CISM COURSES AND LEC
INTERNATIONAL CENTRE

MULTISCALE
OF DAMAGE
FRACTURE PR
COMPOSITE

SpringerWienNewYork

CISM COURSES AND LECTURES

The series presents lecture notes, monographs, edited works and proceedings in the field of Mechanics, Engineering, Computer Science and Applied Mathematics.
Purpose of the series is to make known in the international scientific and technical community results obtained in some of the activities organized by CISM, the International Centre for Mechanical Sciences.

INTERNATIONAL CENTRE FOR MECHANICAL SCIENCES

COURSES AND LECTURES - No. 474

MULTISCALE MODELLING OF DAMAGE AND FRACTURE PROCESSES IN COMPOSITE MATERIALS

EDITED BY

TOMASZ SADOWSKI
LUBLIN UNIVERSITY OF TECHNOLOGY, POLAND

SpringerWienNewYork

The publication of this volume was co-sponsored and co-financed by the UNESCO Venice Office - Regional Bureau for Science in Europe (ROSTE) and its content corresponds to a CISM Advanced Course supported by the same UNESCO Regional Bureau.

This volume contains 204 illustrations

Printed in Italy
SPIN 11569626

In order to make this volume available as economically and as rapidly as possible the authors' typescripts have been reproduced in their original forms. This method unfortunately has its typographical limitations but it is hoped that they in no way distract the reader.

ISBN-10 3-211-29558-5 SpringerWienNewYork
ISBN-13 978-3-211-29558-8 SpringerWienNewYork

PREFACE

Various types of composites are used in engineering practice. The most important are fibrous composites, laminates and materials with a more complicated geometry of reinforcement in the form of short fibres and particles of various properties, shapes and sizes.

The aim of course was to understand the basic principles of damage growth and fracture processes in ceramic, polymer and metal matrix composites. Nowadays, it is widely recognized that important macroscopic properties like the macroscopic stiffness and strength, are governed by processes that occur at one to several scales below the level of observation. Understanding how these processes influence the reduction of stiffness and strength is essential for the analysis of existing and the design of improved composite materials.

The study of how these various length scales can be linked together or taken into account simultaneously is particular attractive for composite materials, since they have a well-defined structure at the micro and meso-levels. Moreover, the microstructural and mesostructural levels are well-defined: the microstructural level can be associated with small particles or fibres, while the individual laminae can be indentified at the mesoscopic level. For this reason, advances in multiscale modelling and analysis made here, pertain directly to classes of materials which either have a range of relevant microstructural scales, such as metals, or do not have a very well-defined microstructure, e.g. cementitious composites.

In particular, the fracture mechanics and optimization techniques for the design of polymer composite laminates against the delamination type of failure was discussed. Computational modelling of laminated composites at different scales: microscopic mesoscopic and macroscopic with application of suitable plate/shell elements for thin composites was presented. The application of fracture and damage mechanics approaches to the description of the complete constitutive behaviour of high performance fibre-reinforced cementitious composites was discussed. With regard to ceramic matrix composites (CMC) the damage and fracture processes was described in three scales. The important problem of damage process of interfaces surrounding particles, grains or fibres in composites was analysed for different properties of the components of composites and in different scales.

The course brought together experts dealing with materials science, mechanics, experimental and computational techniques at the three mentioned scales. I acknowledge the commitment of Professors: H.Altenbach, R. de Borst, P.Ladeveze, B.Karihaloo and Z.Mroz in making the course possible in the nice atmosphere of the Palazzo del Torso in Udine. Lectures delivered by mentioned Professors presenting the latest achievements in the topic of the course and discussions with the course participants significantly enriched the scientific aim of this course. 58 participants PhD students, postdocs, senior researchers and engineers had good opportunity to

listen to interesting lectures and discuss their on going research problems with leading persons in the field of the course.

I thank to the Rectors and staff of CISM for help and co-operation in the organization of the course and printing these lecture notes.

Tomasz Sadowski

CONTENTS

Modelling of anisotropic behavior in fiber and particle reinforced composites

Holm Altenbach

Lehrstuhl Technische Mechanik, Fachbereich Ingenieurwissenschaften,
Martin-Luther-Universität Halle-Wittenberg, D-06099 Halle (Saale), Germany

Abstract Fiber and particle reinforced composites are widely used in aircraft, spacecraft and automotive industries, but also in various branches of the traditional mechanical engineering. They substitute classical materials like steel, aluminium, etc. since their specific stiffness is significant higher. The optimal design of structures made of reinforced composites demands the mathematical description of the constitutive behavior of these materials characterized by anisotropic mechanical properties and inhomogeneities. This contribution is devoted to the phenomenological modelling of fiber and particle reinforced materials.

After a short introduction the modelling principles are briefly discussed. For a realistic material description the anisotropic elasticity is necessary. The generalized HOOKE's law is introduced and the symmetry relations of the stiffness and compliance tensors are discussed. For the analysis of the limit state of composite materials various failure and strength criteria are presented. Finally, a short introduction into modelling of polymer suspensions is given.

1 Introduction

Fiber and particle reinforced composites are used as structural materials in many application fields: aircraft and rocket industries, mechanical and civil engineering, sport goods and automotive industries, etc. The reason for this is a number of advantages in comparison with the traditional structural materials: high specific stiffness properties, small weight, etc. It must be noted that there are also disadvantages: for example, more complex design rules and failure analysis. The application fields, the advantages and disadvantages are discussed, for example by Altenbach et al. (2004); Altenbach & Becker (2003); Ashbee (1994); Chawla (1987); Ehrenstein (1992); Gay (2002); Gibson (1994); Hult & Rammerstorfer (1994); Jones (1975); Kim (1995) and Powell (1994).

The design of structures made of composites is connected with two main problems:

- the material behavior is usually anisotropic and
- the inhomogeneous distribution of all properties must be considered.

In the first case - anisotropic material behavior - one has to apply the anisotropic constitutive equations of continuum mechanics since the anisotropic behavior can be observed in the elastic, viscoelastic, plastic, etc. range. In addition, the classical failure and strength analysis based on the existence of an equivalent stress and a criterion, which allows to compare complex (multiaxial) stress states with some experimental data based on uniaxial tests must be extended. The problem is that in the case of anisotropic material behavior various failure modes are existing and

a unique criterion for all cases cannot be established. The second item - the inhomogeneity of the material behavior - is more complicated. As is known from many practical applications for the general analysis of the stress or strain states one can use the overall properties assuming that the material is quasi-homogeneous and can be described with the help of effective ("smeared") properties. This approach works successfully in the case of structural elements made of composites if only the global mechanical characteristics (for example, the deflections of plates or the eigenfrequencies) are to be computed. In this case the comparison with the experimental data is satisfying. A quite different situation one obtains if the local behavior plays the main role. Now the averaged properties cannot be applied and the heterogeneity of the material must be considered.

Below the anisotropic analysis of composite materials and structures is discussed. The attention is paid to the elastic range and the limit state only. Both situations are mostly assumed in practical applications. In addition, two types of reinforcement are considered: the unidirectional continuous fiber and the short fiber (particle) reinforcements. They are assumed as a satisfying approximation in many practical cases. From the theoretical point of view the analysis of continuous fiber reinforced composites is much simpler - in the case of particle reinforcement the heterogeneity plays an important role.

After this brief introduction the basics of modelling the material behavior and anisotropic elasticity are presented. Some remarks concerning the principles of the global failure analysis are presented. Finally, some models of particle reinforced composites are discussed.

2 Materials behavior modelling

The modelling of the material behavior is a necessary first step for the engineering analysis of any structure. Since the geometry, the loading cases, etc. are often very complex the analysis must be performed computer-aided mostly. For this purpose one needs mathematical expressions describing the material behavior. In this section some problems in material behavior modelling will be discussed. For further reading one can recommend, for example, Altenbach & Skrzypek (1999); Haddad (2000a,b); Hergert et al. (2004); Lemaitre (2001); Lemaitre & Chaboche (1985) and Skrzypek & Ganczarski (2003).

2.1 Continuum mechanics background

The basic equations in *Continuum Mechanics* of deformable bodies can be divided into to groups, see Lai et al. (1993)

- the material independent equations and
- the material dependent equations.

The first group is following from the general balance equations, added by the statement of stresses and geometrical relations. As the main result one gets the equilibrium equations or the equations of motion. Since the material behavior can be reversible or irreversible from the energy and the entropy balance some statements of the physical admissibility of the deformation processes can be made.

The second group of equations allows the description of the individual response of any material on the applied stresses/forces or strains. The so-called constitutive equations (added, may be, by evolution equations) are related to some of the general balances (they describe the theoreti-

cal and the mathematical framework), but the concretion must be performed without any general physical rules. The theoretical framework for the concretion is presented by Haupt (2002); Krawietz (1886) or Palmov (1998).

In addition, the coefficients or parameters of the constitutive and the evolution equations must be identified by tests. There are different possibilities, discussed in Altenbach et al. (1995). Let us assume a macroscopic test, for example, the tension test. In this case one observes the stress-strain curve assuming that the stress and the strain is acting in the same direction. The problem is now how to describe mathematically this curve. At first, it is impossible to find a general analytical function for all stress and strain values. At second, it is clear that such a description is acceptable only for a very specific situation (for example, some parameters like the temperature or the moisture are fixed, the stresses lie in a small range, etc.). So we get from the tension test only a special law of the constitutive behavior.

It must be noted that this approach cannot be used for the modelling and simulation of the three-dimensional behavior, especially in the case of anisotropy since one needs experimental benefit from an infinite number of tests. In such a situation one has to perform a finite number of tests, that means one has to realize, for example, the tension test, the compression test, the shear test (torsion of a thin-walled cylindrical specimen), the two-dimensional tension test (biaxial tension test) and the hydrostatic compression test. In all these cases as a result one obtains stress-strain curves, but the curves can differ significantly. In addition, since the choice of tests is not unique the results depend on the kind of tests that are performed. Note that tests realizing homogeneous stress and strain states are preferred.

Limiting our further discussions to pure mechanical performances the mathematical description of the material behavior can be simplified since for the formulation of the constitutive and evolution equations one needs only a few variables. Let us introduce these variables.

At first let us focus our attention on the strains. In Fig. 1 typical strains are shown. One can

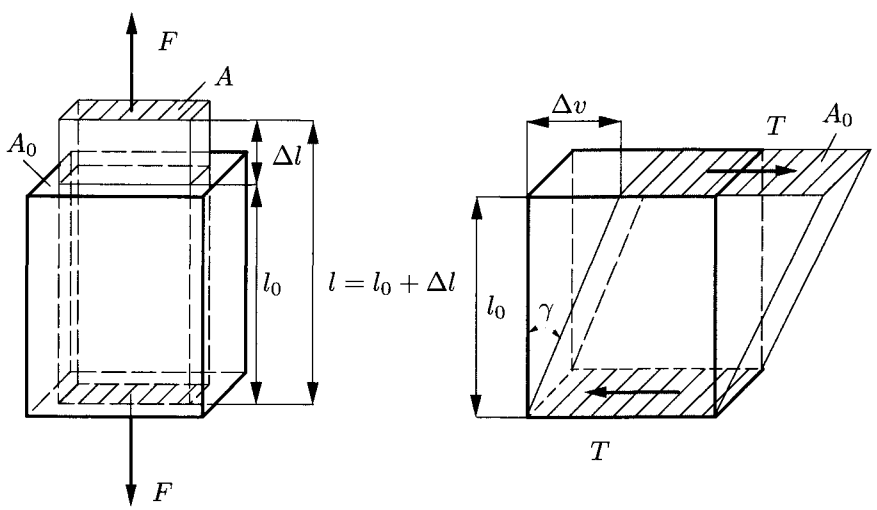

Figure 1. Possible strains: extensional (left) and shear (right) strains

consider that there are two types of strains:

- Extensional strains ε: The body changes only its volume but not its shape.
- Shear strains γ: The body changes only its shape but not its volume.

Concerning Fig. 1 in the one-dimensional case one can define the stresses and strains as follows. Assuming a uniform distribution of the forces F and T on the cross-section we introduce

$$\begin{aligned}
\sigma &= \frac{F}{A_0} && && \text{normal stress} \quad \sigma, \\
\varepsilon &= \frac{l - l_0}{l_0} &= \frac{\triangle l}{l_0} && \text{extensional strain} \quad \varepsilon, \\
\tau &= \frac{T}{A_0} && && \text{shear stress} \quad \tau, \\
\gamma &\approx \tan\gamma &= \frac{\triangle v}{l_0} && \text{shear strain} \quad \gamma
\end{aligned}$$

In the general case of the classical material behavior the stress state is characterized by the stress tensor $\boldsymbol{\sigma}$. This is from the mathematical point of view a second rank tensor and assuming a orthonormal co-ordinate system (Cartesian co-ordinates x_i with the unit basic vectors $\boldsymbol{e}_i$ which have to fulfil the following conditions: $|\boldsymbol{e}_i| = 1, \boldsymbol{e}_i \cdot \boldsymbol{e}_j = \delta_{ij}$, δ_{ij} is the KRONECKER symbol, $i, j = 1, 2, 3$). The following representation is valid

$$\boldsymbol{\sigma} = \sigma_{ij} \boldsymbol{e}_i \boldsymbol{e}_j \tag{2.1}$$

Using $\boldsymbol{\sigma}$ we are applying the absolute or invariant notation, σ_{ij} are the coordinates in the index notation. The invariant notation used here is presented, for example, by Lurie (1990).

Let us discuss the meaning of the components of the stress tensor. The normal stresses are related to $i = j$ and the shear stresses to $i \neq j$. Note that $\sigma_{ij} = \sigma_{ji}$ and for this case the stresses are shown in Fig. 2 The three-dimensional state of strains is characterized by the strain tensor

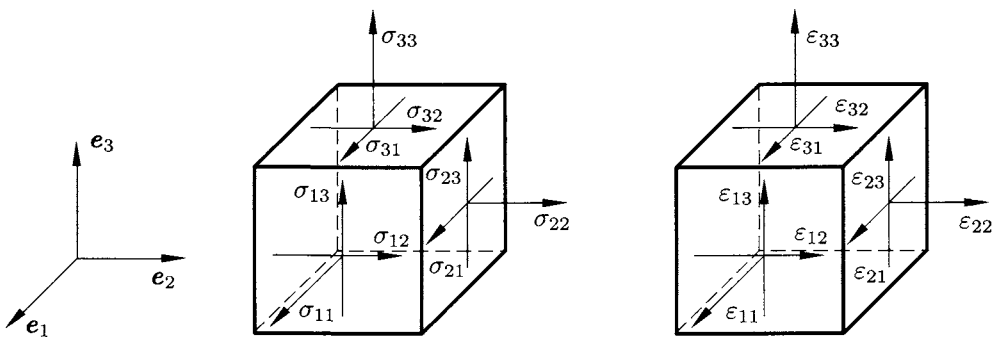

Figure 2. Stress and strain tensor components for Cartesian coordinates

ε_{ij} with the extensional strains in the case $i = j$ and the shear strains for $i \neq j$. Note that ε_{ij} with $i \neq j$ are the tensor shear coordinates, $2\varepsilon_{ij} = \gamma_{ij}, i \neq j$ the engineering shear strains. The coordinates of the strain tensor are also shown in Fig. 2.

Any second rank tensor can also be presented as a $[3 \times 3]$ matrix. For the stresses we obtain

$$\begin{bmatrix} \sigma_{11} & \sigma_{12} & \sigma_{13} \\ \sigma_{21} & \sigma_{22} & \sigma_{23} \\ \sigma_{31} & \sigma_{32} & \sigma_{33} \end{bmatrix} = \begin{bmatrix} \sigma_1 & \tau_{12} & \tau_{13} \\ \tau_{21} & \sigma_2 & \tau_{23} \\ \tau_{31} & \tau_{32} & \sigma_3 \end{bmatrix} \tag{2.2}$$

Since the symmetry of the stress tensor is assumed ($\boldsymbol{\sigma} = \boldsymbol{\sigma}^{\mathrm{T}}$ or $\sigma_{ij} = \sigma_{ji}$) the representation can be simplified as

$$\begin{bmatrix} \sigma_{11} & \sigma_{12} & \sigma_{13} \\ \sigma_{12} & \sigma_{22} & \sigma_{23} \\ \sigma_{13} & \sigma_{23} & \sigma_{33} \end{bmatrix} = \begin{bmatrix} \sigma_1 & \tau_{12} & \tau_{13} \\ \tau_{12} & \sigma_2 & \tau_{23} \\ \tau_{13} & \tau_{23} & \sigma_3 \end{bmatrix} \tag{2.3}$$

In addition, the following vector representation is possible

$$\boldsymbol{\sigma} = [\ \sigma_1 \quad \sigma_2 \quad \sigma_3 \quad \sigma_4 \quad \sigma_5 \quad \sigma_6\ ]^{\mathrm{T}} \tag{2.4}$$

Between the components of the stress tensor (2.1) or the stress matrix (2.3) and the stress vector (2.4) the following relations exist

$$\sigma_{11} = \sigma_1, \quad \sigma_{22} = \sigma_2, \quad \sigma_{33} = \sigma_3, \quad \sigma_{23} = \sigma_4, \quad \sigma_{13} = \sigma_5, \quad \sigma_{12} = \sigma_6$$

Considering small deformations the following strain tensor can be introduced

$$\boldsymbol{\varepsilon} = [\boldsymbol{\nabla u}]^{\mathrm{sym}} = \frac{1}{2}[\boldsymbol{\nabla u} + (\boldsymbol{\nabla u})^{\mathrm{T}}] \tag{2.5}$$

Here $\boldsymbol{u}$ denotes the displacement vector and $\boldsymbol{\nabla}$ is the Nabla operator. Assuming again Cartesian coordinates one can write

$$\varepsilon_{ij} = \frac{1}{2}\left(\frac{\partial u_j}{\partial x_i} + \frac{\partial u_i}{\partial x_j}\right) \equiv \frac{1}{2}(u_{j,i} + u_{i,j}) \tag{2.6}$$

The strain tensor written down as a matrix

$$\boldsymbol{\varepsilon} = \begin{bmatrix} \varepsilon_{11} & 2\varepsilon_{12} & 2\varepsilon_{13} \\ 2\varepsilon_{12} & \varepsilon_{22} & 2\varepsilon_{23} \\ 2\varepsilon_{13} & 2\varepsilon_{23} & \varepsilon_{33} \end{bmatrix} = \begin{bmatrix} \varepsilon_{11} & \gamma_{12} & \gamma_{13} \\ \gamma_{12} & \varepsilon_{22} & \gamma_{23} \\ \gamma_{13} & \gamma_{23} & \varepsilon_{33} \end{bmatrix} \tag{2.7}$$

or as a vector

$$\boldsymbol{\varepsilon} = [\ \varepsilon_1 \quad \varepsilon_2 \quad \varepsilon_3 \quad 2\varepsilon_4 = \gamma_4 \quad 2\varepsilon_5 = \gamma_5 \quad 2\varepsilon_6 = \gamma_6\ ]^{\mathrm{T}} \tag{2.8}$$

The components of the strain tensor are shown in Fig. 2.

It can be established that the symmetry of the stress tensor results in a symmetry of the strain tensor. This is not a general statement in *Continuum Mechanics*, but writing down the elastic energy, for example, one can see that only the symmetric part of the strain tensor plays a role in further discussions if the stress tensor is symmetrically. From the symmetry condition of the strain tensor follows that the strains can be represented by (2.8).

Remark: The starting point of discussion of the anisotropic behavior is connected with three principal assumptions:

- classical continuum assumption (no polar continua),

- small strains assumption, and
- elastic behavior assumption.

For many composite material applications these assumptions are valid since composites are mostly brittle, that means they behave linear elastically with the exception of the limit state characterized by the failure. From the *Material Science* it is well known that brittleness can be observed at small strains and after the elastic range the fracture starts immediately. The assumption of the stress tensor symmetry is under discussion, but using non-symmetric stress tensors the identification of the material properties is more complicated (Nowacki (1985)). So we decided for the main part of this contribution that the assumption of the stress tensor symmetry is valid.

2.2 Elastic behavior

The history of the theory of elasticity is presented in several monographs and textbooks (Todhunter & Pearson (1886), Todhunter & Pearson (1893), Love (1927), Timoshenko (1953), Hetnarski & Ignaczak (2004) among others). In parallel the theory of strength and failure was developed. Some important steps in the development of models for the elastic behavior were

- the establishment of HOOKE's law,
- the introduction of the YOUNG's modulus,
- the stress and strain concepts,
- the theory of linear elasticity,
- the discussion related to the number of material parameters,
- the anisotropic elasticity,
- isotropic failure and strength criteria,
- the anisotropic failure and strength,
- the application of continuous fiber reinforced composites, and
- particle reinforced composites.

It is easy to see that both the theory of elasticity and the failure/strength theories were developed by the inductive way (the generalization was made step by step). Only during the last fifty years the deductive theory was formulated by Truesdell & Noll (1992) and others.

Let us now discuss the elasticity condition more in detail. The starting point is the introduction of two second rank tensors (the stress tensor $\boldsymbol{\sigma}$ and the strain tensor $\boldsymbol{\varepsilon}$) which are symmetrically and characterize the stress and the strain state. Now the question is how to formulate a constitutive equation for the elastic behavior.

The simplest case is the HOOKE's law

$$\sigma = E\varepsilon \tag{2.9}$$

containing only one material parameter. From the mathematical point of view the HOOKE's law is an algebraic linear equation of two scalar variables (the stress σ and the strain ε). The general form of a linear function of two variables is

$$\sigma = a\varepsilon + b$$

The coefficients can be estimated as follows: a is equal to E (the YOUNG's modulus) and b in many applications can be assumed to be 0 otherwise b characterizes the eigenstress. The result

$b = 0$ is identical to the statement that from the stress free state assumption follows no strains and vice versa.

The HOOKE's law is a special constitutive equation connecting the mechanical variables only. So, for example, isothermal conditions must be considered. The basic idea is coming from the original HOOKE's proposal that the loading state and the deformation state are proportional. At present this statement can be formulated for the normal stresses and strains as (2.9). For the shear stresses and shear strains the following relation is valid

$$\tau = G\gamma, \qquad G = \frac{\tau}{\gamma}, \qquad G \quad \text{shear modulus} \tag{2.10}$$

From the mathematical point of view (2.9) is, as was mentioned, a linear function of two variables. By this equation eigenstresses and eigenstrains cannot be described, and the nonlinear behavior cannot be presented. Since the stress and the strain states in the three-dimensional case are presented by the stress tensor and the strain tensor one has to built up a linear function between second rank tensors

$$\boldsymbol{\sigma} = {}^{(4)}\boldsymbol{E} \cdot\cdot\, \boldsymbol{\varepsilon}, \quad \sigma_{ij} = E_{ijkl}\varepsilon_{kl}; k, l = 1, 2, 3 \tag{2.11}$$

The role of the proportionality factor plays the fourth rank HOOKEan tensor ${}^{(4)}\boldsymbol{E}$. Now the main problem is the analysis of the fourth rank tensor ${}^{(4)}\boldsymbol{E} = E_{ijkl}\boldsymbol{e}_i\boldsymbol{e}_j\boldsymbol{e}_k\boldsymbol{e}_l$ which must be related to the material properties of the linear-elastic anisotropic continuum. The experimental identification of the components of this tensor is non-trivial.

Considering the three-dimensional space $\mathbb{R}^3$ the number of the elasticity tensor components E_{ijkl} is $3^4 = 81$ with 3 as the dimension of the space and 4 as the rank of the tensor. With respect to the experimental effort one has to reduce this number. There are three main ideas for the reduction:

- to use general statements of the theory like the statements of symmetry for the stress and for the strain tensor or the statement of the elastic potential,
- to use symmetry considerations for the material behavior like the statement of monoclinic, orthotropic or transversally-isotropic material behavior and
- the statements of approximative stress or strain states (plane stress or plain strain conditions).

Let us focus our attention to the first and the second item. From the first item, see for example Altenbach & Altenbach (1994), $\sigma_{ij} = \sigma_{ji}$ results in $E_{ijkl} = E_{jikl}$ and $\varepsilon_{kl} = \varepsilon_{lk}$ in $E_{ijkl} = E_{ijlk}$. Using both assumptions the number of tensor components is reduced to 36. In addition, further reduction one gets from the existence of the elastic potential W. In this case one can write down

$$W = \frac{1}{2}\boldsymbol{\sigma} \cdot\cdot\, \boldsymbol{\varepsilon} = \frac{1}{2}\boldsymbol{\varepsilon} \cdot\cdot\, {}^{(4)}\boldsymbol{E} \cdot\cdot\, \boldsymbol{\varepsilon}, \quad W = \frac{1}{2}\sigma_{ij}\varepsilon_{ij} = \frac{1}{2}E_{ijkl}\varepsilon_{ij}\varepsilon_{kl} \tag{2.12}$$

Calculating the first and the second derivatives with respect to the strain tensor

$$\frac{\partial W}{\partial \boldsymbol{\varepsilon}} = \boldsymbol{\sigma} = {}^{(4)}\boldsymbol{E} \cdot\cdot\, \boldsymbol{\varepsilon}, \quad \frac{\partial^2 W}{\partial \boldsymbol{\varepsilon}^2} = {}^{(4)}\boldsymbol{E}$$

or

$$\frac{\partial W}{\partial \varepsilon_{ij}} = \sigma_{ij} = E_{ijkl}\varepsilon_{kl}, \quad \frac{\partial^2 W}{\partial \varepsilon_{ij}\partial \varepsilon_{kl}} = E_{ijkl}$$

one can conclude that $E_{ijkl} = E_{klij}$. So finally, from the statements of the first item we obtain a reduction of the number of independent components E_{ijkl} from 81 to 21.

The discussed possibility of reducing the number of components allows to use a second representation of the elastic behavior. Considering the six stresses and the six strains as vectors (2.4) and (2.8) a linear functional relationship between these vectors can be formulated with the help of a $[6 \times 6]$ matrix (instead of the fourth rank elasticity tensor)

$$[\sigma_i] = [E_{ij}][\varepsilon_j]; \quad i,j = 1,2,\ldots,6$$

with the elasticity matrix E_{ij}. Assuming again the existence of an elastic potential one gets further reduction of the number of independent coordinates of the elasticity tensor. The elastic strain energy can be expressed by the strain energy density function

$$W(\varepsilon_i) = \frac{1}{2}\sigma_i\varepsilon_i = \frac{1}{2}E_{ij}\varepsilon_j\varepsilon_i$$

Let us calculate once more the first and the second derivatives of this function with respect to the strain vector

$$\frac{\partial W}{\partial \varepsilon_i} = \sigma_i, \quad \frac{\partial^2 W}{\partial \varepsilon_i \partial \varepsilon_j} = E_{ij}, \quad \frac{\partial^2 W}{\partial \varepsilon_j \partial \varepsilon_i} = E_{ji}, \quad \frac{\partial^2 W}{\partial \varepsilon_i \partial \varepsilon_j} = \frac{\partial^2 W}{\partial \varepsilon_j \partial \varepsilon_i}$$

From the last equation one can make the conclusion that the elasticity matrix must be symmetrically

$$E_{ij} = E_{ji}$$

and the number of the independent material coefficients is only 21.

The generalized relations in the contracted vector-matrix form in the case of the linear anisotropic elastic behavior can be written as follows

$$\begin{bmatrix} \sigma_1 \\ \sigma_2 \\ \sigma_3 \\ \sigma_4 \\ \sigma_5 \\ \sigma_6 \end{bmatrix} = \begin{bmatrix} E_{11} & E_{12} & E_{13} & E_{14} & E_{15} & E_{16} \\ & E_{22} & E_{23} & E_{24} & E_{25} & E_{26} \\ & & E_{33} & E_{34} & E_{35} & E_{36} \\ & & & E_{44} & E_{45} & E_{46} \\ \mathrm{S} & \mathrm{Y} & \mathrm{M} & & E_{55} & E_{56} \\ & & & & & E_{66} \end{bmatrix} \begin{bmatrix} \varepsilon_1 \\ \varepsilon_2 \\ \varepsilon_3 \\ \varepsilon_4 \\ \varepsilon_5 \\ \varepsilon_6 \end{bmatrix} \tag{2.13}$$

Let us summarize the basic formulae for transformation of the stress, the strain and the elasticity tensors in the relevant vectors or matrices. In Table 1 the transformation rules for the stress and the strain tensor coordinates are shown. Table 2 summarizes the transformation rules for the elasticity tensor.

In some cases it is more convenient to use the elasticity equation in the inverse form

$$\begin{bmatrix} \varepsilon_1 \\ \varepsilon_2 \\ \varepsilon_3 \\ \varepsilon_4 \\ \varepsilon_5 \\ \varepsilon_6 \end{bmatrix} = \begin{bmatrix} S_{11} & S_{12} & S_{13} & S_{14} & S_{15} & S_{16} \\ & S_{22} & S_{23} & S_{24} & S_{25} & S_{26} \\ & & S_{33} & S_{34} & S_{35} & S_{36} \\ & & & S_{44} & S_{45} & S_{46} \\ \mathrm{S} & \mathrm{Y} & \mathrm{M} & & S_{55} & S_{56} \\ & & & & & S_{66} \end{bmatrix} \begin{bmatrix} \sigma_1 \\ \sigma_2 \\ \sigma_3 \\ \sigma_4 \\ \sigma_5 \\ \sigma_6 \end{bmatrix} \tag{2.14}$$

Table 1. Transformation of the tensor coordinates σ_{ij} and ε_{ij} to the vector coordinates σ_p and ε_p

σ_{ij}	σ_p	ε_{ij}	ε_p
σ_{11}	σ_1	ε_{11}	ε_1
σ_{22}	σ_2	ε_{22}	ε_2
σ_{33}	σ_3	ε_{33}	ε_3
$\sigma_{23} = \tau_{23}$	σ_4	$2\varepsilon_{23} = \gamma_{23}$	ε_4
$\sigma_{31} = \tau_{31}$	σ_5	$2\varepsilon_{31} = \gamma_{31}$	ε_5
$\sigma_{12} = \tau_{12}$	σ_6	$2\varepsilon_{12} = \gamma_{12}$	ε_6

Table 2. Transformation of the tensor coordinates E_{ijkl} to the matrix coordinates E_{pq}

E_{ijkl}				E_{pq}			
$ij:$	11,	22,	33	$p:$	1,	2,	3
	23,	31,	12		4,	5,	6
$kl:$	11,	22,	33	$q:$	1,	2,	3
	23,	31,	12		4,	5,	6

It is easy to show that

$$[E_{ij}][S_{jk}] = [\delta_{ik}] = \begin{cases} 1 & i = k \\ 0 & i \neq k \end{cases} \qquad i, j, k = 1, \ldots, 6$$

and

$$\boldsymbol{\sigma} = \boldsymbol{E\varepsilon}, \sigma_i = E_{ij}\varepsilon_j, \quad \boldsymbol{\varepsilon} = \boldsymbol{S\sigma}, \varepsilon_i = S_{ij}\sigma_j; \quad i, j = 1, \ldots, 6$$

with $\boldsymbol{E} \equiv [E_{ij}]$ as the stiffness matrix and $\boldsymbol{S} \equiv [S_{ij}]$ as the compliance (flexibility) matrix.

2.3 Material science background

Further reduction of the number of independent components is possible if we take into account the material symmetry, see Nye (1992) among others. In dependence of the scale size each material has a special kind of symmetry. For example, metals have a crystalline microstructure. In this case each crystal has an individual orientation and the symmetry of each crystal can differ. In addition, they are oriented arbitrarily. On the macroscopic level the materials are polycrystalline materials with a huge number of crystals. Averaging the properties and the individual orientations over the volume one obtains an isotropic behavior on the macroscopic level in contrast to the anisotropic behavior on the microscopic level.

Another situation follows from technological treatment of materials. For example, anisotropic behavior can be established for initially isotropic materials after rolling processes. In the case of reinforced materials the situation is more complicated. The individual response of the matrix and the reinforcement can be isotropically, but the combination of both results in a macroscopic anisotropic behavior. The analysis of possible reductions of the number of the fourth rank material tensor components which are related to the independent material properties will be shown for special cases of the anisotropic behavior later.

In material science structural materials are classified as follows: metals, ceramics, and polymers. It is difficult to give an exact assessment of the advantages and disadvantages of these three basic material classes, because each category covers whole groups of materials within which the range of properties is often as broad as the differences between the three material classes. But at the simplistic level some obvious characteristic properties can be identified:

- Most metals are of medium to high density. They have good thermal stability and can be made corrosion-resistant by alloying. Metals have useful mechanical characteristics and it

is moderately easy to shape and join. Metals became the preferred engineering material, they posed less problems to the designer than either ceramic or polymer materials.

- Ceramic materials have great thermal stability and are resistant to corrosion, abrasion, etc. They are very rigid but mostly brittle and can only be shaped with difficulty.
- Polymer materials (plastics) are of low density, have good chemical resistance but lack thermal stability. They have poor mechanical properties, but are easily fabricated and joined. Their resistance to environmental degradation, e.g. the photomechanical effects of sunlight, is moderate.

The main problem in modelling the material behavior is the necessity to describe the similar behavior (for example, the elastic behavior) using similar equations. This is the reason for the introduction of some basic terms.

A material is called *homogeneous* if its properties are the same at every point and therefore independent of the location. Homogeneity is associated with the scale of modelling and the so-called characteristic volume. In this sense the definition can be useful only for the average material behavior on a macroscopic level. On a microscopic level all materials are more or less inhomogeneous but depending on the scale, materials can be described approximately as homogeneous, otherwise as inhomogeneous. A material is inhomogeneous or heterogeneous if its properties depend on location. But in the average sense a material can be regarded as homogeneous, quasi-homogeneous or heterogeneous.

A material is *isotropic* if its properties are independent of the orientation, they do not vary with direction. Otherwise the material is anisotropic. A general anisotropic material has no planes or axes of material symmetry, but some special cases of material symmetries like orthotropy, transverse isotropy, etc., will be discussed later in detail.

Furthermore, a material can depend on several constituents or phases, single phase materials are called *monolithic*. The above three mentioned classes of conventional materials are on the macroscopic level more or less monolithic, homogeneous and isotropic.

3 Composites

3.1 Classification

The group of materials which can be defined as composite materials is extremely large. Its boundaries depend on definition. In the most general definition one can consider a composite as any material that is a combination (composition) of two or more materials (constituents) and have material properties derived from the individual constituents. These properties may have the combined characteristics of the constituents (for example, established by the weighted mixture rules) or they are substantially different. Sometimes the material properties of a composite material may exceed those of the constituents.

This general definition of composites includes natural materials like wood, traditional structural materials like concrete, as well as modern synthetic composites such as fiber or particle reinforced plastics which are now an important group of engineering materials where low weight in combination with high strength and stiffness are required in structural design.

In the more restrictive sense a structural composite consists of an assembly of two materials of different nature. In general, one material is discontinuous and is called the reinforcement, the

other material is mostly less stiff and weaker, but continuously distributed. It is called the matrix. The properties of a composite material depend on

- the properties of the constituents,
- the geometry of the reinforcements,
- their distribution, orientation and concentration usually measured by the volume fraction or fiber volume ratio, and
- the nature and quality of the matrix-reinforcement interface.

In a less restrictive sense, a structural composite can consist of two or more phases on the macroscopic level. The mechanical performance and properties of composite materials are superior to those of their components or constituent materials taken separately. The concentration of the reinforcement phase is a determining parameter of the properties of the new material, their distribution determines the homogeneity or the heterogeneity on the macroscopic scale. The most important aspect of composite materials in which the reinforcement are fibers is the anisotropy caused by the fiber orientation. It is necessary to give special attention to this fundamental characteristic of fiber reinforced composites and the possibility to influence the anisotropy by material design for a desired quality.

The reinforcement constituent can be described as fibrous or particulate. The fibers are continuous or discontinuous. Continuous fibers are arranged usually uni- or bidirectional, but also irregular reinforcements by continuous fibers are possible. The arrangement and the orientation of continuous or short fibers determines the mechanical properties of composites and the behavior ranges between a general anisotropy to a quasi-isotropy. Particulate reinforcements have different shapes. They may be spherical, platelet or of any regular or irregular geometry. Their arrangement may be random or regular with preferred orientations. In the majority of practical applications particulate reinforced composites are considered to be randomly oriented and the mechanical properties are homogeneous and isotropic. The preferred orientation in the case of continuous fiber composites is unidirectional (UD) for each layer or lamina (UD-lamina). Examples of composite materials with different constituents and distributions of the reinforcements are shown in Fig. 3. Various classifications of composites are presented in the literature. One possibility is shown in Fig. 4.

Composite materials can also be classified by the nature of their constituents. According to the nature of the matrix material we classify organic, mineral or metallic matrix composites.

- Organic matrix composites are polymer resins or thermoplastics with fillers. The fibers can be mineral (glass, etc.), organic (Kevlar, etc.) or metallic (aluminium, etc.).
- Mineral matrix composites are ceramics with metallic fibers or with metallic or mineral particles.
- Metallic matrix composites are metals with mineral or metallic fibers.

The use of composites is connected with several functional requirements of fibers and matrices:

- fibers should have a high modulus of elasticity and a high ultimate strength,
- fibers should be stable and retain their strength during handling and fabrication,
- the variation of the mechanical characteristics of the individual fibers should be low, their diameters uniform and their arrangement in the matrix regular,
- matrices have to interface the fibers and protect their surfaces from damage,
- matrices have to transfer stress to the fibers by adhesion and/or friction, and
- matrices have to be chemically compatible with fibers over the whole working period.

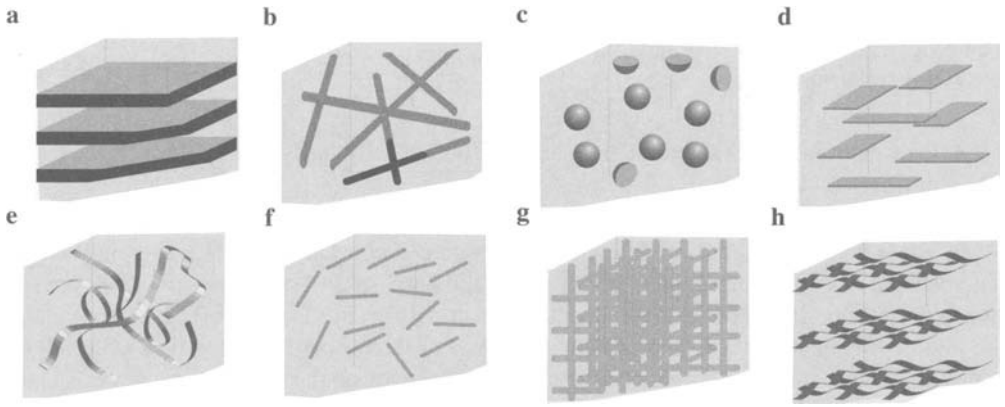

Figure 3. Classification of laminates. **a** Laminate with uni- or bidirectional layers, **b** irregular reinforcement with long fibers, **c** reinforcement with particles, **d** reinforcement with plate strapped particles, **e** random arrangement of continuous fibers, **f** irregular reinforcement with short fibers, **g** spatial reinforcement, **h** reinforcement with surface tissues as mats, woven fabrics, etc.

At present the main topics of composite material research and technology are

- investigation of all characteristics of the constituents and the composite material,
- material design and optimization for the given working conditions,
- development of analytical modelling and solution methods for determining material and structural behavior,

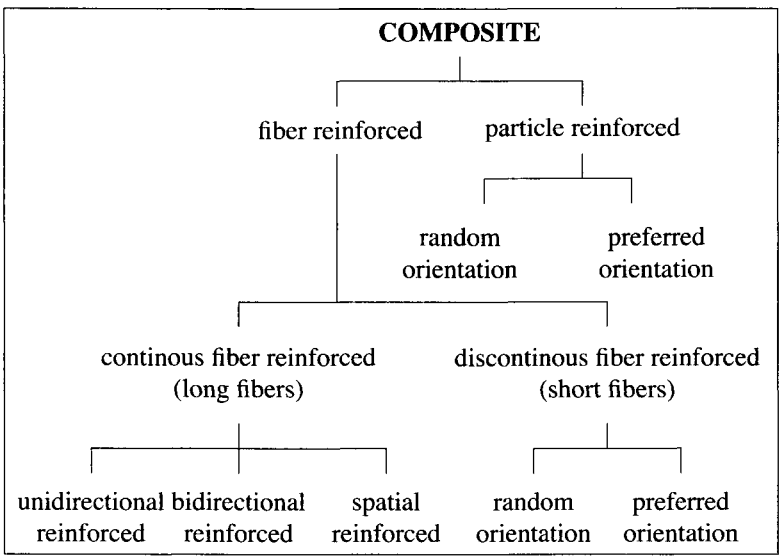

Figure 4. Classification of composites after Agarwal & Broutman (1990)

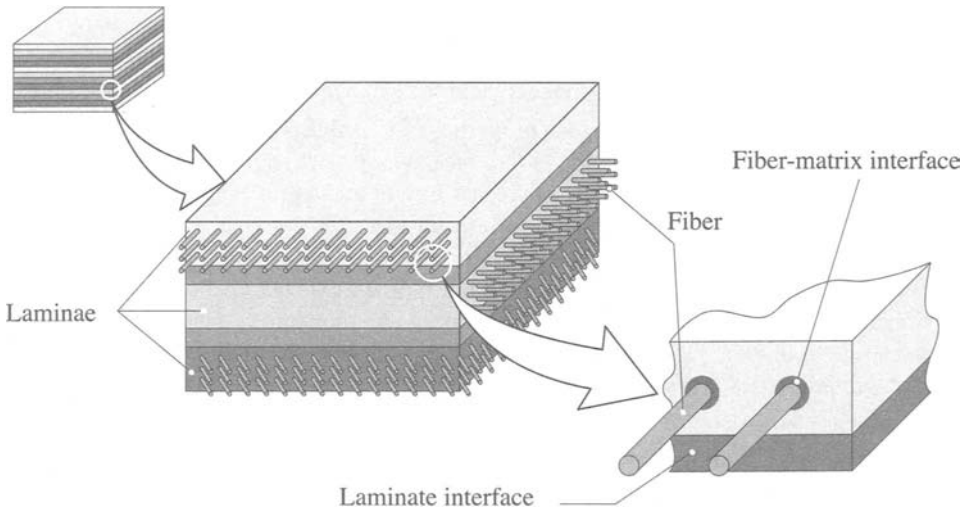

Figure 5. Hierarchical modelling of laminates

- experimental methods for material properties, stress and deformation states, failure, etc. characterization,
- modelling and analysis of creep and damage behavior of composites and their life prediction,
- development of new and efficient fabrication and recycling procedures.

The most significant mainspring in the composite research and application was weight saving in comparison to structures of conventional materials such as steel, alloys, etc. However, to have only material density, stiffness and strength in mind when thinking of composites is a very narrow view of the possibilities of such materials like fiber-reinforced plastics because they often may score over conventional materials like metals not only owing to their mechanical properties. Fiber reinforced plastics are extremely corrosion-resistant and have interesting electromagnetic properties. In consequence they are used for chemical plants and for structures which require non-magnetic materials. Further carbon fiber reinforced epoxy is used in medical applications because it is transparent to X-rays.

3.2 Modelling

Composite materials consist of two or more constituents and the modelling, analysis and design of structures built up of composites are different from conventional materials such as steel. There are three levels of modelling (Fig. 5):

- At the *micro-mechanical level* the average properties of a single reinforced layer have to be determined from the individual properties of the constituents, the fibers and the matrix. The average characteristics include the elastic moduli, the thermal and moisture expansion coefficients, etc. The micro-mechanics of a lamina does not consider the internal structure of the constituent elements, but the heterogeneity of the ply is regarded. The

micro-mechanics is based on some simplifying approximations. These concern the fiber geometry and packing arrangement, so that the constituent characteristics together with the volume fractions of the constituents yield the average characteristics of the lamina.

- The calculated values of the average properties of a lamina provide the basis to predict the macrostructural properties. At the *macro-mechanical level*, only the averaged properties of a lamina are considered and the microstructure of the lamina is ignored. The properties along and perpendicular to the fiber direction, these are the principal directions of a lamina, are recognized and the so-called on-axis stress-strain relations for a unidirectional lamina can be developed. Loads may be applied not only on-axis but also off-axis and the relationships for stiffness and flexibility, for thermal and moisture expansion coefficients and the strength of an angle ply can be determined. Failure theories of a lamina are based on strength properties. This topic is called the macro-mechanics of a single layer or a lamina.
- A laminate is a stack of laminae. Each layer of fiber reinforcement can have different orientations and in principle each layer can be made of different materials. Knowing the macro-mechanics of a lamina, one develops the macro-mechanics of the laminate. Average stiffness, flexibility, strength, etc. can be determined for the whole laminate. The structure and orientation of the laminae in prescribed sequences to a laminate lead to significant advantages of composite materials when compared to a conventional monolithic material. In general, the mechanical response of laminates is anisotropic.

When the micro- and macro-mechanical analysis for laminae and laminates are carried out, the global behavior of laminated composite materials is known. The last step is the modelling on the structure level where the global behavior of a structure made of a composite material is to analyze.

By adapting the classical tools of structural analysis on anisotropic elastic structure elements the analysis of simple structures like beams or plates may be achieved by analytical methods, but for more general boundary conditions and/or loading and for complex structures, numerical methods are used. For laminated composites, assumptions are necessary to enable the mathematical modelling. These are an elastic behavior of fibers and matrices, a perfect bonding between fibers and matrices, a regular fiber arrangement in regular or repeating arrays, etc. Summarizing the different size scales of mechanical modelling of structure elements composed of fiber reinforced composites it must be noted that, independent of the different possibilities to formulate beam, plate or shell theories, three modelling levels must be considered:

- The microscopic level, where the average mechanical characteristics of a lamina have to be estimated from the known characteristics of the fibers and the matrix material taking into account the fiber volume fracture and the fiber packing arrangement. The micro-mechanical modelling leads to a correlation between constituent properties and average composite properties. In general, simple mixture rules are used in engineering applications. If possible, the average material characteristics of a lamina should be verified experimentally. On the micro-mechanical level a lamina is considered as a quasi-homogeneous orthotropic material.
- The macroscopic level, where the effective (average) material characteristics of a laminate have to be estimated from the average characteristics of a set of laminae taking into account their stacking sequence. The macro-mechanical modelling leads to a correlation between the known averaged laminae properties and effective laminate properties. On the macro-

mechanical level a laminate is considered generally as an equivalent single layer element with a quasi-homogeneous, anisotropic material behavior.

- The structural level, where the mechanical response of structural members like beams, plates, shells etc. have to be analyzed taking into account possibilities to formulate structural theories of different order.

4 Elastic composites as anisotropic solids

4.1 Basic assumptions

The classical theory of elastic solids is based on the following assumptions:

- The material behavior can be approximated as ideal linear elastic.
- All elastic properties are the same in tension and compression.
- All strains are small.
- The stress and the strain tensors are symmetric.
- The material behavior is homogeneous and isotropic.

All these assumptions are fulfilled in a satisfactory manner in the case of modelling and analysis of structure elements made of conventional monolithic materials like steel. The structural analysis of elements composed of composite materials is more complicated and based on the theory of anisotropic elasticity (see, for example, Ambarcumyan (1991), Berthelot (1999), Decolon (2002), Lekhnitskij (1981), Mālmeisters et al. (1977) and Rabinovich (1970)) since the elastic properties of composite materials now depend on the direction. In addition, the material is not homogeneous at all. The material is piecewise homogeneous and only after averaging it can be regarded as quasi-homogeneous.

For materials with isotropic and anisotropic behavior the governing equations are mostly the same. The equilibrium equations, the kinematic equations and the compatibility equations are identical because they do not depend on the behavior of the material. Let us summarize the material independent equations (see Altenbach & Altenbach (1994), Hahn (1985), Lai et al. (1993) among others). At first, we have the dynamic equilibrium equations

$$\boldsymbol{\nabla} \cdot \boldsymbol{\sigma} + \boldsymbol{p} = \rho \ddot{\boldsymbol{u}}, \quad \sigma_{ij,i} + p_j = \rho \ddot{u}_j \tag{4.1}$$

with ρ as the density and $\boldsymbol{p}$ being the body force vector. In the index notation the spatial differentiation is written as $(\ldots)_{,i}$ (differentiation with respect to the coordinate x_i). At second, in the case of small strains the Eqs. (2.5) or (2.6) are valid. And last but not least the compatibility can be expressed as

$$\boldsymbol{\nabla} \times \boldsymbol{\varepsilon} \times \boldsymbol{\nabla} = \boldsymbol{0}, \quad \varepsilon_{ij,kl} + \varepsilon_{kl,ij} - \varepsilon_{il,jk} - \varepsilon_{jk,il} = 0 \tag{4.2}$$

All these equations are independent of the elastic properties of the material. Only the constitutive equations differ significantly for an isotropic and an anisotropic body.

Let us now consider that the material behavior can be anisotropically. Below the anisotropic elasticity in the most general form of the linear constitutive equations will be assumed. In addition, special cases of elastic symmetries are deduced (for example, the classical HOOKE's law for an isotropic body and the plane stress and plane strain cases). The final constitutive equations are applied in the analysis of the laminate stiffness and compliances.

4.2 Elastic constitutive equations, transformation rules

The composite material engineering modelling neglects the real on the microscopic scale discontinuous structure and considers on a macroscopic or phenomenological scale the material models as continuous (quasi-homogeneous). Fiber and particle reinforced composites are highly heterogeneous materials as the consequence of the two constituents (fibers/particles and matrix). It must be defined a representative volume element of the material on a characteristic scale at which the properties of the material can be averaged and such a procedure results in a good approximation. If such an averaging is possible the composite material is macroscopic homogeneous, the designing structural elements composed of composite materials can be solved in an analogous manner as for conventional materials with the help of the average material properties (effective properties concept).

Let us present the main approaches in averaging material properties. We assume that a prismatic bar is composed of different materials as shown in Fig. 6. The starting point of the

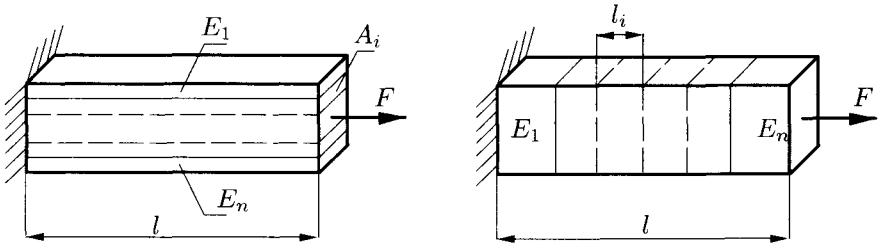

Figure 6. Prismatic bar composed of different materials

analysis of the mechanical behavior of such a bar is the stress definition $\sigma = F/A$ and the one-dimensional elastic law $\sigma = E\varepsilon$. From this follow $\sigma A = F = EA\varepsilon$ and finally $\varepsilon = (EA)^{-1}F$. EA is the tensile stiffness and $(EA)^{-1}$ the tensile flexibility or compliance. Now we assume that the different materials of the prismatic bar are arranged in parallel or series.

In the first case the arrangement is in parallel (VOIGT's model) that means

$$F = \sum_{i=1}^{n} F_i, \quad A = \sum_{i=1}^{n} A_i, \quad \varepsilon = \varepsilon_i$$

The F_i are the loading forces on A_i and the strains ε_i are equal for the total cross-section

$$F = EA\varepsilon \Rightarrow F_i = E_i A_i \varepsilon, \qquad \sum_{i=1}^{n} F_i = F = \sum_{i=1}^{n} E_i A_i \varepsilon$$

By coupling the equations for the stiffness $E_i A_i$ one observes the effective stiffness

$$EA = \sum_{i=1}^{n} E_i A_i, \qquad (EA)^{-1} = \frac{1}{\sum_{i=1}^{n} E_i A_i}$$

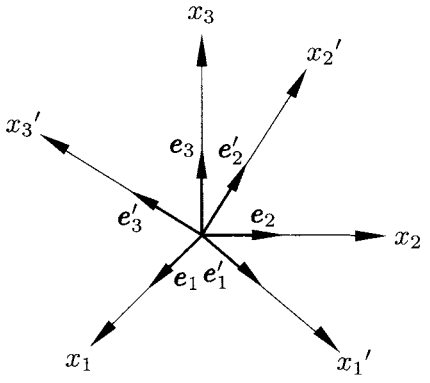

Figure 7. Rotation of the coordinate system. Reference system: e_1, e_2, e_3, rotated system: e_1', e_2', e_3'

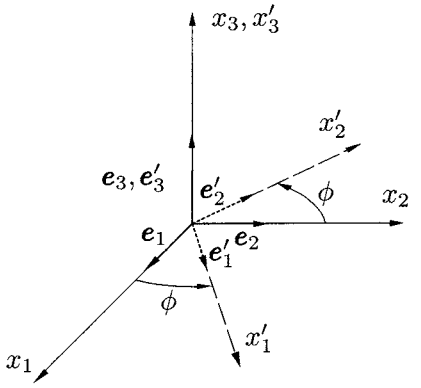

Figure 8. Rotation of the coordinate system around the direction e_3

The second case is the arrangement in series (REUSS' model). With $\triangle l = \sum_{i=1}^{n} \triangle l_i$ and $F = F_i$ one gets

$$\triangle l = l\varepsilon = l(EA)^{-1}F, \quad \triangle l_i = l_i\varepsilon_i = l_i(E_iA_i)^{-1}F$$

and

$$\sum_{i=1}^{n} \triangle l_i = \left[\sum_{i=1}^{n} l_i(E_iA_i)^{-1}\right] F$$

By coupling the equations for the stiffness E_iA_i one observes the effective stiffness as

$$EA = \frac{l}{\sum_{i=1}^{n} l_i(E_iA_i)^{-1}}, \quad (EA)^{-1} = \frac{\sum_{i=1}^{n} l_i(E_iA_i)^{-1}}{l}$$

The averaging in the VOIGT's or REUSS' sense can be applied as a first approximation for the properties of unidirectional reinforced layers. This is demonstrated, for example, by Altenbach et al. (2004). But it is well-known that the agreement with experimental data is partly not satisfying, see Hult & Rammerstorfer (1994) and Mālmeisters et al. (1977). So there are many proposals for improvements of the effective properties.

4.3 Transformation rules

Let us consider the rotation of the coordinate system as shown in Fig. 7. In this case the following transformation rules

$$e_i' = R_{ij}e_j, \quad e_i = R_{ji}e_j', \quad R_{ij} \equiv \cos(e_i', e_j), \quad R_{ji} \equiv \cos(e_i, e_j')$$

and

$$\boldsymbol{e}' = \boldsymbol{R}\boldsymbol{e}, \quad \boldsymbol{e} = \boldsymbol{R}^{-1}\boldsymbol{e}' = \boldsymbol{R}^T\boldsymbol{e}'$$

are valid. $\boldsymbol{R}$ is the transformation or rotation matrix. $\boldsymbol{R}$ is symmetric and unitary (Det $\boldsymbol{R} = |R_{ij}| = 1, \boldsymbol{R}^{-1} = \boldsymbol{R}^T$).

Considering the special case of rotation ϕ around the direction $\boldsymbol{e}_3$ (Fig. 8) the transformation matrix takes the form

$$\left[\overset{3}{R}_{ij}\right] = \begin{bmatrix} c & s & 0 \\ -s & c & 0 \\ 0 & 0 & 1 \end{bmatrix}, \quad \left[\overset{3}{R}_{ij}\right]^{-1} = \left[\overset{3}{R}_{ij}\right]^T = \begin{bmatrix} c & -s & 0 \\ s & c & 0 \\ 0 & 0 & 1 \end{bmatrix},$$

Now the transformation rules are

$$\begin{bmatrix} \boldsymbol{e}_1' \\ \boldsymbol{e}_2' \\ \boldsymbol{e}_3' \end{bmatrix} = \begin{bmatrix} c & s & 0 \\ -s & c & 0 \\ 0 & 0 & 1 \end{bmatrix} \begin{bmatrix} \boldsymbol{e}_1 \\ \boldsymbol{e}_2 \\ \boldsymbol{e}_3 \end{bmatrix}, \begin{bmatrix} \boldsymbol{e}_1 \\ \boldsymbol{e}_2 \\ \boldsymbol{e}_3 \end{bmatrix} = \begin{bmatrix} c & -s & 0 \\ s & c & 0 \\ 0 & 0 & 1 \end{bmatrix} \begin{bmatrix} \boldsymbol{e}_1' \\ \boldsymbol{e}_2' \\ \boldsymbol{e}_3' \end{bmatrix}$$

with $c = \cos\phi, s = \sin\phi$.

After the introduction of the transformation rules for the coordinate axes one has to discuss the transformation rules for the tensors. Let us start with the second-rank tensors. For the stress tensor one gets

$$\sigma_{ij}' = R_{ik}R_{jl}\sigma_{kl}, \quad \sigma_{ij} = R_{ki}R_{lj}\sigma_{kl}' \tag{4.3}$$

The transformation rules for the contracted notation result in

$$\sigma_p' = T_{pq}^{\sigma}\sigma_q, \quad \sigma_p = \left(T_{pq}^{\sigma}\right)^{-1}\sigma_q', \quad p,q = 1,\ldots,6 \tag{4.4}$$

The transformation matrices T_{pq}^{σ} and $(T_{pq}^{\sigma})^{-1}$ follow by comparing (4.3) and (4.4). By analogy one gets for the strain tensor (contracted notation)

$$\varepsilon_p' = T_{pq}^{\varepsilon}\varepsilon_q, \quad \varepsilon_p = \left(T_{pq}^{\varepsilon}\right)^{-1}\varepsilon_q', \quad p,q = 1,\ldots,6$$

Summarizing all derivations the following equations can be established

$$\boldsymbol{\sigma}' = \boldsymbol{T}^{\sigma}\boldsymbol{\sigma}, \quad \boldsymbol{\varepsilon}' = \boldsymbol{T}^{\varepsilon}\boldsymbol{\varepsilon}, \quad \boldsymbol{\sigma} = (\boldsymbol{T}^{\sigma})^{-1}\boldsymbol{\sigma}', \quad \boldsymbol{\varepsilon} = (\boldsymbol{T}^{\varepsilon})^{-1}\boldsymbol{\varepsilon}' \tag{4.5}$$

Considering these equations the transformation relations for the elasticity matrix can be deduced. The starting point is the HOOKE's law

$$\boldsymbol{\sigma} = \boldsymbol{E}\boldsymbol{\varepsilon}, \quad \boldsymbol{\sigma}' = \boldsymbol{E}'\boldsymbol{\varepsilon}'$$

With Eqs (4.5) one can write down

$$\begin{aligned} &(\boldsymbol{T}^{\sigma})^{-1}\boldsymbol{\sigma}' = \boldsymbol{\sigma} = \boldsymbol{E}\boldsymbol{\varepsilon} = \boldsymbol{E}(\boldsymbol{T}^{\varepsilon})^{-1}\boldsymbol{\varepsilon}' \quad &\Rightarrow \quad &\boldsymbol{\sigma}' = \boldsymbol{T}^{\sigma}\boldsymbol{E}(\boldsymbol{T}^{\varepsilon})^{-1}\boldsymbol{\varepsilon}' = \boldsymbol{E}'\boldsymbol{\varepsilon}', \\ &\boldsymbol{T}^{\sigma}\boldsymbol{\sigma} = \boldsymbol{\sigma}' = \boldsymbol{E}'\boldsymbol{\varepsilon}' = \boldsymbol{E}'\boldsymbol{T}^{\varepsilon}\boldsymbol{\varepsilon} \quad &\Rightarrow \quad &\boldsymbol{\sigma} = (\boldsymbol{T}^{\sigma})^{-1}\boldsymbol{E}'\boldsymbol{T}^{\varepsilon}\boldsymbol{\varepsilon} = \boldsymbol{E}\boldsymbol{\varepsilon}, \end{aligned}$$

and the transformation relations for the stiffness matrix are

$$\boldsymbol{E}' = \boldsymbol{T}^{\sigma}\boldsymbol{E}(\boldsymbol{T}^{\sigma})^T, \quad \boldsymbol{E} = (\boldsymbol{T}^{\varepsilon})^T\boldsymbol{E}'\boldsymbol{T}^{\varepsilon}$$

or in index notation

$$E'_{ij} = T^{\sigma}_{ik} T^{\sigma}_{jl} E_{kl}, \quad E_{ij} = T^{\varepsilon}_{ik} T^{\varepsilon}_{jl} E'_{kl}$$

Analogically the transformation relations for the compliance matrix can be formulated. The starting point is now

$$\boldsymbol{\varepsilon} = \boldsymbol{S}\boldsymbol{\sigma}, \quad \boldsymbol{\varepsilon}' = \boldsymbol{S}'\boldsymbol{\sigma}'$$

and after some calculations

$$\begin{aligned} (\boldsymbol{T}^{\varepsilon})^{-1}\boldsymbol{\varepsilon}' = \boldsymbol{\varepsilon} = \boldsymbol{S}\boldsymbol{\sigma} = \boldsymbol{S}(\boldsymbol{T}^{\sigma})^{-1}\boldsymbol{\sigma}' \quad &\Rightarrow \quad \boldsymbol{\varepsilon}' = \boldsymbol{T}^{\varepsilon}\boldsymbol{S}(\boldsymbol{T}^{\sigma})^{-1}\boldsymbol{\sigma}' = \boldsymbol{S}'\boldsymbol{\sigma}', \\ \boldsymbol{T}^{\varepsilon}\boldsymbol{\varepsilon} = \boldsymbol{\varepsilon}' = \boldsymbol{S}'\boldsymbol{\sigma}' = \boldsymbol{S}'\boldsymbol{T}^{\sigma}\boldsymbol{\sigma} \quad &\Rightarrow \quad \boldsymbol{\varepsilon} = (\boldsymbol{T}^{\varepsilon})^{-1}\boldsymbol{S}'\boldsymbol{T}^{\sigma}\boldsymbol{\sigma} = \boldsymbol{S}\boldsymbol{\sigma}, \end{aligned}$$

one finally gets

$$\boldsymbol{S}' = \boldsymbol{T}^{\varepsilon}\boldsymbol{S}(\boldsymbol{T}^{\varepsilon})^{T}, \quad \boldsymbol{S} = (\boldsymbol{T}^{\sigma})^{T}\boldsymbol{S}'\boldsymbol{T}^{\sigma},$$

or in index notation

$$S'_{ij} = T^{\varepsilon}_{ik} T^{\varepsilon}_{jl} S_{kl}, \quad S_{ij} = T^{\sigma}_{ik} T^{\sigma}_{jl} S'_{kl}$$

The complete estimation of the transformation rules is presented in Altenbach et al. (1996) and Altenbach et al. (2004).

For the special case of a rotation ϕ around the $\boldsymbol{e}_3$-direction (Fig. 8) the transformation matrices take the form

$$\left[\overset{3}{T}{}^{\sigma}_{pq}\right] = \begin{bmatrix} c^2 & s^2 & 0 & 0 & 0 & 2cs \\ s^2 & c^2 & 0 & 0 & 0 & -2cs \\ 0 & 0 & 1 & 0 & 0 & 0 \\ 0 & 0 & 0 & c & -s & 0 \\ 0 & 0 & 0 & s & c & 0 \\ -cs & cs & 0 & 0 & 0 & c^2 - s^2 \end{bmatrix}, \qquad \left[\overset{3}{T}{}^{\sigma}_{pq}\right]^{-1} = \left[\overset{3}{T}{}^{\varepsilon}_{pq}\right]^{T}$$

$$\left[\overset{3}{T}{}^{\varepsilon}_{pq}\right] = \begin{bmatrix} c^2 & s^2 & 0 & 0 & 0 & cs \\ s^2 & c^2 & 0 & 0 & 0 & -cs \\ 0 & 0 & 1 & 0 & 0 & 0 \\ 0 & 0 & 0 & c & -s & 0 \\ 0 & 0 & 0 & s & c & 0 \\ -2cs & 2cs & 0 & 0 & 0 & c^2 - s^2 \end{bmatrix}, \qquad \left[\overset{3}{T}{}^{\varepsilon}_{pq}\right]^{-1} = \left[\overset{3}{T}{}^{\sigma}_{pq}\right]^{T}$$

4.4 Symmetry Relations of Stiffness and Compliance Matrices

The most general case of the three-dimensional generalized HOOKE's law is connected with the stiffness and the compliance matrices containing 36 non-zero material parameters E_{ij} or S_{ij}, but due to the potential assumption only 21 are independent constants. In many cases the material show symmetries in their behavior. Important material symmetries are

- monoclinic material behavior,
- orthotropic material behavior,
- transversally isotropic material behavior, and
- isotropic material behavior.

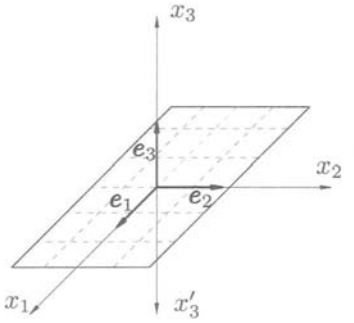

Figure 9. Example of monoclinic material behavior. 20 non-zero elements E_{ij} or S_{ij}, 13 independent elements

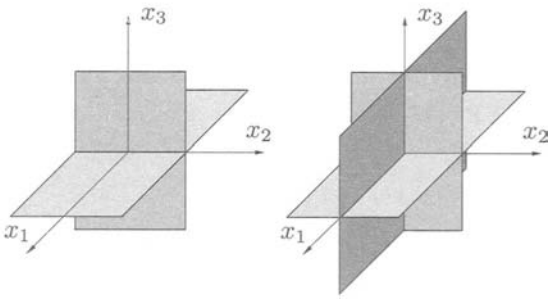

Figure 10. Example of orthotropic material behavior. 12 non-zero elements E_{ij} or S_{ij}, 9 independent elements

In all these cases the number of independent components of the stiffness or compliance matrices can be reduced.

Let us assume monoclinic (monotropic) material behavior. If we have one plane of symmetry (for example, Fig. 9) the elasticity matrix takes the form

$$[E_{ij}]^{\mathrm{MC}} = \begin{bmatrix} E_{11} & E_{12} & E_{13} & 0 & 0 & E_{16} \\ E_{12} & E_{22} & E_{23} & 0 & 0 & E_{26} \\ E_{13} & E_{23} & E_{33} & 0 & 0 & E_{36} \\ 0 & 0 & 0 & E_{44} & E_{45} & 0 \\ 0 & 0 & 0 & E_{45} & E_{55} & 0 \\ E_{16} & E_{26} & E_{36} & 0 & 0 & E_{66} \end{bmatrix}$$

Assuming orthotropic material behavior (for example, Fig. 10) the elasticity matrix takes the following form

$$[E_{ij}]^{\mathrm{O}} = \begin{bmatrix} E_{11} & E_{12} & E_{13} & 0 & 0 & 0 \\ E_{12} & E_{22} & E_{23} & 0 & 0 & 0 \\ E_{13} & E_{23} & E_{33} & 0 & 0 & 0 \\ 0 & 0 & 0 & E_{44} & 0 & 0 \\ 0 & 0 & 0 & 0 & E_{55} & 0 \\ 0 & 0 & 0 & 0 & 0 & E_{66} \end{bmatrix}$$

The next example is the transversely isotropic material behavior. Now one obtains 12 non-zero elements and 5 independent elements

$$[E_{ij}]^{\mathrm{TI}} = \begin{bmatrix} E_{11} & E_{12} & E_{12} & 0 & 0 & 0 \\ E_{12} & E_{22} & E_{23} & 0 & 0 & 0 \\ E_{12} & E_{23} & E_{22} & 0 & 0 & 0 \\ 0 & 0 & 0 & \frac{1}{2}(E_{22} - E_{23}) & 0 & 0 \\ 0 & 0 & 0 & 0 & E_{55} & 0 \\ 0 & 0 & 0 & 0 & 0 & E_{55} \end{bmatrix}$$

Table 3. Compliance matrix elements

Material model	Compliance matrix $[S_{ij}]$
Anisotropy: 21 independent material parameters	$\begin{bmatrix} S_{11} & S_{12} & S_{13} & S_{14} & S_{15} & S_{16} \\ & S_{22} & S_{23} & S_{24} & S_{25} & S_{26} \\ & & S_{33} & S_{34} & S_{35} & S_{36} \\ & & & S_{44} & S_{45} & S_{46} \\ \text{S} & \text{Y} & \text{M} & & S_{55} & S_{56} \\ & & & & & S_{66} \end{bmatrix}$
Monoclinic: 13 independent material parameters	Symmetry plane $x_3 = 0$: $S_{14} = S_{15} = S_{24} = S_{25} = S_{34} = S_{35} = S_{46} = S_{56} = 0$ Symmetry plane $x_2 = 0$: $S_{14} = S_{16} = S_{24} = S_{26} = S_{34} = S_{36} = S_{45} = S_{56} = 0$ Symmetry plane $x_1 = 0$: $S_{15} = S_{16} = S_{25} = S_{26} = S_{35} = S_{36} = S_{45} = S_{46} = 0$
Orthotropic: 9 independent material parameters	3 planes of symmetry $x_1 = 0, x_2 = 0, x_3 = 0$ $S_{14} = S_{15} = S_{16} = S_{24} = S_{25} = S_{26} = S_{34}$ $= S_{35} = S_{36} = S_{45} = S_{46} = S_{56} = 0$
Transversely isotropic: 5 independent material parameters	Plane of isotropy $x_3 = 0$: $S_{11} = S_{22}, S_{23} = S_{13}, S_{44} = S_{55}, S_{66} = 2(S_{11} - S_{12})$ Plane of isotropy $x_2 = 0$: $S_{11} = S_{33}, S_{12} = S_{23}, S_{44} = S_{66}, S_{55} = 2(S_{33} - S_{13})$ Plane of isotropy $x_1 = 0$: $S_{22} = S_{33}, S_{13} = S_{12}, S_{55} = S_{66}, S_{44} = 2(S_{22} - S_{23})$ all other S_{ij} like orthotropic
Isotropy: 2 independent material parameters	$S_{11} = S_{22} = S_{33}, S_{12} = S_{13} = S_{23},$ $S_{44} = S_{55} = S_{66} = 2(S_{11} - S_{12})$ all other $S_{ij} = 0$

The classical isotropic material behavior can be represented by

$$[E_{ij}]^{\mathrm{I}} = \begin{bmatrix} E_{11} & E_{12} & E_{12} & 0 & 0 & 0 \\ E_{12} & E_{11} & E_{12} & 0 & 0 & 0 \\ E_{12} & E_{12} & E_{11} & 0 & 0 & 0 \\ 0 & 0 & 0 & E_* & 0 & 0 \\ 0 & 0 & 0 & 0 & E_* & 0 \\ 0 & 0 & 0 & 0 & 0 & E_* \end{bmatrix}$$

with $E_* = \frac{1}{2}(E_{11} - E_{12})$. There are 12 non-zero elements, but only 2 independent parameters. The results for the tree-dimensional compliance matrices are shown in Table 3. The results for the three-dimensional stiffness matrices can be summarized as shown in Table 4.

The structural analysis in engineering is mostly based on the so-called engineering constants. Considering orthotropic material behavior with material parameters E_i, G_{ij} and ν_{ij} one can write

Table 4. Stiffness matrix elements

Material model	Elasticity matrix $[E_{ij}]$
Anisotropy: 21 independent material parameters	$\begin{bmatrix} E_{11} & E_{12} & E_{13} & E_{14} & E_{15} & E_{16} \\ & E_{22} & E_{23} & E_{24} & E_{25} & E_{26} \\ & & E_{33} & E_{34} & E_{35} & E_{36} \\ & & & E_{44} & E_{45} & E_{46} \\ \text{S} & \text{Y} & \text{M} & & E_{55} & E_{56} \\ & & & & & E_{66} \end{bmatrix}$
Monoclinic: 13 independent material parameters	Symmetry plane $x_3 = 0$: $E_{14} = E_{15} = E_{24} = E_{25} = E_{34} = E_{35} = E_{46} = E_{56} = 0$ Symmetry plane $x_2 = 0$: $E_{14} = E_{16} = E_{24} = E_{26} = E_{34} = E_{36} = E_{45} = E_{56} = 0$ Symmetry plane $x_1 = 0$: $E_{15} = E_{16} = E_{25} = E_{26} = E_{35} = E_{36} = E_{45} = E_{46} = 0$
Orthotropic: 9 independent material parameters	3 planes of symmetry $x_1 = 0, x_2 = 0, x_3 = 0$ $E_{14} = E_{15} = E_{16} = E_{24} = E_{25} = E_{26} = E_{34}$ $= E_{35} = E_{36} = E_{45} = E_{46} = E_{56} = 0$
Transversely isotropic: 5 independent material parameters	Plane of isotropy $x_3 = 0$: $E_{11} = E_{22}, E_{23} = E_{13}, E_{44} = E_{55}, E_{66} = \frac{1}{2}(E_{11} - E_{12})$ Plane of isotropy $x_2 = 0$: $E_{11} = E_{33}, E_{12} = E_{23}, E_{44} = E_{66}, E_{55} = \frac{1}{2}(E_{33} - E_{13})$ Plane of isotropy $x_1 = 0$: $E_{22} = E_{33}, E_{12} = E_{13}, E_{55} = E_{66}, E_{44} = \frac{1}{2}(E_{22} - E_{23})$ all other E_{ij} like orthotropic
Isotropy: 2 independent material parameters	$E_{11} = E_{22} = E_{33}, E_{12} = E_{13} = E_{23},$ $E_{44} = E_{55} = E_{66} = \frac{1}{2}(E_{11} - E_{12})$ all other $E_{ij} = 0$

down

$$\begin{aligned} \sigma_1 &= E_{11}\varepsilon_1 + E_{12}\varepsilon_2 + E_{13}\varepsilon_3, & \sigma_4 &= E_{44}\varepsilon_4, \\ \sigma_2 &= E_{12}\varepsilon_1 + E_{22}\varepsilon_2 + E_{23}\varepsilon_3, & \sigma_5 &= E_{55}\varepsilon_5, \\ \sigma_3 &= E_{13}\varepsilon_1 + E_{23}\varepsilon_2 + E_{33}\varepsilon_3, & \sigma_6 &= E_{66}\varepsilon_6 \end{aligned}$$

The inverted generalized HOOKE's law takes the form

$$\begin{aligned} \varepsilon_1 &= S_{11}\sigma_1 + S_{12}\sigma_2 + S_{13}\sigma_3, & \varepsilon_4 &= S_{44}\sigma_4, \\ \varepsilon_2 &= S_{12}\sigma_1 + S_{22}\sigma_2 + S_{23}\sigma_3, & \varepsilon_5 &= S_{55}\sigma_5, \\ \varepsilon_3 &= S_{13}\sigma_1 + S_{23}\sigma_2 + S_{33}\sigma_3, & \varepsilon_6 &= S_{66}\sigma_6 \end{aligned}$$

Let us now identify the constants.

At first, we perform the tension test. The uniaxial tension in x_i-direction, $\sigma_1 \neq 0$, $\sigma_i = 0$, $i = 2, \ldots, 6$ can be presented by

$$\varepsilon_1 = S_{11}\sigma_1, \quad \varepsilon_2 = S_{12}\sigma_1, \quad \varepsilon_3 = S_{13}\sigma_1, \quad \varepsilon_4 = \varepsilon_5 = \varepsilon_6 = 0,$$

Physical tensile tests yield the elastic constants E_1, ν_{12}, ν_{13}

$$E_1 = \frac{\sigma_1}{\varepsilon_1} = \frac{1}{S_{11}}, \quad \nu_{12} = -\frac{\varepsilon_2}{\varepsilon_1} = -S_{12}E_1, \quad \nu_{13} = -\frac{\varepsilon_3}{\varepsilon_1} = -S_{13}E_1$$

or

$$S_{11} = \frac{1}{E_1}, \quad S_{12} = -\frac{\nu_{12}}{E_1}, \quad S_{13} = -\frac{\nu_{13}}{E_1}$$

Analogous relations resulting from uniaxial tension in x_2- and x_3-directions and all S_{ij} are related to the nine measured engineering constants (3 YOUNG's moduli and 6 POISSON's ratios) by uniaxial tension tests in three directions x_1, x_2 and x_3. From the symmetry of the compliance matrix one can conclude

$$\frac{\nu_{12}}{E_1} = \frac{\nu_{21}}{E_2}, \quad \frac{\nu_{23}}{E_2} = \frac{\nu_{32}}{E_3}, \quad \frac{\nu_{31}}{E_3} = \frac{\nu_{13}}{E_1}$$

or

$$\frac{\nu_{ij}}{E_i} = \frac{\nu_{ji}}{E_j}, \quad \frac{\nu_{ij}}{\nu_{ji}} = \frac{E_i}{E_j}, \quad i,j = 1,2,3 \quad (i \neq j)$$

Remember that the first and the second subscript in POISSON's ratios denote stress and strain directions, respectively.

At second, one can perform the shear test

$$\varepsilon_4 = S_{44}\sigma_4, \quad \varepsilon_5 = S_{55}\sigma_5, \quad \varepsilon_6 = S_{66}\sigma_6$$

The compliances can be estimated as

$$S_{44} = \frac{1}{G_{23}} = \frac{1}{E_4}, \quad S_{55} = \frac{1}{G_{13}} = \frac{1}{E_5}, \quad S_{66} = \frac{1}{G_{12}} = \frac{1}{E_6}$$

Finally one gets

$$\begin{bmatrix} \varepsilon_1 \\ \varepsilon_2 \\ \varepsilon_3 \\ \varepsilon_4 \\ \varepsilon_5 \\ \varepsilon_6 \end{bmatrix} = \begin{bmatrix} \frac{1}{E_1} & -\frac{\nu_{12}}{E_1} & -\frac{\nu_{13}}{E_1} & 0 & 0 & 0 \\ & \frac{1}{E_2} & -\frac{\nu_{23}}{E_2} & 0 & 0 & 0 \\ & & \frac{1}{E_3} & 0 & 0 & 0 \\ & & & \frac{1}{E_4} & 0 & 0 \\ & \text{S} & \text{Y} & \text{M} & \frac{1}{E_5} & 0 \\ & & & & & \frac{1}{E_6} \end{bmatrix} \begin{bmatrix} \sigma_1 \\ \sigma_2 \\ \sigma_3 \\ \sigma_4 \\ \sigma_5 \\ \sigma_6 \end{bmatrix}$$

Let us now estimate the components of the elasticity matrix. The following trivial relations between stiffness and compliance matrices can be obtained

$$E_{44} = \frac{1}{S_{44}} = G_{23}, \quad E_{55} = \frac{1}{S_{55}} = G_{13}, \quad E_{66} = \frac{1}{S_{66}} = G_{12}$$

In addition, a symmetric [3x3]-matrix must be inverted

$$E_{ij} = S_{ij}^{-1} = \frac{(-1)^{i+j} U_{ij}}{\mathrm{Det}[S_{ij}]}, \quad \mathrm{Det}[S_{ij}] = \begin{vmatrix} S_{11} & S_{12} & S_{13} \\ S_{12} & S_{22} & S_{23} \\ S_{13} & S_{23} & S_{33} \end{vmatrix}$$

The U_{ij} are submatrices of $\boldsymbol{S}$ to the element S_{ij}

$$E_{11} = \frac{S_{22}S_{33} - S_{23}^2}{\mathrm{Det}[S_{ij}]}, \quad E_{12} = \frac{S_{13}S_{23} - S_{12}S_{33}}{\mathrm{Det}[S_{ij}]}, \quad E_{22} = \frac{S_{33}S_{11} - S_{13}^2}{\mathrm{Det}[S_{ij}]},$$
$$E_{23} = \frac{S_{12}S_{13} - S_{23}S_{11}}{\mathrm{Det}[S_{ij}]}, \quad E_{33} = \frac{S_{11}S_{22} - S_{12}^2}{\mathrm{Det}[S_{ij}]}, \quad E_{13} = \frac{S_{12}S_{23} - S_{13}S_{22}}{\mathrm{Det}[S_{ij}]}$$

Finally, the stiffness matrix can be expressed by engineering constants as follows

$$E_{11} = \frac{(1 - \nu_{23}\nu_{32})E_1}{\Delta}, \quad E_{12} = \frac{(\nu_{12} + \nu_{13}\nu_{32})E_2}{\Delta}, \quad E_{13} = \frac{(\nu_{13} + \nu_{12}\nu_{23})E_3}{\Delta},$$
$$E_{22} = \frac{(1 - \nu_{31}\nu_{13})E_2}{\Delta}, \quad E_{23} = \frac{(\nu_{23} + \nu_{21}\nu_{13})E_3}{\Delta}, \quad E_{33} = \frac{(1 - \nu_{21}\nu_{12})E_3}{\Delta}$$

with $\Delta = 1 - \nu_{21}\nu_{12} - \nu_{32}\nu_{23} - \nu_{13}\nu_{31} - 2\nu_{21}\nu_{13}\nu_{32}$.

Taking into account $E_i/\Delta \equiv \overline{E}_i$, $1/S_i \equiv E_i$ one gets

$$\begin{bmatrix} \sigma_1 \\ \sigma_2 \\ \sigma_3 \end{bmatrix} = \begin{bmatrix} (1 - \nu_{23}\nu_{32})\overline{E}_1 & (\nu_{12} + \nu_{13}\nu_{32})\overline{E}_2 & (\nu_{13} + \nu_{12}\nu_{23})\overline{E}_3 \\ & (1 - \nu_{31}\nu_{13})\overline{E}_2 & (\nu_{23} + \nu_{21}\nu_{13})\overline{E}_3 \\ \text{SYM} & & (1 - \nu_{21}\nu_{12})\overline{E}_3 \end{bmatrix} \begin{bmatrix} \varepsilon_1 \\ \varepsilon_2 \\ \varepsilon_3 \end{bmatrix},$$

$$\begin{bmatrix} \sigma_4 \\ \sigma_5 \\ \sigma_6 \end{bmatrix} = \begin{bmatrix} E_4 & 0 & 0 \\ & E_5 & 0 \\ \text{SYM} & & E_6 \end{bmatrix} \begin{bmatrix} \varepsilon_4 \\ \varepsilon_5 \\ \varepsilon_6 \end{bmatrix}$$

The most general case of monoclinic material behavior with the plane of elastic symmetry $(x_1 - x_2)$ results in

$$\begin{bmatrix} \varepsilon_1 \\ \varepsilon_2 \\ \varepsilon_3 \\ \varepsilon_4 \\ \varepsilon_5 \\ \varepsilon_6 \end{bmatrix} = \begin{bmatrix} \frac{1}{E_1} & -\frac{\nu_{21}}{E_2} & -\frac{\nu_{31}}{E_3} & 0 & 0 & \frac{\eta_{61}}{E_6} \\ -\frac{\nu_{12}}{E_1} & \frac{1}{E_2} & -\frac{\nu_{32}}{E_3} & 0 & 0 & \frac{\eta_{62}}{E_6} \\ -\frac{\nu_{13}}{E_1} & -\frac{\nu_{23}}{E_2} & \frac{1}{E_3} & 0 & 0 & \frac{\eta_{63}}{E_6} \\ 0 & 0 & 0 & \frac{1}{E_4} & \frac{\mu_{54}}{E_5} & 0 \\ 0 & 0 & 0 & \frac{\mu_{45}}{E_4} & \frac{1}{E_5} & 0 \\ \frac{\eta_{16}}{E_1} & \frac{\eta_{26}}{E_2} & \frac{\eta_{36}}{E_3} & 0 & 0 & \frac{1}{E_6} \end{bmatrix} \begin{bmatrix} \sigma_1 \\ \sigma_2 \\ \sigma_3 \\ \sigma_4 \\ \sigma_5 \\ \sigma_6 \end{bmatrix}$$

with the following reciprocal relations

$$\frac{\eta_{61}}{E_6} = \frac{\eta_{16}}{E_1}, \quad \frac{\eta_{62}}{E_6} = \frac{\eta_{26}}{E_2}, \quad \frac{\eta_{63}}{E_6} = \frac{\eta_{36}}{E_3}, \quad \frac{\mu_{54}}{E_5} = \frac{\mu_{45}}{E_4}$$

The μ_{ij} are the shear-shear stress coupling parameters, the η_{ij} the normal-shear stress coupling parameters (Lai et al. (1993)).

4.5 Two-dimensional Material Equations

A thin lamina can be considered to be under the condition of plane stress with all stress components in the out-of-plane direction being approximately zero (Fig. 11). The two-dimensional

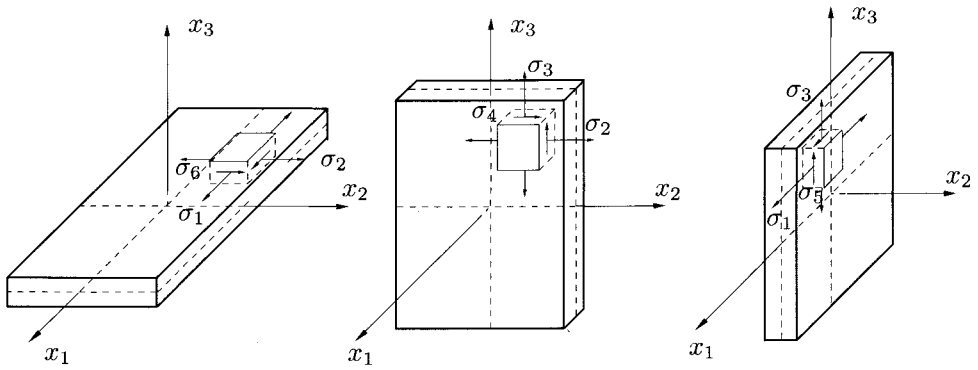

Figure 11. Plane stress statements

generalized HOOKE's law for the plane stress state with respect to the $x_1 - x_2$ plane can be formulated as follows

$$\begin{bmatrix} \varepsilon_1 \\ \varepsilon_2 \\ \varepsilon_3 \\ \varepsilon_4 \\ \varepsilon_5 \\ \varepsilon_6 \end{bmatrix} = \begin{bmatrix} S_{11} & S_{12} & S_{13} & S_{14} & S_{15} & S_{16} \\ & S_{22} & S_{23} & S_{24} & S_{25} & S_{26} \\ & & S_{33} & S_{34} & S_{35} & S_{36} \\ \mathrm{S} & & & S_{44} & S_{45} & S_{46} \\ & \mathrm{Y} & & & S_{55} & S_{56} \\ & & \mathrm{M} & & & S_{66} \end{bmatrix} \begin{bmatrix} \sigma_1 \\ \sigma_2 \\ 0 \\ 0 \\ 0 \\ \sigma_6 \end{bmatrix}$$

In this equation is assumed $\sigma_3 = \sigma_4 = \sigma_5 = 0$. In addition we ignore the shear strains $\varepsilon_4 \approx \varepsilon_5 \approx 0$. Based on these statements so-called reduced constitutive equations can be set up. Three in-plane constitutive equations can be established

$$\begin{aligned} \varepsilon_1 &= S_{11}\sigma_1 + S_{12}\sigma_2 + S_{16}\sigma_6 \\ \varepsilon_2 &= S_{12}\sigma_1 + S_{22}\sigma_2 + S_{26}\sigma_6, \qquad S_{ij} = S_{ji} \\ \varepsilon_6 &= S_{16}\sigma_1 + S_{26}\sigma_2 + S_{66}\sigma_6 \end{aligned}$$

and an additional equation for the strain ε_3 in x_3-direction can be formulated

$$\varepsilon_3 = S_{13}\sigma_1 + S_{23}\sigma_2 + S_{36}\sigma_6$$

The inverse relations are

$$\begin{bmatrix} \sigma_1 \\ \sigma_2 \\ 0 \\ 0 \\ 0 \\ \sigma_6 \end{bmatrix} = \begin{bmatrix} E_{11} & E_{12} & E_{13} & E_{14} & E_{15} & E_{16} \\ & E_{22} & E_{23} & E_{24} & E_{25} & E_{26} \\ & & E_{33} & E_{34} & E_{35} & E_{36} \\ \mathrm{S} & & & E_{44} & E_{45} & E_{46} \\ & \mathrm{Y} & & & E_{55} & E_{56} \\ & & \mathrm{M} & & & E_{66} \end{bmatrix} = \begin{bmatrix} \varepsilon_1 \\ \varepsilon_2 \\ \varepsilon_3 \\ 0 \\ 0 \\ \varepsilon_6 \end{bmatrix}$$

or again three in-plane equations

$$\begin{aligned}\sigma_1 &= E_{11}\varepsilon_1 + E_{12}\varepsilon_2 + E_{13}\varepsilon_3 + E_{16}\varepsilon_6,\\ \sigma_2 &= E_{12}\varepsilon_1 + E_{22}\varepsilon_2 + E_{23}\varepsilon_3 + E_{26}\varepsilon_6, \qquad E_{ij} = E_{ji}\\ \sigma_6 &= E_{16}\varepsilon_1 + E_{26}\varepsilon_2 + E_{36}\varepsilon_3 + E_{66}\varepsilon_6\end{aligned}$$

The reduced stiffness can be deduced taking into account the condition

$$\sigma_3 = E_{13}\varepsilon_1 + E_{23}\varepsilon_2 + E_{33}\varepsilon_3 + E_{36}\varepsilon_6 = 0$$

Now the strain ε_3 can be eliminated

$$\varepsilon_3 = -\frac{1}{E_{33}}(E_{13}\varepsilon_1 + E_{23}\varepsilon_2 + E_{36}\varepsilon_6)$$

and the three in-plane equations can be rewritten

$$\sigma_i = \left(E_{ij} - \frac{E_{i3}E_{j3}}{E_{33}}\right)\varepsilon_j = Q_{ij}\varepsilon_j, \quad i,j = 1,2,6$$

Q_{ij} denotes the reduced stiffness matrix since the values of the elasticity (stiffness) matrix will be partly reduced. The number of unknown independent parameters of each of the matrices S_{ij}, E_{ij} or Q_{ij} is six. In Table 5 the elements of the compliance matrix are shown. The results for the reduced stiffness matrix are presented in Table 6. Similar discussion one can perform for the plan strain state. In this case a reduced compliance matrix with the components V_{ij} can be

Table 5. Compliance matrix representation (plane stress state)

Material model	$\boldsymbol{\varepsilon = S\sigma}$
Anisotropy: 6 independent material parameters	Compliances S_{ij} $\begin{bmatrix}\varepsilon_1\\ \varepsilon_2\\ \varepsilon_6\end{bmatrix} = \begin{bmatrix}S_{11} & S_{12} & S_{16}\\ & S_{22} & S_{26}\\ & & S_{66}\end{bmatrix}\begin{bmatrix}\sigma_1\\ \sigma_2\\ \sigma_6\end{bmatrix}$
Orthotropy: 4 independent material parameters Reference system: on-axis	$S_{16} = S_{26} = 0,\ S_{11} = \dfrac{1}{E_1},$ $S_{22} = \dfrac{1}{E_2},\ S_{12} = \dfrac{-\nu_{12}}{E_1} = \dfrac{-\nu_{21}}{E_2}$ $S_{66} = \dfrac{1}{G_{12}}$
Isotropy: 2 independent material parameters Reference system arbitrary	$S_{16} = S_{26} = 0$ $S_{11} = S_{22} = \dfrac{1}{E},\quad S_{12} = -\dfrac{\nu}{E},$ $S_{66} = 2(S_{11} - S_{12}) = \dfrac{2(1+\nu)}{E} = \dfrac{1}{G}$

Table 6. Stiffness matrices (plane stress state)

Material model	$\boldsymbol{\sigma = Q\varepsilon}$
Anisotropy: 6 independent parameters	Reduced stiffness Q_{ij} $\begin{bmatrix} \sigma_1 \\ \sigma_2 \\ \sigma_6 \end{bmatrix} = \begin{bmatrix} Q_{11} & Q_{12} & Q_{16} \\ & Q_{22} & Q_{26} \\ & & Q_{66} \end{bmatrix} \begin{bmatrix} \varepsilon_1 \\ \varepsilon_2 \\ \varepsilon_6 \end{bmatrix}$
Orthotropy: 4 independent parameters Reference system: on-axis	$Q_{16} = Q_{26} = 0,\ Q_{66} = \dfrac{1}{S_{66}} = G_{12}$ $Q_{11} = \dfrac{S_{22}}{\Delta} = \dfrac{E_1}{1-\nu_{12}\nu_{21}},\ Q_{22} = \dfrac{S_{11}}{\Delta} = \dfrac{E_2}{1-\nu_{12}\nu_{21}}$ $Q_{12} = -\dfrac{S_{12}}{\Delta} = \dfrac{\nu_{12}E_2}{1-\nu_{12}\nu_{21}}$ $\Delta = S_{11}S_{22} - S_{12}^2$
Isotropy: 2 parameters Reference system arbitrary	$Q_{16} = Q_{26} = 0,\ Q_{11} = Q_{22} = \dfrac{E}{1-\nu^2}$ $Q_{12} = \dfrac{\nu E}{1-\nu^2},\quad Q_{66} = \dfrac{E}{2(1+\nu)} = G$

Table 7. Number of non-zero elements

Material model	Non-zero parameters	Independent parameters
Three-dimensional stress- or strain state	$E_{ij}; S_{ij}$ $i,j = 1,\ldots,6$	$E_{ij}; S_{ij}$ $i,j = 1,\ldots,6$
Anisotropic	36	21
Monotropic	20	13
Orthotropic	12	9
Transversely isotropic	12	5
Isotropic	12	2
Plane stress state $(x_1 - x_2)$-plane	$Q_{ij}; S_{ij}$ $i,j = 1,2,6$	$Q_{ij}; S_{ij}$ $i,j = 1,2,6$
Anisotropic	9	6
Orthotropic	5	4
Isotropic	5	2
Plane strain state $(x_1 - x_2)$-plane	$E_{ij}; V_{ij}$ $i,j = 1,2,6$	$E_{ij}; V_{ij}$ $i,j = 1,2,6$
Anisotropic	9	6
Orthotropic	5	4
Isotropic	5	2

introduced. All details are presented in Altenbach et al. (2004). Finally, the number of non-zero elements for the three-dimensional and the two-dimensional equations are presented in Table 7.

5 Failure and strength criteria

5.1 Introductional remarks

The description of the material behavior which is the basis of the engineering analysis of structural elements, etc., should be mathematically correct and correspond to some physically based experiences. Due to the complexity of the behavior of real materials the establishment of suitable equations for the material behavior description is sometimes connected with difficulties and increasing effort. At present the models of isotropic and anisotropic elastic behavior are well established, but the formulation of models for the inelastic and failure behavior is under discussion. This statement is valid for all materials including composites.

In this section we pay our attention on the failure behavior. In the literature one can find various proposals for modelling the failure behavior, see Paul (1968); Altenbach et al. (1995); Yu (2004) among others. The main problem is the selection of the description level reflecting adequate the knowledge of the physics of solids and/or material science. Concerning this fact one can classify again the proposed models as microscopic, mesoscopic, macroscopic, etc. (cp. Sect. 3.2). Note that the use of microscopic models in the analysis and calculation of structural elements, which geometry is much larger in comparison with the characteristic size of the microstructure, is impossible since the computer power till now has been limited. On the other hand, there exist various phenomenological (engineering) models which are unable to reflect all details of the microstructure but they are a powerful tool for engineering calculations.

Limiting the discussion below by failure analysis two phenomenological models are introduced and discussed. The starting point of both is the assumption that a limit stress can be established. For example, in the case of the loss of the overall stiffness this is the ultimate strength, which is a material characteristic specific for the given material. It must be underlined that its experimental estimation is connected with difficulties but the accuracy is enough for engineering applications.

Modelling the limit behavior the use of the equivalent stress concept allows to compare the multi-axial limit states with uniaxial experimental data. For many materials and loading conditions the classical proposals of HUBER, VON MISES and HENCKY or TRESCA describe with the necessary accuracy the failure condition or the beginning of yielding. In addition, for the case of monolithic materials such as metals it is sufficient to use one observable characteristic such as the ultimate tensile, compressive, or shear stress to describe the failure, see Vinson & Sierakowski (1987). Taking into account non-classical effects like different behavior in tension and compression a generalization of the classical limit criteria must be introduced. In this case like in the case of composites one has to select a suitable failure criterion based upon a number of observable characteristics.

Let us assume that the stress estimated $\sigma_{\text{estimated}}$ (from the calculations) must be compared with a critical stress (from tests) σ_{critical}

$$\sigma_{\text{estimated}} \leq \sigma_{\text{critical}}$$

The problem is that the three-dimensional stress state is characterized by the stress tensor $\boldsymbol{\sigma}$. How to compare this tensorial quantity with any scalar-valued critical stress σ_{critical}? There is one engineering solution: the definition of an equivalent stress $\sigma_{\text{eq}} = \sigma_{\text{eq}}(\boldsymbol{\sigma}, \ldots)$ which is scalar-valued

$$\sigma_{\text{eq}} \leq \sigma_{\text{critical}}$$

This method is well-established in the case of classical isotropic structural materials like steel. For composites one has to consider the anisotropy and the existence of various, quite different failure modes (see, for example, Vinson & Sierakowski (1987); Puck (1996)). So the question is how to define the equivalent stress. A similar situation we have if we introduce strain based criteria.

From the strength of materials we know that we have to make at first some engineering assumptions, after that we have to formulate a criterion (hypothesis), and last but not least we have to perform an experimental proof. The anisotropy can be included if we are able to extend the classical isotropic criteria. The extension of the classical criteria can be based mathematically, but the identification of the material parameters can not be solved in a satisfying manner since relevant tests can not be performed.

Let us briefly discuss the main classical isotropic limit criteria which are summarized, for example, in Paul (1968); Altenbach et al. (1995); Lemaitre (2001); Yu (2004):

- *Maximum principal stress criterion*

  $$\sigma_{\text{eq}} = \sigma_1$$

  Assuming this criterion the solution steps are: solving the eigenvalue problem for the stress tensor, estimation of σ_1 which is the maximum of the eigenvalues.

- *Maximum strain criterion*

  $$\sigma_{\text{eq}} = \sigma_1 - \nu(\sigma_2 + \sigma_3)$$

  Here the solution steps are: solving the eigenvalue problem for the strain tensor, estimation of the maximum strain, recalculation of the stresses assuming the HOOKE's law.

- *Maximum shear stress criterion*

  $$\sigma_{\text{eq}} = \sigma_1 - \sigma_3$$

  Now the solution steps are: solving the eigenvalue problem for the stress tensor, estimation of the maximum eigenvalue and the minimum eigenvalue.

- *Distorsion energy criterion*

  $$\sigma_{\text{eq}} = \sqrt{\frac{1}{2}[(\sigma_1 - \sigma_2)^2 + (\sigma_2 - \sigma_3)^2 + (\sigma_3 - \sigma_1)^2]}$$

  After calculating the eigenvalues the criterion can be applied.

The use of isotropic failure and strength criteria is connected with the following statements:

- the comparison of the estimated stresses and the critical values must be performed for each point of the structure,
- the first and the second criterion are suitable for very brittle materials,
- the third and the fourth criterion are more suitable for ductile materials,

- the experimental verification must be performed with respect to the material behavior (ductile, brittle), the loading and other conditions, and
- the anisotropy is not taken into account.

With these statements one can make the conclusion that the introduced criteria can be used also in the case of yielding.

5.2 Failure mechanisms and criteria for composites

The failure of structural elements can be defined in a different manner:

- As in the case of buckling, a structural element may be considered as failure though the material is still intact, but there are excessive deformations.
- Here failure will be considered to be the loss of integrity of the composite material itself.

In the case of monolithic materials stress concentrations, e.g. around notches and holes, cause localized failures. For brittle materials local failure may lead to complete fracture and therefore to a total loss of load-carrying capability. For ductile materials local failure may be in the form of yielding and remains localized, i.e., it is tolerated better than brittle failure. Since composites are not monolithic materials now we have to consider a more complex situation.

The fail-safe philosophy has been employed in the design of metallic structures and is standard in engineering applications. Similar procedures for composite materials are not well defined and are the object of intensive scientific research up to now, see Puck (1996); Christensen (1997). Main causes of failure are design errors, fabrication and processing errors or unexpected service conditions. Design errors can be made in both material and structure. The stress level carried by each lamina in a laminate depends on the elastic moduli. This may cause large stress gradients between laminae which are oriented at considerably large angles to each other (e.g. 90^0). Such high levels of internal stresses in adjacent laminae may develop a result of external applied loads but also by temperature and moisture changes. Service anomalies can include improper operation, faulty maintenance, overloads or environmental incurred damage.

If structural loadings produce local discontinuities inside the material we speak of a crack. Micro-cracking is considered as the nucleation of micro-cracks at the microscopic level starting from defects and may cause the initiation of material fracture. Macro-cracking is the propagation of a fracture by the creation of new fracture surfaces at the macroscopic level. For composite materials the fraction initiation is generally well developed before a change in the macroscopic behavior can be observed. If in a laminate macro-cracks occur, it may not be catastrophic, for it is possible that some layers fail first and the composite continues to take more loads until all laminae fail. The failure of a single layer plays a central function in failure analysis of laminates.

Composite fracture mechanisms are rather complex because of their anisotropic nature. Failure modes depend on:

- the applied loads and
- the distribution of reinforcements in the composites.

Continuous fiber reinforced composites show

- intralaminar fracture,
- interlaminar fracture, and
- translaminar fracture.

Intralaminar fracture is located inside a lamina, interlaminar fracture shows the failure developed between laminae and translaminar fracture is oriented transverse to the laminate plane. The fracture of a UD-lamina is the result of the accumulation of various elementary fracture mechanisms:

- fiber fracture,
- transverse matrix fracture,
- longitudinal matrix fracture, and
- fracture of the fiber-matrix interface.

Elementary failure mechanisms are shown in Fig. 12. How to estimate the basic strength

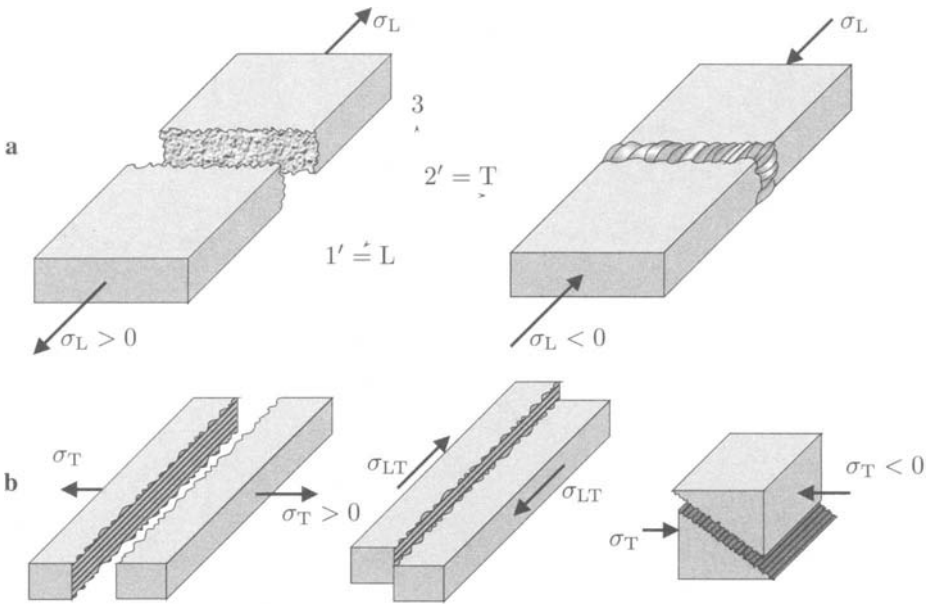

Figure 12. Elementary failure mechanisms. **a** Fiber fracture by pure tension $\sigma_L > 0$ or compression $\sigma_L < 0$ (micro-buckling), **b** Matrix fracture by pure tension $\sigma_T > 0$, pure shearing σ_{LT} and pure compression $\sigma_T < 0$

parameters can be seen in Fig. 13. The in-plane shear failure modes are shown in Fig. 14.

Besides the basic failure mechanisms for a single layer another fracture mode occurs: delamination (separation of layers). The matrix material that sticks the laminae of a laminate together has substantially smaller strength than the in-plane strength of the layers. Stresses perpendicular to the interface between laminae may cause breaking of the bond between the layers in mostly localized, small regions. They may affect the integrity of a laminate and can degrade their in-plane load-carrying capability.

The definition of failure may change from case to case and depends on the composite material and the kind of loads. For composite materials, such as UD-laminates, the end of the elastic domain is associated with the development of micro-cracking. But in the first stage, the initiated cracks do not propagate and their development changes the stiffness of the material very gradually but the degradation is irreversible.

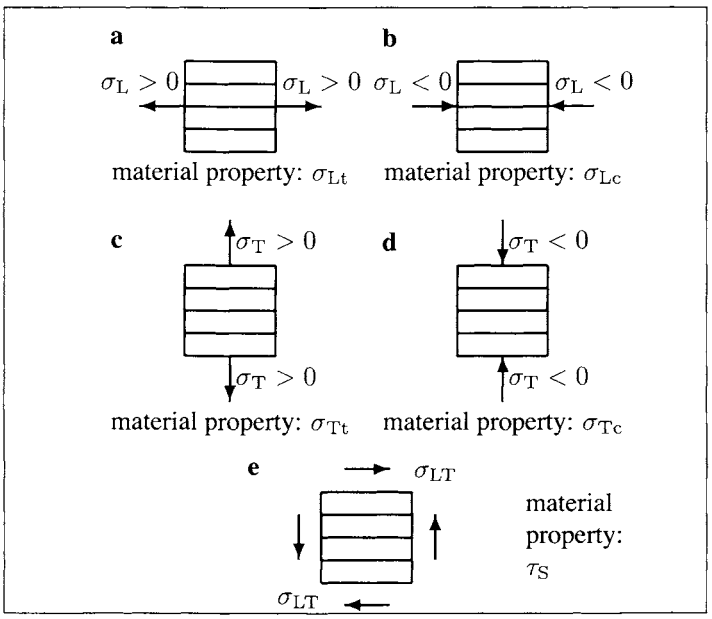

Figure 13. Definition of basic strength parameters. **a** Longitudinal tensile strength σ_{Lt}, **b** longitudinal compressive strength σ_{Lc}, **c** transverse tensile strength σ_{Tt}, **d** transverse compressive strength σ_{Tc}, **e** in-plane (intralaminar) shear strength τ_S

Let us now discuss failure criteria for composites. This must be done with respect to the following items:

- The simplest form of such criteria is similar to those used for isotropic materials.
- The major difference between isotropic materials and unidirectional fibrous composite materials is the directional dependence of the strength on a macrosopic scale.
- The criteria presented here are purely empirical with the minimum of test data.
- The failure criteria are usually grouped in literature into three different classes: limit criteria, interactive criteria, and hybrid criteria.

In the following we discuss only selected criteria of the first two classes.

Laminate failure criteria are applied on a ply-by-ply basis and the load-carrying capability of the entire composite is predicted by the laminate or sandwich theories. A laminate may be assumed to have failed when the strength criterion of any of its laminae is reached (first-ply failure). However, the failure of a single layer not necessarily leads to a total fracture of the laminate structure. The following criteria are mostly applied (note that here the English terms are used, in the Russian literature are similar criteria proposed, but named by other scientists, Mālmeisters et al. (1977); Tamuzh & Protasov (1986)):

- maximum stress theory,
- maximum strain theory,
- deviatoric or distorsion strain energy criteria of TSAI-HILL, and
- interactive tensor polynomial criterion of TSAI-WU (1971).

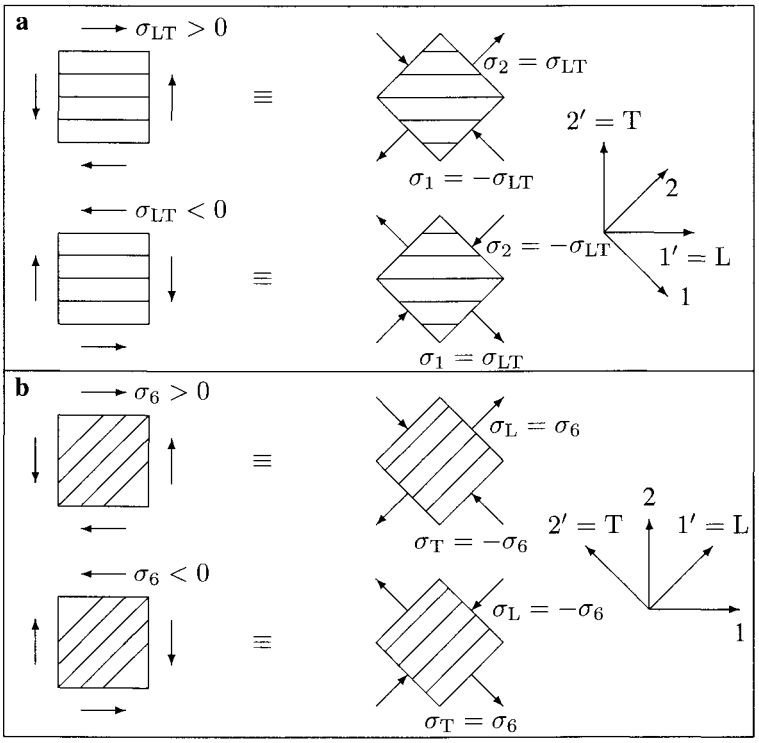

Figure 14. In-plain shear failure. **a** Positive and negative shear stresses along the principal material axes, **b** positive and negative shear stresses at 45^0 with the principal material axes

Other criteria which are completely different are presented, for example, in Hashin (1980), but they are not discussed here.

Let us present criteria for UD-laminates considering plane stress state and assuming

- orthotropic material behavior,
- thin layers, and
- quasi-homogeneous behavior.

The maximum stress and the maximum strain criteria assume no stress interaction while the other ones include full stress interaction. The maximum stress theory assumes that failure occurs when at least one stress component along one of the principal material axes exceeds the corresponding strength parameter in that direction

$$\begin{array}{lllll} \sigma_L = \sigma_{Lt}, & \sigma_L > 0, & \sigma_T = \sigma_{Tt}, & \sigma_T > 0, \\ \sigma_L = \sigma_{Lc}, & \sigma_L < 0, & \sigma_T = \sigma_{Tc}, & \sigma_T < 0, \\ |\sigma_{LT}| = \tau_S, & & & \end{array}$$

The layer failure does not occur if

$$\begin{array}{lll} -\sigma_{Lc} < \sigma_L < \sigma_{Lt}, \\ -\sigma_{Tc} < \sigma_T < \sigma_{Tt}, \\ -\tau_S < \sigma_{LT} < \tau_S \end{array}$$

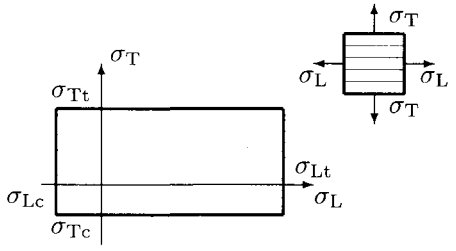

Figure 15. Maximum stress criterion

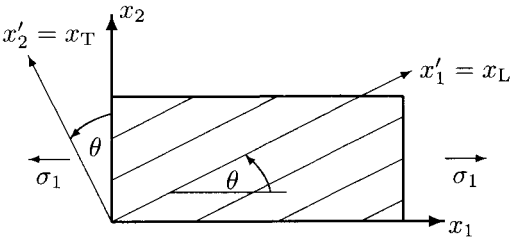

Figure 16. Off-axis tension or compression of a UD-lamina

For a two-dimensional state of normal stresses, i.e. $\sigma_L \neq 0, \sigma_T \neq 0, \sigma_{LT} = 0$, the failure envelope takes the form of a rectangle (Fig. 15). Note that the formulated criterion contains the assumption of different behavior in tension and compression. Such a behavior is typical for composites.

In the case of off-axis loading (Fig. 16) the strength properties must be recalculated.

$$\begin{array}{rclcrcl} \sigma_L &=& \sigma_1 \cos^2\theta &=& \sigma_1 c^2 & \sigma_1 &=& \sigma_L/c^2 \\ \sigma_T &=& \sigma_1 \sin^2\theta &=& \sigma_1 s^2 \Rightarrow & \sigma_1 &=& \sigma_T/s^2 \\ \sigma_{LT} &=& -\sigma_1 \sin\theta\cos\theta &=& -\sigma_1 sc & \sigma_1 &=& -\sigma_{LT}/sc \end{array}$$

$$\begin{array}{rcccl} -\sigma_{Lc} &<& \sigma_1 c^2 &<& \sigma_{Lt}, \\ -\sigma_{Tc} &<& \sigma_1 s^2 &<& \sigma_{Tt}, \\ -\tau_S &<& \sigma_1 sc &<& \tau_S \end{array}$$

Ultimate strength for σ_1 corresponds to the smallest of the following six values

$$\begin{array}{llll} \sigma_{1t} = \sigma_{Lt}/c^2, & \sigma_{1t} = \sigma_{Tt}/s^2, & \sigma_{1t} = \tau_S/sc, & \sigma_1 > 0, \\ \sigma_{1c} = \sigma_{Lc}/c^2, & \sigma_{1c} = \sigma_{Tc}/s^2, & \sigma_{1c} = \tau_S/sc, & \sigma_1 < 0 \end{array}$$

The failure modes depend on the corresponding ultimate strength σ_{1u}

$$\begin{array}{ll} \sigma_{1u} = \sigma_{Lt}/c^2 & \text{fiber failure,} \\ \sigma_{1u} = \sigma_{Tt}/s^2 & \text{transverse normal stress failure,} \\ \sigma_{1u} = \tau_S/sc & \text{in-plane shear failure} \end{array}$$

Because of the orthotropic symmetry, shear strength is independent of the sign of σ_{LT} and there are five independent failure modes. There is no interaction among the modes although in reality the failure processes are highly interacting. The maximum stress criterion can be applied to brittle failure modes.

Maximum strain theory is similar to the maximum stress theory

$$\begin{array}{rclcrcrcl} \varepsilon_L &=& \varepsilon_{Lt} & \varepsilon_L > 0, & \varepsilon_T &=& \varepsilon_{Tt} & \varepsilon_T &> 0, \\ \varepsilon_L &=& \varepsilon_{Lc} & \varepsilon_L < 0, & \varepsilon_T &=& \varepsilon_{Tc} & \varepsilon_T &< 0, \\ |\varepsilon_{LT}| &=& \varepsilon_S & & & & & & \end{array}$$

The lamina failure does not occur if

$$-\varepsilon_{Lc} < \varepsilon_L < \varepsilon_{Lt}, \quad -\varepsilon_{Tc} < \varepsilon_T < \varepsilon_{Tt}, \quad -\varepsilon_S < \varepsilon_{LT} < \varepsilon_S$$

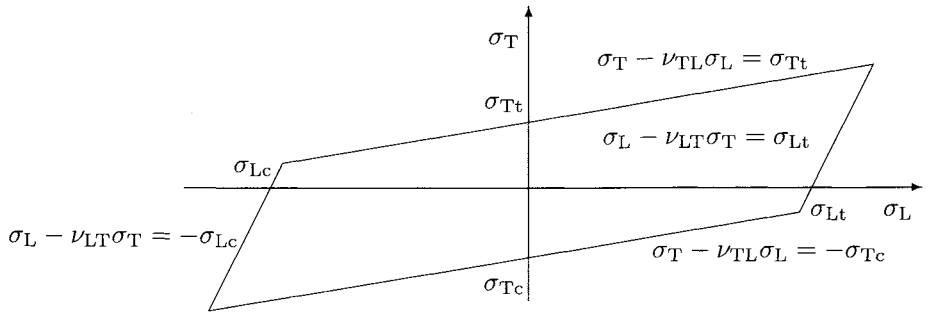

Figure 17. Maximum strain criterion

The engineering moduli in the principal directions $E_L, E_T, G_{LT}, \nu_{LT}, \nu_{TL}$ can be introduced

$$\varepsilon_L = \frac{1}{E_L}(c^2 - \nu_{LT}s^2)\sigma_1, \varepsilon_T = \frac{1}{E_T}(s^2 - \nu_{TL}c^2)\sigma_1, \varepsilon_{LT} = -\frac{1}{G_{LT}}sc\sigma_1$$

The maximum strain and stress criteria must lead to identical values in the cases of longitudinal loading and $\theta = 0^0$ or transverse unidirectional loading and $\theta = 90^0$. The identity of the shear equations is given in both cases. This implies that

$$\varepsilon_{Lt} = \frac{\sigma_{Lt}}{E_L}, \varepsilon_{Lc} = -\frac{\sigma_{Lc}}{E_L}, \varepsilon_{Tt} = \frac{\sigma_{Tt}}{E_T}, \varepsilon_{Tc} = -\frac{\sigma_{Tc}}{E_T}, \varepsilon_S = \frac{\tau_S}{G_{LT}}$$

and the maximum strain criterion may be rewritten as follows

$$\begin{array}{lcll} -\sigma_{Lc} & < & \sigma_1(c^2 - \nu_{LT}s^2) & < \sigma_{Lt}, \\ -\sigma_{Tc} & < & \sigma_1(s^2 - \nu_{TL}c^2) & < \sigma_{Tt}, \\ -\tau_S & < & \sigma_1 sc & < \tau_S \end{array}$$

By comparing maximum stress and strain theories we establish that the two criteria differ by the introduction of the POISSON's ratio ν_{LT} in the strain criterion. In practice these terms modify the numerical results only slightly. In the special case of a two-dimensional stress state $\sigma_L \neq 0$, $\sigma_T \neq 0, \sigma_{LT} = 0$ the failure envelope takes the form of a parallelogram for the maximum strain criterion (Fig. 17).

The next criterion is the distorsion strain energy criterion of TSAI-HILL (Hill (1950)). This is an interactive criterion applied to anisotropic materials and was introduced by HILL. The starting point is the classical isotropic HUBER-VON MISES-HENCKY criterion

$$\sigma_I^2 + \sigma_{II}^2 - \sigma_I\sigma_{II} = \sigma_{eq}$$

or in a general reference system

$$\sigma_1^2 + \sigma_2^2 - \sigma_1\sigma_2 + 3\sigma_6^2 = \sigma_{eq}$$

with σ_I, σ_{II} as the principal stresses. HILL's modification can be formulated as

$$A\sigma_1^2 + B\sigma_2^2 + C\sigma_1\sigma_2 + D\sigma_6^2 = 1$$

A, B, C, D are material parameters. Note, in in the case of anisotropy distorsion and dilatation energies cannot be separated like in the isotropic case. The proposed criterion was applied to UD-laminae by TSAI et al.

$$A\sigma_{\mathrm{L}}^2 + B\sigma_{\mathrm{T}}^2 + C\sigma_{\mathrm{L}}\sigma_{\mathrm{T}} + D\sigma_{\mathrm{LT}}^2 = 1$$

A, B, C, D must be identified by tests

$$\begin{aligned}
&\sigma_{\mathrm{L}} = \sigma_{\mathrm{Lu}}, \quad \sigma_{\mathrm{T}} = 0, \quad \sigma_{\mathrm{LT}} = 0 \quad \Rightarrow \quad A = \frac{1}{\sigma_{\mathrm{Lu}}^2},\\
&\sigma_{\mathrm{L}} = 0, \quad \sigma_{\mathrm{T}} = \sigma_{\mathrm{Tu}}, \quad \sigma_{\mathrm{LT}} = 0 \quad \Rightarrow \quad B = \frac{1}{\sigma_{\mathrm{Tu}}^2},\\
&\sigma_{\mathrm{L}} = 0, \quad \sigma_{\mathrm{T}} = 0, \quad \sigma_{\mathrm{LT}} = \tau_{\mathrm{u}} \quad \Rightarrow \quad D = \frac{1}{\tau_{\mathrm{u}}^2}
\end{aligned}$$

In dependence on the failure mode, the superscript u must be substituted by t, c or s and denotes the ultimate stress value at failure under tension, compression or shear. The remaining parameter C must be determined by a biaxial test. Under identical biaxial normal loading $\sigma_{\mathrm{L}} = \sigma_{\mathrm{T}} \neq 0, \sigma_{\mathrm{LT}} = 0$ it can be assumed that the failure follows the maximum stress criterion, i.e failure will occur when the transverse stress reaches the transverse strength σ_{Tu} which is much lower than the longitudinal strength σ_{Lu}

$$\left(\frac{\sigma_{\mathrm{L}}}{\sigma_{\mathrm{Lu}}}\right)^2 + \left(\frac{\sigma_{\mathrm{T}}}{\sigma_{\mathrm{Tu}}}\right)^2 + C\sigma_{\mathrm{T}}^2 = 1, \quad \sigma_{\mathrm{T}} = \sigma_{\mathrm{Tu}} \Longrightarrow C = -\frac{1}{\sigma_{\mathrm{Lu}}^2}$$

The TSAI-HILL criterion in the case of plane stress state and on-axis loading can be formulated

$$\left(\frac{\sigma_{\mathrm{L}}}{\sigma_{\mathrm{Lu}}}\right)^2 + \left(\frac{\sigma_{\mathrm{T}}}{\sigma_{\mathrm{Tu}}}\right)^2 - \frac{\sigma_{\mathrm{L}}\sigma_{\mathrm{T}}}{\sigma_{\mathrm{Lu}}^2} + \left(\frac{\sigma_{\mathrm{LT}}}{\tau_{\mathrm{u}}}\right)^2 = 1$$

In the case of tension or compression off the principal material directions the TSAI-HILL criterion becomes

$$\left(\frac{\sigma_1 c^2}{\sigma_{\mathrm{Lu}}}\right)^2 + \left(\frac{\sigma_1 s^2}{\sigma_{\mathrm{Tu}}}\right)^2 - \left(\frac{\sigma_1 cs}{\sigma_{\mathrm{Lu}}}\right)^2 + \left(\frac{\sigma_1 sc}{\tau_{\mathrm{u}}}\right)^2 = 1$$

and the strength parameter $\sigma_{1\mathrm{u}}$ in x_1-direction is

$$\left(\frac{1}{\sigma_{1\mathrm{u}}}\right)^2 = \left(\frac{c^2}{\sigma_{\mathrm{Lu}}}\right)^2 + \left(\frac{s^2}{\sigma_{\mathrm{Tu}}}\right)^2 + \left(\frac{1}{\tau_{\mathrm{u}}^2} - \frac{1}{\sigma_{\mathrm{Lu}}^2}\right) c^2 s^2 \approx \left(\frac{c^2}{\sigma_{\mathrm{Lu}}}\right)^2 + \left(\frac{s^2}{\sigma_{\mathrm{Tu}}}\right)^2 + \left(\frac{cs}{\tau_{\mathrm{u}}^2}\right)^2$$

The approximated form presumes $\sigma_{\mathrm{Lu}} \gg \tau_{\mathrm{u}}$. The TSAI-HILL criterion is a single criterion instead of the three subcriteria required in maximum stress and strain theories.

Another suggestion for an anisotropic failure criterion was made by GOL'DENBLAT and KOPNOV (1968): the tensor polynomial criterion. TSAI and WU modified this criterion by assuming the existence of a failure surface in stress space. The general statement is that fracture of an anisotropic material occurs if

$$a_{ij}\sigma_{ij} + a_{ijkl}\sigma_{ij}\sigma_{kl} = 1$$

or in a contracted notation

$$a_i\sigma_i + a_{ij}\sigma_i\sigma_j = 1$$

For an orthotropic composite material one gets

$$a_{\mathrm{L}}\sigma_{\mathrm{L}} + a_{\mathrm{T}}\sigma_{\mathrm{T}} + a_{\mathrm{S}}\sigma_{\mathrm{S}} + a_{\mathrm{LL}}\sigma_{\mathrm{L}}^2 + a_{\mathrm{TT}}\sigma_{\mathrm{T}}^2 + a_{\mathrm{SS}}\sigma_{\mathrm{S}}^2 + 2(a_{\mathrm{LT}}\sigma_{\mathrm{L}}\sigma_{\mathrm{T}} + a_{\mathrm{LS}}\sigma_{\mathrm{L}}\sigma_{\mathrm{S}} + a_{\mathrm{TS}}\sigma_{\mathrm{T}}\sigma_{\mathrm{S}}) = 1$$

Here $\nu_{\mathrm{LT}} \equiv a_{\mathrm{S}}$.

In a similar way the VON MISES-HILL criterion can be introduced. Now the representation is made for the principal stress axes

$$E_1\sigma_1^2 + E_2\sigma_2^2 + E_3(\sigma_1 - \sigma_2)^2 + 2E_4\tau_{12}^2 = 1$$

$E_1, \ldots, E_4$ are material parameters. The first application of this criterion was made by NORRIS (1950). His formulation can be given as

$$\frac{\sigma_1^2}{\sigma_{\mathrm{u1}}} + \frac{\sigma_2^2}{\sigma_{\mathrm{u2}}} - \frac{\sigma_1\sigma_2}{\sigma_{\mathrm{u1}}\sigma_{\mathrm{u2}}} + \frac{\tau_{12}^2}{\tau_{\mathrm{u}}^2} = 1$$

Here $\sigma_{\mathrm{u1}}, \sigma_{\mathrm{u2}}$ are the tension strength in the principal direction 1 and 2, respectively. τ_{u} is the shear strength for the plane 1,2. The problem in application of this criterion is the identical behavior in the case of tension and compression (the principal axes are symmetry axes).

Another criterion for composites was introduced by ZAKHAROV (1961; 1963). The starting point is the 6-dimensional stress space

$$\sum_{i,j=1}^{6} \alpha_{ij}\omega_i\omega_j + \sum_{j=1}^{6} \beta_j\omega_j = 1$$

with $\omega_1, \omega_2, \omega_3$ as normal stresses and $\omega_4, \omega_5, \omega_6$ as shear stresses. α_{ij}, β_j are material parameters estimated by tension, compression and shear tests.

MALMEISTER (1966) also discussed a polynomial criterion

$$p_{\alpha\beta}\sigma_{\alpha\beta} + p_{\alpha\beta\gamma\delta}\sigma_{\alpha\beta}\sigma_{\gamma\delta} + \ldots = 1$$

The matrix representation can be given as

$$p_i\sigma_i + p_{ij}\sigma_i\sigma_j + \ldots = 1$$

In the plane stress state one obtains

$$p_1\sigma_1 + p_2\sigma_2 + p_6\sigma_6 + p_{11}\sigma_1^2 + p_{22}\sigma_2^2 + 2p_{12}\sigma_1\sigma_2 + 4p_{66}\sigma_6^2 + 4p_{16}\sigma_1\sigma_6 + 4p_{26}\sigma_2\sigma_6 = 1$$

Assuming the invariant form (no linear contribution of σ_6) one gets

$$p_1\sigma_1 + p_2\sigma_2 + p_{11}\sigma_1^2 + p_{22}\sigma_2^2 + 2p_{12}\sigma_1\sigma_2 + 4p_{66}\sigma_6^2 = 1$$

Let us now discuss the interactive tensor polynomial criterion of TSAI-WU. The linear terms take into account the actual differences between composite material behavior under tension and compression. The term $a_{\mathrm{LT}}\sigma_{\mathrm{L}}\sigma_{\mathrm{T}}$ represents independent interaction among the stresses σ_{L} and

σ_T and the remaining quadratic terms describe an ellipsoid in stress space. Since the strength of a lamina loaded under pure shear stress τ_S in the on-axis system is independent of the sign of the shear stress, all linear terms in σ_S must vanish

$$a_S = a_{LS} = a_{TS} = 0$$

The TSAI-WU criterion for a single layer in on-axis system can be expressed as

$$a_L\sigma_L + a_T\sigma_T + a_{LL}\sigma_L^2 + a_{TT}\sigma_T^2 + a_{SS}\sigma_S^2 + 2a_{LT}\sigma_L\sigma_T = 1$$

The four quadratic terms correspond to the four independent elastic characteristics of orthotropic materials, the linear terms allow the distinction between tensile and compressive strength. The coefficients of the quadratic TSAI-WU criterion are obtained by applying elementary basic loading conditions to the lamina

$$\begin{array}{l}\sigma_L = \sigma_{Lt}, \quad \sigma_T = \sigma_S = 0 \\ \sigma_L = -\sigma_{Lc}, \quad \sigma_T = \sigma_S = 0\end{array} \quad \Rightarrow \quad \begin{array}{l}a_L\sigma_{Lt} + a_{LL}\sigma_{Lt}^2 = 1 \\ -a_L\sigma_{Lc} + a_{LL}\sigma_{Lc}^2 = 1\end{array} \quad \Rightarrow \quad \begin{array}{l}a_L = \dfrac{1}{\sigma_{Lt}} - \dfrac{1}{\sigma_{Lc}} \\ a_{LL} = \dfrac{1}{\sigma_{Lt}\sigma_{Lc}}\end{array}$$

$$\begin{array}{l}\sigma_T = \sigma_{Tt}, \quad \sigma_L = \sigma_S = 0 \\ \sigma_T = -\sigma_{Tc}, \quad \sigma_L = \sigma_S = 0\end{array} \quad \Rightarrow \quad \begin{array}{l}a_T\sigma_{Tt} + a_{TT}\sigma_{Tt}^2 = 1 \\ -a_T\sigma_{Tc} + a_{TT}\sigma_{Tc}^2 = 1\end{array} \quad \Rightarrow \quad \begin{array}{l}a_T = \dfrac{1}{\sigma_{Tt}} - \dfrac{1}{\sigma_{Tc}} \\ a_{TT} = \dfrac{1}{\sigma_{Tt}\sigma_{Tc}}\end{array}$$

$$\sigma_S = \tau_S, \quad \sigma_L = \sigma_T = 0 \quad \Rightarrow \quad a_{SS}\tau_S^2 = 1 \quad \Rightarrow \quad a_{SS} = \frac{1}{\tau_S^2}$$

The remaining coefficient a_{LT} must be obtained by biaxial testing

$$\sigma_L = \sigma_T = \sigma_U, \quad \sigma_S = 0 \quad \Rightarrow \quad (a_L + a_T)\sigma_U + (a_{LL} + a_{TT} + 2a_{LT})\sigma_U^2 = 1$$

σ_U is the experimentally measured strength under identical biaxial tensile loading $\sigma_L = \sigma_T$. In many cases the interaction coefficient is not critical and is given approximately, e.g.

$$a_{LT} \approx -\frac{1}{2}\sqrt{a_{LL}a_{TT}}$$

Summarizing the considerations on interactive failure criteria leads to the conclusion that the TSAI-HILL and the TSAI-WU failure criteria are quadratic interaction criteria which have the general form

$$F_{ij}\sigma_i\sigma_j + F_i\sigma_i = 1, \quad i,j = \mathrm{L,T,S}$$

F_{ij} and F_i are strength parameters and σ_i, σ_j the on axis stress components. For plane stress state six strength parameters $F_{LL}, F_{TT}, F_{SS}, F_{LT}, F_L, F_T$ have to be implemented into the failure criterion, $F_{LS} = F_{TS} = F_S = 0$. Five of these strength parameters are conventional tensile, compressive or shear strength terms which can be measured in a conventional experimental test programme. The strength parameter F_{LT} is more difficult to obtain, since a biaxial test is necessary and such a test is not easy to perform. The two-dimensional representation of the general quadratic criterion in the stress space can be given in the equation below

$$\frac{\sigma_L^2}{\sigma_{Lt}\sigma_{Lc}} + \frac{\sigma_T^2}{\sigma_{Tt}\sigma_{Tc}} + \frac{\sigma_{LT}^2}{\tau_S^2} + 2F_{LT}\sigma_L\sigma_T + \left(\frac{1}{\sigma_{Lt}} - \frac{1}{\sigma_{Lc}}\right)\sigma_L + \left(\frac{1}{\sigma_{Tt}} - \frac{1}{\sigma_{Tc}}\right)\sigma_T = 1$$

The general form is reduced, e.g., for

$$\sigma_{\mathrm{Lt}} = \sigma_{\mathrm{Lc}}, \quad \sigma_{\mathrm{Tt}} = \sigma_{\mathrm{Tc}}, \quad F_{\mathrm{LT}} = -\frac{1}{2\sigma_{\mathrm{Lt}}^2}$$

to the TSAI-HILL criterion, for

$$\sigma_{\mathrm{Lt}} \neq \sigma_{\mathrm{Lc}}, \quad \sigma_{\mathrm{Tt}} \neq \sigma_{\mathrm{Tc}}, \quad F_{\mathrm{LT}} = -\frac{1}{2\sigma_{\mathrm{Lt}}\sigma_{\mathrm{Lc}}}$$

to the HOFFMAN criterion, and for

$$\sigma_{\mathrm{Lt}} \neq \sigma_{\mathrm{Lc}}, \quad \sigma_{\mathrm{Tt}} \neq \sigma_{\mathrm{Tc}}, \quad F_{\mathrm{LT}} = -\frac{1}{2\sqrt{\sigma_{\mathrm{Lt}}\sigma_{\mathrm{Lc}}\sigma_{\mathrm{Tt}}\sigma_{\mathrm{Tc}}}}$$

to the TSAI-WU criterion. HOFFMAN's criterion is a simple generalization of the HILL criterion that allows different tensile and compressive strength parameters. Using the dimensionless stresses

$$\sigma_{\mathrm{L}}^* = \sqrt{F_{\mathrm{LL}}}\sigma_{\mathrm{L}}, \quad \sigma_{\mathrm{T}}^* = \sqrt{F_{\mathrm{TT}}}\sigma_{\mathrm{T}}, \quad \sigma_{\mathrm{LT}}^* = \sqrt{F_{\mathrm{SS}}}\sigma_{\mathrm{LT}}$$

and the normalized strength coefficients

$$F_{\mathrm{L}}^* = F_{\mathrm{L}}/\sqrt{F_{\mathrm{LL}}}, \quad F_{\mathrm{T}}^* = F_{\mathrm{T}}/\sqrt{F_{\mathrm{T}}}, \quad F_{\mathrm{LT}}^* = F_{\mathrm{LT}}/\sqrt{F_{\mathrm{LL}}F_{\mathrm{TT}}}$$

one gets

$$\sigma_{\mathrm{L}}^{*2} + \sigma_{\mathrm{T}}^{*2} + \sigma_{\mathrm{LT}}^{*2} + 2F_{\mathrm{LT}}^*\sigma_{\mathrm{L}}^*\sigma_{\mathrm{T}}^{*2} + F_{\mathrm{L}}^*\sigma_{\mathrm{L}}^{*2} + F_{\mathrm{T}}^*\sigma_{\mathrm{T}}^{*2} = 1$$

For isotropic materials with $\sigma_{\mathrm{Lt}} = \sigma_{\mathrm{Lc}} = \sigma_{\mathrm{Tt}} = \sigma_{\mathrm{Tc}}$ follows $F_{\mathrm{L}}^* = F_{\mathrm{T}}^* = 0$. For the principal stress state $\sigma_{\mathrm{LT}}^* = \sigma_{\mathrm{LT}} = 0$ is valid. A reducing with $F_{\mathrm{LT}}^* = -\frac{1}{2}$ leads to the known VON MISES criterion.

5.3 Generalized Criteria

Considering classical and non-classical material behavior (Altenbach et al., 1995, 1999) the following statements can be given. The classical material behavior equations are based on several assumptions:

- identical behavior under tension and compression,
- the identity of the equivalent stress-equivalent strain diagrams in the case of tension and torsion,
- the independence of the inelastic material behavior from hydrostatic pressure,
- etc.

If we ignore one or more of these assumptions the mathematical expressions of the constitutive equations and the limit conditions must reflect non-classical effects.

The classical approach of formulating a limit state criterion is connected with the following items: the stress state in the material or in a structural element will be represented by the stress tensor $\boldsymbol{\sigma}$, based on the stress tensor one can construct an equivalent stress $\sigma_{\mathrm{eq}} = F(\boldsymbol{\sigma})$, this equivalent stress will be compared with an experimental limit value by $\sigma_{\mathrm{eq}} \leq \sigma_{\mathrm{limit}}^{\mathrm{exp}}$ ($\sigma_{\mathrm{limit}}^{\mathrm{exp}}$ is a material characteristic for the description of the limit case). This approach is not restricted by the assumed limit state of the material and can be extended to the non-classical cases.

For the classical material behavior one assumes

$$\sigma^{\exp}_{\text{limit}}(\text{Tension}) \approx -\sigma^{\exp}_{\text{limit}}(\text{Compression}), \quad \sigma^{\exp}_{\text{limit}}(\text{Tension}) \approx \pm\sqrt{3}\tau^{\exp}_{\text{limit}}(\text{Torsion})$$

and the influence of the hydrostatic pressure can be ignored.

Non-classical behavior is named the material behavior if different behavior in tension and compression is obtained. The strength-differential effect is well known

$$\sigma^{\exp}_{\text{limit}}(\text{Tension}) \approx -0,9\sigma^{\exp}_{\text{limit}}(\text{Compression})$$

In addition, the material behavior is called non-classically if the tension behavior cannot be described by torsion tests (experimentally observed for some polymers, graphite, etc.), since a fixed relation between both states cannot be established, etc. Several experimental results manifest non-classical behavior, an overview is given, for example, by Altenbach et al. (1995).

Let us formulate generalized limit criteria which are able to reflect non-classical effects of the material behavior. The first one is based on three basic invariants of the stress tensor (see, for example, Życzkowski (1981)) and is more suitable for ductile materials. The second one is based on the NOVOZHILOV's invariants, Novozhilov (1951), and is suitable for a satisfying description of the loss of stiffness which is more characteristic for brittle materials. In both cases we assume monotonic quasi-static loading under isothermal conditions, isotropic material behavior, non-polar material, stress based criteria presuming an equivalent stress $\sigma_{\text{eq}} \geq 0$.

Let us introduce the invariants. The basic invariants are

$$I_1(\boldsymbol{\sigma}) = \boldsymbol{\sigma} \cdot\cdot \boldsymbol{I}, \quad I_2(\boldsymbol{\sigma}) = \boldsymbol{\sigma} \cdot\cdot \boldsymbol{\sigma}, \quad I_3(\boldsymbol{\sigma}) = (\boldsymbol{\sigma} \cdot \boldsymbol{\sigma}) \cdot\cdot \boldsymbol{\sigma} \tag{5.1}$$

The NOVOZHILOV's invariants can be introduced as

$$I_1(\boldsymbol{\sigma}) = \boldsymbol{\sigma} \cdot\cdot \boldsymbol{I}, \quad \sigma_{\text{vM}} = \sqrt{\frac{3}{2}\boldsymbol{s} \cdot\cdot \boldsymbol{s}}, \quad \sin 3\xi = -\frac{27}{2}\frac{\det \boldsymbol{s}}{\sigma^3_{\text{vM}}} \quad \text{with} \quad |\xi| \leq \frac{\pi}{6} \tag{5.2}$$

with $\boldsymbol{s}$ as the stress deviator. Using these invariants two 6-parameter criteria can be formulated:

- using the basic invariants $I_1(\boldsymbol{\sigma}), I_2(\boldsymbol{\sigma}), I_3(\boldsymbol{\sigma})$

$$\sigma_{\text{eq}} = \sigma_1 + \sigma_2 + \sigma_3 = \mu_1 I_1 + \sqrt{\mu_2 I_1^2 + \mu_3 I_2} + \sqrt[3]{\mu_4 I_1^3 + \mu_5 I_1 I_2 + \mu_6 I_3} \tag{5.3}$$

- using the NOVOZHILOV's invariants $I_1(\boldsymbol{\sigma}), \sigma_{vM}(\boldsymbol{\sigma}), \xi(\boldsymbol{\sigma})$

$$\sigma_{\text{eq}} = \lambda_1 \sigma_{\text{vM}} \sin\xi + \lambda_2 \sigma_{\text{vM}} \cos\xi + \lambda_3 \sigma_{\text{vM}} + \lambda_4 I_1 + \lambda_5 I_1 \sin\xi + \lambda_6 I_1 \cos\xi \tag{5.4}$$

In both cases one gets as a special case the VON MISES-criterion. The unknown parameters μ_i and λ_i must be specified.

The identification can be performed as follows. As an example we show the identification for the criterion based on the NOVOZHILOV's invariants. In this case one can perform the following tests:

1. uniaxial tension $\sigma_{11} > 0$

$$\sigma_{11} = \sigma_{\text{T}}$$

σ_{T} is the limit stress in tension.

2. uniaxial compression $\sigma_{11} < 0$

$$\sigma_{11} = -\sigma_{\mathrm{C}}$$

σ_{C} is the limit stress in compression.

3. torsion $\sigma_{12} \neq 0$

$$\sigma_{12} = \tau_{\mathrm{L}}$$

τ_{L} is the limit stress in torsion.

4. thin-walled tube under inner pressure

$$\sigma_{11} = \frac{\sigma_{\mathrm{B}}}{2}, \quad \sigma_{22} = \sigma_{\mathrm{B}}$$

with

$$\sigma_{\mathrm{B}} = \frac{pR}{h}$$

p is the inner pressure, R the radius of the tube and h the tube thickness. From this follows $2\sigma_{11} = \sigma_{22} = \sigma_{\mathrm{B}}$ and σ_{B} plays the role of a limit stress.

5. thin-walled tube under inner pressure and tension

$$\sigma_{11} = \frac{F}{A} + \frac{\sigma_{\mathrm{t}}}{2}, \quad \sigma_{22} = \sigma_{\mathrm{t}}$$

with the tensile force F and

$$\sigma_{\mathrm{t}} = \frac{pR}{h}$$

The tensile force and the inner pressure are controlled by the limit stress σ_{E}

$$\sigma_{11} = \sigma_{22} = \sigma_{\mathrm{E}}$$

6. uniaxial tension in a high pressure chamber

$$\sigma_{11} = \frac{F}{A} - p, \quad \sigma_{22} = \sigma_{33} = -p$$

The pressure and the tensile force are controlled by the limit stress σ_{H}

$$\sigma_{11} = \frac{2}{3}\sigma_{\mathrm{H}}, \quad \sigma_{22} = \sigma_{33} = -\frac{1}{3}\sigma_{\mathrm{H}}$$

As a result of the tests one estimates the limit stresses $\sigma_{\mathrm{T}}, \sigma_{\mathrm{C}}, \tau_{\mathrm{L}}, \sigma_{\mathrm{B}}, \sigma_{\mathrm{E}}$ and σ_{H}.

The mathematical analysis of these tests results in

1. uniaxial tension

$$-\lambda_1 + \sqrt{3}\lambda_2 + 2\lambda_3 + 2\lambda_4 - \lambda_5 + \sqrt{3}\lambda_6 = 2$$

2. uniaxial compression

$$\lambda_1 + \sqrt{3}\lambda_2 + 2\lambda_3 - 2\lambda_4 - \lambda_5 - \sqrt{3}\lambda_6 = 2\frac{\sigma_{\mathrm{T}}}{\sigma_{\mathrm{C}}}$$

3. torsion

$$\lambda_2 + \lambda_3 = \frac{\sigma_T}{\sqrt{3}\tau_L}$$

4. thin-walled tube under inner pressure

$$\sqrt{3}\lambda_2 + \sqrt{3}\lambda_3 + 3\lambda_4 + 3\lambda_6 = 2\frac{\sigma_T}{\sigma_B}$$

5. thin-walled tube under inner pressure and tension force

$$\lambda_1 + \sqrt{3}\lambda_2 + 2\lambda_3 + 4\lambda_4 + 2\lambda_5 + 2\sqrt{3}\lambda_6 = 2\frac{\sigma_T}{\sigma_E}$$

6. uniaxial tension in a high pressure chamber

$$-\lambda_1 + \sqrt{3}\lambda_2 + 2\lambda_3 = 2\frac{\sigma_T}{\sigma_H}$$

Solving the last six equations with respect to the unknown coefficients λ_i one obtains

$$\begin{aligned}
\lambda_1 &= \frac{1}{3}\left(2\frac{\sigma_T}{\sigma_C} - 3\frac{\sigma_T}{\sigma_H} + \frac{\sigma_T}{\sigma_E}\right),\\
\lambda_2 &= -\frac{1}{3(2-\sqrt{3})}\left(2\frac{\sigma_T}{\sigma_C} - 2\sqrt{3}\frac{\sigma_T}{\tau_L} + 3\frac{\sigma_T}{\sigma_H} + \frac{\sigma_T}{\sigma_E}\right),\\
\lambda_3 &= \frac{1}{3(2-\sqrt{3})}\left(2\frac{\sigma_T}{\sigma_C} - 3\frac{\sigma_T}{\tau_L} + 3\frac{\sigma_T}{\sigma_H} + \frac{\sigma_T}{\sigma_E}\right),\\
\lambda_4 &= \frac{1}{3(2-\sqrt{3})}\left(3 - \frac{\sigma_T}{\sigma_C} + \sqrt{3}\frac{\sigma_T}{\tau_L} - 2\sqrt{3}\frac{\sigma_T}{\sigma_B} - 3\frac{\sigma_T}{\sigma_H} + \frac{\sigma_T}{\sigma_E}\right),\\
\lambda_5 &= -\frac{1}{3}\left(3 + \frac{\sigma_T}{\sigma_C} - 3\frac{\sigma_T}{\sigma_H} - \frac{\sigma_T}{\sigma_E}\right),\\
\lambda_6 &= -\frac{1}{3(2-\sqrt{3})}\left(3 - \frac{\sigma_T}{\sigma_C} + 2\frac{\sigma_T}{\tau_L} - 4\frac{\sigma_T}{\sigma_B} - 3\frac{\sigma_T}{\sigma_H} + \frac{\sigma_T}{\sigma_E}\right)
\end{aligned}$$

From this system we can make the following conclusions:

- If one can perform the six tests and estimate the material properties $\sigma_T, \sigma_C, \tau_L, \sigma_B, \sigma_E, \sigma_H$ the coefficients λ_i can be established in a unique way.
- By changing the tests and estimating other material properties one gets other coefficients. An example is given in Altenbach et al. (1993). The choice of the basic tests is connected with technical feasibilities in the laboratories, with the kind of material, with the kind of loading conditions, etc., Altenbach & Zolochevsky (1996).
- In addition, fixing the λ_i one can find the needful conditions for the practical use of special criteria.

The last item can be explained as follows. For example, from the generalized criterion (5.4) the VON MISES-criterion can be deduced setting $\lambda_1 = \lambda_2 = \lambda_4 = \lambda_5 = \lambda_6 = 0, \lambda_3 = 1$. Taking into account these values one can calculate the relations for the material properties

$$\frac{\sigma_T}{\sigma_C} = 1, \quad \frac{\sigma_T}{\tau_L} = \sqrt{3}, \quad \frac{\sigma_T}{\sigma_B} = \frac{1}{2}\sqrt{3}, \quad \frac{\sigma_T}{\sigma_E} = 1, \quad \frac{\sigma_T}{\sigma_H} = 1$$

If these relations are fulfilled the use of the VON MISES-criterion can be recommended. That means a material must show a behavior which is connected with identical properties in tension and compression and a fixed relation between the tension and the shear limit stress. The last statement is a standard statement in several textbooks on solid mechanics and agrees with experimental results, see e.g. Kachanov (1974).

5.4 Outlook

The use of limit criteria is till now under discussion. The reason for this is that the designer want to predict the safety of structures in the early stage of the design process. For this purpose extensions of classical strength and limit criteria can be recommended. The problem is that in contrast to the case of classical structural materials not only one failure mode must taken into account. That means in some cases for composite materials an unique criterion cannot be applied. Considering polymer and composite materials on the application of the generalized criteria is reported, for example, in Altenbach et al. (1996); Altenbach & Zolochevsky (1996), on some improvements in Altenbach & Tushtev (2001).

6 Polymer Suspensions

6.1 Introductional Remarks

Let us now discuss the mechanical behavior of polymers reinforced with short glass fibers. An example of such a material is DuPont Zytel® PA66ZYTEL 70G43L with a polyamide matrix. The typical geometrical and mechanical properties are shown in Fig. 18. With the fiber length l

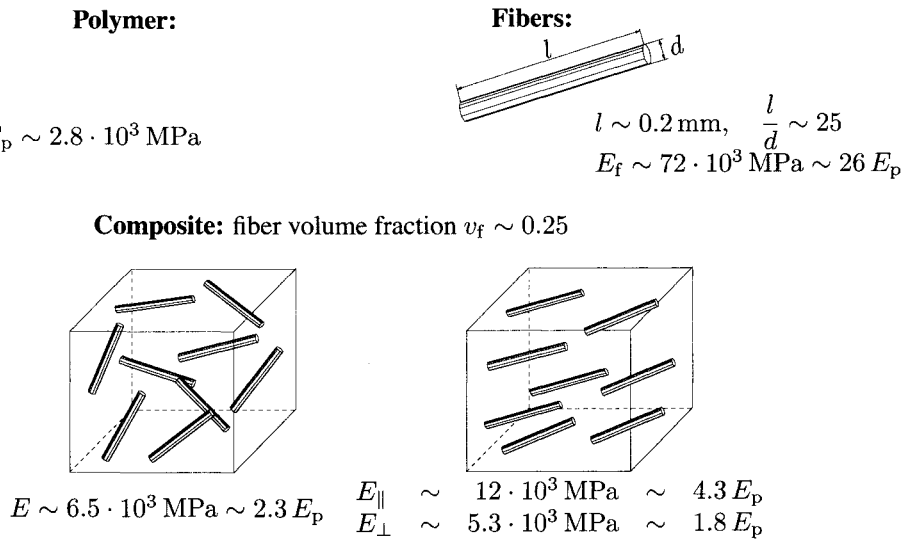

Figure 18. Example of a short fiber reinforced material

and the fiber diameter d one gets for the given material a fiber length to diameter ratio of about 25. In addition, it must be noted that the YOUNG's moduli of the fiber E_{f} and the polymer matrix E_{p} are quite different (the modulus of the fibers is 26 times higher). With respect to this difference the effective mechanical behavior is different: if one obtains an arbitrary distribution of the fibers an isotropic behavior can be assumed, otherwise for the regular distribution as shown in Fig. 18 on the right hand side we get transversally isotropic behavior. For a fiber volume fraction v_{f} of about 25 % the isotropic modulus E ranges between the moduli for the direction parallel to the fiber $E_{\|}$ and the direction perpendicular to the fibers $E_{\perp}$. The geometrical and the mechanical properties of the fibers and the matrix material assumed here were taken from the data basis of the commercial code Moldflow Plastic Inside®. On the application of this material is reported, for example, in Glaser & von Diest (1988), Michaeli (1995) and Whiteside et al. (2000).

Thin-walled structural elements based on particle reinforced composites are manufactured, for example, by injection molding. This technology has a number of advantages compared with other manufacturing techniques: short cycle time of the manufacturing, high degree of automatization, excellent possibilities of manufacturing structural elements with complex geometries. In addition, the injection molding technology allows to improve the stiffness and strength properties of the composite by changing the technological conditions like the temperature, the injection pressure, the injection point, etc. The basic steps of the injection molding technology are shown in Fig. 19 (after Michaeli (1995), Menning (1995) and Altenbach et al. (2003b)).

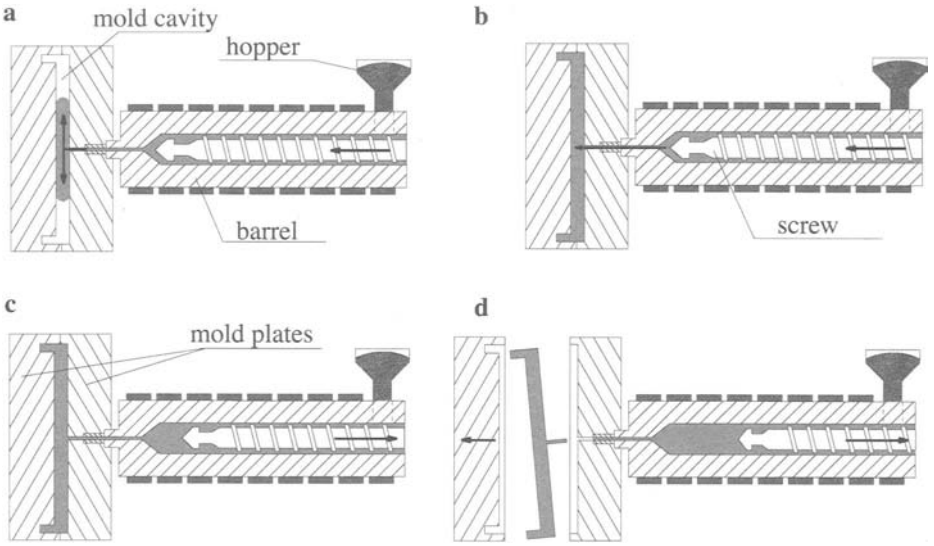

Figure 19. Basic stages of the injection molding processing cycle. **a** filling stage, **b** packing stage, **c** cooling stage, **d** ejection

The mechanical properties of a particle reinforced composite depend significantly on the orientation of the fibers during its manufacture process. During the filling stage the flow translates and rotates the fibers. As a result the distribution of the fibers becomes nonuniform and the overall stiffness characteristics are anisotropically. There are a lot of influence factors like the

viscosity of the polymer melt, the filling conditions, the geometry of the cavity, and so on (Hegler (1984)). All these features must be taken into account during the design process and even then the estimation of the distribution of the reinforcement is possible and the degree of anisotropy can be predicted. The microstructure of the composite is formed during the filling and the established microstructure remains the same after solidification (see, for example, Hegler (1984), Bay & Tucker (1992) and Vincent & Agassant (1986)). Micrographs of the cross section of moldings (Bay & Tucker (1992), Saito et al. (2000)) show that the orientation pattern of fibers has a layered structure. In the core layer, the fibers are oriented predominantly perpendicular to the flow direction. In contrast, in the skin layers close to the mold wall they are oriented mainly parallel to the flow direction. Finally, in the neighborhood to the wall lower fiber concentration and a random orientation can be observed. An example of such a micrograph is presented in Fig. 20.

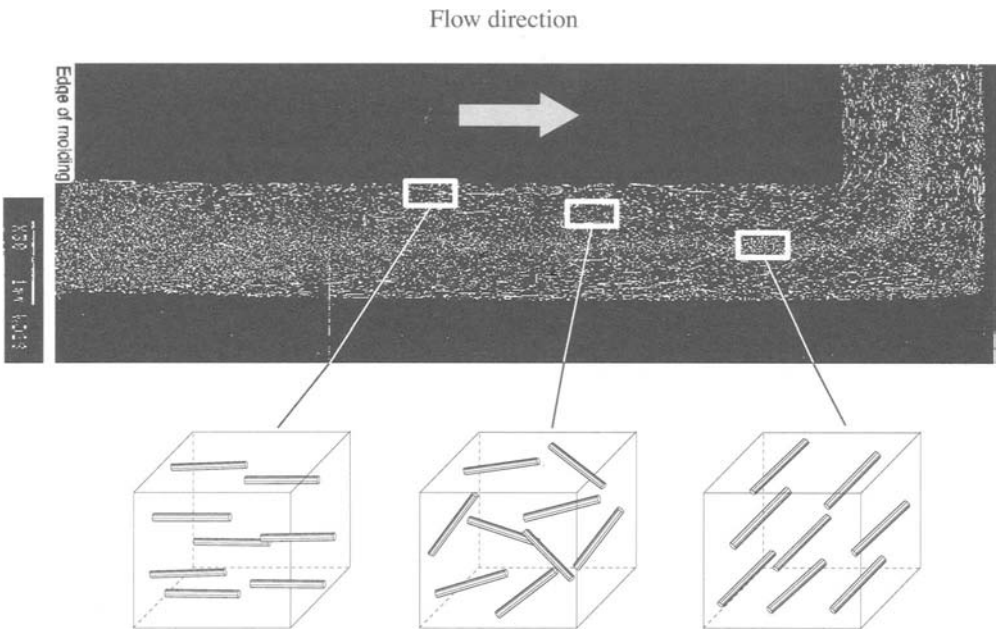

Figure 20. Section of injection molded part (after Saito et al. (2000))

The conditions of the flow of polymer suspensions is discussed in detail by Altenbach et al. (2003b), Dupret & Verleye (1999) and Tucker & Advani (1994). Let us summarize the main items:

- non-isothermal flow with phase transitions,
- non-stationary flow with free surfaces,
- the average volume content of particles is 15 - 45 %, and the local concentration of fibers can vary within the flow region, and
- since the mold cavity is usually thin, its walls affect the movement of fibers considerably.

All these factors play an important role in the design process since the formation of the microstructure (or with other words the arrangement of the fibers) is influenced by them. However,

we do not know of any theory which takes into account all these items mentioned above.

The existing theories can be divided into two classes. The first group includes models based on the concept of an "anisotropic viscous medium". The presence of fibers and their local orientation are taken into account only in the constitutive equations by introducing orientation tensors (see, for example, Dupret et al. (1999), Tucker & Advani (1994) and Dupret & Verleye (1999)). The second group can be related to the so-called micropolar theories, which are based on the assumption of a continuum with independent rotational degrees of freedom (see Altenbach et al. (2003b) or Eringen (2001)). The first approach is the basis of the commercial software Moldflow Plastics Insight® (MPI), which allows to model the complete cycle of the injection molding process. As a result one can determine the particle orientation. The injection molding simulation can be combined with a Finite-Element-Analysis and the stress-strain estimation can be performed. Below this approach will be discussed in detail. Finally some examples are presented.

6.2 Modelling of the microstructure based on Moldflow Plastics Insight®

Let us briefly present the approach realized in the MPI program complex. For details we refer to Tucker & Advani (1994), Dupret et al. (1999) and Dupret & Verleye (1999). The suspension is modelled as a quasi-homogeneous anisotropic medium. According to this approach, the main problem is the formulation of a rheological equation allowing to relate the stresses caused by the liquid flow to local characteristics of the motion $\boldsymbol{V}$ (velocity vector of the particles). For a slow motion of a viscous liquid can be assumed (cp. Batchelor (1970))

$$\boldsymbol{\sigma} = -p\boldsymbol{E} + {}^{(4)}\boldsymbol{\mu} \cdot\cdot\, \boldsymbol{\Lambda}, \quad \boldsymbol{\Lambda} = \boldsymbol{\nabla V}, \tag{6.1}$$

where p is the pressure in the medium and ${}^{(4)}\boldsymbol{\mu}$ is the fourth-rank viscosity tensor. The determination of the viscosity tensor is discussed in the review on suspension rheology published by PETRIE (1999) and in the monograph by Huilgol & Phan-Thien (1997). The applied approach is based on the method of orientational averaging.

As an example, we will consider the model for describing semiconcentrated suspensions (cp. Dinh & Armstrong (1984))

$$\boldsymbol{\sigma} = -p\boldsymbol{E} + \mu(\boldsymbol{\Lambda} + \boldsymbol{\Lambda}^{\mathrm{T}}) \cdot\cdot \left[{}^{(4)}\boldsymbol{E} + \frac{nl^2}{12\mu}\zeta_{\mathrm{p}}\, {}^{(4)}\boldsymbol{A} \right] \tag{6.2}$$

n is the number of fibers in a unit volume, l the length of fibers, μ the polymer viscosity, ζ_{p} an empirical coefficient determined as

$$\zeta_{\mathrm{p}} = \frac{2\pi\mu l}{\ln(2h/d)},$$

where d is the fiber diameter, $h = (nl)^{-1/2}$ for oriented fibers and $h = (nl^2)^{-1}$ for a random orientation. The fourth-rank tensor ${}^{(4)}\boldsymbol{A}$ represents the current fiber orientation

$${}^{(4)}\boldsymbol{A} = \int_{(A)} \Psi(\boldsymbol{m})\boldsymbol{m} \otimes \boldsymbol{m} \otimes \boldsymbol{m} \otimes \boldsymbol{m} dA, \tag{6.3}$$

$\Psi(\boldsymbol{m})$ is the distribution density of the fiber orientation, $\boldsymbol{m}$ the unit vector along the particle axis, dA the differential element on the unit sphere. For the orientation density one can write (cp. Doi

& Edwards (1988) and Tucker & Advani (1994))

$$\dot{\Psi} + \nabla_A \cdot (\Psi \boldsymbol{\omega} - d_r \nabla_A \Psi) = 0 \tag{6.4}$$

$\boldsymbol{\omega}$ is the angular velocity of a particle, d_r the empirical coefficient of rotational diffusion, $\dot{(\ldots)}$ the material derivative and ∇_A the tangential differential operator on the unit sphere

$$\nabla_A(\ldots) = \boldsymbol{e}_k \epsilon_{ijk} m_i \frac{\partial(\ldots)}{\partial m_j}, \quad \boldsymbol{m} \cdot \boldsymbol{m} = 1$$

ϵ_{ijk} denotes the LEVI-CIVITA symbol. For $\boldsymbol{\omega}$ the JEFFERY-solution can be assumed, Jeffery (1922), which was obtained as the angular velocity with which an ellipsoidal particle rotates in an infinite field of a viscous liquid. For an ellipsoid of revolution one gets (Altenbach et al. (2003b))

$$\boldsymbol{\omega} = (\boldsymbol{\phi} + \lambda \boldsymbol{m} \times \boldsymbol{D} \cdot \boldsymbol{m}), \quad \lambda = \frac{a^2 - b^2}{a^2 + b^2}, \tag{6.5}$$

a and b are the semi-axes of the ellipsoid, $\boldsymbol{D}$ the strain rate tensor and $\boldsymbol{\phi}$ the spin vector of the undisturbed flow. For the strain rate tensor $\boldsymbol{D}$ one can consider

$$\boldsymbol{D} = \frac{1}{2}(\nabla \boldsymbol{V} + \nabla \boldsymbol{V}^{\mathrm{T}}), \quad \mathrm{tr} \nabla \boldsymbol{V} = 0, \quad \boldsymbol{\phi} = -\frac{1}{2} \nabla \times \boldsymbol{V}$$

The moments of the distribution function $\Psi(\boldsymbol{m})$ are defined as

$$^{(n)}\boldsymbol{A} = \int_{(A)} \Psi(\boldsymbol{m}) \boldsymbol{m}^{\otimes n} dA, \quad n = 2, 4, \ldots$$

$^{(n)}\boldsymbol{A}$ denotes the nth rank orientation tensor, $(\ldots)^{\otimes n}$ is the nth tensor product. Equation (6.4) with regard to the angular velocity (6.5) is transformed into an infinite system of coupled equations. The first two equations of the infinite system of coupled equations are

$$\begin{aligned}
^{(2)}\dot{\boldsymbol{A}} &= {}^{(2)}\boldsymbol{A} \cdot \boldsymbol{W} - \boldsymbol{W} \cdot {}^{(2)}\boldsymbol{A} + \lambda(\boldsymbol{D} \cdot {}^{(2)}\boldsymbol{A} + {}^{(2)}\boldsymbol{A} \cdot \boldsymbol{D} - 2\,{}^{(4)}\boldsymbol{A} \cdot\cdot \boldsymbol{D}) - 6 d_r \left({}^{(2)}\boldsymbol{A} - \frac{1}{3}\boldsymbol{E} \right), \\
^{(4)}\dot{\boldsymbol{A}} &= {}^{(4)}\boldsymbol{A} \cdot \boldsymbol{W} - \boldsymbol{W} \cdot {}^{(4)}\boldsymbol{A} + \lambda(\boldsymbol{D} \cdot {}^{(4)}\boldsymbol{A} + {}^{(4)}\boldsymbol{A} \cdot \boldsymbol{D} - 4\,{}^{(6)}\boldsymbol{A} \cdot\cdot \boldsymbol{D}) \\
&- \boldsymbol{e}_i \otimes \boldsymbol{W} \cdot {}^{(4)}\boldsymbol{A} \cdot \boldsymbol{e}_i + \boldsymbol{e}_i \cdot {}^{(4)}\boldsymbol{A} \cdot \boldsymbol{W} \otimes \boldsymbol{e}_i \\
&+ \lambda \left(\boldsymbol{e}_i \otimes \boldsymbol{D} \cdot {}^{(4)}\boldsymbol{A} \cdot \boldsymbol{e}_i + \boldsymbol{e}_i \cdot {}^{(4)}\boldsymbol{A} \cdot \boldsymbol{D} \otimes \boldsymbol{e}_i \right) + 2 d_r \left(\boldsymbol{E} \otimes {}^{(2)}\boldsymbol{A} \right. \\
&+ {}^{(2)}\boldsymbol{A} \otimes \boldsymbol{E} + {}^{(2)}\boldsymbol{A} \cdot \boldsymbol{e}_k \otimes \boldsymbol{E} \otimes \boldsymbol{e}_k + \boldsymbol{e}_k \otimes {}^{(2)}\boldsymbol{A} \otimes \boldsymbol{e}_k \\
&+ \left. {}^{(2)}\boldsymbol{A} \cdot \boldsymbol{e}_i \otimes \boldsymbol{e}_k \otimes \boldsymbol{e}_i \otimes \boldsymbol{e}_k + \boldsymbol{e}_i \otimes \boldsymbol{e}_k \otimes \boldsymbol{e}_i \otimes \boldsymbol{e}_k \cdot {}^{(2)}\boldsymbol{A} - 10\,{}^{(4)}\boldsymbol{A} \right)
\end{aligned}$$

$\boldsymbol{W} = \boldsymbol{\phi} \times \boldsymbol{E}$ is the flow vorticity tensor. The two equations are presented in Advani & Tucker (1987) in the coordinate form. In practical calculations $^{(2)}\boldsymbol{A}$ is usually found from the first evolution equation and $^{(4)}\boldsymbol{A}$ from the closure approximation. Mostly used is the hybrid closure

approximation which is incorporated in the MPI code

$$
\begin{aligned}
{}^{(4)}\boldsymbol{A} &\approx (1-f)\,{}^{(4)}\boldsymbol{A}^{\mathrm{L}} + f\,{}^{(4)}\boldsymbol{A}^{\mathrm{Q}}, \quad f = 1 - 27\det {}^{(2)}\boldsymbol{A}, {}^{(4)}\boldsymbol{A}^{\mathrm{Q}} = {}^{(2)}\boldsymbol{A} \otimes {}^{(2)}\boldsymbol{A}, \\
{}^{(4)}\boldsymbol{A}^{\mathrm{L}} &= \frac{1}{7}\Big(\boldsymbol{E} \otimes {}^{(2)}\boldsymbol{A} + {}^{(2)}\boldsymbol{A} \otimes \boldsymbol{E} + {}^{(2)}\boldsymbol{A} \cdot \boldsymbol{e}_k \otimes \boldsymbol{E} \otimes \boldsymbol{e}_k + \boldsymbol{e}_k \otimes {}^{(2)}\boldsymbol{A} \otimes \boldsymbol{e}_k \\
&\quad + {}^{(2)}\boldsymbol{A} \cdot \boldsymbol{e}_i \otimes \boldsymbol{e}_k \otimes \boldsymbol{e}_i \otimes \boldsymbol{e}_k + \boldsymbol{e}_i \otimes \boldsymbol{e}_k \otimes \boldsymbol{e}_i \otimes \boldsymbol{e}_k \cdot {}^{(2)}\boldsymbol{A}\Big) \\
&\quad + \frac{1}{35}\left(\boldsymbol{E} \otimes \boldsymbol{E} + \boldsymbol{e}_k \otimes \boldsymbol{E} \otimes \boldsymbol{e}_k + \boldsymbol{e}_i \otimes \boldsymbol{e}_k \otimes \boldsymbol{e}_i \otimes \boldsymbol{e}_k\right)
\end{aligned}
$$

Finally, let us summarize the governing equations for the filling stage:

- the balance of momentum

$$\rho \frac{D}{Dt}\boldsymbol{V} = \rho \boldsymbol{f} + \boldsymbol{\nabla}\cdot\boldsymbol{\sigma}$$

- the balance of mass

$$\rho = \text{const} \quad \Longrightarrow \quad \boldsymbol{\nabla}\cdot\boldsymbol{V} = 0$$

- the energy balance

$$\rho c_p \frac{DT}{Dt} = \boldsymbol{\sigma} \cdot\cdot\, \boldsymbol{\nabla}\boldsymbol{V} + \boldsymbol{\nabla}\cdot(k\boldsymbol{\nabla}T)$$

- the constitutive equation
- the evolution equation for the structure tensors ${}^{(2)}\boldsymbol{A}$
- the closure approximation for the tensor ${}^{(4)}\boldsymbol{A}$
- the conditions on the boundary Γ

$$\boldsymbol{V} = \bar{\boldsymbol{V}}, \quad T = \bar{T}, \quad \boldsymbol{x} \in \Gamma, \quad p = 0, \quad \boldsymbol{x} \in \Gamma_{\mathrm{f}}$$

- and the initial conditions on a given part of the domain

$$\boldsymbol{V}(\boldsymbol{x}, 0) = \boldsymbol{V}^0, \quad {}^{(2)}\boldsymbol{A}(\boldsymbol{x}, 0) = {}^{(2)}\boldsymbol{A}^0$$

Here $c_p, k, T, \bar{T}$ and $\bar{\boldsymbol{V}}$ denote the heat conductivity at constant pressure, the thermal expansion, the temperature, the given temperature on the boundary and the given velocity on the boundary.

The elastic properties of a short-fiber reinforced composite strongly depend on the volume content and the orientation of the fibers. In the case of randomly distributed and oriented fibers the elastic properties differ significantly. For estimating the influence of the orientation on the elastic properties one can use the method of orientational averaging, Lagzdins et al. (1992). First we write the constitutive equation for the transversely isotropic unidirectional elastic composite, see Boehler (1987),

$$\tilde{\boldsymbol{\sigma}}(\boldsymbol{m}) = \lambda \mathrm{tr}\,\boldsymbol{\epsilon}\,\boldsymbol{E} + \alpha\boldsymbol{\epsilon} \cdot\cdot\, \boldsymbol{N}\,\boldsymbol{E} + 2\mu_{\mathrm{T}}\boldsymbol{\epsilon} + \alpha \mathrm{tr}\,\boldsymbol{\epsilon}\,\boldsymbol{N} + \beta\boldsymbol{\epsilon} \cdot\cdot\, \boldsymbol{N} \otimes \boldsymbol{N} + 2(\mu_{\mathrm{L}} - \mu_{\mathrm{T}})[\boldsymbol{N}\cdot\boldsymbol{\epsilon} + \boldsymbol{\epsilon}\cdot\boldsymbol{N}], \quad (6.6)$$

where $\boldsymbol{N} = \boldsymbol{m} \otimes \boldsymbol{m}$ and α, β, λ, μ_{L} and μ_{T} are five invariants which must be determined from the engineering constants. The second step is connected with the averaging over all directions of

the vector $\boldsymbol{m}$

$$\begin{aligned}\boldsymbol{\sigma} &= \int_{(A)} \Psi(\boldsymbol{m})\,\tilde{\boldsymbol{\sigma}}(\boldsymbol{m})\,dA \\ &= \operatorname{tr}\boldsymbol{\epsilon}\,\boldsymbol{E}\left(\alpha_* + \frac{2}{3}\beta_* + \frac{1}{9}\eta_*\right) + \boldsymbol{\epsilon}\left(2\gamma_* + \frac{4}{3}\xi_*\right) + \left(\beta_* + \frac{1}{9}\eta_*\right)\boldsymbol{\epsilon} \cdot\cdot\, (\boldsymbol{B}\otimes\boldsymbol{E} + \boldsymbol{E}\otimes\boldsymbol{B}) \\ &+ 2\xi_*(\boldsymbol{B}\cdot\boldsymbol{\epsilon} + \boldsymbol{\epsilon}\cdot\boldsymbol{B}) + \eta_*\boldsymbol{\epsilon} \cdot\cdot\, \boldsymbol{B}\otimes\boldsymbol{B},\end{aligned}$$

with

$$\begin{aligned}&\alpha_* = \lambda + \beta\frac{1-f}{35}, && \beta_* = \alpha + \beta\frac{1-f}{7}, \quad \gamma_* = \mu_{\mathrm{T}} + \beta\frac{1-f}{35}, \\ &\xi_* = \mu_{\mathrm{L}} - \mu_{\mathrm{T}} + \beta\frac{1-f}{7}, && \eta_* = f\beta, \\ &\boldsymbol{B} = {}^{(2)}\boldsymbol{A} - \frac{1}{3}\boldsymbol{E}, && f = 1 - 27\det {}^{(2)}\boldsymbol{A}\end{aligned}$$

Let us discuss the representation of the 2nd rank structure tensor. In Fig. 21 the visualization of the fiber orientation is presented. Any second rank tensor can be represented by an ellipsoid

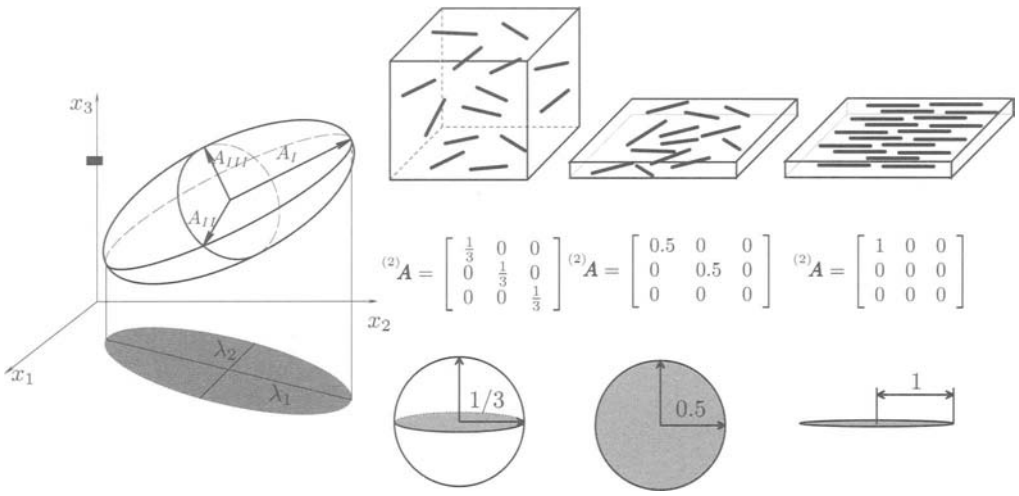

Figure 21. Visualizing the fiber orientation

with the principal values as the semi-axis. Three examples of the structure tensor are shown.

6.3 Examples

Uniformly filled thin strip The first example is related to the filling of a thin strip (Fig. 22). The geometrical parameters of the mold are (Bay & Tucker (1992)): $L = 203.2$ mm, $b = 25.4$ mm and $h = 3.18$ mm. The material is DuPont Zytel® PA66ZYTEL 70G43L 43 % with a relative volume content 25 % of glass fibers of length 0.2 mm and a diameter-length ratio 1/25. The processing conditions are: the inlet temperature of the material $T_{\mathrm{inlet}} = 550$ K, the temperature of the mold walls $T_{\mathrm{wall}} = 297$ K, and the filling time $t_{\mathrm{fill}} = 0.4$ s. Figures 23

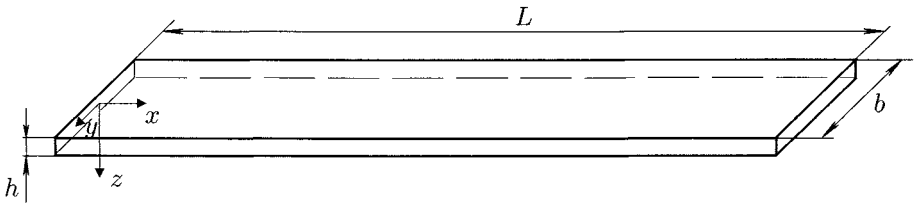

Figure 22. Geometry of a thin strip

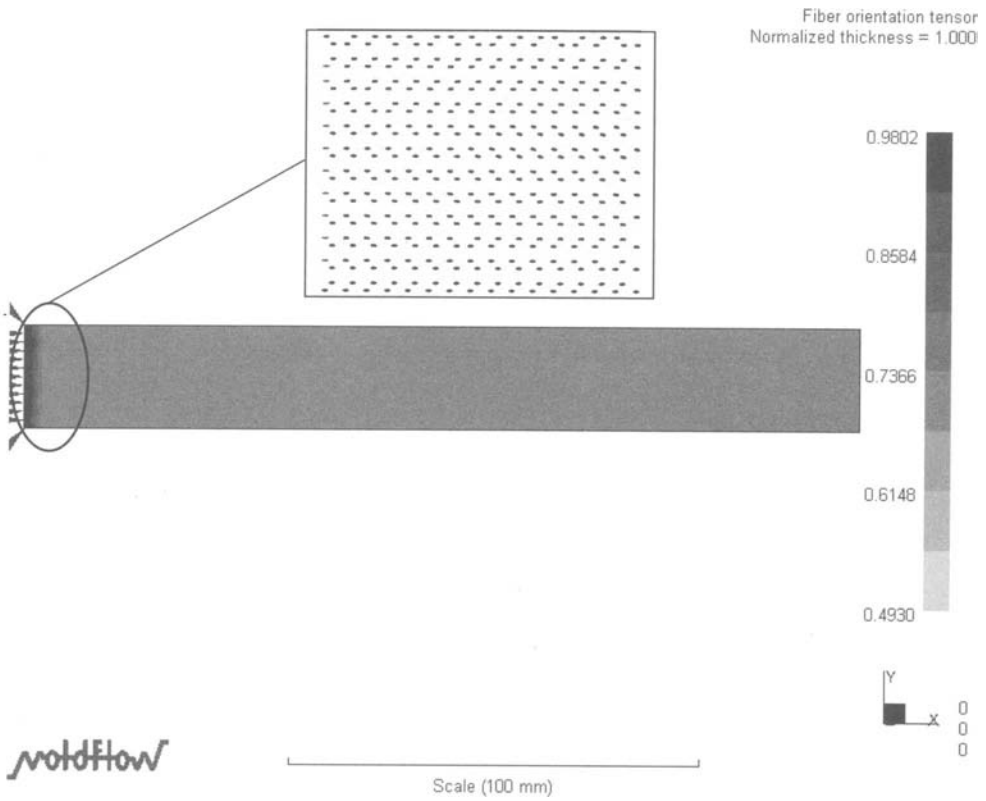

Figure 23. First principal value of the orientation tensor - skin layer

and 24 show the orientational distribution of fibers after the filling stage, as well as the first principal value of the second rank orientation tensor on the skin layer and the core of the strip. In the skin layer one obtains a homogeneous orientation (except the injection part, where the orientation is along the flow direction). In the core layer one gets a significant inhomogeneous orientation. In addition, let us investigate the bending problem under a line load $q = 2560$ N/m (Fig. 25). The unidirectional composite has the following elastic constants (plane of isotropy

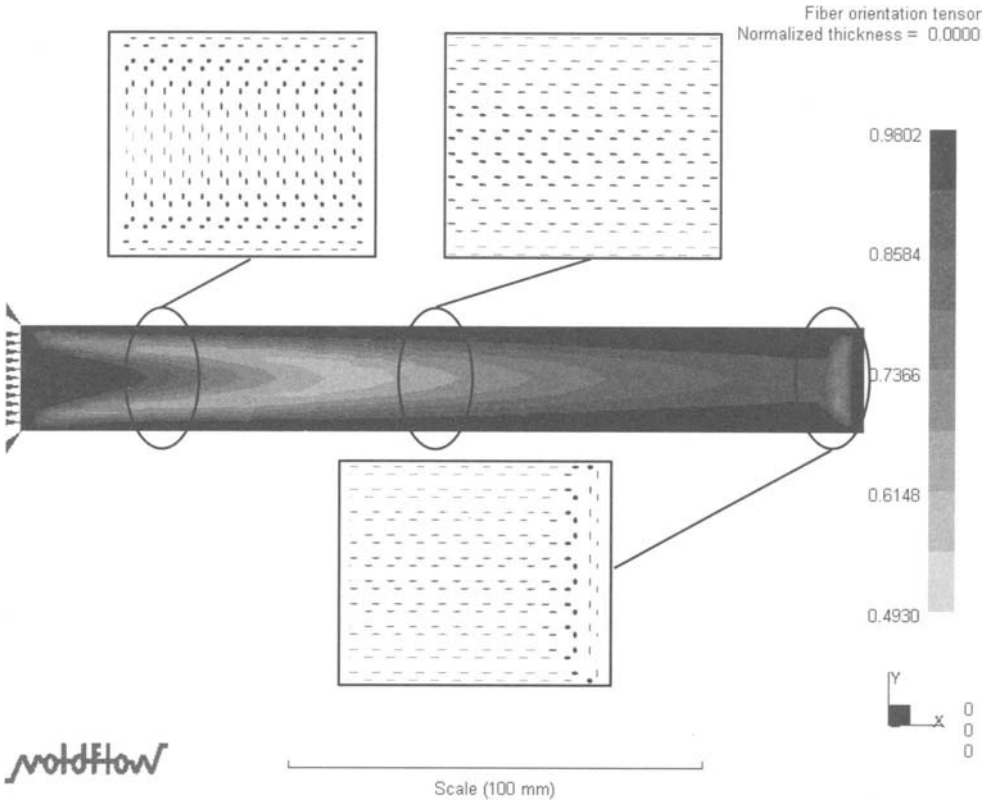

Figure 24. First principal value of the orientation tensor - core layer

2, 3): $E_1 = 8980$ MPa, $E_2 = 5420$ MPa, $\nu_{12} = 0.42$, $\nu_{23} = 0.54$, and $G_{12} = 2260$ MPa. The results of the stress analysis are shown in Figs 26 and 27. The calculations were performed considering large displacements. On the details of the numerical analysis (for example, conver-

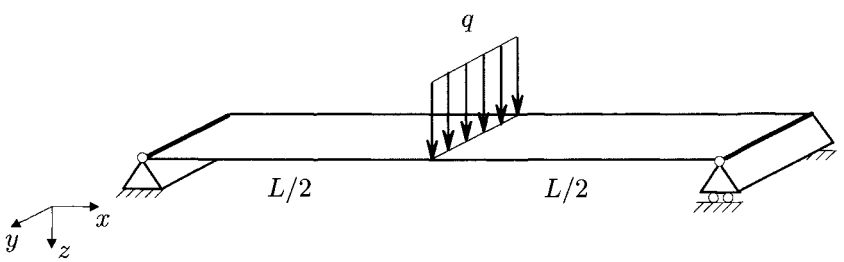

Figure 25. Strip with line load

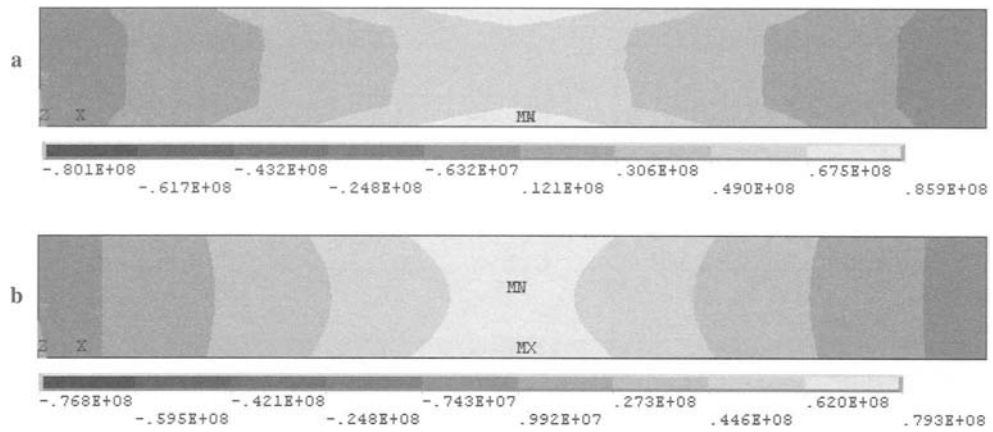

Figure 26. Distributions of normal stresses (in Pa) on the top side of the strip. **a** anisotropic behavior, **b** isotropic behavior

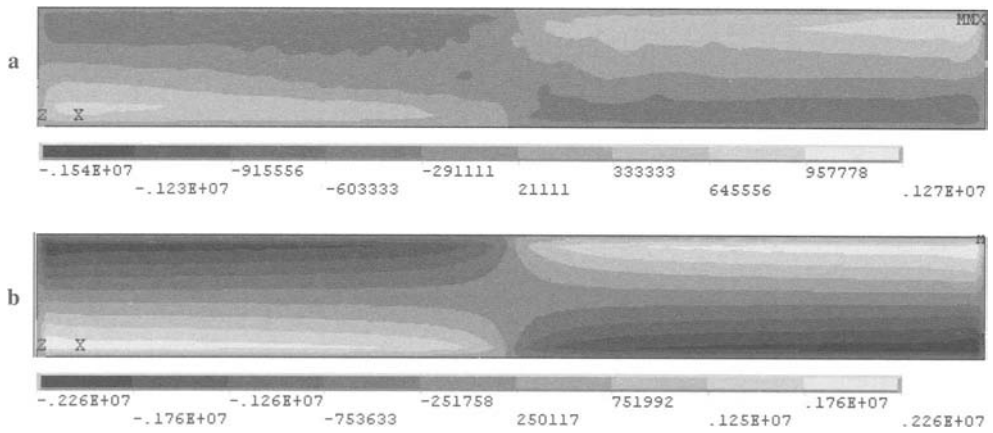

Figure 27. Distributions of shear stresses (in Pa) on the top side of the strip. **a** anisotropic behavior, **b** isotropic behavior

gence) is reported in Altenbach et al. (2003a). The analysis of stresses demonstrates a significant distinction between the anisotropic and the isotropic solution in the case of shear stresses.

Thin rectangular plate In Fig. 28 the geometry and the loading conditions for a thin simply supported plate are presented. The geometrical properties are $L = 150$ mm and $h = 3.18$ mm. The material is the same as in the first example. The processing parameters are: the inlet temperature of the material $T_{\text{inlet}} = 563$ K, the temperature of the mold walls $T_{\text{wall}} = 338$ K, and the filling time $t_{\text{fill}} = 1.5$ s. The filling was performed in different ways: uniformly filling the mold along one edge (injection case **a**), filling by means of a point gate located in one corner (injection

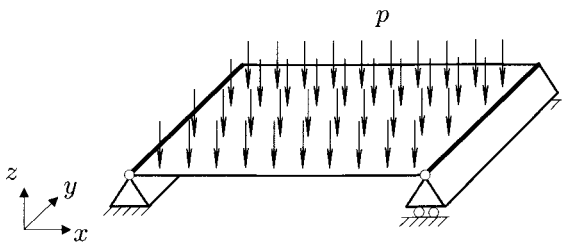

Figure 28. Simply supported plate

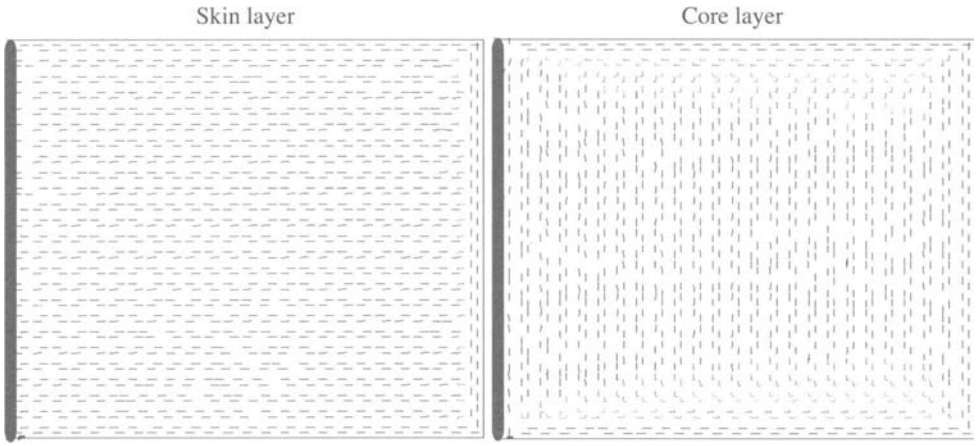

Figure 29. First principal value of the orientation tensor. Case **a**

case **b**) and filling by a point gate at the middle of one mold sides (injection case **c**). Figures 29, 30 and 31 show the distributions of the first principal value of the second rank orientation tensor.

From the analysis of case **a** (Fig. 29) one can make the conclusion that in the skin layer the fibers are oriented mainly in the flow direction, whereas in the core layer they are perpendicular to the flow direction (except the near-edge zones). In case **b** (Fig. 30) one obtains a similar situation. In Fig. 32 the stresses for the three filling cases are shown. The load was $q = 10.000$ N/m^2. For the same loading situation the deflections were estimated too (Fig. 33). The analysis show a significant influence of the processing conditions on the stresses and deflections. One can clearly see that the best results (minimum of stresses and deflections) one gets in the case of the injection along the edge.

Thin-walled shell of revolution In the next example let us consider the manufacture of a thin-walled shell of revolution. The geometry is given in Fig. 34. Let us assume the same material as in the previous cases. The manufacture conditions are: the inlet temperature of the material $T_{\text{inlet}} = 563$ K, the temperature of the mold walls $T_{\text{wall}} = 368$ K, and the filling time $t_{\text{fill}} = 1$ s. In Fig. 37 the distributions of circumferential (**a**) and axial stresses (**b**) are shown. The shell was

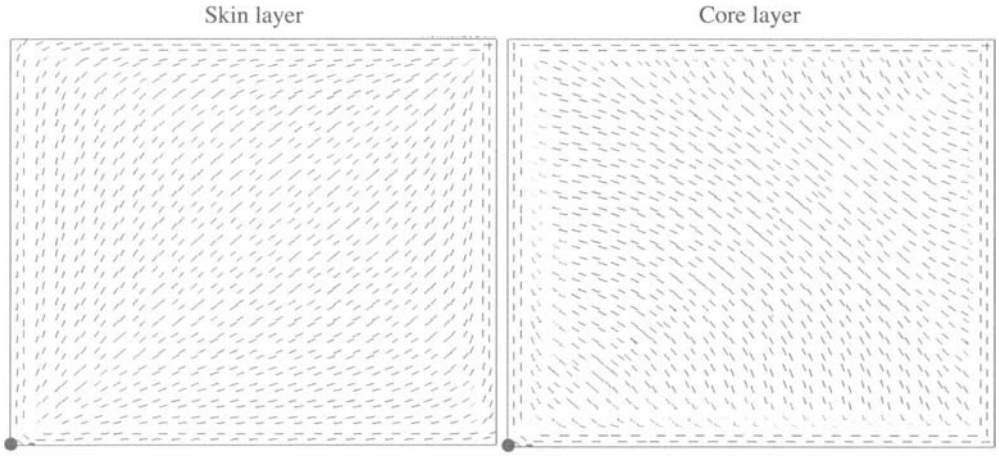

Figure 30. First principal value of the orientation tensor. Case **b**

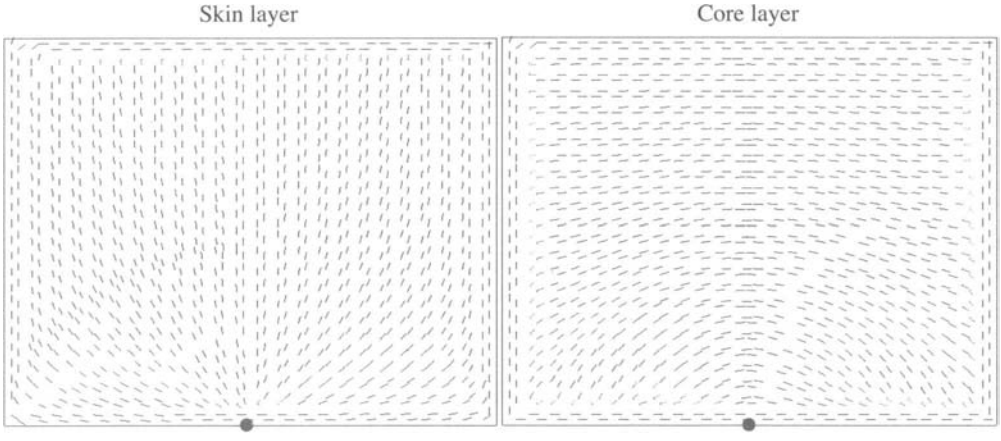

Figure 31. First principal value of the orientation tensor. Case **c**

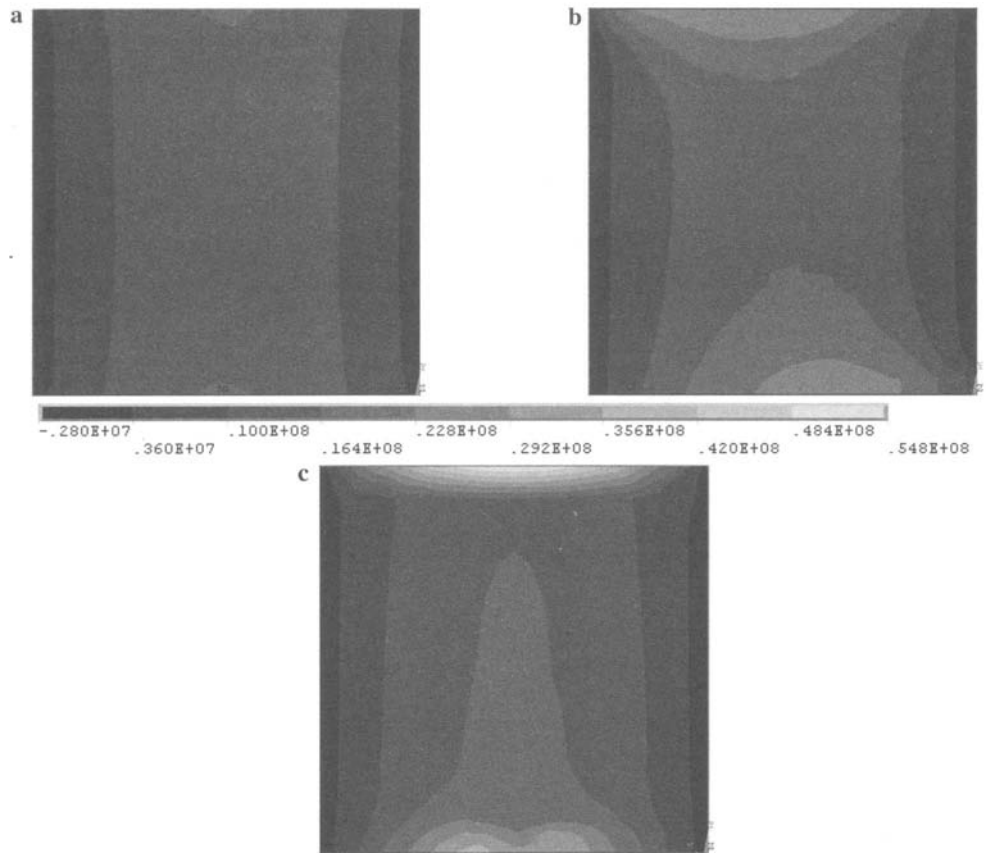

Figure 32. Distribution of stresses σ_x (in Pa) in the surface layer of the plate for the three cases of filling

loaded by internal pressure $q = 1.000.000$ N/m^2. From the analysis one can conclude that the axial stresses are less dangerous to this shell than the circumferential ones, since the fibers in the surface layers of the shell are oriented mainly in the axial direction. The strength will be higher in this direction. However, for the circumferential stresses an opposite situation is observed: these stresses are acting perpendicularly to the fibers. Thus the stresses σ_θ are dangerous and can lead to the crack formation on the shell surface.

Comparison with experimental results In Fig. 35 the model of the filling of a center gated disk is presented. Geometrical parameters of the model are following Bay & Tucker (1992): $R = 76.2$ mm, $h = 3.18$ mm. The material is again DuPont Zytel® PA66ZYTEL 70G43L. The processing conditions are: the inlet temperature of the material - 550 K, the temperature of the mold 347 K, time of filling 2.5 s. Experimental results for this problem were published by Bay & Tucker (1992). The simulation performed by Pylypenko (2003) is compared with the experimen-

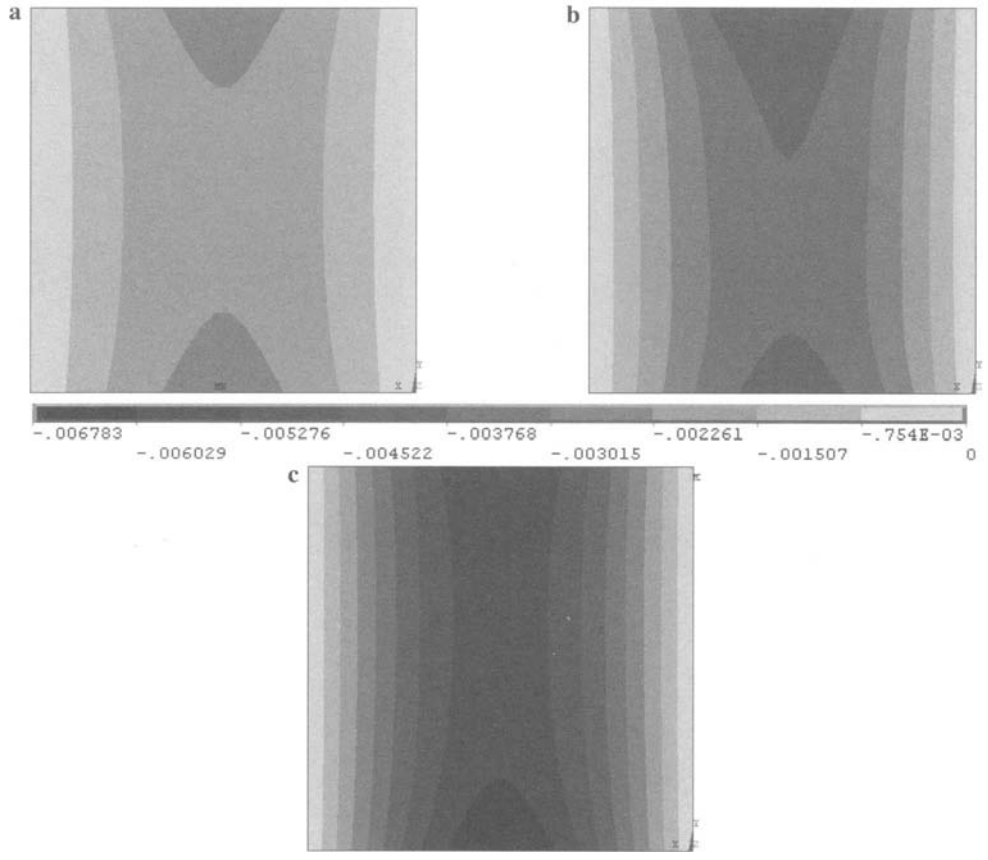

Figure 33. Distribution of deflections (in mm) for the three cases of filling

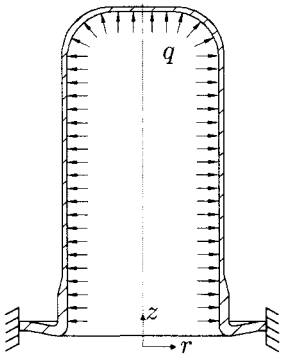

Figure 34. Model of a thin-walled shell

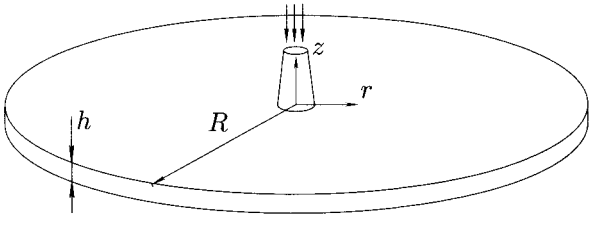

Figure 35. Center gated disk

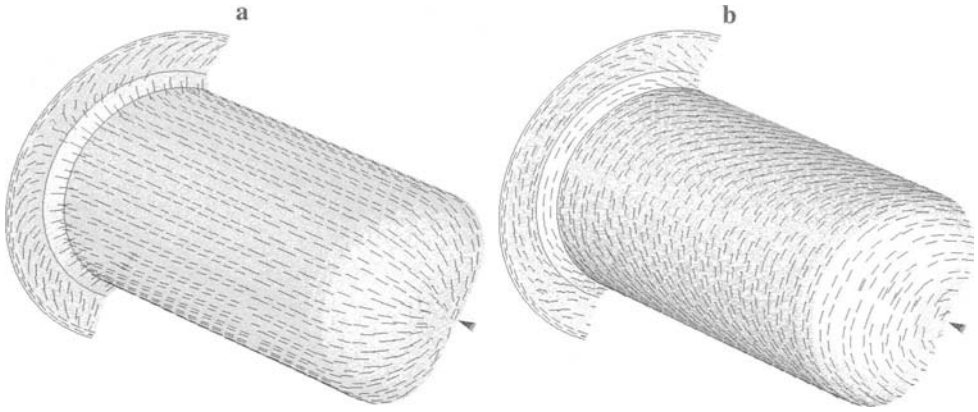

Figure 36. First principal value of the orientation tensor. **a** skin layer, **b** core layer

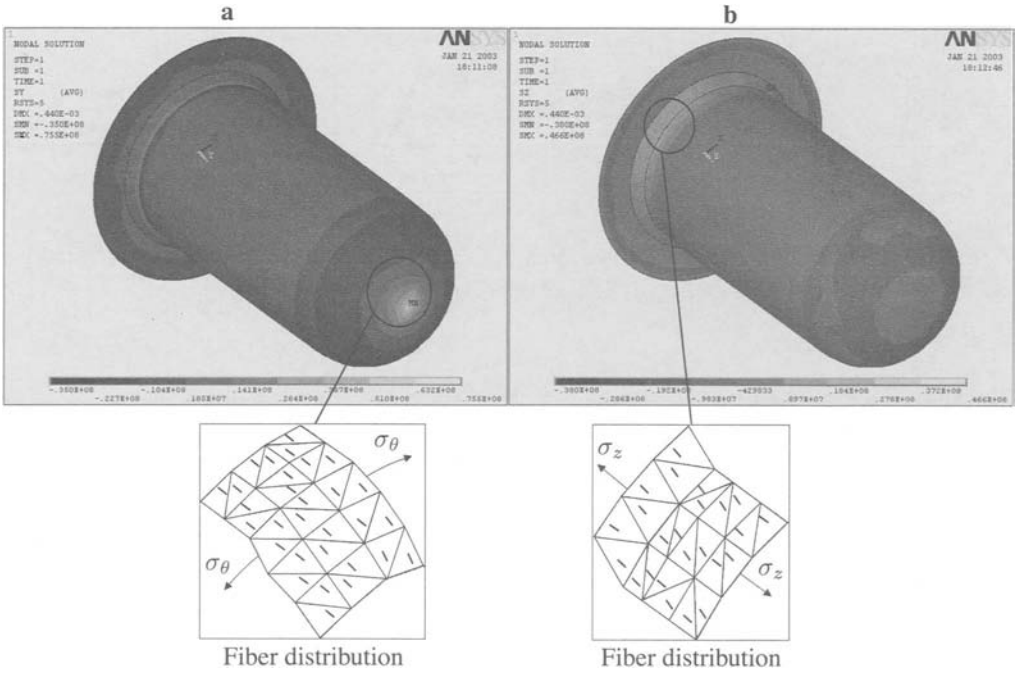

Figure 37. Distributions of circumferential (**a**) and axial stresses (**b**) (in Pa)

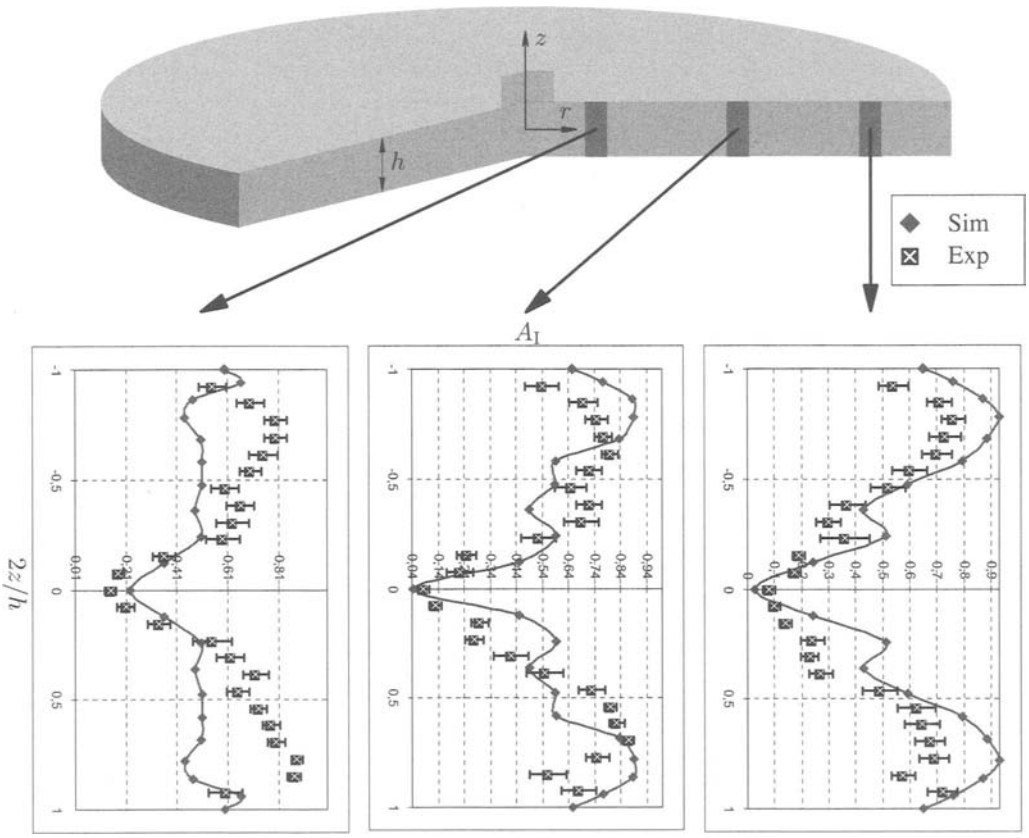

Figure 38. Comparison of MPI results for the first principal value ${}^{(2)}A_{\mathrm{I}}$ of the orientational tensor with experimental data Bay & Tucker (1992)

tal results. This comparison is shown in Fig. 38. The figure illustrates the distributions of the first principal value of the fiber orientation tensor $\boldsymbol{A}$ across the thickness direction z in different radial zones of the disk. The analysis shows a good agreement of experimental with calculated data in zones far from the gate. A non-satisfying agreement was observed in the gate region. This can be explained by the model assumptions of a planar flow used in the simulations.

Acknowledgement

The main part of this contribution is based on the textbooks Altenbach & Altenbach (1994); Altenbach et al. (1995, 1996, 2004), the Lecture Notes Altenbach & Skrzypek (1999); Altenbach & Becker (2003) and the papers Altenbach et al. (2003a,b). I wish to express my special thanks to all co-authors. The preparation of the manuscript was possible with the technical support of O. Dyogtyev, K. Naumenko, S. Pylypenko (creating the figures) and Ms. B. Renner (proof-reading). I acknowledge all of them.

Bibliography

Advani, S.G., and Tucker, C.L. (1987). The use of tensor to describe and predict fiber orientation in short-fiber composites. *J. Rheol.* 31:751–784.

Agarwal, B.D., and L.J. Broutman (1990). *Analysis and Performance of Fibre Composites.* New York: John Wiley & Sons.

Altenbach, H., Altenbach, J., and Kissing, W. (2004). *Mechanics of Composite Structural Elements.* Berlin: Springer.

Altenbach, H., Altenbach, J. und Rikards, R. (1996). *Einführung in die Mechanik der Laminat- und Sandwichtragwerke.* Stuttgart: Dt. Verlag für Grundstoffindustrie.

Altenbach, H., Altenbach, J. und Zolochevsky, A. (1995). *Erweiterte Deformationsmodelle und Versagenskriterien der Werkstoffmechanik.* Stuttgart: Deutscher Verlag für Grundstoffindustrie.

Altenbach, H., and Becker, W., eds., (2003). *Modern Trends in Composite Laminates Mechanics, CISM Courses and Lectures No. 448.* Wien: Springer.

Altenbach, H., and Tushtev, K. (2001). A new static failure criterion for isotropic polymers. *Mechanics of Composite Materials* 37(5/6):475–482.

Altenbach, H., Lauschke, U. und Zolochevsky, A.A. (1993). Ein verallgemeinertes Versagenskriterium und seine Gegenüberstellung mit Versuchsergebnissen. *ZAMM* 73:T372–T375.

Altenbach, H., Naumenko, K., L'vov, G.I., and Pilipenko, S.N. (2003a). Numerical estimation of the elastic properties of thin-walled structures manufactured from short-fiber-reinforced thermoplastics. *Mech. Comp. Mat.* 39:221–234.

Altenbach, H., Naumenko, K., and Zhilin, P. (2003b). A micro-polar theory for binary media with applications to phase-transional flow of fibre suspensions. *Contin. Mech. Thermodyn.*15:539–570.

Altenbach, H., and Skrzypek, J.J., eds., (1999). *Creep and Damage in Materials and Structures, CISM Courses and Lectures No. 399.* Wien: Springer.

Altenbach, H., and Zolochevsky, A. (1996). A generalized failure criterion for three-dimensional behaviour of isotropic materials. *Engng Frac. Mech.* 54(1):75–90.

Altenbach, J. und Altenbach, H. (1994). *Einführung in die Kontinuumsmechanik.* Stuttgart: Teubner.

Ambarcumyan, S.A. (1991). *Theory of Anisotropic Plates.* Washington: Hemispher Publishing.

Ashbee, K. (1994). *Fundamental Principles of Reinforced Composites.* Lancaster: Technomic.

Ashby, M.F. (1987). Technology of the 1990's: advanced materials and predictive design. *Phil. Trans. R. Soc. London* A322:393–407.

Batchelor, G.K. (1970). The stress system in a suspension of force-free particles. *J. Fluid Mech.* 41:545–570.

Bay, R.S., and Tucker, C.L. (1992). Fiber orientation in simple injection moldings, Pt.2 Experimental results. *Polym. Compos.* 13:332–341.

Berthelot, J.-M. (1999). *Composite Materials. Mechanical Behaviour and Structure Analysis.* New York: Springer.

Boehler, J.P. (1987). Anisotropic linear elasticity. In Boehler, J.P., ed. *Application of Tensor Functions in Solid Mechanics, CISM Courses and Lectures No. 292.* Wien: Springer, pp. 55 – 65.

Chawla, K.K. (1987). *Composite Materials.* New York: Springer.

Christensen, R.M. (1997). Stress based yield failure criteria for fiber composites. *Int. J. Solids Structures* 34:529–543.

Decolon, C. (2002). *Analysis of Composite Structures.* London: Hermes Penton Science.

Dinh, S.M., and Armstrong, R.C. (1984). A rheological equation of state for semiconcentrated fibre suspensions. *J. Rheol.* 28:207–227.

Doi, M., and Edwards, S.F. (1988). *The Theory of Polymer Dynamics.* Oxford: University Press.

Dupret, F., Couniot, A., and Mal, L. (1999). Modelling and simulation of injection molding. In Siginer, D.A., Kee, D.D., and Chhabra, R.P., eds., In *Advances in the Flow and Rheology of Non-Newtonian Liquids.* Amsterdam: Elsevier. 939 - 1010.

Dupret, F., and Verleye, V. (1999). Modelling of the flow of fiber suspensions in narrow gaps. In Siginer, D.A., Kee, D.D., and Chhabra, R.P., eds., In *Advances in the Flow and Rheology of Non-Newtonian Liquids.* Amsterdam: Elsevier. 1347 - 1398.

Ehrenstein, G. (1992). *Faserverbund-Kunststoffe.* München: Hanser.

Eringen, A.C. (2001). *Microcontinuum Field Theories. II. Fluent Media.* New York: Springer.

Gay, D. (2002). *Composite Materials: Design and Applications.* Boca Raton: CRC Press.

Glaser, S. und von Diest, K. (1988). Berechnungsverfahren für GFK-Bauteile. *Kunststoffe* 88:537–542.

Gibson, R.F. (1994). *Principles of Composite Material Mechanics.* New York: McGraw-Hill.

Gol'denblat, I.I., and Kopnov, V.A. (1968). *Criteria of Strength and Plasticity of Structural Materials (in Russ.).* Moscow: Mashinostroenie.

Haddad, Y.M. (2000a). *Mechanical Behaviour of Engineering Materials, Vol. 1 Static and Quasi-Static Loading.* Doordrecht: Kluwer.

Haddad, Y.M. (2000b). *Mechanical Behaviour of Engineering Materials, Vol. 2 Dynamic Loading and Intelligent Material Systems.* Doordrecht: Kluwer.

Hahn, H.G. (1985). *Elastizitätstheorie.* Stuttgart: Teubner.

Hashin, Z. (1980). Failure criteria for unidirectional fiber composites. *J. Appl. Mech.* 47:329–334.

Haupt, P. (2002). *Continuum Mechanics and Theory of Materials.* Berlin: Springer.

Hegler, R.P. (1984). Faserorientierung beim Verarbeiten von kurzfaserverstärkter Thermoplaste. *Kunststoffe* 74:271–277.

Hergert, W., Däne, M., and Ernst, A., eds., (2004). *Computational Materials Science, Lect. Notes Phys. No. 642.* Berlin: Springer.

Hetnarski, R.B., and Ignaczak, J. (2004). *Mathematical Theory of Elasticity.* New York: Taylor & Francis.

Hill, R. (1950). *The Mathematical Theory of Plasticity.* London: Oxford University Press.

Huilgol, R.R., and Phan-Thien, N. (1997). *Fluid Mechanics of Viscoelasticity.* Amsterdam: Elsevier.

Hult, J., and Rammerstorfer, F.G., eds., (1994). *Engineering Mechanics of Fibre Reinforced Polymers and Composite Structures, CISM Courses and Lectures No. 348.* Wien: Springer.

Jeffery, G.B. (1922). The motion of ellipsoidal particles immersed in a viscous fluid. *Proc. Roy. Soc. London* A102:161–179.

Jones, R.M. (1975). *Mechanics of composite materials.* Washington: McGraw-Hill.

Kachanov, L.M. (1974). *Foundation of Fracture Mechanics (in Russ.).* Moscow: Nauka.

Kim, D.-H. (1995). *Composite Structures for Civil and Architectural Engineering.* London: E & FN Spoon.

Krawietz, A. (1986). *Materialtheorie. Mathematische Beschreibung des phänomenologischen thermomechanischen Verhaltens.* Berlin: Springer.

Lagzdins, A., Tamuzs, V., Teters, G., and Kregers, A. (1992). *Orientational Averaging in Mechanics of Solids.* London: Longman.

Lai, W.M., Rubin, D., and Krempl, E. (1993). *Introduction to Continuum Mechanics.* Oxford: Pergamon.

Lekhnitskij, S.G. (1981). *Theory of Elasticity of an Anisotropic Body.* Moscow: Mir.

Lemaitre, J., ed., (2001). *Handbook of Materials Behavior Models, Vol. 1 - 3.* San Diego: Academic Press.

Lemaitre, J., et Chaboche, J.L. (1985). *Mécanique des Matériaux Solides.* Paris: Dunod.

Love, A.E.H. (1927). *A Treatise on the Mathematical Theory of Elasticity.* Cambridge: University Press.

Lurie, A. (1990). *Nonlinear theory of elasticity.* Amsterdam: North-Holland.

Malmeister, A.K. (1966). Geometry of strength theory (in Russ.). *Mekhanika Polymerov* (4):519–534.

Mālmeisters, A., Tamužs, V. und Teters, G. (1977). *Mechanik der Polymerwerkstoffe.* Berlin: Akademie-Verlag.

Menning, G. (1995). *Werkzeuge für die Kunststoffverarbeitung.* München: Hanser.

Michaeli, W. (1995). *Plastics Processing.* München: Hanser.

Norris, S.C. (1950). Strength of orthotropic materials subjected to continued stresses, In *Forest Products Lab. Rep.*, No. 1816.

Novozhilov, V.V. (1951). On the relations between the stresses and the strains in non-linear elastic materials (in Russ.), *Prikl. Mat. i Mekh.*, XV(2):183–194.

Nowacki, W. (1985). *Theory of Asymmetric Elasticity.* Oxford: Pergamon.

Nye, J.F. (1992). *Physical properties of crystals.* Oxford: Oxford Science Publications.

Palmov, V.A. (1998). *Vibrations in Elasto-Plastic Bodies.* Berlin: Springer.

Paul, B. (1968). Macroscopic criteria for plastic flow and brittle fracture. In Liebiwitz, H., ed. *Fracture, An Advanced Treatise, Vol. 2.* New York: Academic. 313–496

Petrie, C.J.S. (1999). The rheology of fibre suspensions. *J. Non-Newton. Fluid Mech.* 87:369–402.

Powell, P.C. (1994). *Engineering with Fibre-Polymer Laminates.* London: Chapman & Hall.

Puck, A. (1996). *Festigkeitsanalyse von Faser-Matrix-Laminaten.* München: Hanser.

Pylypenko, S.N. (2003). *Investigation of elastic properties of short fiber composite materials (in Ukrain.).* Master Thesis, Kharkov National Technical University.

Rabinovich, A.L. (1970). *Introduction to Mechanics of Reinforced Polymers (in Russ.).* Moscow: Nauka.

Saito, M., Kukula, S., Kataoka, Y., and Miyata, T. (2000). Practical use of statiscally modified laminate model for injection moldings. *Mat. Sci. Eng.* A285:280-287.

Skrzypek, J.J., and Ganczarski, A.W., eds., (2003). *Anisotropic Behaviour of Damaged Materials, Lect. Notes in Appl. Comp. Mech., Vol. 9.* Berlin: Springer.

Tamuzh, V.P., and Protasov, V.D., eds. (1986). *Failure of Structures made of Composite Materials (in Russ.)*. Riga: Zinatne.

Timoshenko, S.P. (1953). *History of Strength of Materials*. New York: McGraw-Hill.

Todhunter, I., and Pearson, K. (1886). *A History of Elasticity and of the Strength of Materials, Vol. I.* Cambridge: University Press.

Todhunter, I., and Pearson, K. (1893). *A History of Elasticity and of the Strength of Materials, Vol. II.* Cambridge: University Press.

Truesdell, C., and Noll, C.W. (1992). *The Non-linear Field Theories of Mechanics*. Berlin: Springer.

Tsai, S.W., and Hahn, H.T. (1980). *Introduction to Composite Materials*. Lancaster: Technomic.

Tsai, S.W., and Wu, E.M. (1971). A general theory of strength for anisotropic materials. *J. Comp. Mat.* 5:58–80.

Tucker, C.L., and Advani, S.G. (1994). *Processing of short-fiber systems*, In S.G. Advani, ed., *Flow and Rheology in Polymer Composites Manufacturing*. Amsterdam: Elsevier. 147 - 202.

Vincent, M., and Agassant, J.F. (1986). Experimental study and calculations of short glass fiber orientation in a center gated molded disc. *Polym. Compos.* 7:76–83.

Vinson, J.R., and Sierakowski, R.L. (1987). *The Behavior of Structures Composed of Composite Materials*. Dordrecht: Martinus Nijhoff.

Whiteside, P.D., Coates, P.J., Hine, P.J., and Ducket, R.A. (2000). Glass fibre orientation within injection moulded automotive pedal. *Plast. Rubber Compos.* 29:38–45.

Yu, M.-H. (2004). *Unified Strength Theory and its Application*. Berlin: Springer.

Zakharov, K.V. (1961). Strength criterion for laminated plastics (in Russ.). *Plastmassy* (8):59–62.

Zakharov, K.V. (1963). On the strength of laminated plastics (in Russ.). *Plastmassy* (6):57–60.

Życzkowski, M. (1981). *Combined Loadings in the Theory of Plasticity*. Warszawa: PWN-Polish Scientific Publisher.

Computational Mechanics of Failure in Composites at Multiple Scales

René de Borst [†‡]

[†] Koiter Institute Delft / Faculty of Aerospace Engineering, Delft University of Technology, P.O. Box 5058, NL-2600 GB Delft, The Netherlands

[‡] LaMCos C.N.R.S. UMR 5514, I.N.S.A. de Lyon, F-69621 Villeurbanne, France

Abstract The contribution starts with a discussion of various phenomena in laminated composite structures that can lead to failure: matrix cracking, delamination between plies, and debonding and subsequent pull-out between fibres and the matrix material. Next, the different scales are discussed at which the effect of these nonlinearities can be analysed and the ways to couple analyses at these different length scales. From these scales — the macro, meso and micro-levels — the meso-level is normally used for the analysis of delamination, which is the focus of this chapter. At this level, the plies are modelled as continua and interface elements between them conventionally serve as the framework to model delamination and debonding. After a brief discussion of the cohesive–zone concept and its importance for the analysis of delamination, various finite element models for the plies are elaborated: three–dimensional, generalised plane–strain and solid–like shell models. This is followed by a derivation of interface elements and a discussion of advanced techniques for solving the nonlinear equations that ensue after discretisation. In the last part of this chapter a new, recent method to numerically model delamination is discussed. It exploits the partition–of–unity property of finite element shape functions. The approach offers advantages, since interfaces — and more generally, discontinuities — can be inserted at the onset of delamination only and not a priori, as in the conventional approach. As a consequence, artificial elastic compliance of the interface prior to onset of delamination, spurious traction oscillations ahead of the delamination front, and spurious wave reflections because of the presence of a high stiffness value are avoided. Moreover, unstructured meshes can be employed.

1 Introduction

Failure in composites is governed by three mechanisms: matrix cracking, delamination, and fibre debonding and pull-out. Often, matrix cracking occurs first when loading a specimen. Together with stress concentrations that occur near free edges and around holes, matrix cracks trigger delamination. Normally, delamination is defined as the separation of two plies of a laminated composite, although it has been observed that delamination not necessarily occurs exactly at the interface between two plies. For instance, in fibre–metal laminates delamination rather resembles a matrix crack in the epoxy layer near and parallel to the aluminium–epoxy interface.

An important issue when modelling physical phenomena is the proper definition of the scale at which the (failure) mechanism under consideration is modelled. This holds a fortiori for composites, since the in–plane dimensions of a laminated composite structure exceed the length scale at which delamination, matrix cracking and fibre debonding take place by one to several orders of magnitude. This complicates an efficient, accurate and meaningful analysis. Typically, the in–plane dimensions of a laminated structure are in the order of meters, while its thickness can be just a few millimeters. Each ply is then less than a millimeter thick. Since, at least in conventional finite element analysis, each ply has to be modelled separately in order to capture delamination between two plies, and since the aspect ratio of finite elements is limited if one wishes to obtain a reliable stress prediction, the maximum in–plane dimension of a three–dimensional solid element will be around one centimeter. It is obvious that the number of elements that is needed to model each layer is already big, and the total number of elements required to model the entire structure, including possible holes and stiffened areas, can easily exceed computational capabilities when the analyst wishes to simulate nonlinear phenomena, such as delamination.

The same reasoning holds when considering matrix cracking. For most laminated composites, matrix cracks reach a saturation distance, which is in the order of the ply thickness. This implies that, when this phenomenon is to be included in the analysis in a truly discrete format — that is, matrix cracks are modelled individually and not smeared out over the plane — the in–plane discretisation must even be somewhat finer than for an analysis that includes delamination only, roughly one order of magnitude.

A further refinement of the discretisation of several orders of magnitude is required when individual fibres are to be modelled with the aim to include debonding and pull-out of individual fibres. It is evident, that such a type of modelling exceeds computational capabilities even of the most powerful computers nowadays available, if the analysis would consider the entire structure.

Multiscale approaches provide a paradigm to by-pass the problems outlined above. In these methods, the various aspects of the entire structural problem are considered at different levels of observation, each of them characterised by a well–defined *length scale*. The different levels at which analyses are carried out, are connected either through *length scale transitions*, in which the structural behaviour at a given level is homogenised to arrive at mechanical properties at a next higher level (Ladevèze and Lubineau , 2002), or through (finite element) analyses which are conducted at two levels simultaneously and in which are connected by matching the boundary conditions at both levels (Feyel and Chaboche , 2000). In the former class of methods, the *Representative Volume Element (RVE)*, the volume of heterogeneous material that can be considered as representative at a given level of observation and is therefore amenable to homogenisation, plays an important role.

This chapter will not address methods for length scale transition or approaches for carrying out multi-level finite element analyses. Instead, we shall focus on so-called meso-level approaches, in which delamination is assumed to be the main degrading mechanism. For this purpose, the different levels of analysis — macro, meso and micro — are defined in the context of laminated composite structures. At the meso-level as well as at the micro-level, fracture along internal material boundaries, delamination and debonding,

respectively, governs the failure behaviour. While constitutive relations for such *interfaces* are treated elsewhere in this Volume, most of them have in common that a so-called *work of separation* or *fracture energy* plays a central role. For this reason, a succinct discussion of *cohesive–zone* models, which are equipped with such a material parameter, follows the discussion.

Next, we shall formulate the three–dimensional finite element equations for arbitrarily large displacements gradients, but confined to small strains. Both the continuum elements for the plies and the interface elements will be treated. For the continuum elements thermal and/or hygral strains, which are relevant because of the manufacturing process, will be included. Since delamination in strips can often be analysed using a generalised plane-strain formulation, the equations will be elaborated for this case. Furthermore, solid–like shells will be introduced, which can be used to model the plies in a 3D–like manner, but allowing for much larger aspect ratios (up to 1000) than standard solid elements would allow. This section will be concluded by a discussion on solution techniques, where the importance of selecting the proper control parameter is emphasised.

The final part of this chapter discusses a recent development in numerical models for fracture. It exploits the partition-of-unity property of finite element shape functions and allows discontinuities to be inserted during a finite element analysis, either within a matrix, or, as used here, along interfaces between two materials. The concept will be elaborated for large displacement gradients, for the solid–like shell element discussed before and will be complemented by illustrative examples.

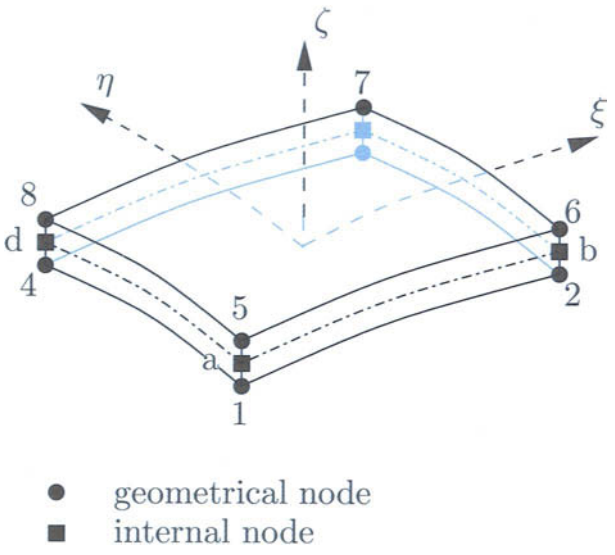

Figure 1. Shell element for macroscopic analysis of a laminated composite structure

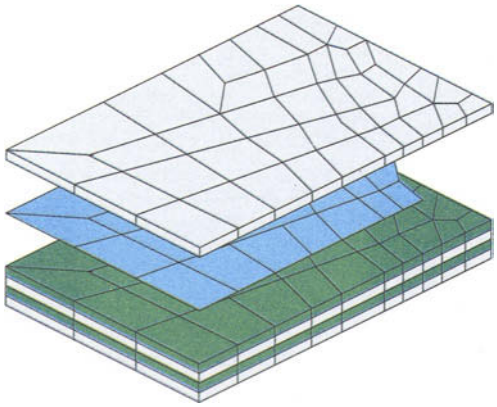

Figure 2. Finite element model of a laminated composite. The individual layers are modelled with three–dimensional, generalised plane–strain or shell elements. Interface elements equipped with a cohesive–zone model are applied between the layers

2 Multi-Level Analysis of Composite Structures

2.1 Levels of Observation

At the macroscopic or structural level the plies are normally modelled via a layered shell approach, where the different directions of the fibres in the layers are taken into account through an anisotropic elasticity model, Figure 1. If this (anisotropic) elasticity model is augmented by a damage or plasticity model, degradation phenomena like matrix cracking, fibre pull-out or fibre breakage can also be taken into account, albeit in a smeared manner. At this level, the in-plane structural dimensions are the length scales that govern the boundary-value problem.

Indeed, discrete modelling of delamination, matrix cracking and fibre-debonding is not possible at this level, as also argued in the Introduction. The level below, where the ply thickness becomes the governing length scale, allows for the modelling of delamination and matrix cracking. At this meso–level the plies are modelled as continua and can either be assumed to behave linearly elastically or can be degraded according to a damage law. In the approach suggested by Schellekens and de Borst (1993, 1994a), elastic anisotropy and curing of composites are taken into account by including possible thermal and hygral effects, but eventual damage which can evolve in the plies is lumped into the interface. This approach is reasonable as long as the energy dissipation due to processes like matrix cracking is small compared to the energy needed for delamination growth, as for mode-I delaminations and for mixed-mode delaminations where the fibres are (almost) parallel to the intralaminar cracks. If this condition is not met, the interface delamination model must be supplemented by a damage model for the ply, which has been proposed by Allix and Ladevèze (1992). A drawback of existing damage approaches

for modelling intralaminar cracks, fibre breakage and debonding is that no localisation limiter is incorporated, which renders the governing equations ill–posed at a generic stage in the loading process and can result in a severe dependence of the results on the spatial discretisation (de Borst , 2004).

At the meso–level, delamination as a discrete process has conventionally been modelled as shown in Figure 2, where the plies are considered as continua — and are discretised using standard finite elements — while the delamination is modelled in a discrete manner using special interface elements (Allix and Ladevèze , 1992; Corigliano , 1993; Schellekens and de Borst , 1993, 1994a; Allix and Corigliano , 1999; Alfano and Crisfield , 2001). Generalised plane–strain elements are often used to model free–edge delamination as in Schellekens and de Borst (1993, 1994a), while stacks of solid or shell elements and interface elements are applicable to cases of delamination near holes or other cases where a three–dimensional modelling is necessary, e.g., (Hashagen *et al.* , 1995; Schipperen and Lingen , 1999).

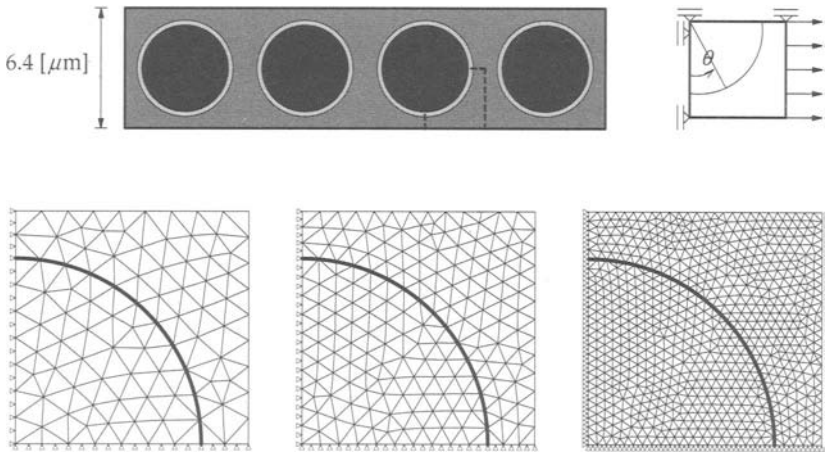

Figure 3. Layer which is unidirectionally reinforced with long fibres (above) and finite element discretisations for three different levels of refinement of a representative volume element composed of a quarter of a fibre, the surrounding epoxy matrix and the interface between fibre and epoxy (Schellekens and de Borst , 1994b)

The greatest level of detail is resolved in the analysis if the fibres are modelled individually. In such micro-level analyses the governing length scale is the fibre diameter. Possible debonding between fibre and matrix material is normally modelled via interface elements, equipped with cohesive–zone models, quite similar to models for delamination. An example is given in Figure 3, which shows an epoxy layer, which has been reinforced uniaxially by long fibres, together with three levels of mesh refinement for a Representative Volume Element of the layer.

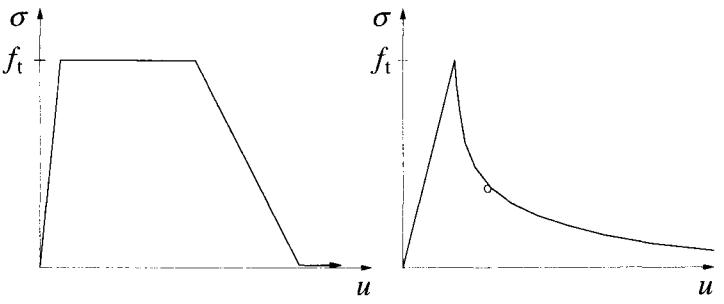

Figure 4. Stress–displacement curves for ductile separation (left) and quasi-brittle separation (right)

2.2 The Cohesive-Zone Concept

Delamination in the interfaces between the plies is modelled using a discrete relation between the interface tractions $\mathbf{t}_i$ and the relative displacements $\mathbf{v}$:

$$\mathbf{t}_i = \mathbf{t}_i(\mathbf{v}, \kappa) \tag{2.1}$$

with κ a history parameter. After linearisation, necessary to use a tangential stiffness matrix in an incremental–iterative solution procedure, one obtains:

$$\dot{\mathbf{t}}_i = \mathbf{T}\dot{\mathbf{v}} \tag{2.2}$$

with $\mathbf{T}$ the material tangent stiffness matrix of the discrete traction–separation law:

$$\mathbf{T} = \frac{\partial \mathbf{t}_i}{\partial \mathbf{v}} + \frac{\partial \mathbf{t}_i}{\partial \kappa} \frac{\partial \kappa}{\partial \mathbf{v}} \tag{2.3}$$

Whichever type of modelling is used, plasticity or damage, a key element is the presence of a work of separation or fracture energy, $\mathcal{G}_c$, which governs delamination growth and enters the interface constitutive relation (2.1) in addition to the tensile strength f_t. It is defined as the work needed to create a unit area of fully developed crack:

$$\mathcal{G}_c = \int_{u=0}^{\infty} \sigma \mathrm{d}u \tag{2.4}$$

with σ and u the stress and the displacement across the *fracture process zone*. It thus equals the area under the decohesion curves as shown in Figure 4. Evidently, cohesive–surface models as defined above are equipped with an *internal length scale*, since the quotient $\mathcal{G}_c/E$, with E a stiffness measure for the plies, has the dimension of length.

3 Standard FE Approach to Debonding and Delamination

3.1 Three–Dimensional Framework

We denote the material coordinates of a point in the undeformed reference configuration by $\mathbf{X} = (X_1, X_2, X_3)$, while in the deformed configuration the spatial coordinates

of the point become $\mathbf{x} = (x_1, x_2, x_3)$. Between $\mathbf{x}$ and $\mathbf{X}$ we have:

$$\mathbf{x} = \mathbf{X} + \mathbf{u} \tag{3.1}$$

with $\mathbf{u}$ the displacement vector. The deformation gradient $\mathbf{F}$ is obtained by differentiating $\mathbf{x}$ with respect to $\mathbf{X}$

$$\mathbf{F} = \frac{\partial \mathbf{x}}{\partial \mathbf{X}} = \boldsymbol{i} + \frac{\partial \mathbf{u}}{\partial \mathbf{X}} \tag{3.2}$$

with $\boldsymbol{i}$ the second–order unit tensor. In the formulation of constitutive relations an objective strain measure is required. Because of its computational convenience the Green–Lagrange strain tensor is often selected:

$$\boldsymbol{\gamma} = \frac{1}{2}\left(\frac{\partial \mathbf{u}}{\partial \mathbf{X}} + \left(\frac{\partial \mathbf{u}}{\partial \mathbf{X}}\right)^{\mathrm{T}} + \left(\frac{\partial \mathbf{u}}{\partial \mathbf{X}}\right)^{\mathrm{T}} \cdot \frac{\partial \mathbf{u}}{\partial \mathbf{X}}\right) \tag{3.3}$$

The incremental strain tensor is then given by:

$$\Delta\boldsymbol{\gamma} = \frac{1}{2}\left(\frac{\partial \Delta\mathbf{u}}{\partial \mathbf{X}} + \left(\frac{\partial \Delta\mathbf{u}}{\partial \mathbf{X}}\right)^{\mathrm{T}} + \left(\frac{\partial \mathbf{u}}{\partial \mathbf{X}}\right)^{\mathrm{T}} \cdot \frac{\partial \Delta\mathbf{u}}{\partial \mathbf{X}} + \left(\frac{\partial \Delta\mathbf{u}}{\partial \mathbf{X}}\right)^{\mathrm{T}} \cdot \frac{\partial \mathbf{u}}{\partial \mathbf{X}} + \left(\frac{\partial \Delta\mathbf{u}}{\partial \mathbf{X}}\right)^{\mathrm{T}} \cdot \frac{\partial \Delta\mathbf{u}}{\partial \mathbf{X}}\right) \tag{3.4}$$

The incremental strain tensor consists of a part that is linear in the incremental displacement field and a part that is quadratic in the incremental displacement field. For computational convenience we introduce

$$\Delta\boldsymbol{\gamma} = \Delta\boldsymbol{\epsilon} + \Delta\boldsymbol{\eta} \tag{3.5}$$

with

$$\Delta\boldsymbol{\epsilon} = \frac{1}{2}\left(\frac{\partial \Delta\mathbf{u}}{\partial \mathbf{X}} + \left(\frac{\partial \Delta\mathbf{u}}{\partial \mathbf{X}}\right)^{\mathrm{T}} + \left(\frac{\partial \mathbf{u}}{\partial \mathbf{X}}\right)^{\mathrm{T}} \cdot \frac{\partial \Delta\mathbf{u}}{\partial \mathbf{X}} + \left(\frac{\partial \Delta\mathbf{u}}{\partial \mathbf{X}}\right)^{\mathrm{T}} \cdot \frac{\partial \mathbf{u}}{\partial \mathbf{X}}\right) \tag{3.6}$$

$$\Delta\boldsymbol{\eta} = \frac{1}{2}\left(\frac{\partial \Delta\mathbf{u}}{\partial \mathbf{X}}\right)^{\mathrm{T}} \cdot \frac{\partial \Delta\mathbf{u}}{\partial \mathbf{X}} \tag{3.7}$$

Furthermore, we introduce the variation of the displacement field as $\delta\mathbf{u}$, so that we can define the variation of the Green–Lagrange strain as:

$$\delta\boldsymbol{\gamma} = \frac{1}{2}\left(\frac{\partial \delta\mathbf{u}}{\partial \mathbf{X}} + \left(\frac{\partial \delta\mathbf{u}}{\partial \mathbf{X}}\right)^{\mathrm{T}} + \left(\frac{\partial \mathbf{u}}{\partial \mathbf{X}}\right)^{\mathrm{T}} \cdot \frac{\partial \delta\mathbf{u}}{\partial \mathbf{X}} + \left(\frac{\partial \delta\mathbf{u}}{\partial \mathbf{X}}\right)^{\mathrm{T}} \cdot \frac{\partial \mathbf{u}}{\partial \mathbf{X}}\right) \tag{3.8}$$

In the actual configuration and ignoring inertia effects, the balance of momentum reads:

$$\nabla_{\mathbf{x}} \cdot \boldsymbol{\sigma} + \rho\mathbf{g} = \mathbf{0} \tag{3.9}$$

where the subscript $\mathbf{x}$ denotes differentiation with respect to the current configuration, $\boldsymbol{\sigma}$ is the Cauchy stress tensor, ρ is the mass density in the current configuration and $\mathbf{g}$ is the gravity acceleration. The weak form of the momentum equation is obtained in

a standard manner by multiplying the balance of momentum by a test function $\boldsymbol{w}$ and integrating over the domain Ω. After using the divergence theorem, one obtains:

$$\int_\Omega \nabla_{\mathbf{x}}^{\mathrm{sym}} \boldsymbol{w} : \boldsymbol{\sigma} \mathrm{d}\Omega = \int_\Omega \boldsymbol{w} \cdot \rho \mathbf{g} \mathrm{d}\Omega + \int_\Gamma \boldsymbol{w} \cdot \mathbf{t} \mathrm{d}\Gamma \tag{3.10}$$

with Γ the external boundary to the body Ω and the superscript *sym* denoting a symmetrised operator. In a total Lagrange description, which is employed predominantly in computational structural analysis, static and kinematic variables are functions of the undeformed, or reference configuration Ω^0 and it is computationally convenient to transform eq. (3.10) to the reference configuration. After some algebraic manipulations, using conservation of mass, $\rho^0 \mathrm{d}\Omega^0 = \rho \mathrm{d}\Omega$, and identifying the test function $\boldsymbol{w}$ with the variation of the displacement field, $\delta \mathbf{u}$, one obtains:

$$\int_{\Omega^0} \delta \boldsymbol{\gamma} : \boldsymbol{\tau} \, \mathrm{d}\Omega^0 = \int_{\Omega^0} \delta \mathbf{u} \cdot \rho^0 \mathbf{g} \, \mathrm{d}\Omega^0 + \int_{\Gamma^0} \delta \mathbf{u} \cdot \mathbf{t}^0 \, \mathrm{d}\Gamma^0 \tag{3.11}$$

where $\mathbf{t}^0$ is the (nominal) traction vector referred to the undeformed state, ρ^0 is the mass density in the undeformed configuration, Γ^0 is the surface in the undeformed state, and $\boldsymbol{\tau}$ is the second Piola–Kirchhoff stress tensor, which is related to the Cauchy stress tensor $\boldsymbol{\sigma}$ by:

$$\boldsymbol{\sigma} = (\mathrm{det}\mathbf{F}) \, \mathbf{F} \cdot \boldsymbol{\tau} \cdot \mathbf{F}^{\mathrm{T}} \tag{3.12}$$

with $\mathrm{det}\mathbf{F} = \rho / \rho^0$.

In general, eq. (3.11) is highly nonlinear, because of the nonlinear dependence of $\boldsymbol{\tau}$ on $\boldsymbol{\gamma}$ and because of the nonlinear dependence of $\boldsymbol{\gamma}$ on $\mathbf{u}$: $\boldsymbol{\tau} = \boldsymbol{\tau}(\boldsymbol{\gamma}(\mathbf{u}))$. Solution of eq. (3.11) is therefore achieved using some iterative procedure, usually the Newton–Raphson method in computational structural analysis. Linearising the stress–strain relation $\boldsymbol{\tau} = \boldsymbol{\tau}(\boldsymbol{\gamma})$ to give the material tangential stiffness tensor,

$$\mathbf{D} = \frac{\partial \boldsymbol{\tau}}{\partial \boldsymbol{\gamma}} \tag{3.13}$$

we obtain for the unknown stress $\boldsymbol{\tau}_j$ at iteration j:

$$\boldsymbol{\tau}_j = \mathbf{D} : \mathrm{d}\boldsymbol{\gamma} + \boldsymbol{\tau}_{j-1} \tag{3.14}$$

with $\boldsymbol{\tau}_{j-1}$ the known stress at the previous iteration $j-1$ and the d-symbol signifying the iterative change of a quantity from iteration $j-1$ to iteration j. With eq. (3.14), we obtain instead of eq. (3.11):

$$\int_{\Omega^0} \delta \boldsymbol{\gamma} : \mathbf{D} : \mathrm{d}\boldsymbol{\gamma} \mathrm{d}\Omega^0 + \int_{\Omega^0} \delta \boldsymbol{\gamma} : \boldsymbol{\tau}_{j-1} \mathrm{d}\Omega^0 = \int_{\Omega^0} \delta \mathbf{u} \cdot \rho^0 \mathbf{g} \mathrm{d}\Omega^0 + \int_{\Gamma^0} \delta \mathbf{u} \cdot \mathbf{t}^0 \mathrm{d}\Gamma^0 \tag{3.15}$$

Elaborating this equation using the strain decomposition (3.5) and consistent linearisation leads to:

$$\int_{\Omega^0} \delta \boldsymbol{\epsilon} : \mathbf{D} : \mathrm{d}\boldsymbol{\epsilon} \mathrm{d}\Omega^0 + \int_{\Omega^0} \delta \boldsymbol{\eta} : \boldsymbol{\tau}_{j-1} \mathrm{d}\Omega^0 = \int_{\Omega^0} \delta \mathbf{u} \cdot \rho^0 \mathbf{g} \mathrm{d}\Omega^0 + \int_{\Gamma^0} \delta \mathbf{u} \cdot \mathbf{t}^0 \mathrm{d}\Gamma^0 - \int_{\Omega^0} \delta \boldsymbol{\epsilon} : \boldsymbol{\tau}_{j-1} \mathrm{d}\Omega^0 \tag{3.16}$$

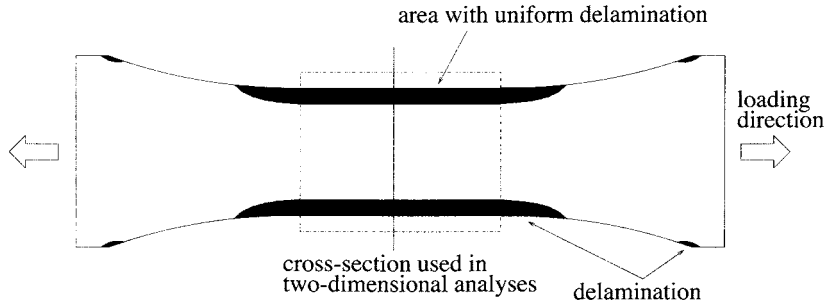

Figure 5. T-bone shaped AS-3501-06 graphite-epoxy laminated strip subjected to uniaxial loading

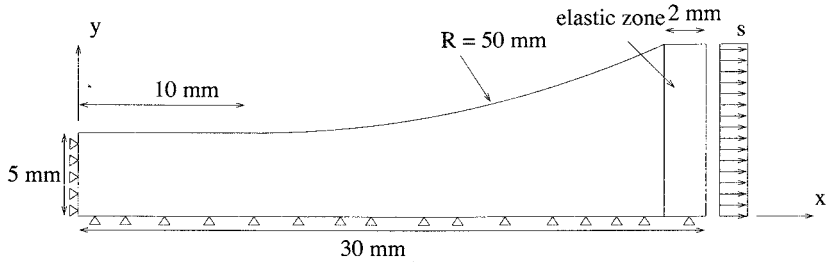

Figure 6. Quarter of T-bone shaped laminated strip

After a standard discretisation of the displacement field $\mathbf{u}$, a discrete set of (nonlinear) algebraic equations is obtained. Such a discretisation will be elaborated in the next subsection for the specific case of generalised plane–strain elements and comments on the solution of the nonlinear set of equations will be made later in this section.

At the beginning of each load increment, so for $j = 0$, the possible influence of hygro–thermal effects is taken into account. Assuming that there are no nonlinear effects in the plies other than hygral and thermal strains the stress increment is then given by

$$\mathrm{d}\boldsymbol{\tau}_0 = \Delta\boldsymbol{\tau} = \mathbf{D} : (\Delta\boldsymbol{\gamma} - \Delta T\boldsymbol{\alpha} - \Delta C\boldsymbol{\beta}) \tag{3.17}$$

with ΔT and ΔC the incremental changes in temperature and moisture content in the current loading step, respectively. The vectors $\boldsymbol{\alpha}$, $\boldsymbol{\beta}$ contain the thermal and hygroscopic expansion coefficients, respectively.

Due to mismatch of the Poisson effect between the layers of a laminated structure, as caused by the different orientation of the fibres, interlaminar stresses will develop between the plies at the free edges. At a generic stage in the loading process, these edge stresses will lead to delamination. Depending on the stacking sequence of the laminate and the position of the delamination zone in the laminate, delamination occurs purely as mode-I delamination or as delamination due to a combination of several cracking modes, so-called mixed-mode delamination. For the three–dimensional example of Figure 5, we will consider a lay-up that causes pure mode–I delamination, which is the dominant

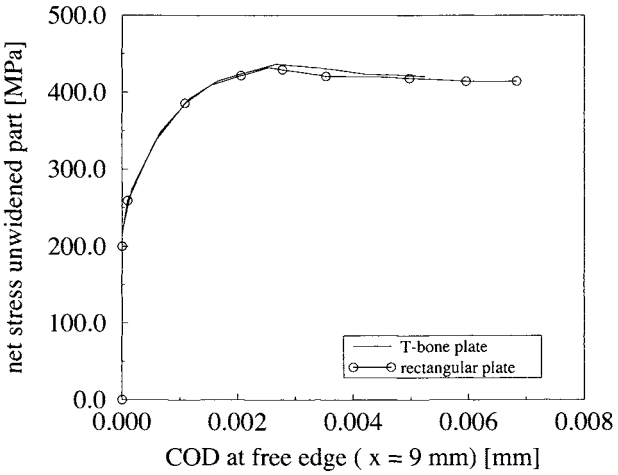

Figure 7. COD *vs* axial stress for the full T–bone specimen and for an approximated 3D solution using the rectangular specimen of Figure 8

mode if delamination occurs in the mid–plane of a symmetric laminate. Consequently, only the upper (or equivalently, the lower) half of the laminate needs to be analysed. The interface delamination model was based on a damage formalism, see Schipperen and Lingen (1999) for details, where also the relevant material parameters can be found.

The strip that has been analysed, has a laminate lay-up of $[25, -25, 90]_s$ and is manufactured of an AS-3501-06 graphite-epoxy. The initiation of delamination occurs at a threshold deformation $\kappa_i = 51.6 \cdot 10^{-7} mm$ in the normal direction of the interface. This threshold deformation is determined from the tensile strength of the material and the normal elastic stiffness in the interface d_n. Because of the zero thickness of the interface this parameter is in fact a dummy stiffness. The use of a dummy stiffness in the determination of κ_i makes the initiation of damage somethat arbitrary. However, the opening of the interface after damage initiation is controlled by the fracture energy of the material, $\mathcal{G}_c = 0.175 N/mm$, which ensures that delamination propagation is predicted properly.

The specimen that has been analysed is depicted in Figure 6 in more detail. The linear elastic ends of the specimen are a simplification of the real situation in an experiment and have been included in the analyses to limit the influence of the boundary conditions. Furthermore, to reduce the computation time, the radius of the transition zone has been taken fairly small compared to data suggested in norms. The COD versus axial stress, measured as the average stress in the narrow part of the strip, is shown in Figure 7.

Numerical solutions of boundary-value problems involving materials that show a descending branch after reaching a peak load level, can be highly mesh sensitive (de Borst , 2004). However, in the present situation, where the degrading phenomena are limited to a discrete interface where the crack opening is controlled by a fracture energy (cohesive–zone approach), the boundary value problem remains well–posed and, consequently, no

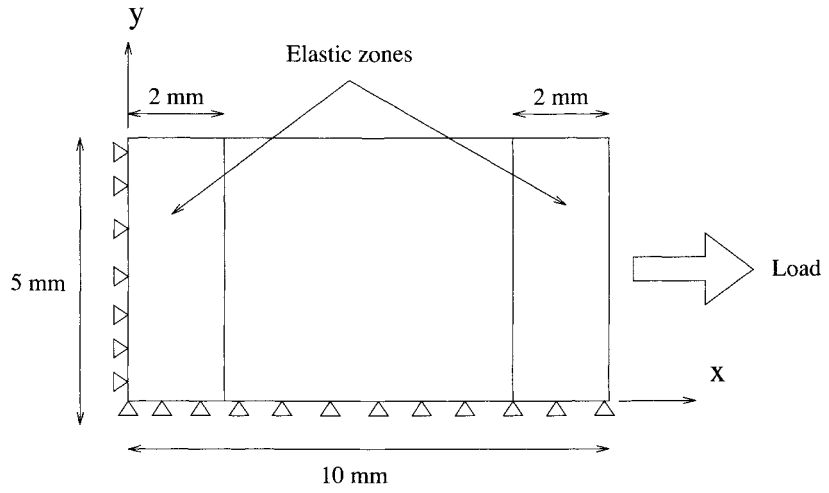

Figure 8. Quarter of the rectangular specimen used in the approximate 3D solutions

mesh sensitivity should be observed. This is confirmed in a mesh refinement study of a three-dimensional rectangular plate, Figure 8, which is used to approximate the original T–bone specimen, but, because of its simpler geometry, is less expensive in mesh refinement studies. The load–displacement curves for the original T–bone specimen and the approximate 3D specimen are close, Figure 7, justifying the approximation for the purpose of a mesh refinement study.

Three different meshes have been used in the calculations. The coarse mesh consisted of 20 elements over the width and 25 elements over the length of the plate. For the two finer meshes the element distribution over the width was not equidistant. For the 2.5 mm of the width of the plate closest to the free edge a finer mesh was used. This leads to 35 elements over the width and 25 elements over the length of the plate for the second mesh and to 70 elements over the width and 50 elements over the length of the place for the finest mesh. The crack opening displacement of a node near the centre of the free edge has been plotted versus the applied axial stress for all three meshes in Figure 9. No mesh sensitivity can be noticed. In Figure 10 the delamination zone of the plate is shown at several stages during the computation. Until the peak load the delamination is uniform, since the slight waviness is purely due to visualisation aspects. However, in the descending branch of Figure 9 the delamination zone becomes more and more non–uniform.

3.2 Generalised Plane-Strain Formulation

If the length of a laminate is large compared to the width and the thickness we may assume that, for uniaxial tensile or compressive loadings, at a certain distance from the ends of the specimen, the in–plane displacements in the X_2, X_3–plane are independent of the X_1-coordinate, Figure 11. This results in the following set of equations for the

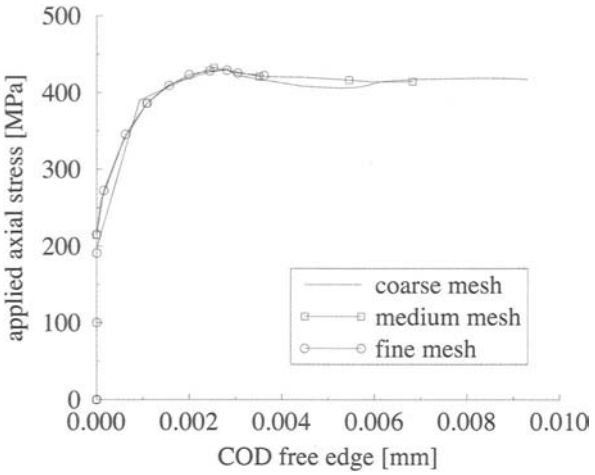

Figure 9. Mesh sensitivity studies for the 3D rectangular specimen

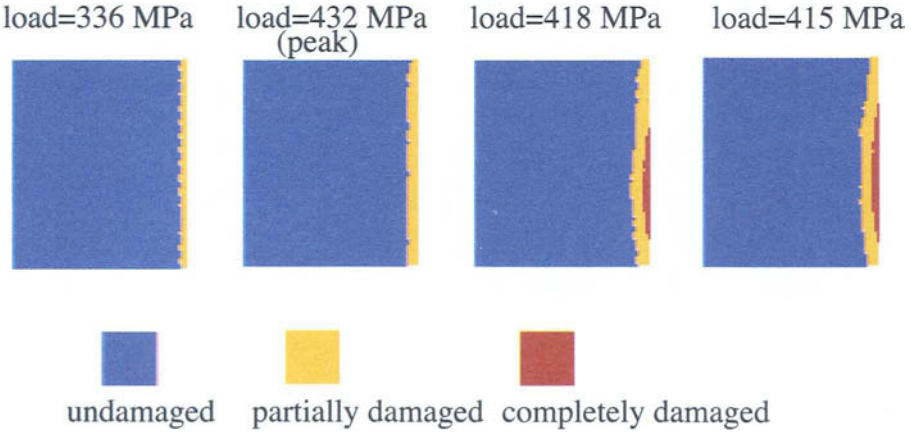

Figure 10. Evolution of the delamination zone in simplified three–dimensional analysis

displacement field of a cross section (Pipes and Pagano , 1970; Pagano , 1974; Schellekens and de Borst , 1993):

$$u_1(X_1, X_2, X_3) = \lambda \epsilon_{11} X_1 + u_1(X_2, X_3) \tag{3.18a}$$

$$u_2(X_1, X_2, X_3) = u_2(X_2, X_3) \tag{3.18b}$$

$$u_3(X_1, X_2, X_3) = u_3(X_2, X_3) \tag{3.18c}$$

with ϵ_{11} a normalised strain that is prescribed in the X_1–direction of the specimen and λ a load parameter. With the increment of the Green–Lagrange strain tensor, eq. (3.4),

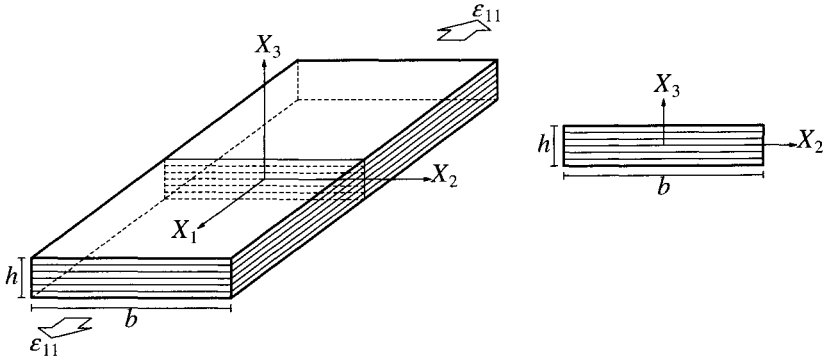

Figure 11. Uniaxially loaded laminate strip

and noting that, for generalised plane–strain conditions, $\Delta u_{1,X_1} = \Delta\lambda\epsilon_{11}$, $\Delta u_{2,X_1} = 0$ and $\Delta u_{3,X_1} = 0$, we obtain for the strain increment $\Delta\boldsymbol{\gamma}$

$$\Delta\boldsymbol{\gamma} = \Delta\lambda\boldsymbol{\epsilon}_l + \Delta\boldsymbol{\epsilon}_0 + \Delta\boldsymbol{\epsilon}_1 + \Delta\boldsymbol{\eta} \tag{3.19}$$

where, using Voigt's notation, the contribution $\Delta\lambda\boldsymbol{\epsilon}_{11}$ is due to the applied strain loading,

$$\boldsymbol{\epsilon}_l = \begin{pmatrix} \epsilon_{11} \\ 0 \\ 0 \\ 0 \\ 0 \\ 0 \end{pmatrix} \tag{3.20}$$

$\Delta\boldsymbol{\epsilon}_0$ is of the order zero in the incremental displacements,

$$\Delta\boldsymbol{\epsilon}_0 = \begin{pmatrix} (F_{11}-1)\Delta\lambda\epsilon_{11} + \frac{1}{2}\Delta\lambda^2\epsilon_{11}^2 \\ 0 \\ 0 \\ F_{12}\Delta\lambda\epsilon_{11} \\ 0 \\ F_{13}\Delta\lambda\epsilon_{11} \end{pmatrix} \tag{3.21}$$

and $\Delta\boldsymbol{\epsilon}$ and $\Delta\boldsymbol{\eta}$ are linear and quadratic in the displacement increments, respectively:

$$\Delta\boldsymbol{\epsilon} = \begin{pmatrix} 0 \\ F_{12}\Delta u_{1,X_2} + F_{22}\Delta u_{2,X_2} + F_{32}\Delta u_{3,X_2} \\ F_{13}\Delta u_{1,X_3} + F_{23}\Delta u_{2,X_3} + F_{33}\Delta u_{3,X_3} \\ (F_{11} + \Delta\lambda\epsilon_{11})\Delta u_{1,X_2} \\ F_{12}\Delta u_{1,X_3} + F_{13}\Delta u_{1,X_2} + F_{22}\Delta u_{2,X_3} + F_{23}\Delta u_{2,X_2} + F_{32}\Delta u_{3,X_3} + F_{33}\Delta u_{3,X_2} \\ (F_{11} + \Delta\lambda\epsilon_{11})\Delta u_{1,X_3} \end{pmatrix} \tag{3.22}$$

and

$$\Delta\boldsymbol{\eta} = \begin{pmatrix} 0 \\ \frac{1}{2}\left(\Delta u^2_{1,X_2} + \Delta u^2_{2,X_2} + \Delta u^2_{3,X_2}\right) \\ \frac{1}{2}\left(\Delta u^2_{1,X_3} + \Delta u^2_{2,X_3} + \Delta u^2_{3,X_3}\right) \\ 0 \\ \Delta u_{1,X_2}\Delta u_{1,X_3} + \Delta u_{2,X_2}\Delta u_{2,X_3} + \Delta u_{3,X_2}\Delta u_{3,X_3} \\ 0 \end{pmatrix} \tag{3.23}$$

Because of the absence of external loadings in the X_2, X_3–plane the weak form of the balance of momentum (3.16) reduces to:

$$\int_{\Omega^0} \delta\boldsymbol{\epsilon}^{\mathrm{T}}\mathbf{D}\mathrm{d}\boldsymbol{\epsilon}\mathrm{d}\Omega^0 + \int_{\Omega^0} \delta\boldsymbol{\eta}^{\mathrm{T}}(\boldsymbol{\tau}_{j-1} + \mathrm{d}\lambda\mathbf{D}\boldsymbol{\epsilon}_l + \mathbf{D}\mathrm{d}\boldsymbol{\epsilon}_0)\mathrm{d}\Omega^0 = -\int_{\Omega^0} \delta\boldsymbol{\epsilon}^{\mathrm{T}}(\boldsymbol{\tau}_{j-1} + \mathrm{d}\lambda\mathbf{D}\boldsymbol{\epsilon}_l + \mathbf{D}\mathrm{d}\boldsymbol{\epsilon}_0)\mathrm{d}\Omega^0 \tag{3.24}$$

where, in conformity with the use of Voigt's notation, matrix–vector notation has been adopted. $\mathrm{d}\boldsymbol{\epsilon}$ is linear in the iterative nodal corrections $\mathrm{d}\mathbf{a}$:

$$\mathrm{d}\boldsymbol{\epsilon} = \mathbf{B}_L \mathrm{d}\mathbf{a} \tag{3.25}$$

with $\mathbf{B}_L$ given by, cf eq. 3.22:

$$\mathbf{B}_L = \begin{bmatrix} \mathbf{0} & \mathbf{0} & \mathbf{0} \\ F_{12}\mathbf{h}_{,X_2} & F_{22}\mathbf{h}_{,X_2} & F_{32}\mathbf{u}_{,X_2} \\ F_{13}\mathbf{h}_{,X_3} & F_{23}\mathbf{h}_{,X_3} & F_{33}\mathbf{u}_{,X_3} \\ (F_{11} + \mathrm{d}\lambda\epsilon_{11})\mathbf{h}_{,X_2} & \mathbf{0} & \mathbf{0} \\ F_{12}\mathbf{h}_{,X_3} + F_{13}\mathbf{h}_{,X_2} & F_{22}\mathbf{h}_{,X_3} + F_{23}\mathbf{h}_{,X_2} & F_{32}\mathbf{h}_{,X_3} + F_{33}\mathbf{h}_{,X_2} \\ (F_{11} + \mathrm{d}\lambda\epsilon_{11})\mathbf{h}_{,X_2} & \mathbf{0} & \mathbf{0} \end{bmatrix} \tag{3.26}$$

where $\mathbf{h}_{,X_i}$ contains the derivatives of the interpolation functions in the X_i–direction. Using eq. (3.25), the first term in eq. (3.24) becomes

$$\int_{\Omega^0} \delta\boldsymbol{\epsilon}^{\mathrm{T}}\mathbf{D}\mathrm{d}\boldsymbol{\epsilon}\mathrm{d}\Omega^0 = \delta\mathbf{a}^{\mathrm{T}} \int_{\Omega^0} \mathbf{B}_L^{\mathrm{T}}\mathbf{D}\mathbf{B}_L \mathrm{d}\Omega^0 \, \mathrm{d}\mathbf{a} \tag{3.27}$$

We next introduce the matrix

$$\mathbf{B}_{NL} = \begin{bmatrix} 0 & 0 & 0 \\ 0 & 0 & 0 \\ 0 & 0 & 0 \\ \partial_{,X_2} & 0 & 0 \\ 0 & \partial_{,X_2} & 0 \\ 0 & 0 & \partial_{,X_2} \\ \partial_{,X_3} & 0 & 0 \\ 0 & \partial_{,X_3} & 0 \\ 0 & 0 & \partial_{,X_3} \end{bmatrix} \tag{3.28}$$

with $\partial_{,X_i} = \partial/\partial X_i$. Now, the second term in the left hand of eq. (3.24) becomes

$$\int_{\Omega^0} \boldsymbol{\eta}^{\mathrm{T}}(\boldsymbol{\tau}_{j-1} + \mathrm{d}\lambda\mathbf{D}\boldsymbol{\epsilon}_l + \mathbf{D}\mathrm{d}\boldsymbol{\epsilon}_0)\mathrm{d}\Omega^0 = \delta\mathbf{a}^{\mathrm{T}} \int_{\Omega^0} \mathbf{B}_{NL}^{\mathrm{T}}(\mathbf{T}_{j-1} + \mathbf{E}_j)\mathbf{B}_{NL} \, \mathrm{d}\Omega^0 \, \mathrm{d}\mathbf{a} \tag{3.29}$$

where

$$\mathbf{T}_{j-1} = \begin{bmatrix} \tau_{11,j-1}\mathbf{I} & \tau_{12,j-1}\mathbf{I} & \tau_{31,j-1}\mathbf{I} \\ \tau_{12,j-1}\mathbf{I} & \tau_{22,j-1}\mathbf{I} & \tau_{23,j-1}\mathbf{I} \\ \tau_{31,j-1}\mathbf{I} & \tau_{23,j-1}\mathbf{I} & \tau_{33,j-1}\mathbf{I} \end{bmatrix}_{9\times 9} \tag{3.30}$$

and

$$\mathbf{E}_j = \begin{bmatrix} \tau_{g,11}\mathbf{I} & \tau_{g,12}\mathbf{I} & \tau_{g,31}\mathbf{I} \\ \tau_{g,12}\mathbf{I} & \tau_{g,22}\mathbf{I} & \tau_{g,23}\mathbf{I} \\ \tau_{g,31}\mathbf{I} & \tau_{g,23}\mathbf{I} & \tau_{g,33}\mathbf{I} \end{bmatrix}_{9\times 9} \tag{3.31}$$

with

$$\boldsymbol{\tau}_g = \mathbf{D}(\mathrm{d}\boldsymbol{\epsilon}_0 + \mathrm{d}\lambda\boldsymbol{\epsilon}_l) \tag{3.32}$$

Substitution of eqs (3.27) and (3.29) into eq. (3.24), and requiring that the result holds for any virtual displacement yields:

$$\mathbf{K}_j \mathrm{d}\mathbf{a} = -\int_{\Omega^0} \mathbf{B}_L^{\mathrm{T}}(\boldsymbol{\tau}_{j-1} + \mathrm{d}\lambda\mathbf{D}\boldsymbol{\epsilon}_l + \mathbf{D}\mathrm{d}\boldsymbol{\epsilon}_0)\mathrm{d}\Omega^0 \tag{3.33}$$

with

$$\mathbf{K}_j = \int_{\Omega^0} \mathbf{B}_L^{\mathrm{T}}\mathbf{D}\mathbf{B}_L \mathrm{d}\Omega^0 + \int_{\Omega^0} \mathbf{B}_{NL}^{\mathrm{T}}(\mathbf{T}_{j-1} + \mathbf{E}_j)\mathbf{B}_{NL}\ \mathrm{d}\Omega^0 \tag{3.34}$$

the tangential stiffness matrix.

The three–dimensional analysis of the preceding subsection has been repeated using generalised plane–strain elements. The analyses have been carried out for two–dimensional meshes of a cross section of a laminate subjected to a uniaxial strain under the assumption of uniform delamination at a certain distance away from the loaded edges, see Figure 5.

The first analysis has been performed on a strip with an individual ply height of 0.132 *mm* and a specimen width of 25 *mm*. For this specimen three different finite element discretisations have been considered, with element lengths of 0.05, 0.1 and 0.2 *mm*, respectively, near the free edge. This fine discretisation has been used only at the 5 *mm* nearest to the free edge of the specimen. The remainder of the laminate has been modelled with a coarser mesh with an element length of 2.5 *mm*. For the two–dimensional analyses, symmetry has been assumed, so that only one quarter of the cross section of the laminate has been modelled. This assumption has been made to reduce the problem size and thus the computation time. Of course, the assumed symmetry axis in the midplane of the laminate is valid due to the symmetrical ply lay–up. The other assumed symmetry axis is not a real symmetry axis of the laminate due to the fibre orientation in the plies. At the symmetry edges of the model supports were added according to the symmetry conditions, viz. $u_1(0,0,X_3) = 0, u_2(0,0,X_3) = 0$ and $u_3(0,X_2,0) = 0$. Prior to delamination, the interface elements have been assigned a high dummy stiffness $d_n = d_s = 10^{+8} N/mm^2$, in order to minimise the artificial elastic deformations in the interface.

The average axial stress (total axial load divided by the surface of the cross section) *vs* the applied axial strain is shown in Figure 12 for all three meshes. Clearly, no mesh sensitivity occurs. A comparison of the computed value for the ultimate strain, $\epsilon_l = 0.00518$,

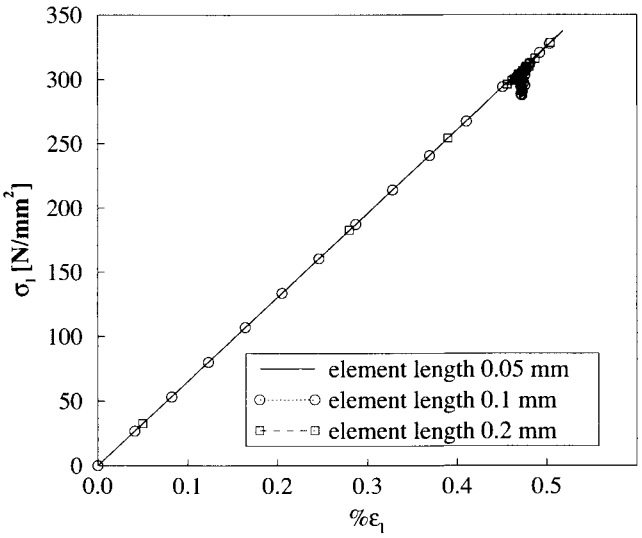

Figure 12. Average axial load *vs* applied axial strain for $[25, -25, 90]_s$ laminate using a generalised plane–strain approximation

with numerical results using a plasticity–based interface model, $\epsilon_l = 0.00516$ (Schellekens and de Borst , 1993), and with experimental data, $\epsilon_l = 0.0053$ (Wang , 1989), shows a good agreement.

The influence of the temperature drop that occurs during the manufacturing process has been taken into account by simulating a temperature drop $\Delta T = -125$ °C. If the temperature drop that occurs in the manufacturing process is not taken into account, the ultimate strain of the laminate is overestimated significantly, Figure 14, in which the delamination length from the free edge versus the applied axial strain is shown for the mesh with an element length of 0.1 mm near the free edge.

A comparison of the results of a two-dimensional analyses of this laminate and the three–dimensional analysis is given in Figure 14. The two–dimensional approximation is close, but it should be noted that this three–dimensional analysis has been carried out for the simplified three-dimensional model of Figure 8.

As an example of mixed–mode free–edge delamination, a composite strip loaded in uniaxial tension has been considered. The material was a Fibredux 6376C/35/135/HTA graphite epoxy. To introduce the initial stresses that are caused by the manufacturing process, a temperature drop $\Delta T = -150$ °C has been imposed prior to incrementing the axial elongation. A cross section of the example that we have considered, is shown in Figure 15. For this specific lay–up, the delamination jumps from one of the -35/90 interfaces to that which is located at the other side of the symmetry line and back (mixed–mode delamination). The energy that is dissipated in the crack that runs through the

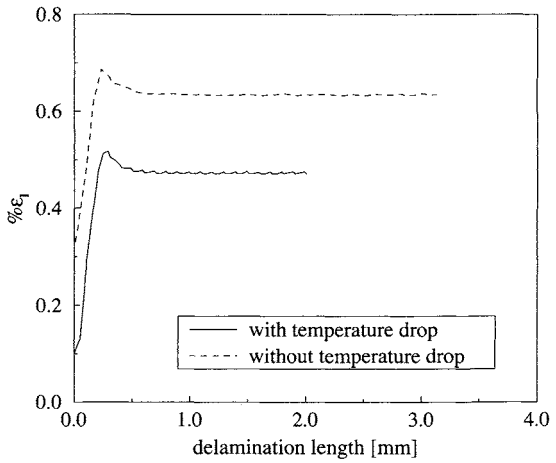

Figure 13. Delamination length *vs* applied strain with and without temperature drop

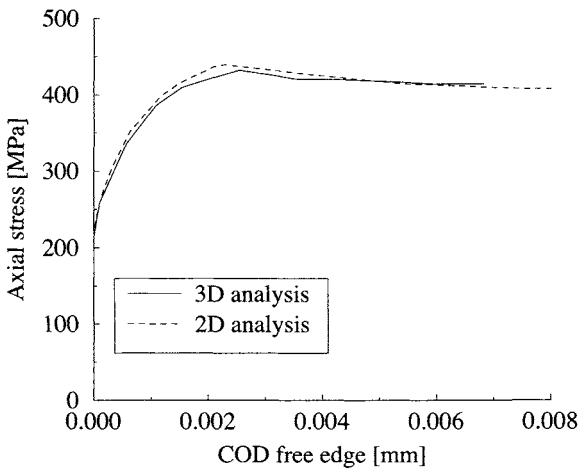

Figure 14. Comparison of load–displacement curves obtained from generalised plane–strain and from three–dimensional analyses

plies is negligible, because the fibres in this layer are parallel to the crack. Figure 16 shows the results in terms of the axial strain at onset of delamination for three different lay–ups. A clear size (thickness) effect is predicted because of the presence of the energy of separation $\mathcal{G}_c$ in the constitutive model for the interface. This computed size effect was confirmed by experiments carried out at the Catholic University of Leuven after completion of the computations (Schellekens and de Borst , 1994a).

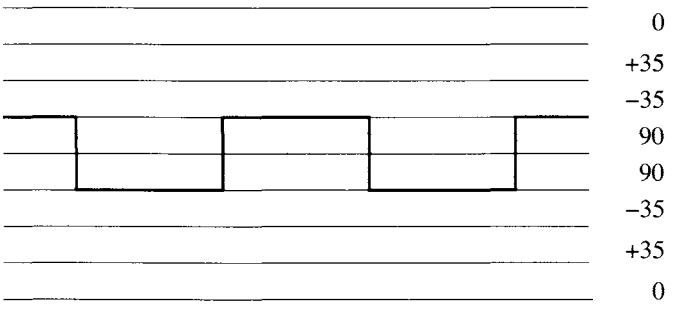

Figure 15. Mixed–mode delamination in a uniaxially loaded laminated strip: jumping of a delamination front between two -35/90 interfaces

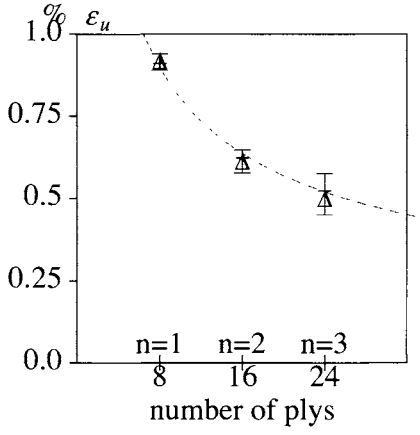

Figure 16. Computed and experimentally determined values for the ultimate strain ϵ_u as a function of the number of plies (Schellekens and de Borst , 1994a). Results are shown for laminates consisting of eight plies ($n = 1$), sixteen plies ($n = 2$) and twenty-four plies ($n = 3$). The triangles, which denote the numerical results, are well within the band of experimental results. The dashed line represents the inverse dependence of the ultimate strain on the laminate thickness

3.3 Solid-Like Shell Formulation

We consider the thick shell shown in Figure 17. The position of a material point in the shell in the undeformed configuration can be written as a function of the three curvilinear coordinates $[\xi, \eta, \zeta]$:

$$\mathbf{X}(\xi, \eta, \zeta) = \mathbf{X}_0(\xi, \eta) + \zeta \mathbf{D}(\xi, \eta) \tag{3.35}$$

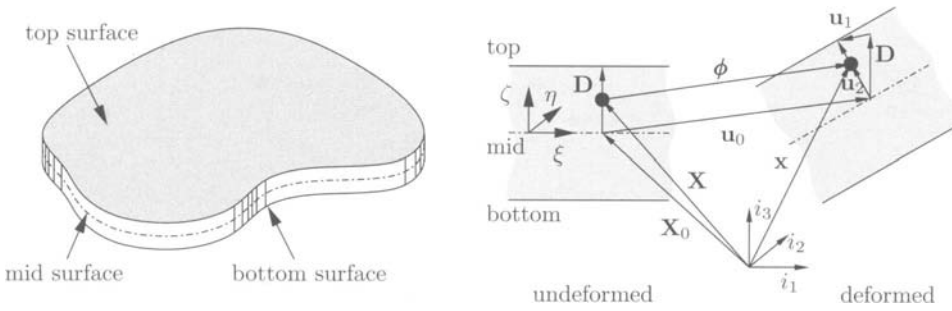

Figure 17. Kinematic relations of the solid–like shell element

where $\mathbf{X}_0(\xi, \eta)$ is the projection of the point on the mid-surface of the shell and $\mathbf{D}(\xi, \eta)$ is the thickness director in this point:

$$\mathbf{X}_0(\xi, \eta) = \frac{1}{2}\left[\mathbf{X}_t(\xi, \eta) + \mathbf{X}_b(\xi, \eta)\right] \tag{3.36}$$

$$\mathbf{D}(\xi, \eta) = \frac{1}{2}\left[\mathbf{X}_t(\xi, \eta) - \mathbf{X}_b(\xi, \eta)\right] \tag{3.37}$$

The subscripts $(\cdot)_t$ and $(\cdot)_b$ denote the projections of the variable onto the top and bottom surface, respectively. The position of the material point in the deformed configuration $\mathbf{x}(\xi, \eta, \zeta)$ is related to $\mathbf{X}(\xi, \eta, \zeta)$ via the displacement field $\boldsymbol{\phi}(\xi, \eta, \zeta)$ according to:

$$\mathbf{x}(\xi, \eta, \zeta) = \mathbf{X}(\xi, \eta, \zeta) + \boldsymbol{\phi}(\xi, \eta, \zeta) \tag{3.38}$$

where:

$$\boldsymbol{\phi}(\xi, \eta, \zeta) = \mathbf{u}_0(\xi, \eta) + \zeta \mathbf{u}_1(\xi, \eta) + (1 - \zeta^2)\mathbf{u}_2(\xi, \eta) \tag{3.39}$$

In this relation, $\mathbf{u}_0$ and $\mathbf{u}_1$ are the displacements of $\mathbf{X}_0$ on the shell mid-surface, and the thickness director $\mathbf{D}$, respectively:

$$\mathbf{u}_0(\xi, \eta) = \frac{1}{2}\left[\mathbf{u}_t(\xi, \eta) + \mathbf{u}_b(\xi, \eta)\right] \tag{3.40}$$

$$\mathbf{u}_1(\xi, \eta) = \frac{1}{2}\left[\mathbf{u}_t(\xi, \eta) - \mathbf{u}_b(\xi, \eta)\right] \tag{3.41}$$

and $\mathbf{u}_2(\xi, \eta)$ denotes the internal stretching of the element, which is colinear with the thickness director in the deformed configuration and is a function of an additional 'stretch' parameter w:

$$\mathbf{u}_2(\xi, \eta) = w(\xi, \eta)[\mathbf{D} + \mathbf{u}_1(\xi, \eta)] \tag{3.42}$$

The displacement field $\boldsymbol{\phi}$ is considered as a function of two kinds of variables; the ordinary displacement field $\mathbf{u}$, which will be split in a displacement of the top and bottom surfaces $\mathbf{u}_t$ and $\mathbf{u}_b$, respectively, and the internal stretch parameter w:

$$\boldsymbol{\phi} = \boldsymbol{\phi}(\mathbf{u}_t, \mathbf{u}_b, w) \tag{3.43}$$

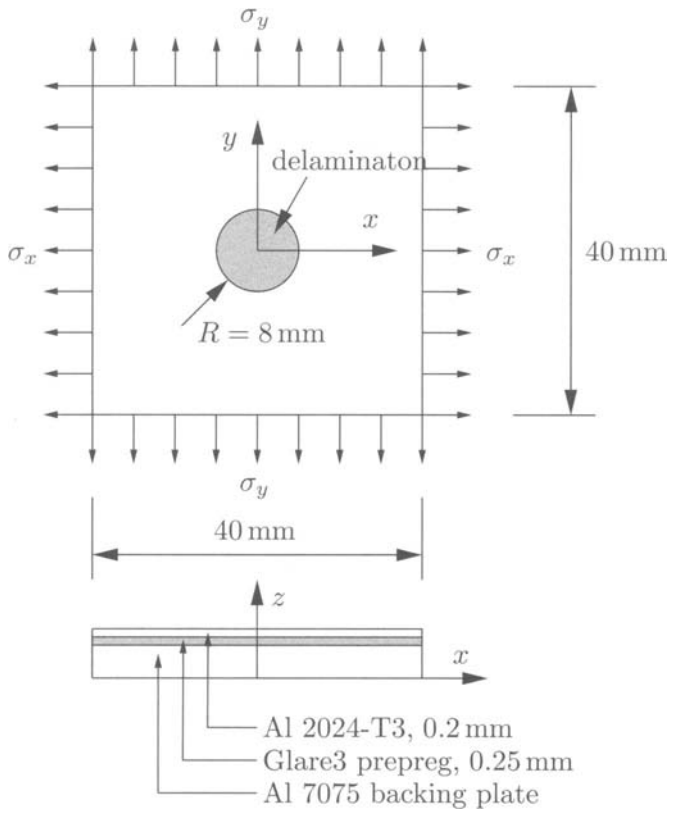

Figure 18. Geometry of a Glare panel with a circular initial delamination

The derivation of the strains and the finite element formulation are given in Hashagen *et al.* (1995) and Parisch (1995).

Using the solid–like shell element, the behaviour of a Glare panel with a circular initial delamination and a sinusoidally shaped out–of–plane imperfection (with an amplitude of 0.003 mm) subject to a compressive load has been examined. The failure mechanism is slightly complicated, since the delaminated zone grows in a direction perpendicular to the main loading direction. As a result, the delaminated area transforms from a circular area into an ellipsoidal one. Consequently, the buckling mode will change as well, and some parts of the top layer will tend to move inwards. For this reason, the possibility of self–contact has been included and a contact algorithm has been activated.

The specimen of Figure 18 consists of an aluminium layer with thickness $h_1 = 0.2\ mm$ and a Glare3 0/90° prepreg layer with a thickness $h_2 = 0.25\ mm$, (Remmers and de Borst , 2002). An initially circular delamination area with radius 8 mm is assumed. The layers are attached to a thick backing plate in order to prevent global buckling. A uniaxial compressive loading in x–direction is considered ($\sigma_x = -\sigma_0$, $\sigma_y = 0.0$).

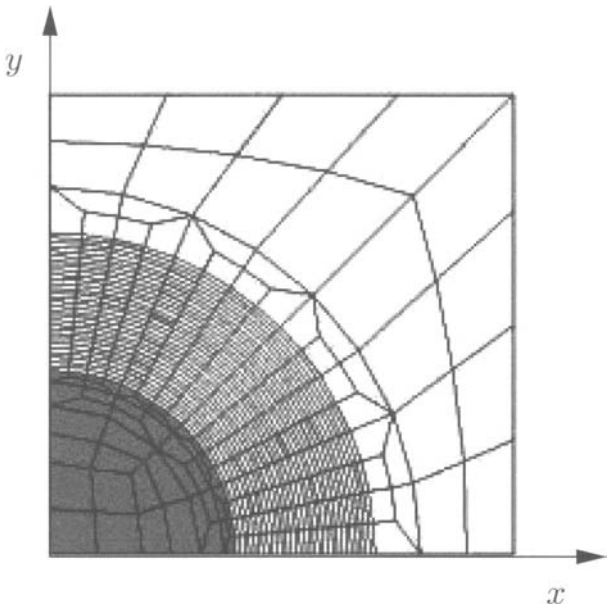

Figure 19. Mesh used for the simulation of delamination growth in the Glare panel. The initial delamination is located at the darker elements. Note that just one quarter of the panel ($x > 0$, $y > 0$) has been modelled

Table 1. Material parameters for 0/90° Glare3

E_{11}	33 170 MPa	G_{12}	5 500 MPa	ν_{12}	0.195
E_{22}	33 170 MPa	G_{23}	5 500 MPa	ν_{23}	0.032
E_{33}	9 400 MPa	G_{13}	5 500 MPa	ν_{13}	0.06

The finite element mesh is shown in Figure 19. The material parameters for the Glare3 layer are taken from Hashagen and de Borst (2000), see Table 1. The ultimate traction in normal direction in tension and compression are assumed to be $\bar{t}_n^t = 50\ MPa$ and $\bar{t}_n^c = 150\ MPa$, respectively, and the ultimate traction in the two transverse directions equals $\bar{t}_{s1} = \bar{t}_{s2} = 25\ MPa$. The work of separation is $\mathcal{G}_c = 1.1\ N/mm$. An initial stiffness of the interface elements of $d_n = 50\,000\ N/mm^2$ has been assumed.

The analytical estimation for the local buckling load of a clamped unidirectional panel with thickness h_1 subjected to an axial compressive load σ_0 was derived in Shivakumar and Whitcomb (1985). For this configuration, the lowest critical buckling load is equal to $\sigma_0 = 113.2\ MPa$.

For the contact algorithm the penalty stiffness has been set equal to the initial stiffness of the interface elements with the delamination model, $d_{pen} = 50\,000\ MPa$. The out-of-plane displacement of the centre point of the panel is shown in Figure 20. The local buckling load is in agreement with an eigenvalue analysis (Remmers and de Borst ,

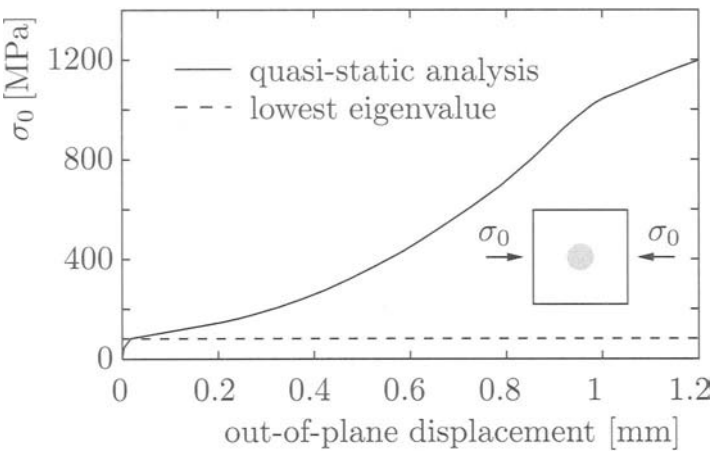

Figure 20. Out–of–plane displacement of top layer versus applied axial compressive load σ_0. The dashed line corresponds to the critical buckling load obtained by an eigenvalue analysis (Remmers and de Borst , 2002)

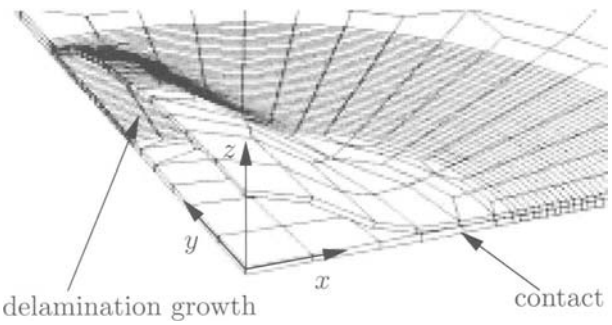

Figure 21. Final deformation of the Glare laminate under uniaxial loading (Remmers and de Borst , 2002)

2002). Initial delamination growth does not start until a load level $\sigma_0 = 300\ MPa$, while progressive delamination begins at an external load level $\sigma_0 \approx 950\ MPa$. As this value is far beyond normal stress levels, the analysis suggests that delamination buckling is of little concern in uniaxially compressed Glare panels. As expected, the delamination extends in a direction perpendicular to the loading direction, Figure 21.

3.4 Interface Elements

We consider an N-noded line or plane interface, e.g. Figure 22 for a line interface. In a general three–dimensional configuration each node has three translational degrees-of-

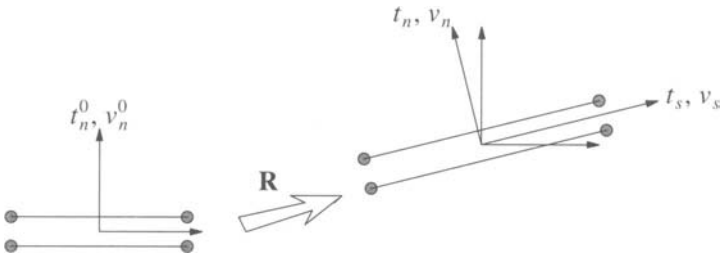

Figure 22. Line interface element and transformation from the reference to the current configuration

freedom, which leads to an element nodal displacement vector $\mathbf{a}$

$$\mathbf{a} = \left(a_n^1, ..., a_n^N, a_s^1, ..., a_s^N, a_t^1, ..., a_t^N\right)^{\mathrm{T}} \tag{3.44}$$

where n denotes the direction normal to the interface surface and s and t denote the directions tangential to the interface surface, respectively. The continuous displacement field is denoted as

$$\mathbf{u} = \left(u_n^u, u_n^l, u_s^u, u_s^l, u_t^u, u_t^l\right)^{\mathrm{T}} \tag{3.45}$$

where the superscripts u and l indicate the upper and lower sides or planes of the interface, respectively. With aid of the interpolation polynomials collected in the array $\mathbf{h}$ the relation between the continuous displacement field and the nodal displacement vector is derived as:

$$\mathbf{u} = \mathbf{H}\mathbf{a} \tag{3.46}$$

with

$$\mathbf{H} = \begin{bmatrix} \mathbf{h} & \mathbf{0} & \mathbf{0} & \mathbf{0} & \mathbf{0} & \mathbf{0} \\ \mathbf{0} & \mathbf{h} & \mathbf{0} & \mathbf{0} & \mathbf{0} & \mathbf{0} \\ \mathbf{0} & \mathbf{0} & \mathbf{h} & \mathbf{0} & \mathbf{0} & \mathbf{0} \\ \mathbf{0} & \mathbf{0} & \mathbf{0} & \mathbf{h} & \mathbf{0} & \mathbf{0} \\ \mathbf{0} & \mathbf{0} & \mathbf{0} & \mathbf{0} & \mathbf{h} & \mathbf{0} \\ \mathbf{0} & \mathbf{0} & \mathbf{0} & \mathbf{0} & \mathbf{0} & \mathbf{h} \end{bmatrix} \tag{3.47}$$

To relate the continuous displacement field to the relative displacements an operator matrix $\mathbf{L}$ is introduced:

$$\mathbf{L} = \begin{bmatrix} -1 & 0 & 0 \\ +1 & 0 & 0 \\ 0 & -1 & 0 \\ 0 & +1 & 0 \\ 0 & 0 & -1 \\ 0 & 0 & +1 \end{bmatrix} \tag{3.48}$$

With the relative displacement vector $\mathbf{v}^{\mathrm{T}} = (v_n, v_s, v_t)$ we obtain

$$\mathbf{v} = \mathbf{L}\mathbf{u} \tag{3.49}$$

The relation between nodal displacements and relative displacements for continuous elements is now derived from eqs (3.46) and (3.49) as:

$$\mathbf{v} = \mathbf{LHa} = \mathbf{Ba} \tag{3.50}$$

where the relative displacement–nodal displacement matrix $\mathbf{B}$ now reads

$$\mathbf{B} = \begin{bmatrix} -\mathbf{h} & \mathbf{h} & \mathbf{0} & \mathbf{0} & \mathbf{0} & \mathbf{0} \\ \mathbf{0} & \mathbf{0} & -\mathbf{h} & \mathbf{h} & \mathbf{0} & \mathbf{0} \\ \mathbf{0} & \mathbf{0} & \mathbf{0} & \mathbf{0} & -\mathbf{h} & \mathbf{h} \end{bmatrix} \tag{3.51}$$

For an arbitrarily oriented interface element the matrix $\mathbf{B}$ subsequently has to be transformed to the local coordinate system of the integration point or node-set.

In interface elements tractions and relative displacements are evaluated between the upper and the lower interface sides or planes. The components of the traction and relative displacement vector are determined by the orientations of the element sides or planes, and are thus fixed. With the Cauchy traction vector at the interface, $\mathbf{t}_i$, a relative displacement vector $\mathbf{v}$ which refers to the current configuration and Γ the actual element surface, the first variation of the internal energy in the current configuration is given by

$$\delta W = \int_{\Gamma} \delta \mathbf{v}^{\mathrm{T}} \mathbf{t}_i \mathrm{d}\Gamma \tag{3.52}$$

which has to be added to the left–hand side of eq. (3.10). Similar to the previous continuum element formulations we will recast this expression in terms of static and kinematic variables that refer to the undeformed reference state. We first introduce $\mathrm{d}\Gamma = (\det\mathbf{J}/\det\mathbf{J}^0)\mathrm{d}\Gamma^0$ with $\det\mathbf{J}$ and $\det\mathbf{J}^0$ the determinants of the Jacobian matrices in the current and the reference configuration, respectively. We next define an interface traction vector that refers to the reference configuration, $\mathbf{t}_i^0 = (\det\mathbf{J}/\det\mathbf{J}^0)\mathbf{R}^{\mathrm{T}}\mathbf{t}_i$, with $\mathbf{R}$ a rotation matrix as in Figure 22, and a relative displacement vector with respect to the reference configuration: $\mathbf{v}^0 = \mathbf{R}^{\mathrm{T}}\mathbf{v}$. Subsequently, we can rewrite eq. (3.52) as:

$$\delta W = \int_{\Gamma^0} (\delta \mathbf{v}^0)^{\mathrm{T}} \mathbf{t}_i^0 \mathrm{d}\Gamma^0 \tag{3.53}$$

Hence, the auxiliary traction vector $\mathbf{t}_i^0$ is energetically conjugate to the relative displacement vector $\mathbf{v}^0$ measured with respect to the reference configuration and can therefore be employed as an interface traction measure in a geometrically nonlinear formulation of interface elements.

In a nonlinear analysis and assuming small strains, a traction vector $\mathbf{t}^0$ at the end of an iteration j can be expressed as

$$\mathbf{t}_j^0 = \mathbf{t}_{j-1}^0 + \mathbf{T}\mathrm{d}\mathbf{v}^0 \tag{3.54}$$

cf., eqs (2.2) and (2.3), and $\mathrm{d}\mathbf{v}^0$ denotes the iterative change in the relative displacement vector. Introducing eqs (3.50) and (3.54) in the virtual work expression (3.53) and considering that no external actions are acting on the interface elements, one obtains:

$$\delta\mathbf{a}^{\mathrm{T}} \int_{\Gamma^0} \mathbf{B}^{\mathrm{T}}\mathbf{T}\mathbf{B}\mathrm{d}\Gamma^0 \mathrm{d}\mathbf{a} = -\int_{\Gamma^0} \mathbf{B}^{\mathrm{T}}\mathbf{t}_{j-1}^0 \mathrm{d}\Gamma^0 \tag{3.55}$$

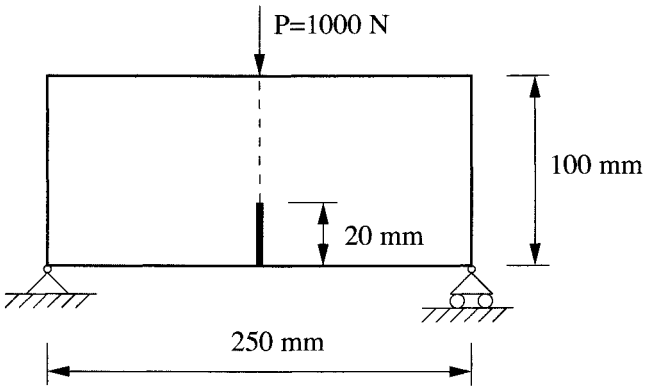

Figure 23. Geometry of symmetric, notched three–point bending beam

The element stiffness matrix $\mathbf{K}$ and the internal force vector $\mathbf{f}_{j-1}$ can thus be defined as

$$\mathbf{K} = \int_{\Gamma^0} \mathbf{B}^{\mathrm{T}}\mathbf{T}\mathbf{B}\mathrm{d}\Gamma^0 \tag{3.56}$$

and

$$\mathbf{f}_{j-1} = -\int_{\Gamma^0} \mathbf{B}^{\mathrm{T}}\mathbf{t}^0_{j-1}\mathrm{d}\Gamma^0 \tag{3.57}$$

In the foregoing examples, interface elements equipped with a cohesive–zone model have been inserted *a priori* in the finite element mesh. Before the tensile strength in the interface element is exceeded, which is monitored in the integration points of the interface element, no deformations should occur, since (elastic) deformations before the onset of fracture only take place in the bulk. Nevertheless, the formulation of conventional interface elements requires a finite stiffness prior to the onset of cracking, thus giving rise to (unphysical) deformations in the interface before crack initiation.

Prior to onset of delamination the stiffness matrix in the interface reads:

$$\mathbf{T} = \begin{bmatrix} d_n & 0 & 0 \\ 0 & d_s & 0 \\ 0 & 0 & d_t \end{bmatrix} \tag{3.58}$$

with d_n the stiffness normal to the interface and d_s and d_t the tangential stiffnesses. The undesired *elastic* deformations can be largely suppressed by choosing a high value for the stiffness d_n. Depending on the chosen spatial integration scheme, this high stiffness value can lead to spurious traction oscillations in the pre–cracking phase, which may cause erroneous crack patterns (Schellekens and de Borst , 1992; Remmers *et al.* , 2001). An example of an oscillatory traction pattern ahead of a notch is given in Figure 24 for the notched three–point bending beam of Figure 23. When analysing dynamic delaminations,

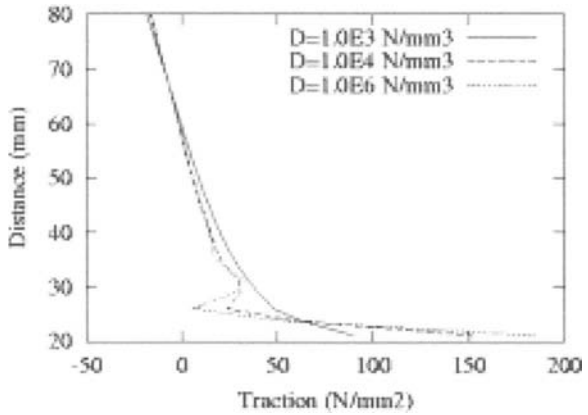

Figure 24. Traction profiles ahead of the notch using linear interface elements with Gauss integration. Results are shown for different values of the stiffness $D = d_n$ in the pre–cracking phase (Schellekens and de Borst , 1992; Remmers *et al.* , 2001)

spurious wave reflections can occur as a result of the introduction of such artificially high stiffness values prior to the onset of delamination. Moreover, the necessity to align the mesh with the potential planes of delamination, restricts the modelling capabilities, in particular for thin composite structures.

3.5 Solution Control

Depending on the lay–up, laminated composite structure can fail in a very brittle, and sometimes explosive manner. When plotting the axial load *vs* the axial elongation, this brittleness translates in snap–through and even in snap–back behaviour, see Figure 12 that contains results for the generalised plane–strain approximation of the T–bone specimen of Figure 5, which fails in mode–I. Use of standard load control prohibits the examination of the post–critical behaviour. However, path–following procedures, also known as arc–length procedures (Riks , 1970, 1972; Ramm , 1981; Crisfield , 1981), provide an elegant way to overcome this limitation of standard load control. This class of methods allows continuation of the computation beyond limit and turning points in the equilibrium path. While originally devised for and applied to purely geometrically nonlinear structural behaviour, there is no conceptual limitation to also apply the method to physically nonlinearities such as delaminations. However, it has been observed that, especially in case of highly localised deformations, the method tends to become less effective and that it can be more efficient to only consider one of more dominant degrees–of–freedom (de Borst , 1987). In delamination analyses the constraint equation is then based on the relative displacements in the delamination front.

Elaborating for the generalised plane–strain case, we observe that in a conventional strain loading the iterative change in nodal displacements $\mathrm{d}\mathbf{a}$ for iteration j is determined

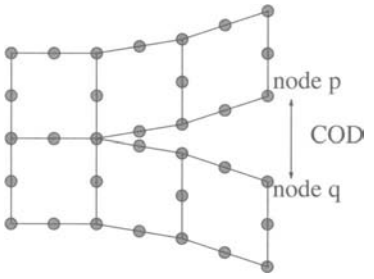

Figure 25. Crack Opening Displacement (COD) control

from eq. (3.33) If we define $\mathbf{q}$ as a normalised external load vector,

$$\mathbf{q} = -\int_{\Omega_0} \mathbf{B}_{\mathrm{L}}^{\mathrm{T}} \mathbf{D}\boldsymbol{\epsilon}_l \mathrm{d}\Omega_0 \tag{3.59}$$

and the internal force vector $\mathbf{p}_{j-1}$ as

$$\mathbf{p}_{j-1} = -\int_{\Omega^0} \mathbf{B}_{\mathrm{L}}^{\mathrm{T}} (\boldsymbol{\tau}_{j-1} - \Delta\lambda_{j-1}\mathbf{D}\boldsymbol{\epsilon}_l + \mathbf{D}\mathrm{d}\boldsymbol{\epsilon}_0)\mathrm{d}\Omega^0 \tag{3.60}$$

eq. (3.33) can be rephrased as:

$$\mathrm{d}\mathbf{a} = \mathbf{K}_j^{-1}(\Delta\lambda_j \mathbf{q} + \mathbf{p}_{j-1}) \tag{3.61}$$

since $\mathrm{d}\lambda = \Delta\lambda_j - \Delta\lambda_{j-1}$. In an arc–length modification of strain loading this process can be represented by the following set of equations

$$\mathrm{d}\mathbf{a}^{\mathrm{I}} = \mathbf{K}_j^{-1}\mathbf{p}_{j-1} \tag{3.62}$$

$$\mathrm{d}\mathbf{a}^{\mathrm{II}} = \mathbf{K}_j^{-1}\mathbf{q} \tag{3.63}$$

$$\mathrm{d}\mathbf{a} = \mathrm{d}\mathbf{a}^{\mathrm{I}} + \Delta\lambda_j \mathrm{d}\mathbf{a}^{\mathrm{II}} \tag{3.64}$$

The correction $\mathbf{da}$ is determined by the requirement that the Crack Opening Displacement (COD) of the interface between the two plies where delamination occurs should have the same value for each iteration, Figure 25:

$$\mathrm{d}(COD) = 0 \rightarrow \mathrm{d}a_p - \mathrm{d}a_q = 0 \tag{3.65}$$

with $\mathrm{d}a_p$ the change in displacement of node p in the direction normal to the interface from iteration $j-1$ to iteration j. Combination of eqs (3.64) and (3.65) yields the value for the change of the load parameter:

$$\Delta\lambda_j = -\frac{\mathrm{d}a_p^{\mathrm{I}} - \mathrm{d}a_q^{\mathrm{I}}}{\mathrm{d}a_p^{\mathrm{II}} - \mathrm{d}a_q^{\mathrm{II}}} \tag{3.66}$$

4 Modelling of Delamination and Debonding Based on the Partition-of-Unity Concept

4.1 The partition–of–unity concept

Considering the restrictions that adhere to the use of interface elements, the search has continued for a proper representation of the discrete character of cracks and interfaces, while allowing for an arbitrary direction of crack propagation, not biased by the initial mesh design. Meshless methods (Huerta *et al.* , 2004) were thought to provide a solution for this problem, but they appear to be less robust than traditional finite element methods, they are computationally more demanding and the implementation in three dimensions appears to be less straightforward. However, out of this research, a method has emerged, in which a discontinuity in the displacement field is captured exactly. It has the added benefit that it can be used advantageously at different scales, from microscopic to macroscopic analyses.

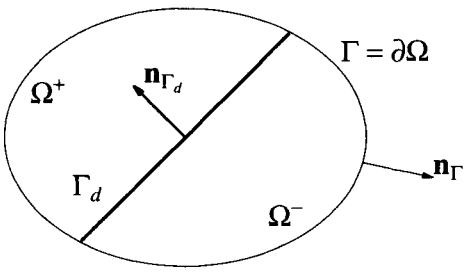

Figure 26. Body composed of continuous displacement fields at each side of the discontinuity Γ_d

The method makes use of the partition–of–unity property of finite element shape functions (Babuška and Melenk , 1997). A collection of functions ϕ_i, associated with nodes i, form a partition of unity if $\sum_{i=1}^{n} \phi_i(\mathbf{x}) = 1$ with n the number of discrete nodal points. For a set of functions ϕ_i that satisfy this property, a field u can be interpolated as follows:

$$u(\mathbf{x}) = \sum_{i=1}^{n} \phi_i(\mathbf{x}) \left(\bar{a}_i + \sum_{j=1}^{m} \psi_j(\mathbf{x}) \tilde{a}_{ij} \right) \tag{4.1}$$

with $\bar{a}_i$ the 'regular' nodal degrees–of–freedom, $\psi_j(\mathbf{x})$ the enhanced basis terms, and $\tilde{a}_{ij}$ the additional degrees–of–freedom at node i which represent the amplitudes of the jth enhanced basis term $\psi_j(\mathbf{x})$. In conventional finite element notation we can thus interpolate a displacement field as:

$$\mathbf{u} = \mathbf{N}(\bar{\mathbf{a}} + \tilde{\mathbf{N}}\tilde{\mathbf{a}}) \tag{4.2}$$

where $\mathbf{N}$ contains the standard shape functions, $\tilde{\mathbf{N}}$ the enhanced basis terms and $\bar{\mathbf{a}}$ and $\tilde{\mathbf{a}}$ collect the conventional and the additional nodal degrees–of–freedom, respectively. A displacement field that contains a single discontinuity, Figure 26, can be represented by

choosing (Belytschko and Black , 1999; Moës *et al.* , 1999):

$$\tilde{\mathbf{N}} = \mathcal{H}_{\Gamma_d}\mathbf{I} \tag{4.3}$$

Substitution into eq. (4.2) gives

$$\mathbf{u} = \underbrace{\mathbf{N}\bar{\mathbf{a}}}_{\bar{\mathbf{u}}} + \mathcal{H}_{\Gamma_d}\underbrace{\mathbf{N}\tilde{\mathbf{a}}}_{\tilde{\mathbf{u}}} \tag{4.4}$$

Identifying $\bar{\mathbf{u}} = \mathbf{N}\bar{\mathbf{a}}$ and $\tilde{\mathbf{u}} = \mathbf{N}\tilde{\mathbf{a}}$ we observe that eq. (4.4) exactly describes a displacement field that is crossed by a single discontinuity, but is otherwise continuous. Accordingly, the partition–of–unity property of finite element shape functions can be used in a straightforward fashion to incorporate discontinuities in a manner that preserves their discontinuous character.

As before, we take the balance of momentum

$$\nabla \cdot \boldsymbol{\sigma} + \rho\mathbf{g} = \mathbf{0} \tag{4.5}$$

as point of departure and multiply this identity by test functions $\boldsymbol{w}$, taking them from the same space as the trial functions for $\mathbf{u}$,

$$\boldsymbol{w} = \bar{\boldsymbol{w}} + \mathcal{H}_{\Gamma_d}\tilde{\boldsymbol{w}} \tag{4.6}$$

Applying the divergence theorem and requiring that this identity holds for arbitrary $\bar{\boldsymbol{w}}$ and $\tilde{\boldsymbol{w}}$ yields the following set of coupled equations:

$$\int_\Omega \nabla^{\mathrm{sym}}\bar{\boldsymbol{w}} : \boldsymbol{\sigma}\mathrm{d}\Omega = \int_\Omega \bar{\boldsymbol{w}} \cdot \rho\mathbf{g}\mathrm{d}\Omega + \int_\Gamma \bar{\boldsymbol{w}} \cdot \mathbf{t}\mathrm{d}\Gamma \tag{4.7}$$

$$\int_{\Omega^+} \nabla^{\mathrm{sym}}\tilde{\boldsymbol{w}} : \boldsymbol{\sigma}\mathrm{d}\Omega + \int_{\Gamma_d} \tilde{\boldsymbol{w}} \cdot \mathbf{t}_i\mathrm{d}\Gamma = \int_{\Omega^+} \tilde{\boldsymbol{w}} \cdot \rho\mathbf{g}\mathrm{d}\Omega + \int_\Gamma \mathcal{H}_{\Gamma_d}\tilde{\boldsymbol{w}} \cdot \mathbf{t}\mathrm{d}\Gamma \tag{4.8}$$

where in the volume integrals the Heaviside function has been eliminated by a change of the integration domain from Ω to Ω^+. With the standard interpolation:

$$\begin{aligned} \bar{\mathbf{u}} &= \mathbf{N}\bar{\mathbf{a}} \quad , \quad \tilde{\mathbf{u}} = \mathbf{N}\tilde{\mathbf{a}} \\ \bar{\boldsymbol{w}} &= \mathbf{N}\bar{\mathbf{w}} \quad , \quad \tilde{\boldsymbol{w}} = \mathbf{N}\tilde{\mathbf{w}} \end{aligned} \tag{4.9}$$

and requiring that the resulting equations must hold for any admissible $\bar{\mathbf{w}}$ and $\tilde{\mathbf{w}}$, we obtain the discrete format:

$$\int_\Omega \mathbf{B}^{\mathrm{T}}\boldsymbol{\sigma}\mathrm{d}\Omega = \int_\Omega \rho\mathbf{B}^{\mathrm{T}}\mathbf{g}\mathrm{d}\Omega + \int_\Gamma \mathbf{N}^{\mathrm{T}}\mathbf{t}\mathrm{d}\Gamma \tag{4.10}$$

$$\int_{\Omega^+} \mathbf{B}^{\mathrm{T}}\boldsymbol{\sigma}\mathrm{d}\Omega + \int_{\Gamma_d} \mathbf{N}^{\mathrm{T}}\mathbf{t}_d\mathrm{d}\Gamma = \int_{\Omega^+} \rho\mathbf{B}^{\mathrm{T}}\mathbf{g}\mathrm{d}\Omega + \int_\Gamma \mathcal{H}_{\Gamma_d}\mathbf{N}^{\mathrm{T}}\mathbf{t}\mathrm{d}\Gamma \tag{4.11}$$

After linearisation, the following matrix–vector equation is obtained:

$$\begin{bmatrix} \mathbf{K}_{\bar{a}\bar{a}} & \mathbf{K}_{\bar{a}\tilde{a}} \\ \mathbf{K}_{\tilde{a}\bar{a}} & \mathbf{K}_{\tilde{a}\tilde{a}} \end{bmatrix} \begin{pmatrix} \mathrm{d}\bar{\mathbf{a}} \\ \mathrm{d}\tilde{\mathbf{a}} \end{pmatrix} = \begin{pmatrix} \mathbf{f}_{\bar{a}}^{ext} - \mathbf{f}_{\bar{a}}^{int} \\ \mathbf{f}_{\tilde{a}}^{ext} - \mathbf{f}_{\tilde{a}}^{int} \end{pmatrix} \tag{4.12}$$

with $\mathbf{f}_{\bar{a}}^{int}, \mathbf{f}_{\tilde{a}}^{int}$ given by the left–hand sides of eqs (4.7)–(4.8), $\mathbf{f}_{\bar{a}}^{ext}, \mathbf{f}_{\tilde{a}}^{ext}$ given by the right–hand sides of eqs (4.7)–(4.8) and

$$\mathbf{K}_{\bar{a}\bar{a}} = \int_{\Omega} \mathbf{B}^{\mathrm{T}}\mathbf{D}\mathbf{B}\mathrm{d}\Omega \tag{4.13}$$

$$\mathbf{K}_{\bar{a}\tilde{a}} = \int_{\Omega^+} \mathbf{B}^{\mathrm{T}}\mathbf{D}\mathbf{B}\mathrm{d}\Omega \tag{4.14}$$

$$\mathbf{K}_{\tilde{a}\bar{a}} = \int_{\Omega^+} \mathbf{B}^{\mathrm{T}}\mathbf{D}\mathbf{B}\mathrm{d}\Omega \tag{4.15}$$

$$\mathbf{K}_{\tilde{a}\tilde{a}} = \int_{\Omega^+} \mathbf{B}^{\mathrm{T}}\mathbf{D}\mathbf{B}\mathrm{d}\Omega + \int_{\Gamma_d} \mathbf{N}^{\mathrm{T}}\mathbf{T}\mathrm{d}\Gamma \tag{4.16}$$

If the material tangential stiffness matrices of the bulk and the interface, $\mathbf{D}$ and $\mathbf{T}$ respectively, are symmetric, the total tangential stiffness matrix remains symmetric. It is emphasised that in this concept, the additional degrees–of–freedom *cannot* be condensed at element level, because it is node–oriented and not element–oriented. It is this property which makes it possible to represent a discontinuity such that it is continuous at interelement boundaries.

At variance with conventional interface elements, a criterion is needed for the placement of the discontinuity upon propagation. This criterion is based on the stress state at the delamination front, which can be monitored by adding temporary sample points. When the criterion exceeds a threshold value, the discontinuity is extended into the new element. The corresponding nodes of this element are enhanced with an additional set of degrees–of–freedom.

Originally, the partition–of–unity concept was applied within the context of linear elastic fracture mechanics (Belytschko and Black , 1999; Moës *et al.* , 1999), thus necessitating special functions to simulate the near–tip singularity. For this reason, close to the crack tip the enhanced basis terms were introduced as:

$$\boldsymbol{\psi} = \left(\sqrt{r}\cos(\theta/2)\ ,\ \sqrt{r}\sin(\theta/2)\ ,\ \sqrt{r}\sin(\theta/2)\sin(\theta)\ ,\ \sqrt{r}\cos(\theta/2)\sin(\theta)\right)^{\mathrm{T}} \tag{4.17}$$

where r is the distance from the crack tip and θ is measured from the current direction of crack propagation. Away from the crack tip Heaviside functions were employed as discussed above.

The partition–of–unity property of finite element shape functions is a powerful method to introduce cohesive surfaces in continuum finite elements (Wells and Sluys , 2001; Wells *et al.* , 2002; Moës and Belytschko , 2002). Using the interpolation of eq. (4.4) the relative displacement at the discontinuity Γ_d is obtained as:

$$\mathbf{v} = \tilde{\mathbf{u}}\,|_{\mathbf{x}\in\Gamma_d} \tag{4.18}$$

and the tractions at the discontinuity are derived from eq. (2.1). A key feature of the method is the possibility of extending a (cohesive) crack during the calculation in an arbitrary direction, independent of the structure of the underlying finite element mesh. It is also interesting to note that the field $\tilde{\mathbf{u}}$ does not have to be constant. The only requirement that is imposed is continuity.

Even though traditional interface elements equipped with cohesive–zone models are able to capture the failure behaviour of laminated composites accurately, the simulation of delamination using the partition–of–unity property of finite element shape functions offers some advantages. Because the discontinuity does not have to be inserted a priori, no (dummy) stiffness is needed in the elastic regime. Indeed, there does not have to be an elastic regime, since the discontinuity can be activated at the onset of cracking. Consequently, the issue of spurious traction oscillations in the elastic phase becomes irrelevant. Also, the lines of the potential delamination planes no longer have to coincide with element boundaries. They can lie at arbitrary locations inside elements and unstructured meshes can be used.

4.2 Extension to Large Displacements

The above approach for capturing discontinuities can be generalised to large displacement gradients in a straightforward and consistent manner. To this end, one extends eq. (4.4) as:

$$\mathbf{x} = \mathbf{X} + \bar{\mathbf{u}} + \mathcal{H}_{\Gamma_d^0}\tilde{\mathbf{u}} \tag{4.19}$$

with $\mathcal{H}_{\Gamma_d^0}$ the Heaviside function at the interface in the reference configuration, Γ_d^0. The deformation gradient follows by differentiation:

$$\mathbf{F} = \bar{\mathbf{F}} + \mathcal{H}_{\Gamma_d^0}\tilde{\mathbf{F}} + \delta_{\Gamma_d^0}(\tilde{\mathbf{u}} \otimes \mathbf{n}_{\Gamma_d^0}) \tag{4.20}$$

with $\bar{\mathbf{F}} = \boldsymbol{i} + \partial\bar{\mathbf{u}}/\partial\mathbf{X}$, $\tilde{\mathbf{F}} = \partial\tilde{\mathbf{u}}/\partial\mathbf{X}$ and $\delta_{\Gamma_d^0}$ the Dirac function at the interface in the reference configuration.

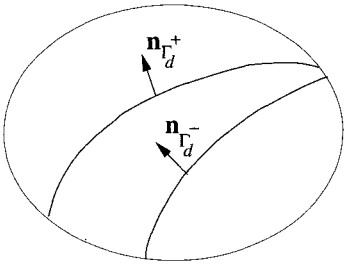

Figure 27. Body crossed by a discontinuity Γ_d with normals $\mathbf{n}_{\Gamma_d^-}$ and $\mathbf{n}_{\Gamma_d^+}$ at both sides of the discontinuity

With aid of Nanson's relation for the normal $\mathbf{n}$ to a surface Γ:

$$\mathbf{n} = \det\mathbf{F}(\mathbf{F}^{-\mathrm{T}})\mathbf{n}_{\Gamma^0}\frac{\mathrm{d}\Gamma^0}{\mathrm{d}\Gamma} \tag{4.21}$$

the expressions for the normals at the - side and at the + side of the interface can be derived:

$$\mathbf{n}_{\Gamma_d^-} = \det\bar{\mathbf{F}}(\bar{\mathbf{F}}^{-\mathrm{T}})\mathbf{n}_{\Gamma_d^0}\frac{\mathrm{d}\Gamma_d^0}{\mathrm{d}\Gamma_d^-} \tag{4.22a}$$

$$\mathbf{n}_{\Gamma_d^+} = \det(\bar{\mathbf{F}} + \tilde{\mathbf{F}})(\bar{\mathbf{F}} + \tilde{\mathbf{F}})^{-\mathrm{T}} \mathbf{n}_{\Gamma_d^0} \frac{\mathrm{d}\Gamma_d^0}{\mathrm{d}\Gamma_d^+} \tag{4.22b}$$

see Figure 27. Distinction between $\mathbf{n}_{\Gamma_d^-}$ and $\mathbf{n}_{\Gamma_d^+}$ is possible because $\tilde{\mathbf{u}}$ is not spatially constant. In the cohesive–zone approach, interface tractions $\mathbf{t}_i$ are transmitted between Γ^- and Γ^+ with different normals $\mathbf{n}_{\Gamma_d^-}$ and $\mathbf{n}_{\Gamma_d^+}$. In a heuristic assumption, it has been assumed that an average normal can be defined for use within the cohesive–zone model (Wells *et al.* , 2002):

$$\mathbf{n}_{\Gamma_d^*} = \det(\bar{\mathbf{F}} + \frac{1}{2}\tilde{\mathbf{F}})(\bar{\mathbf{F}} + \frac{1}{2}\tilde{\mathbf{F}})^{-\mathrm{T}} \mathbf{n}_{\Gamma_d^0} \frac{\mathrm{d}\Gamma_d^0}{\mathrm{d}\Gamma_d^*} \tag{4.23}$$

We now recall the equilibrium equation in the current configuration, cf. eq. (3.9):

$$\nabla_{\mathbf{x}} \cdot \boldsymbol{\sigma} + \rho \mathbf{g} = \mathbf{0}$$

In a Bubnov–Galerkin method the test functions $\boldsymbol{w}$ for a single discontinuity are given by:

$$\boldsymbol{w} = \bar{\boldsymbol{w}} + \mathcal{H}_{\Gamma_d^0} \tilde{\boldsymbol{w}} \tag{4.24}$$

Multiplying with this test function, integrating over the current domain Ω and requiring that the result holds for arbitrary $\bar{\boldsymbol{w}}$ and $\tilde{\boldsymbol{w}}$ yields:

$$\int_\Omega \nabla_{\mathbf{x}} \bar{\boldsymbol{w}} : \boldsymbol{\sigma} \mathrm{d}\Omega = \int_\Omega \bar{\boldsymbol{w}} \cdot \rho \mathbf{g} \mathrm{d}\Omega + \int_\Gamma \bar{\boldsymbol{w}} \cdot \mathbf{t} \mathrm{d}\Gamma \tag{4.25a}$$

$$\int_{\Omega^+} \nabla_{\mathbf{x}} \tilde{\boldsymbol{w}} : \boldsymbol{\sigma} \mathrm{d}\Omega + \int_{\Gamma_d} \tilde{\boldsymbol{w}} \cdot \mathbf{t}_i \mathrm{d}\Gamma = \int_{\Omega^+} \tilde{\boldsymbol{w}} \cdot \rho \mathbf{g} \mathrm{d}\Omega + \int_\Gamma \mathcal{H}_{\Gamma_d} \tilde{\boldsymbol{w}} \cdot \mathbf{t} \mathrm{d}\Gamma \tag{4.25b}$$

with the subscript $\mathbf{x}$ signifying differentiation with respect to the current configuration and $\mathbf{t}_d = \mathbf{n}_{\Gamma_d^*} \cdot \boldsymbol{\sigma}$ the traction at the discontinuity in the current configuration. With a standard interpolation:

$$\bar{\boldsymbol{w}} = \mathbf{N}\bar{\mathbf{w}} \quad , \quad \tilde{\boldsymbol{w}} = \mathbf{N}\tilde{\mathbf{w}} \tag{4.26}$$

where $\mathbf{N}$ contains the interpolation polynomials and $\bar{\mathbf{w}}$ and $\tilde{\mathbf{w}}$ contain the discrete values for the test functions, the discrete format of eqs (4.25a)–(4.25b) reads:

$$\int_\Omega \mathbf{B}^{\mathrm{T}} \boldsymbol{\sigma} \mathrm{d}\Omega = \int_\Omega \rho \mathbf{B}^{\mathrm{T}} \mathbf{g} \mathrm{d}\Omega + \int_\Gamma \mathbf{N}^{\mathrm{T}} \mathbf{t} \mathrm{d}\Gamma \tag{4.27a}$$

$$\int_{\Omega^+} \mathbf{B}^{\mathrm{T}} \boldsymbol{\sigma} \mathrm{d}\Omega + \int_{\Gamma_d} \mathbf{N}^{\mathrm{T}} \mathbf{t}_i \mathrm{d}\Gamma = \int_{\Omega^+} \rho \mathbf{B}^{\mathrm{T}} \mathbf{g} \mathrm{d}\Omega + \int_\Gamma \mathcal{H}_{\Gamma_d} \mathbf{N}^{\mathrm{T}} \mathbf{t} \mathrm{d}\Gamma \tag{4.27b}$$

After substitution of the constitutive relations for the plies and that for the interface, and transforming back to the reference configuration, a nonlinear set of algebraic equations results, which can be solved in a standard manner using an incremental–iterative procedure. If a Newton–Raphson procedure is used, these equations have to be linearised in order to derive the structural tangential stiffness matrix, see Wells *et al.* (2002) for details.

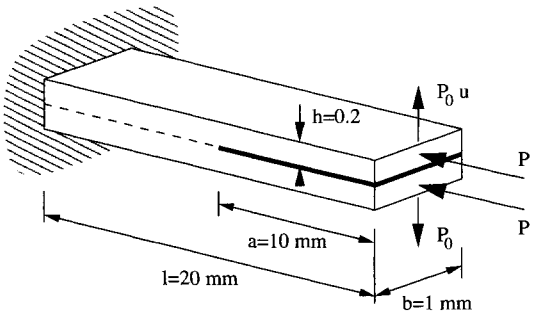

Figure 28. Double cantilever beam with initial delamination under compression

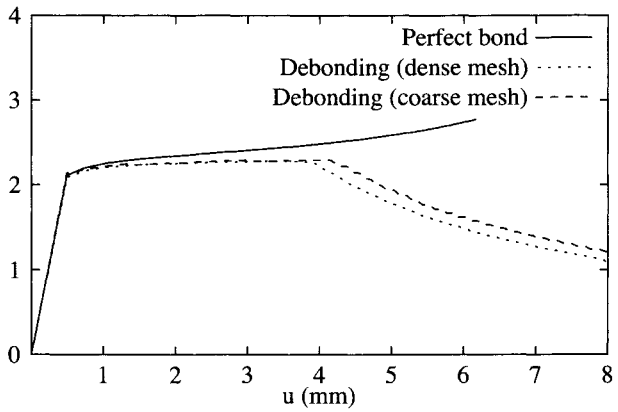

Figure 29. Load–displacement curves for delamination–buckling test (Wells *et al.* , 2003)

To exemplify the possibilities of this approach to model the combined failure mode of delamination growth and local buckling we consider the double cantilever beam of Figure 28 with an initial delamination length $a = 10\ mm$. Both layers are made of the same material with Young's modulus $E = 135\,000\ N/mm^2$ and Poisson's ratio $\nu = 0.18$. Due to symmetry in the geometry of the model and the applied loading, delamination propagation can be modelled with an exponential mode–I decohesion law:

$$t^n_{\text{dis}} = t_{\text{ult}} \exp\left(-\frac{t_{\text{ult}}}{\mathcal{G}_c} v^n_{\text{dis}}\right) \tag{4.28}$$

where t^n_{dis} and v^n_{dis} are the normal traction and displacement jump respectively. The ultimate traction t_{ult} is equal to $50\ N/mm^2$, the work of separation is $\mathcal{G}_c = 0.8\ N/mm$.

This case, in which failure is a consequence of a combination of delamination growth

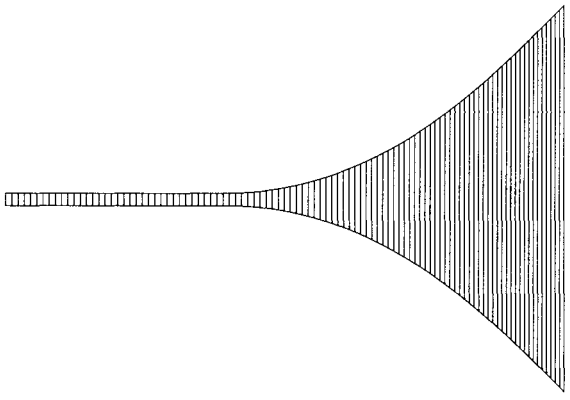

Figure 30. Deformation of coarse mesh after buckling and delamination growth (true scale) (Wells *et al.* , 2003)

and structural instability, has been analysed using conventional interface elements in Allix and Corigliano (1999). The beam is subjected to an axial compressive force $2P$, while two small perturbing forces P_0 are applied to trigger the buckling mode. Two finite element discretisations have been employed, a fine mesh with three elements over the thickness and 250 elements along the length of the beam, and a coarse mesh with only one (!) element over the thickness and 100 elements along the length. Figure 29 shows that the calculation with the coarse mesh approaches the results for the fine mesh closely. For instance, the numerically calculated buckling load is in good agreement with the analytical solution. Steady–state delamination growth starts around a lateral displacement $u = 4\ mm$. From this point onwards, delamination growth interacts with geometrical instability. Figure 30 presents the deformed beam for the coarse mesh at a tip displacement $u = 6\ mm$. Note that the displacements are plotted at true scale, but that the difference in displacement between the upper and lower parts of the beam is for the major part due to the delamination and that the strains remain small.

4.3 Delamination in a Solid–Like Shell Element

The excellent results obtained in this example for the coarse discretisation have motivated the development of a layered plate/shell element in which delaminations can occur inside the element between each of the layers (Remmers *et al.* , 2003). Because of the absence of rotational degrees–of–freedom, the solid–like shell element was taken as a point of departure. The shell of Figure 31 is crossed by a discontinuity surface Γ_d^0 which is assumed to be parallel to the mid–surface of the thick shell. The displacement field $\boldsymbol{\phi}(\xi, \eta, \zeta)$ can now be regarded as a continuous regular field $\bar{\boldsymbol{\phi}}$ with an additional continuous field $\tilde{\boldsymbol{\phi}}$ that determines the magnitude of the displacement jump. The position of a

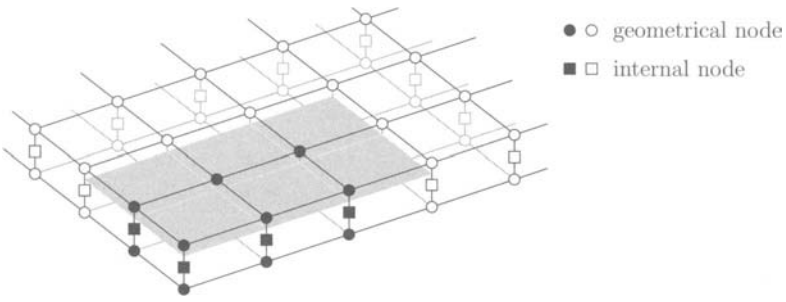

Figure 31. Enhanced nodes (black) whose support contains a discontinuity (grey surface). The nodes on the edge of the discontinuity are not enhanced in order to ensure a zero delamination opening at the tip

material point in the deformed configuration can then be written as:

$$\mathbf{x} = \mathbf{X} + \bar{\boldsymbol{\phi}} + \mathcal{H}_{\Gamma_d^0}\tilde{\boldsymbol{\phi}} \tag{4.29}$$

Since the displacement field $\boldsymbol{\phi}$ is a function of the variables $\mathbf{u}_t$, $\mathbf{u}_b$ and w, we need to decompose these three terms as:

$$\begin{aligned} \mathbf{u}_t &= \bar{\mathbf{u}}_t + \mathcal{H}_{\Gamma_d^0}\tilde{\mathbf{u}}_t \\ \mathbf{u}_b &= \bar{\mathbf{u}}_b + \mathcal{H}_{\Gamma_d^0}\tilde{\mathbf{u}}_b \\ w &= \bar{w} + \mathcal{H}_{\Gamma_d^0}\tilde{w} \end{aligned} \tag{4.30}$$

Inserting eq. (4.30) into eqs (3.40)–(3.42) gives:

$$\begin{aligned} \mathbf{u}_0 &= \bar{\mathbf{u}}_0 + \mathcal{H}_{\Gamma_d^0}\tilde{\mathbf{u}}_0 \\ \mathbf{u}_1 &= \bar{\mathbf{u}}_1 + \mathcal{H}_{\Gamma_d^0}\tilde{\mathbf{u}}_1 \\ \mathbf{u}_2 &= \bar{\mathbf{u}}_2 + \mathcal{H}_{\Gamma_d^0}\tilde{\mathbf{u}}_2 \end{aligned} \tag{4.31}$$

where:

$$\begin{aligned} \bar{\mathbf{u}}_0 &= \frac{1}{2}\left[\bar{\mathbf{u}}_t + \bar{\mathbf{u}}_b\right] & \tilde{\mathbf{u}}_0 &= \frac{1}{2}\left[\tilde{\mathbf{u}}_t + \tilde{\mathbf{u}}_b\right] \\ \bar{\mathbf{u}}_1 &= \frac{1}{2}\left[\bar{\mathbf{u}}_t - \bar{\mathbf{u}}_b\right] & \tilde{\mathbf{u}}_1 &= \frac{1}{2}\left[\tilde{\mathbf{u}}_t - \tilde{\mathbf{u}}_b\right] \\ \bar{\mathbf{u}}_2 &= \bar{w}\left[\mathbf{D} + \bar{\mathbf{u}}_1\right] & \tilde{\mathbf{u}}_2 &= \tilde{w}\left[\mathbf{D} + \bar{\mathbf{u}}_1 + \tilde{\mathbf{u}}_1\right] + \bar{w}\tilde{\mathbf{u}}_1 \end{aligned} \tag{4.32}$$

It is noted that the enhanced part of the internal stretch parameter $\mathbf{u}_2$, i.e. $\tilde{\mathbf{u}}_2$, contains regular variables as well as additional variables. The elaboration of the strains, the equilibrium equations and the linearisation follows standard lines (Remmers *et al.* , 2003).

The magnitude of the displacement jump at the discontinuity is governed by an additional set of degrees–of–freedom which are added to the existing nodes of the model.

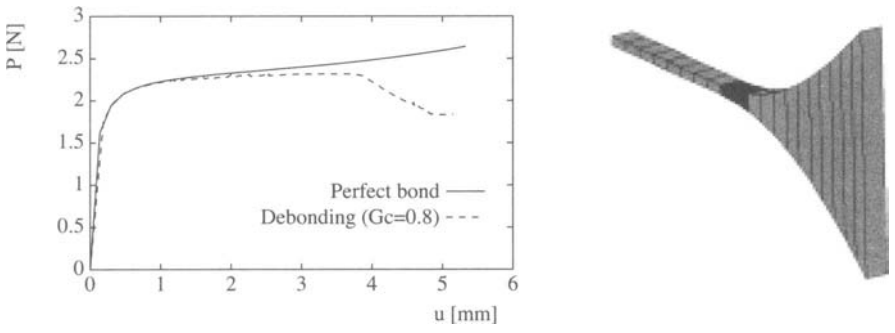

Figure 32. Load–displacement curve and deformations of shell model after buckling and delamination growth (true scale) (Remmers *et al.* , 2003)

Figure 31 shows the activation of these additional sets of degrees of freedom for a given (static) delamination surface in the model. Both the geometrical and the internal nodes are enhanced when the corresponding element is crossed by the discontinuity. This implies that each geometrical node now contains three additional degrees–of–freedom next to the three regular ones, giving six degrees–of–freedom in total. Each internal node has one extra degree–of–freedom added to the single regular degree–of–freedom. As in the continuum elements, the discontinuity is assumed to always stretch through an entire element. This avoids the need for complicated algorithms to describe the stress state in the vicinity of a delamination front within an element. As a consequence, the discontinuity 'touches' the boundary of an element. The geometrical and internal nodes that support this boundary are not enhanced in order to assure a zero crack tip condition.

The example of Figure 28 has been reanalysed with a mesh composed of eight node enhanced solid–like shell elements (Remmers *et al.* , 2003). Again, only one element in thickness direction has been used. In order to capture delamination growth correctly, the mesh has been refined locally. Figure 32 shows the lateral displacement u of the beam as a function of the external force P. The load–displacement response for a specimen with a perfect bond (no delamination growth) is given as a reference. The numerically calculated buckling load is in agreement with the analytical solution. Steady delamination growth starts around a lateral displacement $u \approx 4\ mm$, which is in agreement with the previous simulations (Allix and Corigliano , 1999; Wells *et al.* , 2003).

5 Concluding Remarks

Numerical models with separate finite elements for interfaces and plies are a powerful tool to analyse delaminations in composite structures, but have some restrictions. Because the interface elements have to be inserted a priori, spurious elastic deformations will occur

prior to delamination onset. These undesired deformations can be partially suppressed by assigning a high value to the normal stiffness modulus in the elastic range, but this can result in traction oscillations ahead of the crack tip and in erroneous wave reflections when dynamic delaminations are analysed. Furthermore, this methodology restricts the freedom of the discretisation in the sense that element boundaries have to be aligned with surfaces of potential delamination.

Exploiting the partition–of–unity property of finite element shape functions enables placement of (cohesive) interfaces at arbitrary positions at the onset of delamination. Since interfaces are created at the moment when they are needed, the necessity of assigning an artificially high stiffness in the elastic regime no longer exists and traction oscillations or spurious wave reflections are no longer an issue. The fact that alignment of the discretisation with potential planes of delamination is no longer necessary, makes possible that unstructured meshes can be used. The versatility of the method is further enhanced by a consistent extension to large strains and by the incorporation in a solid–like shell element. It is the latter extension which enables large–scale computations of composite structures taking into account delaminations.

Bibliography

G. Alfano and M.A. Crisfield, Finite element interface models for the delamination analysis of laminated composites: mechanical and computational issues, *International Journal for Numerical Methods in Engineering*, 50: 1701–1736, 2001.

O. Allix and P. Ladevèze, Interlaminar interface modelling for the prediction of delamination, *Composite Structures*, 22: 235–242, 1992.

O. Allix and A. Corigliano, Geometrical and interfacial non-linearities in the analysis of delamination in composites, *International Journal of Solids and Structures*, 36: 2189–2216, 1999.

I. Babuška and J.M. Melenk, The partition of unity method, *International Journal for Numerical Methods in Engineering*, 40: 727–758, 1997.

T. Belytschko and T. Black, Elastic crack growth in finite elements with minimal remeshing, *International Journal for Numerical Methods in Engineering*, 45: 601–620, 1999.

R. de Borst, Computation of post–bifurcation and post–failure behaviour in strain–softening solids, *Computers and Structures*, 25: 211–224, 1987.

R. de Borst, Damage, material instabilities, and failure. In E. Stein, R. de Borst, and T.J.R. Hughes, editors, *Encyclopedia of Computational Mechanics*, J. Wiley & Sons, Chichester, Volume 2, Chapter 10, 2004.

A. Corigliano, Formulation, identification and use of interface models in the numerical analysis of composite delamination, *International Journal of Solids and Structures*, 30: 2779–2811, 1993.

M.A. Crisfield, A fast incremental/iterative procedure that handles snap-through, *Computers and Structures*, 13: 55–62, 1981.

F. Feyel and J.L. Chaboche, FE^2 multiscale approach for modelling the elastoviscoplastic behaviour of long fibre SiC/Ti composite materials, *Computer Methods in Applied Mechanics and Engineering*, 183: 309–330, 2000.

F. Hashagen, J.C.J. Schellekens, R. de Borst, and H. Parisch, Finite element procedure for modelling fibre-metal laminates, *Composite Structures*, 32: 255–264, 1995.

F. Hashagen and R. de Borst, Numerical assessment of delamination in fibre metal laminates, *Computer Methods in Applied Mechanics and Engineering*, 185: 141–159, 2000.

A. Huerta, T. Belytschko, S. Fernández-Mendéz, and T. Rabczuk, Meshfree methods. In E. Stein, R. de Borst and T.J.R. Hughes, editors, *Encyclopedia of Computational Mechanics*, J. Wiley & Sons, Chichester, Volume 1, Chapter 10, 2004.

P. Ladevèze and G. Lubineau, An enhanced mesomodel for laminates based on micromechanics, *Composites Science and Technology*, 62: 533–541, 2002.

N. Moës, J. Dolbow, and T. Belytschko, A finite element method for crack growth without remeshing, *International Journal for Numerical Methods in Engineering*, 46: 131–150, 1999.

N. Moës and T. Belytschko, Extended finite element method for cohesive crack growth, *Engineering Fracture Mechanics*, 69: 813–833, 2002.

N.J. Pagano, On the calculation of interlaminar normal stresses in composite laminates, *Journal of Composite Materials*, 8: 65–81, 1974.

H. Parisch, A continuum–based shell theory for non–linear applications, *International Journal for Numerical Methods in Engineering*, 38: 1855–1883, 1995.

R.B. Pipes and N.J. Pagano, Interlaminar stresses in composite laminates under uniform uniaxial extension, *Journal of Composite Materials*, 4: 538–544, 1970.

E.. Ramm, Strategies for tracing nonlinear response near limit points. In W. Wunderlich, E. Stein, and K.J. Bathe, editors, *Nonlinear Finite Element Analysis in Structural Mechanics*, Springer Verlag, Berlin, 63–89, 1981.

J.J.C. Remmers, G.N. Wells, and R. de Borst, Analysis of delamination growth with discontinuous finite elements, In J. Pamin, editor, *Solids, Structures and Coupled Problems (Proceedings of the Second European Conference on Computational Mechanics)*. Cracow University of Technology, Cracow, CD-ROM, 2001.

J.J.C. Remmers and R. de Borst, Delamination buckling of Fibre-Metal Laminates under compressive and shear loadings, *43rd AIAA/ASME/ASCE/AHS/ASC Structures, Structural Dynamics and Materials Conference*, Denver, Colorado, CD-ROM, 2002.

J.J.C. Remmers, G.N. Wells, and R. de Borst, A solid–like shell element allowing for arbitrary delaminations, *International Journal for Numerical Methods in Engineering*, 58: 2013–2040, 2003.

E.. Riks, *On the Numerical Solution of Snapping Problems in the Theory of Elastic Stability*. SUDAAR No. 401, Stanford University, Stanford, 1970.

E.. Riks, The application of Newtons method to the problem of elastic stability, *Journal of Applied Mechanics*, 39: 1060–1065, 1972.

J.C.J. Schellekens and R. de Borst, On the numerical integration of interface elements, *International Journal for Numerical Methods in Engineering*, 36: 43–66, 1992.

J.C.J. Schellekens and R. de Borst, A non–linear finite element approach for the analysis of mode–I free edge delamination in composites, *International Journal of Solids and Structures*, 30: 1239–1253, 1993.

J.C.J. Schellekens and R. de Borst, Free edge delamination in carbon-epoxy laminates: a novel numerical/experimental approach, *Composite Structures*, 28: 357–373, 1994.

J.C.J. Schellekens and R. de Borst, The application of interface elements and enriched or rate-dependent continuum models to micro-mechanical analyses of fracture in composites, *Computational Mechanics*, 14: 68–83, 1994.

J.H.A. Schipperen and F.J. Lingen, Validation of two–dimensional calculations of free edge delamination in laminated composites, *Composite Structures*, 45: 233–240, 1999.

K. Shivakumar and J. Whitcomb, Buckling of a sublaminate in a quasi-isotropic composite laminate, *Journal of Composite Materials*, 19: 2–18, 1985.

A.S.D. Wang, Fracture analysis of interlaminar cracking. In N.J. Pagano, editor, *Interlaminar Response of Composite Materials*, Elsevier, Amsterdam, 69–109, 1989.

G.N. Wells and L.J. Sluys, A new method for modeling cohesive cracks using finite elements, *International Journal for Numerical Methods in Engineering*, 50: 2667–2682, 2001.

G.N. Wells, R. de Borst, and L.J. Sluys, A consistent geometrically non–linear approach for delamination, *International Journal for Numerical Methods in Engineering*, 54: 1333–1355, 2002.

G.N. Wells, J.J.C. Remmers, R. de Borst, and L.J. Sluys, A large strain discontinuous finite element approach to laminated composites. In C. Miehe, editor, *IUTAM symposium on computational mechanics of solid materials at large strains*, Kluwer, Dordrecht, 355–364, 2003.

Micromechanical modelling of strain hardening and tension softening in cementitious composites

B. L. Karihaloo
School of Engineering, Cardiff University
Cardiff CF24 OYF, U.K.

Abstract These lecture notes will describe a procedure for modelling the complete macroscopic response (including strain hardening and tension softening) of two short fibre reinforced cementitious composites and show how their microstructural parameters influence this response. From a mathematical point of view it is necessary to examine how bridging forces imposed by the fibres alter the opening of multiple cracks in elastic solids under unidirectional tensile loading. The strain hardening is essentially due to elastic bridging forces which are proportional to crack opening displacements. After a certain critical crack opening displacement is reached, some fibres progressively debond from the elastic matrix and thereafter provide a residual bridging force by frictional pull-out, while others continue to provide full bridging. This results in a kind of elasto-plastic bridging law which governs the initial tension softening response of the composite.

Besides the usual square-root singularity at crack tips, the elasto-plastic bridging law introduces a logarithmic singularity at the point of discontinuity in the bridging force. These singularities have been analytically isolated, so that only regular functions are subjected to numerical integration. Unbridged multiple crack problems have in the past been solved using double infinite series which have been found to be divergent. Here, a superposition procedure will be described that eliminates the use of double infinite series and thus the problem of divergence. It is applicable to both unbridged and bridged multiple cracks.

These developments will then be used to show how the model of multiple bridged cracks can accurately predict the prolonged nonlinear strain hardening and the initial tension softening response of two cementitious composites. Finally, we will study the transition from the strain hardening to the tension softening behaviour as an instability phenomenon.

1 Introduction

The nonlinear behaviour of quasi-brittle materials such as concrete and other cementitious composites is most often caused by the growth of pre-existing microcracks and by the nucleation and growth of new microcracks, which eventually lead to crack localization and failure. In order to include this phenomenon in the constitutive relationships, Kachanov (1958) introduced a scalar damage variable D, which increased linearly under increasing stress. More sophisticated continuous damage concepts for brittle materials

were later developed by Krajcinovic and Fonseka (1981), Fonseka and Krajcinovic (1981), and others. One simplified way to model a microcracked solid from a fracture mechanics point of view is to assume that the cracks are arranged in regular patterns. Most studies so far have been devoted to modelling of doubly periodic rectangular arrays of cracks. Sahasakmontri et al. (1987), using the pseudo-traction technique and double infinite summations, revealed an anomaly in the use of double infinite series (Delameter et al. (1975); Karihaloo (1978)). They showed that if a superposition procedure was implemented first for an array of R rows by C columns of cracks, and the number of the cracks was then increased while keeping the ratio C/R constant, the mode I and mode II stress intensity factors depended on the chosen ratio C/R. This anomaly was resolved by Karihaloo et al. (1996) by using a proper superposition procedure and pseudo-traction technique.

Here we shall first present the mathematical details for solving the problem of doubly periodic arrays of cracks when the cracks are free of traction and when they are subjected to a closure pressure. The solution is also based on pseudo-traction formalism, but the superposition procedure makes use of the exact solution for an array (a row) of cracks, thus avoiding divergent double infinite summations (Delameter et al. (1975)). The results for unbridged (traction-free) crack arrays are shown to be identical to those obtained by Isida et al. (1981) who used the boundary collocation method.

The mathematical solutions are then used to study the influence of microstructure upon the complete macroscopic tensile response, including strain hardening and tension softening, of a conventional fibre-reinforced cementitious composite and a high performance DSP-based fibre composite.

A full description of the observed strain hardening behaviour will be given by considering elastically bridged doubly periodic arrays of cracks. The strain hardening regime is assumed to end when the fibres begin to pull out from the matrix. Thereafter, the crack bridging force drops to the level of frictional pull-out force, so that the crack opening increases. This results in a progressive reduction in the tensile carrying capacity of the composite and a corresponding increase in deformation, i.e. in tension softening.

The tension softening response will be modelled by a collinear array (row) of cracks subjected to bilinear bridging forces. This model is akin to that used by Horii et al. (1989) and Ortiz (1988) for the tension softening of unreinforced quasi-brittle materials. It differs from that used by Li et al. (1991) in that the localized damage in the present model is regarded as being discontinuous, whereas Li et al. (1991) assumed that the localized damage has resulted in a through crack. The model developed here is therefore suitable for describing the initial post-peak tension softening response of a fibre-reinforced quasi-brittle matrix. Finally, we will study the transition from the strain hardening to the tension softening behaviour as a material instability phenomenon and derive the conditions for instability on the macroscopic level.

2 Formulation of the problem

An infinite, isotropic elastic solid containing a doubly periodic array of bridged cracks is shown in Fig. 1a. It is subjected to a uniform remote stress σ normal to the cracks. As the cracks are bridged, their faces are subjected to a normal bridging traction p_n. This

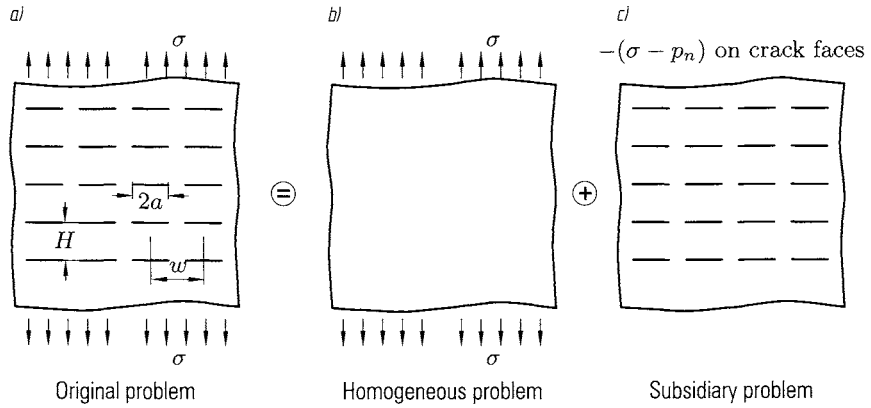

Figure 1. A doubly periodic array of cracks and the decomposition of the problem

traction is not uniformly distributed along the surfaces of a crack but, by symmetry, has the same distribution along all cracks.

In terms of the standard superposition procedure, the original problem shown in Fig. 1a can be decomposed into the homogeneous problem of Fig. 1b and the subsidiary problem shown in Fig. 1c. It is only needed to solve the subsidiary problem. Its solution can be obtained by the pseudo-traction technique and by proper superposition. To apply the method of the pseudo-tractions (Horii and Nemat-Nasser (1985)), the problem 1c is further decomposed into an infinite number of sub-problems, designated $1, \ldots, j, \ldots, \infty$ in Fig. 2. Each sub-problem contains only one row of cracks, each of which is subjected to a normal pseudo-traction σ^p. Because of the inherent symmetry of the original problem, the pseudo-tractions are the same for all cracks.

Sahasakmontri et al. (1987) decomposed the subsidiary problem of Fig. 1c differently. In their decomposition, each sub-problem contained only one crack, so that superposition required summation of two infinite series. The decomposition in the present paper is such that superposition requires the summation of a single infinite series. As we shall see below, the elimination of double infinite series overcomes the problems of divergence and results in highly accurate solutions.

The distribution of unknown pseudo-tractions σ^p will be determined in such a way that the traction-free condition on the crack faces of the problem 2(a) is satisfied when the stress perturbations caused by all the sub-problems are superposed (Hu et al. (1994)). We shall use the basic solution for an infinite body containing a row of cracks each of which is subjected to two pairs of concentrated normal surface loads of opposite direction, as shown in Fig. 3. The exact solution for this problem can be readily deduced from the results in the handbook by Tada et al. (1985). In the sequel, the loads shown in Fig. 3 will be referred to as a set of crack surface tractions at position x.

Because of symmetry, we need consider only one crack in a sub-problem, e.g. the one labelled with the set of crack surface tractions $\sigma^p(x)$ and coordinate system in Fig. 3.

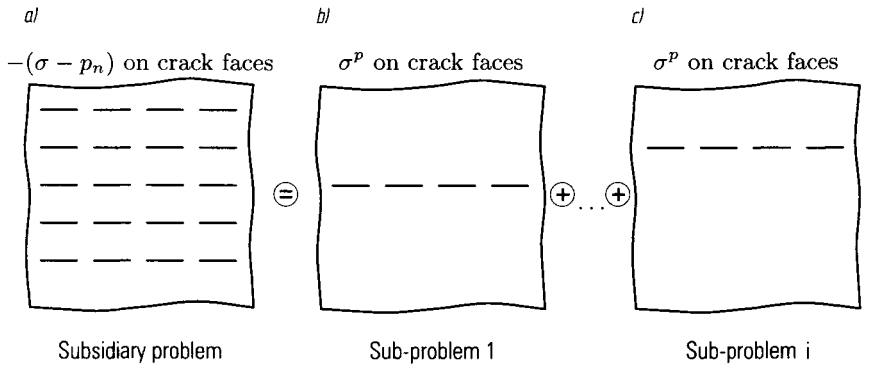

Figure 2. Decomposition of the subsidiary problem of Fig. 1c into an infinite number of sub-problems. σ^p is the pseudo-traction on the faces of each crack in the row in each sub-problem

The stress σ_{yy} at point x of the crack i is given by the superposition of the contributions from all the sub-problems

$$-\sigma^p(x) + \sum_{j=-\infty, j\neq i}^{+\infty} \int_0^{+a} K_\sigma(x, x^j)\sigma^p(x^j)dx^j, \quad x, x^j \in [0, +a) \tag{2.1}$$

where the kernel $K_\sigma(x, x^j)$ represents the stress at x induced by a set of unit crack surface tractions at x^j in sub-problem j. Denoting the distance between the crack rows i and j (Fig. 3) by y, $K_\sigma(x, x^j)$ can be written as

$$\begin{aligned} K_\sigma(x, x^j) = \frac{2}{W}\mathrm{Re}\left\{ \frac{\cos\frac{\pi x^j}{W}\sqrt{\left(\sin\frac{\pi a}{W}\right)^2 - \left(\sin\frac{\pi x^j}{W}\right)^2}}{\left[\left(\sin\frac{\pi z}{W}\right)^2 - \left(\sin\frac{\pi x^j}{W}\right)^2\right]\sqrt{1 - \left(\sin\frac{\pi a}{W}/\sin\frac{\pi z}{W}\right)^2}} \right\} \\ -\frac{2}{W}\mathrm{Im}\left\{ \frac{\cos\frac{\pi x^j}{W}\sqrt{\left(\sin\frac{\pi a}{W}\right)^2 - \left(\sin\frac{\pi x^j}{W}\right)^2}}{\left[\left(\sin\frac{\pi z}{W}\right)^2 - \left(\sin\frac{\pi x^j}{W}\right)^2\right]^2\sqrt{1 - \left(\sin\frac{\pi a}{W}/\sin\frac{\pi z}{W}\right)^2}} \right. \\ \cdot \left[2\frac{\pi}{W}\sin\frac{\pi z}{W}\cos\frac{\pi z}{Z}\sqrt{1 - \left(\sin\frac{\pi a}{W}/\frac{\pi z}{W}\right)^2} \right. \\ \left. \left. + \frac{\pi}{W}\frac{\left(\sin\frac{\pi a}{W}\right)^2\cos\frac{\pi z}{W}\left[\left(\sin\frac{\pi a}{W}\right)^2 - \left(\sin\frac{\pi x^j}{W}\right)^2\right]}{\left(\sin\frac{\pi z}{W}\right)^3\sqrt{1 - \left(\sin\frac{\pi a}{W}/\sin\frac{\pi z}{W}\right)^2}} \right] \right\} \end{aligned} \tag{2.2}$$

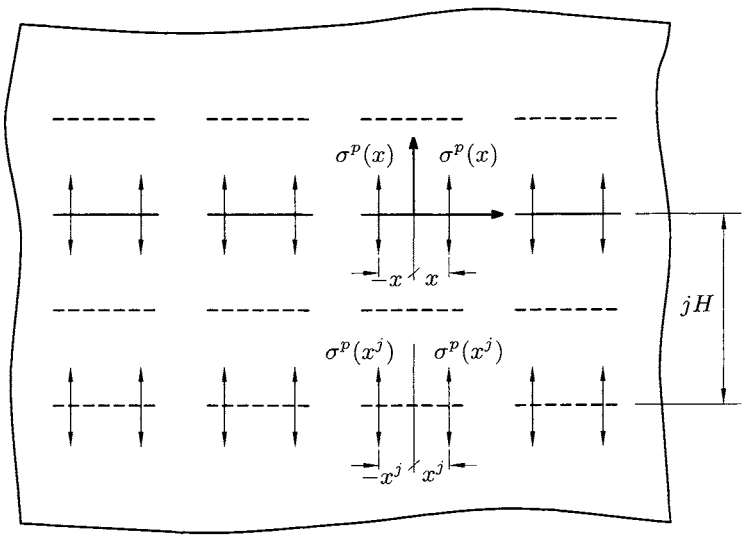

Figure 3. Superposition of sub-problems, showing pseudo-tractions on faces of cracks in rows i and j. Note that because of symmetry, x and x^j only vary from 0 to a (half-crack length)

where $z = x + iy$ and $i = \sqrt{-1}$.

For the crack configuration of Fig. 3, the summation in Eq. (2.1) is obviously carried out subject to the geometrical condition

$$y = jH, \quad j = -\infty, \ldots, -1, +1, \ldots, +\infty. \tag{2.3}$$

Because of the symmetry of the problem with respect to the x axis, eqn (2.1) can be rewritten as

$$-\sigma^p(x) + 2\sum_{j=1}^{+\infty} \int_0^{+a} K_\sigma(x, x^j)\sigma^p(x^j)dx^j, \quad x, x^j \in [0, +a) \tag{2.4}$$

By superposition of the sub-problems, the traction-free condition on each crack in the subsidiary problem of Fig, 2a can be written as

$$-\sigma^p(x) + 2\sum_{j=1}^{+\infty} \int_0^{+a} K_\sigma(x, x^j)\sigma^p(x^j)dx^j = -(\sigma - p_n), \quad x, x^j \in [0, +a) \tag{2.5}$$

Equation (2.5) is a simplified form of the general formula for two-dimensional interacting cracks derived by Hu et al. (1994). It can be rewritten as

$$\sigma^p(x) - 2\sum_{j=1}^{+\infty} \int_0^{+a} K_\sigma(x, x^j)\sigma^p(x^j)dx^j + p_n = \sigma, \quad x, x^j \in [0, +a) \tag{2.6}$$

In common with many previous works, the bridging traction p_n is expressed as a function of the crack opening displacement

$$p_n = f_n(v(x)) \tag{2.7}$$

where $v(x)$ is solely induced by the pseudo-tractions $\sigma^p(x^i)$ on the cracks in sub-problem i (Hu et al. (1994)). It can be easily obtained from

$$v(x) = \int_0^{+a} K_v(x, x^i)\sigma^p(x^i)dx^i, \quad x, x^i \in [0, +a) \tag{2.8}$$

where the kernel $K_v(x, x^i)$ represents the crack opening displacement at x induced by a set of concentrated unit loads at x^i on the crack surfaces in sub-problem i, see Fig. 4. This kernel can be derived in a closed form from the results in the handbook by Tada et al. (1985)

$$K_v(x, x^i) = \frac{1-\nu}{\pi G} \ln \left| \frac{\sqrt{1 - \left(\cos\frac{\pi a}{W} / \cos\frac{\pi x}{W}\right)^2} + \sqrt{1 - \left(\cos\frac{\pi a}{W} / \cos\frac{\pi x^i}{W}\right)^2}}{\sqrt{1 - \left(\cos\frac{\pi a}{W} / \cos\frac{\pi x}{W}\right)^2} - \sqrt{1 - \left(\cos\frac{\pi a}{W} / \cos\frac{\pi x^i}{W}\right)^2}} \right| \tag{2.9}$$

Under general plane stress conditions ν is replaced by $\nu/(1+\nu)$.

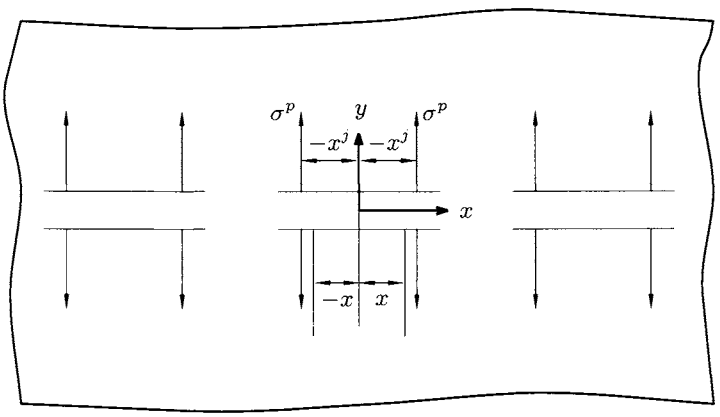

Figure 4. Sub-problem i, showing a set of pseudo-tractions on faces of a crack in a row. Note that because of symmetry, x^i only varies from 0 to a (half-crack length)

It is seen that by substituting Eq. (2.6) into Eq. (2.5), and using the relation between the pseudo-traction and the crack opening displacement (2.8), we need only to solve an integral equation for the pseudo-traction $\sigma^p(x)$. The kernel $K_\sigma(x, x^j)$ is not singular provided that $H > 0$. The kernel $K_v(x, x^i)$ has an integrable logarithmic singularity at

$x = x^i$ which can easily be handled by the regularization

$$\begin{aligned} v(x) &= \int_0^{+a} K_v(x, x^i)\sigma^p(x^i)dx^i \\ &= \int_0^{+a} K_v(x, x^i)\left[\sigma^p(x^i) - \sigma^p(x)\right]dx^i + \\ &\quad + \sigma^p(x)\int_0^{+a} K_v(x, x^i)dx^i \quad x, x^i \in [0, +a). \end{aligned} \tag{2.10}$$

The integrand in the first integral of (2.10) is finite everywhere. The singularity of the integrand $K_v(x, x^i)$ in the second integral can be isolated by introducing a function which has a singularity of the same order at $x = x^i$. The isolated singular integral can then be calculated analytically. To show this, we rewrite (2.9) as

$$K_v(x, x^i) = \frac{1-\nu}{\pi G} \ln \left| \frac{\sqrt{1 - \left(\cos\frac{\pi a}{W} / \cos\frac{\pi x}{W}\right)^2} + \sqrt{1 - \left(\cos\frac{\pi a}{W} / \cos\frac{\pi x^i}{W}\right)^2}}{\sqrt{1 - \left(\cos\frac{\pi a}{W} / \cos\frac{\pi x}{W}\right)^2} - \sqrt{1 - \left(\cos\frac{\pi a}{W} / \cos\frac{\pi x^i}{W}\right)^2}} \frac{x - x^i}{x - x^i} \right| \tag{2.11}$$

Substituting (2.11) into the second integral on the right hand side of Eq. (2.10) and after some algebraic manipulations, we get

$$\int_0^{+a} K_v(x, x^i)dx^i = \int_0^{+a} K_v^{ns}(x, x^i)dx^i + \int_0^{+a} K_v^{s}(x, x^i)dx^i \tag{2.12}$$

Here

$$K_v^{ns}(x, x^i) = \frac{1-\nu}{\pi G} \ln(F_1 F_2) \tag{2.13}$$

where

$$F_1 = \left| \frac{\left(\cos\frac{\pi x}{W}\cos\frac{\pi x^i}{W}\right)^2 \left[\sqrt{1 - \left(\cos\frac{\pi a}{W} / \cos\frac{\pi x}{W}\right)^2} + \sqrt{1 - \left(\cos\frac{\pi a}{W} / \cos\frac{\pi x^i}{W}\right)^2}\right]^2}{2\sin\frac{\pi a}{2W}(x + x^i)\left(\cos\frac{\pi a}{2W}\right)^2\left(\cos\frac{\pi x}{W} + \cos\frac{\pi x^i}{W}\right)} \right| \tag{2.14}$$

$$F_2 = \begin{cases} \left| \dfrac{x - x^i}{\sin\frac{\pi a}{2W}(x - x^i))} \right| & x \neq x^i, \\ \dfrac{2W}{\pi a} & x = x^i. \end{cases} \tag{2.15}$$

The second integral on the right hand side of Eq. (2.12) is

$$\begin{aligned} \int_0^{+a} K_v(x, x^i)dx^i &= -\frac{1-\nu}{\pi G}\int_0^{+a} \ln|x - x^i|\, dx^i = \\ &= -\frac{1-\nu}{\pi G}[x\ln x + (a - x)\ln(a - x) - a] \end{aligned} \tag{2.16}$$

We shall use Gauss-Legendre quadrature to solve the integral Eq. (2.5) and write (with $t = x/a$)

$$\sigma^p(t_l) - 2\sum_{j=1}^{+\infty} a \sum_{k=1}^{N} \left[K_\sigma\left(t_l, t_k^j\right) \sigma^p\left(t_k^j\right)\right] w_k + p_n(t_l) = \sigma$$

$$t_l, t_l^j \in (t_1, \ldots, t_N);\ l = 1, \ldots, N. \quad (2.17)$$

The equation for the crack opening displacement (2.10) can be similarly discretized

$$v(t_l) = a \sum_{k=1, k\neq l}^{N} K_v(t_l, t_k^j) \left[\sigma^p\left(t_k^j\right) - \sigma^p(t_l)\right] w_k +$$

$$+ \sigma^p(t_l) a \left[\sum_{k=1}^{N} K_v^{ns}(t_l, t_k^j) w_k + \int_0^1 K_v^s\left(t_l, t^j\right) dt^j\right]$$

$$t_l, t_l^j \in (t_1, \ldots, t_N); \quad l = 1, \ldots, N. \quad (2.18)$$

In Eqs. (2.17) and (2.18), $t_1, \ldots, t_N$ are the collocation points and, at the same time, the integration points of the Gauss-Legendre quadrature, w_k $(k = 1, \ldots, N)$ are the corresponding weights.

It can be seen from (2.2) and (2.3) that as $j \to +\infty$, $K_\sigma(x, x^j)$ decays exponentially so the infinite summation in Eq. (2.17) is uniformly convergent for $x \in [0, W/2)$. This feature makes it possible to approximate the infinite summation using the sum of finite terms while the truncation error can be made as small as desired.

3 Unbridged cracks

When the cracks are not bridged ($p_n = 0$), the integral Eq. (2.5) is particularly easy to solve with the numerical quadrature (2.17)–(2.18), whereafter the mode I stress intensity factor at each crack tip in the array and the overall effective Young's modulus E_y along the direction of loading can be determined. The non-dimensional mode I stress intensity factor is shown in Fig. 5, as a function of the density of cracks defined by $a^2/(WH)$ and the arrangement (or shape) of the rectangular array characterized by H/W. When $H/W < 0.8$, the SIF decreases with increasing density of cracks suggesting that the mutual influence of closely spaced cracks reduces the crack driving force. On the other hand, when H/W is large, the mode I SIF increases rapidly with the density of cracks. This is due to the fact that in order to maintain a high density when H is large, the neighbouring crack tips in a row must approach each other.

Table 1 compares the results obtained by the present superposition technique with those reported earlier by Isida et al. (1981) and with the first-order approximation of Sahasakmontri et al. (1987). It is seen that the present method gives exactly the same results as those of Isida et al. (1981) for all crack geometries. For small values of a/W, the results of Sahasakmontri et al. (1987) are also quite close to both the present results and those of Isida et al. (1981). This is because for small a/W and a/H, the interactions among the cracks are not significant, so that the pseudo-traction on the crack faces is

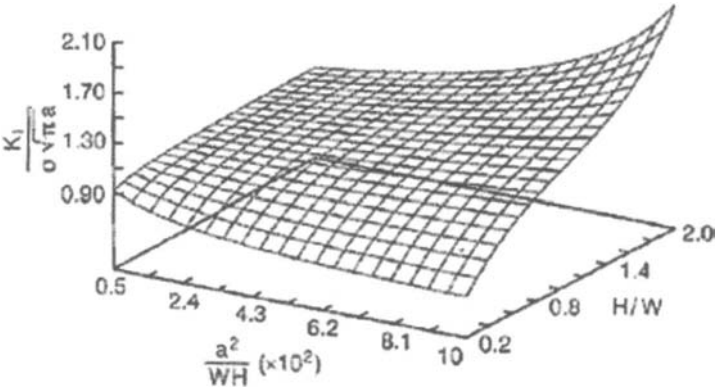

Figure 5. Variation of normalized mode I stress intensity factor with the density and shape of crack arrays

Table 1. Comparison of the normalized mode I SIF

a/W H/W	0.0	0.05	0.10	0.15	0.20	
	1.0	0.984	0.948	0.922		Present method
0.5	1.0	0.983	0.948	0.922		Isida et al.
	1.0	0.982	0.948	0.838		First-order approximation
	1.0	1.003	1.012	1.031		Present method
1.0	1.0	1.003	1.012	1.031		Isida et al.
	1.0	1.003	1.011	1.025		First-order approximation
	1.0	1.004	1.017	1.039	1.074	Present method
1.5	1.0	1.004	1.017	1.039	1.074	Isida et al.
	1.0	1.004	1.016	1.036	1.074	First-order approximation

reasonably accurately approximated by a constant value. The interactions are significant for large values of a/W, thus rendering the first-order approximation less accurate.

The overall tangent modulus of the body along the direction of loading is of prime interest. However, it is obvious that the cracked body is no longer a macroscopically isotropic medium but an orthotropic one. Its instantaneous shear modulus in the xy plane can be calculated by subjecting the body to an in-plane (xy) shear stress, but we shall not attempt this calculation here. Horii and Nemat-Nasser (1993) have given the constitutive relations for a cracked body

$$\bar{\varepsilon}_{ij} = D_{ijkl}\bar{\sigma}_{kl} + \frac{1}{V}\int_S \frac{1}{2}([v_i]n_j + [v_j]n_i)dS \tag{3.1}$$

where $[v_j]$ denotes the displacement jump across the crack with unit normal vector n_i, D_{ijkl} is the elastic compliance tensor of the uncracked body, and the integration is carried over the crack surface S contained in a representative volume V of the solid. Application of (3.1) to the stress and strain in the loading direction gives the tangent modulus E_y in that direction

$$\frac{E_y}{E} = \frac{1}{1 + \frac{8a^2}{WH}\int_0^1 v^*(t)dt} \tag{3.2}$$

with

$$v^*(t) = \frac{v(t)E}{2a\ \sigma}; \quad t \in [0,1] \tag{3.3}$$

$v(t)$ is half crack opening displacement at the position $t = x/a$, and E is plane stress Young's modulus of the uncracked body. Under plane strain, E is replaced with $E/(1-\nu^2)$.

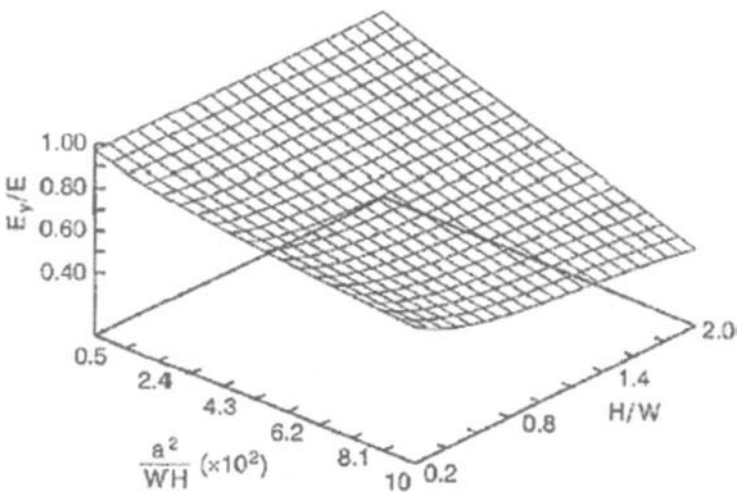

Figure 6. Variation of normalized tangent modulus with the density and shape of the array of cracks

Figure 6 shows the variation of E_y/E with the density and shape of the array of cracks. In contrast to the stress intensity factor, the instantaneous elastic modulus in the direction of loading does not seem to be very sensitive to the shape of the array (i.e. H/W). It depends primarily on the crack density (i.e. $a^2/(WH)$). The tangent modulus E_y in the direction of loading for the crack geometry under consideration may be regarded as a lower bound on the value for a solid containing randomly oriented cracks.

4 Bridged cracks

4.1 Elastic bridging

In this section we shall study the effect of the bridging stiffness on the stress intensity factor at the tips of cracks and on the crack opening displacement, assuming that the bridging force is linearly proportional to the latter

$$p_n(t_l) = k\nu(t_l). \tag{4.1}$$

Here, k is the bridging stiffness and t_l ($l = 1, \ldots, N$) denote positions on the crack surface in the notation of Eqs. (2.17)–(2.18).

Figure 7 shows the non-dimensional crack opening displacement (for a quarter of the crack) for different values of the non-dimensional bridging stiffness $c = k\frac{2(1-\nu^2)}{E}a$. The geometry of the array of cracks is described by $W/a = 2.5$ and $H/a = 2.0$. The results indicate that the crack opening displacement is very sensitive to small bridging stiffness. The same is also true for the mode I stress intensity factor at the crack tips (Fig. 8) and the tangent modulus (Fig. 9). It appears that the influence of bridging stiffness peaks at about $c \approx 10$. A similar variation of the mode I stress intensity factor for three parallel, but offset bridged cracks is also seen in the work of Hu et al. (1994).

4.2 Bilinear bridging

It is assumed that when the crack opening displacement reaches a critical value v_{cr} some of the fibres bridging the crack will debond from the matrix, resulting in a sudden drop in the bridging force (BC in Fig. 10), whereafter these fibres will exert a reduced closure force by frictional pull-out (CD in Fig. 10). If the fibres bridging the crack break, then $\alpha = 0$. A bridging law with $\alpha = 0$ has been earlier considered by Bao and Suo (1992). Several analytical models for fibre pull-out in cementitious composites have been developed by Gopalaratman and Shah (1987), Stang and Shah (1986), and Lim et al. (1987). These are based on single fibre pull-out tests giving a relationship between pull-out force P (or interfacial shear stress $\tau = P/(\pi d l_e)$ where d is the fibre diameter and l_e its embedded length) and fibre slip v (Fig. 11a). From this single-fibre ($\tau - v$) relationship, the average closure force on crack faces bridged by many fibres is obtained through an approximation to the fibre distribution function (Fig. 11b). The slope of the elastic part of this averaged pull-out diagram gives directly the parameter k in (4.1). When the crack opening exceeds the critical value v_{cr}, the bridging stress $p = kv(t_l)$ drops to the constant frictional pull-out value p_g.

As the stress drop introduces a logarithmic singularity in the gradient of the crack opening displacement, the problem is subdivided into two sub-problems: (a) perfect elasto-plastic bond with no stress drop (Fig. 12a), and (b) a constant stress drop $\Delta p = p_v - p_g$ (Fig. 12b). The superposition of the two solutions gives the final result. The first sub-problem is solved exactly as an elastically bridged crack but with the closure stress replaced by an constant stress p_v over the part of the crack where $v(t_l)$ exceeds the critical crack opening v_{cr}.

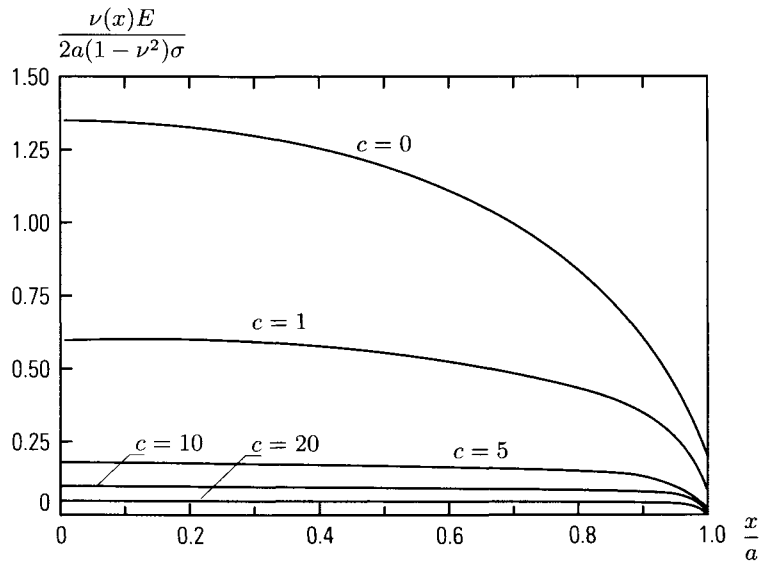

Figure 7. Influence of bridging stiffness on normalized crack opening displacement

The crack opening displacement caused by the partial crack surface traction in Fig. 12b can be calculated as follows

$$v^s(x) = (p_v - p_g)\int_0^b K_v^{ns}(x, x^i)dx^i - \frac{1-\nu}{G}\frac{p_v - p_g}{\pi}\int_0^b \ln|x - x^i|dx^i \qquad x \in [0, a] \text{ and } b \leq a \tag{4.2}$$

where $K_v^{ns}(x, x^i)$ is non-singular and is given by Eq. (2.13).

It is easy to show that

$$\int_0^b \ln|x - x^i|dx^i = \begin{cases} x\ln x + (b-x)\ln(b-x) - b & \text{for } x \leq b, \\ x\ln x - (x-b)\ln(x-b) - b & \text{for } x \geq b. \end{cases} \tag{4.3}$$

From Eqs. (4.2) and (4.3), it is clearly seen that the gradient of crack opening displacement has a logarithmic singularity at $x = b$.

5 Application to short fibre reinforced concrete

In the following, we shall use the above model to predict the pre-peak (strain hardening) and initial post-peak (tension softening) behaviour of short fibre reinforced conventional and DSP-based cementitious composites. The material parameters are given in Table 2. DSP stands for *Densified Systems containing homogeneously arranged ultrafine Particles.*

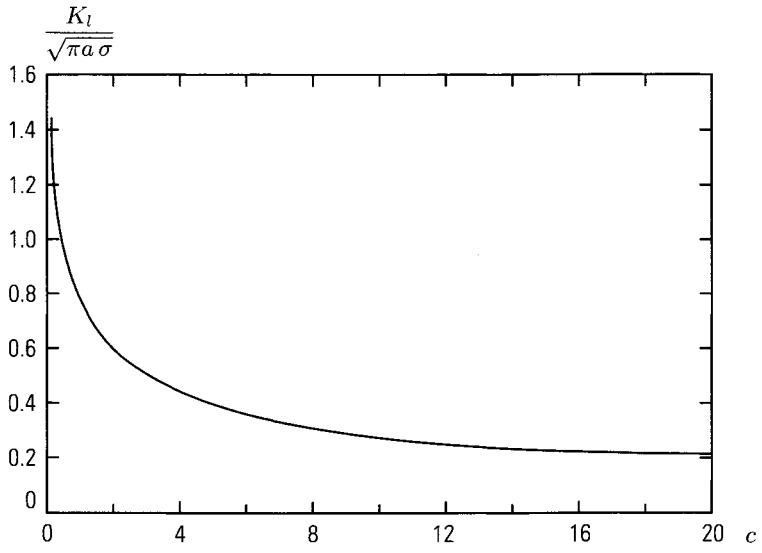

Figure 8. Influence of bridging stiffness on normalized stress intensity factor

5.1 Strain hardening due to multiple cracking

The decrease in the elastic modulus in the direction of loading induced by multiple elastically-bridged cracks can be used to predict the tensile strain hardening behaviour of random short fibre reinforced composites. There is ample experimental evidence from tests on fibre-reinforced brittle (Kim and Pagano (1991)) and quasi-brittle matrices (Mobasher et al. (1990); Tjiptobroto and Hansen (1993)) that suggests that the tensile strain hardening in these composites is due to the formation of microcracks whose density increases with increasing tensile/flexural loading until it reaches a saturation level.

To account for the increase in the density (number) of microcracks during the stage of strain hardening, we need a proper evolution law for the multiple cracks. Since the distribution of the size and spacing of multiple cracks in fibre-reinforced composites is of random nature, investigations have been conducted to predict the stochastic tendency of the development of the multiple cracks. Zok and Spearing (1992) considered a nonlinear relation between the spacing of cracks and applied stress. However, experimental observations on glass/ceramic GAS/SiC composite and theoretical predictions of Spearing and Zok (1993) based on stochastic simulations showed that the average spacing of cracks is reasonably linear in the applied stress during the course of multiple cracking until a state of saturation is reached. A linear relation between the average crack spacing and applied stress was also reported by Evans et al. (1994)

$$\ell = \ell_s \frac{[\sigma_s/\sigma_{mc} - 1]}{[\sigma/\sigma_{mc} - 1]} \tag{5.1}$$

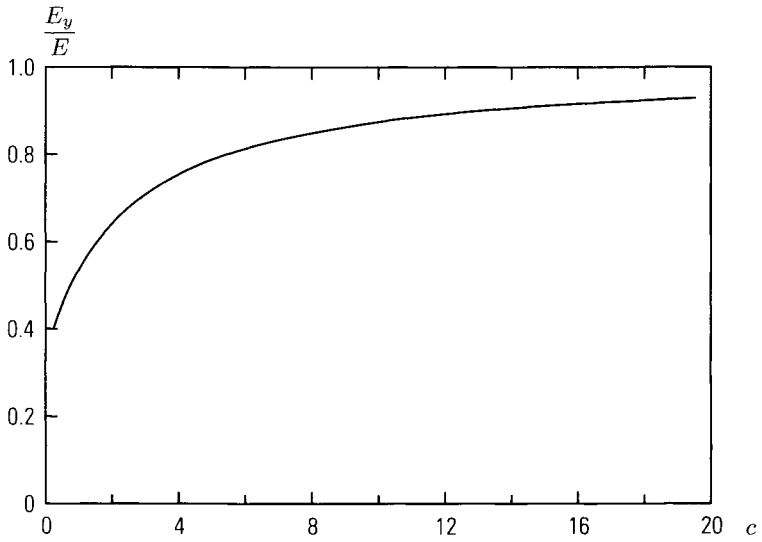

Figure 9. Influence of bridging stiffness on normalized tangent modulus

where σ_{mc} is the stress level at the initiation of the cracks; ℓ is the crack spacing at stress level σ and ℓ_s is the saturation spacing at stress level σ_s.

Following the same line of reasoning as in the works just cited, we propose the following two-dimensional linear evolution law for multiple cracks analogous to the one-dimensional law (5.1)

$$\frac{\sigma}{\sigma_{mc}} = 1 + \frac{\left(\frac{WH}{a^2}\right)_s [\sigma_s/\sigma_{mc} - 1]}{\frac{WH}{a^2}} \tag{5.2}$$

where σ_{mc} is the stress level at the initiation of the cracks, and the subscript s denotes the value of the corresponding parameter at the saturation of multiple cracks. The initiation value σ_{mc} may be equated to the tensile strength of the matrix, whereas the saturation value σ_s will represent the ultimate tensile capacity of the composite.

The variation of tangent modulus with the applied stress during the evolution of the multiple cracks can be determined from Eqs. (3.2) and (5.2). Once the variation of tangent modulus with the applied stress during the evolution of the multiple cracks is known, the stress-strain relation past the initiation stress level σ_{mc} can be obtained incrementally via

$$\dot{\varepsilon} = \dot{\sigma}/E_y(\sigma) \tag{5.3}$$

or

$$\frac{\dot{\varepsilon}}{\varepsilon_{mc}} = \left(\frac{\dot{\sigma}}{\sigma_{mc}}\right) \Big/ \left(\frac{E_y}{E}\right) \tag{5.4}$$

where we have used the definition $\varepsilon_{mc} = \sigma_{mc}/E$. When $\sigma \leq \sigma_{mc}$, $E_y \equiv E$, so that the stress-strain relation is linear. When $\sigma > \sigma_{mc}$, E_y/E changes with $\dot{\sigma}/\sigma_{mc}$ so that we

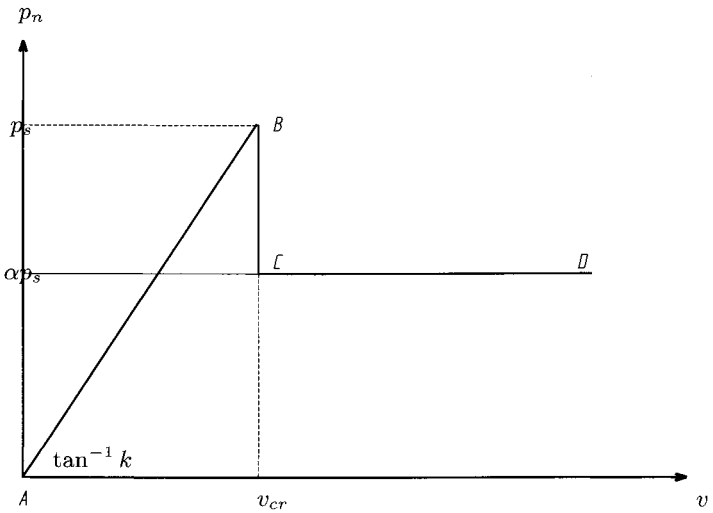

Figure 10. A linearized bridging law describing the relation between the bridging force and the crack opening displacement

have to calculate the increment of the strain using the current value of E_y/E at each step. The accuracy of the incremental formulation is the better, the smaller the step length. The normalized stress-strain curves predicted by (5.4) via Eqs. (3.2) and (5.2) are shown in Fig. 13. The curves predicted by the one-dimensional evolution law (5.1) are shown for comparison.

From Fig. 13, it is seen that both evolution laws (5.1) and (5.2) produce similar variations of the stress-strain curves. As the final crack densities are assumed to be the same for the two evolution processes, the final values of E_y/E are also equal, for the same value of σ_s/σ_{mc}. As expected, the two-dimensional evolution law predicts a stiffer response than does the one-dimensional law. The response of a composite with randomly oriented cracks can be expected to be even more stiff.

5.2 Modelling of tension softening

The microcrack model of Horii et al. (1989) and Ortiz (1988) for modelling the tension softening process of un-reinforced cementitious materials will be extended to short fibre reinforced composites. In this model (Fig. 14) the damage at peak load is assumed to localize along the eventual failure plane. The damage is in the form of fragmented cracks interspersed by unbroken material. At peak load each crack is bridged by fibres, some of which are on the verge of pulling out from the matrix. Let the average maximum opening displacement at this instant be $\bar{v}_{cr}$. The initial part of tension softening is a result of the progressive growth of the cracks into the unbroken material, for which two conditions must be simultaneously met: the stress intensity factor at the tips of each crack K_{Ij} must attain the critical value K_{Ic} of the composite and the fibres must pull out when

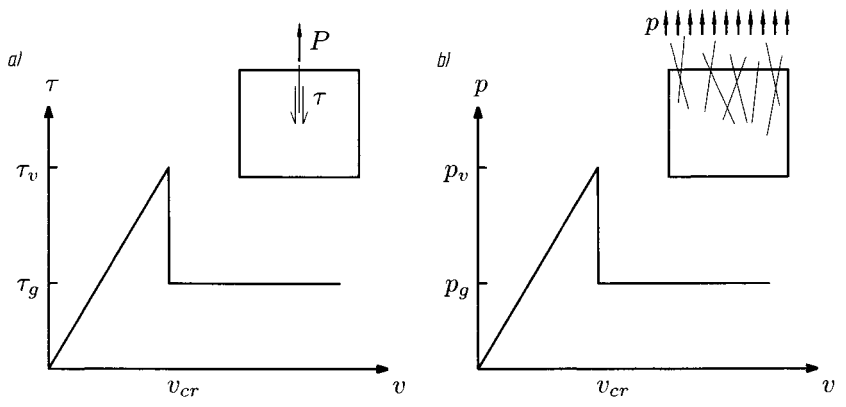

Figure 11. Conversion from pull-out properties of a single fibre to interfacial properties averaged over the cross-section, a) Single fibre pull-out b) averaged interfacial properties for many fibres randomly distributed

Table 2. Material parameters

Parameter			DSP-based FRC	Conventional FRC
E	(Young's modulus)	[GPa]	40.0	40.0
σ_m	(matrix strength)	[MPa]	10.0	3.0
ν	(Poisson's ratio)		0.2	0.2
τ_v	(interfacial shear strength)	[MPa]	9.0	2.0
τ_g	(frictional shear strength)	[MPa]	5.0	1.0
l	(fibre length)	[mm]	20.0	20.0
d	(fibre diameter)	[mm]	0.4	0.4

the crack opening reaches $\bar{v}_{cr}$. Mathematically these two dynamic conditions for crack growth are

$$K_I(\sigma, a, l) = K_{Ic} \tag{5.5}$$

$$v(\sigma, a, l) = \bar{v}_{cr} \tag{5.6}$$

where $v(\sigma, a, l)$ is the crack opening at $x = l$ and σ denotes the reduced tensile carrying capacity. Note that at the onset of tension softening $l = 0$, so that Eq. (3.3) can be used to calculate the average critical crack opening $\bar{v}_{cr}$. K_{Ic} is related to the fibre content, the critical stress intensity factor of the matrix and the interfacial bond strength.

Here, we introduce an equivalent critical stress intensity factor K_{Ic} based upon the ultimate tensile strength of short fibre-reinforced concrete. The ultimate tensile strength of a composite containing a moderate fraction of fibre can be calculated using the simple

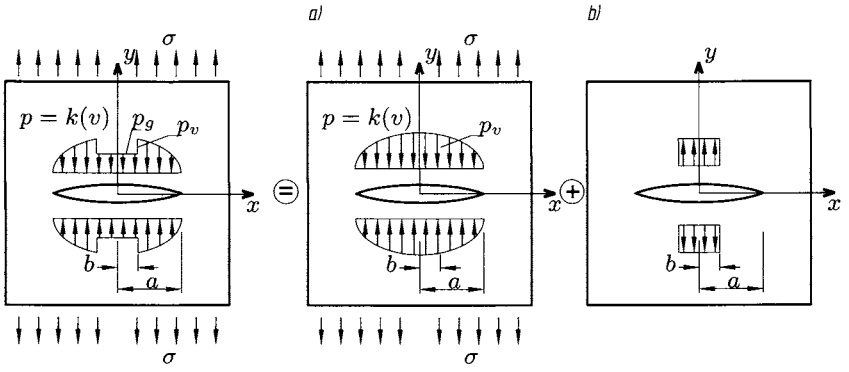

Figure 12. The superposition of closing tractions

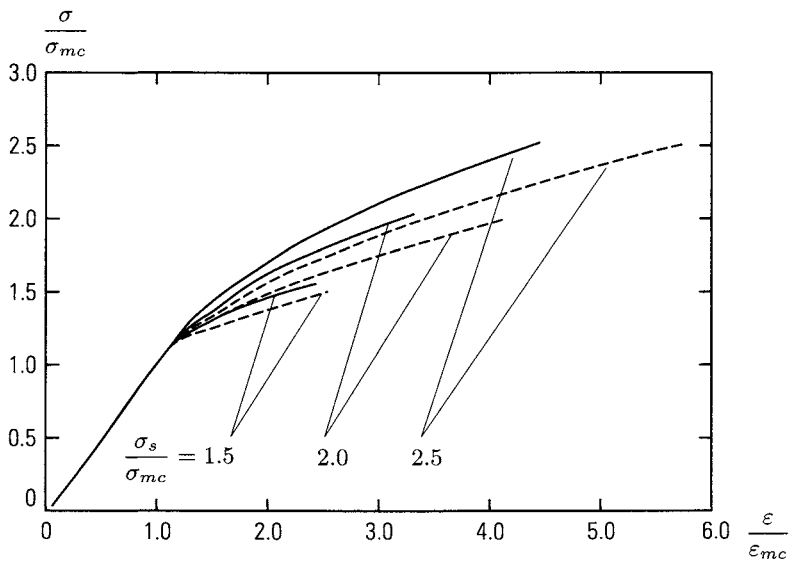

Figure 13. Normalized stress-strain curves during multiple cracking (strain hardening). Solid line corresponds to Eq. (5.2), and dashed line to Eq. (5.1)

law of mixtures (Karihaloo (1995))

$$\sigma_c = \alpha\sigma_m(1 - V_f) + \beta\tau V_f \frac{\ell}{d} \tag{5.7}$$

where V_f is the volume fraction of fibre, τ is the average bond strength of the fibre-matrix interface, and l/d is the aspect ratio of the fibre, α and β are empirical constants which are to be determined from tests. In order to retrieve $\sigma_c \equiv \sigma_m$ when $V_f = 0$, we take

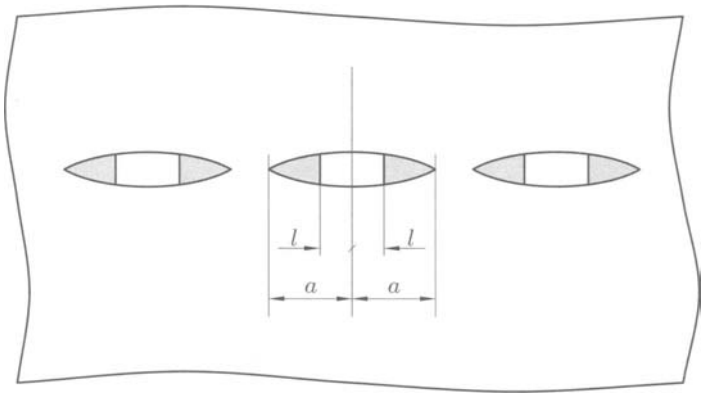

Figure 14. A microcrack model for tension softening process. The fibres in the central region of length $2l$ of each crack are assumed to pull out, so that the bridging traction in this region is reduced from p_s to αp_s as shows in Fig. 10. The bridging traction in the shaded regions where the fibres are still fully bonded to the matrix is proportional to crack opening, kv

$\alpha = 1$. Aveston et al. (1971) have proposed a value $\beta = 0.5$ for randomly distributed short fibres. Note that σ_c equals σ_s in the present model.

In the initial part of tension softening regime the growth of fragmented bridged cracks takes place at constant stress intensity factor equal to the effective fracture toughness of composite K_{Ic}. Its value can therefore be calculated using the stress and crack length at the onset of tension softening. The stress equals σ_c ($\equiv \sigma_s$) given by (5.7) and the half crack length is a_0, so that

$$K_{Ic} = \Gamma_0 \sqrt{\pi a_0} \left[\alpha \sigma_m (1 - V_f) + \beta \tau V_f \frac{l}{d} \right] \tag{5.8}$$

The geometrical factor Γ_0 for the row of elastically bridged cracks at the onset of tension softening is calculated using the procedure described in Sect. 4 with $H \to +\infty$.

From Eqs. (5.5), (5.6) and (5.8) it is now possible to determine the reduced tensile carrying capacity σ and the length of crack l over which the fibres exert closure force due to frictional pull-out only. To complete the description of tension softening process it remains to determine the average inelastic crack opening along the localized damage band, given by

$$w^* \equiv \langle v_i \rangle = \frac{1}{W} \int_{-a}^{a} [v_t] dx - \frac{1}{W} \int_{-a_0}^{a_0} [v_e] dx \tag{5.9}$$

where $[v_t]$ is the total opening of the crack faces ($[v_t] = v_t^+ - v_t^-$, with "+" and "−" referring to the upper and lower crack faces), and $[v_e]$ is the elastic (recoverable) opening of the crack faces. Note that over the unbroken ligaments $|x| < \frac{W}{2} - a$, $[v_t] = 0$.

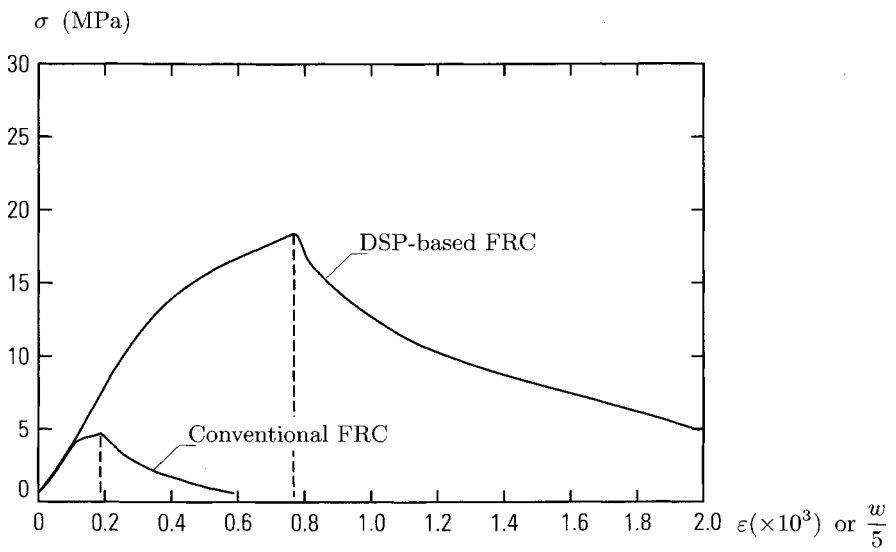

Figure 15. Complete pre- and post-peak tensile response of the materials of Table 2 and $V_f = 0.04$. Note that the pre-peak response is given in terms of stresses and strains, whereas the post-peak response is via a stress-average crack opening measure

Figure 15 shows the complete pre- and post-peak curves for the material parameters of Table 2. The values of W and a_0 in eqn (5.9) are assumed to be 50 mm and 4.83 mm, respectively. β in Eq. (5.7) is taken as 0.5. For convenience of graphical presentation of strain hardening and tension softening on the same diagram, it is assumed that $\sigma_c = \sigma_s$ and $\sigma_{mc} = \sigma_m$, although in the latter instance it might be more appropriate to set $\sigma_{mc} = \sigma_m/(1 - V_f)$. Moreover, the pre-peak behaviour is presented as a relation between the applied remote stress σ and strain ε, whereas the post-peak behaviour is presented as a relation between the diminishing applied stress σ and the average inelastic crack opening $w = w^* E/\pi a_0 \sigma_m$. Again for ease of comparison of the two response curves σ_m has been arbitrarily chosen equal to 4 MPa. In reality, E of DSP-based FRC is nearly twice that of the conventional FRC (60 GPa compared with 30 GPa), while its σ_m is more than three times that of the latter (see Table 2). The ratio E/σ_m is DSP-based FRC is therefore around 6, whereas that of conventional FRC is around 10. This difference should be borne in mind in evaluating the response curves in Fig. 15.

Figure 15 is in very good agreement with the typical load-elongation responses of these two materials. The stress-strain curve of DSP-based matrix is in excellent agreement with that measured in four-point bending by Tjiptobroto and Hansen (1993). The present model predicts that the improvement in the toughness of the material is primarily due to the enhancement of the ultimate strength (or the equivalent critical stress intensity factor K_{Ic}) of the composite. The high strength of the DSP-based matrix itself and the high interfacial bonding strength between the fibre and this matrix makes significant contribution to the improvement in the overall properties of the composite.

6 Material instability in the tensile response of short fibre reinforced quasi-brittle composites

We described above the complete constitutive behaviour of short-fibre-reinforced cementitious composites under unidirectional tension. We could not however predict the transition from the strain-hardening to tension-softening. This led to a discontinuity in the slope of the stress-strain/displacement curve at the peak load (see Fig. 15). In other words, conditions for localisation are still not clear. In this section, the mechanisms for the material instability which lead to deformation localisation and tension softening will be revealed. The study will be based upon an analytical procedure which allows the conditions for the material instability in short-fibre-reinforced composites to be highlighted. The material instability is examined using the classical bifurcation criterion, with an emphasis on the role played by fibre bridging in the macroscopic instability. It is found that while the microscopic instability in the bridging traction plays a major role in the macroscopic instability of the composite, it is the level of damage in the matrix that determines when the macroscopic instability is induced by the bridging instability. The satisfaction of the classical bifurcation criterion is identified with several failure modes, depending on the degree of damage in the matrix. The phrase 'microscopic instability' is used to define the instant when the bridging stiffness momentarily vanishes.

6.1 General formulae for multiple cracks

The prediction of the effective elastic and fracture properties of a medium containing multiple cracks has received considerable attention. Among the studies are the solutions based upon the non-interacting approximation, when the interaction among the cracks is neglected. Under this assumption, the effective elastic properties can be expressed in explicit forms. The interactions among multiple cracks complicate the prediction of the overall material behaviour. The schemes based upon indirect considerations of crack interactions, such as the self-consistent method and the differential scheme may considerably underestimate the overall moduli, as has been pointed by Wang et al. (2000a).

Here, we shall present an analytical approach for the calculation of the overall tensile modulus of bodies containing multiple parallel bridged cracks. For this, we shall make use of the procedures described above, and those in the works of Wang et al. (2000a), Wang et al. (2000b).

The overall (average) strain and stress of a cracked body are related via (e.g. [6])

$$\varepsilon_{ij} = C^0_{ijkl}\sigma_{kl} + \frac{1}{2V}\sum_N \int_{S_N} ([u_i]n_j + [u_j]n_i)\, dS_N \tag{6.1}$$

where ε_{ij} and σ_{kl} are the average strain and stress components, respectively. u_i and n_i are the total crack opening/sliding displacement (COD/CSD) and the component of the unit vector normal to the crack faces. C^0_{ijkl} is the compliance tensor of the uncracked material. For parallel flat cracks when n_i is a constant, eqn (6.1) can be rewritten as

$$\varepsilon_{ij} = C^0_{ijkl}\sigma_{kl} + \frac{1}{2V}\sum_N \left(\overline{[u_i]}n_j + \overline{[u_j]}n_i\right) S_N \tag{6.2}$$

where $\overline{[u_i]}$ is the average COD/CSD for a single crack over its faces, and S_N is its area.

We note that eqn (6.2) can be written as

$$\varepsilon_{ij} = C^0_{ijkl}\sigma_{kl} + \frac{\omega}{L}\left(\overline{[u_i]}n_j + \overline{[u_j]}n_i\right) \tag{6.3}$$

where ω is a non-dimensional crack density parameter, and L is an internal length scale, which will be defined later. In the above expression, $\overline{[u_i]}$ is taken to be the COD/CSD for a representative crack.

We consider only infinitesimal deformation and rotation. Taking the time-derivative of the above equation gives

$$\dot{\varepsilon}_{ij} = C^0_{ijkl}\dot{\sigma}_{kl} + \frac{1}{L}\left(\overline{[u_i]}n_j + \overline{[u_j]}n_i\right)\frac{\partial\omega}{\partial\sigma_{kl}}\dot{\sigma}_{kl} + \frac{\omega}{L}\left(\frac{\partial\overline{[u_i]}}{\partial\sigma_{kl}}n_j + \frac{\partial\overline{[u_j]}}{\partial\sigma_{kl}}n_i\right)\dot{\sigma}_{kl} \tag{6.4}$$

Here, we have assumed that the crack density is a function of the applied stress. Strictly speaking, $\overline{[u_i]}$ is also a function of ω, which is in turn a function of σ_{kl}. However, eqn (6.3) implies that $\overline{[u_i]}$ is a generic crack opening/sliding displacement in a representative element. In analogy with the usual non-interacting solution, we assume at this stage that this generic crack opening/sliding displacement is not related to the crack density, so that the derivative of $\overline{[u_i]}$ with respect to ω vanishes. Equation (6.4) gives the tangent compliance tensor

$$C_{ijkl} = C^0_{ijkl} + \frac{1}{L}\left(\overline{[u_i]}n_j + \overline{[u_j]}n_i\right)\frac{\partial\omega}{\partial\sigma_{kl}} + \frac{\omega}{L}\left(\frac{\partial\overline{[u_i]}}{\partial\sigma_{kl}}n_j + \frac{\partial\overline{[u_j]}}{\partial\sigma_{kl}}n_i\right) \tag{6.5}$$

whence the rate form of the constitutive relation (6.4) can be written as

$$\dot{\varepsilon}_{ij} = C_{ijkl}\dot{\sigma}_{kl} \tag{6.6}$$

We now return to the determination of $\overline{[u_i]}$. For bodies containing multiple cracks, the effect of crack interactions and of any bridging tractions must be taken into account in the calculation of the crack opening displacement. Using the pseudo-traction formalism Horii and Nemat-Nasser (1985), the average crack opening displacement is calculated by applying a pseudo-traction on the faces of a single crack, as we did in the preceding sections. In order to determine $\overline{[u_i]}$ and thus C_{ijkl} for a body containing randomly distributed multiple parallel bridged cracks, we shall first invoke the analytical procedures in the works of Wang et al. (2000a), Wang et al. (2000b) for two regular arrays of bridged cracks, namely, a doubly periodic rectangular array and a doubly periodic diamond-shaped array of bridged cracks, shown in Figure 16. We consider the two-dimensional case, when the parallel cracks are perpendicular to, say, the direction 2. Following the procedures in the above works, the traction consistency condition on each crack in either of the two doubly periodic configurations is expressed as follows:

$$\sigma^p_{ij}(x) - 2\sum_{j=1}^{+\infty}\int_0^a K_{ijkl}(x,x^j)\sigma^p_{kl}(x^j)dx^j + p_{ij}(x) = \sigma^0_{ij} \quad x \in [0,a) \tag{6.7}$$

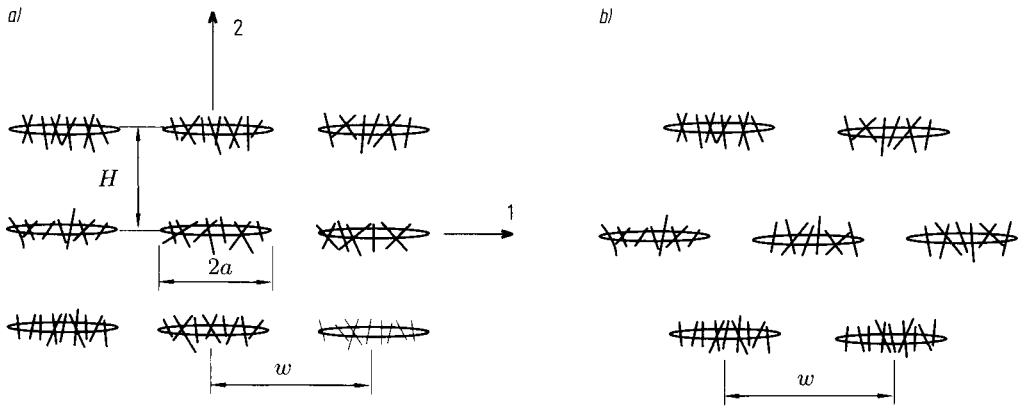

Figure 16. Doubly periodic rectangular (a) and diamond-shaped array (b) of bridged cracks

where σ_{ij}^p is the pseudo-traction on the crack faces, σ_{ij}^0 is the applied stress, p_{ij} is the bridging stress exerted by the fibres, and a is the half length of a crack. $K_{ijkl}(x, x^j)$ is the stress influence tensor which was described above (see Eq. (2.6), where we used a slightly different notation).

However, in this section, in order to trace the non-linear behaviour of the material, we shall recast the traction consistency condition (6.7) in an incremental form

$$\Delta\sigma_{ij}^p(x) - 2\sum_{j=1}^{+\infty}\int_0^a K_{ijkl}(x, x^j)\Delta\sigma_{kl}^p(x^j)dx^j + \Delta p_{ij}(x) = \Delta\sigma_{ij}^0 \quad x \in [0, a) \tag{6.8}$$

For the two-dimensional case under study, the parallel cracks are perpendicular to direction 2, so that we need only the pseudo-tractions σ_{22}^p and σ_{12}^p for calculating the crack opening/sliding displacements. Following the procedure in the work by Wang et al. (2000a), it is found that the incremental pseudo-tractions for the two periodic arrays of cracks shown in Figure 16 can be written as

$$\begin{Bmatrix} \Delta\sigma_{22}^{pr} \\ \Delta\sigma_{22}^{pd} \end{Bmatrix} = \begin{Bmatrix} \zeta^r \\ \zeta^d \end{Bmatrix} \Delta\sigma_{22}^0 \tag{6.9}$$

$$\begin{Bmatrix} \Delta\sigma_{12}^{pr} \\ \Delta\sigma_{12}^{pd} \end{Bmatrix} = \begin{Bmatrix} \eta^r \\ \eta^d \end{Bmatrix} \Delta\sigma_{12}^0 \tag{6.10}$$

where

$$\zeta^r = \left\{1 + 4\sin^2\frac{\pi a}{W}e^{-2\frac{H}{W}\pi}\left[1 + 2\frac{H}{W}\pi\right] - \frac{2\overline{k}_{22}W^2}{\pi a\ E'}\ln\left(\cos\frac{\pi a}{W}\right)\right\}^{-1} \tag{6.11}$$

$$\zeta^d = \left\{1 - 4\sin^2\frac{\pi a}{W}e^{-2\frac{H}{W}\pi}\left[1 + 2\frac{H}{W}\pi\right] - \frac{2\overline{k}_{22}W^2}{\pi a\ E'}\ln\left(\cos\frac{\pi a}{W}\right)\right\}^{-1} \tag{6.12}$$

$$\eta^r = \left\{1 + 4\sin^2\frac{\pi a}{W}e^{-2\frac{H}{W}\pi}\left[1 - 2\frac{H}{W}\pi\right] - \frac{2\overline{k}_{12}W^2}{\pi a\ E'}\ln\left(\cos\frac{\pi a}{W}\right)\right\}^{-1} \tag{6.13}$$

$$\eta^d = \left\{1 - 4\sin^2\frac{\pi a}{W}e^{-2\frac{H}{W}\pi}\left[1 - 2\frac{H}{W}\pi\right] - \frac{2\overline{k}_{12}W^2}{\pi a\ E'}\ln\left(\cos\frac{\pi a}{W}\right)\right\}^{-1} \tag{6.14}$$

$E' = E$ for plane-stress, and $E' = E/(1-\nu^2)$ for plane-strain deformation. In deriving eqns (6.9)–(6.10), a linear relationship between the incremental bridging stress $\Delta p_{22}(x)$ and incremental COD/CSD has been assumed

$$\Delta p_{22}(x) = \overline{k}_{22}\Delta[u_2](x); \qquad \Delta p_{12}(x) = \overline{k}_{12}\Delta[u_1](x) \tag{6.15}$$

where $[u_1](x)$ and $[u_2](x)$ are the crack opening/sliding displacements. It is evident that $\overline{k}_{12}$ and $\overline{k}_{22}$ in the above expression should be the tangent bridging stiffnesses.

We presented above the incremental pseudo-tractions on the crack faces following the asymptotic analysis of Wang et al. (2000a), Wang et al. (2000b). They are found to be constants (in an average sense only) and dependent upon the geometry of the crack arrays and the instantaneous tangent bridging stiffnesses. $\Delta\sigma_{22}^{pr}(\Delta\sigma_{12}^{pr})$ and $\Delta\sigma_{22}^{pd}(\Delta\sigma_{12}^{pd})$ are the two incremental pseudo-tractions for the doubly periodic rectangular array and diamond-shaped array, respectively. According to the analysis in the work by Wang et al. (2000a), these two regular patterns should represent the two extreme interactions among multiple parallel cracks, namely, the maximum "shielding" and "magnification" effects under unidirectional tension and the maximum "magnification" and "shielding" effects under in-plane shear. Based upon this analysis, Wang et al. (2000a) deduced that the overall modulus of a body containing randomly distributed multiple parallel cracks should be within a pair of bounds corresponding to the moduli for the doubly periodic rectangular and diamond-shaped array, respectively. Moreover, it was found that when the the terms $4\sin^2\frac{\pi a}{W}e^{-2\frac{H}{W}\pi}\left[1 + 2\frac{H}{W}\pi\right]$ and $4\sin^2\frac{\pi a}{W}e^{-2\frac{H}{W}\pi}\left[1 - 2\frac{H}{W}\pi\right]$ were neglected in the expressions (6.11)–(6.14), i.e., when these expressions reduced to

$$\zeta = \left\{1 - \frac{2\overline{k}_{22}W^2}{\pi a\ E'}\ln\left(\cos\frac{\pi a}{W}\right)\right\}^{-1} \tag{6.16}$$

$$\eta = \left\{1 - \frac{2\overline{k}_{12}W^2}{\pi a\ E'}\ln\left(\cos\frac{\pi a}{W}\right)\right\}^{-1} \tag{6.17}$$

the overall moduli so calculated for low to moderate crack density were always in the middle of the range bounded by those obtained when the terms $4\sin^2\frac{\pi a}{W}e^{-2\frac{H}{W}\pi}\left[1 + 2\frac{H}{W}\pi\right]$ and $4\sin^2\frac{\pi a}{W}e^{-2\frac{H}{W}\pi}\left[1 - 2\frac{H}{W}\pi\right]$ were retained. Expressions (6.16)–(6.17) are nothing

but the so-called non-interacting solution. Numerical computations of Kachanov (1992) for random discrete unbridged parallel cracks also were found to be close to the non-interacting solution. Thus, it is reasonable to use the expressions (6.16)–(6.17) to calculate the pseudo-tractions

$$\Delta\sigma_{22}^{p} = \zeta\Delta\sigma_{22}^{0}, \qquad \Delta\sigma_{12}^{p} = \eta\Delta\sigma_{12}^{0} \tag{6.18}$$

Having obtained the pseudo-tractions, the average crack opening/sliding displacements can be easily found

$$\begin{Bmatrix} \Delta\overline{[u_1]} \\ \Delta\overline{[u_2]} \end{Bmatrix} = \frac{1}{2a}\int_{-a}^{+a} \begin{Bmatrix} \Delta[u_1](x) \\ \Delta[u_2](x) \end{Bmatrix} dx = -\frac{2W^2}{\pi a\, E} \ln\left(\cos\frac{\pi a}{W}\right) \begin{Bmatrix} \Delta\sigma_{12}^{p} \\ \Delta\sigma_{22}^{p} \end{Bmatrix} \tag{6.19}$$

The subsequent development is for plane-stress deformation condition. Substituting (6.18) into (6.19) gives

$$\begin{Bmatrix} \Delta\overline{[u_1]} \\ \Delta\overline{[u_2]} \end{Bmatrix} = -\frac{2W^2}{\pi a\, E} \ln\left(\cos\frac{\pi a}{W}\right) \begin{Bmatrix} \eta\Delta\sigma_{12}^{0} \\ \zeta\Delta\sigma_{22}^{0} \end{Bmatrix} \tag{6.20}$$

which can be rewritten as

$$\begin{Bmatrix} \dfrac{\Delta\sigma_{12}^{0}}{E} \\ \dfrac{\Delta\sigma_{22}^{0}}{E} \end{Bmatrix} = \begin{bmatrix} -\dfrac{1}{\frac{2W}{\pi a}\eta \ln\left(\cos\frac{\pi a}{W}\right)} & 0 \\ 0 & -\dfrac{1}{\frac{2W}{\pi a}\zeta \ln\left(\cos\frac{\pi a}{W}\right)} \end{bmatrix} \cdot \begin{Bmatrix} \dfrac{\Delta\overline{[u_1]}}{W} \\ \dfrac{\Delta\overline{[u_2]}}{W} \end{Bmatrix} \tag{6.21}$$

Expression (6.21) describes the local behaviour of the cracked material. The global constitutive behaviour of the material can be determined from (6.6), together with (6.5).

6.2 Analysis of Material Instability

In this Section, we shall study the material instability in the macroscopic tensile response of the composite, especially that induced by the microscopic bridging mechanism. For this, we use the classical bifurcation criterion for discontinuity localisation across parallel planes of Rudnicki and Rice (1975). As will be seen later, for the case studied here, this criterion is equivalent to other bifurcation criteria identified by Neilsen and Schreyer (1993) for the study of material instabilities. The classical bifurcation criterion is

$$\det[Q_{ij}] = 0 \tag{6.22}$$

where Q_{ij} is the acoustic tensor defined as

$$Q_{ij} = n_k D_{kijl} n_l \tag{6.23}$$

D_{kijl} is the tangent stiffness tensor which is the inverse of the tangent compliance tensor C_{kijl} in Eq (6.5).

In order to obtain the acoustic tensor (6.23), we need to calculate the tangent compliance tensor from eqn (6.5). For this, we need the total crack opening/sliding displacement $\overline{[u_i]}$, and its partial derivative with respect to σ_{kl}. As pointed out previously, in fibre-reinforced quasi-brittle composites, it is observed in experiments that the density of the multiple cracks increases with increasing load until it reaches a saturation level ω_s, when the localisation sets in. Moreover, in these materials the damage localisation usually coincides with the pull-out of fibres from the matrix. This implies that at localisation, the partial derivative $\partial\omega/\partial\sigma_{kl}$ in Eq (6.5) can be equated to zero. Of course, the second term in Eq (6.5) is essential to the strain hardening description which may be found in the work of Karihaloo and Wang (2000). The tangent compliance tensor (6.5) at the instant of localisation therefore reduces to

$$C_{ijkl} = C^0_{ijkl} + \frac{\omega_s}{L}\left(\frac{\partial\overline{[u_i]}}{\partial\sigma_{kl}}n_j + \frac{\partial\overline{[u_j]}}{\partial\sigma_{kl}}n_i\right) \tag{6.24}$$

Let us consider the localisation into a planar band under unidirectional tension σ_{22}. For the considered two-dimensional case, the conventional crack density parameter ω is defined as

$$\omega = \frac{a^2}{WH} \tag{6.25}$$

The rate form of the stress-strain relations (6.6), after making use of (6.24), are

$$\begin{Bmatrix}\dot\varepsilon_{11}\\ \dot\varepsilon_{22}\\ \dot\varepsilon_{12}\end{Bmatrix} = \begin{bmatrix}\frac{1}{E} & -\frac{\nu}{E} & 0\\ -\frac{\nu}{E} & \frac{1}{E}+2\frac{\omega_s}{L}\frac{\partial\overline{[u_2]}}{\partial\sigma_{22}} & 0\\ 0 & 0 & \frac{2(1+\nu)}{E}+2\frac{\omega_s}{L}\frac{\partial\overline{[u_1]}}{\partial\sigma_{12}}\end{bmatrix}\cdot\begin{Bmatrix}\dot\sigma_{11}\\ \dot\sigma_{22}\\ \dot\sigma_{12}\end{Bmatrix} \tag{6.26}$$

Calculating $\partial\overline{[u_2]}/\partial\sigma_{22}$ and $\partial\overline{[u_1]}/\partial\sigma_{12}$ from Eq (6.20), and noting that for the considered case, $L = a$, we get the tangent compliance matrix

$$[C_{ij}] = \begin{bmatrix}\frac{1}{E} & -\frac{\nu}{E} & 0\\ -\frac{\nu}{E} & \frac{1}{E}-4\left(\frac{W}{a}\right)^2\frac{\omega_s}{\pi E}\zeta\ln\left(\cos\frac{\pi a}{W}\right) & 0\\ 0 & 0 & \frac{2(1+\nu)}{E}-4\left(\frac{W}{a}\right)^2\frac{\omega_s}{\pi E}\eta\ln\left(\cos\frac{\pi a}{W}\right)\end{bmatrix} \tag{6.27}$$

and, by inversion, the corresponding tangent stiffness matrix

$$[D_{ij}] = \begin{bmatrix}\frac{E[1-4\left(\frac{W}{a}^2\right)\frac{\omega_s}{\pi}L_t]}{[1-\nu^2-4\left(\frac{W}{a}\right)^2\frac{\omega_s}{\pi}L_t]} & \frac{E\nu}{[1-\nu^2-4\left(\frac{W}{a}\right)^2\frac{\omega_s}{\pi}L_t]} & 0\\ \frac{E\nu}{[1-\nu^2-4\left(\frac{W}{a}\right)^2\frac{\omega_s}{\pi}L_t]} & \frac{E}{[1-\nu^2-4\left(\frac{W}{a}\right)^2\frac{\omega_s}{\pi}L_t]} & 0\\ 0 & 0 & \frac{E}{2[(1+\nu)-2\left(\frac{W}{a}\right)^2\frac{\omega_s}{\pi}L_s]}\end{bmatrix} \tag{6.28}$$

Here, we have introduced two non-dimensional parameters

$$L_t \equiv \zeta \ln\left(\cos\frac{\pi a}{W}\right) \tag{6.29}$$

$$L_s \equiv \eta \ln\left(\cos\frac{\pi a}{W}\right) \tag{6.30}$$

where the subscripts t and s denote tension and shear, respectively.

Substituting the tangent stiffness tensor into Eq (6.23) gives the acoustic tensor whose components in a matrix form are

$$[Q_{ij}] = \begin{bmatrix} \frac{E}{2[(1+\nu)-2\left(\frac{W}{a}\right)^2\frac{\omega_s}{\pi}L_s]} & 0 \\ 0 & \frac{E}{[1-\nu^2-4\left(\frac{W}{a}\right)^2\frac{\omega_s}{\pi}L_t]} \end{bmatrix} \tag{6.31}$$

As we are interested in the unidirectional tensile case, we only discuss L_t in the sequel. We first rewrite L_t (6.29), using Eq (6.16), and omit the subscript 22 from $\overline{K}_{22}$ for brevity,

$$L_t = \frac{\ln\left(\cos\frac{\pi a}{W}\right)}{1 - \frac{2\bar{k}W^2}{\pi a E}\ln\left(\cos\frac{\pi a}{W}\right)} \tag{6.32}$$

The ratio $2a/W$ represents the cracked area to the nominal area in the direction perpendicular to the loading direction. It therefore represents the conventional damage parameter in the context of damage mechanics. Denoting $\Omega = 2a/W$, L_t can be rewritten as

$$L_t = \frac{\ln\left(\cos\frac{\pi}{2}\Omega\right)}{1 - \frac{8\bar{k}a}{\pi E}\frac{1}{\Omega^2}\ln\left(\cos\frac{\pi}{2}\Omega\right)} \tag{6.33}$$

It is seen from Eq (6.31) that the satisfaction of the localisation criterion (6.22) requires that $L_t \to \infty$. When this condition is met, it is seen from (6.28) that the determinant of the tangent stiffness matrix, $\det[D_{ij}]$, also vanishes. $[D_{ij}]$ is symmetric, as is $[Q_{ij}]$. Therefore, the condition $L_t \to \infty$ leads to the satisfaction of all bifurcation criteria identified by Neilsen and Schreyer (1993), namely, the classical bifurcation criterion (6.22), the general bifurcation criterion, the limit point bifurcation criterion and the loss of strong ellipticity criterion. In the following, we shall use the phrases "localisation" or "material instability" to refer to the consequences of $\det[Q_{ij}] = 0$, i.e. when $L_t \to \infty$.

6.3 Conditions for Material Instability

Several features of the material instability are revealed by the above results. First, for unbridged material ($\bar{k} = 0$), it seen from eqn (6.33) that the satisfaction of the localisation criterion $\det[Q_{ij}] = 0$ requires that $L_t = \ln\left(\cos\frac{\pi}{2}\Omega\right) \to \infty$. This simply means that the damage parameter, or any effective quantity, Ω, tends to 1. In this case, L_s also becomes zero. So the material loses instability both under unidirectional tension perpendicular to the crack and under in-plane shear. Thus, the bifurcation criterion is identified with the damage induced rupture of the material.

When $\bar{k} \neq 0$, it is seen from (6.33) that L_t is determined by the tangent bridging stiffness $\bar{k}$. For short-fibre-reinforced cementitious composites, a trilinear bridging law,

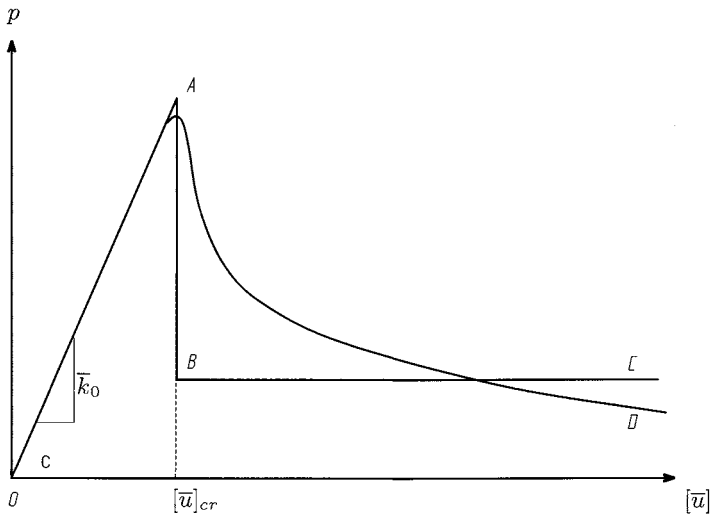

Figure 17. An idealised trilinear bridging law OABC and a more realistic smooth bridging law OAD with continuous slope

such as OABC shown in Figure 17, is commonly used. This is obviously an idealisation of the actual fibre pull-out test results. The problem with the idealised trilinear bridging law is the discontinuity in the tangent bridging stiffness k. In real materials, especially when the average effect of randomly distributed fibres is considered, the tangent bridging stiffness varies gradually, as shown by OAD in Figure 17. This continuous bridging traction can, for example, be described by

$$p = \overline{k}[\overline{u}]e^{-\frac{[\overline{u}]}{[\overline{u}]_{cr}}} \tag{6.34}$$

The tangent bridging stiffness can thus be written as

$$\overline{k} = \overline{k}_0 \left\{ 1 - \frac{[\overline{u}]}{[\overline{u}]_{cr}} \right\} e^{-\frac{[\overline{u}]}{[\overline{u}]_{cr}}} \tag{6.35}$$

where $\overline{k}_0$ is the initial tangent bridging stiffness when the fibres are bonded to the matrix (Figure 17). It is evident that the tangent bridging stiffness vanishes at $[\overline{u}] = [\overline{u}]_{cr}$ and it becomes negative, when $[\overline{u}] > [\overline{u}]_{cr}$. The expression (6.35) is in line with the simple local constitutive law that Jirasek and Bažant (1994) used in their study of the localisation phenomenon within the formalism of the non-local theory. The initial tangent bridging stiffness $\overline{k}_0$ can be calculated from the linear bridging model developed by Lange-Kornbak and Karihaloo (1997).

$$\overline{k}_0 = V_f \frac{\tau_v}{\tau_g} E_f \frac{h}{L} \tag{6.36}$$

where τ_g and τ_v are the frictional bond strength and the adhesive bond strength, respectively. h is the so-called snubbing factor, L is the length of fibres, and E_f their modulus of elasticity.

When $\overline{k} > 0$, it follows from (6.33) that L_t has the following property

$$\Omega \to 0: \qquad L_t \to 0 \tag{6.37}$$

In other words, no instability can set in, if there is no damage in the material. Thus, as expected, the case $\Omega \to 0$ can be excluded from the instability analysis.

When $0 < \Omega < 1$, the bifurcation criterion ($L_t \to \infty$) can only be satisfied when the following condition is met (cf. (6.33))

$$1 - \frac{8\overline{k}a}{\pi E}\frac{1}{\Omega^2}\ln\left(\cos\frac{\pi}{2}\Omega\right) = 0 \tag{6.38}$$

that is

$$\overline{k}^{cr} = \frac{\pi E}{8a}\frac{\Omega^2}{\ln\left(\cos\frac{\pi}{2}\Omega\right)} \qquad \text{for} \quad 0 < \Omega < 1 \tag{6.39}$$

with

$$\Omega \to 1: \qquad \overline{k}^{cr} \to 0 \tag{6.40}$$

The variation of the normalised $\overline{k}^{cr}$ with Ω given by (6.39) is shown in Figure 18.

From the above analysis and Figure 18, we are able to discern several features of incipient material instability. First, it follows from eqn (6.39) that for all values of Ω in the range $0 < \Omega < 1$, no instability can set in, if the tangent bridging stiffness $\overline{k}$ is greater than 0. In other words, no matter how much the matrix is damaged, as long as the fibres are still bonded to it ($\overline{k} > 0$) , the composite will not exhibit any instability at the macroscopic level, even when a through crack has formed in the matrix (Figure 19(a)). The tangent stiffness of the composite will continue to be positive. This is exactly what happens, for example, in strong continuous fibre-reinforced composites, as is demonstrated by the ACK model Aveston et al. (1971).

The second feature is that $\overline{k}$ can vanish before or after a through crack has formed, i.e., $\Omega \to 1$. Here, we discuss the formation of a through crack ($\Omega \to 1$) when the fibres are still bonded to the matrix, i.e., $\overline{k} \geq 0$. In this case, L_t can be approximated by

$$L_t = -\frac{\pi a\, E}{4\overline{k}W} \tag{6.41}$$

Here, W loses its meaning, although its appearance in the above formula simply points to the existence of an internal length scale. The expression (6.41) indicates that the bifurcation condition ($L_t \to \infty$) requires that the fibre bridging stiffness vanishes $\overline{k} = 0$. In other words, after a through crack has formed or is about to form, the macroscopic instability of the composite coincides with the (microscopic) bridging instability (Figure 19(b)).

The third feature is that when the localisation band is still not a through crack (i.e. $0 < \Omega < 1$), the localisation criterion can still be satisfied when $\overline{k}^{cr}$ is given by (6.39). We

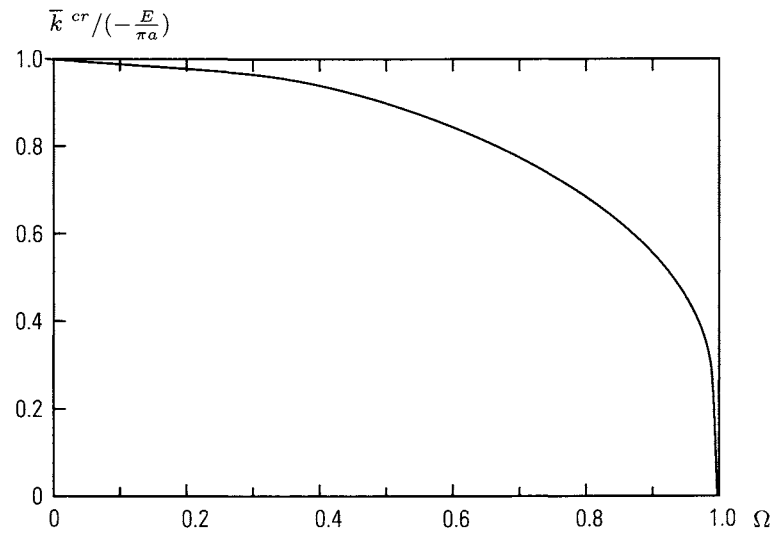

Figure 18. Variation of normalised tangent bridging stiffness at macroscopic instability with damage parameter. No instability is possible when $\Omega = 0$. Thus the point on the axis of ordinates at 1 is excluded, as highlighted by the open circle

recall that the average crack opening displacement for a row of periodic cracks without the bridging action of fibres can be rewritten as (see, e.g. Karihaloo (1995)).

$$\Delta\sigma_m = -\frac{\pi E}{8a}\frac{\Omega^2}{\ln\left(\cos\frac{\pi}{2}\Omega\right)}\Delta\overline{[u]} \tag{6.42}$$

When the cracks are bridged by fibres, the total instantaneous resistance of the composite material to crack opening can be written as the sum of matrix and fibre contributions

$$-\frac{\pi E}{8a}\frac{\Omega^2}{\ln\left(\cos\frac{\pi}{2}\Omega\right)} + \overline{k} \tag{6.43}$$

Thus the condition (6.39) implies that the resistance of the composite material to crack opening displacement vanishes because the instantaneous resistance of the matrix itself to crack opening is exactly counterbalanced by the loss of the bridging resistance (Fig. 19(c)).

The parameter $\overline{k}^{cr}$ in (6.39) includes the physical effect of several factors on the inception of localisation. First, instability of the composite at the macrolevel is possible, when $\overline{k} < 0$, i.e., the fibres are only exerting the residual friction bridging action. The closer Ω is to 1, the smaller the absolute value of $\overline{k}^{cr}$. When $\Omega = 1$, the macroscopic instability occurs at $\overline{k} = 0$, i.e. it coincides with the microscopic (bridging) instability. Second, the dependence of the absolute value of $\overline{k}^{cr}$ on the modulus E of the uncracked matrix indicates that the stiffer the matrix, the less susceptible the material is to microscopic

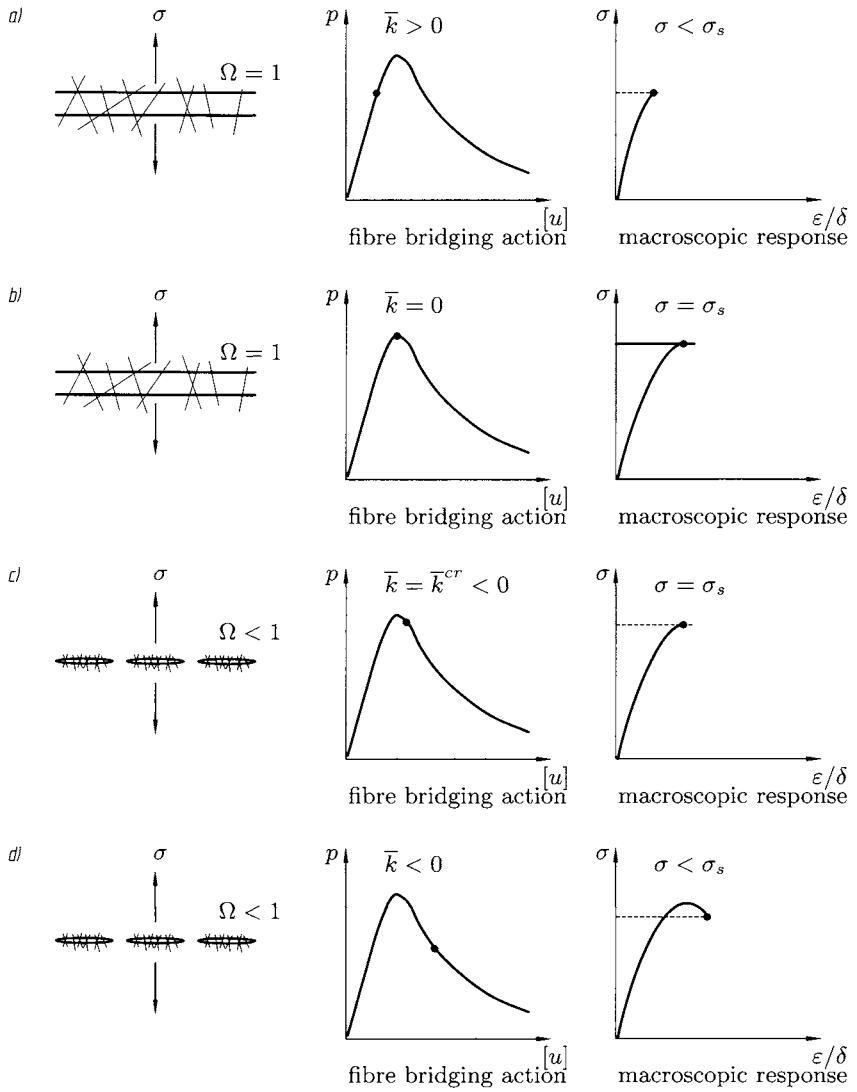

Figure 19. Relationship between bridging stiffness and macroscopic response of the composite material, (a) no instability, when the fibres are bonded to matrix ($\overline{k} > 0$) even though a through crack has formed in it ($\Omega = 1$); (b) macroscopic instability induced by loss of bridging stiffness ($\overline{k} = 0$) and formation of a through crack ($\Omega = 1$); (c) macroscopic instability induced by a combination of matrix damage ($\Omega < 1$) and initial softening of bridging stiffness equal to $\overline{k}^{cr} < 0$; (d) macroscopic tension-softening caused by matrix damage ($\Omega < 1$) and considerable softening of bridging stiffness ($\overline{k} < 0$)

instability. Third, $\overline{k}^{cr}$ contains a length scale, here the half length a of a crack. As the parameters Ω and E are scale insensitive, $\overline{k}^{cr}$ introduces a scale effect into the loss of macroscopic instability of short-fibre-reinforced materials. The macroscopic response of large specimens made from these composites will be more sensitive to vanishing of bridging stiffness than that of small specimens with the same level of damage ($0 < \Omega < 1$).

It is seen from Figure 18 that the absolute value of $\overline{k}^{cr}$ increases rapidly when the value of Ω deviates from 1. This means that in order to delay macroscopic instability of the composite, it is very important to prevent or delay the coalescence of the discrete microcracks. In principle, if the microcracks are somehow prevented from coalescing whilst at the same time the tangent bridging stiffness is maintained above the critical value given by (6.39), macroscopic instability of the composite cannot occur. In practice though, the discrete microcracks are likely to propagate and coalesce once the fibres begin to be pulled out, i.e., once $\overline{k}$ reaches zero. Figure 19(d) illustrates such a possibility whereby the composite exhibits tension-softening, while the cracks in the localisation band are still fragmented ($0 < \Omega < 1$) but the tangent bridging stiffness is equal to or less than the critical value (6.39). This provides a softening model which is different from that introduced by Li et al. (1991) in which the softening is a result of fibre pull-out from a through crack ($\Omega = 1$).

Based upon the pseudo-traction technique and an asymptotic analysis, the tensile stress-strain relation was established analytically for short-fibre-reinforced composites containing multiple parallel bridged microcracks. This allows an analysis to be made of the macroscopic material instability in the tensile deformation process of these composites. The material instability at the macrolevel is examined using the classical bifurcation criterion, with an emphasis on the role of the bridging action of fibres. Conditions for the incipient macroscopic instability are obtained as functions of damage in the matrix, crack length, and the microscopic bridging stiffness. It is found that no macroscopic instability is possible as along as the tangent bridging stiffness is positive, i.e., as long as the fibres remain bonded to the matrix. However, whilst the bridging instability at the microievel plays a major role in the macroscopic instability, it is the damage in the matrix that determines when the macroscopic instability is induced by the bridging instability. The microscopic bridging instability does not necessarily induce macroscopic instability. Indeed, macroscopic instability may be delayed until the fibres are only exerting residual frictional action. Likewise, the formation of a through crack is neither a necessary nor a sufficient condition for the onset of tension-softening in the composite. The results also suggest that in order to delay macroscopic instability in the tensile response, it is very important to prevent or to delay the coalescence of the discrete microcracks that form in the strain-hardening stage.

Bibliography

J. Aveston, G.A. Cooper, and A. Kelly. Single and multiple fracture. In *The properties of fibre composites*, Conference Proceedings of National Physical Laboratory, pages 15–26, London, 1971.

G. Bao and Z. Suo. Remarks on crack bridging concepts. *Applied Mechanics Reviews*, 45:355–366, 1992.

W.R. Delameter, G. Herrmann, and D.M. Barnett. Weakening of an elastic solid by a rectangular array of cracks. *Journal of Applied Mechanics*, 42:74–80, 1975.

A.G. Evans, J.M. Domergue, and E. Vagaggini. Methodology for relating the tensile constitutive behaviour of ceramic-matrix composites to constituent properties. *Journal of the American Ceramic Society*, 77:1425–1435, 1994.

G.U.J. Fonseka and D. Krajcinovic. The continuous damage theory of brittle materials; Part 2: uniaxial and plane response modes. *Journal of Applied Mechanics*, 48:816–824, 1981.

V.S. Gopalaratman and S.P. Shah. Tensile failure of steel fiber-reinforced mortar. *ASCE Journal of Engineering Mechanics*, 113:635–652, 1987.

H. Horii, A. Hasegawa, and F. Nishino. Process zone model and influencing factors in fracture of concrete. In S.P. Shah and S.E. Swartz, editors, *Fracture of Concrete and Rocks*, pages 205–219. Springer-Verlag, New York, 1989.

H. Horii and S. Nemat-Nasser. Elastic fields of interacting inhomogeneities. *International Journal of Solids and Structures*, 21:731–745, 1985.

H. Horii and S. Nemat-Nasser. Overall moduli of solids with microcracks: load-induced anisotropy. *Journal of the Mechanics and Physics of Solids*, 31:155–171, 1993.

K.X. Hu, A. Chandra, and Y. Huang. On interacting bridged-crack systems. *International Journal of Solids and Structures*, 31:599–611, 1994.

M. Isida, N. Ushijima, and N. Kishine. Rectangular plates, strips and wide plates containing internal cracks under various boundary conditions. *Transactions of the Japan Society of Mechanical Engineers*, Series A 47:27–35, 1981.

M. Jirasek and Z.P. Bažant. Localization analysis of nonlocal model based upon crack interactions. *ASCE Journal of Engineering Mechanics*, 120:1521–1542, 1994.

L.M. Kachanov. *Time of the rupture process under creep conditions*, pages 26–31. Izv. Akad. Nauk SSR, 1958.

M. Kachanov. Effective elastic properties of cracked solids: critical review of some basic concepts. *Applied Mechanics Reviews*, 45:304–335, 1992.

B.L. Karihaloo. Fracture characteristics of solids containing doubly-periodic arrays of cracks. *Proceedeings of Royal Society London*, A360:373–387, 1978.

B.L. Karihaloo. *Fracture Mechanics and Structural Concrete*. Addison Wesley Longman, 1995.

B.L. Karihaloo and J. Wang. Mechanics of fibre-reinforced cementitious composites. *Computers & Structures*, 76:19–34, 2000.

B.L. Karihaloo, J. Wang, and M. Grzybowski. Doubly periodic arrays of bridged cracks and short fibre-reinforced cementitious composites. *Journal of the Mechanics and Physics of Solids*, 44:1565–1586, 1996.

R.Y. Kim and N.J. Pagano. Crack initiation in unidirectional brittle-matrix composites. *Journal of the American Ceramic Society*, 74:1082–1090, 1991.

D. Krajcinovic and G.U. Fonseka. The continuous damage theory of brittle materials. Part 1: general theory. *Journal of Applied Mechanics*, 48:809–815, 1981.

D. Lange-Kornbak and B.L. Karihaloo. Tension softening of fibre-reinforced cementitious composites. *Cement and Concrete Composites*, 19:315–328, 1997.

V.C. Li, Y. Wang, and S. Backer. A micromechanical model of tension-softening and bridging toughening of short random fibre reinforced brittle matrix composites. *Journal of the Mechanics and Physics of Solids*, 39:607–625, 1991.

T.Y. Lim, P. Paramasivan, and S.L. Lee. Analytical model for tensile behavior of steel-fiber concrete. *ACI Material Journal*, 84:286–298, 1987.

B. Mobasher, H. Stang, and S.P. Shah. Microcracking in fibre reinforced concrete. *Cement and Concrete Research*, 20:665–676, 1990.

M.K. Neilsen and H.L. Schreyer. Bifurcations in elastic-plastic materials. *International Journal of Solids and Structures*, 30:521–544, 1993.

M. Ortiz. Microcrack coalescence and macroscopic crack growth initiation in brittle solids. *International Journal of Solids and Structures*, 24:231–250, 1988.

J.W. Rudnicki and J.R. Rice. Conditions for the localization of deformation in pressure-sensitive dilatant materials. *Journal of the Mechanics and Physics of Solids*, 23: 371–394, 1975.

K. Sahasakmontri, H. Horii, A. Hasegawa, and F. Nishino. Mechanical properties of solids containing a doubly periodic rectangular array of cracks. *Structural Engineering / Earthquake Engineering*, 4:125s–135s, 1987.

S.M. Spearing and F.W. Zok. Stochastic aspects of matrix cracking in brittle matrix composites. *Journal of Engineering Materials and Technology*, 115:314–318, 1993.

H. Stang and S.P. Shah. Failure of fibre-reinforced composites by pull-out fracture. *Journal of Materials Science*, 21:953–957, 1986.

H. Tada, P.C. Paris, and G.R. Irwin. *The Stress Analysis of Cracks Handbook.* Paris Productions Inc., St. Louis, Missouri, 1985.

P. Tjiptobroto and W. Hansen. Tensile strain hardening and multiple cracking in high-performance cement-based composites containing discontinuous fibres. *ACI Material Journal*, 90:16–35, 1993.

J. Wang, J. Fang, and B.L. Karihaloo. Asymptotic bounds on overall moduli of cracked bodies. *International Journal of Solids and Structures*, 37:6221–6237, 2000a.

J. Wang, J. Fang, and B.L. Karihaloo. Asymptotics of multiple crack interactions and prediction of effective modulus. *International Journal of Solids and Structures*, 37: 4261–4273, 2000b.

F.W. Zok and S.M. Spearing. Matrix crack spacing in brittle matrix composites. *Acta Metallurgica et Materialia*, 40:2033–2043, 1992.

Optimum Composite Laminates Least Prone to Delamination under Mechanical and Thermal Loads

B. L. Karihaloo
School of Engineering, Cardiff University
Cardiff CF24 OYF, U.K.

Abstract In this Chapter we will describe how optimum laminate configurations are sought for multidirectional fibre-reinforced composite laminates under combined in-plane mechanical and thermal loads. The design objective is to enhance the value of the loads over and above the first-ply-failure loads which are judged by a transverse failure criterion and the Tsai-Hill criterion, respectively. The in situ strength parameters previously obtained are incorporated in these criteria. It is found that the optimum designs under combined mechanical and thermal loads are not the same as those under pure mechanical loads for three of the four loading cases studied. For all cases the optimum loads are significantly larger than those for a quasi-isotropic design.

1 Introduction

Optimum strength designs of continuous fibre-reinforced composite laminates have been pursued since the early days of these materials. For example, Sandhu (1969) used a parametric study to investigate the fibre orientation of a unidirectional lamina yielding maximum strength under in-plane stress conditions. Brandmaier (1970) found that the strength of a unidirectional lamina under in-plane stresses could be maximized analytically with respect to the fibre orientation. The results based upon Tsai-Hill failure criterion indicated that the optimum fibre orientation depended upon the stress state and the relative value of the transverse and in-plane shear strengths of the lamina. When the strength of a multidirectional composite laminate is to be maximized, more complicated and explicit optimization techniques are needed. The work by Chao et al. (1975) was probably the earliest study that sought the optimum strength design of multidirectional laminates using a search technique. Many studies have been devoted to the optimum strength design of multidirectional laminates in the recent two decades. Among these are the works by Park (1982), Fukunaga and Chou (1988), Miravete (1989), Fukunaga and Vanderplaats (1991). Considering that most of the advanced fibre-reinforced composite laminates are prone to cracking and delamination, and that the properties of laminates are tailorable, Wang and Karihaloo (1994a), Wang and Karihaloo (1996c), Wang and Karihaloo (1996b) posed optimum strength design problems of multidirectional laminates in a different way from the conventional ones. They applied fracture mechanics analyses in the optimum strength designs of multidirectional laminates against delamination and transverse cracking. We shall summarise these results in later sections.

In measuring the in situ transverse strength of unidirectional laminae in laminates, it was found by Flaggs and Kural (1982) that the thermal residual stress resulting from the manufacturing process might consist of a large portion of the in situ strength (more than half for $[0_2/90_n]_s$ and $[\pm 30/90_n]_s$ for $n = 1, 2, \ldots, 8$). A composite structure will also experience temperature variations in service. Because of the remarkable difference in the thermal expansion coefficients as well as the stiffnesses of a unidirectional lamina in its longitudinal and transverse directions, the stresses caused by temperature variations may be quite significant in practice. It is obvious that the thermal stresses in a multidirectional laminate are functions of the laminate configuration, that is, functions of the ply angles in the laminate. In the present chapter, we shall pursue the optimum in situ strength design of multidirectional composite laminates subjected to combined mechanical and thermal loads. We shall first introduce the in situ strength parameters, and then incorporate them into the formalism of optimization problems. Details of these calculations will be given in later sections. The optimization problems will be solved by a nonlinear mathematical programming technique.

2 In situ strength formulae

Chang and Lessard (1991) fitted experimental data with two formulae to calculate the in situ transverse tensile and in-plane shear strengths of unidirectional laminae in general multidirectional laminates, namely,

$$\frac{Y_t}{T_t^0} = 1 + \frac{A}{N^B} \sin(\Delta\theta), \tag{2.1}$$

$$\frac{S_C}{S_C^0} = 1 + \frac{C}{N^D} \sin(\Delta\theta), \tag{2.2}$$

where T_t^0 and S_C^0 are the transverse tensile strength and in-plane shear strength measured with a thick unidirectional lamina. A, B, C and D are to be determined by experiments. N is the number of plies in a unidirectional lamina in a multidirectional laminate. $\Delta\theta$ represents the minimum difference between the ply angle of a lamina and those of its neighbouring plies.

In order to reveal the physics of the phenomenon of in situ strengths, Wang and Karihaloo (1996c) studied the in situ strengths using fracture mechanics . Based upon the fracture mechanics analyses, they proposed two formulae to calculate the in situ strengths

$$\frac{Y_t}{T_t^0} = 1 + \frac{A}{N^B} f_t(\Delta\theta), \tag{2.3}$$

$$\frac{S_C}{S_C^0} = 1 + \frac{C}{N^D} f_s(\Delta\theta), \tag{2.4}$$

Here, the two functions $f_t(\Delta\theta)$ and $f_s(\Delta\theta)$ represent the influence of the neighbouring

laminae on the strengths of a lamina. They are given by

$$f_t(\Delta\theta) = \min\left[\frac{\sin^2(\Delta\theta_a)}{1+\sin^2(\Delta\theta_a)}, \frac{\sin^2(\Delta\theta_b)}{1+\sin^2(\Delta\theta_b)}\right], \tag{2.5}$$

$$f_s(\Delta\theta) = \min\left[\frac{\sin^2(2\Delta\theta_a)}{1+\sin^2(2\Delta\theta_a)}, \frac{\sin^2(2\Delta\theta_b)}{1+\sin^2(2\Delta\theta_b)}\right]. \tag{2.6}$$

The parameters A, B, C and D in formulae (2.1)–(2.4) are to be determined from experimental results. As these formulae also contain the ply-angle influence functions, i.e. $\sin(\Delta\theta)$, $f_t(\Delta\theta)$ and $f_s(\Delta\theta)$, the investigation of the dependence of A, B, C and D on the laminate configuration is very important. They must be independent of the laminate configuration, if they are to be regarded as material constants. Otherwise the above in situ strength formulae cannot be applied to a general multidirectional laminate. Therefore, in order to determine the values of these constants for a particular composite material, extensive experiments are needed. Currently, there are very few experimental results available, of which the results of the in situ transverse tensile strength obtained by Flaggs and Kural (1982) are widely cited in the literature. Regarding the in-plane shear strength, Chang and Chen (1987) studied its dependence on the ply thickness in unidirectional and cross-ply laminates. There is a dearth of experimental data to determine the dependence of the in situ shear strength on the laminate configuration.

In Fig. 1, the in situ transverse strength predicted by Eqs. (2.1) and (2.3) are compared with the experimental results of Flaggs and Kural (1982) for the material T300/934. In fitting the experimental data, different values of A are used in Eqs. (2.1) and (2.3) (1.7 and 3.4, respectively). Chang and Lessard (1991) used $A = 1.3$ and $B = 0.8$ previously to fit the experimental data. It is seen that both the theoretical formulae fit the experimental data reasonably well. The most important conclusion drawn from Fig. 1 is that for the material and laminate configurations studied by Flaggs and Kural (1982) the parameters A and B appear to be independent of the laminate configuration. It appears that they can indeed be treated as material constants. On the other hand, due to lack of experimental data, the dependence of the parameters C and D on the laminate configuration cannot be judged. Chang and Lessard (1991) found that formula (2.2) fits the experimental data well for T300/976 cross-ply laminates with $D = 2.0$ and $C = 1.0$. In the sequel, we shall use formula (2.3), which has a fracture mechanics basis, to calculate the in situ shear strength of laminae in multidirectional laminates with $C = 4.0$ and $D = 1.0$.

In most cases, transverse cracking is the first noticeable damage in a laminate. Although the transverse cracks generally do not result in the immediate failure of the whole laminate, they have the potential to induce failure by stress concentration and delamination. For instance, the experimental results of Herakovich (1982) indicate that the failure of angle-ply laminates with thick laminae under in-plane unidirectional tension is entirely due to transverse cracking. In the optimum strength design to follow, we shall use a transverse tensile failure criterion (Chang and Lessard (1991)) to judge the transverse failure of a unidirectional lamina in a multidirectional laminate. This criterion,

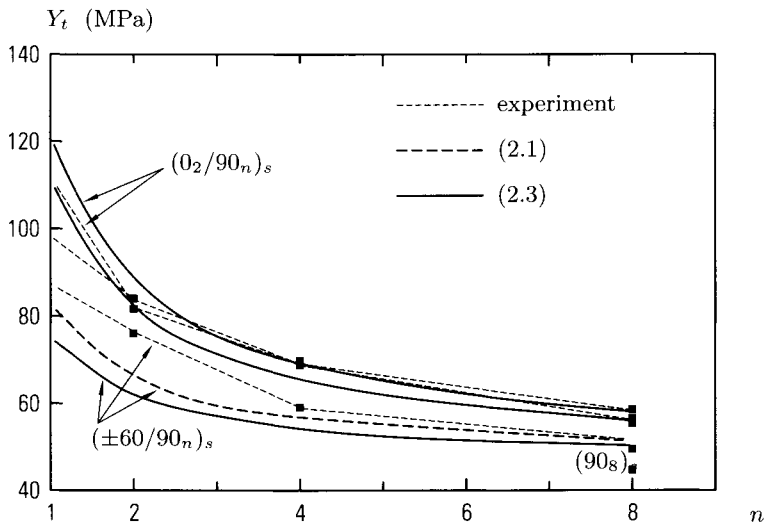

Figure 1. Comparison of theoretical and experimental results of the in situ transverse tensile strength. $A = 1.7$ and $B = 0.8$ are used in formula (2.1), and $A = 3.4$ and $B = 0.8$ are used in formula (2.3)

into which the in situ strengths are incorporated, is written as

$$\left(\frac{Y}{Y_t}\right)_i^2 + \left(\frac{S}{S_c}\right)_i^2 \leq 1 \quad (i = 1, 2, \ldots, L), \tag{2.7}$$

where Y and S are the in-plane transverse and shear stresses in the lamina. L is the total number of unidirectional laminae in the laminate. In the previous optimum strength design of laminates by Wang and Karihaloo (1996b), it was found that the optimizer aims at distributing the stresses according to the strengths of an anisotropic material in different directions. In the failure criterion (2.7), the strength and stress in the fibre direction are not taken into account. Therefore, the optimizer always gives optimum designs of laminates in which the stresses in the fibre directions of the laminae are very large. This may increase the risk of failure in the fibre direction. Thus, here we also use the following simplified Tsai-Hill criterion to consider the effect of the stress in the fibre direction in the optimum design

$$\left(\frac{\sigma_L}{F_L}\right)_i^2 + \left(\frac{Y}{Y_t}\right)_i^2 + \left(\frac{S}{S_c}\right)_i^2 \leq 1 \quad (i = 1, 2, \ldots, L), \tag{2.8}$$

where σ_L and F_L are the stress and strength of a unidirectional lamina in the fibre direction.

3 Formulation of optimization problem

For a multidirectional laminate subjected to in-plane loads, let us denote the left-hand terms of Eqs. (7) and (8) by q_i^2. For a composite laminate under given in-plane loads, if the ply angles and thicknesses of the constituent laminae are so chosen that the values of q_i^2 for all laminae are reduced, then the loads corresponding to the transverse cracking or failure will be enhanced. This objective is achieved by minimizing the maximum value of q_i^2. Following the procedure in the work by Wang and Karihaloo (1996b), the optimization problem is formulated as

$$\min_{\theta_i, t_i, \gamma} \gamma \tag{3.1}$$

subject to

$$q_i - \gamma \leq 0, \tag{3.2}$$

$$-\frac{\pi}{2} \leq \theta_i \leq \frac{\pi}{2}, \tag{3.3}$$

$$\sum_i t_i = h \quad (i = 1, \ldots, L), \tag{3.4}$$

$$\underline{t} \leq t_i \leq \bar{t}. \tag{3.5}$$

The above optimization problem is solved by a constrained variable metric method. The non-differentiability of $f_t(\Delta\theta)$ and $f_s(\Delta\theta)$ with respect to the design variables θ_i is treated using the procedure in the work by Wang and Karihaloo (1996b).

As mentioned in Section 1, the thermal residual stresses resulting from the manufacturing process may constitute a large portion of the in situ strength (more than half for $[0_2/90_n]_s$ and $[\pm 30/90_n]_s$ for $n = 1, 2, \ldots, 8$). It is obvious that the thermal residual stresses in a multidirectional laminate are also functions of the laminate configuration, that is, functions of the ply angles in the laminate. Therefore, in the optimum strength design of laminates, the laminates are assumed to be under combined thermal and mechanical loads. Thus, following the classical lamination theory, the total stresses in a generic lamina in a multidirectional laminate are calculated from

$$\sigma_i = \bar{Q}_{ij} \left[A_{jk}^{-1} (N_k + N_k^t) - \varepsilon_j^t \right] \quad (i, j, k = 1, 2, 6), \tag{3.6}$$

where σ_i the stress components in the reference coordinate system for the laminate, $\bar{Q}_{ij}$ the off-axis stiffnesses of the lamina, and A_{ij} the in-plane stiffnesses of the laminate, N_k^t the equivalent thermal loads, and ε_j^t the thermal strains.

4 Design examples

The above optimization procedure was applied to the optimum design of a multidirectional laminate shown in Figure 2. Fig. 2(a) shows the in-plane loads, and Fig. 2(b) shows the detailed configuration of one half of the laminate. This laminate is composed of L laminae of different ply angles and thicknesses. It is physically symmetric with respect to its geometric middle plane, i.e. the laminae are stacked in the order

$(\theta_{L/2}/\ldots/\theta_1)_s$. The stiffness and strength constants used in the calculation of the in situ strengths are adapted from the work by Chang and Lessard (1991) on T300/976. The thermal expansion coefficients are taken as those of T300/934 (Flaggs and Kural (1982)), i.e. $\alpha_L = 0.09$ μstrain/°C, $\alpha_T = 28.8$ μstrain/°C. The thickness of a single ply is assumed to be 0.14 mm. The temperature variation is taken as $\Delta T = -147\,°\mathrm{C}$, i.e. the temperature drop in the manufacturing process. It can be arbitrary otherwise.

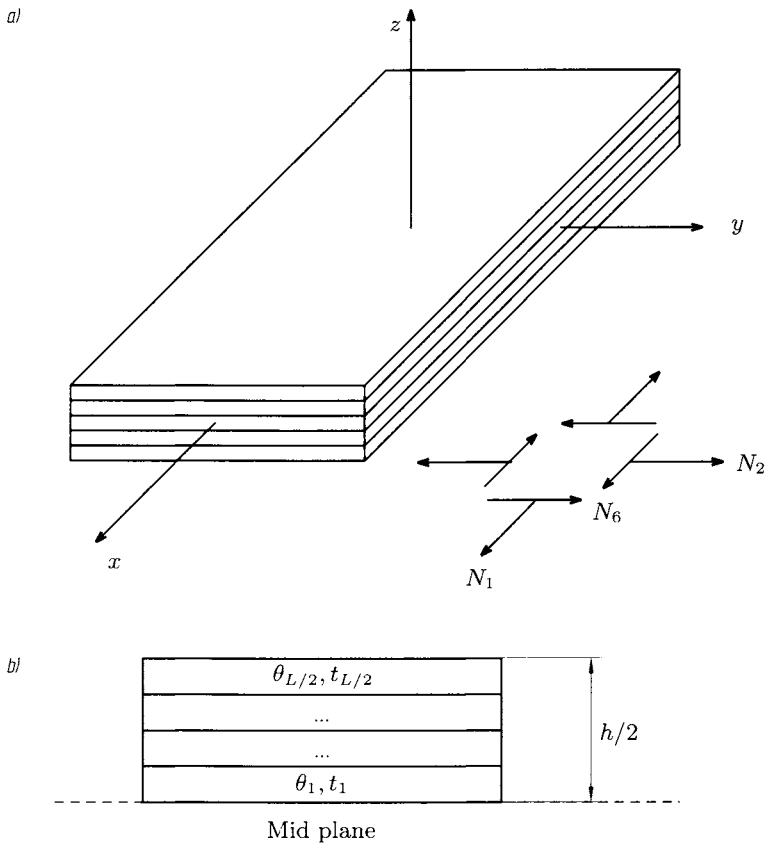

Figure 2. The laminate configuration. The in-plane loads shown represent the resultant mechanical forces over the thickness

Because of the highly nonlinear nature of the functions q_i, and of the fact that they can attain their minima at different combinations of design variables, the above optimization problem can have many local minima. In the computational scheme, the global minimum is sought by a random search technique. The optimization process is begun from different initial design points $(x_j^0)_m^T$ $(j = 1, \ldots, L;\ m = 1, \ldots, M)$ (m denotes the mth initial design point) in the space of design variables $(x_j)^T$ $(j = 1, \ldots, L)$. These random initial design points are chosen so that they are uniformly distributed in the design space, and the

global minimum is sought from among the local minima corresponding to these randomly chosen initial designs. In all cases, M was chosen to be equal to 400.

The above optimum design is demonstrated on an eight-ply symmetric laminate with the four ply angles being the design variables. Given a mechanical load $[N_1^0, N_2^0, N_6^0]$, the improvement in the design is represented by

$$k = \frac{1}{\max q_i} \quad (i = 1, 2, \ldots, 4) \tag{4.1}$$

We first seek the optimum designs without the thermal effect, that is, the laminate is only subjected to mechanical loads. The change of the load factor k during the optimization process for four in-plane loading combinations is shown in Figs. 3 and 4 for the failure criteria (2.7) and (2.8), respectively. The initial guesses to ply angles (chosen pseudo-randomly) and their final optimum values, the optimum load factor $k_{\max}$ and the ratio of $k_{\max}$ to the initial load factor k_{in}, are given in Table 1, where the load factor k_{iso} is for a quasi-isotropic laminate design $[45/90/-45/0]_s$.

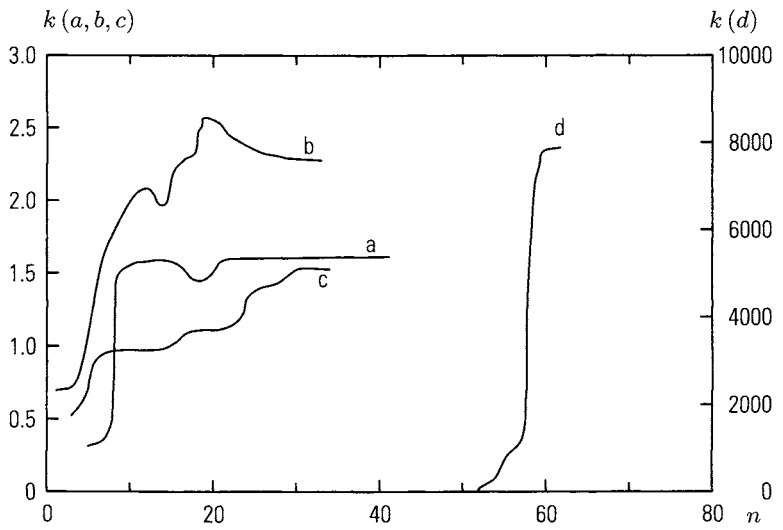

Figure 3. Evolution of load factor k for a symmetric laminate of four ply angles for four mechanical loading cases without thermal effect: (a) $[N_1^0, N_2^0, N_6^0]^T = [200, 200, 0]^T$ kN/m; (b) $[N_1^0, N_2^0, N_6^0]^T = [200, 0, 200]^T$ kN/m; (c) $[N_1^0, N_2^0, N_6^0]^T = [400, 200, 0]^T$ kN/m; (d) $[N_1^0, N_2^0, N_6^0]^T = [200, 200, 200]^T$ kN/m. The transverse cracking criterion (2.7) is used

The results shown in Table 1 and in Figs. 3 and 4 exhibit several features. First, for each of the loading cases (a)–(c), the mechanical load corresponding to the first-ply-failure in the optimally designed laminate is increased several fold compared with that of a randomly chosen design. Secondly, when the transverse cracking criterion (2.7) is

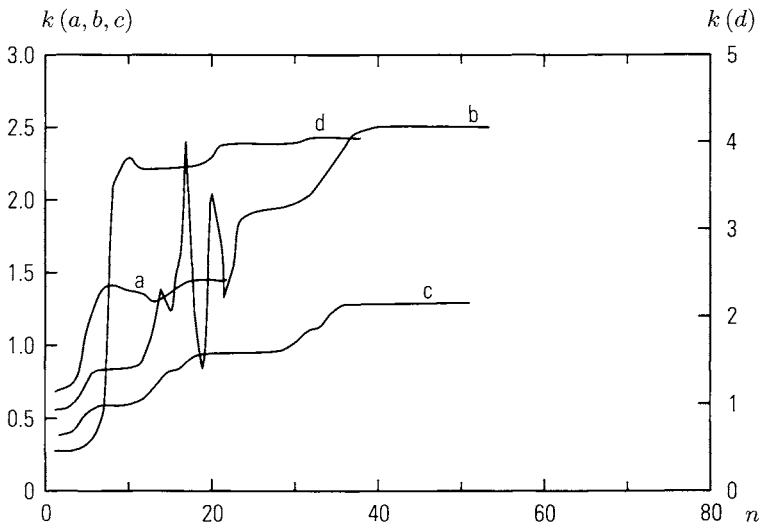

Figure 4. Evolution of load factor k for a symmetric laminate of four ply angles without thermal effect. The mechanical loading cases are the same as those in Fig. 3. The Tsui-Hill failure criterion (2.8) is used

used in the optimization, the optimizer aims at reducing the transverse and in-plane shear stresses and distributing the stress in the fibre direction of a lamina in a laminate. For example, for loading case (b) in Fig. 3, the final stresses in the four laminae in the optimized laminate are $\{\sigma_1, \sigma_2, \sigma_6\} = [\{-349, 39, 0.5\}, \{541, -19, 0.3\}, \{-36, 18, -38\},$

Table 1. Summary of optimized ply angles in a symmetric laminate of four ply angles without thermal effect

In-plane loading	Initial design $\theta_1, \theta_2, \theta_3, \theta_4$	Final design $\theta_1, \theta_2, \theta_3, \theta_4$	$k_{\max}$	$k_{\max}/k_{\text{in}}$	k_{iso}
	Transverse cracking criterion				
a	82.4, 88.5, 75.3, 46.6	46.8, 89.6, 44.0, −30.4	1.62	5.34	1.37
b	−78.1, 72.5, 82, 5, 18.2	−56.6, 32.7, 86.6, 30.5	2.28	3.27	0.93
c	−0.9, 76.1, −2.2, 48.3	−33.5, 70.0, −33.8, 20.4	1.5	3.0	1.40
d	33.9, 27.3, 35.2, 38.9	45.0, 45.0, 45.0, 45.0	∞	∞	0.77
	Tsai-Hill failure criterion				
a	21.1, 7.2, 38.6, −40.9	40.6, −4.4, 54.7, −58.5	1.45	2.13	1.32
b	−61.5, 10.6, −59.7, 86.1	−58.4, 32.0, −57.6, 31.3	2.50	4.5	0.90
c	13.6, 54.2, −74.0, 61.7	−48.9, 52.3, −44.7, 10.6	1.28	3.46	1.18
d	23.0, 55.2, 52.5, 21.4	45.5, 43.6, 47.0, 43.7	4.22	3.08	0.76

$\{540, -19, 3\}$] MPa. For loading case (c), these values are $\{\sigma_1, \sigma_2, \sigma_6\}$ = [$\{439, 48, 24\}$, $\{364, 53, -23\}$, $\{436, 28, 24\}$, $\{726, 29, 5\}$] MPa, In terms of the optimum design under loading case (b), the failure load corresponding to the first transverse cracking will be $k_{\max} \times [N_1^0, N_2^0, N_6^0]$, in which case the maximum tensile stress in the fibre direction of the second ply (lamina) will be 2.28 × 541 MPa = 1233 MPa. This value is close to the longitudinal tensile strength 1515 MPa of the material 1300/976. For this reason, optimum strength designs are pursued using the Tsai-Hill failure criterion (2.8) in which the contribution of the stress component in the fibre direction is also taken into account.

The results obtained using the Tsai-Hill failure criterion are also shown in Table 1. However, it is found that the use of the Tsai-Hill criterion does not result in a significant change in the stress distribution in the laminae in the optimally designed laminate. For instance, for loading case (b) in Fig. 4, the final stresses in the four laminae in the optimized laminate are $\{\sigma_1, \sigma_2, \sigma_6\}$ = [$\{-213, 41, 2\}$, $\{537, -8, -5\}$, $\{-213, 41, 10\}$, $\{537, -8, 3\}$] MPa. The reason for this may be due to the large strength of the unidirectional lamina in the fibre direction. The optimizer always distributes the stresses according the strengths in different directions of the anisotropic material.

Loading case (d) is simply to check the "smartness" of the optimizer. As this loading case is simply a unidirectional tension along 45° with respect to the 1-axis of the reference coordinate system for the laminate, the theoretical optimum design should be a unidirectional laminate in which all the fibres are along 45°. In this case, all q_i are 0, which is obviously the absolute minimum of the optimization problem. This theoretical optimum design is captured by the optimizer for both failure criteria, as shown in Table 1. This theoretical optimum design was not obtained in the previous work by Wang and Karihaloo (1995).

The results of the optimum designs when the thermal effect is included are shown in Table 2 again for the two failure criteria. The evolutions of the load factor it are shown in Figs. 5 and 6 for the two failure criteria, respectively. Due to the thermal stresses,

Table 2. Summary of optimized ply angles in a symmetric laminate of four ply angles with thermal effect

In-plane loading	Initial design $\theta_1, \theta_2, \theta_3, \theta_4$	Final design $\theta_1, \theta_2, \theta_3, \theta_4$	$k_{\max}$	$k_{\max}/k_{\text{in}}$	k_{iso}
	Transverse cracking criterion				
a	$-29.9, -13.6, -75.6, 13.6$	$-56.3, -30.5, -49.2, 44.4$	0.81	1.66	0.60
b	$-7.1, -35, -19.2, 16.4$	$23.7, -36.5, 23.7, 27.0$	2.24	8.75	0.72
c	$-27.37, -63.1, 69.8, -63.4$	$43.7, -51.1, 43.7, -18.6$	0.82	3.31	0.62
d	$57.3, 41.3, 45.8, 35.6$	$45.0, 45.0, 45.0, 45.0$	∞	∞	0.50
	Tsai-Hill failure criterion				
a	$-32.6, -27.7, -77.8, 14.9$	$-53.0, -29.2, -47.2, 45.8$	0.79	1.56	0.60
b	$86.6, 73.4, -36.0, 61.2$	$27.4, 24.3, -36.6, 24.3$	1.91	5.66	0.71
c	$-64.8, 11.1, -88.6, -44.0$	$-42.8, 49.1, -42.8, 19.4$	0.77	1.95	0.60
d	$86.7, 61.6, 22.8, 22.6$	$45.0, 45.0, 45.0, 45.0$	4.24	5.75	0.50

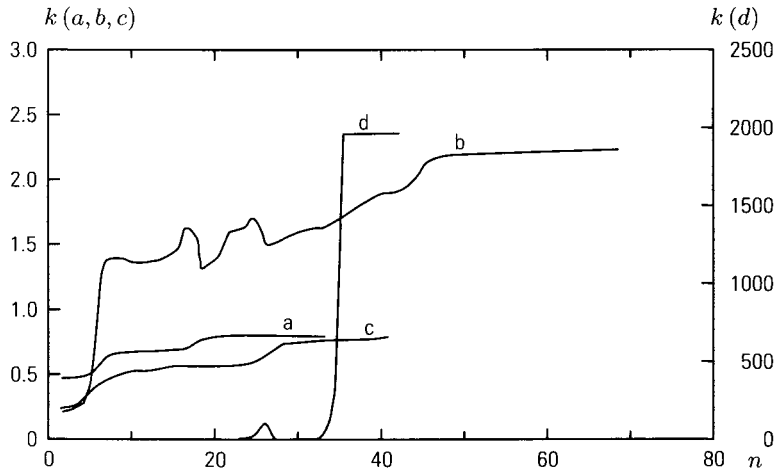

Figure 5. Evolution of load factor k for a symmetric laminate of four ply angles subjected to mixed thermal and mechanical loads. The mechanical loading cases are the same as those in Fig. 3. The transverse cracking criterion (2.7) is used

the absolute enhancement of the load factor is not as large as those in Table 1.

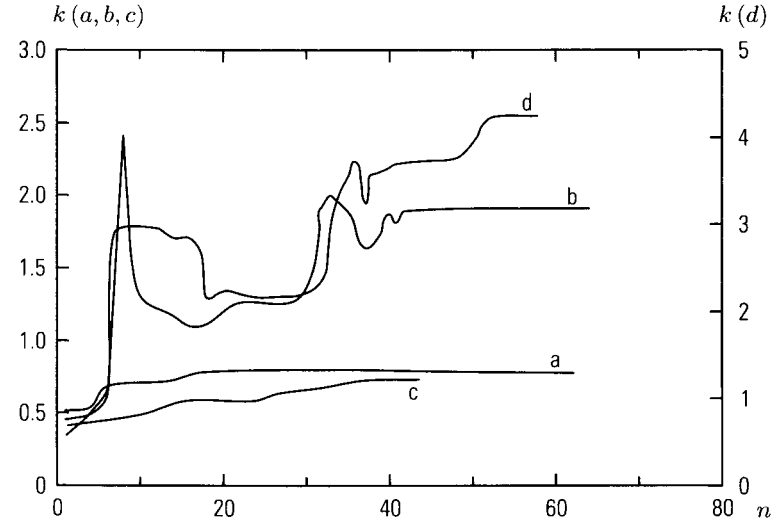

Figure 6. Evolution of load factor k for a symmetric laminate of four ply angles subjected to mixed thermal and mechanical loads. The mechanical loading cases are the same as those in Fig. 3. The Tsai-Hill failure criterion (2.8) is used

Table 3. Summary of optimized ply angles in a symmetric laminate of four ply angles with thermal effect using the initial designs in Table 1

In-plane loading	Initial design $\theta_1, \theta_2, \theta_3, \theta_4$	Final design $\theta_1, \theta_2, \theta_3, \theta_4$	$k_{\max}$	$k_{\max}/k_{\text{in}}$
	Transverse cracking criterion			
a	82.4, 88.5, 75.3, 46.6	35.2, 60.7, 41.8, −44.9	0.81	2.7
b	−78.1, 72.5, 82, 5, 18.2	−84.7, 39.6, 37.0, 37.0	1.78	2.59
c	−0.9, 76.1, −2.2, 48.3	−43.9, 50.9, −43.9, 18.4	0.82	2.16
d	33.9, 27.3, 35.2, 38.9	45.0, 45.0, 45.0, 45.0	∞	∞
	Tsai-Hill failure criterion			
a	27.1, 7.2, 38.6, −40, 9	54.2, 30.3, 48.1, −45.1	0.79	1.37
b	−61.5, 10.6, −59.7, 86.1	−55.9, 33.2, −69.0, 32.9	1.66	4.05
c	13.6, 54.2, −74.0, 61.7	−42.9, 49.2, −42.9, 19.3	0.77	2.64
d	23.0, 55.2, 52.5, 21.4	45.5, 45.0.45.0, 45.0	4.24	4.08

However, the values of the ratio $k_{\max}/k_{\text{in}}$ are of the same level as those in Table 1. Because all the optimum designs are sought starting from multiple random initial designs, the initial designs in Table 2 are not necessarily the same as those in Table 1.

Although the optimum values of $k_{\max}$ in Tables 1 and 2 are likely to be the global maxima in the design domain, the optimum ply angles as well as the initial ply angles leading to the same optimum angles are not unique because of the high nonlinearity and the inherent symmetry of the problem. To get a better insight into the influence of the thermal effect on the optimum strength design, we use the initial ply angles in Table 1 to seek the optimum designs of the laminate when subjected to the combined mechanical and thermal loads. The results are shown in Table 3.

A comparison of the results in Tables 1 and 3 shows that for loading cases (a), (b), and (c), the optimum designs without the thermal effect are not the optimum designs under mixed mechanical and thermal loads. On the other hand, for loading case (d), the optimum design under pure mechanical loads is the optimum design under mixed mechanical and thermal loads, for both the failure criteria.

5 Matrix crack-induced delamination in composite laminates under transverse loading

Fibre-reinforced multidirectional composite laminates are observed in experiments under transverse static or low-velocity impact loading to suffer considerable delamination damage. The intensity of this damage depends on the difference in the ply angles above and below the interface. Here a fracture mechanics model is presented for investigating the role of matrix cracks in triggering delaminations and the influence of ply angles in adjacent plies on delamination cracking. The fracture mechanics analysis shows that for a graphite fibre-reinforced composite laminate containing a transverse intraply crack, the crack-induced largest interfacial principal tensile stress is the maximum when the

difference between the ply angles across the interface is 90°, and it attains a minimum when the difference is 40°. When the crack tips touch the interfaces, the minimum mode II stress singularity which is weaker than the usual square-root type appears when the difference between the ply angles is about 45° for one glass fibre-reinforced laminate and three graphite fibre-reinforced laminates. These results are in agreement with the experimental observation that the largest delaminations appear at the interface across which the difference between the ply angles is the largest, i.e. 90°. The analytical results indicate that in the commonly used quasi-isotropic laminate in which the ply angles are usually 0°, ±45° and 90°, it would be advantageous to interleave the 0° and 90° plies with the ±45° plies in order to increase its damage tolerance to transverse static or low-velocity impact loading.

5.1 Introduction

It is widely known that under transverse static or low-velocity impact loading, matrix cracks in the laminae of a fibre-reinforced multidirectional laminate can cause delaminations between the laminae (Chester and Clark (1992); Doxsee et al. (1993); Jih and Sun (1993); Liu et al. (1993); Pavier and Clarke (1995); Wang and Karihaloo (1994a)). As the low-velocity impact-induced delaminations in laminates are the major source of the reduction in their post-impact-compressive strength, the mechanisms of onset of the impact-induced delaminations has attracted the attention of many researchers in recent years (Chester and Clark (1992); Choi and Chang (1992); Davies et al. (1997); Jih and Sun (1993); Pavier and Clarke (1995)). There have been numerous experimental observations and finite element computations in this area. As the damage in laminates is always related to cracks (matrix and/or interfacial cracks), a strict fracture mechanics analysis is likely to provide a better physical insight into the damage mechanisms in these materials than the finite element analysis.

For fibre-reinforced multidirectional composite laminates under low-velocity impact, Chester and Clark (1992), and Pavier and Clarke (1995) found that the intensity of delaminations depended on the difference between the ply angles above and below the interface. Figure 7 shows the relative intensity of the observed delaminations in a composite laminate caused by transverse impact. It is seen that the largest delaminations appear at the interface across which the difference between the ply angles is the largest, i.e. 90°. A damage model which shows the matrix cracks and delaminations in a composite laminate under transverse impact has been presented by Chester and Clark (1992), and is reproduced in Figure 8.

In this section an idealized fracture mechanics model is presented for investigating the role of a transverse shear crack in triggering delaminations and the influence of ply angles in adjacent plies on delamination cracking. The model consists of a cracked $[(\pm\theta)_{n_2}/(90)_{n_1}/(\mp\theta)_{n_2}]$ laminate. The inner layer is assumed to contain an intraply or interply crack, whereas the two outer layers are assumed to have no cracks (Wang and Karihaloo (1994a); Wang and Karihaloo (1994b)). A solution is obtained when the crack is subjected to transverse shear, i.e. mode II in fracture mechanics, for two crack configurations. First, when the crack is contained wholly within the inner layer, the crack driving-force and the *crack-induced* interfacial stresses are calculated. The fracture

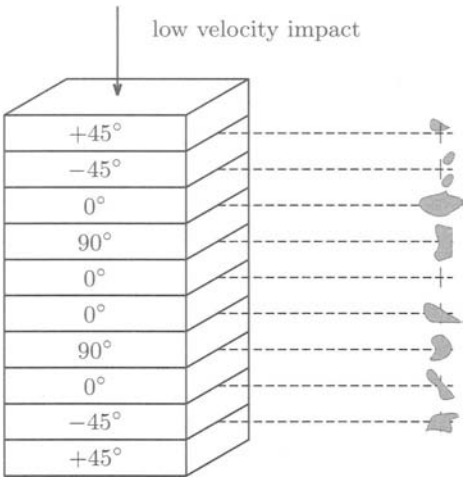

Figure 7. A composite laminate subjected to transverse impact and the relative intensity of delaminations at the interfaces caused by the impact (after Chester and Clark (1992))

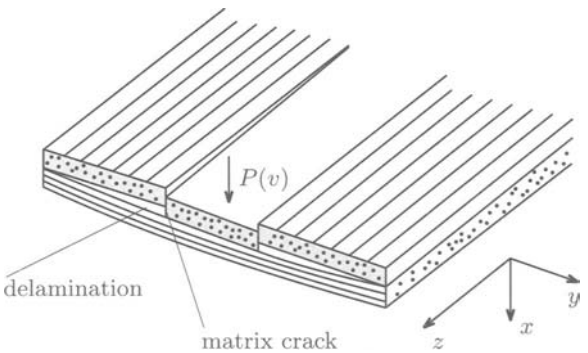

Figure 8. A damaged composite laminate showing matrix cracks and delaminations caused by a transverse load or low-velocity impact (after Chester and Clark (1992))

mechanics analysis shows that for a graphite fibre-reinforced composite laminate, when the transverse crack is an intraply crack, the *crack-induced* largest interfacial principal tensile stress is the maximum when $\theta = 0°$, that is, the difference between the ply angles across the interface is 90°, and it attains a minimum when $\theta = 50°$. Secondly, when the crack tips touch the interfaces, the minimum mode II stress singularity, which is weaker than the usual square-root type, appears when θ is about 45° for one glass fibre-reinforced laminate and three graphite fibre-reinforced laminates. These analytical results indicate that in the commonly used quasi-isotropic laminate in which the ply angles are usually

0°, ±45° and 90°, it would be advantageous to interleave the 0° and 90° plies with the ±45° plies in order to increase its damage tolerance to transverse static or low-velocity impact loading.

5.2 Fracture mechanics model

The damage model in Figure 8 clearly shows that the delaminations are related to the transverse cracks. Clark and Saunders (1991) also noted that delaminations in fibre-reinforced composite laminates under impact appear to initiate at the crossover points of matrix cracks in adjacent plies. It is noted in Figure 8 that the matrix cracks are mainly subjected to a shear stress in the xy-plane. Only when the top layer fails at this stress state can the transverse load be transferred to the lower layer and the delaminations result. Liu et al. (1993), and Jih and Sun (1993) have classified the matrix cracks caused by a transverse load or low-velocity impact into two types: transverse shear cracks and bending cracks. The transverse shear cracks occur near the loading site due to the high transverse shear stress in this area, whereas the transverse bending cracks are mainly caused by the flexing of the laminate. It is concluded by Liu et al. (1993) that the delaminations caused by a transverse shear crack are catastrophic in that, once formed, they propagate unstably. On the other hand, the delaminations caused by a transverse bending crack are stable. Therefore, in order to investigate the role of a transverse shear crack in triggering the delaminations, the idealized fracture mechanics model of the composite laminate shown in Figure 9 (Wang and Karihaloo (1994a); Wang and Karihaloo (1994b)) is used.

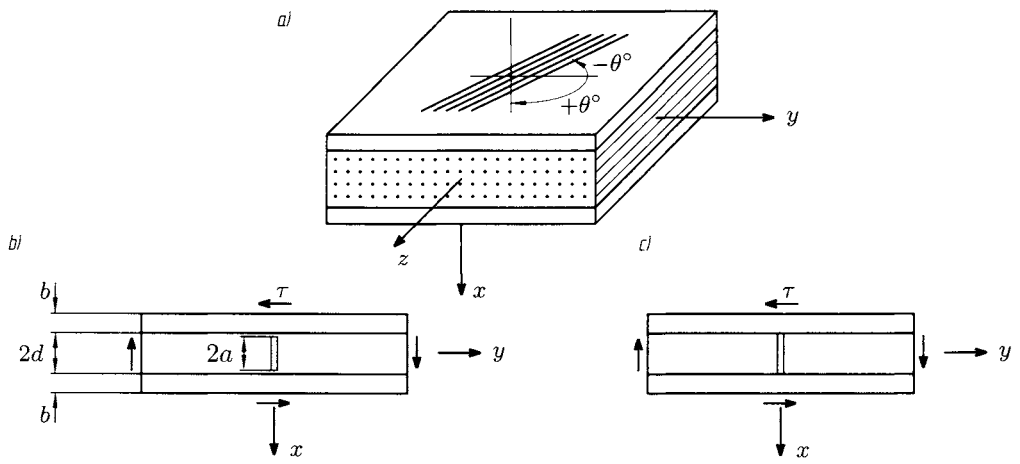

Figure 9. A fracture mechanics model for investigating the role of a transverse matrix crack in triggering delaminations when the crack is subjected to an in-plane shear stress, mode II in fracture mechanics, (a) laminate configuration; (b) an intraply transverse matrix crack; (c) an interply transverse matrix crack

In the idealized fracture mechanics model of Figure 9, the two outer layers of thickness b are assumed to be each an $(\pm\theta)_{n_2}$ angle-ply laminate. They are regarded as transversely orthotropic in the xy-plane whose principal elastic axes are parallel with the x and y axes, respectively. The elastic constants are calculated using the classical lamination theory (Wang and Karihaloo (1994a)). The inner layer of thickness $2d$ is taken as a transversely isotropic material in the xy-plane. Figure 9(b) shows an intraply transverse matrix crack of length $2a$ which is in the center of the inner layer, whereas Figure 9(c) shows an interply matrix crack whose tips touch the interfaces.

5.3 Solution of intraply crack

The fracture mechanics problems shown in Figures 9(b) and 9(c) can be solved using the Fourier transforms and superposition procedure (Wang and Karihaloo (1994a); Wang and Karihaloo (1994b)). We first give the results for the intraply crack problem of Figure 9(b). For this problem, the most relevant parameters which are related to the damage of the laminate are the mode II stress intensity factor at the crack tips and the *crack-induced* interfacial stresses. The mode II stress intensity factor at each of the tips of the crack is

$$K_{II} = F_{II}\tau\sqrt{a} \tag{5.1}$$

where F_{II} is determined by the configuration of the laminate. For a typical graphite/epoxy fibre-reinforced composite material (M1 in Table 4), the variation of F_{II} is shown in Figure 10. In the figure, $F(a/d)$ represents the value of F_{II} when the two outer layers are absent. It is seen that these layers considerably reduce the crack-driving force at the tips of the crack. From this point of view, the outer layers have the strongest constraining effect on the propagation of the crack when θ is 0°, that is, the laminate is a cross-ply one. The constraining effect decreases when θ increases from 0° to 90°.

The presence of the transverse matrix crack will inevitably cause stress concentration in the areas ahead of the crack tips. As the interfacial area is generally a weak part of the laminate, we now consider the *crack-induced* interfacial stresses. The non-dimensional (normalized by τ) *crack-induced* largest interfacial principal tensile stress σ_T, which occurs immediately ahead of the crack tips ($x = \pm d$, $y = 0$), is shown in Figure 11.

The results show that the magnitude of σ_T is influenced by the outer ply angle θ. In contrast to the mode II intensity factor, whose magnitude is determined by F_{II}, θ_T has

Table 4. Material properties

Property Materials	E_L [GPa]	E_T [GPa]	G_{LT} [GPa]	G_{TT} [GPa]	ν_{LT} [–]	ν_{TT} [–]
M1: T300/934 (Gr/Ep)	138.0	11.7	4.56	4.18	0.29	0.40
M2: Glass/Ep	41.7	13.0	3.40	4.57	0.30	0.42
M3: AS4/3501-6 (Gr/Ep)	140.1	8.36	4.31	3.20	0.253	0.297
M4: AS4/Tactix 556 (Gr/Ep)	151.1	7.09	3.63	2.72	0.241	0.304

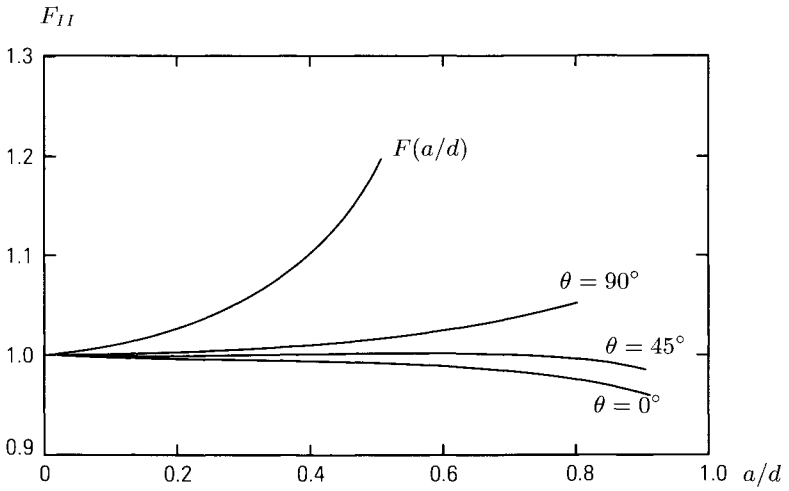

Figure 10. Variation of F_{II} with the relative crack length $\frac{a}{d}$ and the outer ply angle θ

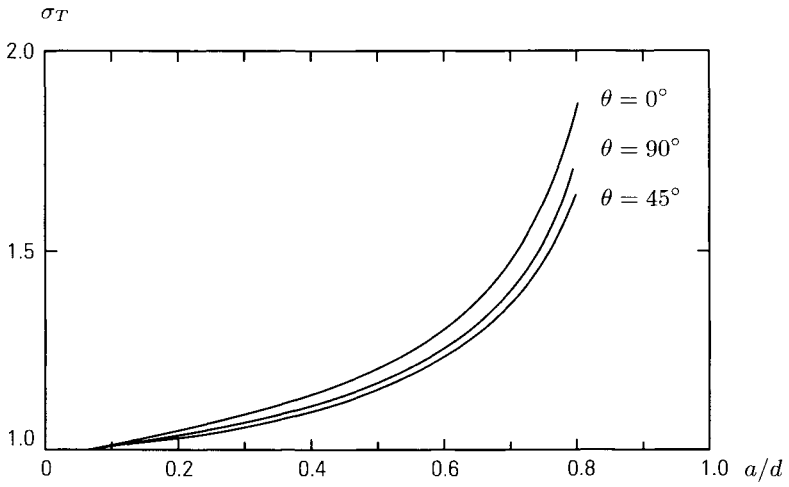

Figure 11. Variation of the normalized *crack-induced* largest interfacial principal tensile stress with the relative crack length a/d and the outer ply angle θ

the maximum value when θ is 0°. The situation worsens as the tips of the crack approach the interfaces, as the influence of θ becomes more prominent.

If the design objective is to minimize the crack-driving force at the tips of the crack so that the laminate is least prone to transverse cracking when subjected to a transverse load, $\theta = 0°$ should be chosen. However, if the design objective is to minimize the

crack-induced, interfacial stress so that the risk of delamination is minimized or delayed, θ should take on a non-zero value. We can deal with these conflicting design objectives by trying to find a compromise design using optimization techniques. The compromise design can be obtained by solving two optimization problems (Wang and Karihaloo (1994a)).

In the first optimization problem, the crack-driving force, represented by F_{II}, is minimized, whereas constraints are imposed on σ_T, $\sigma_T < (1+\alpha)$ and the flexural rigidity of the laminate, $\bar{D} \geq (1-\gamma)D_0$. $\bar{D}$ is the normalized flexural rigidity of the laminate, and D_0 is its value, when $\theta = 0°$. α and γ are tolerance factors on the stress gain and stiffness loss, respectively. Upper $(\bar{\theta}, \bar{b})$ and lower limits $(\underline{\theta}, \underline{b})$ are also placed on the design variables θ and b/d, respectively ($\bar{\theta} = 90°$, $\bar{b} = 4.0$; $\underline{\theta} = 0°$, $\underline{b} = 0.0$). From the solution of this optimization problem it was found that for small a/d, the active constraints were the lower limit on θ and the upper limit on b/d. The minimum of F_{II} always occurred at $\theta = 0°$. When a/d was large, the interfacial stress constraint became critical to the design. For the satisfaction of this constraint the design angle θ had to take on a non-zero value. It was found that for $\alpha = 0.5$, $\gamma = 0.15$ and $\bar{b} = 4.0$, when a/d exceeded 0.73, no optimum design was possible because of the violation of the constraint on interfacial strength. For this reason an alternative formulation of the optimization problem was considered.

In the second optimization problem, the largest interfacial tensile stress σ_T was minimized subject to the constraint that $\Phi(1)$ not exceed 1.0 and that the flexural stiffness be adequate. The solution of this minimization problem is shown in Figure 12. In this case, σ_T reaches its minimum when $\theta = 50°$ and $b/d = \bar{b}$.

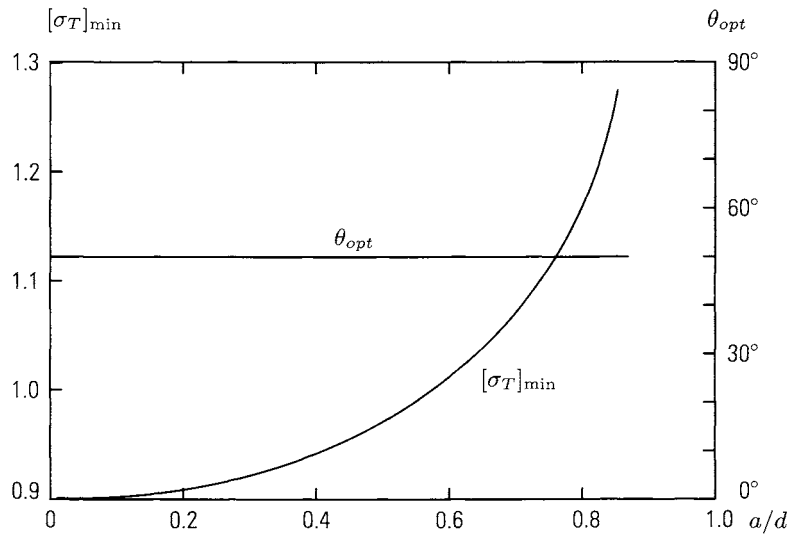

Figure 12. Results of the optimization problem in which the normalized *crack-induced* largest interfacial principal tensile stress σ_T is minimized

5.4 Solution of interply crack

In this section, we show the results of the fracture mechanics solution of the crack problem shown in Figure 9(c). In this case, the problem leads to the solution of a singular integral equation (Wang and Karihaloo (1994b)). When the tips of the crack touch the interfaces, the asymptotic value of the stresses near the tips can be expressed as

$$\sigma_{ij} = \frac{K_{II}}{\sqrt{2}r^{\gamma_2}} f_{ij}(r,\theta) \tag{5.2}$$

where σ_{ij} $(i,j = 1,2)$ are the stress components in the xy-plane. K_{II} is the mode II stress intensity factor and γ_2 is the singularity of the stress field, r is the distance away from the tips of the crack, and $f_{ij}(r,\theta)$ are the angular functions with the origin of polar coordinates at the crack tip.

The variation of the stress singularity γ_2 for the four composite materials (three graphite/epoxy composites and one glass/epoxy composite) listed in Table 4 is shown in Figure 13. The strongest and weakest mode II singularities are given in Table 5. It is seen from Figure 13 and Table 5 that the mode II stress singularity has its minimum value when the outer ply angle θ is about 45°, that is, the difference between the ply angles in the adjacent plies is about 45°. For the three graphite/epoxy composites the strongest singularity occurs at $\theta = 90°$, that is when the composite laminate in Figure 9(a) degenerates into a transversely isotropic layer.

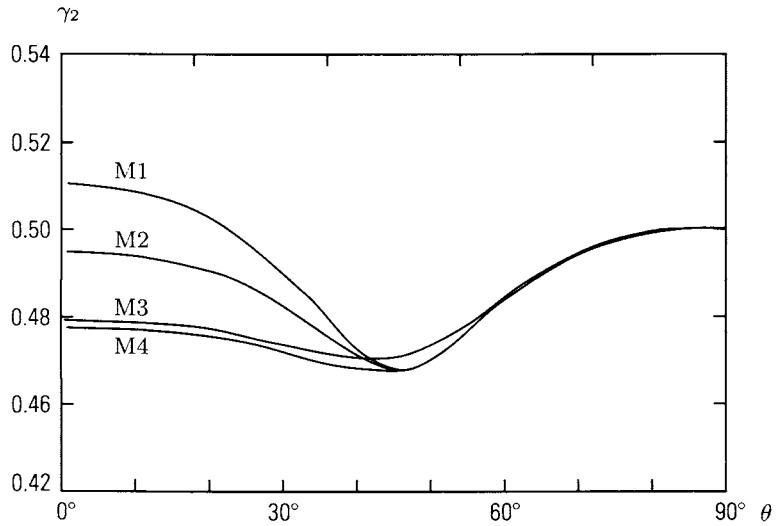

Figure 13. Variation of the mode II stress singularity γ_2 with the outer ply angle θ for four composites. M1, M3 and M4 are graphite/epoxy composites, whereas M2 is a glass/epoxy composite

Table 5. Strongest and weakest mode II stress singularities

Materials	M1	M2	M3	M4
$\gamma_{2\,\max}$	0.500	0.510	0.500	0.500
$\theta_{\max}$	90°	0°	90°	90°
$\gamma_{2\,\min}$	0.468	0.468	0.470	0.468
$\theta_{\min}$	45°	45°	41°	42°

5.5 Discussion

For a multidirectional composite laminate under transverse static or low-velocity impact loading, the matrix cracks are obviously caused by a combination of the tensile stress perpendicular to the fibre direction and the shear stress, as shown in Figure 8. It was shown by Davies and Zhang (1995) that for quasi-isotropic laminates, the transverse shear stress near the impacted site is very high. Following this observation and the analyses by Liu et al. (1993), and by Jih and Sun (1993), it is quite reasonable to assume that the occurrence of transverse cracks near the loading point is dominated by the transverse shear stress.

From the idealized fracture mechanics model presented above, the following conclusions may be drawn:

1. When the transverse crack is wholly within the inner layer (intraply transverse crack), the *crack-induced* interfacial principal tensile stress is influenced by the difference between the ply angles in the inner and outer layers. When the difference between the ply angles is 40°, the stress reaches its minimum for the graphite/epoxy composite material considered.
2. For an interply transverse crack where the crack has run through the thickness of the inner layer, the mode II stress singularity reaches its minimum for the three graphite/epoxy composites and one glass/epoxy composite when the difference between the ply angles is about 45°.
3. It is therefore suggested that in the design of the commonly used quasi-isotropic laminates, say, $[(\pm 45°/90°/0°)_r]_s$, it would be advantageous to interleave the 0° and 90° plies with the ±45° plies in order to increase its damage tolerance to transverse static or low-velocity impact loading. The configuration $[(+45°/90°/-45°/0°)_n]_s$ would be more damage tolerant than the configuration mentioned above.

6 Multiple cracking in angle-ply composite laminates

The stress field in a cracked $[(\pm\theta°)_{n2}/(90°)_{n1}]_s$ angle-ply fibre-reinforced composite laminate is solved by using Fourier transforms and dual integral equation formulation. The $(90°)_{n1}$ sublaminate is characterized by periodically distributed multiple transverse intralaminar cracks. The stress intensity factor at each crack tip and the *crack-induced* interfacial stresses are calculated. Both are found to be significantly influenced by the closeness of the crack tip to the bimaterial interface, the crack spacing and ply angle θ

of the constraining sublaminates. The variation of the SIF explains the physical mechanisms behind constrained cracking in composite laminates, while the perturbation of the interfacial stress field caused by the transverse cracks reveals that as the cracks approach the bimaterial interface, there is a considerable increase in interfacial stresses. The crack driving force and the *crack-induced* interfacial stresses decrease considerably when the multiple cracks are densely distributed. From the design point of view, the results also suggest that by a proper choice of ply angles in angle-ply laminates the crack growth in the individual lamina can be greatly retarded.

6.1 Introduction

The strength and stiffness of unidirectional fibre-reinforced composite laminae are quite sensitive to the direction of load with respect to the fibre orientation. For this reason, they are often used in the form of multi-angle-ply laminates. In these laminates, because of the inherent weakness of the laminae in their transverse direction, multiple transverse cracks are the most frequently observed form of damage. They can be found in the very early loading stage or even before external service loading Bailey and Parvizi (1981). The propagation of these cracks results not only in the fracture of the lamina, but also in the delamination failure between the sublaminates. Experimental results and theoretical calculations Crossman and Wang (1982), Fish and Lee (1990), Kim (1989), Wang and Karihaloo (1994a) have revealed that transverse cracks, especially when they are close to the interfaces, are directly responsible for the delamination failure.

Recognizing the transverse cracks as a basic damage feature of fibre-reinforced angle-ply laminates, many studies have been devoted to estimating the perturbations induced in the stress fields and laminate properties by these cracks. Thus Garrett and Bailey (1977) used a one-dimensional shear-lag model to predict the stress redistribution due to multiple transverse cracks in the 90° ply of cross-ply laminates. Crossman and Wang (1982) made detailed experimental observations of the phenomena of multiple transverse cracks in 90° and delamination in $[\pm 25°/90°_n]_s$ angle-ply laminates. The stress redistribution and the stiffness reduction due to the existence of multiple transverse cracks were extensively investigated in the works of others (Gudmundson and Zang (1993); Hashin (1985); Highsmith and Reifsnider (1982); Lee et al. (1989); Nairn (1989); Talreja (1985); Tan and Nuismer (1989)). Most of these works considered pre-existing through-thickness transverse cracks in the 90° plies. However, through-thickness cracks do not normally exist in laminates but originate as microcracks or small flaws in the 90° ply and propagate under increasing load until they reach the interfaces, resulting in the complete fracture of the 90° ply. Moreover, because of the weak constraint provided by the adjacent plies on the crack propagation, the initial microcracks are most likely to occur away from the interfaces (Kaw and Besterfield (1992); Wang and Karihaloo (1994a)) so that they are wholly within the 90° ply. On the aspect of the intralaminar crack problem, Fan et al. (1989) calculated the stress intensity factor at the tip of a single transverse crack in the 90° ply of a cross-ply laminate. Bai (1989) studied the tensile stiffness reduction of cross-ply laminates due to the existence of these multiple intralaminar cracks in the 90° ply. For angle-ply laminates under out-of-plane shear load, Wang and Karihaloo (1994a) calculated the stress intensity factor at the tip of a single intralaminar crack in the 90°

sublaminate and the *crack-induced* interfacial stresses. These results were applied to the design of angle-ply laminates that were least prone to delamination failure Wang and Karihaloo (1994a).

In this section, the results of Wang and Karihaloo (1994a) for a single transverse crack wholly within the $(90°)_{n_1}$, sublaminate are generalised to $[(\pm\theta°)_{n_2}/(90°)_{n_1}]_s$ angle-ply laminates with multiple intralaminar cracks in the $(90°)_{n1}$ sublaminate. The generalisation is accomplished by the superposition procedure of Nied (1987), and Kaw and Besterfield (1992) and requires the solution of a boundary-value problem. This solution is obtained by an extension of Copson (1961) procedure (Sih and Chen (1981); Wang and Karihaloo (1994a)). In this procedure the stress intensity factor is computed from the solution of a Fredholm integral equation rather than a singular integral equation. The effect of the crack spacing and ply angle θ on the in situ stress intensity factor is studied. The relationship between the *crack-induced* interfacial stresses and the crack geometry is also investigated.

The results reveal the constraining effect of the outer $\pm\theta°$ sublaminates on the crack driving force at the crack tips in the 90° sublaminate. This constraining effect can be exploited in designing the ply angle configurations of multi-angle-ply laminates so that the crack propagation in the individual unidirectional lamina can be retarded. As in a homogeneous medium containing a parallel array of cracks under mode I, the stress intensity factor (SIF) at each crack tip decreases with decreasing crack spacing. The interactive effect of multiple cracks considerably decreases the SIF when the cracks are densely distributed. At the same time the *crack-induced* interfacial stress is also reduced by the existence of the multiple cracks, which therefore serve as stress relaxers.

6.2 Boundary-Value Problem and Solution

Model and Basic Solution We consider a symmetric (or antisymmetric) angle-ply $[(\pm\theta°)_{n2}/(90°)_{n1}]_s$ fibre-reinforced laminate under unidirectional in-plane (yz) tension, shown in Figure 14. It consists of a central sublaminate in which the fibres are oriented normal to the plane of the paper (90° ply) and two outer sublaminates which are composed of an equal number of $+\theta°$ and $\theta°$ angle plies. The $(90°)_{n1}$ sublaminate of thickness $2d$ is transversely isotropic (in xy plane) and is assumed to contain a series of parallel, periodically distributed transverse cracks of length $2c$. Each outer sublaminate of thickness b is treated as being homogeneous orthotropic with average elastic properties of $[\pm\theta°]_s$ laminate, consistent with the classical lamination theory.

It is assumed that the composite laminate is subjected remotely to a uniform tensile deformation along y direction. Because of the orthotropy of the outer sublaminates, the 90° sublaminate also undergoes a uniform tensile deformation along y direction except near the free edges. This free-edge effect is not considered here. From a mathematical point of view, one needs only to solve the problem of cancellation of a uniform stress over the faces of all the cracks. Because of symmetry, it is enough to consider a quarter of the laminate, say $x \geq 0$, $y \geq 0$.

The solution to the above problem must satisfy the following boundary, and symmetry

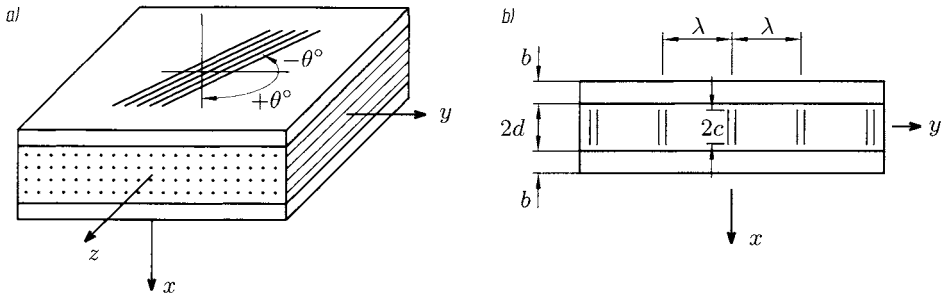

Figure 14. The cracked composite laminate and co-ordinate axes

conditions

$$\sigma_{yy}^{90}(x, n\lambda) = -\sigma; \qquad 0 \le x < c; \qquad n = 0, 1, 2, \ldots, +\infty \tag{6.1}$$

$$u^{90}(x, n\lambda) = 0; \qquad x > c; \qquad n = 0, 1, 2, \ldots, +\infty \tag{6.2}$$

$$u^{\theta}(x, n\lambda) = 0; \qquad d \le x \le d + b; \qquad n = 0, 1, 2, \ldots, +\infty \tag{6.3}$$

$$\tau_{xy}^{90}(x, n\lambda) = 0; \qquad c < x \le d; \qquad n = 0, 1, 2, \ldots, +\infty \tag{6.4}$$

$$\tau_{xy}^{\theta}(x, n\lambda) = 0; \qquad d \le x \le d + b; \qquad n = 0, 1, 2, \ldots, +\infty \tag{6.5}$$

and the following continuity and free surface conditions ($0 \le y < +\infty$):

$$\sigma_{xx}^{90}(d, y) = \sigma_{xx}^{\theta}(d, y) \tag{6.6}$$

$$\tau_{xy}^{90}(d, y) = \tau_{xy}^{\theta}(d, y) \tag{6.7}$$

$$u^{90}(d, y) = u^{\theta}(d, y) \tag{6.8}$$

$$v^{90}(d, y) = v^{\theta}(d, y) \tag{6.9}$$

$$\sigma^{\theta_{xx}}(d + b, y) = 0 \tag{6.10}$$

$$\tau_{xy}^{\theta}(d + b, y) = 0 \tag{6.11}$$

The solution of the above boundary-value problem for multiple cracks is simplified by the superposition procedure of Nied (1987), and Kaw and Besterfield (1992) applied to the solution of the boundary-value problem for a single crack, given by Wang and Karihaloo (1996a). The relevant expressions from that solution, identified by $n = 0$ will be cited here without detail. With the single crack located at $y = 0$, the stress $\sigma_{yy}^{90}(x, y)$

and displacement $v^{90}(x,y)$ are

$$\sigma_{yy}^{90}(r,y)|_{n=0} = \frac{2}{2\pi}\int_0^{+\infty} \mathcal{G}_1\left(\frac{s}{c},r\right)\cos\left(s\frac{y}{c}\right)ds+ \frac{2}{\pi c}\int_0^{+\infty} E\left(\frac{s}{c}\right)\left(1+s\frac{y}{c}\right)e^{-s\frac{y}{c}}\cos(sr)ds \tag{6.12}$$

$$v^{90}(r,y)|_{n=0} = \frac{2}{2\pi}\int_0^{+\infty} \mathcal{G}_2\left(\frac{s}{c},r\right)\sin\left(s\frac{y}{c}\right)ds+ -\frac{2}{\pi}\int_0^{+\infty}\frac{1}{s}E\left(\frac{s}{c}\right)[2a_{11}-(a_{12}-a_{11})sy]\,e^{-s\frac{y}{c}}\cos(sr)ds \tag{6.13}$$

where

$$\mathcal{G}_1\left(\frac{s}{c},r\right) = A\left(\frac{s}{c}\right)\cosh(sr)+B\left(\frac{s}{c}\right)[2\cosh(sr)+sr\sinh(sr)] \tag{6.14}$$

$$\mathcal{G}_2\left(\frac{s}{c},r\right) = \frac{1}{s}\left\{-A\left(\frac{s}{c}\right)(a_{12}-a_{11})\cosh(sr)+ +B\left(\frac{s}{c}\right)[2a_{11}\cosh(sr)-(a_{12}-a_{11})sr\sinh(sr)]\right\} \tag{6.15}$$

and

$$r = \frac{x}{c} \tag{6.16}$$

The functions $A(s/c)$ and $B(s/c)$ are determined from the continuity and free surface conditions (6.6)–(6.11).

The perturbation of the stress and displacement fields caused by the infinite array of cracks can be obtained by superposing the contributions of cracks located at $y = \pm n\lambda$, $n = 0, ..., +\infty$. Using the above superposition procedure on (6.12) and (6.13) and noting that $v^{90}(x,y)$ must be an odd function of y, we get the following two integral equations

$$\int_0^{+\infty}\left[1+\mathcal{G}\left(\frac{s}{c}\right)\right]E\left(\frac{s}{c}\right)\cos(sr)ds = -\left\{\frac{\pi c}{2}\sigma+\int_0^{+\infty}\mathcal{G}_1\left(\frac{s}{c},r\right)\cdot \cdot\left[1+2\sum_{n=1}^{+\infty}\cos\left(sn\frac{\lambda}{c}\right)\right]ds\right\};\quad 0\le r<1 \tag{6.17}$$

$$\int_0^{+\infty}\frac{1}{s}E\left(\frac{s}{c}\right)\cos(sr)ds = 0;\quad r>1 \tag{6.18}$$

where

$$\mathcal{G}\left(\frac{s}{c}\right) = \frac{2e^{-s\frac{\lambda}{c}}}{1-e^{-s\frac{\lambda}{c}}}\left[1+s\frac{\lambda}{c}\frac{1}{1-e^{-s\frac{\lambda}{c}}}\right]. \tag{6.19}$$

Denoting

$$F(s) = \left(\frac{\pi}{2s}\right)^{\frac{1}{2}}E\left(\frac{s}{c}\right) \tag{6.20}$$

and noting that

$$\cos(sx) \equiv \left(\frac{\pi sx}{2}\right)^{\frac{1}{2}}J_{-\frac{1}{2}}(sx) \tag{6.21}$$

where $J_{-\frac{1}{2}}$ is the Bessel function of the first kind, the dual integral eqns. (6.17)–(6.18) can be rewritten as

$$\int_0^{+\infty} s\left[1+\mathcal{G}(s)\right]F(s)J_{-\frac{1}{2}}(sr)ds = -\frac{1}{\sqrt{r}}\left\{\frac{\pi c}{2}\sigma + \int_0^{+\infty}\mathcal{G}_1(s,r)\cdot \right.$$
$$\left.\cdot\left[1+2\sum_{n=1}^{+\infty}\cos\left(sn\frac{\lambda}{c}\right)\right]ds\right\}; \quad 0\le r<1 \tag{6.22}$$

$$\int_0^{+\infty} F(s)J_{-\frac{1}{2}}(sr)\,ds = 0; \quad r>1 \tag{6.23}$$

The above dual integral equations can be solved by generalising the procedure of Copson (1961) (see also Sih and Chen (1981)), as shown in the Appendix. From (6.40) of the Appendix, $E(s)$ can be expressed as

$$E(s) = -\frac{\pi c}{2}\sigma\left\{\Phi(1)J_1(sc) - \int_0^1 \xi J_1(sc\xi)\frac{d}{d\xi}\left[\frac{\Phi(\xi)}{\sqrt{\xi}}\right]d\xi\right\}, \tag{6.24}$$

where $\Phi(\xi)$ is the solution of the following Fredholm integral equation

$$\Phi(\xi) + \int_0^1 \left[K_1(\xi,\eta)+K_2(\xi,\eta)\right]\Phi(\eta)d\eta = \sqrt{\xi} \tag{6.25}$$

The kernels $K_1(\xi,\eta)$ and $K_2(\xi,\eta)$ in eqn (6.25) are

$$K_1(\xi,\eta) = \sqrt{\xi\eta}\int_0^{+\infty}\frac{se^{-s\frac{d}{c}}}{\Delta(s)}\left\{I_0(s\xi)\sum_{j=1}^{4}K_{1j}E_j + \right.$$
$$\left.+\left[2I_0(s\xi)+s\xi I_1(s\xi)\right]\sum_{j=1}^{4}K_{2j}E_j\right\}\left[1+2\sum_{n=1}^{+\infty}\cos\left(sn\frac{\lambda}{c}\right)\right]ds \tag{6.26}$$

$$K_2(\xi,\eta) = \sqrt{\xi\eta}\int_0^{\infty} s\frac{2e^{-s\frac{\lambda}{c}}}{1-e^{-s\frac{\lambda}{c}}}\left[1+s\frac{\lambda}{c}\frac{1}{1-e^{-s\frac{\lambda}{c}}}\right]J_0(\xi s)J_0(\eta s)ds \tag{6.27}$$

where K_{ij} $(i=1,2;\ j=1,\ldots,4)$ may be found in Wang and Karihaloo (1996a), and

$$E_1 = \left(2-s\frac{d}{c}\right)I_0(s\eta) + s\eta I_1(s\eta),$$
$$E_2 = \left(1-s\frac{d}{c}\right)I_0(s\eta) + s\eta I_1(s\eta),$$
$$E_3 = a_{12}E_1 + a_{11}\left[s\frac{d}{c}I_0(s\eta) - s\eta I_1(s\eta)\right],$$
$$E_4 = (2a_{11}-a_{12})E_2 + a11\left[\left(1+s\frac{d}{c}\right)I_0(s\eta) - s\eta I_1(s\eta)\right].$$

$I_0()$ and $I_1()$ are the modified Bessel functions of the first kind.

That the integral of $K_1(\xi,\eta)$ is convergent follows from the integral

$$\int_0^{+\infty} s^m e^{-\beta s}\cos(n\alpha s)ds = (-1)^m \frac{\partial^m}{\partial\beta^m}\left(\frac{\beta}{n^2\alpha^2+\beta^2}\right) \tag{6.28}$$

The integral of $K_2(\xi,\eta)$ is evidently convergent.

The necessary stress and displacement components can be obtained, once $E(s)$ has been found from the solution of (6.24)–(6.27).

Stress intensity factor We now calculate the mode I stress intensity factor at each crack tip. The relevant normal stress component around the crack tip is

$$\begin{aligned}\sigma_{yy}^{90}(x,0) =& \frac{2}{\pi}\int_0^{+\infty}[1+\mathcal{G}(s)]\,E(s)\cos(sx)ds+\\ &+\frac{2}{\pi}\int_0^{+\infty}\mathcal{G}_1(s,x)\left[1+2\sum_{n=1}^{+\infty}\cos(sn\lambda)\right]ds\end{aligned} \tag{6.29}$$

Substituting eqn (6.24) into eqn (6.29) gives

$$\begin{aligned}\sigma_{yy}^{90} =& -c\sigma\int_0^{+\infty}[1+\mathcal{G}(s)]\left\{\Phi(1)J_1(sc)-\int_0^1 \xi J_1(sc\xi)\frac{d}{d\xi}\left[\frac{\Phi(\xi)}{\sqrt{\xi}}\right]d\xi\right\}\cos(sx)ds+\\ &+\frac{2}{\pi}\int_0^{+\infty}\mathcal{G}_1(s,x)\left[1+2\sum_{n=1}^{+\infty}\cos(sn\lambda)\right]ds\end{aligned} \tag{6.30}$$

The mode I stress intensity factor at the crack tip is

$$K_I = \lim_{x\to c^+}\sqrt{s(x-c)}\,\sigma_{yy}^{90}(x,0) = \Phi(1)\sigma\sqrt{c} \tag{6.31}$$

If the θ° plies on the two sides are absent then the stress intensity factor is

$$K_{I0} = F\left(\frac{c}{d}\right)\sigma\sqrt{c} \tag{6.32}$$

$\Phi(1)$ alone is affected by stiffness properties of the sublaminates, the density of the cracks and the laminate configuration, i.e. the ply-angle θ and the relative thicknesses of the sublaminates. For the graphite/epoxy material properties (Tan and Nuismer

Table 6. Material properties

Properties and material	E_L (GPa)	E_T (GPa)	G_{LT} (GPa)	G_{TT} (GPa)	ν_{LT} –	ν_{TT} –	Ply thickness (mm)
T300/934	138	11.7	4.56	4.18	0.29	0.40	0.132

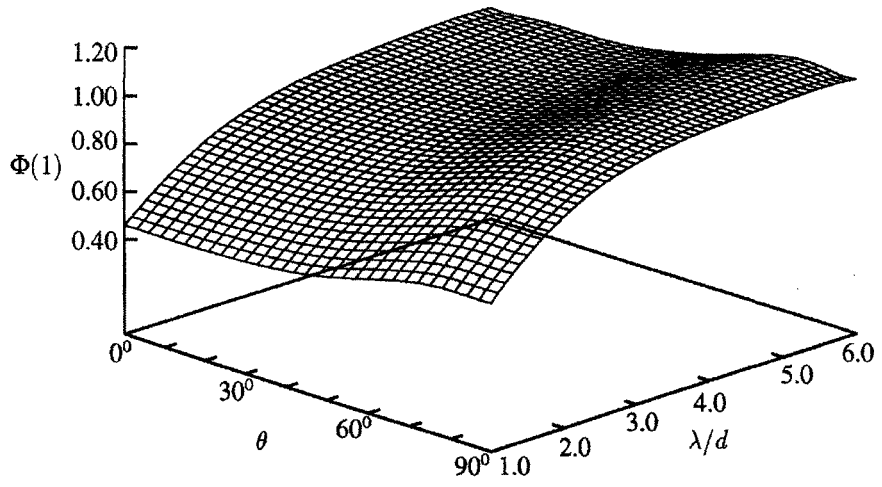

Figure 15. Variation of $\Phi(1)$ with c/d and θ for a single crack

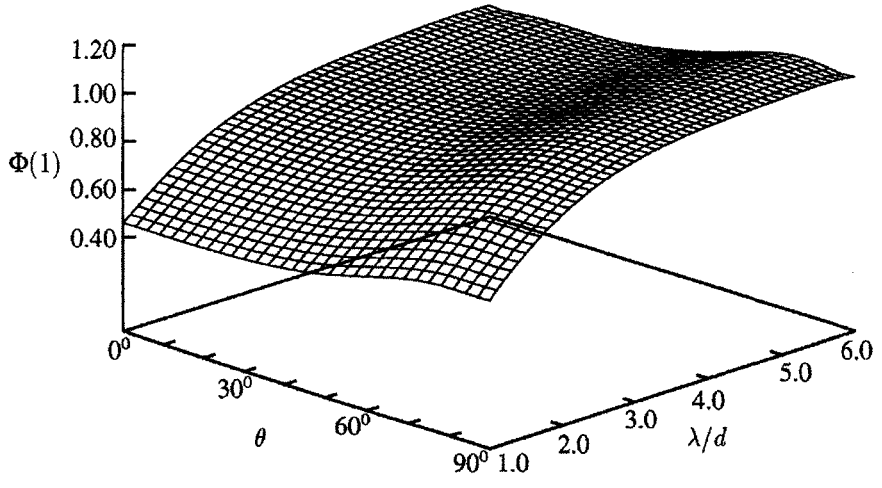

Figure 16. Variation of $\Phi(1)$ with θ and λ/d for multiple cracks of length $c/d = 0.7$

(1989))listed in Table 6 in the notation of Tsai and Hahn (1980) , the variation of $\Phi(1)$ with c/d, λ/d, and different θ are shown in Figures 15 and 16.

In order to examine the constraining effect of the outer sublaminates, we first show in

Figure 15 the variation of $\Phi(1)$ with θ and c/d, for a single crack (i.e. when $\lambda/d \to \infty$). $b/d = 1$ is used here and throughout the computations presented below.

$\Phi(1)$ exhibits two notable features. First, it always increases with increasing θ, irrespective of the crack size. This means that the constraining effect of the outer plies decreases with increasing θ. In other words, transverse cracks in the 90° ply of $[\pm\theta^\circ/90^\circ]_s$ laminates will propagate at smaller stress levels, the larger the ply angle θ. This result agrees with the experimental observations which show that *in situ* tensile strength of the 90°_n layer in $[\pm 0^\circ/90^\circ_n]_s$ laminates reduces with an increase in θ (Flaggs and Kural (1982)). It is also seen that if the size of the initial cracks or flaws is less than a certain critical value, the *in situ* stress intensity factor increases with an increase in the thickness of the 90° sublaminate. Thus, the thicker the 90° layer, the smaller the *in situ* transverse tensile strength. This deduction also confirms experimental observations made by Garrett and Bailey (1977), Parvizi et al. (1978), and Flaggs and Kural (1982).

Secondly, for $0^\circ \leq \theta \leq 90^\circ$, $\Phi(1)$ is always less than $F(\frac{c}{b+d})$ – the corresponding geometry factor at each crack tip in a finite homogeneous isotropic strip, otherwise there would be no point in using composite materials. It is also for this reason that the θ° sublaminates are regarded as constraints for the central layer. However, it is found that this constraining effect has the following important characteristic which can be exploited in the design of crack-insensitive laminates. When θ is not greater than a certain critical value θ_c, $\Phi(1)$ decreases with the increasing crack length, so that the crack-driving force decreases during the propagation of the crack. This suggests that for arbitrary multi-ply-angle laminates, the difference between the fibre orientations in the adjacent plies should exceed a certain minimum value θ_m, if the laminae are going to play the role of mutual crack arrestors. For the material properties of Table 6, this critical value θ_c is around 70°, i.e. the ply angle difference between the central sublaminate and the outer sublaminates should exceed $\theta_m = 20^\circ$. The configurations with smaller ply angle differences should be avoided in order not to exaggerate the crack growth in the central sublaminate.

Figure 16 shows the variation of $\Phi(1)$ with θ and c/d. The interaction among the multiple cracks helps to reduce the value of the stress intensity factor at each crack tip. This effect comes from the stress relaxation caused by the crack arrays on the two sides of a particular crack. Theoretically, when $\lambda/d \to 0$, $\Phi(1) \to 0$ (a paradoxical result from a practical view point). Experimental results (e.g. Highsmith and Reifsnider (1982)) reveal that the number of the multiple cracks (the crack density) in the 90° sublaminate increases with increasing tensile load, reaching a saturation value at a certain load level. This saturation phenomenon is evidently a result of the interplay between $\Phi(1)$ and λ/d just mentioned.

Interfacial Stresses The non-dimensional *crack-induced* stresses at the interfacial point in front of each crack tip are

$$\frac{\sigma_{xx}(d,0)}{\sigma} = \int_0^{+\infty} \frac{se^{-s\frac{d}{c}}}{\Delta(s)} \left[\cosh\left(s\frac{d}{c}\right)\sum_{j=1}^{4} K_{1j}G_j + s\frac{d}{c}\sinh\left(s\frac{d}{c}\right)\sum_{j=1}^{4} K_{2j}G_j\right] \cdot \left[1 + 2\sum_{n=1}^{\infty}\cos\left(sn\frac{\lambda}{c}\right)\right] ds + \int_0^1 \Phi(\xi)G(\xi)d\xi - \int_0^{+\infty} K_5G_5 ds \tag{6.33}$$

$$\frac{\sigma_{yy}(d,0)}{\sigma} = \int_0^{+\infty} \frac{se^{-s\frac{d}{c}}}{\Delta} \left\{\cosh\left(s\frac{d}{c}\right)\sum_{j=1}^{4} K_{1j}G_j + \left[2\cosh\left(s\frac{d}{c}\right) + \frac{d}{c}\sinh\left(s\frac{d}{c}\right)\right] \cdot \sum_{j=1}^{4} K_{2j}G_j\right\} \cdot \left[1 + 2\sum_{n=1}^{\infty}\cos\left(sn\frac{\lambda}{c}\right)\right] ds + \int_0^1 \Phi(\xi)G(\xi)d\xi - \int_0^{+\infty} K_6G_6 ds \tag{6.34}$$

where

$$G(\xi) = \left(\frac{c}{d}\right)^2 \frac{\sqrt{\xi}}{\sqrt{1-\left(\frac{c}{d}\xi\right)^2}\left[1+\sqrt{1-\left(\frac{c}{d}\xi\right)^2}\right]} \left\{2 + \frac{\left(\frac{c}{d}\xi\right)^2\left[1+2\sqrt{1-\left(\frac{c}{d}\xi\right)^2}\right]}{\left[1-\left(\frac{c}{d}\xi\right)^2\right]\left[1+\sqrt{1-\left(\frac{c}{d}\xi\right)^2}\right]}\right\} \tag{6.35}$$

$$G_i = \int_0^1 \sqrt{\xi}\Phi(\xi)E_i(s,\xi)d\xi \quad (i = 1,\ldots,4)$$

$$G_5 = G_6 = \int_0^1 \sqrt{\xi}\Phi(\xi)J_0(s\xi)d\xi$$

$$K_5 = 2s\frac{e^{-s\frac{\lambda}{c}}}{1-e^{-s\frac{\lambda}{c}}}\left[1 - s\frac{\lambda}{c}\frac{1}{1-e^{-s\frac{\lambda}{c}}}\right]\cos\left(s\frac{d}{c}\right) \tag{6.36}$$

$$K_6 = 2s\frac{e^{-s\frac{\lambda}{c}}}{1-e^{-s\frac{\lambda}{c}}}\left[1 + s\frac{\lambda}{c}\frac{1}{1-e^{-s\frac{\lambda}{c}}}\right]\cos\left(s\frac{d}{c}\right) \tag{6.37}$$

The tensile stress perpendicular to the interface area is most likely to cause delamination. For the crack configuration and loading, the interfacial stresses in front of each crack tip σ_{xx} and σ_{yy} are found to be always positive. Therefore, under plane strain conditions, the interfacial area is subjected to an unfavourable three-dimensional tensile field. The variation of *crack-induced* interfacial normal stress σ_{xx} with λ/d and c/d for $\theta = 0°$ and $\theta = 45°$ is shown in Figures 17(a,b), respectively. The *crack-induced interfacial* σ_{yy} is almost of the same order as σ_{xx}. The total interfacial σ_{yy} is obtained by adding the applied homogeneous stress σ to the *crack-induced* value.

As the crack tip approaches the interface ($c/d \to 1$), the interfacial stresses increase rapidly for all θ. For small cracks though, the interfacial stresses are fairly insensitive to changes in θ, but as c/d increases so also does its sensitivity to outer ply angle θ. An examination of Figures 16 and 17 shows that for all c/d, both the crack driving force $\Phi(1)$

and the interfacial stresses take on their minimum values when $\theta = 0°$. It confirms the fact that the outer sublaminates of a cross-ply laminate have the strongest constraining effect on the inner 90° layer. The crack-induced interfacial stress field due to an isolated crack that terminates at the interface ($c/d = 1$) has been given for modes I, II and III by Wang and Karihaloo (1994b), Wang and Karihaloo (1996a).

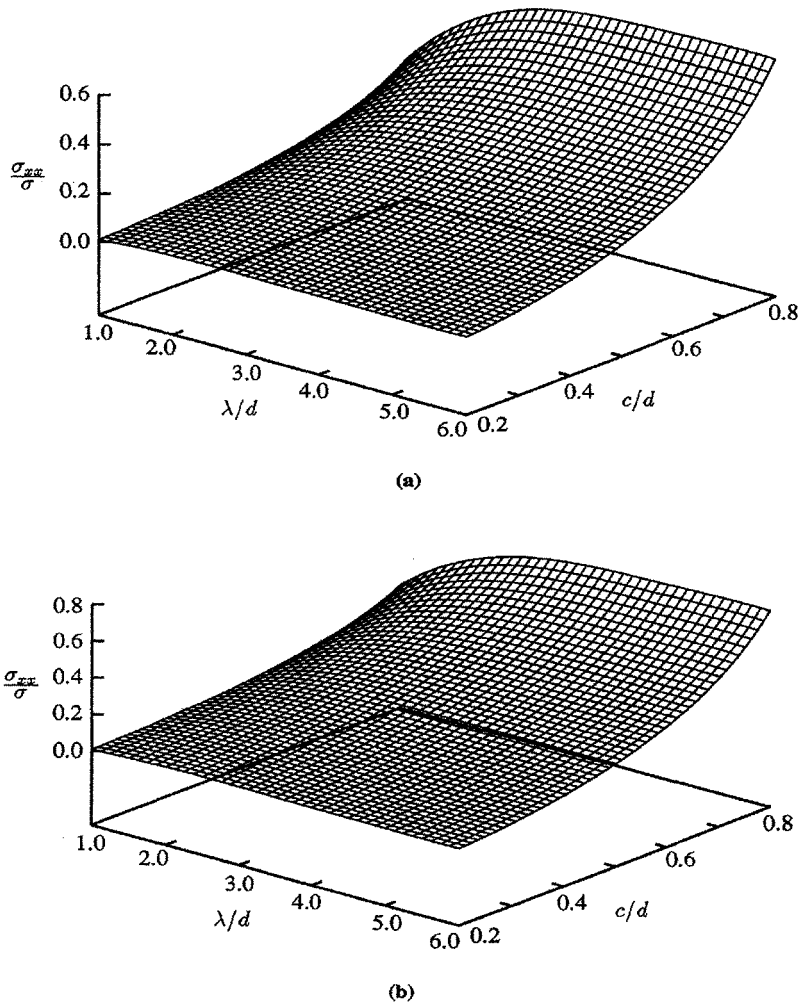

Figure 17. Normalised interfacial normal stress: (a) $\theta = 0°$; (b) $\theta = 45°$

6.3 Discussion

In a $[(\pm\theta^\circ)_{n_2}/(90^\circ)_{n_1}]]_s$ angle-ply laminate, the constraining effect of the outer $[(\pm\theta^\circ)_{n_2}]$ sublaminates on the inner $[(90^\circ)_{n_1}]$ sublaminate is determined by the stiffness, geometry and ply angle θ, with the stiffness of the outer sublaminates playing the most dominant role. In order to retard the growth of transverse cracks in the inner sublaminate the difference in the fibre orientations in the adjacent laminae must exceed a certain critical value. For the same reason, the inner sublaminate should not be very thick.

Transverse cracks can induce high interfacial stresses, the more so when these cracks are close to the interface. This is a major cause of the crack-induced delamination in angle-ply laminates.

Appendix

Solution of dual integral equations

Copson (1961) showed that the dual integral equations

$$\int_0^\infty A(s)J_\nu(rs)ds = 0 \quad r > c \tag{6.38}$$

$$\int_0^\infty s^{2\alpha}A(s)J_\nu(rs)ds = f(r) \quad r < c \tag{6.39}$$

are solved by

$$A(s) = s^{1-\alpha}\int_0^c \phi(t)J_{\nu+\alpha}(st)dt \tag{6.40}$$

provided that

$$0 < \alpha < 1 \tag{6.41}$$

$$\nu > -\alpha \tag{6.42}$$

$$\lim_{t\to 0^+}[t^{\nu+\alpha-1}\phi(t)] = 0 \tag{6.43}$$

The function $\phi(t)$ is given by

$$\phi(t) = \frac{2^{1-\alpha}}{\Gamma(\alpha)}t^{1-\nu-\alpha}\int_0^t \frac{r^{1+\nu}f(r)}{(t^2-r^2)^{1-\alpha}}dr \tag{6.44}$$

provided that the function $r^\nu f(r)$ and its first derivative are continuous in the interval $[0, c]$. The above solution procedure was also cited by Sih and Chen (1981) in relation to crack problems in composite materials.

Wang and Karihaloo (1994a) showed that the solution (6.40) is also valid when $\alpha = \nu = 1/2$ as in the dual integral equations

$$\int_0^\infty A(s)J_{-\frac{1}{2}}ds = 0 \quad r > c \tag{6.45}$$

$$\int_0^\infty sA(s)J_{-\frac{1}{2}}ds = f(r) \quad r < c \tag{6.46}$$

resulting from the boundary-value problem for a single crack.

The dual integral equations (6.5)–(6.6) are a variation upon (6.38)–(6.39)

$$\int_0^\infty A(s)J_\nu(rs)ds = 0 \quad r > c \tag{6.47}$$

$$\int_0^\infty s^{2\alpha}F(s)A(s)J_\nu ds = f(r) \quad r < c \tag{6.48}$$

These may however be formally given the form of (6.21)-(6.22)

$$\int_0^\infty A(s)J_\nu(rs)ds = 0 \quad r > c \tag{6.49}$$

$$\int_0^\infty s^{2\alpha}A(s)J_\nu ds = f*(r) \quad r < c \tag{6.50}$$

where

$$f*(r) = f(r) - \int_0^\infty s^{2\alpha}[F(s)-1]A(s)J_\nu(rs)ds \tag{6.51}$$

The solution (6.44) now becomes

$$\phi(t) + \int_0^c \phi(\xi)K(\xi,\eta)d\eta = \frac{2^{1-\alpha}}{\Gamma(\alpha)}t^{1-\nu-\alpha}\int_0^t \frac{r^{1+\nu}f(r)}{(t^2-r^2)^{1-\alpha}} \tag{6.52}$$

in which the additional kernel $K(\xi,\eta)$ is

$$K(\xi,\eta) = t\int_0^\infty s[F(s)-1]J_{\alpha+\nu}(s\xi)J_{\alpha+\nu}(st)ds \tag{6.53}$$

Bibliography

J.M. Bai. Stiffness reduction analysis of cracked cross-ply laminates by using integral equation approach. *Engineering Fracture Mechanics*, 34:245–251, 1989.

J.E. Bailey and A. Parvizi. On fibre debonding effects and the mechanism of transverse-ply failure in cross-ply laminates. *Journal of Material Science*, 16:649–659, 1981.

H.E. Brandmaier. Optimum filament orientation criteria. *Journal of Composite Materials*, 4:422–425, 1970.

F.K. Chang and M.H. Chen. The in situ ply shear strength distributions in graphite/epoxy laminated composite. *Journal of Composite Materials*, 21:708–733, 1987.

F.K. Chang and L.B. Lessard. Damage tolerance of laminated composites containing an open hole and subjected to compressive loadings Part I: analysis. *Journal of Composite Materials*, 25:2–43, 1991.

C.C. Chao, C.T. Sun, and S.L. Koh. Strength optimization for cylindrical shells of laminated composites. *Journal of Composite Materials*, 9:53–66, 1975.

R.J. Chester and G. Clark. Modelling of impact damage features in graphite/epoxy laminates. In J.E. Masters, editor, *Damage Detection in Composite Materials*, volume ASTM STP 1128, pages 200–212, 1992.

H.Y. Choi and F.K. Chang. A model for predicting damage in graphite/epoxy laminated composites resulting from low-velocity point impact. *Journal of Composite Materials*, 26:2134–2169, 1992.

G. Clark and D.S. Saunders. Morphology of impact damage growth by fatigue in carbon fibre composite laminates. *Materials Forum*, 15:333–342, 1991.

E.T. Copson. On certain dual integral equations. *Proceedings of the Glasgow Mathematical Association*, 5:19–24, 1961.

F.W. Crossman and A.S.D. Wang. The dependence of transverse cracking and delamination on ply thickness in graphite/epoxy laminates. In *Damage in Composite Materials*, volume ASTM STP 775, pages 118–139. American Society for Testing and Materials, 1982.

G.A. Davies and X. Zhang. Impact damage prediction in carbon composite structures. *International Journal of Impact Engineering*, 16:149–170, 1995.

G.A.O. Davies, D. Hitchings, and J. Wang. Prediction of threshold impact energy for onset of delamination in quasi-isotropic carbon/epoxy composite laminates under low-velocity impact. *Composite Science and Technology*, 1997.

L.E. Doxsee, P. Rubbrecht, L. Li, I. Verpoest, and M. Scholle. Delamination growth in composite plates subjected to transverse loads. *Journal of Composite Materials*, 27: 764–781, 1993.

F.W. Fan, W. Dong, and J. Wang. A study of the *in situ* transverse tensile lamina strength and the solution of the opening mode crack in $0°/90°/0°$ laminate. *Acta Mechanica Sinica*, 21:450–458, 1989.

J.C. Fish and S.W. Lee. Three-dimensional analysis of combined free-edge and transverse-crack-tip delamination. In *Composite Materials: Testing and Design*, volume ASTM STP 1059, pages 271–286. American Society for Testing and Materials, 1990.

D.L. Flaggs and M.H. Kural. Experimental determination of in situ transverse lamina strength in graphite/epoxy laminates. *Journal of Composite Materials*, 16:103–116, 1982.

H. Fukunaga and T.W. Chou. On laminate configurations for simultaneous failure. *Journal of Composite Materials*, 22:271–286, 1988.

H. Fukunaga and G.N. Vanderplaats. Strength optimization of laminated composites with respect to layer thickness and/or layer orientation angle. *Computers nad Structures*, 40:1429–1439, 1991.

K.W. Garrett and J.E. Bailey. Multiple transverse fracture in $90°$ cross-ply laminates of a glass fibre-reinforced polyester. *Journal of Material Science*, 12:157–168, 1977.

P. Gudmundson and W. Zang. An analytic model for thermoelastic properties of composite laminates containing transverse matrix cracks. *International Journal of Solids and Structures*, 30:3211–3231, 1993.

Z. Hashin. Analysis of cracked laminates: a variational approach. *Mechanics of Materials*, 4(121–136), 1985.

C.T. Herakovich. Influence of layer thickness on the strength of angle-ply laminates. *Journal of Composite Materials*, 16:216–227, 1982.

A.L. Highsmith and K.L. Reifsnider. Stiffness-reduction mechanisms in composite laminates. In *Damage in Composite Materials*, volume ASTM STP 775, pages 103–117. American Society for Testing and Materials, 1982.

C.J. Jih and C.T. Sun. Prediction of delamination in composite laminates subjected to low velocity impact. *Journal of Composite Materials*, 27:684–701, 1993.

A.K. Kaw and G.H. Besterfield. Mechanics of multiple periodic brittle matrix cracks in unidirectional fiber-reinforced composites. *International Journal of Solids and Structures*, 29:1193–1207, 1992.

R.Y. Kim. Experimental observations of free-edge delamination. In N.J. Pagano, editor, *Interlaminar Response of Composite Materials*, pages 111–160. Elsevier, Amsterdam, 1989.

J.W. Lee, D.H. Allen, and C.E. Harris. Internal state variable approach for predicting stiffness reductions in fibrous laminated composites with matrix cracks. *Journal of Composite Materials*, 23:1273–1291, 1989.

S. Liu, Z. Kutlu, and F.K. Chang. Matrix cracking and delamination in laminated composite beams subjected to a transverse concentrated line load. *Journal of Composite Materials*, 27:436–470, 1993.

A. Miravete. Optimization of symmetrically laminated composites rectangular plates. In Y. Wu, Z. Gu, and R. Wu, editors, *Proceedings of the Seventh International Conference on Composite Materials*, volume 3, pages 289–294, Beijing, 1989. International Academic Publishers.

J.A. Nairn. The strain energy release rate of composite microcracking: a variational approach. *Journal of Composite Materials*, 23:1106–1129, 1989.

H.F. Nied. Periodic array of cracks in a half-plane subjected to arbitrary loading. *Journal of Applied Mechanics*, 54:642–648, 1987.

W.J. Park. An optimal design of simple symmetric laminates under the first ply failure criterion. *Journal of Composite Materials*, 16:341–355, 1982.

A.K. Parvizi, K.W. Garrett, and J.E. Bailey. Constrained cracking in glass fibre-reinforced epoxy cross-ply laminates. *Journal of Material Science*, 13:195–201, 1978.

M.J. Pavier and M.P. Clarke. Experimental techniques for the investigation of the effects of impact damage on carbon-fibre composites. *Composite Science and Technology*, 55: 157–169, 1995.

R.S. Sandhu. Parametric study of Tsai's strength criterion for filamentary composites. Technical Report TR-68-168, Air Force Flight Dynamic Laboratory, Wright-Patterson AFB, 1969.

G.C. Sih and E.P. Chen. *Mechanics of Fracture-Cracks in Composite Materials*. Martinus Nijhoff Publisher, The Hague, 1981.

R. Talreja. Transverse cracking and stiffness reduction in composite laminates. *Journal of Composite Materials*, 19:355–375, 1985.

S.C. Tan and R.J. Nuismer. A theory for progressive matrix cracking in composite laminates. *Journal of Composite Materials*, 23:1029–1047, 1989.

S.W. Tsai and H.T. Hahn. *Introduction to Composite Materials.* Technomic Publishing Co Inc, Westport, 1980.

J. Wang and B.L. Karihaloo. Cracked composite laminates least prone to delamination. *Proceedeings of Royal Society London*, A444:17–35, 1994a.

J. Wang and B.L. Karihaloo. Mode II and mode III stress singularities and intensities at a crack tip terminating on a transversely isotropic-orthotropic bimaterial interface. *Proceedeings of Royal Society London*, A444:447–460, 1994b.

J. Wang and B.L. Karihaloo. Fracture mechanics and optimization – a useful tool for fibre-reinforced composite design. *Computers and Structures*, 31:151–162, 1995.

J. Wang and B.L. Karihaloo. Mode I stress singularity and intensity factor at a crack tip terminating at a transversely isotropic-orthotropic bimaterial interface. *International Journal of Fracture*, (74):325–340, 1996a.

J. Wang and B.L. Karihaloo. Optimum *in situ* strength design of composite laminates Part II: optimum design. *Journal of Composite Materials*, 30:1338–1358, 1996b.

J. Wang and B.L. Karihaloo. Optimum in situ strength design of composite laminates Part I: in situ strength parameters. *Journal of Composite Materials*, 30:1314–1337, 1996c.

Multiscale Computational Damage Modelling of Laminate Composites

Ladevèze Pierre[1]

[1] LMT Cachan (ENS Cachan/CNRS/Paris 6 Univ.), 61 avenue du Président-Wilson, 94235 Cachan, France

Abstract. The main questions discussed here are how to bridge the micro- and mesomechanics of laminates and how this affects the understanding and prediction of localization and final fracture of engineering composite structures.

1 Motivations: the Scientific and Industrial Challenges

The last quarter-century has witnessed considerable research efforts in the mechanics of composites in order to understand their behavior and to model or calculate them – the ultimate goal being the design of the materials/structures/manufacturing processes. Even in the case of stratified composites (which are the most studied and, therefore, the best understood), the prediction of damage evolution up to and including final fracture remains a major challenge in the modern mechanics of composite materials and structures. Today, the use of stratified composites in the aerospace industry always involves characterization procedures consisting of huge numbers of tests, which shows the low level of confidence in models. A significant improvement in this situation, *i. e.* a drastic reduction in the number of industrial tests, could be achieved if one could create a real synergy among the approaches on different scales which, today, are followed quite independently of one another in the case of stratified composites. One could jokingly say that there is, on the one hand, the micromechanics of laminates where one counts cracks and, on the other, the meso- or macromechanics of laminates where one measures stiffnesses – with only few links between the two. How to bridge the micro- and mesomechanics aspects and how this affects the understanding and prediction of localization and final fracture are the two main questions discussed here.

Up to now, there have been numerous theoretical and experimental works on the micromechanics of laminates (see the two review papers Nairn and Hu, 1994, Berthelot, 2003, our references herein, and in particular the book of Herakovich, 1998); the micromechanics approach provides a relatively good understanding of damage mechanisms, such as matrix microcracking. However, these micromechanics models are lacking in some respects: in particular, they are far from being complete for the prediction of localization and final fracture.

Alternative, pragmatic computational approaches have also been developed. In our lab, we focus on what we call a "damage mesomodel for laminates" (see Ladevèze, 1986, Ladevèze *et al.*, 2000, and our references herein). In this approach, one assumes that the behavior of any

laminated composite for any loading and any stacking sequence can be modeled using two elementary constituents which are continuous media: the ply and the interface. Another important point is that the state of damage is assumed to remain constant throughout the thickness of the single layer (of course, it can vary from one layer of the laminate to the next).

The central question we aim to discuss here is: how can one bridge the micro- and mesomechanics of damage? The belief that such a complete bridge could exist is not shared by all the people working in micromechanics. A first attempt at building such a bridge was made in Ladevèze and Lubineau (2001, 2002) for plane macrostresses. The mesomodel was found to be fully compatible with the microdamage mechanisms. The micro-meso relations introduce quantities or relations which we call "approximately ply-material", which are intrinsically related to the cracked ply's characteristics and, therefore, independent of the characteristics of the other plies. Recently, additional work has extended this approach to out-of-plane stresses (see Ladevèze *et al.*, 2004). This more complex situation involves non-local mesomodels, as there are interactions between the interface's damage and the microcracking mechanisms of the adjacent plies. The method of investigation is now entering what is called a "virtual testing" stage, in which numerous numerical experiments using the micromodel and involving various possible stacking sequences, thicknesses... are performed. One can show that the micromechanisms within the plies and interfaces can be homogenized; relations between the micro- and mesoquantities can be obtained through the resolution of several basic problems.

The second question being discussed here is the impact of such a bridge on the micro- and mesomodels themselves, the objective being to calculate the intensities of the damage mechanisms at any point of a laminated structure subjected to complex loading and at any time until final fracture resulting from strain and damage localization. These improved models require a multiscale approach. A first example is an improved damage mesomodel for laminates allowing the calculation of the intensities of the damage micromechanisms. A second example is a "computational damage micromodel" which is rather simple, yet semi-discrete and probabilistic. It is detailed here for the first time. Unfortunately, this model leads to prohibitive calculation costs if one uses current industrial codes. The use of a multiscale computational strategy is absolutely essential. Several examples are worked out in order to show the capabilities and the limitations of the different models.

2 The Micromechanics of Laminates – Damage Modelling

2.1 The Working Scale

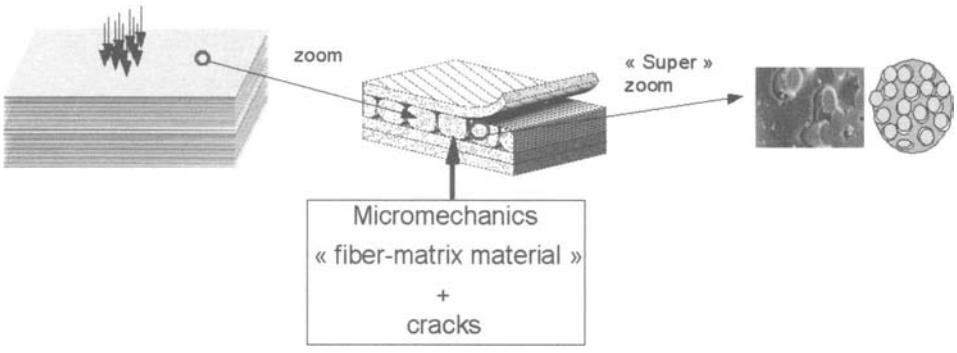

Figure 1. The studied structure at the microscale.

Up to now, there have been numerous theoretical and experimental works on the micromechanics of laminates (see the two review papers Nairn and Hu, 1994, Berthelot, 2003, our references herein, and in particular the book of Herakovich, 1998). The working scale in micromechanics is between the dimension of the structure and the diameter of a fiber. The structure at state is in fact described as an assembly of cracked interfaces and cracked layers made with a "fiber-matrix" material prescribed homogeneous or quasi-homogeneous.

2.2 Phenomenology at the Microscale

Figures 2, 3, 4 show the different scenarios on the microscale. Scenarios 3 and 4 are generally missing in micromechanics.

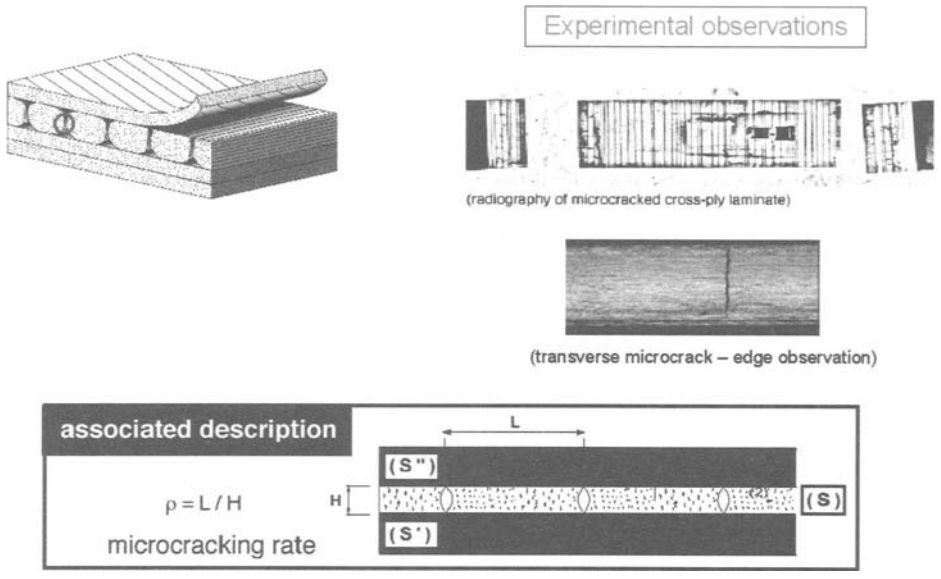

Figure 2. **Scenario 1: transverse microcracking.**

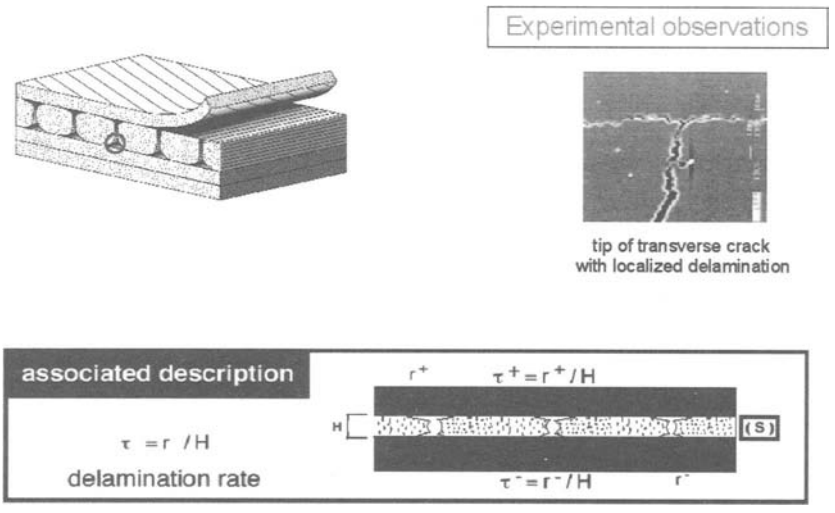

Figure 3. **Scenario 2: local delamination.**

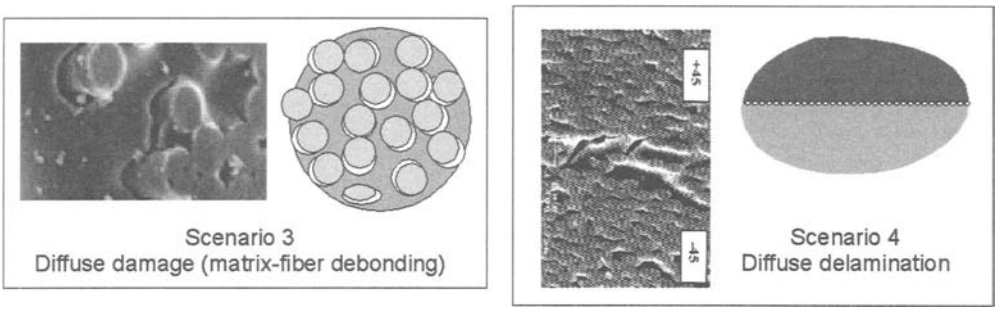

Figure 4. **Scenarios 3 and 4: diffuse damage inside the plies and interfaces.**

In most practical cases, the chain of scenarios follows the figure 5. Scenarios 3 and 4 start, leading to a rather diffuse damage inside the plies and interfaces. Through a percolation phenomenon, transverse microcracks appear and then Scenario 1 is active. The competition between transverse microcracking and local delamination ends with the saturation of Scenario 1 and is relayed by the catastrophic development of Scenario 2. Finally, the final fracture arrives with fiber breaking and delamination.

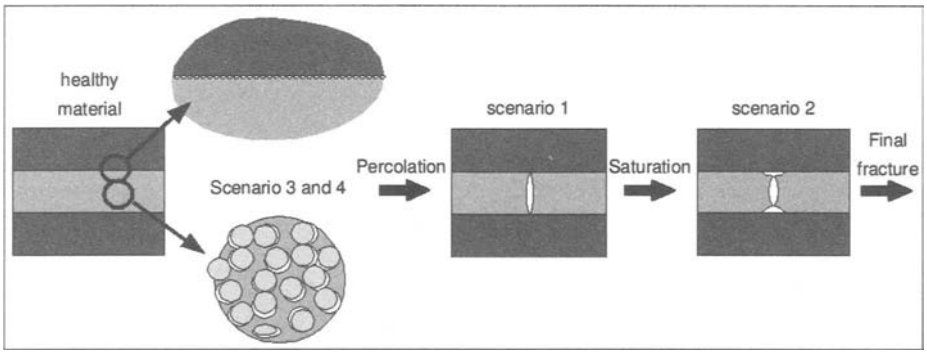

Figure 5. **The chain of scenarios.**

2.3 Several Keypoints in Micromechanics

Hereafter are displayed several keypoints which characterize in our opinion the behavior of a laminate on the microscale.

Keypoint 1: need of Scenarios 3 and 4. The Scenarios 3 and 4 which are usually missing in micromechanics can be witnessed when performing the tension test $[45°, -45°]_{2n}$; a clear definitive experimental proof has been done recently in Lagattu and Lafarie-Frénot, 2000:

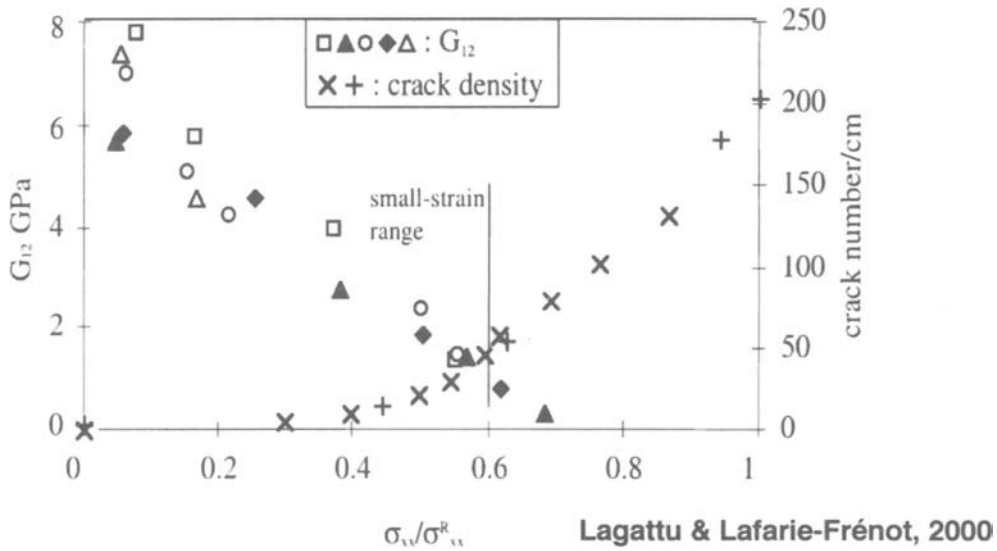

Figure 6. **Shear modulus and microcracking density versus the longitudinal stress for the tension test $[45°, -45°]_{2S}$.**

A major consequence is that there are at least two main damage mechanisms: Scenarios 1 and 3. Therefore, mesomodels with one mesodamage variable per layer are only valid for particular loading; that is the case for the most alternative approaches to our mesomodel (see Paragraph 3).

Remarks:

- These scenarios are also responsible of the (visco)plastic behavior which can be observed at the mesoscale.
- The better understanding at the scale of the fiber of the surprising non-percolation phenomenon which occurs with shear is an open question.

Keypoint 2: Initiation/propagation modelling – thickness effect. Most of the basic papers are not recent: Garrett and Bailey (1977), Parvizi *et al.* (1978), Wang and Crossman (1980), Boniface *et al.* (1997), Yang *et al.* (2003). For stacking sequences built with 0° and 90° plies, two main observations have been done for tension tests.

First, the behavior of thick 90° plies is different from the one of thin 90° plies. For thick plies, the transverse microcracks always cross the width of the tension test specimen. For thin plies, they can stop near the edges.

Another observation is related to thickness effect (see Figures 7 and 8) which is quite important. Let us note that the longitudinal stiffnesses of the different stacking sequences are very

similar: the contribution of the 90° plies is negligible. The transition thickness h is about twice the thickness of the elementary ply.

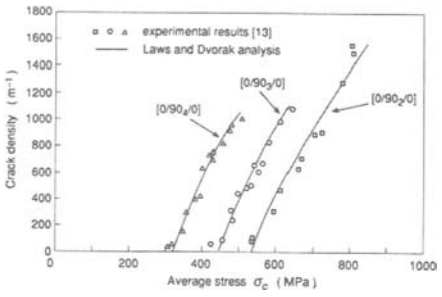

Figure 7. **Microcracking density versus the longitudinal stress for different stacking sequences.**

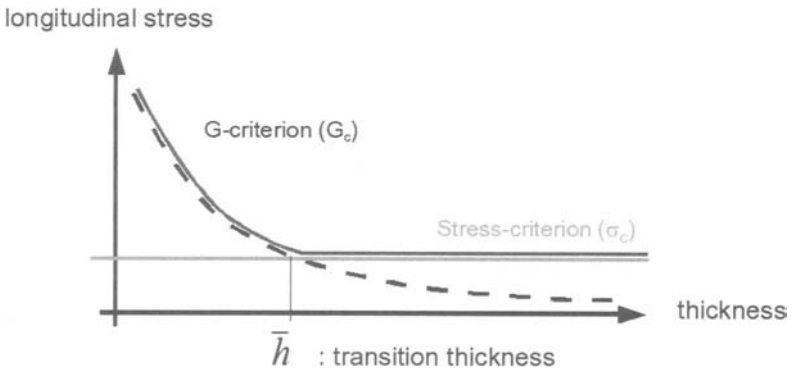

Figure 8. **Failure stress versus the number of 90° plies.**

The theoretical explanation is both quite old and well-known. Let us consider a flaw *i. e.* a penny-shape crack (see Figure 9) which could propagate in the longitudinal direction or in the transverse one (thickness direction). It has been proved that the transverse value of the energy release rate is much larger than the longitudinal one; consequently, the flaw primarily propagates itself in the transverse direction.

Before introducing a cracking process modelling, let us build the damage force. Let $G_{tunneling}$ be the tunneling energy release rate used classically in micromechanics. A significant property is shown in Figure 9; its value is practically independent of the ratio $\varnothing = l/H$ for $\varnothing \geq 0.8$ .Then, the transverse damage force is:

$$G_{trans} = \min\left[G_{tunneling}, G_{tunneling}\frac{\bar{h}}{h}\right] \tag{1}$$

and the longitudinal one: $G_{tunneling}$.

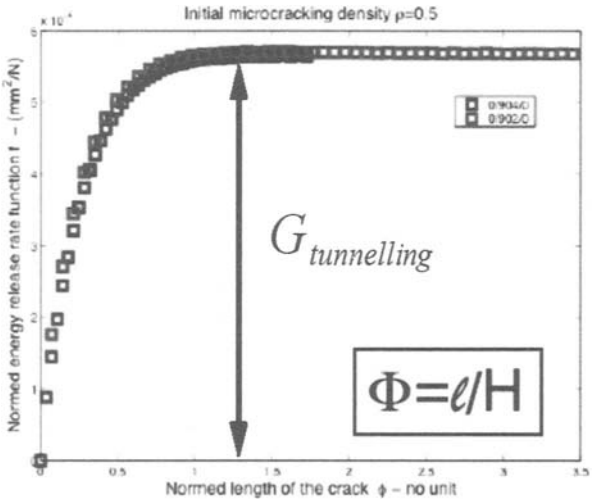

Figure 9. **Energy release rate versus the ratio** $\varnothing = {}^{l}/_{H}$.

The cracking process modelling is then without separating the different modes for staking sequences made with 0° and 90° plies:

- initiation

$$G_{trans} \geq G_c \tag{2}$$

- propagation of existing cracks

$$G_{tunneling} \geq G_c \tag{3}$$

Applied to thick and thin 90° plies, one gets for tension tests:

- Thick plies: $h \geq \bar{h}$

If the initiation criterion is active, the propagation one is also active. A rapid crack propagation in the width direction follows.

• Thin plies: $h \leq \bar{h}$

There is only one criterion for both initiation and propagation. An overstress occurs near the edges that explains why the cracks start at the edges. After, they cand stop if the energy release rate diminishes. Such an edge effect has been stressed recently in Pagano *et al.* (1998). We add that it is responsible for the odd behavior of certain stacking sequences.

Keypoint 3: Microcracking as a stochastic phenomenon. Several probabilistic models have already been proposed: Wang *et al.* (1984), Fukunaga *et al.* (1984), Laws and Dvorak (1988), Masters and Reifsnider (1982), Berthelot and Le Corre (2000). Heuristic coefficients have been introduced to characterize the non-perfect periodicity for large cracking density (see Laws and Dvorak, 1988, Nairn *et al.*, 1993, and Ladevèze and Lubineau, 2002). This is necessary in order to get a reasonable agreement with experiment (see Yahvac *et al.*, 1991).

Here, we defend the idea that the process is stochastic but quasi-independent of the probabilistic law. Let us consider the *G*-curve defined Figure 10; a new crack should appear at the maximum. Being piecewise flat, the cracking process is necessarily stochastic at the beginning. Our proposed model is very simple. It is prescribed a uniform probability density to get a new crack over the domain:

$$\left\{ \underline{M} \middle| \max_{\underline{M}'} G(\underline{M}') - G(\underline{M}) \leq \Delta \right\} \tag{4}$$

with $\max_{\underline{M}'} G(\underline{M}') = G_C$.

G denotes the tunneling energy release rate and Δ a small parameter. G_C is the critical value associated to the fiber-matrix material.

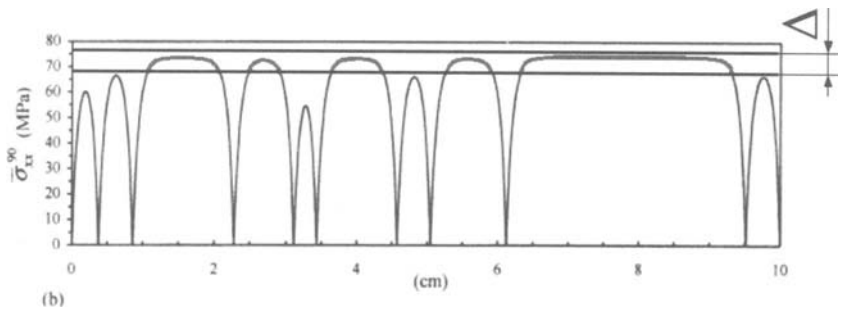

Figure 10. **G-curve as the function of the longitudinal abscissa – domain associated to Δ.**

Figure 11 shows several samples for different values of Δ; the "mean" curve which is used for identification appears to be insensitive to Δ and to the samples. It is a quasi-deterministic curve (practically independent of Δ) which is quite different from the curve related to a perfect periodic pattern.

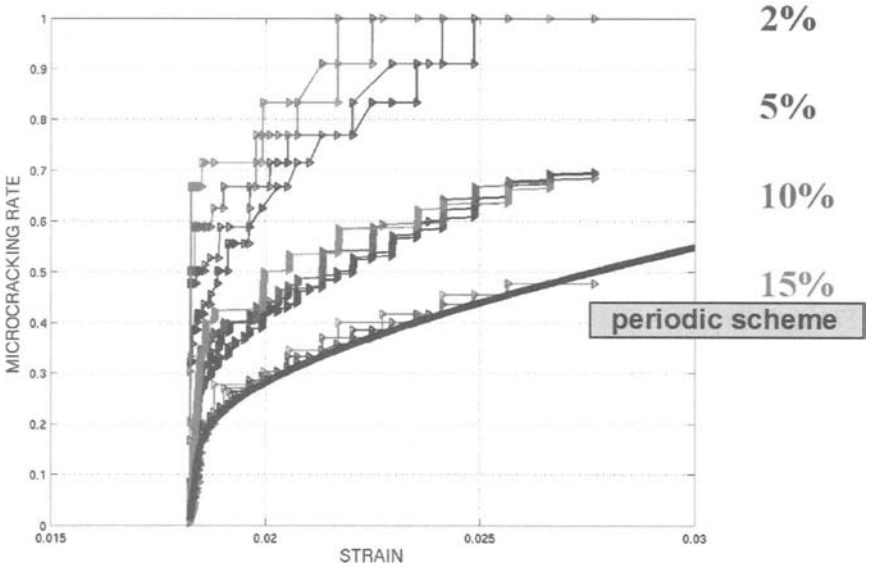

Figure 11. **Max., mean and min. values for the microcracking rate versus the longitudinal strain.**

Such a model has a reasonable agreement with experiments (see Figure 12); the test results are given in Nairn and Hu (1994) for AS4/Hercules 3501-6.

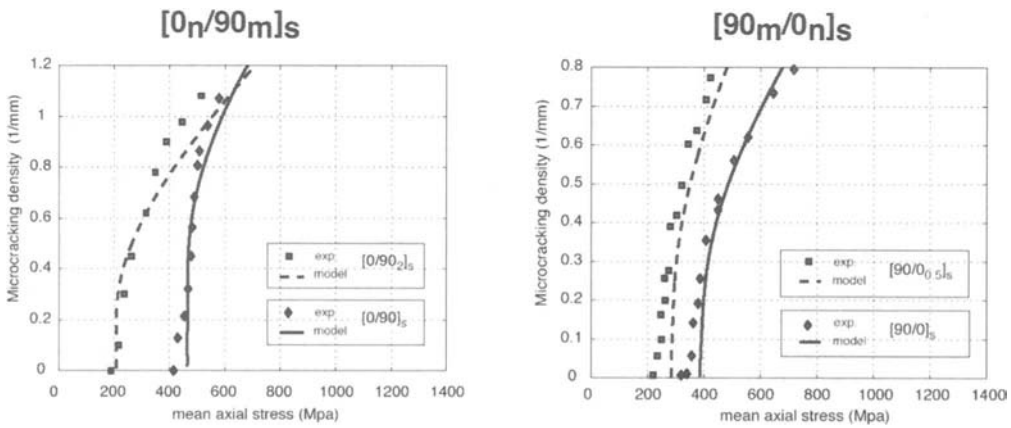

Figure 12. **Comparison tests-model.**

3 A First Damage Mesomodel: a Pragmatic Approach

3.1 Basic Aspects

An initial step is to define what we call a laminate mesomodel (see Ladevèze, 1986, 1989). At the mesoscale, characterized by the thickness of the ply, the laminate structure is described as a stacking sequence of homogeneous layers through the thickness and of interlaminar interfaces (see Figure 13). The main damage mechanisms are described as: fiber breaking, matrix microcracking and debonding of adjacent layers. The single-layer model includes both damage and inelasticity. The interlaminar interface is defined as a two-dimensional mechanical model which ensures traction and displacement transfer from one ply to the next. Its mechanical behavior depends on the angle between the fibers of two adjacent layers. *A priori*, 0°/0° interfaces are not introduced. Herakovich (1998), in his book, calls this theory "mesoscale composite damage theory".

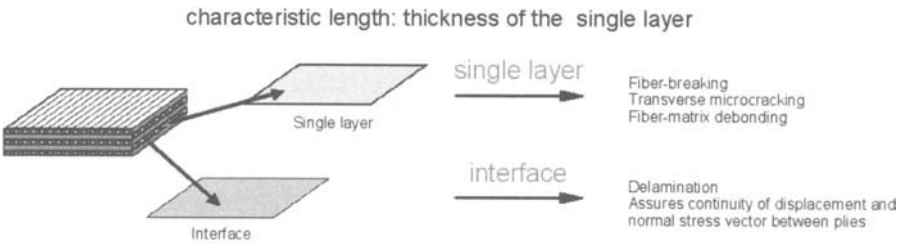

Figure 13. **Laminate modelling.**

The damage mechanisms are taken into account by means of internal damage variables. A mesomodel is then defined by adding another property; a uniform damage state is prescribed throughout the thickness of the elementary ply. This point plays a major role when trying to simulate a crack with a damage model. As a complement, delayed damage models are introduced.

One limitation of the proposed mesomodel is that material fracture is described by means of only two types of macrocracks:

- delamination cracks within the interfaces,
- cracks orthogonal to the laminate's mid-plane, each cracked layer being completely cracked through its thickness.

The layers – in our sense – are assumed to be not too thick. Another limitation is that very severe dynamic loadings cannot be studied; the dynamic wavelength must be larger than the thickness of the plies.

Two models have to be identified: the single-layer model (see Ladevèze and Le Dantec, 1992) and the interface model (see Allix and Ladevèze, 1992, and Allix *et al.*, 1999). The appropriate tests used consist of: tension, bending and delamination. Each composite specimen, which contains several layers and interfaces, is analyzed in order to derive the material quantities intrinsic to the single-layer or to the interlaminar interface.

Various comparisons with experimental results have been performed to show the possibilities and limits of our proposed computational damage mechanics approach for laminates (see Ladevèze, 1995, Daudeville and Ladevèze, 1993, and Allix, 1992).

The Ply Mesomodel

Damage kinematics. The composite materials under investigation in this study have only one reinforced direction. In the following, subscripts 1, 2 and 3 designate the fiber direction, the transverse direction inside the layer and the normal direction respectively. The energy of the damaged material defines the damage kinematics. Using common notations, this energy is:

$$E_D \equiv \frac{1}{2(1-d_F)}\left[\frac{\langle\sigma_{11}\rangle^2}{E_1^0}+\frac{\varnothing(\langle-\sigma_{11}\rangle)}{E_1^0}-\left(\frac{\nu_{21}^0}{E_2^0}+\frac{\nu_{12}^0}{E_1^0}\right)\sigma_{11}\sigma_{22}-\left(\frac{\nu_{31}^0}{E_3^0}+\frac{\nu_{13}^0}{E_1^0}\right)\sigma_{11}\sigma_{33}\right.$$
$$\left.-\left(\frac{\nu_{32}^0}{E_3^0}+\frac{\nu_{23}^0}{E_2^0}\right)\sigma_{22}\sigma_{33}\right]+\frac{\langle-\sigma_{22}\rangle^2}{2E_2^0}+\frac{\langle-\sigma_{33}\rangle^2}{2E_3^0} \qquad (5)$$
$$+\frac{1}{2}\left[\frac{1}{(1-d')}\left(\frac{\langle\sigma_{22}\rangle^2}{E_2^0}+\frac{\langle\sigma_{33}\rangle^2}{E_3^0}\right)+\frac{1}{(1-d)}\left(\frac{\sigma_{12}^2}{G_{12}^0}+\frac{\sigma_{23}^2}{G_{23}^0}+\frac{\sigma_{31}^2}{G_{31}^0}\right)\right]$$

$\varnothing$ is a material function which takes into account the nonlinear response in compression (see Allix *et al.*, 1994). d_F, d and d' are three scalar internal variables which remain constant through the thickness of each single-layer and serve to describe the damage mechanisms inside. The unilateral aspect of microcracking is taken into account by splitting the energy into a "tension" energy and a "compression" energy; $\langle\cdot\rangle$ denotes the positive part.

The thermodynamic forces associated with the mechanical dissipation are:

$$Y_d \equiv \frac{\partial}{\partial d}\langle\langle E_D\rangle\rangle\Big|_{\varpi\,:\,cst} = \frac{1}{2(1-d)^2}\left\langle\left\langle\frac{\sigma_{12}{}^2}{G_{12}^0}+\frac{\sigma_{23}{}^2}{G_{23}^0}+\frac{\sigma_{31}{}^2}{G_{31}^0}\right\rangle\right\rangle$$
$$Y_{d'} \equiv \frac{\partial}{\partial d'}\langle\langle E_D\rangle\rangle\Big|_{\varpi\,:\,cst} = \frac{1}{2(1-d')^2}\left\langle\left\langle\frac{\langle\sigma_{22}\rangle^2}{E_2^0}+\frac{\langle\sigma_{33}\rangle^2}{E_3^0}\right\rangle\right\rangle \qquad (6)$$
$$Y_F \equiv \frac{\partial}{\partial d_F}\langle\langle E_D\rangle\rangle\Big|_{\varpi\,:\,cst} = \frac{1}{2(1-d_F)^2}\left\langle\left\langle\frac{\langle\sigma_{11}\rangle^2}{E_1^0}+\frac{\varnothing(\langle-\sigma_{11}\rangle)}{E_1^0}\right.\right.$$

$$-\left(\frac{\nu_{12}^0}{E_1^0}+\frac{\nu_{21}^0}{E_2^0}\right)\sigma_{11}\sigma_{22}-\left(\frac{\nu_{13}^0}{E_1^0}+\frac{\nu_{31}^0}{E_3^0}\right)\sigma_{11}\sigma_{33}-\left(\frac{\nu_{32}^0}{E_3^0}+\frac{\nu_{23}^0}{E_2^0}\right)\sigma_{22}\sigma_{33}\Big\rangle\Big\rangle$$

$\langle\langle\cdot\rangle\rangle$ denotes the mean value through the thickness.

Damage evolution law. From experimental results, it follows that the governing forces of damage evolution are:

$$Y = \left[Y_d + bY_{d'}\right]Y' = \left[Y_{d'} + b'Y_d\right]Y_F$$

where b and b' are material constants which balance the influence of the transverse energy and the shear energy. For small damage rates and quasi-static loading, we get:

$$\begin{aligned} d &= f_d\left(\underline{Y}^{1/2}\right) \text{ for } d \le 1 \\ d' &= f_{d'}\left(\underline{Y'}^{1/2}\right) \text{ for } d' \le 1 \\ d_F &= f_F\left(\underline{Y}_F^{1/2}\right) \text{ for } d_F \le 1 \end{aligned} \tag{7}$$

where: $\underline{r}_{|t} = \sup_{\tau \le t} r_{|\tau}$.

f_d, $f_{d'}$ and f_F are material "functions"; progressive damage evolution (generally defined by a linear function) and brittle damage evolution (defined by a threshold) are both present. The thresholds involve the thickness because they are related to Scenarios 1 and 2. f_F is generally associated with a brittle damage mechanism. The model stays valid for a rather large temperature range (see Allix *et al.*, 1996). At room temperature, a typical material function f_d is given in figure 14. For large damage rates, we have introduced a damage model with delay effects:

$$\begin{aligned} d &= \frac{1}{\tau_c}\left[1-\exp\left(-a\left\langle f_d\left(Y^{1/2}\right)-d\right\rangle\right)\right] \text{ if } d<1, d = 1 \text{ otherwise} \\ d' &= \frac{1}{\tau_c}\left[1-\exp\left(-a\left\langle f_{d'}\left(Y'^{1/2}\right)-d'\right\rangle\right)\right] \text{ if } d'<1, d' = 1 \text{ otherwise} \\ d_F &= \frac{1}{\tau_c}\left[1-\exp\left(-a\left\langle f_F\left(Y_F^{1/2}\right)-d_F\right\rangle\right)\right] \text{ if } d_F<1, d_F = 1 \text{ otherwise} \end{aligned} \tag{8}$$

The same material constants, τ_C and a, are taken for the three damage evolution laws. For this damage model with delay effects, the variations of the forces Y, Y' and Y_F do not lead to instantaneous variations of the damage variables d, d' and d_F. There is a certain delay, defined

by the characteristic time τ_c . Moreover, a maximum damage rate, which is $1/\tau_c$, does exist. A first identification consists of taking half the Rayleigh wave speed combined with the critical value of the energy release rate. Let us also point out here that a clear distinction can be made between this damage model with delay effects and viscoelastic or viscoplastic models: the characteristic time introduced in the damage model with delay effects is several orders of magnitude less than in the viscous case. This characteristic time is, in fact, related to the fracture process.

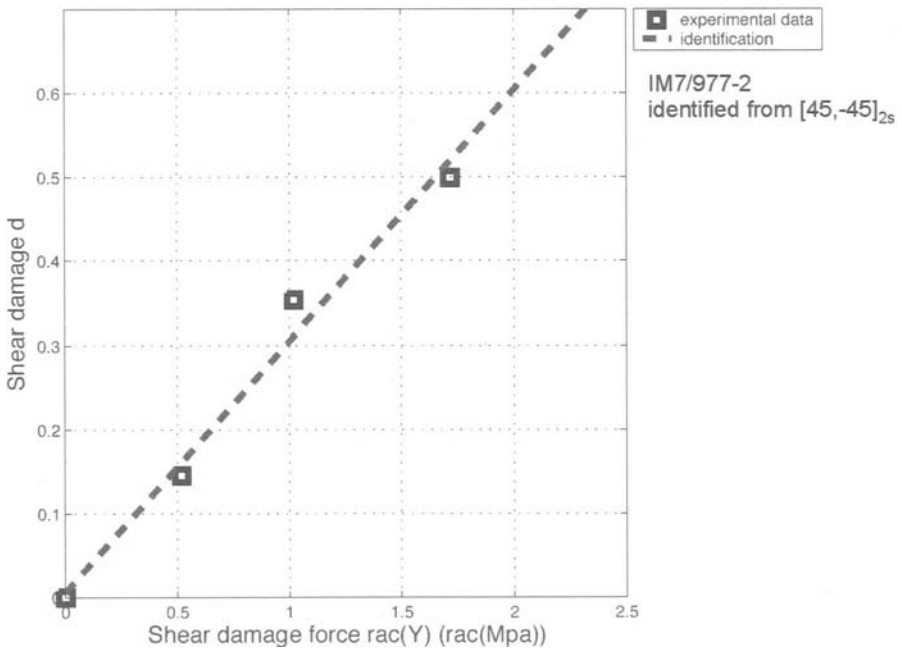

Figure 14. **Shear damage material function $Y_d^{1/2} \rightarrow f_d\left(Y_d^{1/2}\right)$ of the single-layer for the M55J/M18 material at room temperature.**

Remarks:

- Two damage variables are used to describe the damage associated with matrix microcracking and fiber-matrix debonding. They seem to account for all the proposed damage kinematics, including all of them starting from an analysis of the microcracks. Many works have established, experimentally or theoritically, a relation between the microcrack density and our damage variable *d*, which can be very useful for the identification of a damage fatigue model.
- What we call the single-layer is the assemblage of adjacent usual elementary plies of the same direction. The damage forces, being mean values through the thickness of the single-layer, can be interpreted as energy release rates divided by the thickness. It follows that the

damage evolution law of the progressive part is thickness-independent. At the contrary, the thresholds are thickness-dependent.

- The damage variables are active for $[0°, 90°]_n$ laminates even if the apparent modulus does not change. The model predicts this hidden damage (see Ladevèze, 1992).
- For fatigue loadings, we introduce:

$$\begin{aligned} d &= d_S + d_F \\ d' &= d'_S + d'_F \end{aligned} \tag{9}$$

where d_S and d'_S are the quasi-static part of the damage defined by Equations 4 and 5. d_F and d'_F denote the fatigue part characterized by the following fatigue evolution laws:

$$\begin{aligned} \frac{\partial d_F}{\partial N} &= \boldsymbol{a}\left(d, \left[Y_d + bY_{d'}\right]\right) \\ \frac{\partial d'_F}{\partial N} &= \boldsymbol{a}'\left(d', \left[Y_{d'}\right]\right) \end{aligned} \tag{10}$$

where $\boldsymbol{a}, \boldsymbol{a}'$ are two material functions. $[\cdot]$ denotes the maximum value over the cycle.

Coupling between damage and (visco)plasticity. The microcracks, *i. e.* the damage, lead to sliding with friction, and thus to inelastic strains. The effective stress and inelastic strain are defined by:

$$\begin{aligned} &\sigma_{11} \equiv \sigma_{11} \quad \sigma_{22} \equiv -\langle -\sigma_{22}\rangle + \frac{\langle \sigma_{22}\rangle}{(1-d')} \quad \sigma_{33} \equiv -\langle -\sigma_{33}\rangle + \frac{\langle \sigma_{33}\rangle}{(1-d')} \\ &\sigma_{12} \equiv \frac{\sigma_{12}}{(1-d)} \quad \sigma_{23} \equiv \frac{\sigma_{23}}{(1-d)} \quad \sigma_{31} \equiv \frac{\sigma_{31}}{(1-d)} \\ &\varepsilon_{11p} \equiv \varepsilon_{11p} \quad \varepsilon_{22p} \equiv \langle \varepsilon_{22p}\rangle(1-d') - \langle -\varepsilon_{22p}\rangle \quad \varepsilon_{33p} \equiv \langle \varepsilon_{33p}\rangle(1-d') - \langle -\varepsilon_{33p}\rangle \\ &\varepsilon_{12p} \equiv \varepsilon_{12p}(1-d) \quad \varepsilon_{23p} \equiv \varepsilon_{23p}(1-d) \quad \varepsilon_{31p} \equiv \varepsilon_{31p}(1-d) \end{aligned} \tag{11}$$

ε_{ijp} for $ij \in \{1, 2, 3\}$ denotes the usual inelastic strain. The idea is to apply classical plasticity or viscoplasticity models to effective quantities. A very simple plasticity model is defined by the following elastic domain:

$$f(\tilde{\boldsymbol{\sigma}}, R) = \left[\sigma_{12}^2 + \sigma_{23}^2 + \sigma_{31}^2 + a^2\left(\sigma_{22}^2 + \sigma_{33}^2\right)\right]^{1/2} - R - R_0 \tag{12}$$

Hardening is assumed to be isotropic, which means that the threshold R is a function of the cumulated strain p; $p \to R(p)$ is a material function, p being defined by:

$$p = \int_0^t dt \left[\varepsilon_{12p}^2 + \varepsilon_{23p}^2 + \varepsilon_{31p}^2 + \frac{1}{a^2}\left(\varepsilon_{22p}^2 + \varepsilon_{33p}^2\right) \right]^{1/2} \tag{13}$$

a is a material coupling constant. The yield conditions are:

$$\begin{aligned} &\bullet\ pf = 0,\ p \geq 0,\ f \leq 0 \\ &\bullet\ \varepsilon_{ijp} = \frac{1}{2} p \frac{\sigma_{ij}}{R + R_0} \text{ for } i \neq j;\ i, j \in \{1, 2, 3\} \\ &\bullet\ \varepsilon_{iip} = p \frac{a^2 \sigma_{ii}}{R + R_0} \text{ for } i \in \{2, 3\} \end{aligned} \tag{14}$$

An example of such a hardening curve is given for the T300-914 material in figure 15.

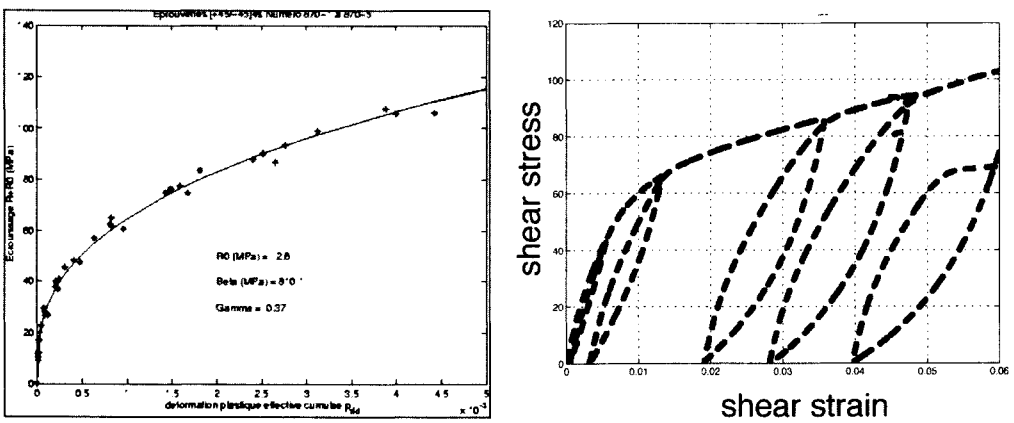

Figure 15. **Hardening curve at room temperature for IM6/914.**

Identification of the material parameters. The single-layer model and the interface model have been identified for various materials. Aside from the elastic constants, the model depends on:

- three coupling coefficients b, b', a^2,
- the damage "functions" $f_d, f_{d'}, f_F$ describing progressive and brittle evolutions,
- the hardening function $p \to R(p)$,

- the function $\varnothing$ defined practically by one parameter characterizing the compressive stiffness loss in the fiber direction (see Allix *et al.*, 1994).

The identification is developed here for low-stiffness matrixes. It is based on three canonic tests $[0°, 90°]_{2S}$, $[+45°, -45°]_{2S}$, $[+67.5°, -67.5°]_{2S}$. The measured experimental quantities are:

- the tension F which is related to the macrostress σ_L^* by $\sigma_L^* = F/S$ where S is a specimen's section,
- the laminate's axial strain ε_L^* and the transverse one ε_T^*.

Consequently, the inelastic strains and moduli variations are determined.

- Tensile test on $[0°, 90°]_{2S}$ laminate

This test defines f_F, *i. e.*, in many cases, the fiber's limit tensile strain.

- Tensile test on $[+45°, -45°]_{2S}$ laminate

The following relations allow to reconstitute the ply's shear behavior:

$$\begin{aligned} \sigma_{12} &= \frac{\sigma_L^*}{2} \\ \varepsilon_{12} &= \frac{\left(\varepsilon_L^* - \varepsilon_T^*\right)}{2} = \varepsilon_{12e}^* + \varepsilon_{12p}^* \\ \sigma_{11} &= \sigma_L^* \end{aligned} \tag{15}$$

For many materials, one has:

$\varepsilon_{12} \geq (\varepsilon_{11}, \varepsilon_{22})$

$\sigma_L^* \geq \sigma_{22}$

Consequently, the transverse stress and strain do not affect the behavior. The damage function f_d is defined using:

$$\begin{aligned} Y &= \sqrt{2G_{12}^0}\ \varepsilon_{12e}^* \\ (1-d) &= \frac{\sigma_L^*}{2G_{12}^0\ \varepsilon_{12e}^*} \end{aligned} \tag{16}$$

$$R + R_0 = G_{12}^0 \varepsilon_{12e}^*$$
$$p = \int_0^{\varepsilon_{12e}^*} 2(1-d)d\varepsilon_p \tag{17}$$

• Tensile test on $[+ 67.5°, - 67.5°]_s$ laminate

b' can be taken to zero for many materials. Then, the stresses and strains in the upper layer are:

$$\sigma_{11} = s\sigma_L^* \quad \sigma_{22} = s'\sigma_L^* \quad \sigma_{12} = s''\sigma_L^* \quad \theta = 67.5°$$
$$\varepsilon_{11} \approx 0 \quad \varepsilon_{22} = \cos^2\theta\,\varepsilon_L^* + \sin^2\theta\,\varepsilon_T^* \quad \varepsilon_{12} = \cos\theta\sin\theta\left(\varepsilon_L^* - \varepsilon_T^*\right)$$

where s, s', s'' are coefficients depending on θ and the single-layer's characteristics. This test allows one to identify the two coupling coefficients b and a^2 and the material function $f_{d'}$. A complete numerical simulation of the model is needed here. Let us note that a more robust test should be welcome.

3.2 The Interface Mesomodel

Damage kinematics of the interface. The interlaminar connection is thus modeled as a two-dimensional entity which ensures stress and displacement transfers from one ply to another. The interlaminar connection can be classically interpreted as a ply of matrix whose thickness (denoted by e) is small compared to the in-plane dimension.

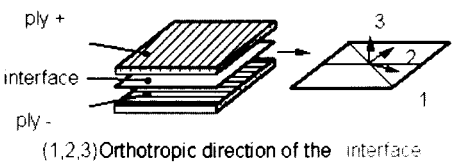

Figure 16. **"Orthotropic" directions of the interface.**

$[U] = U^+ - U^- = [U_1]N_1 + [U_2]N_2 + [U_3]N_3$ denotes the difference in displacements between the upper and lower surfaces of the "3D interface". Thus, at the first order, the strain energy is:

$$E_D \approx \frac{1}{2} e \int_{\tilde{A}} \frac{[U]^T}{e} \mathbf{H} \frac{[U]}{e} d\tilde{A} \tag{18}$$

where Γ is the area of the mid-plane interface, and $\mathbf{H}$ is a (3,3) symmetrical matrix. For the 2D interface model, $[U]$ is the displacement discontinuity between two adjacent layers. We assume that the bisectors (N_1 and N_2) of the angle formed by the fiber directions of the adjacent plies are orthotropic directions. The interface material model is built following the same approach used for deriving the single-layer model. The effect of the deterioration of the interlaminar connection is taken into account by means of internal damage variables. The behaviors in "tension" and in "compression" are distinguished by splitting the strain energy into a "tension energy" and a "compression energy".

More precisely, we use the following expression for the energy per unit area:

$$E_D = \frac{1}{2}\int_{\Gamma}\left[\frac{\langle -\sigma_{33}\rangle^2}{k_3^0} + \frac{\langle \sigma_{33}\rangle^2}{k_3^0(1-d_3)} + \frac{\sigma_{13}^2}{k_1^0(1-d_1)} + \frac{\sigma_{23}^2}{k_2^0(1-d_2)}\right]d\Gamma \qquad (19)$$

Three internal damage indicators, associated with the three Fracture Mechanics modes, are thereby introduced.

Damage evolution laws of the interface. These evolution laws must satisfy the Clausius-Duheim inequality. Classically, the damage forces, associated with the dissipated energy ω, are introduced as follows:

$$Y_{d_3} = \frac{1}{2}\frac{\langle \sigma_{33}\rangle^2}{k_3^0(1-d_3)^2}; Y_{d_1} = \frac{1}{2}\frac{\sigma_{31}^2}{k_1^0(1-d_1)^2}; Y_{d_2} = \frac{1}{2}\frac{\sigma_{32}^2}{k_2^0(1-d_2)^2} \qquad (20)$$

with $\omega = Y_{d_3}d_3 + Y_{d_1}d_1 + Y_{d_2}d_2 \ (\omega \geq 0)$.

The damage evolution laws used in this study are based on the assumption that the evolutions of the various damage indicators are strongly coupled and driven by a unique equivalent damage force. The following model considers that the damage evolution is governed by means of the following equivalent damage force:

$$\begin{aligned} Y(t) &\equiv \left[\left(Y_{d_3}^{\alpha} + \left(\gamma_1 Y_{d_1}\right)^{\alpha} + \left(\gamma_2 Y_{d_2}\right)^{\alpha}\right)^{1/\alpha}\right] \\ \underline{Y}_{|t} &\equiv \sup_{\tau \leq t} Y_{|\tau} \end{aligned} \qquad (21)$$

where γ_1, γ_2 and α are material parameters. In terms of delamination modes, the first term is associated with the first opening mode, and the two others are associated with the second and

third modes. A damage evolution law is then defined by the choice of a material function W, such that:

$$W(\underline{Y}) = \left[\frac{n}{n+1}\frac{\langle \underline{Y} - Y_0 \rangle_+}{Y_C - Y_0}\right]^n \tag{22}$$

where a critical value Y_C and a threshold value Y_0 are introduced. A high value of n corresponds to a brittle interface. For small damage rates, one obtains:
$d_3 = d_1 = d_2 \approx W(\underline{Y})$ if $d < 1$; $d_3 = d_1 = d_2 = 1$ otherwise.

In the general case, a damage model with delay effects is used:

$$\begin{aligned} &\delta = d_3 = d_1 = d_2 = \frac{1}{\tau_c'}\left[1 - \exp\left(-a'\langle W(Y) - \delta \rangle\right)\right] \text{ if } \delta < 1 \\ &\delta = d_3 = d_1 = d_2 = 1 \text{ otherwise} \end{aligned} \tag{23}$$

To summarize, the damage evolution law is defined, except for τ_C' and a', by means of six intrinsic material parameters $Y_C, Y_0, \gamma_1, \gamma_2, \alpha$ and n. The threshold value Y_0 is introduced here in order to expand the possibility of describing both the initiation of a delamination crack and its propagation. As regards the initiation of a delamination crack, the significant parameters are Y_0, n and α. It will be shown hereafter that Y_C, γ_1, γ_2 and α are related to the critical damage forces.

Identification of the interface model's material constants. A simple way to identify the various material constants is by comparing the mechanical dissipation yielded by our damage mechanics approach and classical linear fracture mechanics; classical delamination tests are used (see Daudeville and Ladevèze, 1993, and Allix *et al.*, 1998). One main result reported in Ladevèze *et al.* (1998) is that the interface parameters seem to be independent of θ for all $\pm\theta$ interfaces with $\theta \neq 0°$ (see Table 1). Let us also note that the (0°/0°) interface appears to be something artificial. However, such an "artificial" interface can be introduced, for example, to describe a crack inside a thick layer. It should also be pointed out that the same model is applicable for both delamination propagation and delamination initiation.

0°/0°	:	$Y_c = 0,1$ N/mm, $\gamma_1 = \gamma_2 = 0,35$, $\alpha = 2$
$\pm\theta$	:	$Y_c = 0,18$ N/mm, $\gamma_1 = \gamma_2 = 0,35$, $\alpha = 1$

Table 1. Interface model parameters.

Remarks:

- γ_1 *and* γ_2 characterize the ratio between interface toughness in mode II and mode I, and mode III and mode I, respectively. Until now, we have taken practically: $\gamma_1 = \gamma_2$. The α value can be different from 2; its value is identified from the measured interface toughness for combined delamination modes. Interface material parameters have been characterized in Daudeville and Ladevèze (1993) and Allix *et al.* (1998). τ_C' and a' could be identified using pressure-shear impact test (see Espinoza, 1995); however, they do not play an important role for fracture prediction in most engineering quasi-static situations.
- The different damage indicators must be equal for the completely destroyed zones; their value is one. It follows that to define same damage rate for modes I, II and III is very convenient for calculation; it means that the interface damage state is characterized by a scalar state internal variable. However, a model with different damage rate for modes I, II and III is given in Allix and Ladevèze (1992) and Ladevèze (1992, 1995).

3.3 Objective Prediction of Final Fracture

An important issue is the objective prediction of final fracture which is rather well-understood nowadays. It is well known that classical damage models are non-consistent. A visible lack is the abnormal sensitivity to the mesh of the finite element solution. Several remedies have been proposed, in particular:

- non local damage model (see Bazant and Pijaudier-Cabot, 1988)
- second-gradient regularization (see Belytschko and Lasry, 1988, and Slyuis and De Borst, 1992)
- rate dependent damage model (see Needleman, 1988, and Loret and Prevost, 1990).

Here, we have followed a specific approach to laminate composites introduced in Ladevèze (1989, 1992). It is prescribed that the damage state is piecewise constant in the thickness of the laminate. Moreover, as a complement, we use damage models with delay effect combined with a dynamic analysis. Further developments can be found in Ladevèze (1992, 1995) and Ladevèze *et al.* (2000).

3.4 An Illustration

Several calculations done with the mesomodel are presented in the special issue (see Allix and Johnson, 2004). Here, it is shown that the damage mesomodel predicts the response of a composite structure in dynamics until its ultimate fracture. This response is computed using the explicit dynamic code LS-DYNA3D. Figure 17 defines the studied structure and its loading. It is a $[+ 22.5°, - 22.5°]_s$ holed laminated plate; the material is a SiC/MAS-L composite with silicon carbide fibers and a glass matrix made by EADS. The fiber stiffness (200 GPa) is higher than the matrix stiffness (75 GPa), and cracks first appear in the matrix. Let us note that reasonable values have been chosen for the material constants of the interlaminar interface model.

In particular, the values of the critical times τ_c and τ'_c and the constants a and a' are:

$$\begin{aligned} \tau_c &= \tau'_c = 2\,10^{-6}\mathrm{s} \\ a &= a' = 1 \end{aligned} \tag{24}$$

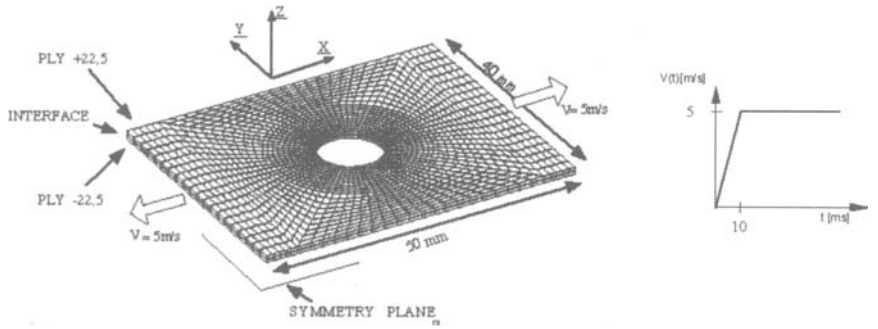

Figure 17. **Holed laminate submitted to dynamic tension loading.**

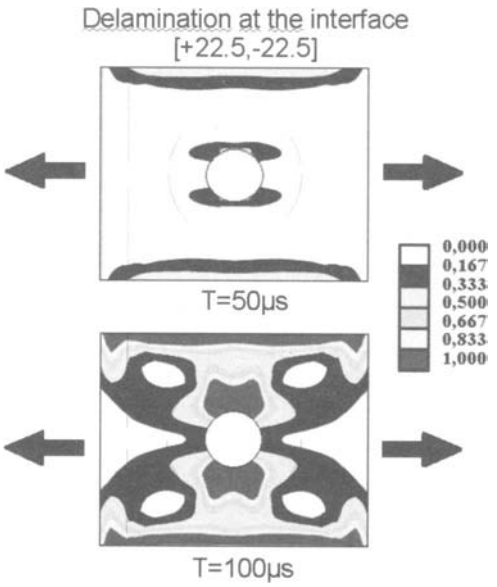

Figure 18. **Interface damage map at several times.**

Several computations have been performed especially for the stacking sequence $[n0°]_S$. These reasonable constant values correspond to a fracture zone size whose order of magnitude corresponds to the ply's thickness. Figure 18 reveals the degradation of the [± 22.5°] interface; the dark area represents the completely destroyed zone and then the delamination crack. Figures 19 and 20 present the microcracking intensity maps and the fiber-direction damage maps at different times. It is clear that a transverse crack orthogonal to the fibers appears and then grows inside each ply. One can consider that the final fracture occurs around t = 100 is ; the size of the transverse cracks is about 2 mm. Last, the global load versus the prescribed displacement is plotted in Figure 21. No particular numerical difficulty with respect to time discretization and mesh sensitivity has appeared.

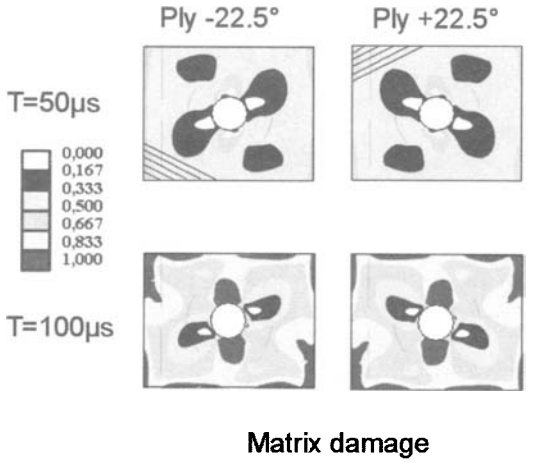

Figure 19. **Shear damage maps for the plies at several times.**

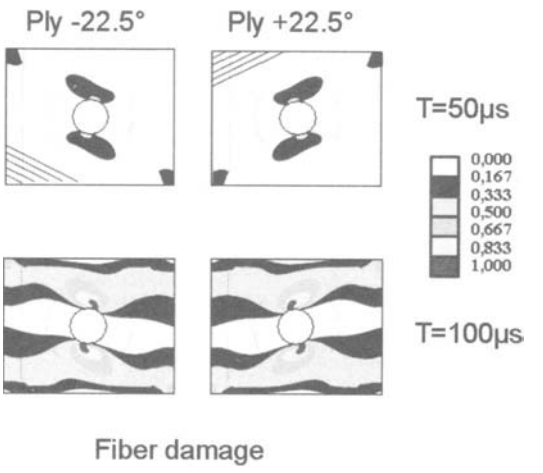

Figure 20. **Longitudinal damage maps for the plies at several times.**

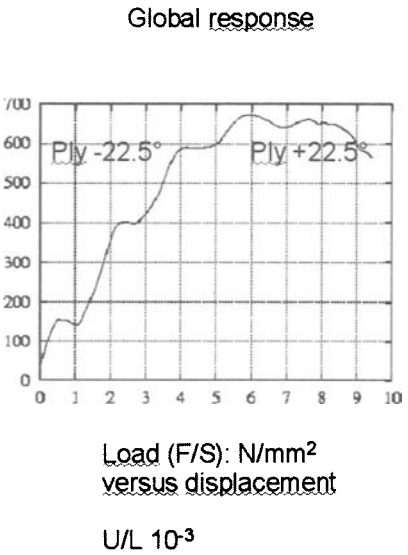

Figure 21. **Global load versus the prescribed displacement.**

3.5 Concluding Remarks

The laminate mesomodel proposed herein is able to compute the intensities of the damage mechanisms inside both the plies and the interfaces at any time, until final fracture; the main limitation for severe dynamic loadings is that the dynamic wavelength has to be larger than the thickness of the plies. Simulations have shown the macrocracks' initiation and propagation. Comparisons with experimental results have proved to be satisfactory; however, a better agreement could be welcome for delamination prediction.

4 A Bridge Between the Micro- and Mesomechanics of Laminates

A rather complete bridge has been built in Ladevèze and Lubineau (2001, 2002) and Ladevèze *et al.* (2004).

4.1 The Method to Bridge

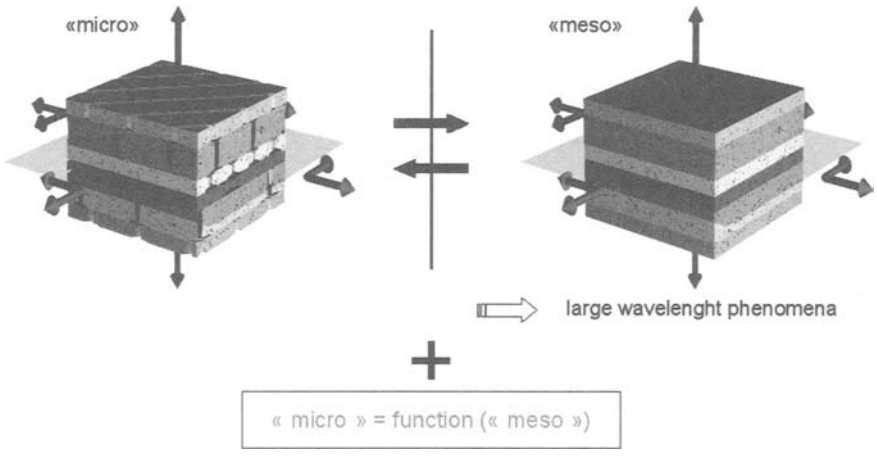

Figure 22. **The two-scale computational scheme.**

Figure 22 describes the used two-scale computational scheme. At the left, the real structure submitted to a given loading is defined at the "microscale". It is made with the fiber-matrix material and there are crack, delamination and transverse ones. The problem to solve is clearly a two-scale one, and then the solution consists in two parts: the large wavelength part for which the characteristic length is the structure dimension and the small wavelength part which has a characteristic length equal to the ply thickness.

A classical scheme to solve this two-scale problem is to separate the calculation of the two parts. In a first step, one determines the large wavelength part solving the so-called homogenized problem where the real structure is replaced by the homogenized structure. Its solution defines the mesoquantities. In a second step, the microquantities that make the small wavelength part of the solution are determined in term of the mesoquantities.

This approach is applied to two basic problems which represent all engineering situations: the ply basic problem and the interface basic problem. They are defined Figures 23 and 24. Periodic conditions and elastic behavior are prescribed. The upper and lower parts of the studied cell are homogenized.

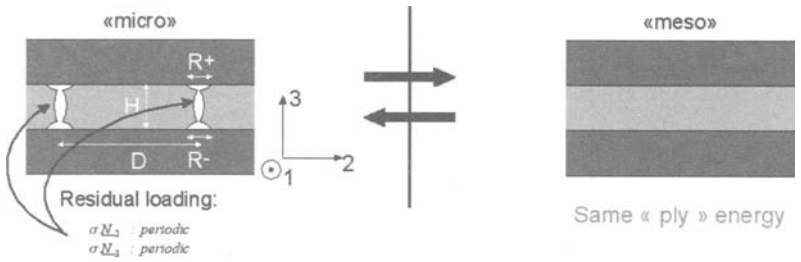

Figure 23. **The ply basic problem.**

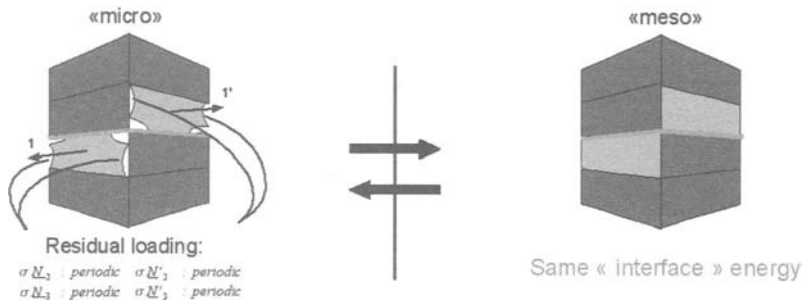

Figure 24. **The interface basic problem.**

As classically, the solution of the homogenized problem is built first (see Figure 25). For the real structure, this solution needs to be corrected; the residuals associated with discontinuities have to be equilibrated.

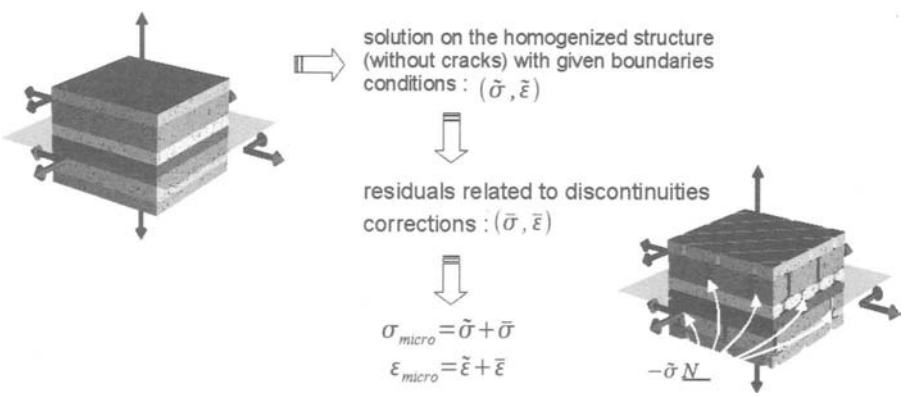

Figure 25. **To solve the "micro" problem.**

It is supposed that the wavelength of the homogenized problem is smaller or of the same order of the ply thickness. It follows that the residuals can be considered as locally uniform. Another interesting property comes from the fact that the resultant and the moment of each residual are zero-value; according to Saint-Venant's principle, corrections are relatively local.

The equivalence should hold for any value of the residual which can be written in term of mesoquantities. The fundamental micro-meso link which defines the so-called homogenized structure holds exactly for the two basic problems; it could be written:

$$\forall \Gamma \quad \Pi\!\!\!\text{æ}_{meso}\, \Pi\!\!\!\Pi = < \Pi\!\!\!\text{æ}_{micro}\, \Pi\!\!\!\Pi > \qquad \text{ϖ}_{meso}\, \underline{N}_3 = < \text{ϖ}_{micro}\, \underline{N}_3 > \tag{25}$$

where $< \cdot > \equiv \frac{1}{mes\ \Gamma} \int_{\Gamma} \cdot\, dS$.

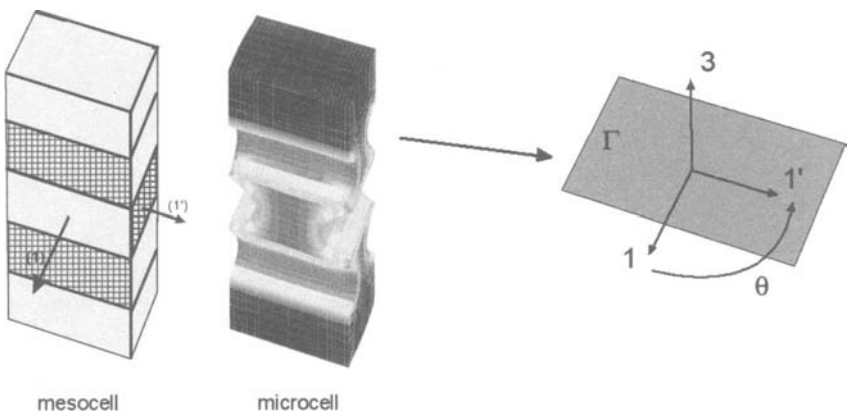

Figure 26. **Fundamental micro-meso link – the cell for the interface basic problem.**

Γ is any cross-section orthogonal to $\underline{N}_3$ and compatible to the periodicity associated to the layer or interface containing Γ. Practically for large crack densities, Γ could be replaced by any large cross-section with respect to the plate thickness. $\Pi\!\!\!\Pi$ is the projector on the plane orthogonal to $\underline{N}_3$.

4.2 The Solving of the Microproblem

The solving of the microproblem has been a major issue in micromechanics; quasi-analytical approximations have been derived (see Hashin, 1985, Nairn, 1989, Aboudi *et al.*, 1988, Nuismer and Tan, 1988, Zhang *et al.*, 1992, McCartney, 1992, 2000, Schoeppner and Pagano, 1998, Varna *et al.*, 1992, Berthelot *et al.*, 1996, Selvarathinam and Weitsman, 1999...) Such approximations have been quite interesting for a better understanding of laminate behavior but they have some

limits which are displayed in Figure 27. It computs three stacking sequences which follow three very close curve microcracking rate/transverse mesodamage; using Hashin approximation, one gets three different curves and consequently, one loses a remarkable property. It is why we follow here another calculation method which is in fact a functional analysis: the solution is first determined in term of material operators which depend on the microdamage variables and the different additional parameters. After that, these operators are computed for all the values of parameters and microdamage variables (practical range: $\rho \in [0, 0.7] \tau \in [0, 0.4]$). Consequently, a very large amount of calculations have been performed.

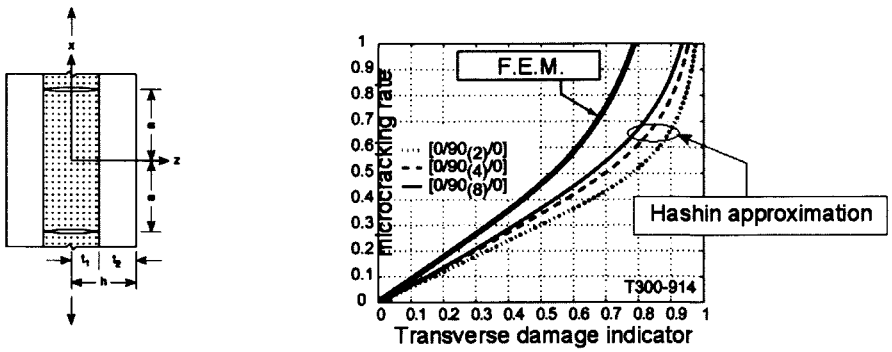

Figure 27. **Limit of quasi-analytical calculation.**

4.3 Virtual Testing Dealing With the Ply

The ply basic problem. The mesoenergy of the cracked ply can be written:

$$e_{meso}(\varepsilon_{meso}, \underline{\underline{N}}_3) = \frac{1}{2} T_r[\mathbf{H}\varepsilon_{meso}\varepsilon_{meso}]$$

$$+ \frac{1}{2} \underline{\underline{N}}_3 \cdot \mathbf{A}\underline{\underline{N}}_3 + \underline{\underline{N}}_3 \cdot \mathbf{B}\varepsilon_{meso} \tag{26}$$

where **H**, **A**, **B** depend on the microdamage variables and the parameters of the upper and lower parts.

Numerically, it has been proved:

Fundamental property:

The operators **H**, **A**, **B** are quasi-intrinsic homogenized operators. They do not depend practically on the parameters of the upper and lower parts. An illustration is given Figure 28 for two coefficients, the mesodamages d_{22} and d_{33}.

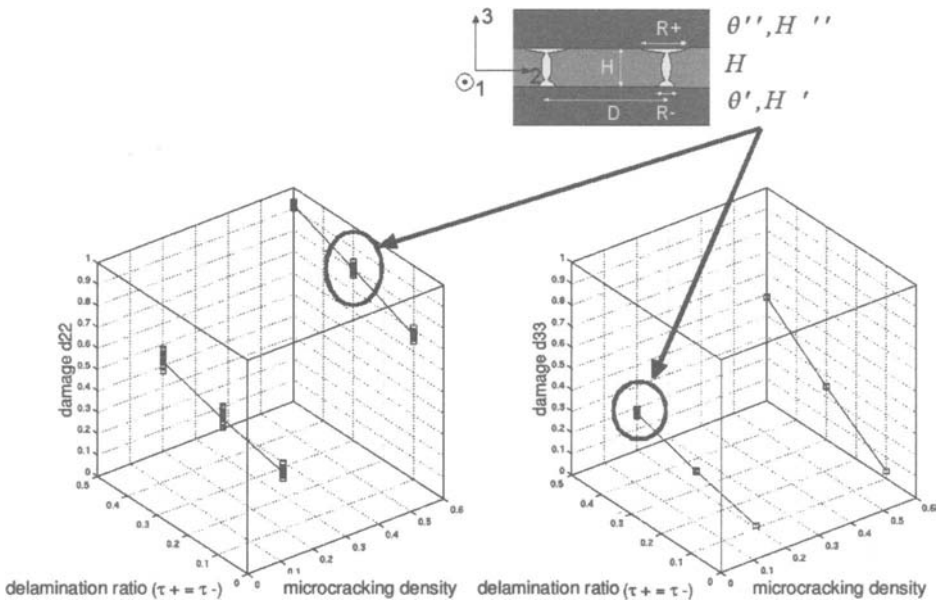

Figure 28. **Mesodamages d_{22} and d_{33} in term of parameters for different values of the microdamage variables.**

Additional results:

The mesoenergy has the following remarkable expression:

$$e_{meso}(\text{Πæ}_{meso}\text{Π},\varpi_{meso}\underline{N}_3) - e^{0}_{meso} =$$

$$-\frac{1}{2}\left[\frac{d_{22}}{1-d_{22}}\frac{{\sigma_{22}}^2}{E_2^0}+\frac{d_{12}}{1-d_{12}}\frac{{\sigma_{12}}^2}{G_{12}^0}\right] \tag{27}$$

$$-\frac{1}{2}\left[\frac{d_{33}}{1-d_{33}}\frac{{\sigma_{33}}^2}{E_3^0}+\text{Π}\varpi\,\underline{N}_3\,.\,\text{C}\text{Π}\varpi\,\underline{N}_3\right]$$

All stresses involved are mesoquantities; moreover, the mesodamage variables d_{22}, d_{12}, d_{33} and $\mathbf{C}$ which is diagonal can be computed in a very simple way in terms of the microdamage variables:

$$d_{ij}(\rho,\tau^+,\tau^-) = f_{ij}(\rho,\tau^+) + f_{ij}(\rho,\tau^-) \tag{28}$$

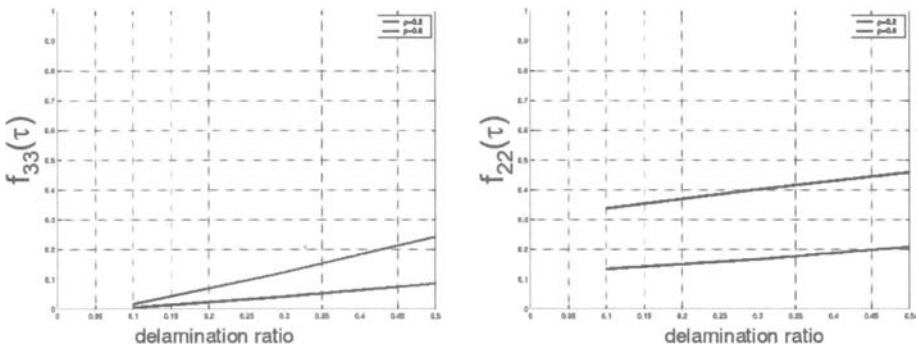

Figure 29. **Functions f_{22} and f_{33} related to the ply basic problem.**

The extended ply basic problem.

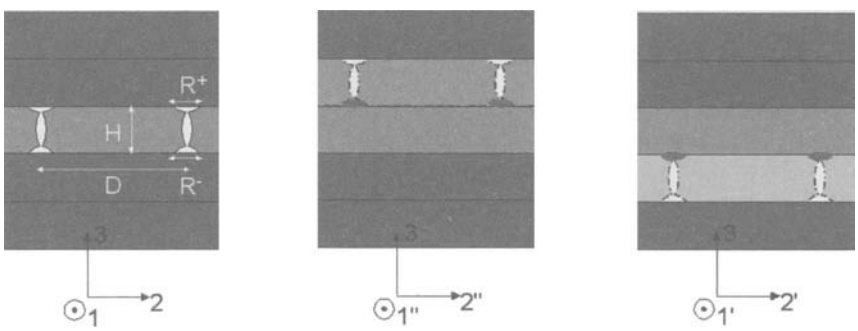

$$\lambda = \frac{R}{D}, \rho = \frac{H}{D}, \tau = \frac{R}{H}$$

Figure 30. **The extended ply basic problem.**

From calculations, it follows that:

Fundamental property:

The damage mesomodel of the ply is quasi-intrinsic to the ply and its adjacent interfaces. Its mesodamage variables are defined in term of the microdamage variables of the ply and its adjacent interfaces.

Additional result:

The damages d_{22} and d_{12} for the ply i depend on $\rho_i, \tau_i^+, \tau_i^-$.

Remarks:

Such results allow an easy calculation of the ply mesomodel. Let us note that it is easy to introduce the different behaviors due to the closure and the opening of microcracks. For example, in the left member of the Equation (27), σ_{22} and σ_{33} should be replaced by $\langle\sigma_{22}\rangle_+$ and $\langle\sigma_{33}\rangle_+$.

4.4 Virtual Testing Dealing With the Interface

The interface basic problem is a 3D one with the following microdamage variables:

- transverse microcracking rates: $\rho = H/D, \rho' = H'/D'$
- local delamination rates:

$$\tau^+ = R^+/H, \tau^- = R^-/H, \tau'^+ = R'^+/H', \tau'^- = R'^-/H'$$

- total delamination ratio: $\lambda = \text{delaminated area}/\text{total area}$.

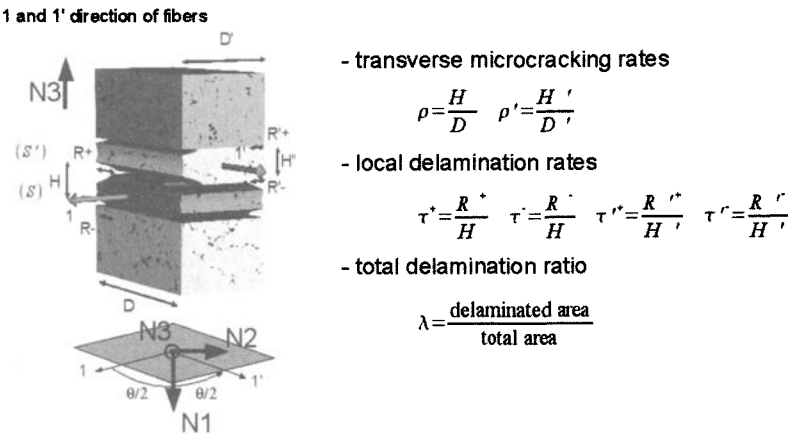

Figure 31. **The interface basic problem and its parameters.**

The interface is only active under out-of-the plane loading. The mesoenergy can be written:

$$E_{meso}(\varpi_{meso}\underline{N}_3)=\frac{1}{2}\varpi_{meso}\underline{N}_3\cdot\mathbf{D}\varpi_{meso}\underline{N}_3 \tag{29}$$

where **D** is a positive definite symmetric operator which depends on the microdamage variables and the parameters of the upper and lower parts. This expression has to be compared with the expression of our previous interface damage mesomodel:

$$E_{meso}(\ddot{\varpi}_{meso}\underline{N}_3)=\frac{1}{2}\left[\frac{\sigma_{33}{}^2}{(1-D_{33})k_3^0}+\frac{\sigma_{13}{}^2}{(1-D_{13})k_1^0}+\frac{\sigma_{23}{}^2}{(1-D_{23})k_2^0}\right] \tag{30}$$

where D_{33}, D_{13}, D_{23} are associated to the delamination modes I, II, III. Numerically, it has been proved:

Fundamental property:

The operator **D** does not depend practically on the parameters of the lower and upper parts. The interface mesomodel does depend on the interface and its adjacent plies. Illustrations of this property are given Figures 32 and 33.

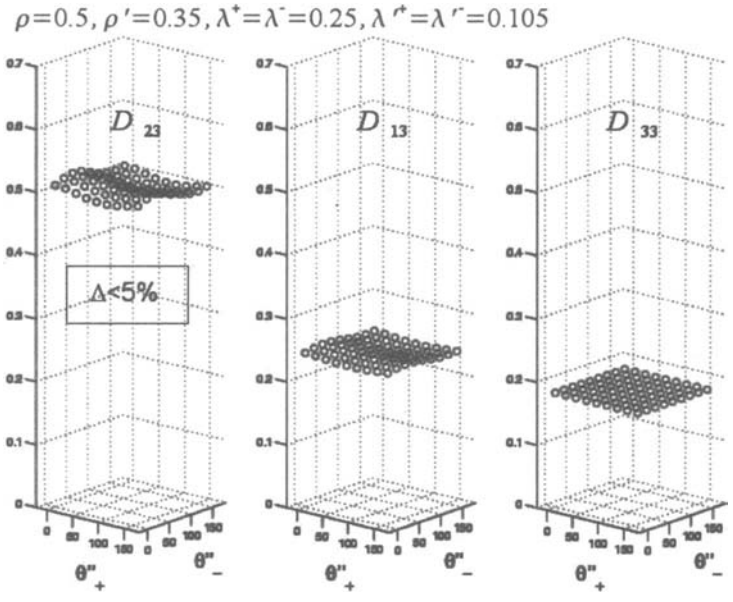

Figure 32. **Mesodamage variables in term of orientation parameters of the upper and lower parts.**

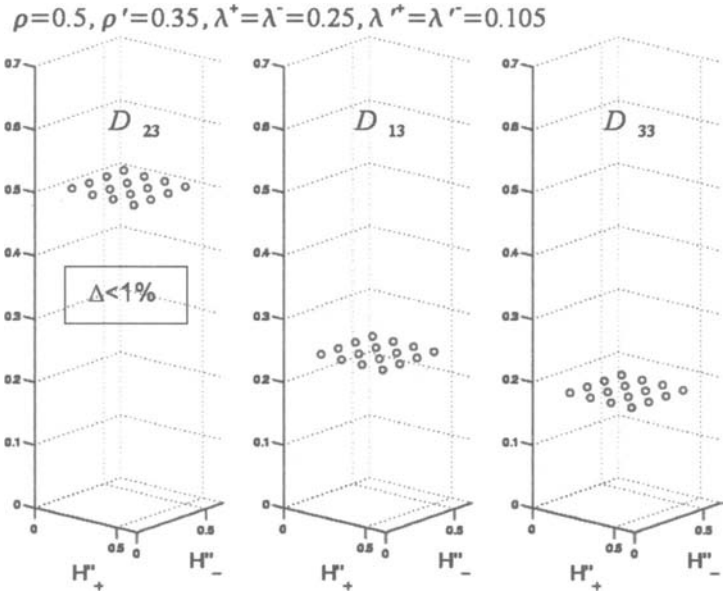

Figure 33. **Mesodamage variables in term of thicknesses of the upper and lower parts.**

Additional results:

The mesodamage D_{33} related to the opening delamination mode (mode I) does depend only on the total delamination ratio (see Figure 34). Figure 35 shows the other mesodamages D_{13} and D_{23} associated to modes II and III when orthotropic conditions are prescribed; it quantifies the interaction between intra and interlaminar mesodamages.

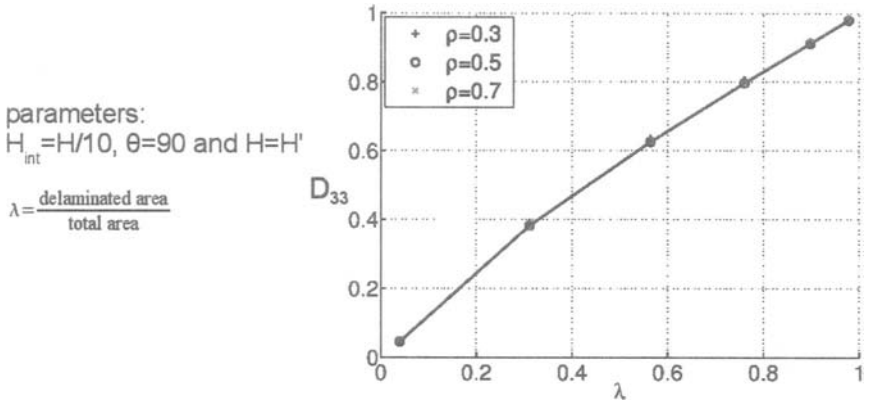

Figure 34. **Mesodamage D_{33} of the interface in term of the total delamination ratio for different values of microcracking rates.**

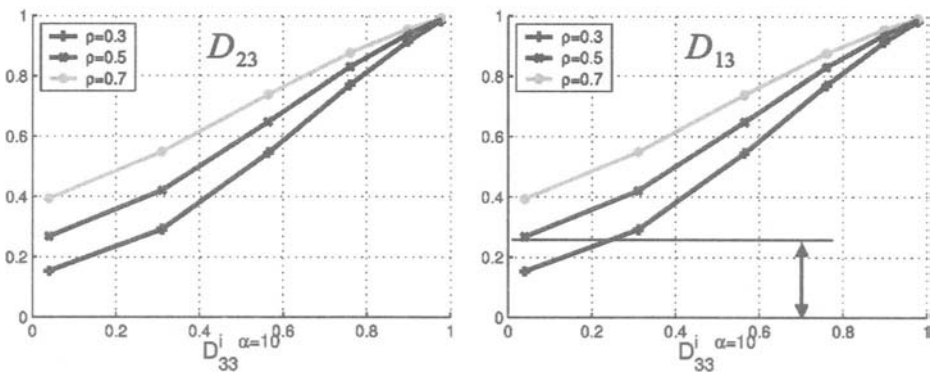

Figure 35. **Interface mesodamages D_{13} and D_{23} related to modes II and III.**

Remarks:

Through calculations, it is relatively easy to build the interface mesomodel. Let us note that a good approximation could be obtained by solving two 2D-problems similar to the ply basic problem.

It is also relatively easy to introduce the different behaviors due to the closure and the opening of the delamination microcracks by considering that the cracks are shut when the meso-stress σ_{33} is negative and that the normal stiffness then remains the initial one.

5 Perspectives to Damage Computation

Two computational approaches could be distinguished:

- an enhanced damage mesomodel
- a computational damage micromodel of laminates.

5.1 An Enhanced Damage Mesomodel

Engineering calculations with the standard mesomodel. An example of a 3D finite element computation is presented in order to demonstrate the ability of the damage mesomodel to predict the response of a composite structure in dynamics until its ultimate fracture (see Paragraph 3.5).

Other engineering examples can be found in Allix and Johnson (2004). They show that the standard mesomodel is a pragmatic and efficient model for engineering problems but it should be improved:

- to get a better coupling between ply-microcracking and delamination
- to get a better answer to Edge Delamination Tension tests.

The enhanced versions. Firstly, the progress lies in the enhancement of the delamination prediction by considering a nonlocal interface damage mesomodel which takes into account the damage of adjacent plies. Another application of the bridge that we have built is the use of micro-meso relations for describing damage in terms of micromechanics.

A first open question is to come back to the identification process by using micro- and macro-information. A further step is to develop the true mesomodel which is nonlocal not only for the interface but also for the ply mesomodel.

5.2 A Computational Damage Micromodel of Laminate

Basic aspects. One starts with the initial state where residual stresses occur which can be calculated from the process simulation. A more pragmatic and standard approach is simply to introduce a uniform negative variation of temperature and then the corresponding residual stresses calculated in elasticity.

At the microscale, the structure is described as an assembly of layers and interfaces which could be cracked; the layers being made with the fiber-matrix material. A hybrid modelling is proposed. The fiber-matrix material is described following the classical continuum mechanics framework and the cracked surfaces follow a discrete model by introducing "minimum cracked surfaces". This enters in what is called "Finite Fracture Mechanics" (see Hashin, 1996).

Modelling of the fiber-matrix material. Here, we follow the mesomodel limited to Scenarios 3 and 4. The Scenarios 1 and 2 which appear through thresholds are not included. Therefore we describe the diffuse damage in plies and interface through a model which includes damage and (visco)plasticity.

Modelling of delamination and microcracking. One introduces minimum cracked surfaces, the characteristic length being the thickness of the elementary ply (see Figure 36).

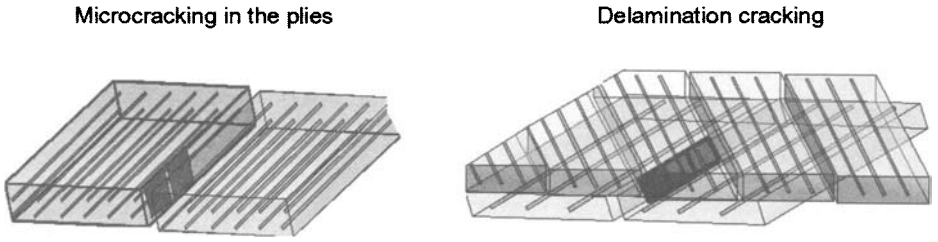

Figure 36. **Minimum cracked surfaces.**

• Initiation criterion of transverse microcracks

$$Y^{\mathrm{I}}_{\mathrm{initiation}} = \begin{cases} h \le \bar{h} & G^{\mathrm{I}} \\ h \ge \bar{h} & G^{\mathrm{I}} \dfrac{\bar{h}}{h} \end{cases}$$

$$Y^{\mathrm{II,\,III}}_{\mathrm{initiation}} = \begin{cases} h \le \bar{h} & G^{\mathrm{II,\,III}} \\ h \ge \bar{h} & G^{\mathrm{II,\,III}} \dfrac{\bar{h}}{h} \end{cases} \tag{31}$$

$$\left[\frac{Y^{\mathrm{I}}_{\mathrm{initiation}}}{G^{\mathrm{I}}_{c}}\right]^{\alpha} + \left[\frac{Y^{\mathrm{II,\,III}}_{\mathrm{initiation}}}{G^{\mathrm{II,\,III}}_{c}}\right]^{\alpha} \ge 1 \tag{32}$$

• Propagation criterion of existing transverse microcracks

$$\left[\frac{G^{\mathrm{I}}}{G^{\mathrm{I}}_{c}}\right]^{\alpha} + \left[\frac{G^{\mathrm{II,\,III}}}{G^{\mathrm{II,\,III}}_{c}}\right]^{\alpha} \ge 1 \tag{33}$$

• Delamination cracking

$$\left[\frac{G_{\text{del}}^{\text{I}}}{G_c^{\text{I}'}}\right]^{\alpha'} + \left[\frac{G_{\text{del}}^{\text{II, III}}}{G_c^{\text{II, III}'}}\right]^{\alpha'} \geq 1 \tag{34}$$

• Fiber breaking

It is supposed brittle. A minimum volume to fracture is introduced: a cube of height h. So, we have:

$$\begin{aligned} \langle \varepsilon_{11} \rangle &\geq 0 \quad {}_{l_T(\langle Y_f \rangle, \langle Y_d \rangle) \geq 1} \\ \langle \varepsilon_{11} \rangle &\leq 0 \quad {}_{l_c(\langle Y_f \rangle, \langle Y_d \rangle) \geq 1} \end{aligned} \tag{35}$$

$\langle \cdot \rangle$ denotes the mean value over the cube of height h. l_T and l_C define the criteria for traction and compression.

• Complements

When an elementary surface is cracked, unilateral contact conditions with friction occur. The critical values G_c, G_c' are stochastic fields for which we suppose that the correlation length is not larger than the thickness h. Then, after discretization, they could be replaced by independent stochastic variables for which a modified normal law is introduced.

• Remarks

The energy release rate related to microcracking could be computed simply by using the tunneling value. More generally, the computation of the different energy release rates could be vastly simplified by using analytical expressions.

Numerical difficulties. Let us consider as an example the low velocity impact problem defined Figure 37.

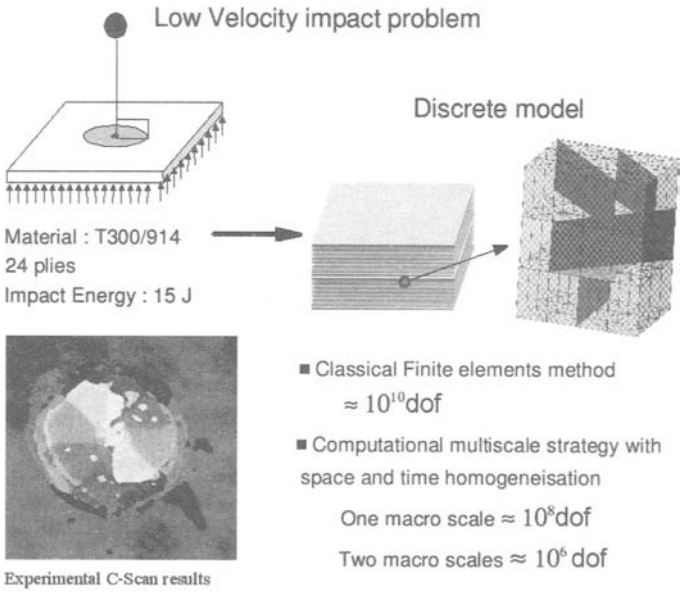

Figure 37. **A low velocity impact problem.**

A reasonable mesh for the classical finite element method leads to 2.10^{10} degrees of freedom! A research challenge is then to derive alternative computational strategies capable of solving such engineering problems. This is a hot topic named "multiscale computational strategies including uncertainties". Several answers have already been given (see Fish *et al.*, 1997, Zohdi, 1998, Oden *et al.*, 1999, Feyel, 2003, Geers *et al.*, 2003, Ghosh, 1995, Ladevèze *et al.*, 2001, Ladevèze and Nouy, 2003...)

Following Ladevèze and Nouy (2003), one gets with two scales: 4.10^8 degrees of freedom. To get reasonable calculations, it is necessary to introduce one more scale, a macro one; one has 10^6 ddls.

6 Conclusion

Let us come back to the central question discussed in this paper: does a bridge exist between the micro- and the mesomechanics of laminates?

The answer is positive but the mesomechanics of laminates is not so simple, it is nonlocal.

Applications of the bridge which has been built are computational approaches for final fracture prediction, the most promising approach being the computational micromodel of laminates. To become true engineering tools, further researches, especially in computational mechanics, are needed.

References

Aboudi, L., Lee, S. W., and Herakowich, C. T. (1988). Three dimensional analysis of laminates with cross cracks. *ASME J. Appl. Mech.* 55: 389-397.

Allen, D. H., Groves, S. E., and Harris, C. E. (1988). A cumulative damage model for continuous fiber composite laminates with matrix cracking and interply delaminations. In Withcomb, J. D., ed., *Composite Materials: Testing and Design*. ASTM STP 972, Washington, DC, USA.. 57-80.

Allix, O. (1992). Damage analysis of delamination around a hole. In Ladevèze, P., and Zienkiewicz, O. C., eds., *New Advances in Computational Structural Mechanics*, Elsevier Science Publishers B. V. 411-421.

Allix, O. (2002). Interface damage mechanics: application to delamination. In Allix, O., and Hild, F., eds., *Continuum Damage Mechanics of Materials and Structures*, Elsevier. 295-324.

Allix, O., Bahlouli, N., Cluzel, N., and Perret, C. (1996). Modelling and identification of temperature-dependent mechanical behavior of the elementary ply in carbon/epoxy laminates. *Comp. Sci. Techn.* 56: 883-888.

Allix, O., and Deü, J. F. (1997). Delay-damage modeling for fracture prediction of laminated composites under dynamic loading. *Engineering Transactions* 45: 29-46.

Allix, O., Guedra-Degeorges, D., Guinard, S., and Vinet, A. (1999). 3D analysis applied to low-energy impacts on composite laminates. In Masard, T., and Vautrin, A., eds., *Proceedings ICCM12T*. 282-283.

Allix, O., and Johnson, A. (1992). Interlaminar interface modelling for the prediction of laminate delamination. *Comp. Sci. Techn.*

Allix, O., and Ladevèze, P. (2004). Advances in the statics and dynamics of delamination – Special issue. *Composite Structures* 22: 235-242.

Allix, O., Ladevèze, P., and Vitecoq, E. (1994). Modelling and identification of the mechanical behaviour of composite laminates in compression. *Comp. Sci. Techn.* 51: 35-42.

Allix, O., Lévêque, D., and Perret, L. (1998). Interlaminar interface model identification and forecast of delamination in composite laminates. *Comp. Sci. Techn.* 56: 671-678.

Bazant, Z., and Pijaudier-Cabot, G. (1988). Non local damage: continuum model and localisation instability. *J. Appl. Mech.* 287-294.

Belytschko, T., and Lasry, D. (1988). *Localisation limiters and numerical strategies softening materials*. In Mazars, J., and Bazant, Z. P., eds., Amsterdam: Elsevier. 349-362.

Berthelot, J. M.0 (2003). Transverse cracking and delamination in cross-ply glass-fiber and carbon-fiber renforced plastic laminates: static and fatigue loading. *Appl. Mech. Rev.* 56(1): 1-37.

Berthelot, J. M., and Le Corre, J. F. (2000). Statistical analysis of the progression of transverse cracking and delamination in cross-ply laminates. *Comp. Sci. Techn.* 60: 2659-2669.

Berthelot, J. M., Leblond, P., El Mahi, A., and Le Corre, J. F. (1996). Transverse cracking of cross-ply laminates, Part 1: Analysis. *Composites*. 27A: 989-1001.

Boniface, L., Smith, P., Bader, M., and Rezaifard, A. (1997). Transverse ply cracking in cross-ply CFRP laminates – Initiation or propagation controlled ? *J. Comp. Materials*. 31: 1080-1112.

Crossman, F. W., and Wang, A. S. D. (1982). The dependence of transverse cracking and delamination on ply thickness in graphite/epoxy laminates. In Reisnider, K. L., ed., *Damage in Composite Materials*, ASTM STP 775. 118-139.

Daudeville, L., and Ladevèze, P. (1993). A damage mechanics tool for laminate delamination. *Composite Structures*. 25: 547-555.

Devries, F., Dumontet, H., Duvaut, G., and Léné, F. (1989). Homogenization and damage for composite structures. *Int. J. for Numerical Methods in Engineering*. 27: 285-298.

Dvorak, G. J., and Laws, N. (1987). Analysis of progressive matrix cracking in composite laminates, II. First ply failure. *J. Comp. Materials*. 21: 309-329.

Espinoza, H. D. (1995). On the dynamic shear resistance of ceramic composites and its dependence on applied multiaxial deformation. *Int. J. Solids and Structures*. 3105-3128.

Feyel, F. (2003). A multilevel finite element method (FE^2) to describe the response of highly non-linear structures using generalized continua. *Comput. Meth. Appl. Mech. Engrg.* 192: 3233-3244.

Fish, J., Sheck, K., Pandheeradi, M., and Shepard, M. S. (1997). Computational plasticity for composite structures based on mathematical homogenization: theory and practice. *Comput. Meth. Appl. Mech. Engrg.* 148: 53-73.

Fukunaga, H., Chou, T. W., Peters, P. W. M., and Schulte, K. (1984). Probabilistic failure strength analyses of graphite/epoxy cross-ply laminates. *J. Comp. Materials*. 18: 339-356.

Garrett, K. W., and Bailey, J. E. (1977). Multiple transverse fracture in 90° cross-ply laminates of a glass fiber reinforced polyester. *J. Mater. Sci.* 12: 157-168.

Geers, M., Kouznetsova, V., and Brekelmans, W. (2003). Multiscale first-order and second-order computational homogenization of microstructures towards continua. *Int. J. for Multiscale Computational Engineering*. 1(4): 371-386.

Ghosh, S., Lee, K., and Moorthy, S. (1995). Multiple scale analysis of heterogeneous elastic structures using homogenization theory and Voronoï cell finite element method. *J. Solids Structures*. 32(1): 27-62.

Gudmunson, P., and Zang, W. (1993). An analytical model for thermoelastic properties of composite laminates containing transverse matrix cracks. *Int. J. Solids Structures*. 30: 3211-3231.

Guild, F. J., Ogin, S. L., and Smith, P. A. (1993). Modelling of 90° ply cracking in cross ply laminates, including three-dimensional effects. *J. Comp. Materials*. 27: 646-667.

Hashemi, S., Kinloch, A., and Williams, J. (1990). Mechanics and mechanisms of delamination in a poly(ether sulphone)-fiber composite. *Comp. Sci. Techn.* 37: 429-462.

Hashin, Z. (1985). Analysis of cracked laminates: a variational approach. *Mech. Mater.* 4: 121-136.

Hashin, Z. (1985). Analysis of orthogonally cracked laminates under tension. *ASME J. Appl. Mech.* 4: 121-136.

Hashin, Z. (1996). Finite thermoelastic fracture criterion with application to laminate cracking analysis. *J. Mech. Phys. Solids*. 44(7): 1129-1145.

Herakovich, C. (1998). *Mechanics of Fibrous Composites*, J. Wiley, ed.

Highsmith, A. L., and Reifsnider, K. L. (1982). Stiffness reduction mechanisms in composite laminates. In Reisnider, K. L., ed., *Damage in Composite Materials*, ASTM STP 775. 103-117.

Kouznetsova, V., Geers, M. G. D., and Brekelmans, W. A. M. (2003). Multiscale constitutive modelling of heterogeneous materials with a gradient-enhanced computational homogenization scheme. *Int. J. for Numerical Methods in Engineering*. 54: 1235-1260.

Ladevèze, P. (1983). On an anisotropic damage theory. In Boehler, J. P., ed., *Failure Criteria of Structured Media*, Report n° 34-LMT-Cachan, Balkema. 355-364.

Ladevèze, P. (1986). About the damage mechanics of composites. In Bathias, C., and Menkés, D., eds., *Comptes-Rendus des JNC5*, Paris: Pluralis Publication. 667-683.

Ladevèze, P. (1989). About a damage mechanics approach. In *Mechanics and Mechanisms of Damage in Composite and Multimaterials*, MEP. 119-142.

Ladevèze, P. (1992). A damage computational method for composite structures. *J. Computer and Structure*. 44(1/2): 79-87.

Ladevèze, P. (1995). A damage computational approach for composites: Basic aspects and micromechanical relations. *Comput. Mech.* 8: 142-150.

Ladevèze, P. (2000). Modelling and computation until final fracture of laminate composites. In Cardon, A. H., *et al.*, eds., *Recent Developments in Durability Analysis of Composite Systems*, Balkema. 39-47.

Ladevèze, P., Allix, O., Deü, J. F., and Lévêque, D. (2000). A mesomodel for localisation and damage computation in laminates. *Comput. Meth. Appl. Mech. Engrg.* 1832: 105-122.

Ladevèze, P., Allix, O., Gornet, L., Lévêque, D., and Perret, L. (1998). A computational damage mechanics approach for laminates: Identification and comparison with experimental results. In Voyiadjis, G. Z., Wu, J. W., and Chaboche, J. L., eds., *Damage Mechanics in Engineering Materials*, Amsterdam: Elsevier. 481-500.

Ladevèze, P., and Le Dantec, E. (1992). Damage modeling of the elementary ply for laminated composites. *Comp. Sci. Techn.* 43(3): 257-267.

Ladevèze, P., Loiseau, O., and Dureisseix, D. (2001). A micro-macro and parallel computational strategy for highly heterogeneous structures. *Int. J. for Numerical Methods in Engineering*. 52: 121-138.

Ladevèze, P., and Lubineau, G. (2001). On a damage mesomodel for laminates: micro-meso relationships, possibilities and limits. *Comp. Sci. Techn.* 61(15): 2149-2158.

Ladevèze, P., and Lubineau, G. (2001). On a damage mesomodel for laminates: micromechanics basis and improvement. *Mech. Materials*. 35: 763-775.

Ladevèze, P., and Lubineau, G. (2002). An enhanced mesomodel for laminates based on micromechanics. *Comp. Sci. Techn.* 62: 533-541.

Ladevèze, P., Lubineau, G., and Marsal, D. (2004). Towards a bridge between the micro- and the mesomechanics of delamination for laminated composites. *Comp. Sci. Techn.* Manuscript submitted for publication.

Ladevèze, P., and Nouy, A. (2003). On a multiscale computational strategy with time and space homogenization for structural mechanics. *Comput. Meth. Appl. Mech. Engrg.* 192: 3061-3087.

Lagattu, F., and Lafarie-Frénot, M. (2000). Variation of PEEK matrix crystallinity in APC-2 composite subjected to large shearing deformation. *Comp. Sci. Techn.* 60: 605-612.

Laws, N., and Dvorak, G. J. (1988). Progressive transverse cracking in composite laminates. *J. Comp. Marerials*. 22: 900-916.

Li, D. S., and Wisnom, M. (1997). Evaluating Weibull parameters for transverse cracking in cross-ply laminates. *J. Comp. Materials*. 31(9): 935-951.

Loret, B., and Prevost, J. H. (1990). Dynamic strain localization in elasto- (visco-)plastic solids, Part 1. General formulation and one-dimensional examples. *Comput. Meth. Appl. Mech. Engrg.* 83: 247-273.

Manders, P. W., Chou, T. W., Jones, F. R., and Rock, J. W. (1983). Statistical analysis of multiple fracture in 0°/90°/0° glass fiber/epoxy resin laminates. *J. Mater. Sci.* 8: 352-362.

Masters, J. E., and Reifsnider, K. L. (1982). An investigation of cumulative damage development in quasi-isotropic graphite/epoxy laminates. In *Damage in Composite Materials*, ASTM STP 77. 40-62.

McCartney, L. N. (1992). Theory of stress transfer in a 0°-90°-0° cross-ply laminate containing a parallel array of transverse cracks. *J. Mech. Phys. Solids*. 40: 27-68.

McCartney, L. N. (2000). Model to predict effects of triaxial loading on ply cracking in general symmetric laminates. *Comp. Sci. Techn.* 60: 2255-2279.

McCartney, L. N., Schoeppner, G. A., and Becker, W. (2000). Comparison of models for transverse ply cracks in composite laminates. *Comp. Sci. Techn.* 60: 2347-2359.

Nairn, J. A. (1989). The strain energy release rate of composite microcracking: a variational approach. *J. Comp. Materials*. 23: 1106-1129.

Nairn, J. A., and Hu, S. (1992). The initiation and growth of delaminations induced by matrix microcracks in laminated composites. *Int. J. Fract.* 57: 1-24.

Nairn, J. A., and Hu, S. (1994). Micromechanics of damage: a case study of matrix cracking. In Talreja, R., ed., *Damage Mechanics of Composite Materials*, Amsterdam: Elsevier. 187-243.

Nairn, J., Hu, S., and Bark, J. (1993). A critical evaluation of theories for predicting microcracking in composite laminates. *J. Materials Science*. 28: 5099-5111.

Needleman, A. (1988). Material rate dependence and mesh sensitivity in localization problems. *Comput. Meth. Appl. Mech. Engrg.* 67: 69-85.

Nuismer, R. J., and Tan, S. C. (1988). Constitutive relations of a cracked composite lamina. *J. Comp. Materials*. 22: 306-321.

Oden, J., Vemaganti, K., and Moes, N. (1999). Hierarchical modelling of heterogeneous solids. *Comput. Meth. Appl. Mech. Engrg.* 172: 2-25.

Ogin, S. L., Smith, P. A., and Beaumont, P. W. R. (1985). Matrix cracking and stiffness reduction during the fatigue of a $(0/90)_S$ GFRP laminate. *Comp. Sci. Techn.* 22: 23-31.

Pagano, N., Schoeppner, G., Kim, R., and Abrams, F. (1998). Steady-state cracking and edge effect in thermo-mechanical transverse cracking of cross-ply laminates. *Comp. Sci. Techn.* 58: 1811-1825.

Parvizi, A., Garrett, K. W., and Bailey, J. E. (1978). Constrained cracking in glass fiber-reinforced epoxy cross-ply laminates. *J. Mater. Sci.* 13: 195-201.

Renard, J., and Jeggy, T. (1989). Modélisation de la fissuration transverse dans les matériaux composites carbone/résine. In *Groupe de Réflexion sur l'Endommagement*, Cetim, Senlis.

Schoeppner, G., and Pagano, N. (1998). Stress fields and energy release rates in cross-ply laminates. *Int. J. Solids and Structures*. 35(11): 1025-1055.

Selvarathimam, A., and Weitsman, J. (1999). A shear-lag analysis of transverse cracking and delamination in cross-ply carbon-fiber/epoxy composites under dry, saturated and immersed fatigue conditions. *Comp. Sci. Techn.* 59: 2115-2123.

Slyuis, L. J., and De Borst, R. (1992). Wave propagation and localisation in a rate-dependent cracked medium: Model formulation and one dimensional examples. *Int. J. Solids and Structures*. 29: 2945-2958.

Takeda, N., and Ogihara, S. (1994). Initiation and growth of delamination from the tips of transverse cracks in CFRP cross-ply laminates. *Comp. Sci. Techn.* 52: 309-318.

Talreja, R. (1980). Stiffness based fatigue damage characterization of fibrous composites. In Bunsell, A. R., *et al.*, eds., *Advances in Composite Materials*, Oxford: Pergamon Press. 2: 1732-1739.

Talreja, R. (1985). Transverse cracking and stiffness reduction in composite laminates. *J. Comp. Materials*. 19: 355-375.

Tong, J., Guild, F. J., Ogin, S. L., and Smith, P. A. (1997). On matrix crack growth in quasi-isotropic laminates, I. Experimental investigations. *Comp. Sci. Techn.* 57: 1527-1535.

Varna, J., and Berglund, L. A. (1992). A model for prediction of the transverse cracking strain in crosss-ply laminates. *J. Reinf. Plast. Comp.* 11: 708-728.

Wang, A. S. D., Chou, P. C., and Lei, S. (1984). A stochastic model for the growth of matrix cracks in composite laminates. *J. Comp. Materials*. 18: 239-254.

Wang, A. S. D., and Crossman, F. W. (1980). Initiation and growth of transverse cracks and edge delamination in composite laminates, Part 1: An energy method. *J. Comp. Materials*. 14: 71-87.

Yahvac, S., Yats, L., and Wetters, D. (1991). Transverse ply cracking in toughened and untoughened graphite/epoxy and graphite/polycyanate cross-ply laminates. *J. Comp. Materials*. 25: 1653-1667.

Yang, T., Liu, Y., and Wang, J. (2003). A study of the propagation of an embedded crack in a composite laminate of finite thickness. *Composite Structures*. 59: 473-479.

Zhang, J., Fan, J., and Soutis, C. (1992). Analysis of multiple matrix cracking in $[\pm 0_m/90_n]$ composite laminates, *Composites*, 23: 291-298.

Zohdi, T. I., Oden, J. T., and Rodin, G. J. (1996). Hierarchical modeling of heterogeneous bodies. *Comput. Meth. Appl. Mech. Engrg.* 155: 181-192.

Damage Modelling at Material Interfaces

Marcin Białas and Zenon Mróz
Institute of Fundamental Technological Research
Polish Academy of Sciences, Warsaw, Poland

Abstract. Interface damage and delamination is usually accompanied by frictional slip at contacting interfaces under compressive normal stress. Under tensile stress the separation and opening mode develops. The present study provides a simplified analysis of progressive interface failure under applied in plane tractions and normal compressive traction. The cohesive crack model is used to simulate damage frictional traction present at contact. Both monotonic and cyclic loadings are considered for an elastic plate bonded to a rigid substrate by means of cohesive interface. The analysis of progressive delamination process revealed three solution types, namely short, medium and long plate solutions. For cyclic loading the states of frictional slip accompanied by shake down or incremental failure are distinguished. The finite element solutions confirm the validity of simplified analysis. The thermal loading case is studied separately under monotonic and cyclic temperature loading history. The cracking of plate is now accompanied by frictional slip and progressive delamination of the interface layer. The analysis predicts the cracking pattern and the size of delaminated zones.

1 Introduction

The propagation of interlayer cracks and the resulting failure of the interface is one of more important modes occurring in composite materials, rocks and ceramics. A detailed survey of research in this area can be found, for instance, in the article by Hutchinson and Suo (1991) who discussed mixed mode crack propagation using the Griffith energy condition. A promising approach to analyse interface failure seems to be the concept of a cohesive zone assumed ahead of crack tip at the interfacial region. It follows the pioneering works by Barenblatt (1962) and Dugdale (1960) and so far has been used by numerous researchers in investigating crack growth, *cf.* for instance, Ortiz (1996), Hillerborg et al. (1976), Yang and Ravi-Chandar (1997). The asperity interaction modes at cracked interfaces and associated effects were studied in some papers, *cf.* Gross and Mendelsohn (1989), Bennison and Lawn (1989), Evans and Hutchinson (1989). The analysis of asperity models and the effects of interface micro-dilatancy in problems of fiber pulling or pushing was presented by Mróz and Stupkiewicz (1995). However, the effects of interface friction have not yet been fully investigated. In general, several major topics should be considered, namely, formulation of slip and wear rules at the delaminated interface portions, damage zone evolution rules and also localized temperature effects due to cyclic slip and interface dissipation. In fact, the coupled phenomena occur at the interface such

as wear and damage growth, frictional slip and localized temperature effects, asperities crushing or flattening with the associated dilatancy phenomena.

The interface failure can be closely related to segmentation cracking of structures having large surface area subjected to axial strains. Both segmentation and delamination processes can be distinguished as failure modes in thin films technologies, when a film is attached to a thick substrate. The segmentation cracking can result in delamination phenomena, since there are new damaged zones created at the interface in the vicinity of every segmentation crack, leading to a potential slip mechanism. On the other hand, delamination can reduce the risk of potential segmentation. Both cracking and delamination resistance has to be considered in practical applications in a way that a proper balance between these two factors is maintained.

The segmentation and delamination failure is related to systems of either macro and micro scale. Crack development within concrete structures occurring as a result of drying shrinkage or thermal cyclic loading is often observed in engineering practice. In many cases the cracks are formed in structures having either one dimension dominant with respect to the others or when a large surface area is subjected to tension. Failure can be a consequence of either external temperature loading changing in time, or of internal material shrinkage driven by drying or concrete production process, both influencing crack patterns, their development in time and opening gap. Due to the production process, concrete is first subjected to tension stresses owing to drying shrinkage. In order to protect the material from potential failure, reinforcement in the form of randomly distributed steel fibers is needed. If their resistance is not sufficient to compensate tension stresses, a fragmentation occurs which can lead to functional or structural failure. In addition to the drying shrinkage, concrete is also subjected to environmental loading. Daily and seasonal temperature changes play a dominant role as a crack development factor.

It is often observed that uniformly spaced longitudinal cracks are normal to the direction of applied axial strain. The so called thermal cracks can also propagate in asphalt pavements on a granular base, extending across the width of the pavement (Timm et al. (2003), Hiltunen and Roque (1994)) and allowing for infiltration of water leading to structure deterioration. They usually appear as a consequence of a sudden temperature drop causing excessive tension in a pavement system.

Although thermal cracking of pavements is related to large scale systems, the same mechanical modelling can be applied to thin film coatings attached to metal substrates (Shieu et al. (1990), Agrawal and Raj (1989, 1990), Chen et al. (2000), Xia and Hutchinson (2000),. Baker et al. (2002)). When subjected to temperature loading and tension stresses, cracks typically develop within a coating before actual failure of substrate. After initiation they propagate through a film thickness and upon reaching coating-substrate interface several failure mechanisms can follow: cracks enter the substrate material (Chung and Pon (2001), Zhang and Zhao (2002), Chi and Chung (2003)), deviate and propagate along the coating-substrate interface (Nairn and Kim (1992), Kokini and Takeuchi (1998), Erdem Alaca et al. (2002)) or remain arrested. In this particular case new cracks may form during the course of loading (Kim and Nairn (2000a,b), Schulze and Erdogan (1998)). It has been observed that the crack density initially increases and then stabilizes at a constant value, unaffected by further loading (Agrawal and Raj (1989, 1990)).

Fragmentation of thin brittle coatings seem to be well suited to examine the interaction between elastic properties of solids and statistical aspect of failure phenomena. It is obvious that crack formation is strongly dependent upon the existence of randomly distributed microcraks that promote failure. These issues have been addressed in the papers by Handge et al. (2000, 2001), accounting for stochastical effects in multiple cracking.

The present work is aimed at analytical solutions of damage growth at the interface between an elastic plate and a rigid foundation, assuming compressive normal traction acting on the interface. A cohesive zone is assumed ahead of crack tip and an influence of various softening constitutive relations for the bond is analysed. Both mechanical or temperature loadings are assumed, the former leading to delamination process, the latter related to plate segmentation and delamination. The states of frictional slip accompanied by shake down or incremental failure are distinguished in the case of cyclic loading, related to the load amplitude and structural dimensions. With regard to monotonic loadings, the analysis clarifies the character of instability points, occurring due to interaction of damaged zone with the boundary and can serve as a reference solution for more complex cases.

2 Problem Formulation

Consider a plate resting on a rigid foundation as schematically presented in Figure 1. The plate is bonded to the foundation by a thin interface layer of thickness much smaller than the plate thickness. The upper plate surface is acted on by surface tractions $\boldsymbol{t}$ inducing compressive normal stresses at contact interface. The edge traction $\boldsymbol{T}$ may induce three modes of delamination or their combination, namely opening, longitudinal and transverse shear modes, analogous to fundamental modes in fracture mechanics. Assuming the plate thickness to be small as compared to its other dimensions, its response may be described within linear elasticity equations and the interaction tractions of the bonding interface can be treated as in-plane body forces acting on the plate. If there is no opening mode at the interface, the plate deformation state can be described by assuming plane stress conditions.

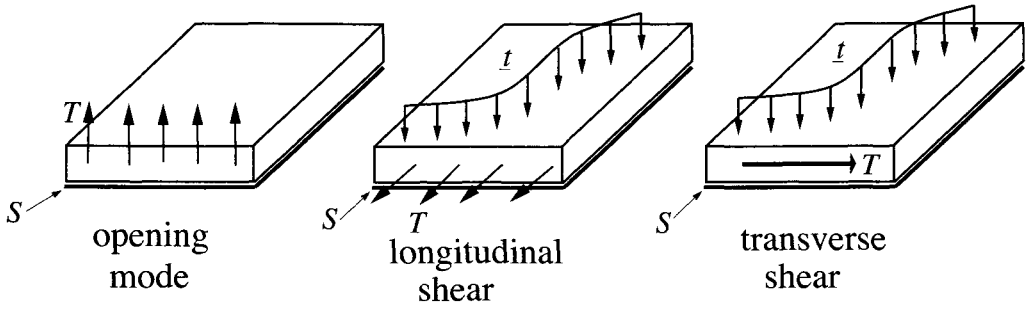

Figure 1. Basic modes of delamination.

By assuming that there is a frictional contact at the interface between the plate and the substrate governed by the Coulomb's law, the traction $\boldsymbol{t}$ normal to the upper

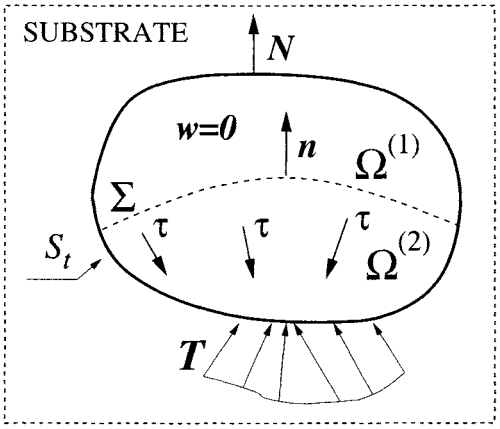

Figure 2. A plate in plane stress condition resting on a rigid substrate.

plate surface induces the frictional stress having the magnitude $|\boldsymbol{\tau}| = \mu|\boldsymbol{t}|$. The friction stress direction remains unknown. When a rigid-frictional interface is assumed, we have two zones developed at the interface, namely $\Omega^{(1)}$, where the structure is fully bonded and $\Omega^{(2)}$, where the bond is damaged and there is a frictional contact. Let Σ denote the delamination front between regions $\Omega^{(1)}$ and $\Omega^{(2)}$, as schematically presented in Figure 2. The displacement field $\boldsymbol{w}$ has to be continuous across Σ:

$$\lceil \boldsymbol{w} \rfloor = \boldsymbol{0}, \tag{2.1}$$

where $\lceil m(\boldsymbol{x}) \rfloor = m(\boldsymbol{x}^+) - m(\boldsymbol{x}^-)$, $\boldsymbol{x} \in \Sigma$ is the discontinuity of function $m(\boldsymbol{x})$ across Σ ($\boldsymbol{x}^+ = \boldsymbol{x}^-$, $\boldsymbol{x}^+ \in \Omega^{(1)}$, $\boldsymbol{x}^- \in \Omega^{(2)}$). On the other hand, for a rigid-frictional interface there is discontinuous switch of shear stresses at the interface across the boundary Σ:

$$\lceil \boldsymbol{\tau n} \rfloor \neq \boldsymbol{0}, \tag{2.2}$$

where $\boldsymbol{n}$ is a unit vector pointing into $\Omega^{(1)}$ and normal to the delamination front.

The time derivative of condition (2.1) provides a relation between the velocity field $\boldsymbol{v} = \dot{\boldsymbol{w}} = \partial \boldsymbol{w}/\partial t$ and the discontinuity of displacement gradient across Σ:

$$\lceil \dot{\boldsymbol{w}} \rfloor + v_n \lceil (\nabla \boldsymbol{w}) \cdot \boldsymbol{n} \rfloor = \boldsymbol{0}, \tag{2.3}$$

where v_n is the velocity of delamination front. The frictional tractions at the interface can be treated as in-plane body forces, so the equation of equilibrium takes the form:

$$\mathrm{Div}\tilde{\boldsymbol{\sigma}} + \boldsymbol{\tau} = \boldsymbol{0}, \tag{2.4}$$

with $\tilde{\sigma}_{ij} = t\sigma_{ij}$ $(i, j = 1, 2)$ being a stress tensor in the plane stress case. The interfacial frictional tractions satisfy the Coulomb's law:

$$\begin{array}{lll} |\boldsymbol{\tau}| \leq \mu|\boldsymbol{t}| & & \text{for } |\dot{\boldsymbol{w}}| = 0, \\ |\boldsymbol{\tau}| = \mu|\boldsymbol{t}|, \qquad \boldsymbol{\tau}/|\boldsymbol{\tau}| = \dot{\boldsymbol{w}}/|\dot{\boldsymbol{w}}| & & \text{for } |\dot{\boldsymbol{w}}| > 0. \end{array} \tag{2.5}$$

The boundary conditions on S_t are

$$\tilde{\boldsymbol{\sigma}}\boldsymbol{N} = \boldsymbol{T}, \tag{2.6}$$

where $\boldsymbol{N}$ is the unit normal vector to S_t. Additional boundary conditions on the delamination front Σ are provided by Equations (2.1) and (2.3) and have the form:

$$\lceil \boldsymbol{w} \rfloor = \boldsymbol{0} \qquad \lceil \dot{\boldsymbol{w}} \rfloor = -v_n \lceil (\nabla \boldsymbol{w}) \cdot \boldsymbol{n} \rfloor. \tag{2.7}$$

To fully formulate the delamination process for an elastic plate bonded to a rigid substrate, we define the strain rate tensor $\dot{\boldsymbol{\varepsilon}}$:

$$\dot{\boldsymbol{\varepsilon}} = \frac{1}{2}(\nabla \dot{\boldsymbol{w}} + \nabla^T \dot{\boldsymbol{w}}) \tag{2.8}$$

and the linear constitutive equation for the plate material:

$$\dot{\tilde{\boldsymbol{\sigma}}} = \boldsymbol{C}\dot{\boldsymbol{\varepsilon}}, \tag{2.9}$$

where $\boldsymbol{C}$ is the elastic tensor.

The rate of dissipated energy is a difference between the rate of work done on the system by external forces $\boldsymbol{T}$ and the rate of change of elastic energy:

$$\dot{D} = \int_{S_t} \boldsymbol{T} \cdot \dot{\boldsymbol{w}} \mathrm{d}S - \frac{\mathrm{d}}{\mathrm{d}t} \int_{\Omega^{(2)}} U(\boldsymbol{\varepsilon}) \mathrm{d}\Omega, \tag{2.10}$$

where $U(\boldsymbol{\varepsilon}) = \frac{1}{2}\boldsymbol{\varepsilon}\boldsymbol{C}\boldsymbol{\varepsilon}$ is the specific elastic energy per unit volume. The time derivative of the total elastic energy can be rewritten in the form:

$$\frac{\mathrm{d}}{\mathrm{d}t} \int_{\Omega^{(2)}} U(\boldsymbol{\varepsilon}) \mathrm{d}\Omega = \int_{\Omega^{(2)}} \tilde{\boldsymbol{\sigma}} \cdot \dot{\boldsymbol{\varepsilon}} \mathrm{d}\Omega + \int_{\Sigma} U(\boldsymbol{\varepsilon}) v_n \mathrm{d}\Sigma, \tag{2.11}$$

where the fact, that the delamination front Σ changes with time and propagates during the loading process has been used to derive the second term on the right side of above equation. By substituting (2.4), (2.6), (2.7) and (2.11) into Equation (2.10) and making use of Gauss theorem, we can write the formula for the rate of dissipated energy

$$D = \int_{\Omega^{(2)}} \boldsymbol{\tau} \cdot \dot{\boldsymbol{u}} \mathrm{d}\Omega + \int_{\Sigma} [(\tilde{\boldsymbol{\sigma}}\boldsymbol{n}) \cdot (\nabla \boldsymbol{u} \cdot \boldsymbol{n}) - U(\boldsymbol{\varepsilon})] v_n \mathrm{d}\Sigma. \tag{2.12}$$

The first term in the above equation refers to frictional dissipation at the interface, the second is related to the energy dissipated at the delamination front.

In the present paper, the bonding layer will be treated as an elastic-plastic interface for which the response is expressed in terms of contact stress components and the conjugate displacement discontinuities. As the substrate is assumed as rigid, the plate displacement field at the interface represents the displacement discontinuity for the interface. The constitutive equations for the interface will be referred to elastic, elastic-plastic and frictional slip regimes. We shall now discuss these relations in more detail.

2.1 Constitutive Relations for the Interface

Considering an interface S, we neglect the in-plane stress components and express the deformation response in terms of the interface traction components σ_n, τ_l, τ_m, where

$$\sigma = \boldsymbol{i}_n \cdot \boldsymbol{\sigma} \boldsymbol{i}_n, \qquad \tau_l = \boldsymbol{i}_l \cdot \boldsymbol{\sigma} \boldsymbol{i}_n, \qquad \tau_m = \boldsymbol{i}_m \cdot \boldsymbol{\sigma} \boldsymbol{i}_n \tag{2.13}$$

and $\boldsymbol{i}_n$ is the unit normal vector to S, $\boldsymbol{i}_l$ and $\boldsymbol{i}_m$ are the unit vectors within the S, forming the orthonormal basis. The displacement discontinuity vector $\boldsymbol{\delta}$ on S can also be decomposed into normal and tangential components δ_n, δ_l and δ_m. The total displacement discontinuity and its rate are decomposed into elastic and slip components, thus:

$$\boldsymbol{\delta} = \boldsymbol{\delta}^e + \boldsymbol{\delta}^s, \qquad \dot{\boldsymbol{\delta}} = \dot{\boldsymbol{\delta}}^e + \dot{\boldsymbol{\delta}}^s. \tag{2.14}$$

The constitutive equations relating the interface tractions and the reversible part of displacement discontinuity are of the form:

$$\dot{\sigma} = K_n \dot{\delta}_n^e, \quad \dot{\tau}_l = K_t \dot{\delta}_l^e, \quad \dot{\tau}_m = K_t \dot{\delta}_m^e, \tag{2.15}$$

where K_n and K_t is an interfacial stiffness respectively in tension and shear. The irreversible part of displacement discontinuity is related to the failure process at the interface and expressed in the framework of theory of plasticity by an evolution of failure function F. The proposed failure function has the form:

$$F(\sigma, \tau) = \begin{cases} \tau + \mu\sigma - \tau_c(\delta_e) \leq 0 & \text{for } \sigma < 0 \\ \sqrt{\left(\frac{\tau_c^0}{\sigma_c^0}\right)^2 \sigma^2 + \tau^2} - \tau_c(\delta_e) \leq 0 & \text{for } \sigma \geq 0, \end{cases} \tag{2.16}$$

where:

$$\tau = \sqrt{\tau_l^2 + \tau_m^2},$$

μ is a friction coefficient and $\tau_c(\delta_e)$ the critical shear stress for $\sigma = 0$. The failure parameter δ_e is defined as

$$\delta_e = \int_0^t \sqrt{(\dot{\delta}_t^s)^2 + M^2(\dot{\delta}_n^s)^2} \mathrm{d}\bar{t} \qquad \dot{\delta}_t^s = \sqrt{(\dot{\delta}_l^s)^2 + (\dot{\delta}_m^s)^2}, \tag{2.17}$$

where M is a material constant expressing the influence of opening mode on failure evolution.

Thus, for the compressive traction acting at the interface we have the Coulomb friction law relating the shear and normal stresses, whereas for tension the damage surface is an ellipse. The function F is presented in Figure 3.

The assumed slip potential is of the form:

$$G(\sigma, \tau) = \begin{cases} \tau - \tau_c(\delta_e) & \text{for } \sigma < 0 \\ \sqrt{\left(\frac{\tau_c^0}{\sigma_c^0}\right)^2 \sigma^2 + \tau^2} - \tau_c(\delta_e) & \text{for } \sigma \geq 0. \end{cases} \tag{2.18}$$

Thus, we have an associated flow rule for positive normal stresses and non-associated flow rule for interface subjected to compression. The reason for doing that is to neglect

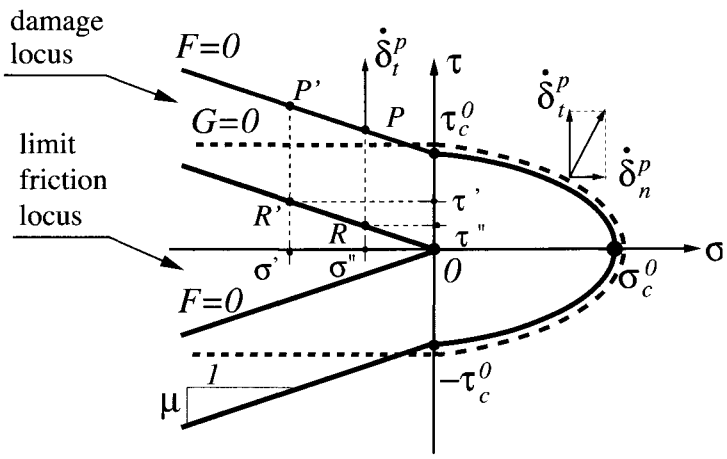

Figure 3. Yield function F and plastic potential G.

the contact dilatancy. It should be noted, that the slip rule remains continuous when the normal stress σ changes sign, though the damage function F has a slope discontinuity for $\sigma = 0$, see Figure 3.

The sliding rule has a form:

$$\dot{\delta}_t^{\,s} = \dot{\lambda}\frac{\partial G}{\partial \tau}, \qquad \dot{\delta}_n^{\,s} = \dot{\lambda}\frac{\partial G}{\partial \sigma}, \qquad F \leq 0, \qquad \dot{\lambda}F = 0, \tag{2.19}$$

where $\dot{\lambda}$ is a positive slip multiplier.

The evolution equation expresses the failure development at the interface and relates the increasing separation $\boldsymbol{\delta}^s$ with the vanishing interfacial traction. In the present study, the linearly decreasing function has been assumed:

$$\tau_c(\delta_e) = \begin{cases} \tau_c^0 - K_r\delta_e, & \delta_e < \frac{\tau_c^0}{K_\delta} \\ 0, & \delta_e \geq \frac{\tau_c^0}{K_r} \end{cases} \tag{2.20}$$

For $\tau_c^0 = 0$ we have only elastic-frictional contact with no stress softening and subsequently the failure function does not evolve in $\{\sigma, \tau\}$ space. For $K_n = K_t \to \infty$ one can neglect the elasticity of interface layer and obtain rigid-softening-friction or rigid-friction interface models.

In the case of monotonically varying shear loading and constant compressive normal traction $\sigma = \text{const}$, Equations (2.19) can be integrated in order to provide the total slip displacement:

$$\delta_t^s = \lambda\frac{\partial G}{\partial \tau} = \lambda, \qquad F^f \leq 0, \qquad \lambda F^f = 0. \tag{2.21}$$

However, when unloading and reverse slip occurs, the memory of the previous slip displacement must be stored and added to the reverse slip displacement. Figure 4(a)

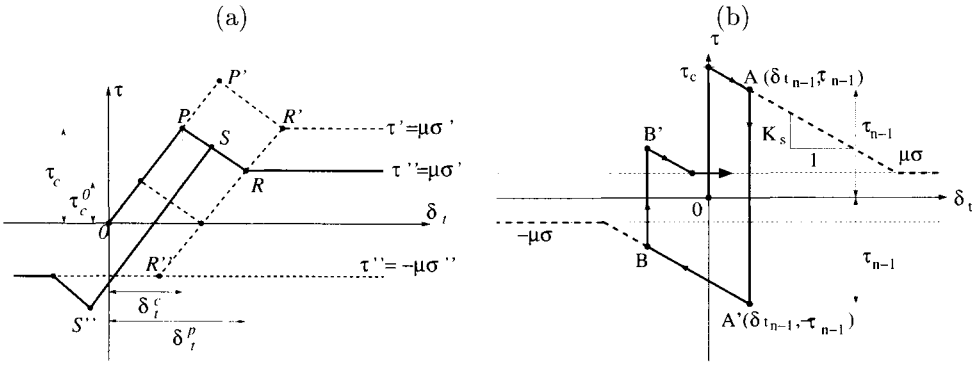

Figure 4. (a) Stress – displacement response for elastic-plastic layer under constant compressive normal stress. (b) Stress – displacement response for rigid-plastic layer under constant compressive normal stress.

presents the shear stress – tangential sliding response for the interface layer in the case of progressive delamination. For specified σ, the shear stress first reaches the maximum critical value τ_c and then in the elasto-plastic softening process, decreases to the limit friction value $\mu\sigma$ in the fully damaged state. We can therefore write:

$$\tau = K_t \delta_t, \qquad 0 < \delta_t < \delta_t^c = \frac{\tau_c}{K_t}, \tag{2.22}$$

$$\tau = \tau_c - K_s(\delta_t - \delta_t^c), \qquad \delta_t^c < \delta_t < \delta_t^p = \delta_t^c + \frac{\tau_c - \mu\sigma}{K_s}, \tag{2.23}$$

$$\tau = \mu\sigma, \qquad \delta_t > \delta_t^p, \tag{2.24}$$

where $K_s > 0$ is the elasto-plastic softening modulus. Figure 4(b) specifies the constitutive relation in the case of rigid-plastic response.

Assuming the decomposition (2.14), we can write in the softening regime:

$$\dot{\delta}_t = \dot{\delta}_t^e + \dot{\delta}_t^s = \frac{\dot{\tau}}{K_t} - \frac{\dot{\tau}}{K_r} = -\frac{\dot{\tau}}{K_s}, \tag{2.25}$$

where K_r is the softening modulus associated with the plastic slip component δ_t^s. From Equation (2.25) we have

$$\frac{1}{K_s} = \frac{1}{K_r} - \frac{1}{K_t}, \quad K_s = \frac{K_r}{1 - K_r/K_t}. \tag{2.26}$$

Thus, the softening response for the elasto-plastic interface is dependent on the ratio K_r/K_t. When $\zeta = K_r/K_t = 1$, we have the brittle response of the interface. On the other hand, when $K_t \to \infty$, that is for rigid-plastic response, there is $K_s = K_r$.

The discussion of a dilatant contact condition can be found in the paper by Mróz and Seweryn (1998).

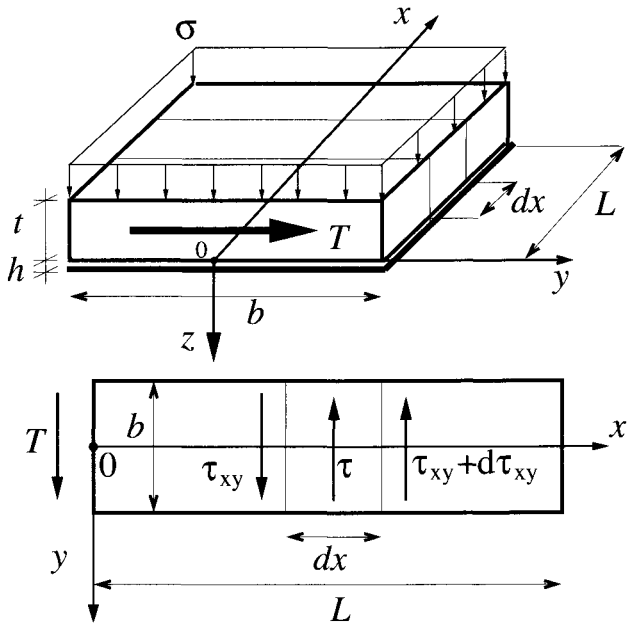

Figure 5. Plate bonded to the substrate. Anti plane shear state $b > L$

2.2 Anti-Plane Shear State

In the present section we shall formulate equations of an anti-plane shear state allowing for analytical solution of delamination process due to mechanical loading. Subsequently longitudinal shear delamination due to temperature loading will be treated resulting in a simple mathematical model for delamination and segmentation.

Let us consider a plate of length L, width b, and thickness t, bonded to a rigid foundation by an interface layer of thickness h, $h << t$, as shown in Figure 5.

The uniform compressive traction $\sigma_{zz} = -\sigma$ is assumed to act at the upper plate surface. The plate is loaded by the shear force $T = \tau_{yx}(0)A$, $A = bt$, at the end section $x = 0$. The other end at $x = L$ remains traction free. Assuming the transverse dimension b to be larger than the plate length L, the flexural effects can be neglected and the state of anti-plane shear can be assumed with two shear stress components τ_{yx} and τ_{yz}, so that the equilibrium equation is:

$$\frac{\partial \tau_{yx}}{\partial x} + \frac{\partial \tau_{yz}}{\partial z} = 0 \tag{2.27}$$

and $\sigma_{zz} = -\sigma = \text{const}$ is the initial stress induced by the lateral compressive traction along the z-axis. Denoting by $w = w(x, z)$ the displacement field along the y-axis and

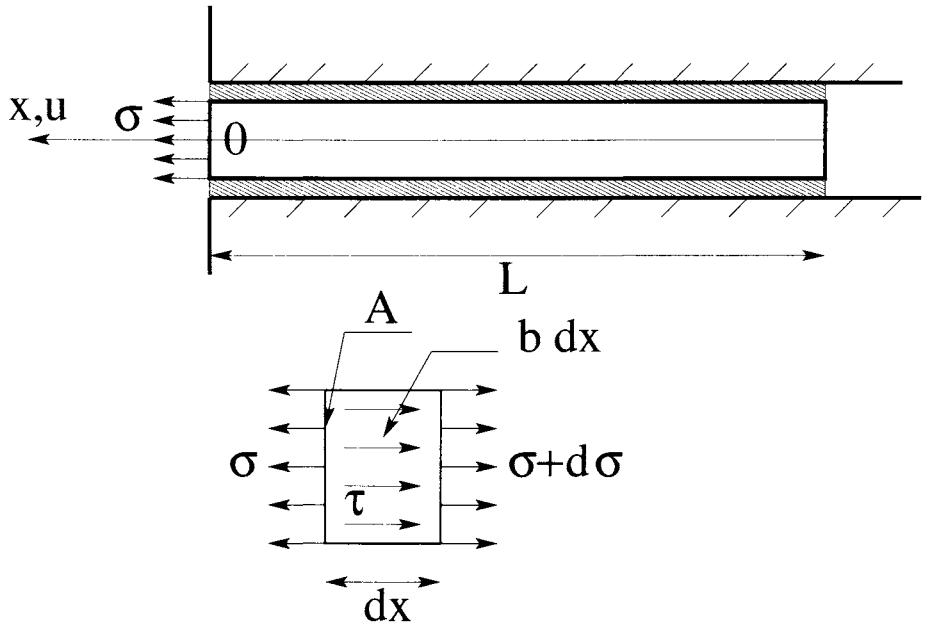

Figure 6. Fiber pullout.

using the Hooke's law:

$$\tau_{yz} = -G_2 \frac{\partial w}{\partial z}, \qquad \tau_{xy} = -G_1 \frac{\partial w}{\partial x}, \tag{2.28}$$

the equilibrium equation (2.27) takes the form :

$$G_1 \frac{\partial^2 w}{\partial x^2} + G_2 \frac{\partial^2 w}{\partial z^2} = 0, \tag{2.29}$$

where G_1 and G_2 are the shear moduli along x and z axes. The boundary conditions at the interface $z = 0$: $\tau_{yz} = -\tau_f$; at the upper boundary $z = -t$: $\tau_{yz} = 0$ and at the transverse boundaries $x = 0 : \tau_{xy}(0) = f_0(y, z)$, $x = L : \tau_{xy}(L) = 0$ should be satisfied.

A simplified solution can be generated by assuming the distribution of τ_{yz}, namely:

$$\tau_{yz} = -\tau(x)\Big(1 + \frac{z}{t}\Big), \tag{2.30}$$

where $\tau(x)$ is the interface shear stress at $z = 0$. The equilibrium (2.27) takes the form:

$$\frac{\partial \tau_{xy}}{\partial x} + \frac{\tau}{t} = 0. \tag{2.31}$$

Let us note that this form of (2.31) can be obtained by assuming the *s*hear beam model, that is assuming $w = w(x)$, $\tau_{xy} = -G\mathrm{d}w/\mathrm{d}x$ and writing the equilibrium equation

for the elastic beam interacting with the interface cohesive layer:

$$A\frac{\mathrm{d}\tau_{xy}}{\mathrm{d}x} + b\tau = 0, \tag{2.32}$$

where $A = bt$ denotes the transverse cross section area. This formula can be rewritten in the form:

$$-AG\frac{\mathrm{d}^2 w}{\mathrm{d}x^2} + b\tau = 0. \tag{2.33}$$

This form of equation can be generated from (2.29) by assuming $G_2 \to \infty$, that is neglecting shear deformation along the z-axis and regarding the shear stress τ_{yz} as a reaction. Alternatively, this equation can be obtained from (2.29) and (2.30) by satisfying the equilibrium equation at the interface $z = 0$. In the following, we shall provide the analytical solution using the simplified equation.

It should be noted, that the same set of equations apply for a fiber pullout problem as presented in Figure 6. By assuming the problem to be axisymmetric and reflecting the deformable medium surrounding the fiber by the interface constitutive equation with the surrounding medium to be rigid, one obtains the equilibrium equation

$$A\frac{\mathrm{d}\sigma}{\mathrm{d}x} + b\tau = 0. \tag{2.34}$$

The three dimensional effects associated with normal stresses due to Poisson's ratio are then ignored. Additionally, treating the fiber as an elastic body, we have the linear constitutive relation between displacement field u and normal stress σ:

$$\sigma = -E\frac{\mathrm{d}u}{\mathrm{d}x}, \tag{2.35}$$

with E being the Young modulus. By substituting (2.34) into (2.35), one obtains a differential equation in the form:

$$-AE\frac{\mathrm{d}^2 u}{\mathrm{d}x^2} + b\tau = 0 \tag{2.36}$$

identical to (2.33). The results of fiber pullout based on such a one dimensional model of decohesion were discussed by Schreyer and Peffer (2000).

2.3 Longitudinal Shear Delamination Due to Temperature Loading

In a similar fashion we shall now derive equations for an elastic plate of length $2L$, width $2B$ and thickness t bonded to a rigid substrate, as presented in Figure 7(a). Due to temperature loading, the structure delaminates and the tractions at plate-substrate interface induce stresses acting on the plate material. In order to obtain an analytical solution for the problem, we shall consider a simple one dimensional strip model presented in Figure 7(b).

The plate material is elastic - perfectly brittle as depicted in Figure 7(c). The critical stress is denoted by σ_c. We want to analyze the plate response under monotonic and

cyclic temperature loadings, assuming different constitutive laws for the bond interface. The equilibrium equation has the form:

$$\frac{\mathrm{d}\sigma}{\mathrm{d}x} - \frac{\tau}{t} = 0 \tag{2.37}$$

with σ denoting the normal stress, τ the shear stress at the interface and t the plate thickness, Figure 8. Since we consider temperature loading, the stress - strain relation takes the form:

$$\epsilon = \frac{\sigma}{E} + \alpha\Delta T, \tag{2.38}$$

where ϵ is the plate elongation along x axis, α denotes the thermal expansion coefficient and ΔT is the temperature variation with respect to reference state. It is assumed that the substrate does not crack, so the problem can be reduced to a model of interaction with the rigid substrate. The strain ϵ is defined as

$$\epsilon = \frac{\mathrm{d}u}{\mathrm{d}x} \tag{2.39}$$

with $u = u(x)$ being the displacement field along x. Combining Equations (2.37), (2.38) and (2.39) provides a formula relating u with the interface shear stress τ:

$$\frac{\mathrm{d}^2u}{\mathrm{d}x^2} + \alpha\frac{\mathrm{d}(\Delta T)}{\mathrm{d}x} - \frac{\tau}{Et} = 0. \tag{2.40}$$

Assume the uniform temperature distribution within the plate material, that is ΔT is not a function of x $\Delta T(x) = \Delta T = \text{const}$. Then Equation (2.40) becomes

$$-Et\frac{\mathrm{d}^2u}{\mathrm{d}x^2} + \tau = 0. \tag{2.41}$$

Equations (2.33), (2.36), and (2.41) have the same structure. As will be presented in the following, the delamination process is identical in nature in the case of transverse and longitudinal shear as well as fiber pull-out problem (Schreyer and Peffer (2000)).

The temperature gradient along the thickness of the plate results in a bending moment to be specified from vanishing curvature of plate deflection, that is assuming a full contact between the plate and the substrate. The appropriate condition takes the form:

$$\kappa = \kappa^M + \kappa^T = 0, \tag{2.42}$$

with κ^M equal:

$$\kappa^M = \frac{M}{EJ}, \qquad J = \frac{(2B)t^3}{12}, \tag{2.43}$$

and the curvature κ^T resulting from temperature gradient:

$$\kappa^T = \alpha\frac{\partial(\Delta T)}{\partial z}, \tag{2.44}$$

where z denotes the normal direction to the plate.

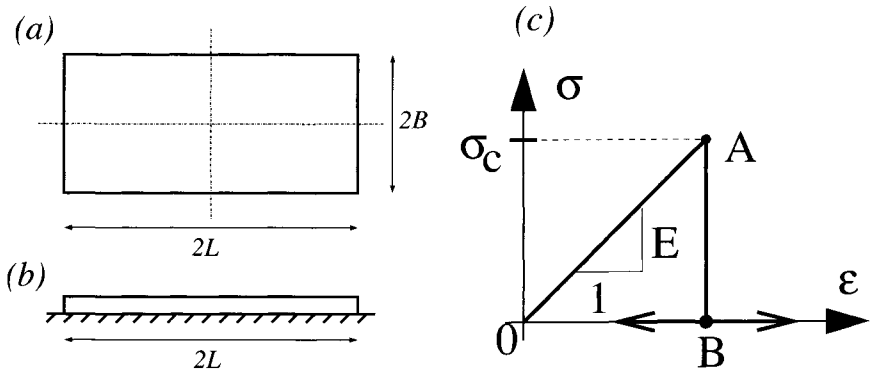

Figure 7. (a) Plate bonded to a rigid substrate. (b) One dimensional strip model. (c) The constitutive law for the plate material.

By substituting Equations (2.43) and (2.44) into Equation (2.42), one obtains:

$$M = -EJ\alpha \frac{\partial(\Delta T)}{\partial z}. \tag{2.45}$$

The value of normal stresses σ^M resulting from temperature gradient is given by:

$$\sigma^M = \frac{Mz}{J} = -\alpha Ez \frac{\partial(\Delta T)}{\partial z}. \tag{2.46}$$

When a linear temperature variation across the plate thickness is assumed, we have:

$$\sigma^M = \alpha Ez \frac{\Delta T_t - \Delta T_b}{t}, \tag{2.47}$$

where ΔT_t is the temperature loading at the upper plate surface and ΔT_b is the temperature change at plate-substrate interface. In the following we shall assume a uniform temperature variation across plate thickness, $\Delta T_t = \Delta T_b$, resulting in $\sigma^M = 0$.

Now the interfacial constitutive model is used to describe the deformation of the interface layer. In the analysis we shall use rigid-friction and rigid-cohesive-friction formulations for the interface material. Two types of temperature loadings shall be considered, namely monotonic and cyclic.

2.4 Cyclic Loading of Interface

Consider now a cyclic loading of interface with varying shear stress τ and normal traction σ kept constant. In order to simplify mathematical considerations let us assume that the interface is rigid-cohesive-frictional as presented in Figure 4(b). We shall distinguish between two consecutive semi-cycles constituting loading and unloading stages, respectively. The interface state variables for the n-th and $n-1$-st stages are δ_{t_n}, τ_n,

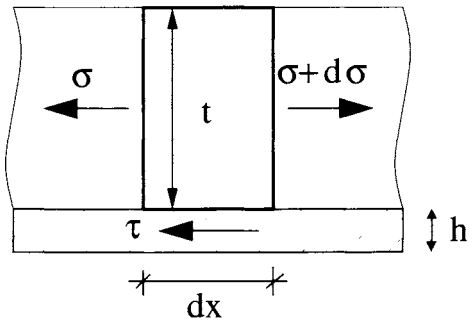

Figure 8. Stresses acting on an infinitesimal strip element.

$\delta_{t_{n-1}}$, τ_{n-1}, with $\dot{\delta}_{t_n} = -\dot{\delta}_{t_{n-1}}$. The constitutive equation for the plastic zone now takes the form:

$$\tau_n(x) = -K_s\big(\delta_{t_n}(x) - \delta_{t_{n-1}}(x)\big) - \tau_{n-1}(x), \tag{2.48}$$

where $\delta_{t_{n-1}}(x)$, $\tau_{n-1}(x)$ are respectively the displacement and stress fields at the end of $n-1$-st semi cycle, as denoted in Figure 4(b). The equilibrium Equations (2.33) and (2.41) provide:

$$\delta''_{t_n} + r_s^2\delta_{t_n} = r_s^2\delta_{t_{n-1}} - \delta''_{t_{n-1}} \tag{2.49}$$

where $r_s = \sqrt{K_s/Gt}$, $\delta_t = w$ for for anti-plane shear and $r_s = \sqrt{K_s/Et}$, $\delta_t = u$ for longitudinal delamination. Equation (2.49) is a recursive relation between functions $\delta_{t_n}(x)$ and $\delta_{t_{n-1}}(x)$ and allows for an analytical solution. Though it is easy to specify the integration constants for a monotonic loading program, a cyclic case requires substantial algebraic manipulations. In practice, it is necessary to use a computer software, eg. *Mathematica* Wolfram (1999), able to perform symbolic mathematics.

3 Anti-Plane Shear – Analytical Solution

Let us now consider transverse delamination of a plate in an anti-plane shear state. In order to obtain formulas that can be easily treated in an analytical fashion we shall neglect the elasticity for interface layer by assuming $K_n = K_t \to \infty$. Thus we have rigid-softening-friction interface constitutive relation. By substituting Equations (2.23) and (2.24) into (2.33), one obtains ordinary differential equations providing formulas for displacement fields w^p and w^f, respectively for plastic and frictional interfaces. Thus, for the plastic case we have

$$w^p(x) = C_1\cos(r_s x) + C_2\sin(r_s x) + \frac{\tau_c}{K_s}\mathrm{sign}(\dot{w}) \qquad r_s = \sqrt{\frac{K_s}{Gt}} \tag{3.1}$$

whereas the displacement field within the frictional zone is given by the following formula

$$w^f(x) = \mathrm{sign}(\dot{w})\frac{\mu\sigma}{2Gt}x^2 + C_3 x + C_4 \tag{3.2}$$

with C_1, C_2, C_3 and C_4 being the integration constants to be specified from boundary and continuity conditions. Here $r_s = \sqrt{K_s/(Gt)}$ is a parameter of dimension `1/length`. In the following, monotonic and cyclic interface failure modes will be discussed separately.

3.1 Monotonic Interface Failure

Let us assume monotonic damage at the material interface and examine the effect of progressive delamination on stress and displacement fields. In order to do that, we shall combine functions (3.1) and (3.2) using appropriate boundary and continuity conditions. Three different solution types can be distinguished, each being defined by the plate dimensions. They are characterized in the following sections where the consecutive stages of delamination process are described.

Short plate solution. There are two zones at the interface during the first stage of loading, namely undamaged and cohesive zone. They are schematically presented in Figure 9. Due to the rigid-plastic interface model, the undamaged zone has zero displacement field, whereas the plate displacement field for the cohesive region is provided by Equation (3.1) with the integration constants C_1 and C_2 to be specified from the boundary conditions:

$$w^p(s_1) = w^{p\prime}(s_1) = 0. \tag{3.3}$$

The value of s_1 specifies the coordinate of the transition point between undamaged and plastic (cohesive) zones. The displacement field w^p takes the form:

$$w^p(x, s_1) = \frac{\tau_c}{K_s}\{1 - \cos[r_s(x - s_1)]\}, \qquad 0 \le x \le s_1 \tag{3.4}$$

where s_1 is taken as a loading parameter describing the damage zone evolution. The corresponding stress in the plate τ_{xy} can be obtained by making use of Equation (2.28), thus:

$$\tau^p_{xy}(x, s_1) = -Gr_s\frac{\tau_c}{K_s}\sin[r_s(x - s_1)], \qquad 0 \le x \le s_1. \tag{3.5}$$

Formula (2.33) provides the shear stress at the plastic interface:

$$\tau^p(x, s_1) = \tau_c \cos[r_s(x - s_1)], \qquad 0 \le x \le s_1. \tag{3.6}$$

The short plate solution takes place when the plate is short enough for the plastic zone to cover the entire length L. This is true when the following condition is satisfied:

$$w^p(x = 0, s_1 = L) \le w_p = \frac{\tau_c - \mu\sigma}{K_s}, \tag{3.7}$$

stating that there is no frictional zone developed at the interface while its undamaged part has finally vanished. The inequality (3.7) reduces to

$$\frac{L}{t} \le \sqrt{\frac{G}{K_s t}}\arccos\frac{\mu\sigma}{\tau_c} \tag{3.8}$$

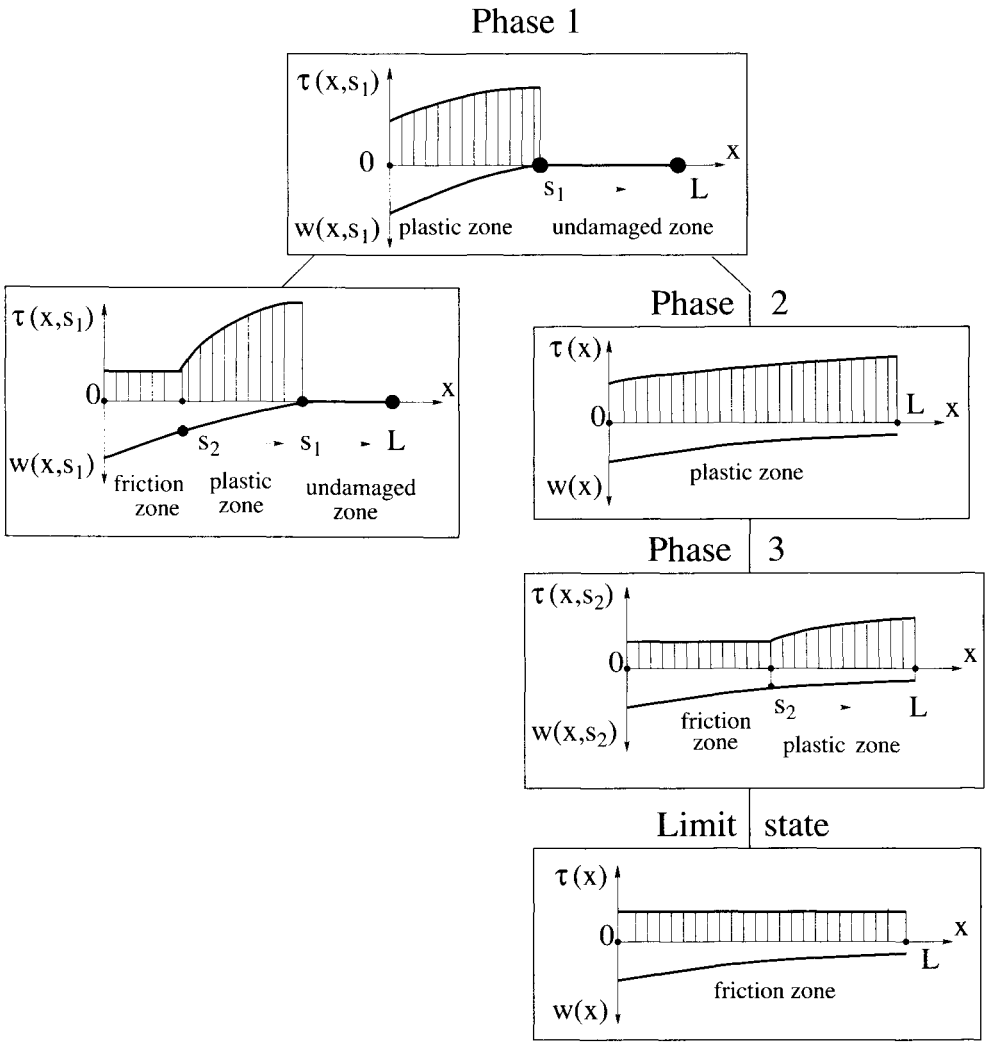

Figure 9. Short plate solution; delamination phases and contact stress distribution.

where the condition put on plate dimensions is shown explicitly. This condition may be rewritten in a dimensionless form:

$$\chi \leq \arccos \eta, \qquad \chi = r_s L, \qquad \eta = \frac{\mu\sigma}{\tau_c}. \tag{3.9}$$

requiring the dimensionless parameter χ to be bounded. In a particular case, we can vary the softening modulus K_s keeping the plate length constant and, as a result, we will obtain a short plate solution for small values of K_s. It is seen that the system response depends on a complex interaction between mechanical and geometrical characteristics to be captured by two dimensionless parameters χ and η.

There is only plastic zone at the interface during the second loading phase, as presented schematically in Figure 9. The displacement field is given by Equation (3.1), where the integration constants can be specified from the boundary conditions:

$$w^{p\prime}(L) = 0, \qquad w^p(0) = w_0^p, \tag{3.10}$$

with w_0^p being the loaded end displacement. At this stage, the value of w_0^p becomes the loading parameter. The displacement field, shear stress τ_{xy}^p and interfacial traction τ^p fields are:

$$w^p(x, w_0^p) = \left(w_0^p - \frac{\tau_c}{K_s}\right)\frac{\cos[r_s(L-x)]}{\cos(r_s L)} + \frac{\tau_c}{K_s}, \qquad 0 \leq x \leq L, \tag{3.11}$$

$$\tau_{xy}^p(x, w_0^p) = -Gr_s\left(w_0^p - \frac{\tau_c}{K_s}\right)\frac{\sin[r_s(L-x)]}{\cos(r_s L)}, \qquad 0 \leq x \leq L, \tag{3.12}$$

$$\tau^p(x, w_0^p) = \left(\frac{\tau_c}{K_s} - w_0^p\right)\frac{\cos[r_s(L-x)]}{\sin(r_s L)}, \qquad 0 \leq x \leq L. \tag{3.13}$$

A friction zone starts to develop at the interface for the displacement w_0^p reaching $w_p = (\tau_c - \mu\sigma)/K_s$ and a subsequent loading phase begins, as presented in Figure 9. There are two interfacial zones, namely plastic and friction with respective displacement fields given by Equations (3.1) and (3.2). The integration constants are specified from the boundary and continuity conditions:

$$w^{p\prime}(L) = 0, \quad w^p(s_2) = w^f(s_2) = \frac{\tau_c - \mu\sigma}{K_s}, \quad w^{p\prime}(s_2) = w^{f\prime}(s_2), \tag{3.14}$$

where s_2 is a coordinate of the transition point between plastic and frictional zones. The displacement and stress fields take the form:

– plastic zone, $s_2 \leq x \leq L$:

$$w^p(x, s_2) = \frac{\tau_c}{K_s} - \frac{\mu\sigma}{K_s}\frac{\cos[r_s(L-x)]}{\cos[r_s(L-s_2)]}, \tag{3.15}$$

$$\tau_{xy}^p(x, s_2) = \frac{\mu\sigma}{K_s} r_s G \frac{\sin[r_s(L-x)]}{\cos[r_s(L-s_2)]}, \tag{3.16}$$

$$\tau^p(x, s_2) = \mu\sigma\frac{\cos[r_s(L-x)]}{\cos[r_s(L-s_2)]}, \tag{3.17}$$

– friction zone, $0 \leq x \leq s_2$:

$$w^f(x, s_2) = \frac{\mu\sigma}{2Gt}(x - s_2)^2 + \frac{\mu\sigma r_s}{K_s}\tan[r_s(L - s_2)](x - s_2) + \frac{\tau_c - \mu\sigma}{K_s}, \tag{3.18}$$

$$\tau^f_{xy}(x, s_2) = -\frac{\mu\sigma}{t}(x - s_2) - \frac{\mu\sigma r_s G}{K_s}\tan[r_s(L - s_2)], \tag{3.19}$$

$$\tau^f(x, s_2) = \mu\sigma, \tag{3.20}$$

so for this loading phase the value of s_2 takes over w^0_p as the loading parameter and its monotonic increase describes the damage growth.

For s_2 equal to L the interface has been fully damaged and progressive delamination is accomplished. The limit shear stress subjected to the plate equals

$$\tau^{lim}_{xy}(0) = \frac{\mu\sigma}{t}L \tag{3.21}$$

and is equilibrated by the frictional forces at the interface.

Figure 10(a) presents a relation between the loading traction $\tau_{xy}(0)$ and the loaded end displacement for various values of the dimensionless parameter $\chi = r_s L$ satisfying the condition (3.9). The dashed line is a solution obtained for an interface with no cohesive strength, simply rigid-frictional interface. It should be noted that there is a slope discontinuity on the load-displacement curves at limit points P_l corresponding to the maximal load value, Figure 10(a). In fact, the limit point P_l corresponds to the state when the damage zone reaches the plate boundary $s_1 = L$. The subsequent response is associated with reduction of length of damage zone when s_2 approaches L.

It also follows from Figure 10 that the normalized maximum traction $\tau_{xy}(0)/\tau^{lim}_{xy}(0)$ subjected to the plate becomes higher while the length L, that is the dimensionless parameter χ, decreases. The reason for this scale effect is the softening law used for the material interface.

Since the solution strategy is similar in the case of short, medium and long plate, the resulting displacement and stress fields will not be included in the following sections. In order to avoid repetitive formulations, only general guidelines and the most important conclusions shall be considered now with the detailed mathematical expressions to be found in Appendix.

Medium length solution. Let us assume now that the condition (3.8) is not satisfied. As opposed to the short plate solution, there are following interface zones during the second loading phase: friction, plastic and undamaged, as schematically presented in Figure 11. The displacement fields for the plastic and friction zones are given by Equations (3.1) and (3.2), respectively. The integration constants can be specified from the boundary and continuity conditions:

$$w^p(s_1) = w^{p\prime}(s_1) = 0, \quad w^p(s_2) = w^f(s_2) = \frac{\tau_c - \mu\sigma}{K_s}, \quad w^{p\prime}(s_2) = w^{f\prime}(s_2), \tag{3.22}$$

where, as before, s_1 is the coordinate of the transition point between undamaged and plastic regions, and s_2 indicates the point between plastic and friction zones. Assume

(a)

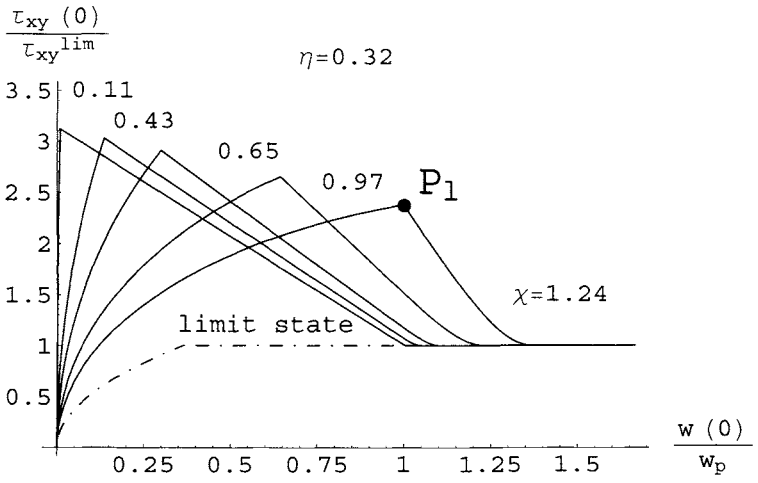

(b)

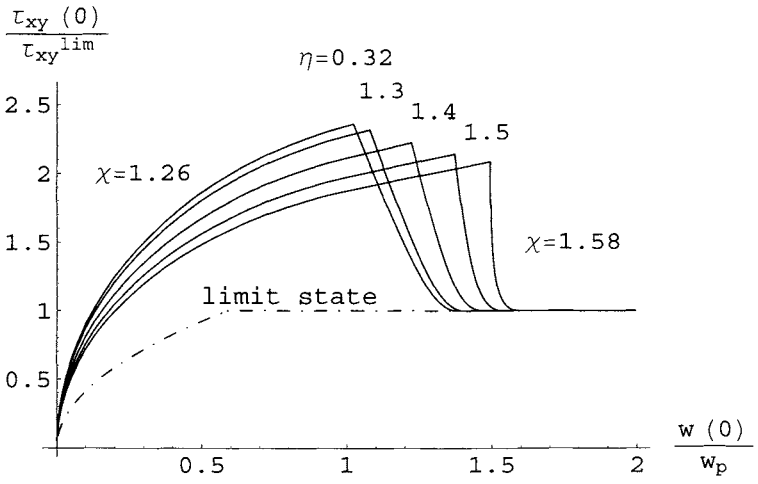

Figure 10. Short (a) and medium length (b) solutions; the loading traction versus displacement for varying values of $\chi = r_s L$, $\eta = 0.32$.

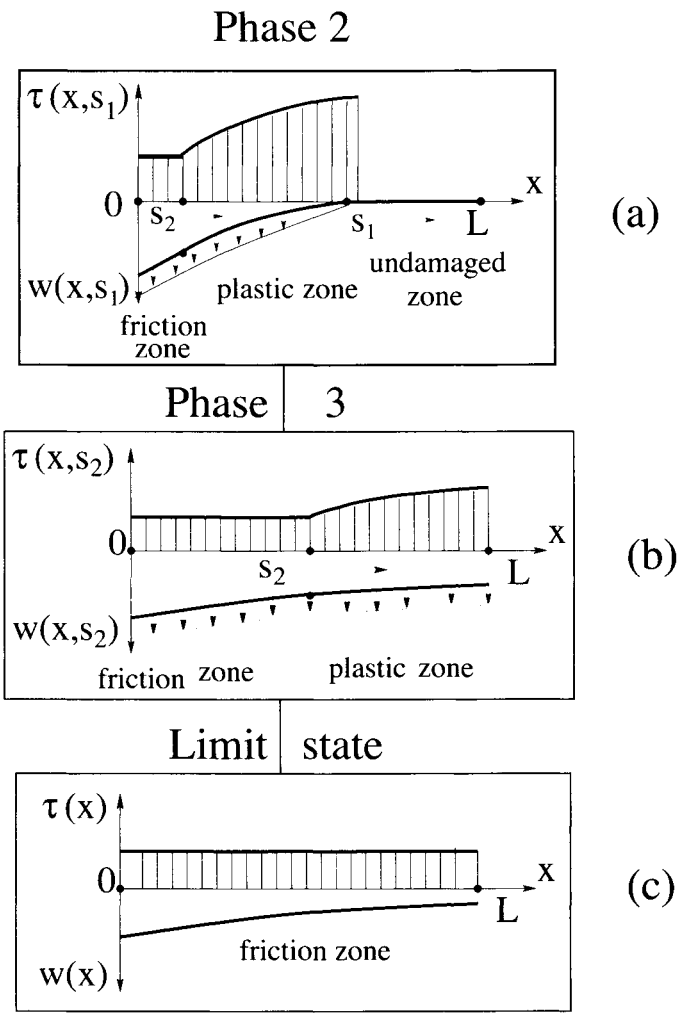

Figure 11. Medium length solution; delamination phases and contact stress distribution: (a) plastic and friction zones inside the interface, $s_1 < L$; (b) plastic zone reaching the boundary, $s_1 = L$; (c) limit friction state.

that s_1 is now a monotonically increasing control parameter of the loading process and both shear stress and displacement at the loaded boundary $x = 0$ are specified in terms of s_1. It subsequently follows from the conditions (3.22):

$$s_2 = s_1 - \frac{1}{r_s}\arccos\eta, \qquad s_d = s_1 - s_2 = \frac{1}{r_s}\arccos\eta, \tag{3.23}$$

that is the plastic zone length s_d is constant during the second loading phase. The displacement and stress fields for plastic and friction zones are presented by Equations (5.4)÷(5.9) in Appendix.

The whole interface is damaged during the subsequent delamination stage, that is for $s_1 = L$. The value of s_2 becomes the control parameter of the loading process, so the considered situation is identical to the third delamination phase of short plate solution, with plastic and friction zones at the interface. The obtained stress and displacement fields are specified by Equations (5.10)÷(5.15) in Appendix. One should remember though, that these formulas are valid for monotonic interface loading only, that is when the following condition is satisfied:

$$\dot{w} \geq 0. \tag{3.24}$$

Having in mind that s_2 is a control parameter during the third delamination stage, the inequality (3.24) can be rewritten as:

$$\frac{\partial w(x, s_2)}{\partial s_2} \geq 0 \qquad \forall x \in < 0, L > . \tag{3.25}$$

This condition is satisfied for the length to height ratio L/t smaller than

$$\frac{L}{t} < \sqrt{\frac{G}{K_s t}}\left(\arccos\eta + \frac{\eta}{\sqrt{1-\eta^2}}\right) \tag{3.26}$$

or in a dimensionless form:

$$\chi \leq \arccos\eta + \frac{\eta}{\sqrt{1-\eta^2}}, \qquad \chi = r_s L, \qquad \eta = \frac{\mu\sigma}{\tau_c}. \tag{3.27}$$

Plate satisfying the inequality (3.27) will provide a medium length solution. In a dimensionless form, it is defined by the following formula

$$\arccos\eta < \chi \leq \arccos\eta + \frac{\eta}{\sqrt{1-\eta^2}}. \tag{3.28}$$

As in the case of short plate solution, it is a condition put on parameter χ and expressed in terms of both the plate length and the softening modulus K_s. It is seen that two dimensionless parameters χ and η govern the system response.

Figure 10(b) presents a relation between the loading traction $\tau_{xy}(0)$ and the loaded end displacement for various values of dimensional parameter $\chi = r_s L$ satisfying the condition (3.28). The dashed line is a solution obtained for an interface with no softening effect, simply rigid-frictional interface. Similarly to the short plate solution, the scale effect is manifested by a decrease in the normalized maximum traction $\tau_{xy}(0)/\tau_{xy}^{lim}(0)$ accompanied by an increase in plate length L, that is in the parameter χ.

Long plate solution. The static solution for this case can be constructed by assuming the existence of a reverse slip zone near the loaded boundary (L-1 solution). For a longer plate, multiple zones may develop near the loaded boundary (L-2 solution). We shall discuss in detail the L-1 solution and specify its domain of validity in terms of plate and interface parameters. The details of L-2 solution will be presented in a companion paper accounting for the elasticity of the interface.

L-1 solution. Let us consider now a long plate solution, when the material and geometric parameters satisfy the following condition:

$$\chi = r_s L > \arccos\eta + \frac{\eta}{\sqrt{1-\eta^2}}.$$

The first two delamination stages are identical to those of medium plate solution, that is there are initially the following zones at the interface:

- first phase: plastic and undamaged zones, Equations (5.1)÷(5.3) in Appendix;
- second phase: friction, plastic and undamaged zones, Equations (5.4)÷(5.9) in Appendix.

A difference appears when the plastic zone reaches the boundary $s_1 = L$. Assume now s_2, specifying the transition between plastic and friction zones, to be the control parameter of the process. For the progressive delamination the value of s_2

increases from $\bar{s}_2$ to L, where $\bar{s}_2$ corresponds to the instant when $s_1 = L$, thus in view of Equation (3.23) we have

$$\bar{s}_2 = L - \frac{1}{r_s}\arccos\eta.$$

Assuming existence of plastic and friction zones within the interface we have the displacement and stress fields given by Equations (5.10)÷(5.15) in Appendix. However, they cannot be accepted as the correct solution, since the rate of deflection changes its sign within the frictional interface. In fact, the derivative $\partial w^f(x,s_2)/\partial s_2$ vanishes at $x = s_3$ and becomes negative for $0 \le x \le s_3$. Thus, there is a transition point between the forward ($\dot{w}^f > 0$) and the reverse ($\dot{w}^f < 0$) displacement zones. By substituting (5.10) into equation

$$\frac{\partial w^f(x,s_2)}{\partial s_2} = 0 \tag{3.29}$$

one obtains a formula relating s_3 to the loading parameter s_2:

$$s_3 = s_2 - \frac{1}{r_s}\cot[r_s(L-s_2)]. \tag{3.30}$$

The constitutive relation for the reverse displacement interface is given by

$$\tau = \mu\sigma\,\mathrm{sign}(\dot{w}) = -\mu\sigma, \tag{3.31}$$

as previously indicated in Figure 4. Upon substituting Equation (3.31) into (2.33), we obtain an ordinary differential equation specifying the reverse deflection field:

$$w^r(x) = -\frac{\mu\sigma}{2Gt}x^2 + C_5 x + C_6 \tag{3.32}$$

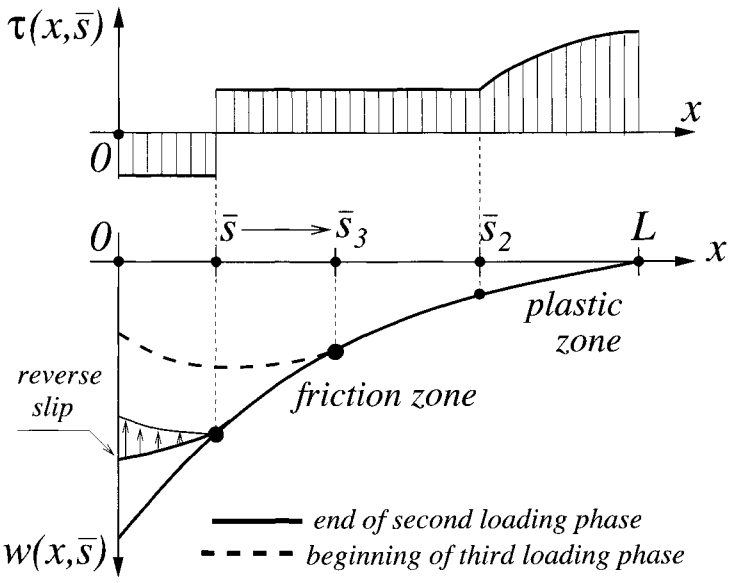

Figure 12. The end of second and beginning of third loading phases - $\bar{s}$ as the control parameter.

where C_5 and C_6 are the integration constants to be specified from the continuity conditions:

$$w^r(s_3) = w^f(s_3), \qquad w^{r\prime}(s_3) = w^{f\prime}(s_3). \tag{3.33}$$

The displacement field takes the form:

$$w^r(x, s_2) = -\frac{\mu\sigma}{2Gt}[2(x-s_3)^2 - (x-s_2)^2] - \frac{\mu\sigma}{Gtr_s}\tan[r_s(L-s_2)](x-s_2) + \frac{\tau_c - \mu\sigma}{K_s}. \tag{3.34}$$

Figure 12 presents the displacement field at the instance when $s_1 = L$, that is at the end of the second loading phase. The dashed line refers to the onset of the subsequent delamination stage when $s_2 = \bar{s}_2$. It is seen that there is a discontinuous switch from forward to reverse displacement within the segment $x \in [0, \bar{s}_3]$ characterized by the snap-back response at the end of beam and accompanied by the discontinuous load variation. Such discontinuous response is typical for the rigid-plastic-friction interface model.

In order to obtain a continuous response, we may assume that s_2 is fixed at the value $s = \bar{s}_2$ and the reverse friction slip zone propagates from the loaded end $x = 0$ until it reaches the length $x = \bar{s}_3$ specified by

$$\bar{s}_3 = \bar{s}_2 - \frac{1}{r_s}\cot[r_s(L - \bar{s}_2)] \tag{3.35}$$

and obtained from Equation (3.30) for $s_2 = \bar{s}_2$. It is schematically presented in Figure 12. Assuming $\bar{s}$ to represent the position of the propagating zone, we can specify the

deflection field from (3.32) and determine the integration constants from the continuity conditions at $x = \bar{s}$:

$$w^r(x = \bar{s}) = w^f(x = \bar{s}, s_2 = \bar{s}_2), \qquad w^{r\prime}(x = \bar{s}) = w^{f\prime}(x = \bar{s}, s_2 = \bar{s}_2). \tag{3.36}$$

The obtained displacement and stress fields within the reverse slip zone are given by Equations (5.16)÷(5.18) in Appendix.

For $\bar{s} = \bar{s}_3$ the reverse slip zone reaches its maximal length. The third delamination phase then begins and formulas (5.10)÷(5.15), *cf.* Appendix, become valid for the progressive slip within the interval $s_3 < x \leq L$. The reverse slip deflection within the interval $0 \leq x \leq s_3$ is characterised by Equation (3.34). It follows from Equation (3.30), that $\partial s_3/\partial s_2 < 0$, so for $\dot{s}_2 > 0$ we have $\dot{s}_3 < 0$ and the reverse slip zone is decreasing and eliminated when $s_3 = 0$. The stress fields within the plate and at the interface can be obtained from Equations (3.34), (2.28) and (2.33) providing

$$\tau^r_{xy}(x, s_2) = \frac{\mu\sigma}{t}[2(x - s_3) - (x - s_2)] + \frac{\mu\sigma}{tr_s}\tan[r_s(L - s_2)], \qquad 0 \leq x \leq s_3, \tag{3.37}$$

$$\tau^r(x, s_2) = -\mu\sigma, \qquad 0 \leq x \leq s_3, \tag{3.38}$$

where the relation between s_3 and s_2 is given by (3.30). The evolution of forward and reverse friction zones is presented schematically in Figure 13.

The fourth phase of deformation is associated with the progressive slip and evolution of s_2 to its limit value $s_2 = L$, when the plastic zone is erased and the limit state is reached. The stress and displacement fields are specified by Equations (5.10)÷(5.15) in Appendix for friction and plastic interfacial zones.

The load-displacement diagrams are presented in Figure 14. The combined decrease in loading traction and loaded end displacement corresponds to the snap-back of the loaded end and generation of the reverse slip zone. It is subsequently erased and the last section of the $\tau(0) \sim w(0)$ diagram refers to progressive slip and failure within the plastic zone, similarly to the case of short and medium plate solutions. Figure 14 presents the calculated response diagram for $\eta = 0.32$ and several values of $\chi = r_s L$.

The present solution describes the quasi static response assuming the process to be controlled by the progressive front of the plastic zone. Figure 14 reveals a complex response, that cannot be realized either by stress or displacement controlled loading. In practice it may lead to an unstable behaviour with a critical point related to the disappearance of undamaged interfacial area. A dynamic mode could follow next starting from this limit state. However, the present solution clarifies the nature of critical points associated with the delamination process and can provide a reference solution for numerical algorithms attempting to generate equilibrium paths in the post critical states. The reason for the combined decrease in loading traction and loaded end displacement is the elastic energy stored in the plate during the previous loading phase and its release to debond the structure. Thus, an extra work by external loadings would produce a dynamic response.

We shall check now, whether the presented scenario is compatible with the slip rule at the interface. In order to do that, one should analyze the sign of the derivative

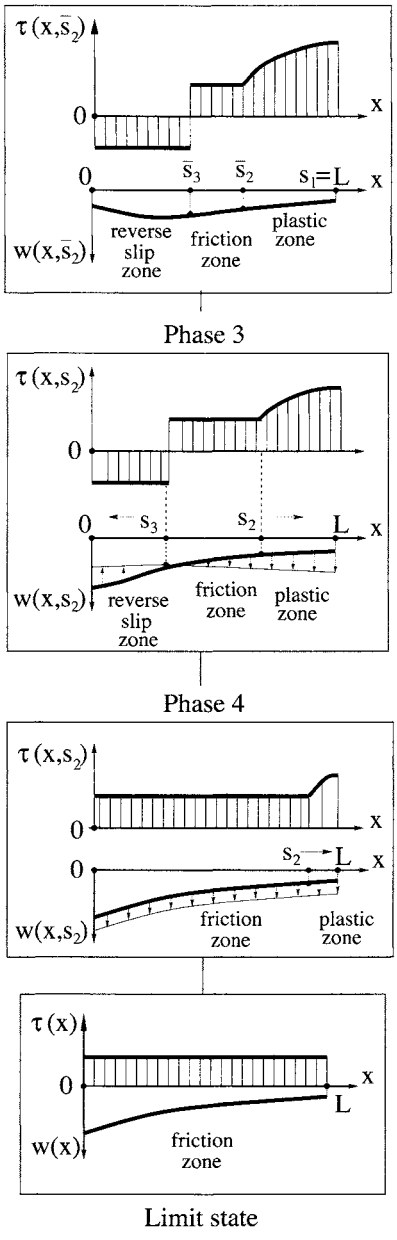

Figure 13. Long plate delamination phases: L-1 solution: (a) plastic, friction and reverse slip zones; (b) moving interfaces: $\dot{s}_2 > 0$, $\dot{s}_3 < 0$); (c) friction and plastic zones; (d) limit friction state.

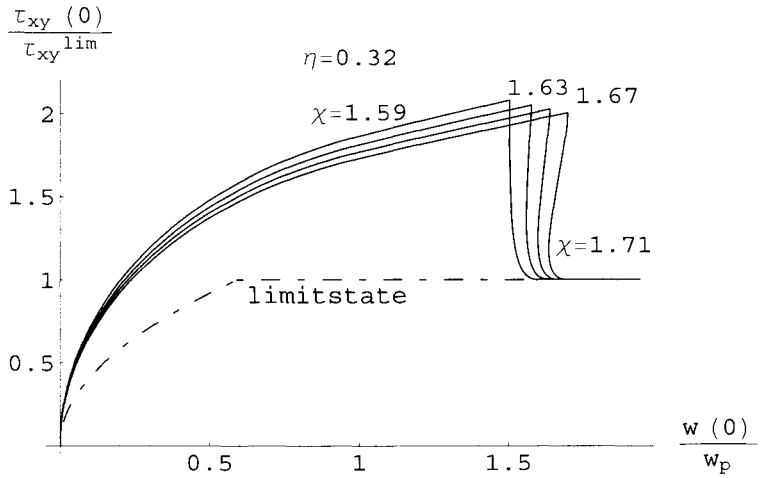

Figure 14. Long plate solution L-1, loading traction versus displacement: illustrative solutions with response curves for $\eta = 0.32$ and varying χ.

$\partial w^r(x, s_2)/\partial s_2$, representing the rate of slip within the reverse slip zone with respect to control parameter s_2. Equations (3.34), (3.37), (3.38) are valid only when the inequality

$$\frac{\partial w^r(x, s_2)}{\partial s_2} \leq 0 \tag{3.39}$$

is satisfied, which is compatible with the interfacial shear stress within the reverse slip zone $\tau = -\mu\sigma$. By substituting (3.34) into (3.39), this condition takes the form:

$$C \cdot D \leq 0, \tag{3.40}$$

where:

$$C = \cos[r_s(L - s_2)] + r_s(x - s_2)\sin[r_s(L - s_2)],$$
$$D = -3 - 12\cos[2r_s(s_2 - L)] - \cos[4r_s(s_2 - L)].$$

The value of C is always negative for every $x \in [0, s_3]$ and the sign of product $C \cdot D$ depends on D only. Thus, in order for the reverse slip zone to be compatible with the slip rule, the condition $D \geq 0$ should be satisfied. That is true only when the control parameter s_2 is lower than the value of $\tilde{s}_2$, thus:

$$s_2 \leq \tilde{s}_2 = L - \frac{1}{2r_s}\arccos(2\sqrt{2} - 3) = L - \frac{0.8716}{r_s}. \tag{3.41}$$

For values of s_2 not satisfying this condition, that is for $s_2 > \tilde{s}_2$, we have the inequality $\partial w^r(x, s_2)/\partial s_2 > 0$, meaning that there is a subsequent change in the rate of slip within the reverse slip zone for $x \in [0, s_3]$ during the course of delamination.

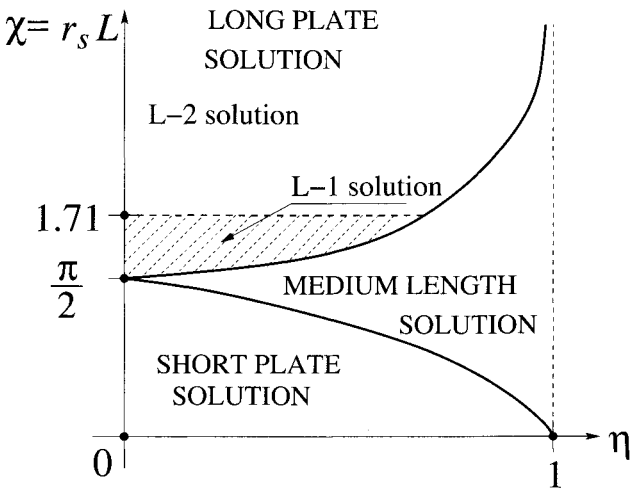

Figure 15. Response domains in the plane $\{\chi, \eta\}$.

Upon substituting (3.41) into Equation (3.30) one obtains the length of reverse slip zone at the instant when the subsequent change in displacement rate takes place:

$$\tilde{s}_3 = s_3(\tilde{s}_2) = L - \frac{1.7125}{r_s}, \tag{3.42}$$

It becomes obvious that for $\tilde{s}_3 = 0$ we have a situation when the reverse slip zone has vanished before the slip rate in this particular area is changed.

In view of (3.42), the delamination process presented in Figure 13 and Figure 14 is valid for a plate of length L satisfying the inequality:

$$\arccos\eta + \frac{\eta}{\sqrt{1-\eta^2}} < \chi \leq 1.7125, \qquad \chi = r_s L. \tag{3.43}$$

The domain of validity of this solution in the plane χ, η is shown in Figure 15.

L-2 solution. For $\chi > 1.7125$ a different type of system response occurs with more complex evolution of slip zones. Now, subsequent changes in the slip rate within the zone $x \in [0, \tilde{s}_3]$ should be considered. Detailed analytical solution cannot be constructed using the rigid-plastic interface model. It can be constructed though by means of finite differences method when the elastic-softening interface is considered. The progressive delamination of the structure occurs in a cyclic deformation process with hysteretic response generated in load-displacement diagram. The length of zone $x \in [0, \tilde{s}_3]$ decreases to zero with progressive increase of control parameter s_2 provided by Equation (3.30). When the value of s_3 reaches zero, there are two interfacial zones left at the interface: friction and plastic. The situation is identical to previously considered and the stresses

and displacement fields are specified by the medium length solution (3.15)÷(3.20). For $s_2 = L$ the plastic zone is erased and the limit state is reached. A complete solution for this case is discussed by Białas and Mróz (2004). Here only the final results are presented. Figure 16 reveals a complex system response. It is seen that in order to perform the progressive delamination, a cyclic loading along a specific loading path is required. The number of hysteretic loops in the $\tau_{xy}(0) - w(0)$ relation depends on the value of dimensionless parameter χ. By keeping the K_s constant and varying only the plate length L, we obtain a different number of loops. The number of loading cycles required to damage the interface increases with increasing L. The results show that the part of the structure in the $x \in < 0, \bar{s}_3 >$ zone performs a flattering movement with subsequent forward and reverse displacements. This process cannot be executed either by stress or displacement controlled loading. In practice it may lead to an unstable behaviour with a critical point related to the disappearance of undamaged interfacial area. A dynamic mode could follow next starting from this limit state. However, the present solution clarifies the nature of critical points associated with the delamination process and can provide a reference solution for numerical algorithms attempting to generate equilibrium paths in the post critical states. The reason for the combined decrease in loading traction and loaded end displacement is the elastic energy, stored in the plate during the previous loading phase and being released to debond the structure. For a longer plate there is more elastic energy in the structure and consequently a greater number of loading cycles is required for its dissipation at the frictional interface. Any extra work by external forces would result in a dynamic response.

Figure 15 presents the response domains provided by conditions (3.8), (3.26), for short, medium and long solution types in $\{\chi, \eta\}$ plane. The L-1 and L-2 regimes are also indicated. It allows for a prediction of structural response when the set of geometric and material parameters is known.

Finite element validation. In the present section the obtained analytical results of the shear beam model will be compared with a finite element analysis of an elastic plate bonded to a rigid substrate by a cohesive interface. The problem presented in Figure 5 shall be treated as two dimensional, with elastic plane stress elements for the plate material and with zero thickness interfacial elements. The delamination process is displacement controlled by an increasing value of displacement $u_y(y, x = 0)$ of plate boundary for $x = 0$. It has been assumed that the displacement $u_x(y, x = 0)$ in x direction is constrained, that is we have $u_x(y, x = 0) = 0$.

Let us assume that the plate is a granite block with the value of Young modulus equal to $E = 4 \cdot 10^4$ MPa and Poisson's ratio $\nu = 0.25$. The shear strength is $\tau_c^0 = 30$ MPa and the friction coefficient $\mu = 0.64$. The resulting Kirchhoff modulus is $G = 1.6 \cdot 10^4$ MPa. The plate dimensions are $L = 2$ m $b = 4$ m $t = 0.2$ m in order to provide the anti-plane shear state. The traction σ acting on the upper surface has the value $\sigma = 20.1$ MPa and the resulting friction stress for the fully damaged interface is $\mu\sigma = 12.9$ MPa. The value of the dimensionless parameter

$\eta = \mu\sigma/(\mu\sigma + \tau_c^0)$ equals $\eta = 0.3$. By varying the interfacial softening modulus K_s, we can obtain the delamination scenario characteristic for short, medium and long plate solutions.

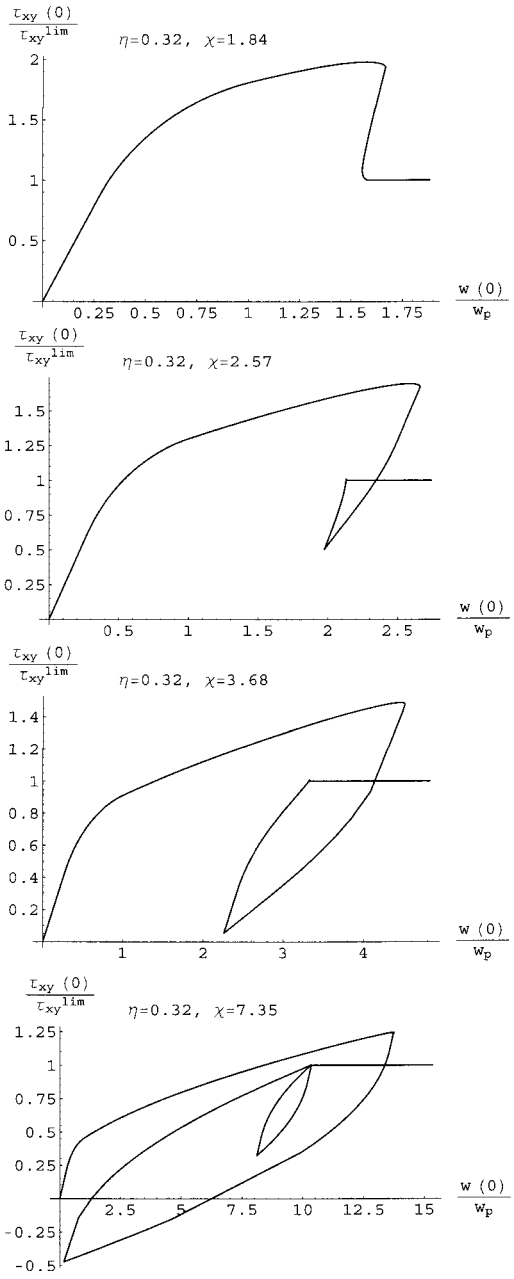

Figure 16. Long plate solution. The loading traction versus loaded end displacement. The solutions for various values of parameter $\chi = r_s L$.

(a)

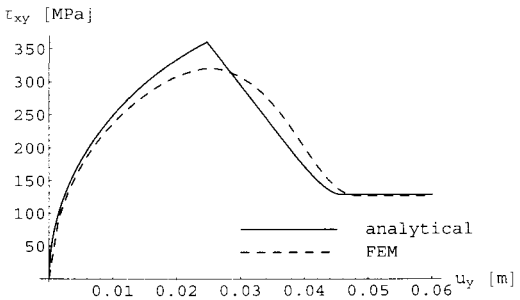

(b)

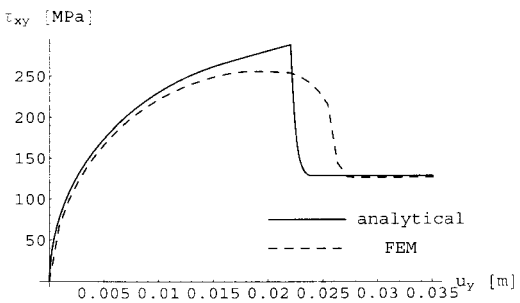

(c)

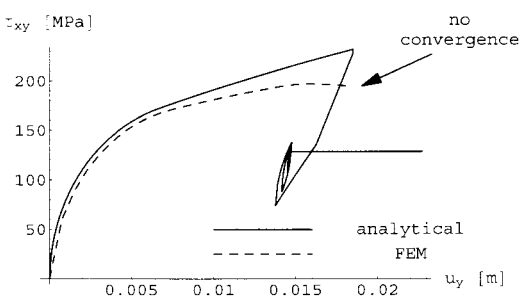

Figure 17. Load – displacement curves for transverse shear delamination; dashed line – results of numerical simulation for two dimensional model; continuous line – analytical solution for shear-beam model; (a) short plate solution, (b) medium plate solution, (c) long plate solution.

Figures 17 presents the relation between the displacement u_x and the stress τ_{xy} at point 0, that is at the origin of coordinate system, see Figure 5. They have been obtained for short, medium and long plates by varying the value of interfacial softening modulus K_s. The continuous line was obtained using the analytical solution for the shear beam model, whereas the dashed line is a result of numerical simulation performed for the two dimensional system. The simulation results are very close to the analytical solution during the early delamination stages. As the failure progresses though, the differences become more visible and disappear only during the last delamination stage, that is when there is only frictional interaction at contact. It is seen, that the decrease of loading force is smoother in the case of two dimensional simulation. In particular, the delamination stage associated with the decrease in loading force after the elastic zone has been terminated, is significantly different for the medium plate solution. The shear beam model provides an abrupt jump in the value of loading traction, whereas the numerical simulation results in a more compliant system response.

For $K_s > 1999$ MPa/m we have a long plate solution. Due to the numerical convergence problems, the full delamination process could not be performed. These difficulties arise from the fact, that displacement controlled simulation does not lead to a progressive failure evolution and the quasi static equilibrium path can not be generated. Figure 17(c) presents the solution for $K_s = 4500$ MPa/m obtained only up to the point of loss of convergence. It is associated with the first loop in the load-displacement curve for the shear beam model. Thus, the simple model of decohesion provides a reference solution for numerical algorithms searching for quasi static equilibrium paths in more complex cases.

Figures 18(a–e) present the variation of interfacial shear stress τ_y during the delamination process obtained for the following values of displacement at point 0: $26{\cdot}10^{-6}$ m, 0.02 m, 0.032 m, 0.042 m, 0.06 m. For clarity, the deformed mesh has been magnified and does not present the exact solution for the displacement field. Figures 18 were obtained for subsequent delamination phases of short plate and thus we have: in (a) the interface is fully elastic and the shear stress is below the critical value τ_c; in Figure 18(b) the interface is in the elastic and plastic regimes; Figure 18(c) presents the evolution of interfacial plastic zone; Figure 18(d) shows both plastic and frictional stresses at the interface, whereas in Figure 18(e) only frictional stress for fully damaged interface is presented. The τ_y stress presents a slight dependence on the y coordinate, so interfacial zones of elastic, plastic and frictional stresses are not exactly parallel. This is due to the flexural effects still present during the course of delamination and playing a dominant role mainly along the stress free boundaries. Moreover, as presented in Figure 18(e), the fully frictional interface becomes unloaded below the frictional stress value $\mu\sigma = 12.9$ MPa, which is also a result of flexural response of the structure.

3.2 Cyclic Loading: Plastic Shake Down and Incremental Failure

Consider now a cyclic loading process induced by the boundary traction $\tau_{xy}(0)$ varying between $+\tau^a_{xy}$ and $-\tau^a_{xy}$, that is a symmetric loading program. It is assumed that the cyclic response is represented by the same softening diagram as in the monotonic case, Figure 4(b). We shall distinguish between two consecutive semi-cycles constituting loading and unloading stages, respectively. The equilibrium Equation (2.49) is a recursive

(a)

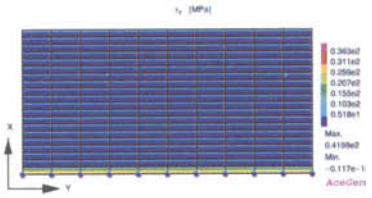

(b)

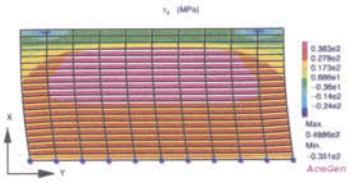

(c)

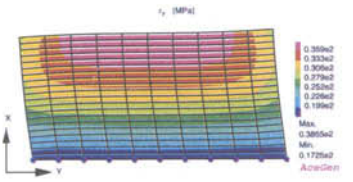

(d)

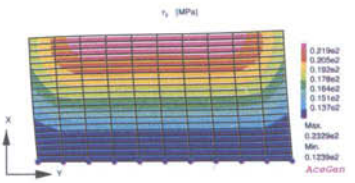

(e)

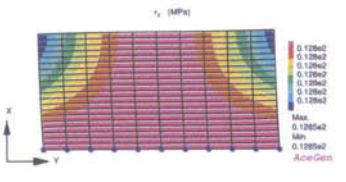

Figure 18. The variation of interfacial shear stress τ_y [MPa] during the course of delamination for the short plate response; the subsequent displacements u_y of boundary $x = 0$: (a) $26 \cdot 10^{-6}$ m; (b) 0.02 m; (c) 0.032 m; (d) 0.042 m; (e) 0.06 m.

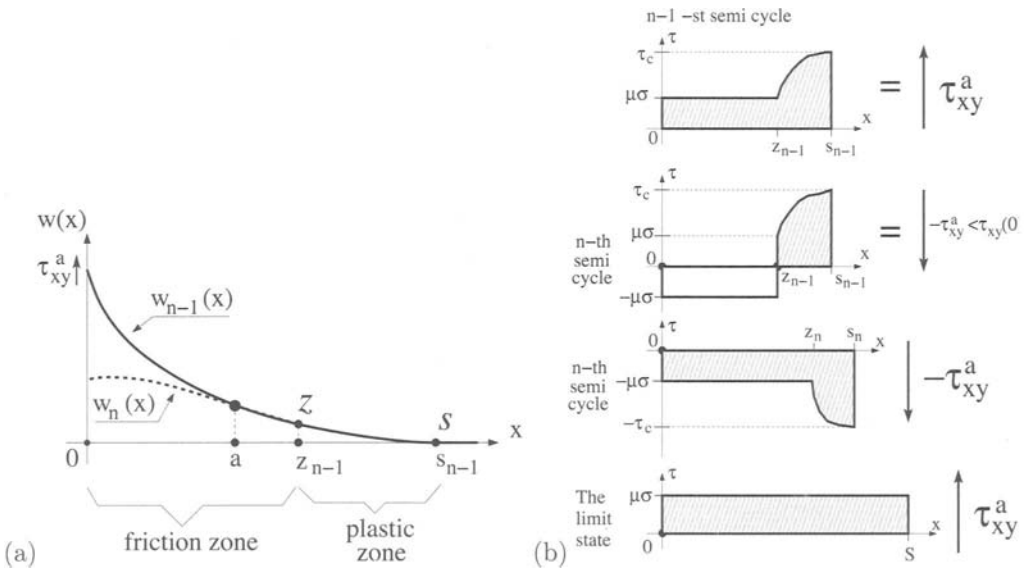

Figure 19. (a) The change in displacement fields during two subsequent semi cycles. (b) The friction zone unloading. The shear stress at the interface.

relation between functions $w_n(x)$ and $w_{n-1}(x)$ and allows for an analytical solution. For $n = 1$ we have the displacement field given by Equation (3.1).

Frictional shake-down solution, $\tau^a_{xy} \leq \mu\sigma L/t$. Let us consider the $n-1$-st semi cycle and assume that there are friction, plastic (damage) and undamaged zones at the interface. The transition point between friction and plastic region has a coordinate z_{n-1}. The value of s_{n-1} specifies the transition point between plastic and undamaged zones, as presented in Figure 19(a). The loading traction at the end of $n-1$-st semi cycle is τ^a_{xy}, so we assume it to be a loading stage. We shall consider the subsequent n-th loading stage. The function $w_{n-1}(x)$ and its derivative $w'_{n-1}(x)$ at the end of $n-1$-st semi cycle provide the continuity conditions:

$$w_n(a) = w_{n-1}(a) \qquad w'_n(a) = w'_{n-1}(a), \tag{3.44}$$

allowing for the specification of integration constants for the displacement field function $w_n(x)$ of n-th semi cycle. The unloading process is presented in Figure 19(a), meaning that there is a change in displacement field only for $x \in [0, a]$ and there are no configuration changes in the remaining plate section, that is for $x \in [a, L]$.

Mróz and Białas (2004) presented a detailed analysis of plate delamination due to cyclic loading, taking the limit case as the number of cycles approaches infinity. The results can be summarised as follows. During the cyclic loading process there are friction slip and damage zones developed at the interface. The interfacial shear stress is

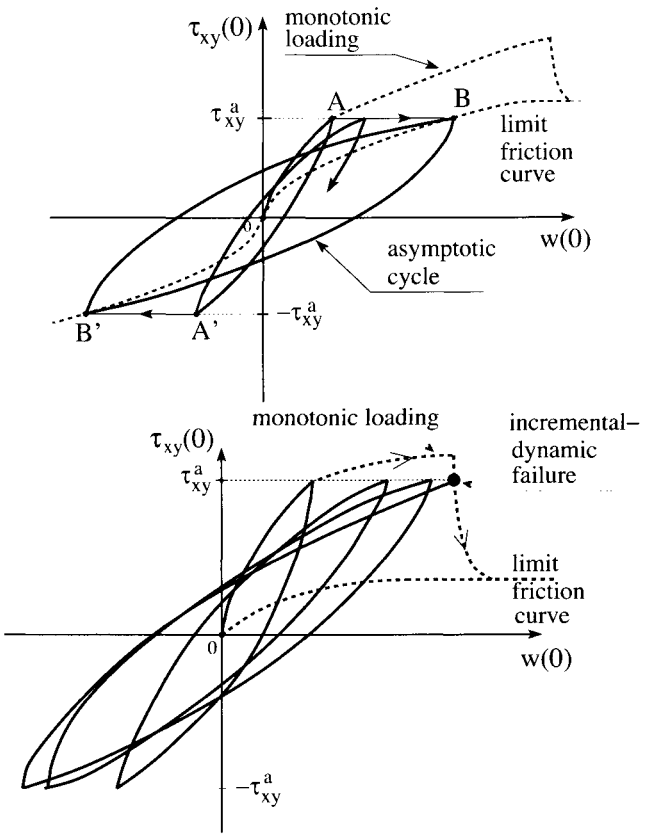

Figure 20. (a) Adaptation mode (shake down). (b) Incremental failure mode.

equilibrated by the external tractions subjected to the structure. As the loading process progresses, the damage zone becomes shorter, whereas the friction zone becomes longer. In the limit case, that is for a number of loading cycles approaching infinity, the cohesive zone vanishes completely and there is only frictional contact at the interface. The friction zone reaches its ultimate length S given by

$$S = \frac{|\tau^a_{xy}|t}{\mu\sigma}. \tag{3.45}$$

which can be easily deduced from Figure 19(b) by considering plate equilibrium in the limit state.

The loading traction $\tau_{xy}(0)$ varying between $-\tau^a_{xy}$ to $+\tau^a_{xy}$ cannot produce any further bond degradation and it is the frictional stress only to equilibrate the external loading. The development of interfacial shear stress is schematically presented in Figure 19.

The reason for this interesting phenomena is the softening response in the damage zone of the interface material providing progressive decrease in stress magnitude regardless the loading path. The actual shape of the softening function is not important and does not change the overall tendency, that is the progressive elongation of the frictional zone and the ultimate disappearance of cohesive area. In the limit state, the applied cyclic loading is fully equilibrated by the friction stress in the slip zone $0 \leq x \leq S$. The length S of friction zone does not depend on the softening function and is dependent on the amplitude τ_{xy}^a of the loading traction and the value of interfacial frictional stress $\tau = \mu\sigma$, *cf.* Equation (3.45).

It should be noted, that the interfacial frictional stress allows for the structural adaptation to steady cyclic response and thus, it governs the delamination process. The interfacial friction equilibrates the loading traction in the steady cyclic state. The ultimate length S of debonded area depends on the value of $\mu\sigma$: it is inversely proportional to the magnitude of friction stress. In fact, the failure zone can be very long, provided the frictional stress $\tau = \mu\sigma$ is small.

The present analysis does not consider wear effects at the interface, that is the degradation of friction coefficient μ. In practice, these effects are also present and cannot be neglected. The wear would reduce the value of friction stresses at the interface and, as a result, the ultimate length S of failure zone would increase. The coupling between wear and cohesive zone development should be treated numerically, as analytical approach faces mathematical difficulties.

Incremental-dynamic failure mode, $\tau_{xy}^a > \mu\sigma L/t$. Our analysis reveals two modes of structural response to cyclic loading, dependent on the value of amplitude τ_{xy}^a and the actual length L of the structure. When the loading traction amplitude τ_{xy}^a satisfies the inequality $\tau_{xy}^a \leq \mu\sigma L/t$, the limit length S of debonded zone is lower than the plate length L. Thus, at any stage during the delamination process, there remains an intact zone at the interface where the bond is not damaged and the loading traction $\tau_{xy}(0)$ can be fully equilibrated by the interfacial shear stress. We have then the case of cyclic shake down with frictional cyclic dissipation generated within the slip zone. As presented in Figure 20, the loading cycles approach the asymptotic cycle obtained for an interface with rigid-frictional constitutive relation with no softening effects. Thus, we have a situation of structural adaptation to cyclic loading, when the plate can sustain even an infinite number of loading cycles. For $\tau_{xy}^a > \mu\sigma L/t$ we have an incremental failure mode. An amplitude satisfying this inequality results in the frictional zone limit length S being longer than the actual length L of the structure, meaning that the entire interface debonds after a specific number of cycles. The equilibrium curve is then reached with a subsequent dynamic failure mode. This type of response is also valid for a frictionless case, $\mu\sigma = 0$, since the friction stress cannot equilibrate the loading traction and the debonded area becomes longer from one cycle to the other. No shake down is then possible as the debonded zone does not stabilize on any length. The structural response is schematically presented in Figure 20(b).

The delamination process is coupled with two types of energy dissipation at the material interface, namely damage and friction dissipation. In the course of delamination the damage zone disappears, so one dissipative process (friction) eliminates the other

(damage growth) in the steady-state response. This phenomenon is believed to be an intrinsic feature of failure evolution at material interfaces subjected to cyclic loading. It can be generalized to any loading conditions involving cyclic changes in external tractions, not only symmetric cycles assumed in the present analysis. This phenomenon is present during any delamination process induced by cyclic loading and the following conclusion can be stated. The steady state cyclic response at the interface is associated with frictional slip and disappearance of the damaged zone. The transient state evolves toward the steady cyclic state or the dynamic failure mode.

Numerical predictions. In order to present the results for the cyclic loading program, we shall introduce two dimensionless parameters:

$$\eta = \frac{\mu\sigma}{\tau_c}, \qquad \beta = \frac{s_1}{S},$$

where s_1 is the overall length of debonded zone at the end of the first semi cycle and S specified by (3.45) denotes the damaged zone length in the limit state. Thus, β specifies the length of the damaged interface zone after the first semi cycle is completed as compared to the overall damage area. The parameter η was already introduced in Section 3.1 and expresses the ratio between interface critical stress and frictional traction for fully damaged interface. The value of s_1 can be obtained from Equations (3.5) and (5.8). So we have:

$$s_1 = \frac{1}{r_s} \arcsin \frac{\tau_{xy}^a K_s}{G\tau_c r_s} \qquad \text{for} \qquad \tau_{xy}^a \leq \frac{\tau_c}{r_s t}\sqrt{1-\eta^2} \tag{3.46}$$

and

$$s_1 = \frac{\tau_{xy}^a}{\mu\sigma} t - \frac{1}{r_s}\frac{\sqrt{1-\eta^2}}{\eta} + \frac{1}{r_s}\arccos\eta \quad \text{for} \quad \tau_{xy}^a > \frac{\tau_c}{r_s t}\sqrt{1-\eta^2}. \tag{3.47}$$

The results are provided under the assumption that the plate is long enough to allow for the adaptation mode. In order to equilibrate the loading traction in the limit cyclic state the following condition should be satisfied:

$$\mu\sigma S < \tau_c s_1$$

providing

$$\beta > \eta. \tag{3.48}$$

So the pair $\{\eta, \beta\}$ should satisfy the inequalities:

$$0 < \eta < 1, \qquad \eta < \beta < 1. \tag{3.49}$$

The dimensionless parameter β can be expressed as a function of ratio $\delta = \tau_{xy}^a/\tau_c$ in the form

$$\beta = \frac{\eta}{r_s t\delta} \arcsin(r_s t\delta) \qquad \text{for} \qquad r_s t\delta \leq \sqrt{1-\eta^2} \tag{3.50}$$

$$\beta = \frac{1}{r_s t\delta}(\eta \arccos\eta - \sqrt{1-\eta^2}) \qquad \text{for} \qquad r_s t\delta > \sqrt{1-\eta^2} \tag{3.51}$$

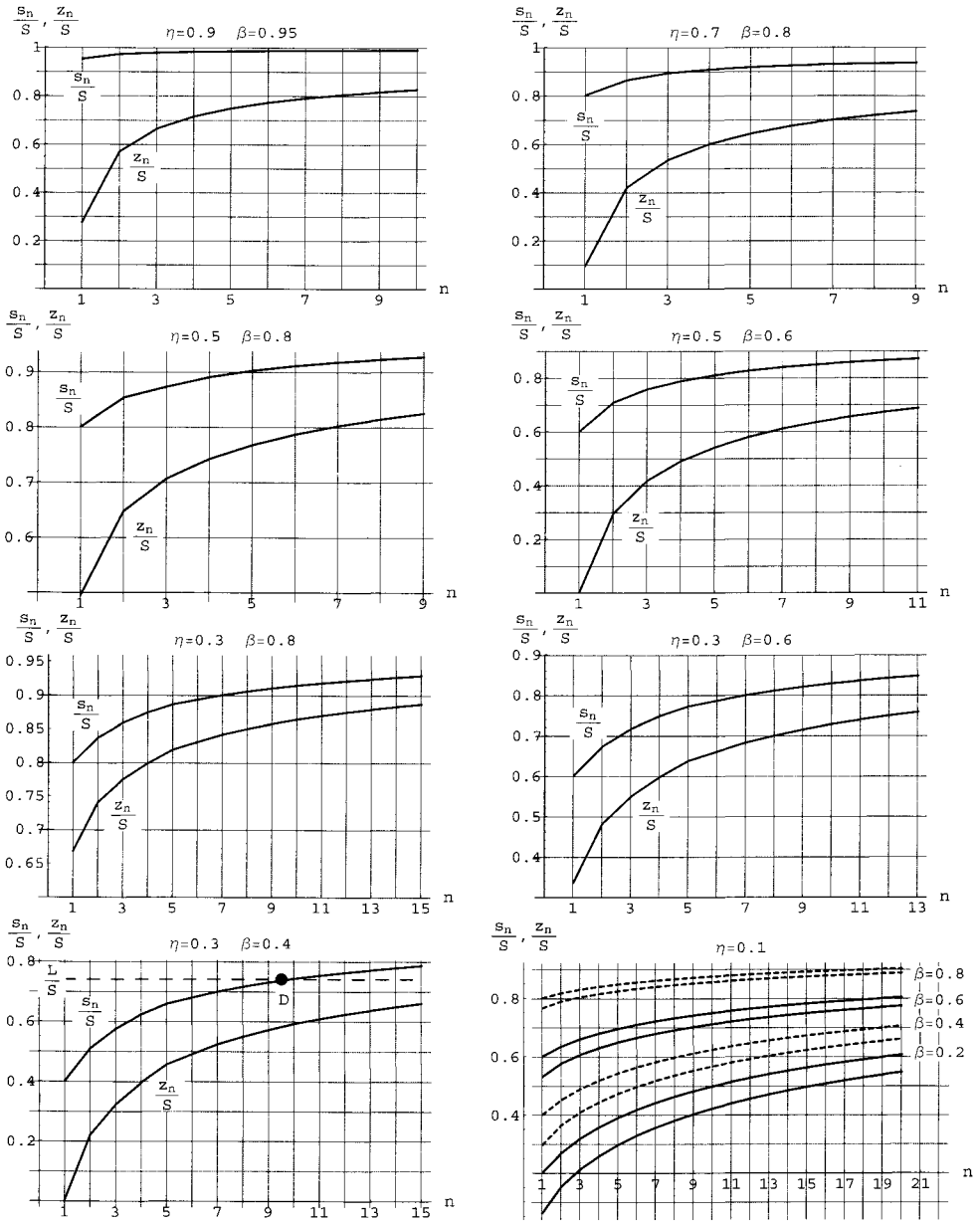

Figure 21. The development of friction and cohesive zones. The intersection of L/S line with s_i/S curve provides the number of semi-cycles to failure. For $\eta = 0.3$ and $\beta = 0.4$ and $L/S = 0.74$ the structure debonds during the tenth semi-cycle (point D in the left bottom diagram) .

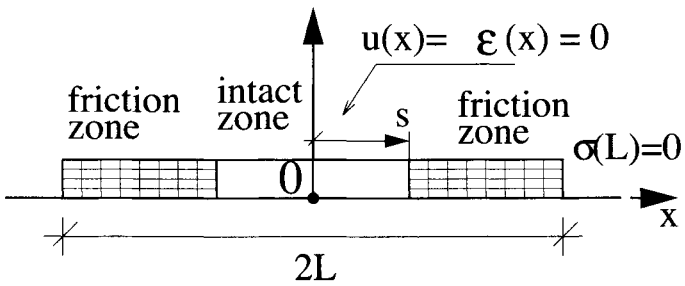

Figure 22. A plate on a substrate. The rigid-friction interface model.

Thus, Equations (3.50) and (3.51) allow for a comparison between the parameter β and more convenient, from a practical point of view, the ratio $\delta = \tau_{xy}^a/\tau_c$.

Figures 21 illustrate the problem solution by showing the evolution of $\{z_n\}$ and $\{s_n\}$, being respectively friction and combined friction and damage zones lengths. They are obtained for various values of parameters η and β satisfying the condition (3.49) by recursively integrating Equation (2.49). The number n indicates a particular semi-cycle. It is seen that throughout the loading process the results come closer to the asymptotic solution described above: the length of damage zone approaches zero and the length of friction zone approaches S. The diagrams (21) provide also the number of semi cycles leading to failure in the case of incremental collapse. For a given $L < S$ and an amplitude τ_{xy}^a, one can read the maximum number of semi cycles the structure can sustain by an intersection of an appropriate s_i/S curve with L/S line, as presented in the nomogram obtained for the values $\eta = 0.3$ and $\beta = 0.4$.

4 Longitudinal Shear Delamination and Segmentation Cracking Due to Temperature Loading

In the following we shall use equations specified in Section 2.3 in order to analyse the plate delamination and segmentation cracking induced by temperature loading. In the analysis we shall use rigid-friction and rigid-cohesive-friction formulations for the interface material. Two types of temperature loadings shall be considered, namely monotonic and cyclic.

4.1 Monotonic Loading

Rigid-friction interface model. Let us assume a frictional relation between the shear stress τ and the interface deformation $\gamma = u/h$, where h denotes interface layer thickness. The interface shear stress equals

$$\tau(x) = \tau_f \text{sign}(\dot{u}) \tag{4.1}$$

with τ_f being the constant value of frictional stress and h the interface thickness. By substituting Equation (4.1) into (2.41) and solving it for u, one can obtain the displacement field in the form:

$$u(x) = \frac{\tau_f}{2Et}\text{sign}(\dot{u})x^2 + A_1 x + A_2, \tag{4.2}$$

where A_1 and A_2 are integration constants. Equation (4.2) together with (2.38), (2.39) and the boundary conditions

$$u(s) = 0, \qquad \sigma(L) = 0, \qquad \lceil \sigma(s) \rfloor = 0 \tag{4.3}$$

presented in Figure 22, provide the problem solution. Here $\lceil \bullet \rfloor$ denotes the discontinuity of the enclosed state field. Equations $(4.3)_2$ and $(4.3)_3$ indicate that the interface in the middle of the plate remains intact and the deformation takes place in the frictional zone only. With s being the loading parameter, we obtain the displacement field $u(x, s)$ in the form:

$$u(x, s) = -\frac{\tau_f}{2Et}(x - s)^2. \tag{4.4}$$

The temperature ΔT is related to s by the formula:

$$\Delta T(s) = -\frac{\tau_f(L - s)}{\alpha t E}. \tag{4.5}$$

The corresponding normal stress $\sigma(x)$ within the friction zone is a linear function:

$$\sigma(x, s) = \frac{\tau_f}{t}(L - x), \tag{4.6}$$

whereas in the intact layer zone its value is independent of x and equals $\sigma = \tau_f(L - s)/t$ in order to compensate the normal strain. The plots of τ, σ, ϵ and u are presented in Figure 23. It should be noted that although the plate is being cooled down and subsequently being shrunken, the normal stress acting on it is positive and therefore the plate is in tension. It is clearly seen that the maximum value of the normal stress σ is achieved for $s = 0$ and equals $\tau_f L/t$. The condition $s = 0$ means that the entire interface has been damaged and further variation in temperature ΔT will not affect the stress state. The limit value of ΔT is equal to $-\tau_f L/(\alpha t E)$ and can be obtained from Equation (4.5) for $s = 0$.

The influence of temperature gradient $\partial(\Delta T)/\partial z$ on the stress state in the plate material can be specified by the ratio σ^M/σ where σ^M is given by Equation (2.47) and σ by Equation (4.6):

$$\frac{\sigma^M}{\sigma} = \frac{\alpha E z(\Delta T_t - \Delta T_b)}{\tau_f(L - x)}. \tag{4.7}$$

Having in the above formula $z = t/2$ and requiring $\sigma^M/\sigma < 0.05$, we obtain the maximal plate thickness for which the influence of temperature gradient on normal stress distribution is less than 5%:

$$t < \frac{0.1\tau_f(L - x)}{\alpha E(\Delta T_t - \Delta T_b)}. \tag{4.8}$$

It is obvious that the temperature gradient effect plays dominant role at stress free end for $x = \pm L$ and reduces in the middle section of the structure.

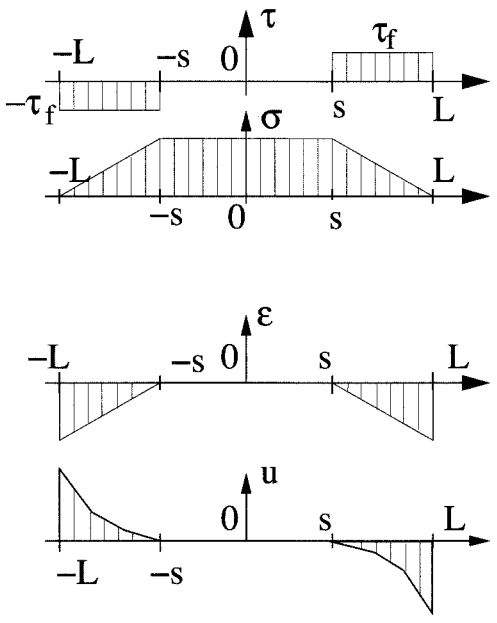

Figure 23. The shear stress at the interface, normal stress, strain and displacement fields for the rigid-friction model.

Let us now consider the brittle fracture of the plate material. The critical stress value σ_c indicates the strength in tension. As it is seen in Figure 23 the maximum value of the normal stress is attained along the entire middle zone, therefore this simple model can not properly predict the place where fracture occurs. As a matter of fact, we assume that the plate would break exactly in the middle. It corresponds to the realistic assumption that interface material cannot be perfectly rigid and, if so, the maximum stress σ is always attained in the middle for $x = 0$. It will be clarified when elastic - frictional model of the interface is considered.

Due to the assumption that the plate would fracture in the middle, a new boundary is created for $x = 0$ and the stress field has to satisfy the condition $\sigma(0) = 0$. This leads to creation of two more frictional zones in the vicinity of the plate fragmentation point. The plateau where $\sigma(x)$ is equal to σ_c still exists though, and the two successive fragments fracture again. The process continues until there are no more critical stresses σ_c attained at any of the plate fragments. Thus, the total number of fragments N may equal $1, 2, 4, 8, ..., n_i, 2n_i, ...$ The fragmentation process is illustrated in Figure 24.

Let N be the number of plate fragments. From the condition

$$\sigma(0) < \sigma_c \tag{4.9}$$

we can derive a formula for N, when all material and geometry parameters are given.

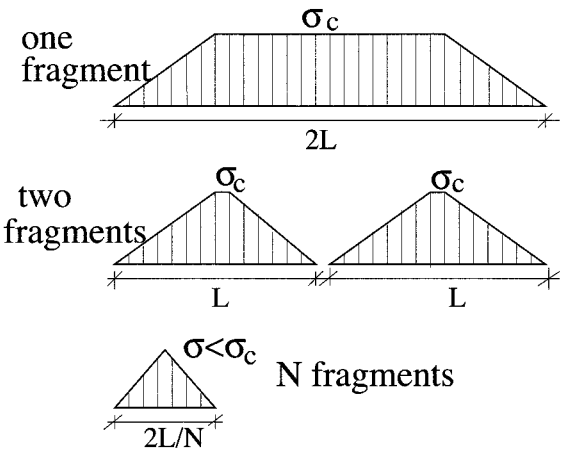

Figure 24. Plate fragmentation process.

Condition (4.9) applied to Equation (4.6) provides

$$\sigma(0) = \frac{\tau_f}{t}\frac{L}{N} < \sigma_c. \tag{4.10}$$

The fact that the length of each of N-th fragments is $2L/N$ now has been used. From inequality (4.10) it can be derived that the total number of plate fragments is the smallest natural number N of the set $\{1, 2, 4, 8, \ldots, n_i, 2n_i, \ldots\}$ that obeys the condition

$$N > \frac{\tau_f}{\sigma_c}\frac{L}{t}. \tag{4.11}$$

It should be noticed, that according to this model all fractures occur at the same temperature $\Delta T_c = \tau_f/(\alpha t E)$.

Rigid-Cohesive-Friction Model Now, let us assume the cohesive interface model and study the progressive delamination at the interface combined with plate cracking. The relation between the shear stress τ and the interface deformation exhibits softening and is that presented in Figure 4(b). In the case of monotonic loading it takes the form:

$$\tau = \tau_c - K_s u, \qquad u \in < 0, u_c >, \qquad u_c = \frac{\tau_c - \tau_f}{K_s}, \tag{4.12}$$

for the cohesive zone, and

$$\tau = \tau_f, \qquad u > u_c \tag{4.13}$$

for the frictional zone. By substituting Equation (4.12) into equilibrium Equation (2.41) and solving for u, it can be obtained that the displacement field within the cohesive zone

is expressed in the form:

$$u(x) = C_1 \cos(r_s x) + C_2 \sin(r_s x) + \frac{\tau_c}{K_s}, \tag{4.14}$$

where $r_s = \sqrt{K_s/(Et)}$ and C_1 and C_2 are the integration constants. The displacement field (4.2) still applies for the frictional zone. To describe the delamination phenomena we have to combine displacement fields (4.2) and (4.14) using appropriate boundary and continuity conditions. It appears that there are two distinct cases to be considered, namely a short and a long plate solution.

During the first stage of delamination there is only the cohesive zone developed at the interface. From Equation (4.14) we can determine the constants C_1 and C_2 which satisfy the boundary conditions:

$$u(s) = 0, \qquad \sigma(L) = 0. \tag{4.15}$$

Similarly to the rigid friction model, there is a central zone where the interface is intact, that is

$$u(x) \equiv \epsilon(x) \equiv 0 \tag{4.16}$$

for $x \in < -s, s >$. From Equation (2.38) it follows that the normal stress within this zone is constant and equals

$$\sigma(x) \equiv \alpha \Delta T E \qquad x \in < -s, s > . \tag{4.17}$$

Equations (4.15) and (4.17) allow us to write the displacement field u, the normal stress field σ, the interface shear stress field τ and the temperature ΔT as functions of s:

$$u(x,s) = -\frac{\tau_c}{K_s} + \frac{\tau_c}{K_s}\frac{\cos[r_s(L-x)]}{\cos[r_s(L-s)]} + \frac{\tau_c}{K_s}\sin[r_s(s-x)]\tan[r_s(L-s)], \tag{4.18}$$

$$\sigma(x,s) = \frac{E r_s \tau_c}{K_s}\Big(\sin[r_s(L-s)] + \sin[r_s(s-x)]\Big), \tag{4.19}$$

$$\tau(x,s) = -\tau_c \cos[r_s(s-x)], \tag{4.20}$$

$$\Delta T(s) = -\frac{r_s \tau_c}{K_s \alpha}\sin[r_s(L-s)]. \tag{4.21}$$

The equality

$$\tau(0)|_{s=0} = -\tau_f \tag{4.22}$$

implies the condition for two types of solution. The plate will be called a long one if there are three zones, namely friction, cohesive and intact, developed at the interface. For the short plate solution there are either one or two zones developed for every stage of the loading process. At first there are cohesive and intact zones developed, next the cohesive one only and subsequently both cohesive and friction zones.

From Equation (4.22) the condition for the short plate solution can be derived in the form:

$$\chi_s \leq \arccos\eta, \tag{4.23}$$

where $\chi_s = r_s L$, $\eta = \tau_f/\tau_c$. The long plate solution applies when

$$\chi_s > \arccos\eta. \tag{4.24}$$

Short plate solution. Let us consider the short plate solution in detail. After the intact zone has disappeared there is only cohesive zone left. The stress and displacement fields can be derived from Equation (4.14) by satisfying boundary conditions:

$$u(0) = \sigma(L) = 0. \tag{4.25}$$

Accounting for Equation (4.25), one obtains:

$$u(x) = -\frac{\tau_c}{K_s} + \frac{\tau_c}{K_s}\frac{\cos[r_s(L-x)]}{\cos(r_s L)} + \frac{\Delta T\alpha}{r_s}\frac{\sin(r_s x)}{\cos(r_s L)}, \tag{4.26}$$

$$\sigma(x) = -E\Delta T\alpha + E\alpha\Delta T\frac{\cos(r_s x)}{\cos(r_s L)} + \frac{Er_s\tau_c}{K_s}\frac{\sin[r_s(L-x)]}{\cos(r_s L)}. \tag{4.27}$$

The decohesion process continues with temperature decreasing from

$$\Delta T_1 = -r_s\tau_c \sin(r_s L)/(K_s\alpha)$$

down to

$$\Delta T_2 = -r_s[\tau_c/\sin(r_s L) + \tau_f \cot(Lr_s)]/(K_s\alpha).$$

When ΔT reaches ΔT_2 the friction zone starts to develop together with the cohesive one. The displacement and stress fields can be obtained from Equation (4.14) by satisfying the boundary conditions:

$$u(0) = 0, \qquad u(z) = -u_c, \tag{4.28}$$

where z is the coordinate of point between the friction and cohesion zones. The continuity condition

$$\sigma(z) = \frac{\tau_f}{t}(L-z) \tag{4.29}$$

provides the relation between the temperature T and the parameter z:

$$u(x) = -\frac{\tau_c}{K_s} - \frac{\tau_c \sin[r_s(x-z)] - \tau_f \sin(r_s x)}{K_s \sin(r_s z)}, \tag{4.30}$$

$$\sigma(x) = -E\Delta T(z)\alpha - \frac{Er_s}{K_s}\frac{\tau_c\cos[r_s(x-z)] - \tau_f\cos(r_s x)}{\sin(r_s z)}, \tag{4.31}$$

$$\Delta T(z) = -\frac{\tau_f}{Et\alpha}(L-z) - \frac{r_s}{Et\alpha}\frac{\tau_c - \tau_f\cos(r_s z)}{\sin(r_s z)}. \tag{4.32}$$

It follows from Equation (4.32) that when z tends to zero ΔT tends to minus infinity. Therefore, the stage when the interface is totally delaminated is attained only asymptotically.

Long plate solution. We shall consider now the long plate solution in detail. During the first stage of the loading process there are two zones at the interface: intact and cohesive and Equations (4.18)–(4.21) apply. During the second stage the friction zone develops additionally. The condition

$$u(x) \equiv \epsilon(x) \equiv 0, \qquad x \in < -s, s > \tag{4.33}$$

still holds within the intact zone providing the value of the normal stress acting in this zone:

$$\sigma(x) = -\alpha \Delta T E, \qquad x \in < -s, s > . \tag{4.34}$$

By satisfying the continuity conditions:

$$\begin{aligned} \sigma(s) &= -\alpha \Delta T E, \\ u(s) &= 0, \\ \sigma(z) &= \frac{\tau_f}{t}(L - z), \\ u(z) &= -u_c, \end{aligned} \tag{4.35}$$

we can obtain displacement and stress fields, temperature ΔT and the value of z in the function of s:

$$u(x) = -\frac{\tau_c}{K_s} - \frac{\tau_c}{K_s}\frac{\sin[r_s(x-z)]}{\sqrt{1-\eta^2}} - \frac{\tau_f}{K_s}\frac{\sin[r_s(s-x)]}{\sqrt{1-\eta^2}}, \tag{4.36}$$

$$\sigma(x) = -E\Delta T\alpha + \frac{E r_s}{K_s}\frac{\tau_f \cos[r_s(s-x)] - \tau_c \cos[r_s(x-z)]}{\sqrt{1-\eta^2}}, \tag{4.37}$$

$$z = s + \frac{1}{r_s}\arccos\eta, \tag{4.38}$$

$$\Delta T(s) = -\frac{\tau_f}{Et\alpha}(L - s - \frac{1}{r_s}\arccos\eta) - \frac{r_s \tau_c}{K_s \alpha}\sqrt{1-\eta^2}. \tag{4.39}$$

It should be noted that the length of the cohesive zone $|z - s|$ is constant and equals $\arccos\eta/r_s$.

The last stage of the loading process starts when the intact zone disappears and there are only two zones left, namely cohesive and frictional. This particular case was solved before and is described by Equations (4.30)–(4.32). All previous remarks apply.

Brittle fracture of plate. Let us discuss now the brittle fracture of the plate. In order to do that, we shall examine the maximum normal stress acting in the plate, that is at the center $x = 0$. It can be done by making use of Equations (4.17), (4.27), (4.31) and (4.34). Results are presented in Figure 25. It is seen that in the short plate case the maximum normal stress is attained at the end of the first loading stage, whereas for the long plate, at the end of the second one.

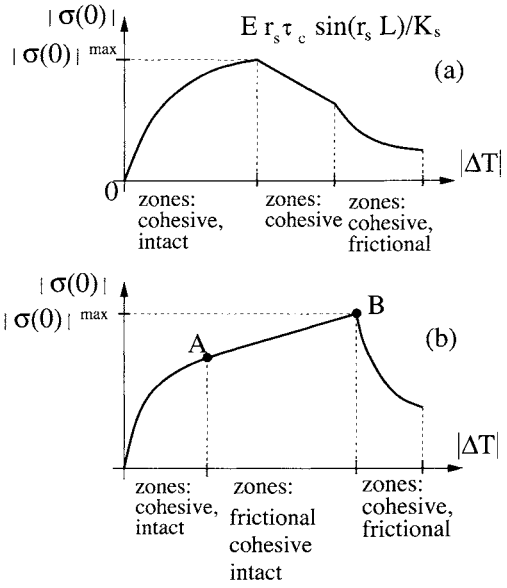

Figure 25. The maximum normal stress $\sigma(0)$ during the loading process: (a) short plate, (b) long plate: $\sigma(0)$ at point A equals $Er_s\tau_c\sqrt{1-\eta^2}/K_s$; $\sigma(0)$ at point B is equal to $Er_s\tau_c\sqrt{1-\eta^2}/K_s + \tau_f(L - \arccos\eta/r_s)/t$.

Let us discuss the fragmentation of the short plate first. If σ_c, that is the fracture strength, is greater than $Er_s\tau_c \sin(r_s L)/K_s$ then no fragmentation occurs. For σ_c satisfying the inequality

$$\sigma_c \leq \frac{Er_s\tau_c}{K_s}\sin(r_s L) \tag{4.40}$$

fractures will appear during the first stage of loading process, that is when there is cohesive zone developed together with the intact one. After a fracture, a new boundary is created for $x = 0$ and the stress field has to satisfy the condition $\sigma(0) = 0$. This leads to creation of two cohesive zones in the vicinity of the plate fragmentation point. The plateau where $\sigma(x) = \sigma_c$ still exists though, and the plate breaks again. The process continues until there are no more critical stresses σ_c attained at any of the plate fragments. The scenario is similar to that of rigid-friction model and can be illustrated by Figure 24.

Let n be the number of plate fragments. From the condition

$$\sigma(0) < \sigma_c \tag{4.41}$$

we will derive a formula for N when all material and geometry parameters are given.

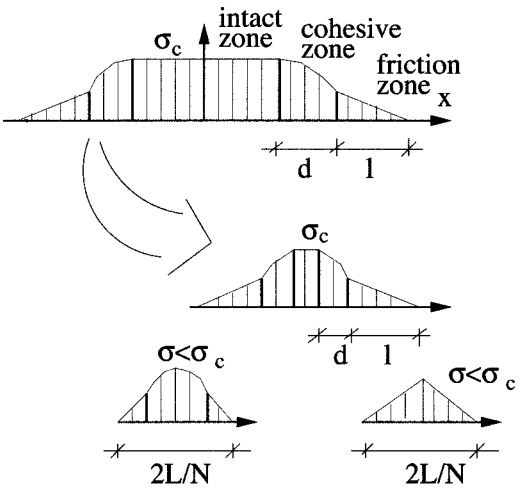

Figure 26. The fracture of a long plate.

Condition (4.41) applied to Equation (4.19) provides

$$N > \frac{r_s L}{\arcsin(\frac{\sigma_c}{\tau_c} t r_s)} \tag{4.42}$$

which means that the total number of fragments is the smallest N in the set $N \in \{1, 2, 4, 8, \ldots, n_i, 2n_i, \ldots\}$ that satisfies condition (4.42).

We shall concentrate now on the long plate solution. Three different cases should be discussed. For

$$\sigma_c \leq \frac{E r_s \tau_c}{K_s} \sqrt{1 - \eta^2} \tag{4.43}$$

fracture occurs when two zones exists, namely intact and cohesive. Equation (4.42) applies since the considerations are identical with those of the short plate. If the critical stress σ_c satisfies the condition:

$$\frac{E r_s \tau_c}{K_s} \sqrt{1 - \eta^2} < \sigma_c \leq \frac{E r_s \tau_c}{K_s} \sqrt{1 - \eta^2} + \frac{\tau_f}{t}(L - \frac{1}{r_s} \arccos \eta), \tag{4.44}$$

then fracture occurs when there are three interfacial zones developed, namely: intact, cohesive and friction. As it is presented in Figure 26 the condition for the cracks to stop occurring can be written in the form:

$$l + d > \frac{L}{N}, \tag{4.45}$$

where l and d are the lengths of friction and damage zones respectively. From (4.45) it follows

$$N > \frac{Lr_s}{\arccos\eta - \frac{\sqrt{1-\eta^2}}{\eta} + \frac{\sigma_c}{\tau_f} tr_s}, \tag{4.46}$$

where N is the smallest number of the set $\{1, 2, 4, 8, \ldots, n_i, 2n_i, \ldots\}$.

For

$$\sigma_c > \frac{Er_s\tau_c}{K_s}\sqrt{1-\eta^2} + \frac{\tau_f}{t}(L - \frac{1}{r_s}\arccos\eta)$$

no cracks occur and there is delamination only.

4.2 Discussion

Let us compare the maximum number of plate fragments provided by discussed models. They are given by expression (4.11) for the rigid-friction model and by formulas (4.42) and (4.46) respectively for the short and long plate solutions in case of rigid-cohesive-frictional interface. In order to compare the results we shall introduce the following dimensionless parameters:

$$\chi_s = Lr_s, \qquad \xi_s = \frac{\sigma_c}{\tau_c} tr_s, \qquad \eta = \frac{\tau_f}{\tau_c}.$$

Having done that, we can rewrite the expressions (4.11), (4.11), (4.42) and (4.46). They take the form:

- the rigid-friction model

$$N > \frac{\chi_s}{\xi_s}, \tag{4.47}$$

- the cohesive-friction model
  - short plate solution

$$N > \frac{\chi_s}{\arcsin\xi_s}, \tag{4.48}$$

  - long plate solution

$$N > \frac{\chi_s}{\arcsin\xi_s} \qquad \text{for } \xi_s \le \sqrt{1-\eta^2}, \tag{4.49}$$

$$N > \frac{\chi_s}{\arccos\eta + \frac{1}{\eta}(\xi_s - \sqrt{1-\eta^2})} \qquad \text{for } \xi_s > \sqrt{1-\eta^2}, \tag{4.50}$$

where N is the smallest natural number of the set $\{1, 2, 4, 8, \ldots, n_i, 2n_i, \ldots\}$.

By having equality in the conditions (4.47), (4.48), (4.49), (4.50) and N being a number of the set $\{1, 2, 4, 8, \ldots, n_i, 2n_i, \ldots\}$, we obtain a family of functions $\xi_s^N(\chi_s)$. They are plotted in Figure 27 and Figure 28. Thus, the plane (χ_s, ξ_s) is divided into separate regions providing the resulting maximum number of plate fragments for given parameters χ_s and ξ_s.

The solutions for the rigid-cohesive-friction model are plotted in Figure 28 for several values of dimensionless parameter $\eta = \tau_f/\tau_c$. It is clearly seen that for η being close

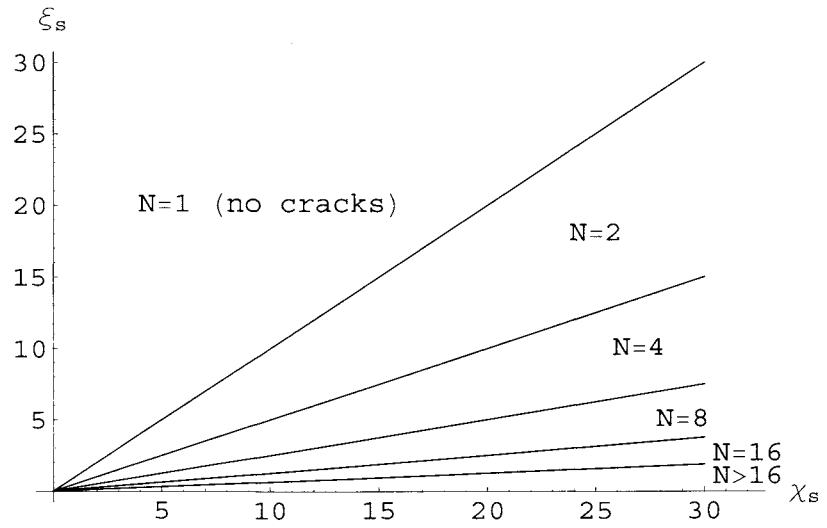

Figure 27. Number of plate fragments in the plane (χ_s, ξ_s) for the rigid-friction and elastic-friction models.

to 1 the resulting number of fragments versus the parameters χ_s, ξ_s is similar to that provided by the rigid-friction model. It can be easily explained since a value of η close to unity means that the softening effect of the rigid-cohesive-friction model is very small. As a consequence, it provides similar results to those of the rigid-friction model.

In order to obtain a high number of plate fragments the ratio ξ_s/χ_s has to be small enough. It can be achieved by several means. Firstly, a small value of the critical stress σ_c results in small ξ_s and, consequently, a high number of fragments. It is not strange since a weaker plate tends to break into more segments. In order to obtain a small value of ξ_s one can also have a high value of τ_c, that is the maximal interfacial strength. As a consequence, it follows that a strong bond between the plate and the substrate may lead to a high damage within the entire structure.

4.3 Cyclic Loading: Rigid-Cohesive-Friction Model

We now consider the cyclic loading case.As in the case of anti-plane shear, formula (2.49) is a recursive relation between the displacement fields of two subsequent semi-cycles. By having u_{n-1} one can solve Equation (2.49) in order to obtain u_n. In the following we shall consider symmetric cyclic loading.

Limit solution. In this section we shall consider a limit solution referring to a situation after an infinite number of cycles. First let us focus on the cooling and heating cycles and assume that the plate is long enough to have three interface zones developed, namely intact, cohesive and friction. The normal stress at the center is constant and its absolute

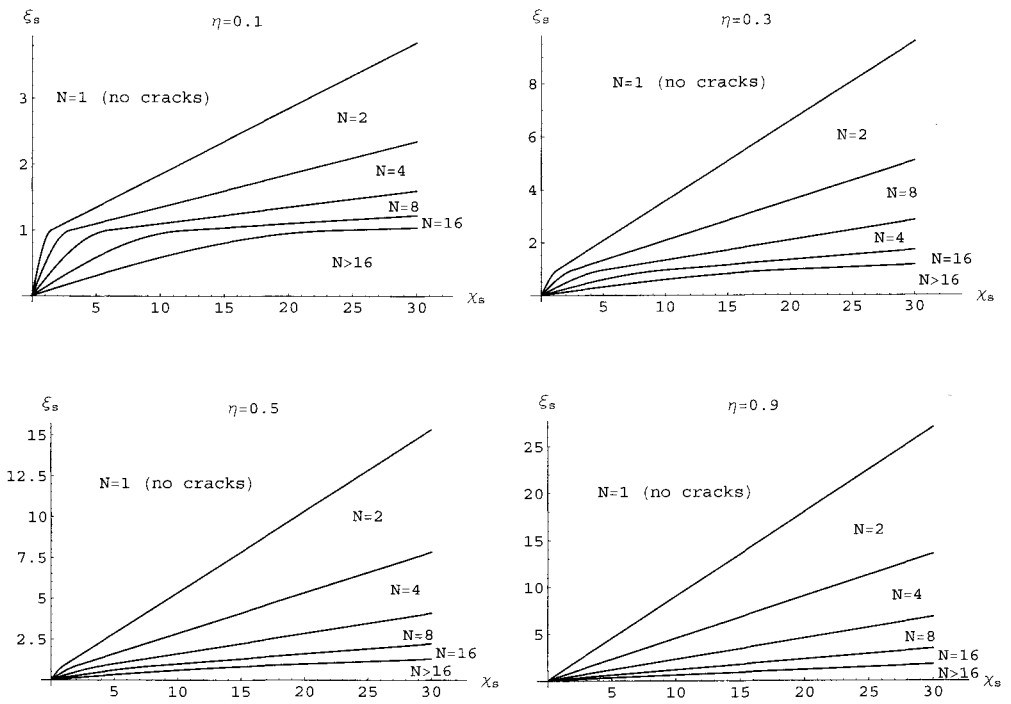

Figure 28. Number of plate fragments in the plane (χ_s, ξ_s) for the rigid-cohesive-friction model and values of η equal to 0.1, 0.3, 0.5, 0.9.

value is $\alpha E \Delta T_a$. It compensates the thermal deformation of this plate portion and therefore there is no shrinkage in this zone.

At the end of the subsequent heating there is an intact zone in the center portion as well, but this time shorter than at the end of previous semi-cycle. In order to compensate its thermal expansion the damage interface zone gets longer. The reason of this is the softening effect in the cohesive zone and subsequent reduction in absolute value of interfacial shear stress. The phenomena continues during the following cycles. An asymptotic solution is that the cohesive zone vanishes completely and there are only friction and intact zones remaining, provided the plate is long enough. The process is illustrated in Figures 29 and is identical to that presented by Mróz and Białas (2004). This scenario can be called *an adaptation mode*, since the structure exhibits only partial delamination and there always remains an undamaged interfacial zone, regardless the number of loading cycles.

Let us derive the limit length S of a single friction zone during the asymptotic limit state. The normal stress $\sigma = \alpha E \Delta T_a$ has to compensate the plate deformation in the central portion. Moreover, it has to be continuous at the transition point between both

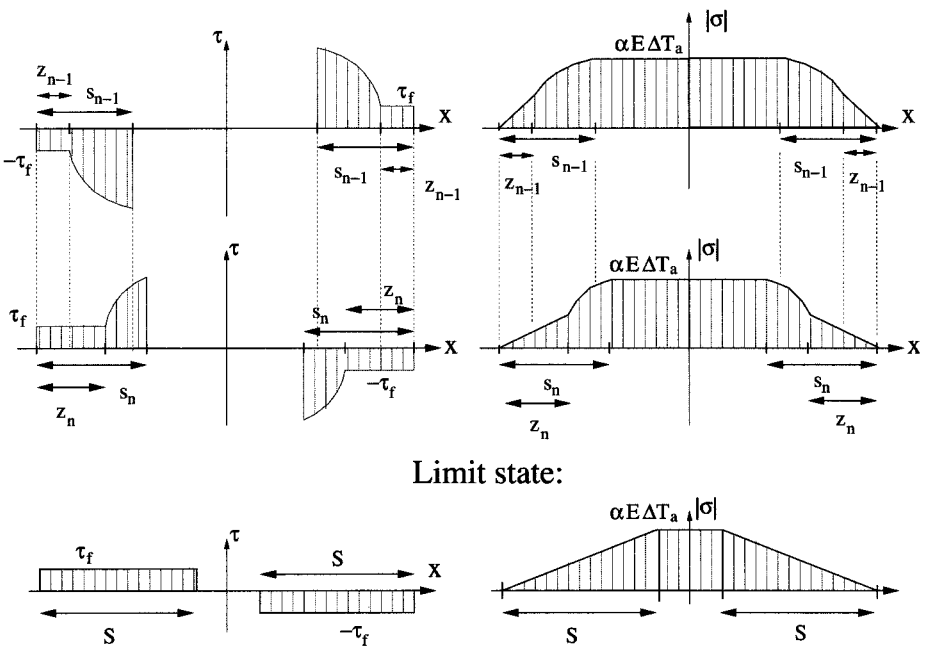

Figure 29. Plate response to cyclic loading for adaptation mode. The limit state: $L \geq S$.

intact and friction zones. Therefore we can write:

$$\sigma = \frac{\tau_f}{t} S = \alpha E \Delta T_a$$

and subsequently:

$$S = \frac{\Delta T_a E t \alpha}{\tau_f}. \tag{4.51}$$

Results. Let us assume that the plate length satisfies the condition:

$$L \geq S,$$

that is there is always an intact interface layer in the middle of the plate. We shall introduce two dimensionless parameters allowing to describe the plate response to cyclic loading. The first one η is given by the formula:

$$\eta = \frac{\tau_f}{\tau_c}.$$

The other dimensionless parameter β is defined as follows:

$$\beta = \frac{s_1}{S}$$

where s_1 is the length of damage zone at the end of first semi-cycle, and S is given by Equation (4.51). Thus, β says how long is the damaged interface zone after the first semi-cycle when compared to the overall length of the damaged zone. The value of s_1 is provided by

$$s_1 = \frac{1}{r_s} \arcsin \frac{|\Delta T_a| K_s \alpha}{r_s \tau_c}$$

for the short plate solution and by

$$s_1 = \frac{1}{r_s} \arccos \eta - \frac{\sqrt{1-\eta^2}}{r_s \eta} - |\Delta T_a| \frac{Et\alpha}{\tau_f}$$

for the long plate solution.

Parameters η and β have already been used in Section 3.2 where anti-plane cyclic shear loading was considered. The same condition applies, namely β and η are bounded by the inequalities:

$$0 < \eta < 1, \qquad \eta < \beta < 1.$$

Figures 21 present the problem solution by providing the evolution of lengths of single friction and cohesive zones. They are obtained for several values of parameters η and β by integrating Equation (2.49). The number n indicates a particular semi-cycle. They are the same as for anti-plane shear cyclic loading, since they were obtained by integrating Equation (2.49), valid both for longitudinal and transverse delamination. It is seen that throughout the loading process the results are closer to the asymptotic solution described above: the lengths of cohesive zone for increasing number of cycles tend to zero and the length of friction zone tends to S.

For $L < S$ the intact zone vanishes and there are only cohesive and friction zones left at the interface. Figures 21 allow for specification of number of thermal cycles leading to failure. For a given set of parameters (η, β) one simply has to read the semi-cycle for which the following condition is satisfied:

$$\frac{s_n}{S} > \frac{L}{S}.$$

A similar failure mode for an interface subjected to cyclic loading was presented in the paper by Mróz and Białas (2004).

For $L < S$ the intact zone vanishes and the whole plate shrinks during cooling or elongates during heating. This is the incremental failure situation, when the interface is damaged after a critical number of cycles. Due to the softening effect the length of cohesive zone tends to zero, but the state when it vanishes completely can be obtained only asymptotically. This is because of the structural symmetry. The point at the center $x = 0$ cannot be displaced and the interface will not be damaged there. The plate response for this particular case is schematically presented in Figure 30.

Figures 31 present the development of friction and cohesive zones when $L < S$. They are obtained for several values of η, β and L/S. Likewise in the previous case, the length of cohesive zone becomes shorter as loading progresses.

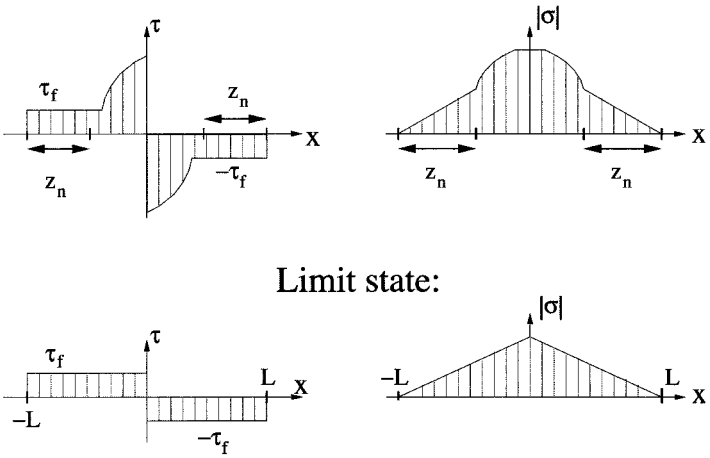

Figure 30. The plate response to cyclic loading – incremental failure mode: $L < S$.

5 Summary and conclusions

The present work was aimed at analytical solutions of damage growth at the interface between an elastic plate and a rigid foundation, assuming compressive normal traction acting on the interface. The concept of plastic damage zone ahead of delamination front was used in order to simulate progressive damage and ultimate failure. The analysis was simplified by assuming two basic delamination modes, namely longitudinal and transverse shear. The assumption of anti-plane shear and the strip model allowed for one dimensional treatment and analytical solutions. The control parameter driving the failure process was the length of damage zone. Thus, a particular attention could be given to the analysis of critical and post-critical states associated with growth of delamination zone under monotonic and cyclic loading. It was shown that two types of response can be specified in terms of two dimensionless parameters χ and η with corresponding short, medium and long plate solutions.

The quasi static solutions were specified assuming monotonic progression of delamination front. Obviously, under boundary traction control the quasi-static deformation process is terminated at the limit point corresponding to maximal load and the dynamic failure mode would be developed. Similarly, for the displacement control the snap-back state is reached in the long plate solution at the maximal load point with snap back associated with the reverse slip effect. In order to execute a quasi-static delamination both the loading traction and the loaded end displacement should follow a unique equilibrium path, resulting in a histeretic response. The structure close to the loaded end performs a flattering movement with subsequent forward and reverse displacements. The number of cycles leading to complete delamination is dependent on the plate length. The reason for the combined traction and displacement interaction is the elastic energy stored in the plate and next released to debond the structure. Thus, an extra work by external forces

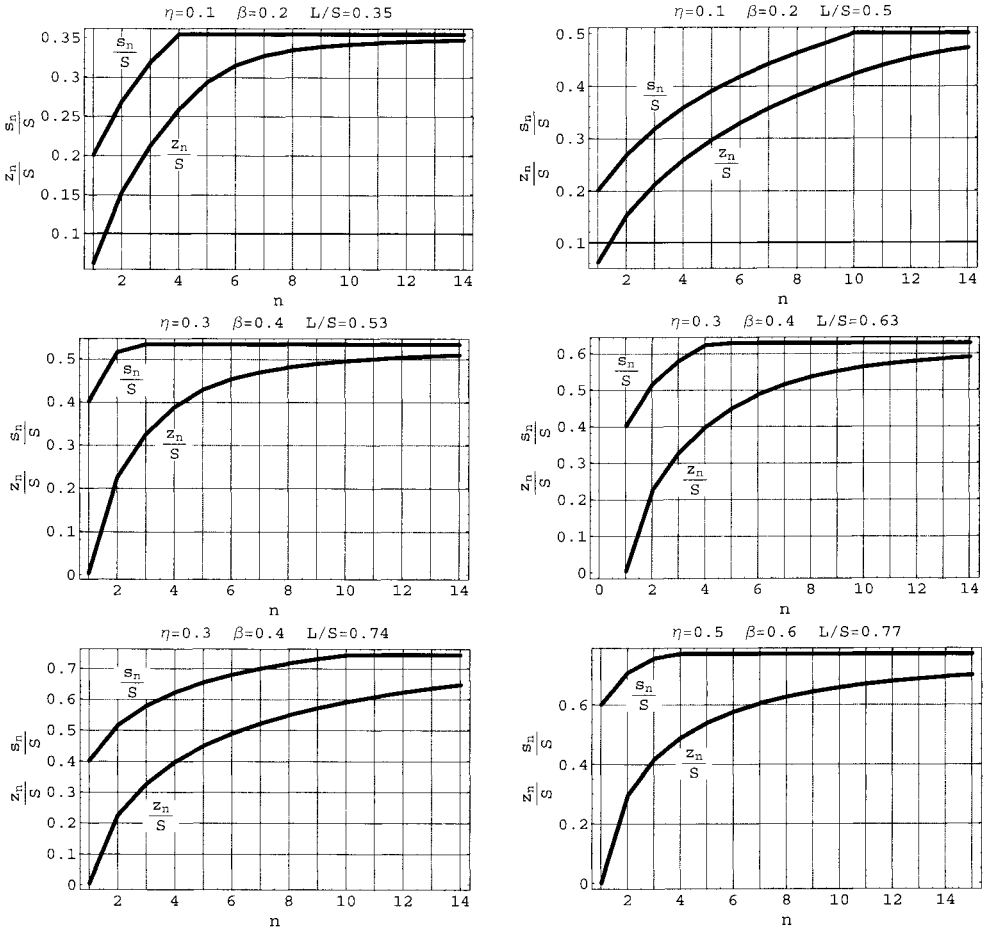

Figure 31. The development of friction and cohesive zones for $L < S$.

would be transformed into kinetic energy and a dynamic mode would follow.

The shear beam model was validated by a finite element analysis. It was shown, that one can neglect the flexural deformation provided that the plate width is greater than its length. The analytical solution describes qualitatively the delamination process and is close to the numerical results during the early delamination phases. Following the critical point associated with maximum value of traction subjected to the structure, differences increase and disappear only when the structure is fully debonded with frictional contact at the interface.

Displacement control does not provide a complete solution for the long plate case. There is a divergence in numerical procedure at the beginning of first hysteretic loop. Thus, the analytical shear beam model provides a reference solution for numerical algorithms searching for quasi-static equilibrium paths.

The softening constitutive relation in the case of rigid-cohesive interfacial model allows to describe the progressive delamination induced by cyclic temperature loading. Two types of structural response can be exhibited: either adaptative delamination and subsequent structural adaptation to cyclic loading, or incremental delamination mode resulting in full delamination after a specific number of loading cycles. The wear effects accompanying cyclic deformation would reduce the friction coefficient, leading to an accelerated incremental failure mode.

In the case of temperature loading, the delamination was coupled with segmentation cracking. The model describes the saturation stage, when the crack density stabilizes at a constant value unaffected by further loading. A common feature for the used interface models is the fact, that strong bond between the plate and the substrate may lead to dense segmentation cracking per unit length. High value of critical shear stress at the interface results in high normal stresses acting on the plate and thus, mitigates the segmentation process. Both cracking and delamination resistance have to be considered in practical applications, in a way that a proper balance between these two factors is maintained.

It follows from the proposed model that the segmentation cracking can result in delamination process, since there are new damaged zones created at the interface in the vicinity of every segmentation crack, leading to a potential slip mechanism. On the other hand, delamination can reduce the risk of potential segmentation cracking, since the resulting normal stress acting on the plate is lower in the case of delaminated layer than for fully bonded structure.

Bibliography

D. C. Agrawal and R. Raj. Measurement of the ultimate shear strength of a metal-ceramic interface. *Acta metall.*, 37(4):1265–1270, 1989.

D. C. Agrawal and R. Raj. Ultimate shear strengths of copper-silica and nickel-silica interfaces. *Materials Science and Engineering*, A126:125–131, 1990.

S. P. Baker, X. Wang, and C.-Y. Hui. Effect of nonlinear elastic behavior on bilayer decohesion of thin metal films from nonmetal substrate. *Journal of Applied Mechanics*, 69:407–414, July 2002.

G. I. Barenblatt. The mathematical theory of equilibrium cracks in brittle fracture. In *Advances in Applied Mechanics*, volume 7, pages 55–129. Academic Press, New York, 1962.

S. J. Bennison and B. R. Lawn. Role of interfacial crack bridging sliding friction in the crack resistance and strength properties of non-transforming ceramics. *Acta Metallurgica*, 37(10):2659–2671, 1989.

M. Białas and Z. Mróz. Modelling of progressive interface failure under combined normal compression and shear stress. Submitted to *International Journal of Solids and Structures*, 2004.

B. F. Chen, J. Hwang, I. F. Chen, G. P. Yu, and J-H. Huang. A tensile-film-cracking model for evaluating interfacial shear strength of elastic film on ductile substrate. *Surface and Coatings Technology*, 126:91–95, 2000.

S. Chi and Y.-L. Chung. Cracking in coating-substrate composite with multi-layered and fgm coatings. *Engineering Fracture Mechanics*, 70:1227–1243, 2003.

Y.-L. Chung and C.-F. Pon. Boundary element analysis of cracked film-substrate media. *International Journal of Solids and Structures*, 38:75–90, 2001.

D. S. Dugdale. Yielding of steel sheets containing slits. *Journal of Mechanics and Physics of Solids*, 8:100–104, 1960.

B. Erdem Alaca, M. T. A. Saif, and Huseyin Sehitoglu. On the interface debond at the edge of a thin film on a thick substrate. *Acta Materialia*, 50:1197–1209, 2002.

A. G. Evans and J. W. Hutchinson. Effect of non-planarity on the mixed mode fracture resistance. *Acta Metallurgica*, 37(3):909–916, 1989.

T. S. Gross and D. A. Mendelsohn. Model I stress intensity factors induced by fracture surface roughness under pure mode III loading: application to the effect of loading models on stress corrosion crack growth. *Metallurgical and Material Transactions A*, 20(10), 1989.

U. A. Handge, Y. Leterrier, G. Rochat, I. M. Sokolov, and A. Blumen. Two scaling domains in multiple cracking phenomena. *Physical Review E*, 62(6):7807–7810, 2000.

U. A. Handge, I. M. Sokolov, and A. Blumen. Disorder and plasticity in the fragmentation of coatings. *Physical Review E*, 64:106–109, 2001.

A. Hillerborg, M. Modeer, and P. E. Peterson. Analysis of crack formation and crack growth in concrete by means of fracture mechanics and finite elements. *Cement and Concrete Research*, 6:773–782, 1976.

D. R. Hiltunen and R. Roque. A mechanics-based prediction model for thermal cracking of asphaltic concrete pavements. *Association of Asphalt Paving Technologists*, 63: 81–117, 1994.

J. W. Hutchinson and Z. Suo. Mixed mode cracking of layered materials. In J. W. Hutchinson and T. Y. Wu, editors, *Advances in Applied Mechanics*, volume 29, pages 63–191. Academic Press, 1991.

S.-R. Kim and J. A. Nairn. Fracture mechanics analysis of coating/substrate systems. part i: Analysis of tensile and bending experiments. *Engineering Fracture Mechanics*, 65:573–593, 2000a.

S.-R. Kim and J. A. Nairn. Fracture mechanics analysis of coating/substrate systems. part ii: Experiments in bending. *Engineering Fracture Mechanics*, 65:595–607, 2000b.

K. Kokini and Y. R. Takeuchi. Multiple surface thermal fracture of graded ceramic coatings. *Journal of Thermal Stresses*, 27:715–725, 1998.

Z. Mróz and M. Białas. A simplified analysis of interface failure under compressive normal stress and monotonic or cyclic shear loading. *International Journal of Numerical and Analytical Methods in Geomechanics*. In press, 2004.

Z. Mróz and A. Seweryn. Non local failure and damage evolution rule: application to a dilatant crack model. *Journal de Physique IV*, 8(Pr 8):257–268, 1998.

Z. Mróz and S. Stupkiewicz. Hysteretic effects and progressive delamination at composite interfaces. In R. Pyrz, editor, *IUTAM Symposium on Microstructure - Property Interactions in Composite Materials*, pages 247–264. Kluwer Academic Publishers, 1995.

J. A. Nairn and S.-R. Kim. A fracture mechanics analysis of multiple cracking in coatings. *Engineering Fracture Mechanics*, 42:195–208, 1992.

M. Ortiz. Computational micro-mechanics. *Computational Mechanics*, 18(5):324–338, 1996.

H. L. Schreyer and A. Peffer. Fiber pullout based on a one-dimensinal model of decohesion. *Mechanics of Materials*, 32:821–836, 2000.

G. W. Schulze and F. Erdogan. Periodic cracking of elastic coating. *International Journal of Solids and Structures*, 35(28-29):3615–3634, 1998.

F.-S. Shieu, R. Raj, and S. L. Sass. Control of mechanical properties of metal-ceramic interfaces through interfacial reactions. *Acta metall. mater.*, 38(11):2215–2224, 1990.

D. H. Timm, B. B. Guzina, and V. R. Voller. Prediction of thermal crack spacing. *International Journal of Solids and Structures*, 40:125–142, 2003.

S. Wolfram. *The Mathematica Book (4th ed.)*. Wolfram Media/Cambridge University Press, 1999.

Z. C. Xia and J. W. Hutchinson. Crack patterns in thin films. *Journal of Mechanics and Physics of Solids*, 48:1107–1131, 2000.

B. Yang and K. Ravi-Chandar. Antiplane shear crack growth under quasistatic loading in a damaging material. *International Journal of Solids and Structures*, 35(28,29): 3695–3715, 1997.

T.-Y. Zhang and M.-H. Zhao. Equilibrium depth and spacing of cracks in a tensile residual stressed thin film deposited on a brittle substrate. *Engineering Fracture Mechanics*, 69:589–596, 2002.

Appendix

1. Plastic and undamaged interface zones.
   - plastic zone: $0 \leq x \leq s_1$

$$w^p(x, s_1) = \frac{\tau_c}{K_s}\{1 - \cos[r_s(x - s_1)]\}, \tag{5.1}$$

$$\tau^p_{xy}(x, s_1) = -Gr_s\frac{\tau_c}{K_s}\sin[r_s(x - s_1)], \tag{5.2}$$

$$\tau^p(x, s_1) = \tau_c \cos[r_s(x - s_1)]. \tag{5.3}$$

2. Undamaged, plastic and friction interface zones.
   - plastic zone: $s_2 \leq x \leq s_1$

$$w^p(x, s_1) = \frac{\tau_c}{K_s}\{1 - \cos[r_s(x - s_1)]\}, \tag{5.4}$$

$$\tau^p_{xy}(x, s_1) = -Gr_s\frac{\tau_c}{K_s}\sin[r_s(x - s_1)], \tag{5.5}$$

$$\tau^p(x, s_1) = \tau_c \cos[r_s(x - s_1)], \tag{5.6}$$

   - friction zone: $0 \leq x \leq s_2$

$$w^f(x, s_1) = \frac{\mu\sigma}{2Gt}\big(x - s_2(s_1)\big)^2 - r_s\frac{\tau_c}{K_s}\sqrt{1 - \eta^2}\big(x - s_2(s_1)\big) + \frac{\tau_c - \mu\sigma}{K_s}, \tag{5.7}$$

$$\tau^f_{xy}(x, s_1) = -\frac{\mu\sigma}{t}\big(x - s_2(s_1)\big) + Gr_s\frac{\tau_c}{K_s}\sqrt{1 - \eta^2}, \tag{5.8}$$

$$\tau^f(x, s_1) = \mu\sigma, \tag{5.9}$$

   where:

$$s_2(s_1) = s_1 - \frac{1}{r_s}\arccos\eta.$$

3. Plastic and friction interface zones.
   - plastic zone: $s_2 \leq x \leq L$

$$w^p(x, s_2) = \frac{\tau_c}{K_s} - \frac{\mu\sigma}{K_s}\frac{\cos[r_s(L - x)]}{\cos[r_s(L - s_2)]}, \tag{5.10}$$

$$\tau^p_{xy}(x, s_2) = \frac{\mu\sigma}{K_s}r_s G\frac{\sin[r_s(L - x)]}{\cos[r_s(L - s_2)]}, \tag{5.11}$$

$$\tau^p(x, s_2) = \mu\sigma\frac{\cos[r_s(L - x)]}{\cos[r_s(L - s_2)]}, \tag{5.12}$$

   - friction zone, $0 \leq x \leq s_2$:

$$w^f(x, s_2) = \frac{\mu\sigma}{2Gt}(x - s_2)^2 + \frac{\mu\sigma r_s}{K_s}\tan[r_s(L - s_2)](x - s_2) + \frac{\tau_c - \mu\sigma}{K_s}, \tag{5.13}$$

$$\tau^f_{xy}(x, s_2) = -\frac{\mu\sigma}{t}(x - s_2) - \frac{\mu\sigma r_s G}{K_s}\tan[r_s(L - s_2)], \tag{5.14}$$

$$\tau^f(x, s_2) = \mu\sigma. \tag{5.15}$$

4. Propagation of reverse slip zone.

– reverse slip zone: $0 \leq x \leq \bar{s}$

$$w^r(x,\bar{s}) = -\frac{\mu\sigma}{2Gt}(x-\bar{s})^2 + w^{r\prime}(\bar{s})(x-\bar{s}) + w^r(\bar{s}), \tag{5.16}$$

$$\tau^r_{xy}(x,\bar{s}) = \frac{\mu\sigma}{t}(x-\bar{s}) - Gw^{r\prime}(\bar{s}), \tag{5.17}$$

$$\tau^r(x,\bar{s}) = -\mu\sigma, \tag{5.18}$$

where:

$$w^r(\bar{s}) = \frac{\mu\sigma}{2Gt}(\bar{s}-\bar{s}_2)^2 - r_s\frac{\tau_c}{K_s}\sqrt{1-\eta^2}(\bar{s}-\bar{s}_2) + \frac{\tau_c-\mu\sigma}{K_s},$$

$$w^{r\prime}(\bar{s}) = \frac{\mu\sigma}{Gt}(\bar{s}-\bar{s}_2) - r_s\frac{\tau_c}{K_s}\sqrt{1-\eta^2}\bar{s},$$

$$\bar{s}_2 = L - \frac{1}{r_s}\arccos\eta.$$

Modelling of Damage and Fracture Processes of Ceramic Matrix Composites

Tomasz Sadowski

Department of Solid Mechanics, Lublin University of Technology, Lublin, Poland

Abstract. The present contribution focuses on the problem of mechanical response of the composite ceramic material containing internal structure. This initial internal structure of the material consists of: grains, intergranular layers, initial defects (like porosity or microcracks) and initial reinforcement. During deformation process the initial structure of the material changes (evolves) due to development of dislocation bands, local stress concentration and further nucleation of microdefects, their growth into mesocracks and finally to macrocracks leading to the failure of the material. This contribution describes all phases of deformation process of polycrystalline of composite ceramic material including phenomena governing changes of internal structure of the material like: nucleation, growth of defects. In particular to the description of the material response including internal damage process, the micromechanical approach will be used by application of averaging procedures. In order to show local stress concentrations the Finite Element Analysis (FEA) will be applied.

1 Introduction

In general, polycrystalline materials - depending on their internal structure - can be treated as multiphase materials. Even one phase ceramic porous material can be analysed as two-phase solid, where gas existing in the pores is considered as a second phase.

The initial internal structure of the composite material consists of: grains, intergranular layers, initial defects (like porosity or microcracks) and initial reinforcement (small particles, whiskers, short or long fibers), see Figure 1. The first problem in modeling of such materials is estimation of the effective behavior of nonlinear composite materials. The overview of different methods was discussed at CISM courses: in 1996 entitled "Continuum Micromechanics" (Sequet ed.), in 2000 entitled "Mechanics of Random and Multiscale Microstructures" (Juelin and Ostoja-Starzewski eds.) and in 2002 entiled "Modern Trends in Composite Laminates Mechanics" (Altenbach and Becker eds.). The non-linearity problem of composites was discussed by Ponte Castañeda and Sequet (1998) whereas mixed mode of cracks in layered materials by Hutchinson and Suo (1991).

In this presentation we will focuse on the problem of modelling ceramic matrix and ceramic polycrystalline materials of the types illustrated in the Figure 1d - h. Even one phase polycrystalline material can be treated as a composite because of different mechanical and fracture properties of grains and grain boundaries, Davidge (1979). It is due to existence of:

- misorientation of crystalline axes on the grain boundaries of two adjacent grains and
- different kind of microdefects generated at grain boundaries during the technological process of material preparation

It means that the initial structure of the material is complicated, changes from point to point inside of the material and is difficult for experimental investigations concerning estimation of local mechanical and fracture properties.

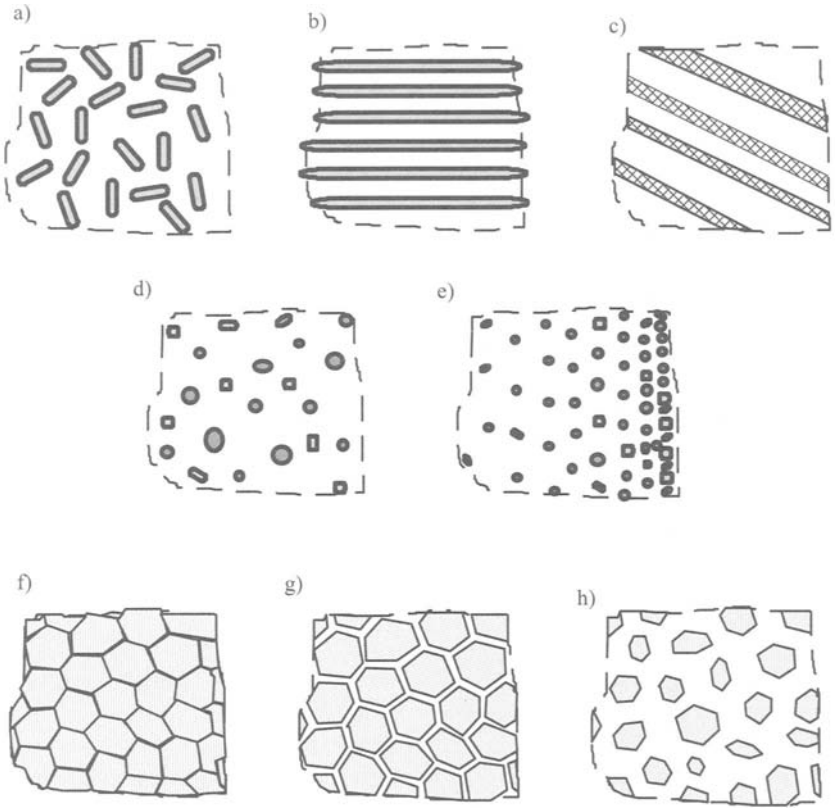

Figure 1. Type of composites: a) short-fiber, b) long fiber, c) layered, d) particle, e) FGM, f) polycrystalline with different grain boundary fracture properties, g) polycrystalline with small interfaces, h) polycrystalline with thick interfaces.

In many cases, ceramic polycrystalline material has the second phase introduced to the material as an interface of the small thickness in comparison to the grain diameter. Such interfaces result from technological process or are intentionally introduced to the material to create a new internal structure.

One can distinguish four kinds of polycrystalline materials containing intergranular phases. The internal structure of the material consists of:

- ceramic grains with brittle interphases. An example of such material is alumina ceramics, where glassy phase added as sintering aid between grains changes significantly response of the material to a mechanical loading, Raiser et al., (1994), Espinosa and Zavattieri

(2003). Under dynamic loading this intergranular glassy phase decreases tensile strength (spall) when the amount of this phase increases. This problem was analysed by Sundaram and Clifton (1998) for alumina ceramics containing 15% glassy binder

- ceramic grains and metallic interphase (cermets). The problem of modelling of a ductile layer in ceramics was considered, for example, by Tvergaard (1997)
- metallic grains surrounded by ceramic interphases(cermets)
- metallic grains surrounded by the layer of a soft ductile material, softer than the grain interior. This case is very important for alluminum alloys applied in aerospace purposes (e.g. Vasudevan et.al. (1987), Pardoen et. al. (2003)

In all cases the role of intergranular phase is very important for the description of such composite materials having very complex internal structure.

Generally the deformation process of the composite materials passes through two stages:

- stage I – purely: elastic, elasto-plastic or elasto-viscoplastic deformations in which we observe the stress concentrations at particular points of the internal structure of the material
- stage II – additional inelastic deformation due to: microdefects initiation (inside of each phase or at the boundary between phases) and their propagation, interphase or transphase failure, fragmentation of phases and flow of metallic phase or crushing of brittle phases (in case of compressive load).

The stage I is very important for the further material behaviour because depending on the type of loading (mechanical, thermal etc.) the stress concentration takes place in different points of the material. It means that the further damage process in composites highly depends on the description of loading process (uniaxial, multiaxial, monotonic, cyclic, etc.) of the material and even initially isotropic treated material becomes anisotropic due to defects growth in the stage II. The above specified stages of the deformation process will be discussed in the next chapters for different kind of composites and different types of loading.

2 Prediction of Mechanical Response under Uniaxial Tension of Polycrystalline Ceramics Containing Brittle or Metallic Inter-granular Layers

Let us consider polycrystalline material containing interfaces between grains, Figure 1g. The theory was formulated by Sadowski et all. (2004) for the case of brittle and metallic intergranular layers. For the theoretical considerations we use the SEM photographs material presenting fracture surface of polycrystalline ceramic, Figure 2a. Figure 2b presents contours of grains and small interface layers. Another examples of the internal structures of the materials can be shown, for example, in Davidge (1979) or Sadowski et al. (1997).

In order to model polycrystalline material containing interphase between grains, it is necessary to have microscopic observations of the internal structure of the material showing:

- interface thickness distribution
- pore size distribution

- grain size distribution,
- pore placement inside the material

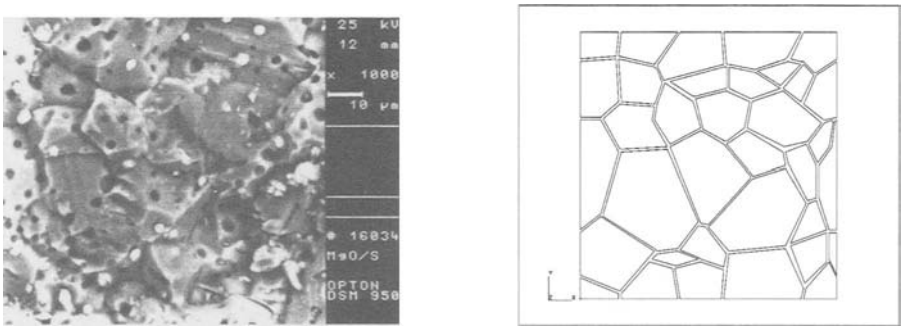

a) b)

Figure 2. Internal structure of polycrystalline ceramics a) SEM photograph, b) contours of grains and interfaces

2.1 Theoretical formulation of the problem

In order to formulate general model of the polycrystalline material containing interfaces between grains, covering all four specified cases in previous chapter, it is important to include time rate effects in description of the material response. This allows to include in the modelling creep effects, viscoplastic response and modelling of the changes of the internal material structure under dynamic and temperature loading. The different phases of the considered composite can exhibit various physical and mechanical features. Therefore in order to describe all the essential characteristics of the visco-elastic-plastic materials response, following Perzyna (1971), the total strain rate $\dot{\varepsilon}_{ij}$ can be split into elastic strain rate $\dot{\varepsilon}^{e}_{ij}$ and viscoplastic strain rate $\dot{\varepsilon}^{vp}_{ij}$:

$$\dot{\varepsilon}_{ij} = \dot{\varepsilon}^{e}_{ij} + \dot{\varepsilon}^{vp}_{ij} \qquad i,j = 1,2,3 \tag{2.1}$$

Dot over the symbol denotes time differentiation. Having the elastic strain rate $\dot{\varepsilon}^{e}_{ij}$ and specified elastic properties defined by elasticity matrix C_{ijkl}, one can calculate the total stress rate:

$$\dot{\sigma}_{ij} = C_{ijkl}\dot{\varepsilon}^{e}_{kl} \tag{2.2}$$

The visco-plastic behaviour of the material occurs, when the following yield condition is satisfied:

$$F(\sigma_{ij}, \varepsilon^{vp}_{kl}) \geq F_0 \tag{2.3}$$

where F_0 denotes the uniaxial yield stress. Assuming associated plasticity theory the viscoplastic strain rate $\dot{\varepsilon}_{ij}^{vp}$ can be postulated in the following form:

$$\dot{\varepsilon}_{ij}^{vp} = \gamma \langle \exp[M(F-F_0)/F_0]-1 \rangle \frac{\partial F}{\partial \sigma_{ij}} \tag{2.4}$$

where γ is the fluidity parameter related to the plastic flow rate and M is the constant describing the particular plastic behaviour of the material. The next step in the problem formulation is calculation of a strain increment $\Delta\varepsilon_{ij}^{vp(n)}$ for a time increment $\Delta t^{(n)} = t^{(n+1)} - t^{(n)}$. Taking into account the Euler time integration scheme we assume that the strain increment is fully described by conditions specified in time $t^{(n)}$:

$$\Delta\varepsilon_{ij}^{vp(n)} = \dot{\varepsilon}_{ij}^{vp(n)} \Delta t^{(n)} \tag{2.5}$$

Similar to Owen and Hinton (1980), one can define viscoplastic strain rate $\dot{\varepsilon}_{ij}^{vp(n+1)}$ for the time while of the loading process $t^{(n+1)}$:

$$\dot{\varepsilon}_{ij}^{vp(n+1)} = \dot{\varepsilon}_{ij}^{vp(n)} + H_{ijkl}^{(n)} \Delta\sigma_{kl}^{(n)} \tag{2.6}$$

where matrix $H_{ijkl}^{(n)}$ is given by:

$$H_{ijkl}^{(n)} = \left(\frac{\partial \dot{\varepsilon}_{ij}^{vp}}{\partial \sigma_{kl}} \right)^{(n)} \tag{2.7}$$

and the stress increment, taking into account strain-displacement relation $\Delta\varepsilon_{ij}^{(n)} = B_{ijk}^{(n)} \Delta d_k^{(n)}$ and (2.5), is expressed by:

$$\Delta\sigma_{ij}^{(n)} = C_{ijkl} (B_{klm}^{(n)} \Delta d_m^{(n)} - \dot{\varepsilon}_{kl}^{vp(n)} \Delta t^{(n)}) \tag{2.8}$$

where $B_{klm}^{(n)}$ is the strain-displacement matrix.

The loading process of the material should satisfy equillibrium equation for any instant of time $t^{(n)}$:

$$\int_{\Omega} [B_{kli}^{(n)}]^T \sigma_{kl}^{(n)} d\Omega + f_i^{(n)} = 0 \tag{2.9}$$

where $f_i^{(n)}$ represents vector of equivalent nodal forces and Ω denotes considered volume of the analysed material. During time increment $\Delta t^{(n)}$ it is necesasary to satisfy also incremental form of equillibrium equation (2.9) expressed in the linearised form:

$$\int_{\Omega} [B_{kli}^{(n)}]^T \Delta\sigma_{kl}^{(n)} d\Omega + \Delta f_i^{(n)} = 0 \tag{2.10}$$

where $\Delta f_i^{(n)}$ is the increase of load corresponding to $\Delta t^{(n)}$. The calculated current component of the total stress $\sigma_{ij}^{(n+1)} = \sigma_{ij}^{(n)} + \Delta\sigma_{ij}^{(n)}$ are not strictly correct. Therefore it is necessary to calculate the residual forces in order to make corrections:

$$\psi_s^{(n+1)} = \int_\Omega [B_{ijs}^{(n+1)}]^T \sigma_{ij}^{(n+1)} d\Omega + f_s^{(n+1)} \neq 0 \tag{2.11}$$

where $B_{ijs}^{(n+1)}$ is evaluated for a current displacement state $d_s^{(n+1)} = d_s^{(n)} + \Delta d_s^{(n)}$. Formula (2.11) as a of set of equation is solved by iteration procedure (Newton-Raphson method). The iterative process is continued until the solution converges to the nonlinear solution, which is indicated by the condition $\psi_s^{(n+1)} \approx 0$.

Introducing tangential stiffness matrix $K_{sm}^{T(n)}$:

$$K_{sm}^{T(n)} = \int_\Omega [B_{ijs}^{(n)}]^T C_{ijkl}^{(n)} B_{klm}^{(n)} d\Omega \tag{2.12}$$

one can calculate the inrease of pseudo-load:

$$\Delta V_m^{(n)} = \int_\Omega [B_{ijm}^{(n)}]^T C_{ijkl}^{(n)} \dot{\varepsilon}_{kl}^{vp(n)} \Delta t^{(n)} d\Omega + \Delta f_m^{(n)} \tag{2.13}$$

and increase of nodal displacements:

$$\Delta d_s^{(n)} = [K_{sm}^{T(n)}]^{-1} \Delta V_m^{(n)} \tag{2.14}$$

Then the current values of the stress state and displacement are: $\sigma_{ij}^{(n+1)} = \sigma_{ij}^{(n)} + \Delta\sigma_{ij}^{(n)}$ and $d_s^{(n+1)} = d_s^{(n)} + \Delta d_s^{(n)}$.

Finally one can calculate the strain increment:

$$\Delta\varepsilon_{ij}^{vp(n)} = B_{ijs}^{(n)} \Delta d_s^{(n)} - C_{ijkl}^{-1} \Delta\sigma_{kl}^{(n)} \tag{2.15}$$

and the current components of the visco-plastic strain for the time $t^{(n+1)}$ take the form:

$$\varepsilon_{ij}^{vp(n+1)} = \varepsilon_{ij}^{vp(n)} + \Delta\varepsilon_{ij}^{vp(n)} \tag{2.16}$$

Moreover, the equivalent visco-plastic strain is calculated according to:

$$\varepsilon_{eq}^{vp} = \sqrt{\left(\frac{2}{3}\right) \varepsilon_{ij}^{vp} \varepsilon_{ij}^{vp}} \tag{2.17}$$

and the Huber - von Mises equivalent stress:

$$\sigma_{eq}^{H-M} = \frac{1}{\sqrt{2}} \sqrt{(\sigma_{xx} - \sigma_{yy})^2 + (\sigma_{yy} - \sigma_{zz})^2 + (\sigma_{zz} - \sigma_{xx})^2 + 6(\sigma_{xy}^2 + \sigma_{yz}^2 + \sigma_{zx}^2)} \tag{2.18}$$

2.2 FEM mesh for polycrystalline material containing interphase and loading conditions

The internal structure of the material was modelled within Finite Element Method (FEM) using eight-node isotropic hexagonal elements to represent grains and interfaces. The Representative Volume Element (RVE) of the following dimensions: 100 μm x 200 μm x 20 μm was cut out. It was assumed that RVE was subjected to a uniform pressure σ and due to appropriate symmetries only one quarter of the RVE was analysed, i.e. sample of the following dimensions: 100 μm x 100 μm x 10 μm . The exemplary internal structure on the surface of the material is shown in Figure 2b. The corresponding FEM mesh is shown in Figure 3, whereas interphase is presented in Figure 4. Number of used elements to model REV was 58,016.

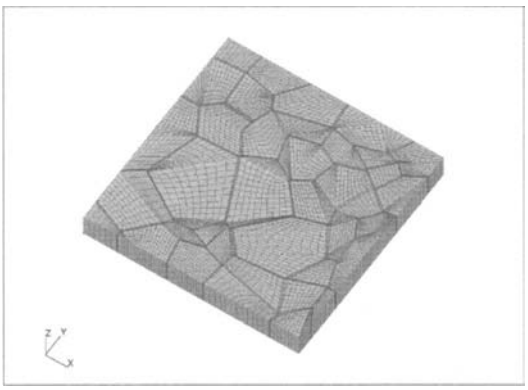

Figure 3. FEM mesh of the material internal structure

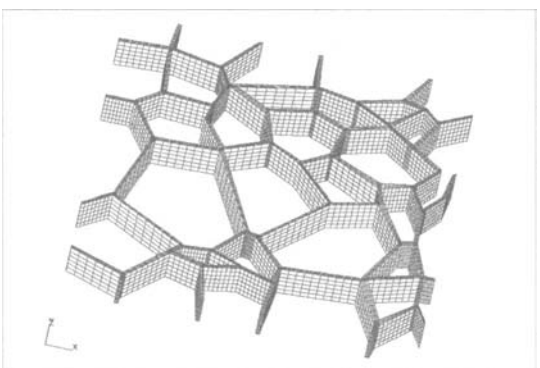

Figure 4. Interphase FEM mesh

In order to present the influence of the heterogeneity of the material on the stress distribution inside RVE, the polycrystalline sample was subjected to the uniaxial tension. The manner of specimen loading and displacement boundary conditions are shown in Figure 5. The poly-

crystalline sample is situated horizontally and on the right hand side is simply supported to constrain free displacement along x-axis. This RVE can model one quarter of the total specimen subjected to uniaxial pressure when we assume that the symmetry plane are coincided with plane xy and yz. The specimen is subjected to quasi-static increase of pressure σ up to the limit corresponding to ultimate strength of alumina oxide.

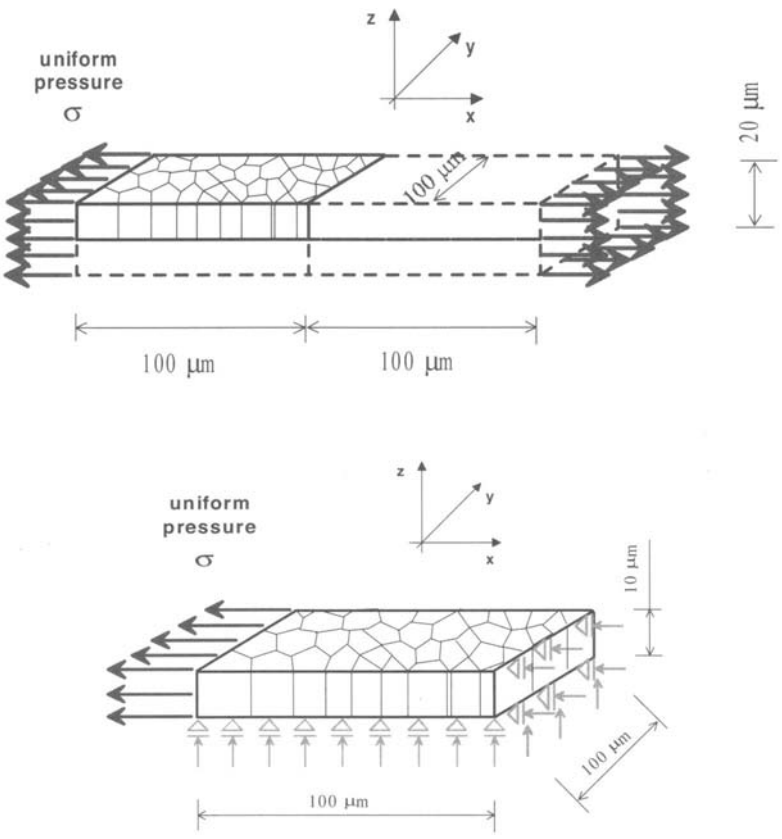

Figure 5. Specimen, RVE loading and boundary conditions.

2.3 Numerical example

The mechanical properties of the polycrystalline samples were presented in Table 1. Two examples with the same grains made of alumina oxide were considered. In the first example interphase was created from a weak elastic material, eg. alumina oxide containing porosity. In the second example the interphase was build up from metallic phase, eg. cobalt. The aim of this work was to show the different behaviour between those two kinds of composite materials with regard to stress distribution.

Table 1: Mechanical properties of the polycrystal

Part of polycrystal	Material in *example 1*	Material in *example 2*
Grains (elastic material - Al_2O_3)	$E_{gr} = 4.1\ 10^{11}$ MPa $\nu_{gr} = 0.25$	
Interphase	*weak elastic material* $E_{in} = 2.1\ 10^{11}$ MPa $\nu_{gr} = 0.235$	*plastic material – cobalt (Co)* $E_{in} = 2.1\ 10^{11}$ MPa $\nu_{gr} = 0.235$ $\sigma_y = 2.97\ 10^{10}$ MPa

Polycrystalline material with strong elastic grains and weak elastic interphase (example 1). Figure 6 illustrates the distribution of stress σ_{xx}. As it was expected, the low values of stress are concentrated along parts of interfaces parallel to loading direction. It is due to quasi-homogeneous distribution of the displacement u_x. The higher values of stress can be observed in parts of grains lying along side surfaces of RVE parallel to x-axis, but they do not exceed fracture stress for Al_2O_3 equal to $\approx$ 400 MPa. The maximum of σ_{xx} appears in interfaces at the bottom of the RVE and is equal to 467 MPa, whereas the minimum amounts 195 MPa. The degree of in-homogeneity

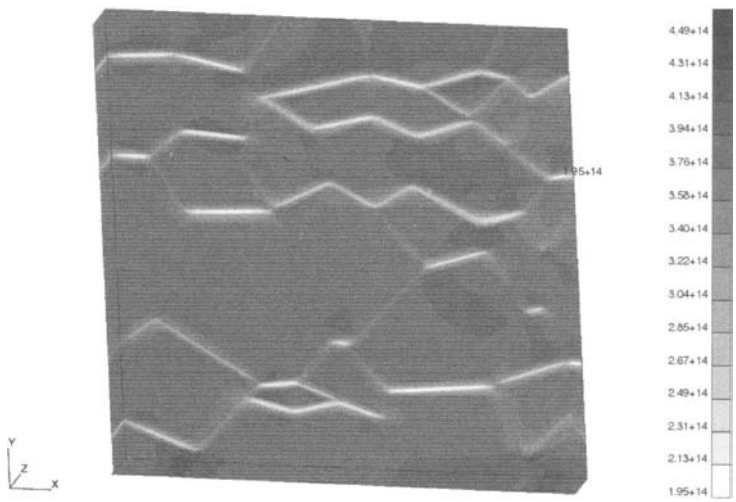

Figure 6. Distribution of stress σ_{xx} for the material with elastic interface.

measured as the relative difference between maximum and minimum values of σ_{xx} in RVE is equal to 58%.

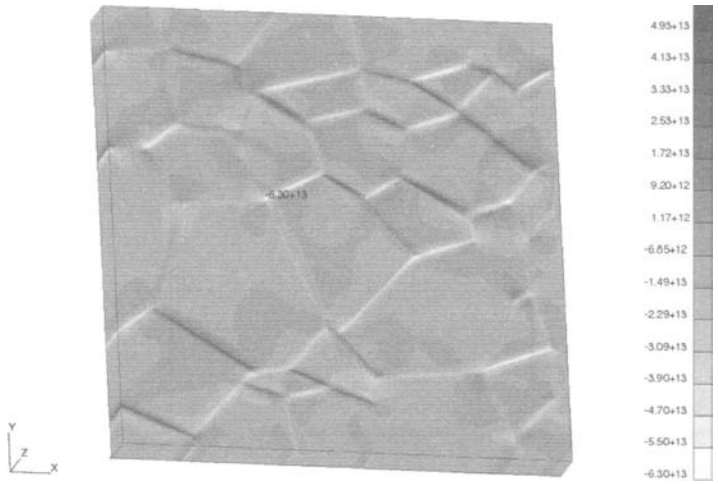

Figure 7. Distribution of stress σ_{xy} for the material with elastic interface.

Figure 7 presents distribution of shear stress σ_{xy}. The shear stress concentrates along interfaces (white and black lines) in the form of bands inclined to the loading direction at $\pm(20-45)^0$. Concentration of such high values of the stress in the narrow bands can cause grain rotation. The values of stress inside the grains are one order less in comparison to interfaces.

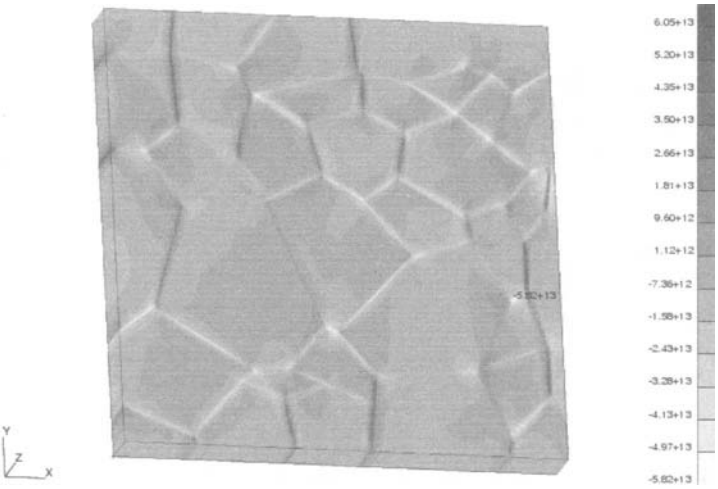

Figure 8. Distribution of stress σ_{yy} for the material with elastic interface.

Figure 8 shows distribution of the stress perpendicular to the loading direction, i.e. σ_{yy}. One can observe that interfaces inclined to the x-axis at the angle 75-90° are subjected to tension, whereas interfaces inclined at the angle 10-45° are subjected to compression. The maximum of tension is equal to 69 MPa, whereas the minimum of compression appears in the interface inclined at the angle 10^0 and is equal to –58 MPa. Nongomogeneity parameter is of order 218%. One can point out that the level of stress σ_{yy} in grains is less more than one order in comparison to the interfaces.

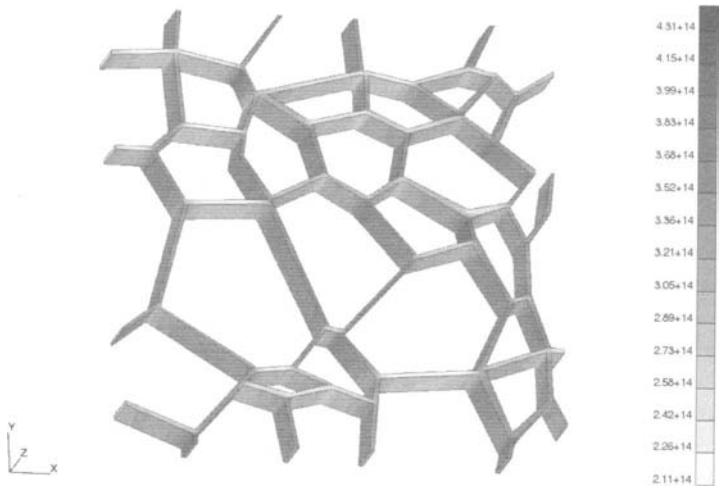

Figure 9. The Huber - von Mises equivalent stress σ_{eq}^{H-M} for the material with elastic interface.

In order to estimate the material effort, the Huber - von Mises equivalent stress, Eq. (2.18), was calculated in the interfaces, Figure 9. It is interesting to notice that the maximum of σ_{eq}^{H-M} appears at the "triple points" of interfaces of polycrystalline structure of the material. These interfaces are inclined at the angle 80-90° to the loading direction. The relative inhomogeneity of the Huber - von Mises stress distribution is of order 53%.

Polycrystalline material with strong elastic grains and visco-plastic interphase (example 2). The material properties of the second polycrystalline are presented in Table 1. In the numerical examples the visco-plastic strain rate (Eq. (2.11)) was modelled using a fluidity parameter within the range $\gamma \in (10^{-10}, 10^{-5})[\text{MPa} \cdot \text{s}]^{-1}$. Figures 14 – 22 show the results obtained for the material containing interfaces characterised by $\gamma = 10^{-5}[\text{MPa} \cdot \text{s}]^{-1}$.

Figure 10 illustrates the distribution of stress σ_{xx}, which is similar to example 1 (Figure 6). The lower value of stresses are concentrated along the interfaces parallel to the loading direction i.e. the x-axis. This is due to the quasi-homogeneous distribution of displacement u_x. The higher values of stress can be observed in parts of grains lying along side the surface of the RVE parallel to the x-axis, but they do not exceed the fracture stress for Al_2O_3 ($\approx$ 400 MPa).

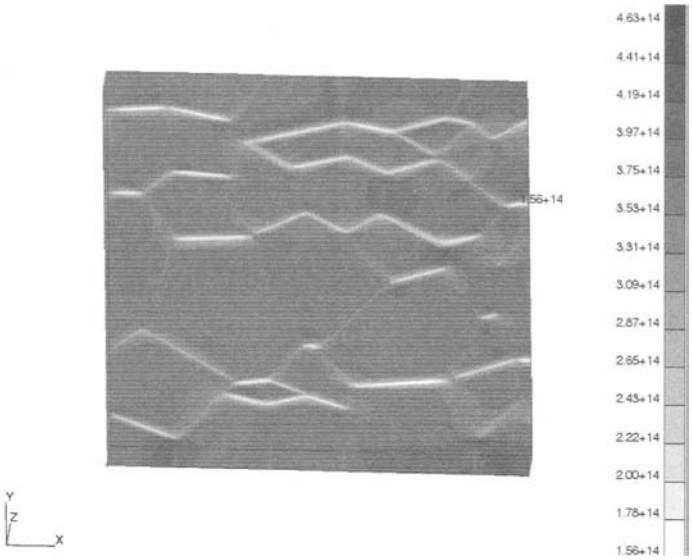

Figure 10. Distribution of stress σ_{xx} for the material with visco-plastic interface.

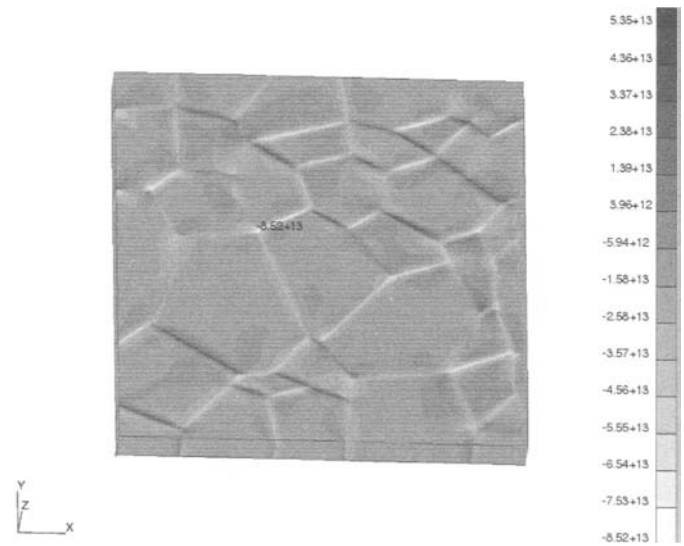

Figure 11. Distribution of stress σ_{xy} for the material with visco-plastic interface.

The maximum value of σ_{xx} appears in the interfaces at the bottom of the RVE and is 484 MPa, an increase in comparison to example 1 of 3,6%. The minimum value of σ_{xx} is 156 MPa and a

decrease in comparison to example 1 of 21%. The degree of inhomogeneity measured as the relative difference between maximum and minimum values of σ_{xx} in the RVE is 68%.

Figure 11 shows the distribution of shear stress σ_{xy}. In a similar way to example 1 (Figure 7), the shear stress concentrates along the interfaces (white and black bands) inclined to the loading direction at $\pm(20-45)^0$. The concentration of such high values of stress in the narrow bands is due to plastic slip and grain rotation. The maximum value of stress is $\approx$ 20% greater than in example 1. The stresses inside the grains have values one order of magnitude less than the interfaces.

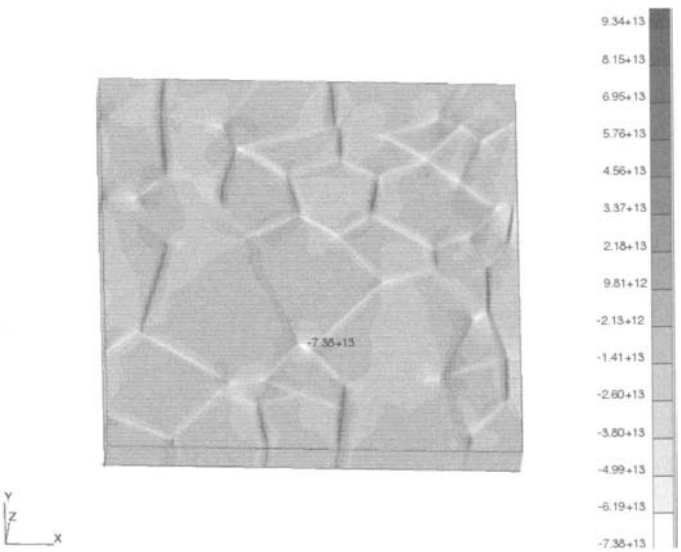

Figure 12. Distribution of stress σ_{yy} for the material with elastic interface.

Figure 12 presents distribution of σ_{yy}. One can observe that the interfaces inclined to the x-axis at an angle of about 90° are subjected to tension, whereas the interfaces inclined at an angle 10-45° are compressed. The maximum tensile stress is 105 MPa, whereas the minimum compressive stress appears in the interfaces inclined at 10° and is -74 MPa. Then the non-homogeneity parameter is of order 242,3%. The level of stress σ_{yy} in the grains is more than one order of magnitude less than the interfaces, similar to example 1.

The equivalent visco-plastic strains were calculated according to Eq. (2.17) and are presented in Figure 13. The equivalent visco-plastic strains are concentrated at the interfaces. The maximum value of ε_{eq}^{vp} appears both in the middle of the straight segments of the interfaces, and at the so-called "triple points". Grains are free of equivalent visco-plastic strains. Therefore it is instructive to plot only the interfaces, Figure 14. The analysis of this plot leads to the conclusion that the third dimension (along the z-axis) plays a very important role in the problem of strain concentration and the initiation of further defects.

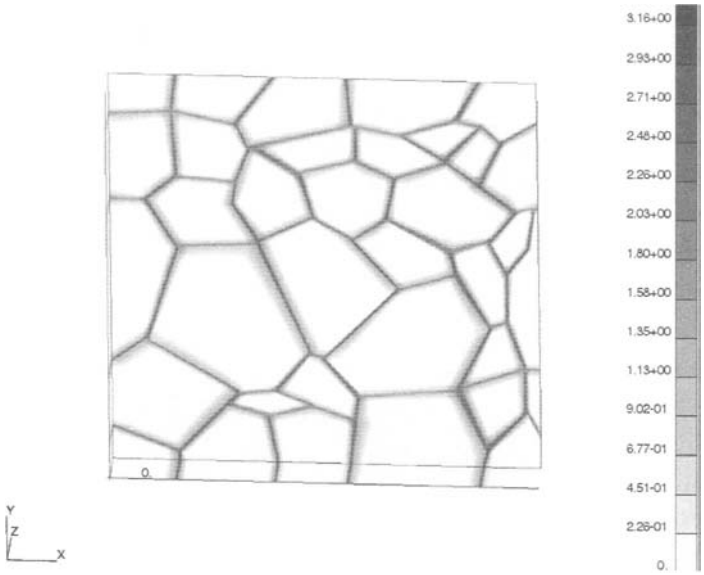

Figure 13. The equivalent strain ε_{eq}^{vp} in RVE for the material with visco-plastic interface.

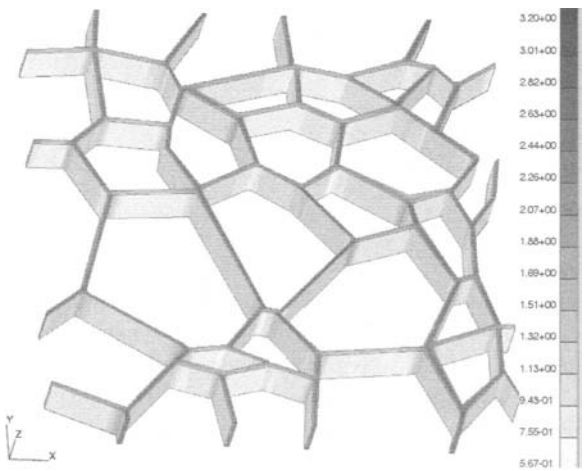

Figure 14. The equivalent strain ε_{eq}^{vp} in the visco-plastic interface.

In order to estimate the material effect in the interfaces, the Huber - von Mises equivalent stress was calculated according to Eq. (2.18), Figure 15. It is interesting to note that the maximum value

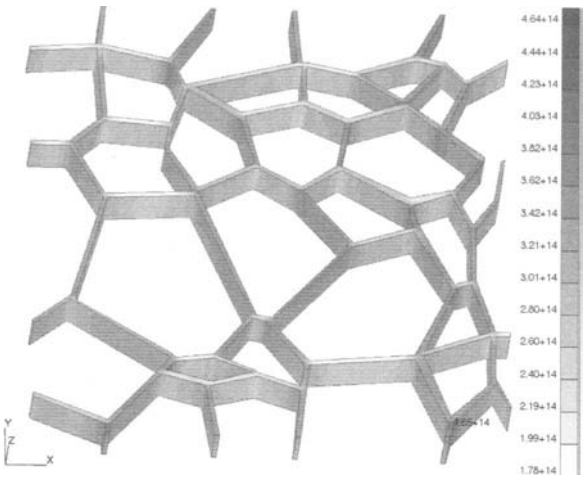

Figure 15. The von Mises equivalent stress σ_{eq}^{H-M} for the material with visco-plastic interface.

of σ_{eq}^{H-M} appears at the "triple points" of the interfaces of the material polycrystalline structure, see Figure16 for more details. These interfaces are inclined to the loading direction at an angle 80-90°.

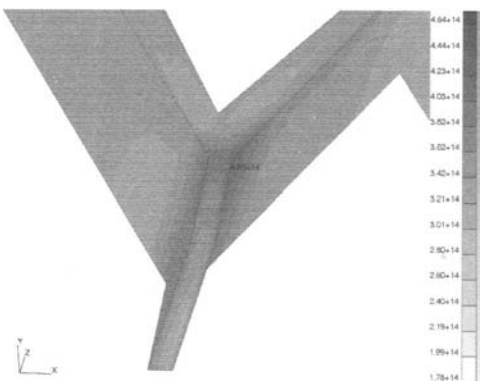

Figure 16. "Triple point" in the visco-plastic interface.

The relative nonhomogeneity of the Huber - von Mises stress distribution is of the order 63%. Figure 16 shows the stress concentration in the "triple point". One can see additionally the change of stress distribution along the z-axis and observe the stress concentration (K_t = 1.21) at the top surface of the RVE. This means that defects can nucleate at the surface of the material and propagate into the volume of the material.

It is important to note that the variation of the fluidity parameter within the range $\gamma \in (10^{-10}, 10^{-5})[\text{MPa} \cdot \text{s}]^{-1}$ causes variation of the equivalent visco-plastic strain, Figure 17, but does not affect the Huber - von Mises equivalent stress.

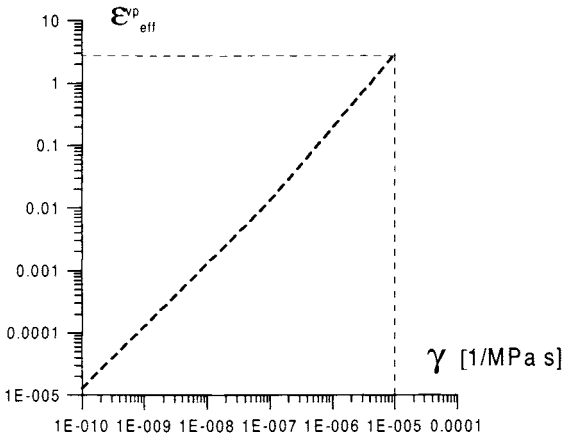

Figure 17. Variation of the equivalent visco-plastic strain with the fluidity parameter.

2.4 Polycrystalline material containing single viod inside of the interface

Let us consider the case of the material containing single void in the interface, Figure 18. The diameters of this void are 0.5 μm x 3.3 μm x 8.5 μm . The existence of any defect strongly disturbs the stress distribution inside of the material. It can be observed in the Figure 19. The stress concentration factor at the border of the void is $K_t = 1.42$.

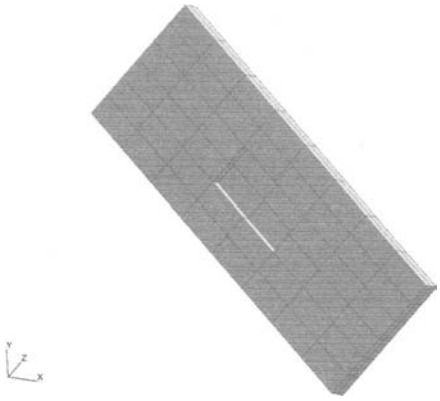

Figure 18. Single void inside one facet of the interface.

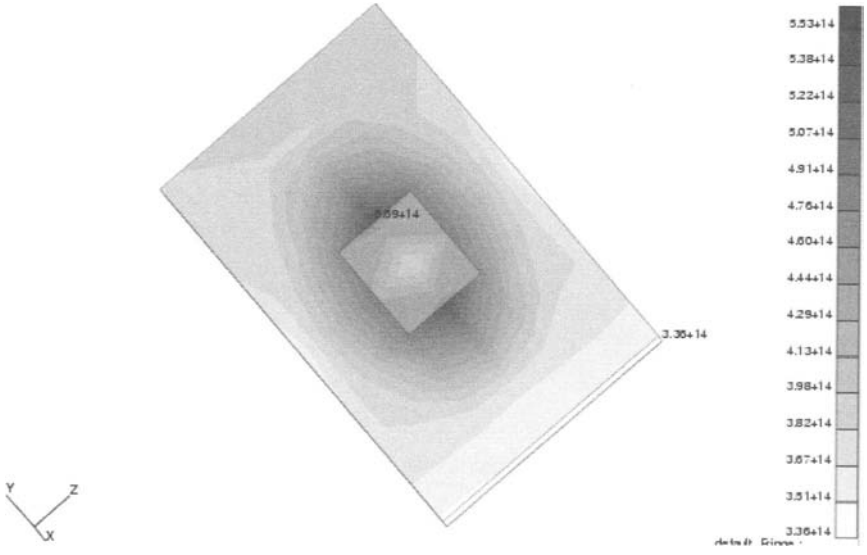

Figure 19. Single void inside one facet of the interface.

2.5 Conclusions and remarks

The aim of this lectures is to highlight qualitatively and quantitatively the problem of non-homogeneity of displacement, stress and strain distributions in real polycrystalline material structures. In particular, the work focuses on the influence of thin inter-granular layers between grains on the material behaviour. The properties of these components of the material structure play a fundamental role in the description of the microscopic and macroscopic material response. In this work, consideration is limited to polycrystalline materials having strong elastic grains and relatively weaker interfaces: purely elastic or visco-plastic.

Presented results show the real micro-stress distributions in the polycrystalline material. In general these distributions are very complicated. The degree of nonhomogeneity is relatively high. One can also observe many sites of the local concentrations:

- at interfaces and particularly at the so called "triple points"
- on the surface of the specimen.

These can act as future sources of defect nucleus, when the local tensile strength is overcome. In the first case, in relation to a particular case of loading: a circular, elliptic or other shaped cracks can initiate and develop as an isolated defect. In the second case the stress concentration on the surface of the material (at the interfaces) can be a source of a semi-circular surface crack (e.g. Fett (2001), Fett and Munz (1997)), which spreads into the volume of the material.

As an example, the stress concentration around the single void inside of interface was analysed. It indicates that the stress concentration factor is of order 1.42 what is higher value in comparison to stress concentration inside the material without defect (1.21). Further investigations are necessary in order to obtain more details of crack initiation and propagation in modern and complicated materials i.e. composites. The model outlined above is currently being developed in order to describe the material behaviour more precisely.

3 Modeling of Porous Ceramics Response to Compressive and Tensile Loading

3.1 Introduction

Popularity of porous ceramic materials results from many engineering applications, like: thermal insulators, filters, grinding wheels, electrodes, surgical implants, etc. Rice (1998), Pampuch (1988).

Porous ceramic materials can be treated as two-phase materials with a gas existing in pores as a second phase. Such materials are widely used in steel making or cement factories as furnace lining because of good thermal stress resistance and relatively good compressive strength.

The volumetric porosity of refractory materials is up to 30%. Grains of ceramic material create a skeleton of the solid phase, which determines the final mechanical properties. Pores of elliptical or spherical shape arise in the material during the technological process (isotropic pressing and sintering at high temperature) e.g. Ostrowski and Rödel (1999). A typical example of a refractory material is magnesium oxide – a semi-brittle ceramic exhibiting limited plasticity at room temperature and microcrack development during loading.

The Scanning Electron Microscopy (SEM) observations of the polycrystalline material structure before and after fracture give the following information:

- grain size distribution,
- pore size distribution,
- pore distribution in the material,
- mode of microcracking process (intergranular or transgranular).

Experimental findings for MgO and Al_2O_3, e.g. Sadowski et al. (1997), show that pores are spherical and their diameters are much smaller than the grain diameter. They are distributed along grain boundaries and inside grains. Crack initiation mechanism for semi-brittle ceramics can be described by Zener-Stroh's model [7], i.e. dislocations pile-up at the grain boundary of the polycrystalline material structure. The observations of the fracture surface (Davidge (1979), Sadowski et al. (1997)) , lead to conclusion that for quasi-static load increase, microcracks propagate mainly intergranularly. Moreover experiments let us establish the distribution of the basic mechanical features as the Young's modulus or the Poisson's coefficient in relation to porosity of the material (Lam et al. (1994) and Nanjangud (1995).
The purpose of this lecture is theoretical modelling of the behaviour of porous ceramic materials under compression and tension, taking into account necessary experimental data. Unfortunately, the behavior of polycrystalline ceramic materials under compression have been studied little, Fett and Munz (1999). This work aims at removing lack in theoretical modeling.

3.2 Modeling of the material response

Micromechanical basis of constitutive equations. Constitutive modeling of polycrystalline semi-brittle and porous materials under active loading process obeys a description of the:

- elastic deformations of initially porous material,
- existence of shear dislocation bands,
- deformations connected with crack growth.

In order to model the considered material behavior for plane strain condition we introduce a Representative Surface Element – RSE (e.g. Krajcinovic (1989), Namat-Nasser and Horii (1993), Kachanov (1993), Kachanov et al. (2001)) with the surface area of A, Figure 20. We assume that RSE contains N hexagonal grains. All defects inside the material: porosity, dislocation bands and microcracks create local microscopic additional strains in comparison to purely elastic material behavior. Let us denote by:
Let us denote by:

- $A_{po}^{(s)}$ the surface area of one pore "s",
- $A_{pl}^{(s)}$ the surface area of the single grain "s" with activated slip system,
- $A_{cr}^{(s)}$ the surface area of one crack "s",
- A_d the surface area of all pores and cracks inside RSE.

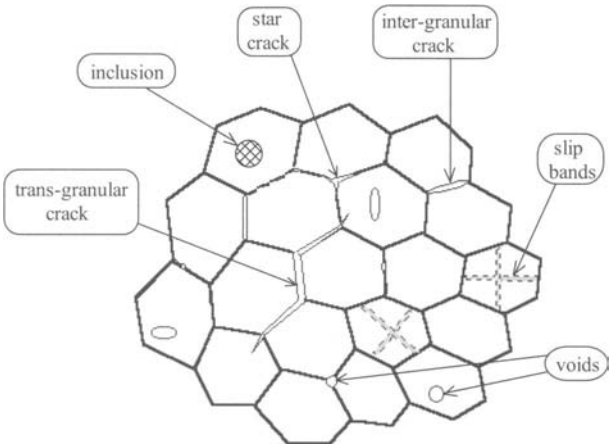

Figure 20. Representative Surface Element.

The RSE area A can be divided into the surface area of grains A_e (deforming elastically or elasto-plastically) and surface area of defects A_d, i.e. $A = A_e + A_d$.
In micromechanical approach we analyze development of all existing (pores) and nucleating (cracks) defects inside RSE. Let us assume that the initially porous polycrystalline material is subjected to monotonically increasing compressive load $\sigma_{22}^{(b)}$, Figure 21. Then within the material, local microstrains at arbitrary point x_m are created $\varepsilon'_{ij}(x_m, \sigma_{22}^{(b)})$ due to the change of pores shape, development of dislocation bands and cracks. Note, that $i, j, m = 1,2$. These microstrains should be averaged over the appropriate areas. As a result we obtain:

- the elastic strains

$$\varepsilon_{ij}^{e}(x_m, \sigma_{22}^{(b)}) = \frac{1}{A_e} \int_{A_e} \varepsilon_{ij}'^{e}(x_m, \sigma_{22}^{(b)}) dA \tag{3.1}$$

- the additional strains due to single pore "s"

$$\varepsilon_{ij}^{po(s)}(x_m, \sigma_{22}^{(b)}) = \frac{1}{A_{po}^{(s)}} \int_{A_{po}^{(s)}} \varepsilon_{ij}'^{po(s)}(x_m, \sigma_{22}^{(b)}) dA\,. \tag{3.2}$$

- the additional strains due to activation of slip system in grain "s"

$$\varepsilon_{ij}^{pl(s)}(x_m, \sigma_{22}^{(b)}) = \frac{1}{A_{pl}^{(s)}} \int_{A_{pl}^{(s)}} \varepsilon_{ij}'^{pl(s)}(x_m, \sigma_{22}^{(b)}) dA\,, \tag{3.3}$$

- the additional strains caused by single crack "s"

$$\varepsilon_{ij}^{cr(s)}(x_m, \sigma_{22}^{(b)}) = \frac{1}{A_{cr}^{(s)}} \int_{A_{cr}^{(s)}} \varepsilon_{ij}'^{cr(s)}(x_m, \sigma_{22}^{(b)}) dA\,. \tag{3.4}$$

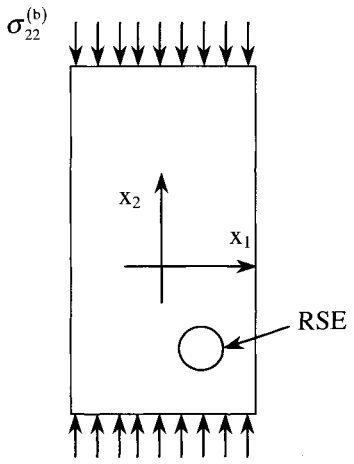

Figure 21. Compressive loading of the specimen.

In order to obtain macroscopic constitutive relation we introduce the following surface densities: $f_d = A_d / A$ characterizing all defects inside RSE, $f_{po}^{(s)} = A_{po}^{(s)} / A$ - for a single pore "s", $f_{pl}^{(s)} = A_{pl}^{(s)} / A$ - for one grain "s" with activated slip system, $f_{cr}^{(s)} = A_{cr}^{(s)} / A$ - for a single crack "s". Applying the mixture rule we can get the constitutive equations:

$$\varepsilon_{ij}(x_m;\ \sigma_{kl}^{(b)}) = \begin{cases} \left[1 - f_d\right]\ \varepsilon_{ij}^{e}(x_m;\ \sigma_{22}^{(b)}) + \sum_{s=1}^{N_{po}} f_{po}^{(s)} \varepsilon_{ij}^{po(s)}(x_m;\ \sigma_{22}^{(b)}) + \\ \sum_{s=1}^{N_{pl}} f_{pl}^{(s)} \varepsilon_{ij}^{pl(s)}(x_m;\ \sigma_{22}^{(b)}) + \sum_{s=1}^{N_{cr}} f_{cr}^{(s)} \varepsilon_{ij}^{cr(s)}(x_m;\ \sigma_{22}^{(b)}) \end{cases} \tag{3.5}$$

N_{po} denotes the number of pores inside RSE. It is estimated on the basis of SEM observations of the fracture surface of the specimen and the measurement of the material density by Archimedes method. In numerical calculations it was assumed $N_{po} = \text{const.}$ during whole loading process. $N_{pl}\left(\sigma_{22}^{(b)}\right)$ denote the number of grains with activated conjugate slip system in RSE. This parameter of the model is estimated according to [17]:

$$N_{pl}\left(\sigma_{22}^{(b)}\right) = \frac{2}{\pi}\left[\beta_{S_2}\left(\sigma_{22}^{(b)}\right) - \beta_{S_1}\left(\sigma_{22}^{(b)}\right)\right] N \tag{3.6}$$

where $\beta_{S_1}\left(\sigma_{22}^{(b)}\right) \le \beta \le \beta_{S_2}\left(\sigma_{22}^{(b)}\right)$ denotes the fan of inclination angles measured in relation to the axis x_1 of activated slip system inside the grains of RSE. Slip system activates, when the shear stress along its direction overcomes a threshold value τ_{so} characterizing dislocation resistance to move:

$$\tau\left(\sigma_{22}^{(b)},\beta\right)\geq\tau_{so} \tag{3.7}$$

τ_{so} results from experimental observations of MgO single crystals.
$N_{cr}\left(\sigma_{22}^{(b)}\right)$ denotes the number of active cracks inside RSE. It is estimated similarly to (3.6), i.e.:

$$N_{cr}\left(\sigma_{22}^{(b)}\right)=\alpha_{cr}\frac{2}{\pi}\left[\beta_{cr_2}\left(\sigma_{22}^{(b)}\right)-\beta_{cr_1}\left(\sigma_{22}^{(b)}\right)\right]N \tag{3.8}$$

The fan of inclination angles of crack to the axis x_1 $\beta_{cr_1}\left(\sigma_{22}^{(b)}\right)\leq\beta\leq\beta_{cr_2}\left(\sigma_{22}^{(b)}\right)$ is calculated from:

$$\tau\left(\sigma_{22}^{(b)},\beta\right)\geq\tau_{cr} \tag{3.9}$$

α_{cr} in (8) plays the role of material parameter depending on grain size in RSE.
The constitutive equations (3.5) are valid for dilute or at most moderate defect concentration. It means that the presented model describes the material with porosity less than 40%, Boccacini (1998) and the interaction of pores is very limited. Taking the above into account, the constitutive equations can be rewritten to the additive form of macroscopic strain components:

$$\varepsilon_{ij}=\varepsilon_{ij}^{e}+\varepsilon_{ij}^{po}+\varepsilon_{ij}^{pl}+\varepsilon_{ij}^{cr}=S_{ijkl}\sigma_{kl} \tag{3.10}$$

where: ε_{ij}^{e} are purely elastic strains, ε_{ij}^{po} are pore existence-dependent strains, ε_{ij}^{pl} are plastic strains, ε_{ij}^{cr} are crack growth-dependent strains. S_{ijkl} is the compliance tensor of the total material response, whereas σ_{kl} is the macroscopic stress tensor.

Porosity of ceramic material. We assume the initial porosity of the material to be closed and distributed in grains (p_g) or along grain boundaries (p_{gb}). Both types of porosity $p=p_g+p_{gb}$ influence the initial components of the compliance tensor S_{ijkl} and the initial (elastic) stage of deformation process. In case of spherical pores, which at the beginning of the loading process are homogeneously distributed inside RSE the porosity parameter can be expressed as:

$$p=\frac{1}{A}\sum_{s=1}^{N_{po}}\pi r_{(s)}^2 \tag{3.11}$$

Considering RSE of circular shape $A=\pi R^2$ we get, see Figure 22:

$$p=\sum_{s=1}^{N_{po}}\left[\frac{r_{(s)}}{R}\right]^2 \tag{3.12}$$

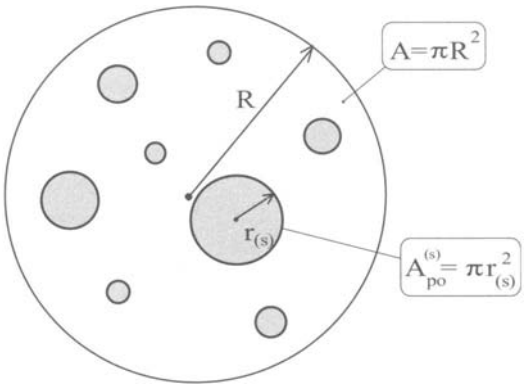

Figure 22. RSE containing dilutely distributed pores.

If the loading process is analyzed for plane strain conditions, we have:

$$\varepsilon_{ij}^{po} = \frac{1-(\nu_0)^2}{E_0}\left[p(4\sigma_{ij}^{(b)} - \sigma_{kk}^{(b)}\delta_{ij})\right] \tag{3.13}$$

for non-interacting pores or

$$\varepsilon_{ij}^{po} = \frac{1-(\nu_0)^2}{E_0}\left[\frac{p}{1-p}(4\sigma_{ij}^{(b)} - \sigma_{kk}^{(b)}\delta_{ij})\right] \tag{3.14}$$

for interacting pores Kachanov (1993).

Crack growth. Cracks inside the MgO material are initiated by Zener-Stroh's mechanism. Microcracks can develop along grain facets changing direction of their propagation, Figure 23.

The description of the crack propagation process is strongly influenced by grain boundary porosity p_{gb}. Namely, any crack (rectilinear or wing) occupying grain boundaries can grow if the energy release rate G satisfies the following condition:

$$G(\sigma_{22}^{(b)}, \phi, \theta, \mu, p_{gb}) \geq \gamma_{gb}^{cr}(p_{gb}) \tag{3.15}$$

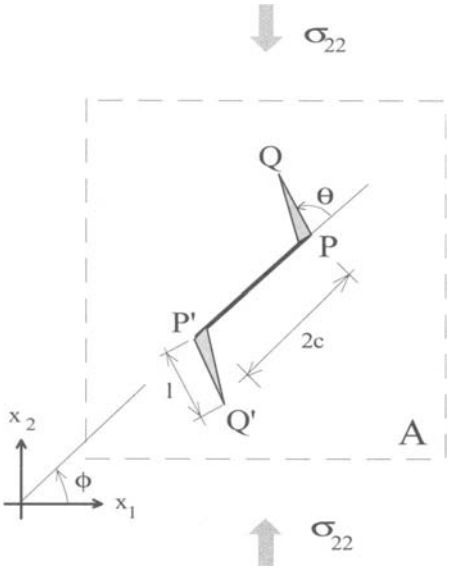

Figure 23. Wing crack model.

where ϕ, θ are inclination angles of straight crack and a wing, respectively Namat-Nasser and Obata (1988) and Sadowski (1994). It is worth pointing out that during compression the straight crack or central parts of the wing cracks are closed. Their growth is highly influenced by friction coefficient μ of the crack surfaces. Moreover $\gamma_{gb}(p_{gb})$ is the critical value of the grain boundary fracture surface energy and is considerably less than the grain fracture surface energy γ_g, Pampuch (1988):

$$\gamma_{gb}(p_{gb}) = (0.5 \text{ - } 0.75)\gamma_g \tag{3.16}$$

In order to describe function $\gamma_{gb}(p_{gb})$ we introduce linear density of holes along grain boundary $\overline{p}_{gb}$. For our purpose let us assume the simplest correlation:

$$\gamma_{gb}(\overline{p}_{gb}) = (1 - \overline{p}_{gb})\gamma_g \tag{3.17}$$

or

$$\gamma_{gb}(\overline{p}_{gb}) = \gamma_g \exp(-\delta\, \overline{p}_{gb}) \tag{3.18}$$

It is easy to find correlation $\overline{p}_{gb}(p_{gb})$ or $\overline{p}_{gb}(p)$ from geometrical considerations and finally $\gamma_{gb}(p_{gb})$ or $\gamma_{gb}(p)$.

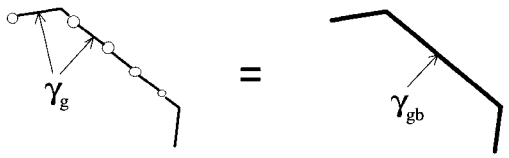

Figure 24. Homogenization procedure of the surface energy for grain boundary.

In order to describe crack growth along grain boundaries we assume (instead of boundary with a certain set of holes – Figure 24a that grain boundaries are homogeneous and their fracture energy is expressed by $\gamma_{gb}(p_{gb})$, i.e. by formula (3.17) or (3.18) – Figure 24b. The growth of microcrack occurs when condition (3.15) is satisfied at the crack tip.

3.3 Experimental and numerical results

Empirical evidences. Our objective was an investigation of the initial porosity effect on the semi-brittle MgO ceramic response to uniaxial compressive stress. In order to estimate the Young's modulus in MgO the specimens with the following porosities were experimentally analyzed: $p = 0.06$, 0.10 and 0.18. The material porosity was estimated by measurement of material density conducted by the Archimedes method using water as the medium. For each level of porosity 4 cylindrical specimens of diameter 13mm and height 50mm were loaded (with the loading rate about 0.01mm/s) to the final failure. The strain gauges were placed at the central part of the specimens' height. The elastic part of the stress-strain curve allows to estimate the values of the Young's modulus of porous MgO ceramic for compression process – continuous line in Figure 25. The dot line corresponds to the theoretical model of porous material containing spherical non-interacting voids, whereas the broken line is related to the case when holes interact. Figure 25 shows small discrepancy between theoretical modeling of the porous material by spherical holes only and the real material behavior. The less values of the Young's modulus can be caused by existence of small amount of microcracks existing in the real material, which are created during technological process.

Numerical example. Numerical calculations were performed according to theoretical formulation presented in section II taking into account the following data (e.g. Davidge (1979) or Pampuch (1988)):

- $E_0(p=0) = 316.4\ GPa$,
- $G_0(p=0) = 121.4\ GPa$,
- $\nu_0(p=0) = 0.20$,
- $\gamma_g(p=0) = 1\ J/m^2$,

The porosity parameter is included within the range $p \in \langle 0; 0.2 \rangle$

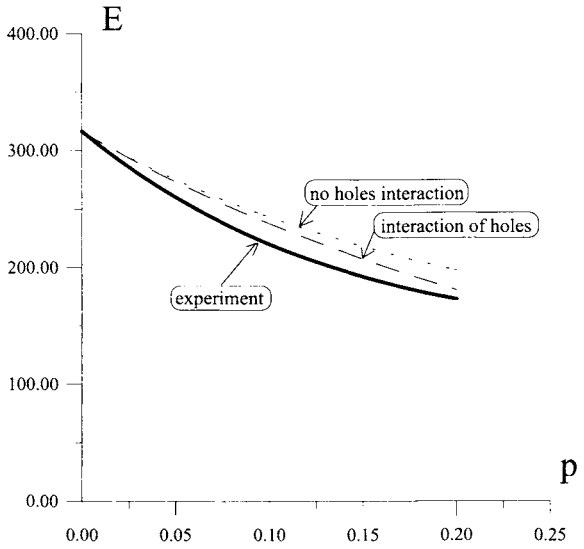

Figure 25. Comparison of numerically and experimentally estimated Young's modulus for porous ceramics (MgO).

Moreover, it was assumed polycrystalline structure of the material consists of hexagonal grains of mean diameter D=45μm . The densities of pores and cracks are here low, therefore we do not take into account interaction between them. As for modeling of grain boundaries it was assumed that the mean pore diameter is equal 2μm (data results from fracture surface SEM observations) and the surface fracture energy of grain boundaries is assumed to be equal $\gamma_{gb}(p_{gb}) = 0.5$.

Figure 26 presents the diagram of normalized compressive stresses versus normalized compressive strains. The normalizing values of stress $\tau_{so} = -75\text{MPa}$ and strain $\varepsilon_{so} = -4{,}75 \cdot 10^{-4}$ correspond to the point of slip lines initiation inside the grains of polycrystalline structure of the material. During the compression process of ceramic materials the initiated microcracks develop as closed cracks with contact friction. It is difficult to estimate the real value of friction coefficient μ along crack facets. Therefore the numerical calculation were performed for the several values of μ = 0.1; 0.2; 0.3; 0.4. It is illustrated for the case of material without porosity (p = 0). The influence of the initial porosity on the material behavior is presented for the case p = 0,10 and 0,18. Comparison with experimental data (dot lines) of deformation process exhibits good confirmation of assumption concerning theoretical modeling.

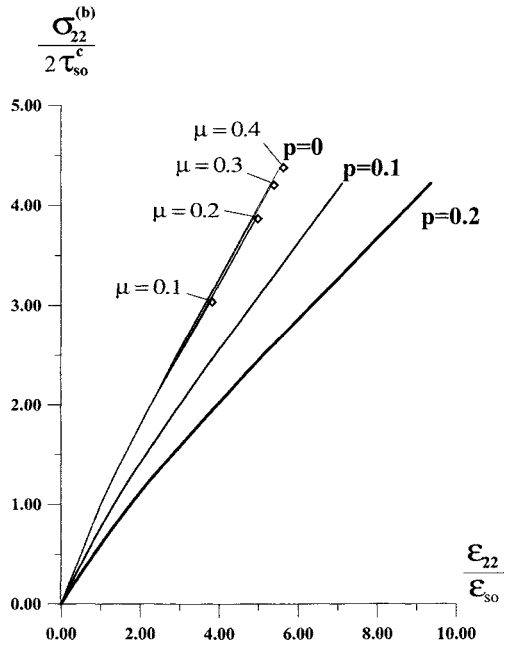

Figure 26. Stress-strain relation for different porosity levels. Experimental data shown by dotted lines; modelling shown by solid lines.

3.4 Summary

Presented results show capability of micromechanical approach in modeling of material with internal structure (Figure 20). One can notice high influence of the porosity on the material response (Figure 26). It is reflected by significant increase of the components of compliance tensor $S_{ijkl}(p)$. Experimental observations of the Poisson's coefficient lead to the conclusion that $\nu(p) > \nu_0(p = 0)$ for the analyzed range of porosity. It confirms the theoretical modeling methods suggesting a small increase of this mechanical property.

4 Thermal shock crack propagation in functionally graded strip

4.1 Introduction

The aim of this lecture is theoretical modelling of the thermal shock problem in a strip made of functionally graded composite with an interpenetrating network microstructure of Al_2O_3 and Al (Sadowski and Neubrand 2003). Such a material could be used in brake disks or cylinder liners in the future. In both applications it is subjected to the thermal shock.

Now this material is used as brittle surface layers in many high temperature applications such as thermal barrier coatings for turbines and combustion engines and chemical reactors because of their superior mechanical properties, oxidation and wear resistance at elevated temperatures. Temperature gradients and differences in thermal expansion can cause high thermal stresses in such layers. Large shear and axial stress concentrations are generated where the interface meets the free edge of the part, Bogy (1970). These stresses promote crack propagation parallel to the interface Hu et al. (1988). It has been shown that the introduction of a layer with a gradual transition of the thermomechanical properties can greatly reduce these stress concentrations, Yang and Munz (1995). Additionally, it has been observed experimentally that the critical energy release rate for delamination is substantially increased in such a FGM which further impedes delamination, Bahr et al. (2004). Unfortunately in-plane thermal stresses parallel to the interface are not always reduced (Itoh and Kishiwaya (1992) and Dröschel et al. (1999)) and the initiation of vertical surface cracks under transient or constant thermal loads is common in FGMs. In the present work which is based on linear elastic fracture mechanics, it will be demonstrated that the additional degree of freedom provided by the gradation of properties can reduce the driving force for the propagation of such vertical cracks substantially. It will be shown that thermal residual stresses resulting from the production process can play an important role and should be taken into account in investigations of thermal shock crack propagation in FGMs. In combination with the increasing crack growth resistance typically encountered in graded composites, an early crack arrest and a high residual strength after thermal shock can be obtained for an optimized composition gradient.

4.2 Formulation of the problem of edge crack problem subjected to high temperature gradient

Let us consider an infinitely long strip made of functionally graded material (FGM), which in the initial state is without any crack, Figure 27a. Both the mechanical and the thermal properties of the strip change gradually along the x direction. Assume that the strip has initial temperature T_0. In an unsymmetrical thermal shock one side of strip ($x = 0$) is cooled by ΔT to the temperature T_a, whereas the second side of the strip ($x = h$) remains under constant temperature T_0. It is assumed that an edge crack (Fig. 28a) is initiated at the cooling surface due to tensile thermal stress (Figure 27b). This crack can propagate as long as the thermal stress intensity factor exceeds the threshold value of the crack resistance of the FGM. The aim of the work is to estimate the equilibrium length b of the edge crack after thermal shock in particular composition of FGM (Al_2O_3/Al).

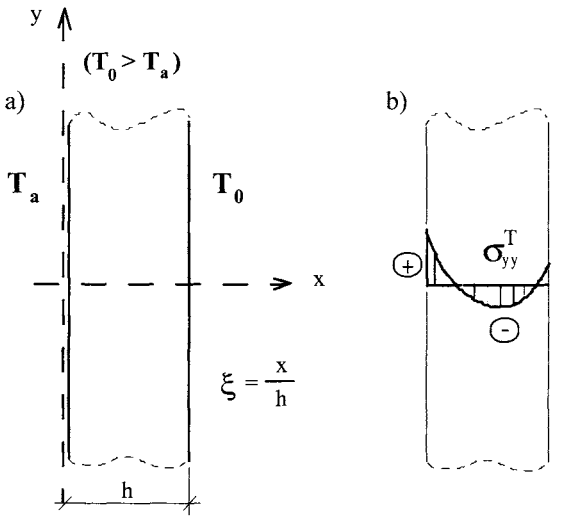

Figure 27. Initial configuration of the strip subjected to thermal shock: a) strip dimensions, b) thermal stress distribution during thermal shock.

The theoretical solution of the considered problem is performed in several steps:

- finding the temperature distribution as a function of time *t*, Figure 27a
- calculation of the thermal shock stress distribution as a function of time *t*, Figure 27b
- estimation of thermal residual stress distribution due to technological cooling process
- calculation of thermal stress intensity factors as a function of time and crack length for an edge crack, Figure 28

Temperature distribution during thermal shock. The temperature function $T(x, y, t)$ can be calculated solving the heat conduction equation, which has the following form in the two dimensional case:

$$\nabla^2 T + \frac{1}{k}\left(\frac{\partial k}{\partial x}\frac{\partial T}{\partial x} + \frac{\partial k}{\partial y}\frac{\partial T}{\partial y}\right) = \frac{1}{\kappa}\frac{\partial T}{\partial t}, \tag{4.1}$$

Here the thermal diffusivity is equal to $\kappa = k/\rho c_v$, where k is the thermal conductivity, ρ is the density and c_v is the specific heat of the material. Taking into account symmetry condition regarding to y axis, Figure 27, and introducing non-dimensional coordinate $\xi = \frac{x}{h}$ and non-dimensional time $t^* = \frac{\kappa_0}{b^2}t$, equation (1) takes the following form for sought temperature function $T = T(\xi, t^*)$

$$\frac{d^2T}{d\xi^2} + \frac{1}{k}\left(\frac{dk}{d\xi}\frac{dT}{d\xi}\right) = \frac{1}{\kappa}\frac{dT}{dt^*} \tag{4.2}$$

Here, $\kappa_0 = \kappa(\xi = 0)$, is the thermal diffusivity at the ceramic side of the strip. The above equation will be solved for the following boundary and initial conditions $T(\xi = 0, t) = T_a$ and $T(\xi = 1, t) = T_0$. The temperature field $T = T(\xi, t^*)$ can be obtained by numerical integration of (2) using the Runge-Kutta method for given thermal conductivity and thermal diffusivity functions of the form $k(\xi) = \sum_i k_i \xi^i$ and $\kappa(\xi) = \sum_i \kappa_i \xi^i$. In the present work the coefficients of these functions were estimated from experimental data.

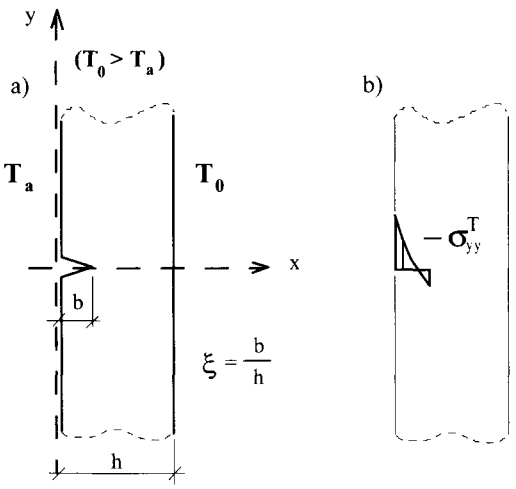

Figure 28. Edge crack formation due to thermal shock: a) crack configuration, b) stress applied to the crack surface.

Thermal shock stress. Having the temperature field inside the strip $T = T(\xi, t^*)$ it is possible to calculate the thermal shock stress by introduction of the Airy stress function (Jin and Batra (1996)) into the equilibrium equation

$$\sigma_{ij,j} + \rho f_i = 0 \tag{4.3}$$

where f_i are components of the body forces per unit mass. Using the Hooke's law in the following form

$$\sigma_{ij} = \frac{E}{(1+\nu)}\left[\frac{\nu}{(1-2\nu)}\varepsilon_{kk}\delta_{ij} + \varepsilon_{ij}\right] - \alpha(T - T_0)\frac{E}{(1-\nu)}\delta_{ij} \tag{4.4}$$

and assuming small strain, i.e. $\varepsilon_{ij} = (u_{i,j} + u_{j,i})/2$ one can calculate the thermal shock stress $\sigma^T_{yy}(\xi, t^*)$ from the equation

$$\frac{d^2}{d\xi^2}\left(\frac{1-\nu^2}{E}\sigma_{yy}^{T}\right)+\frac{d^2}{d\xi^2}\left[(1+\nu)\alpha T\right]=0 \tag{4.5}$$

if body forces are excluded. In equations (4.4) and (4.5) $E(\xi,t^*)$ is the Young modulus, $\nu(\xi,t^*)$ is the Poisson ratio and $\alpha(\xi,t^*)$ is the thermal expansion coefficient. All of them are in general functions of position and time. Equation (4.5) was solved analytically for power law expansions (in x) for $E(\xi,t^*)$, $\nu(\xi,t^*)$ $\alpha(\xi,t^*)$ and stress free boundary conditions, i.e. no additional mechanical loading on the strip boundary. The particular form of the thermal stress function is the following

$$\begin{aligned}\sigma_{yy}^{*T}(\xi,t^*)&=\left(\frac{1-\nu^2}{E_0\alpha_0\Delta T}\right)\sigma_{yy}^{T}(\xi,t^*)=\\&=-\frac{E(\xi,t^*)}{E_0}\frac{\alpha(\xi,t^*)}{\alpha_0}\frac{T(\xi,t^*)}{\Delta T}+\\&+\frac{1}{1-[\nu(\xi,t^*)]^2}\frac{E(\xi,t^*)}{E_0A_0}\left[\begin{array}{l}\{h\xi A_{22}(\xi)-A_{21}(\xi)\}\int_0^1 E(\xi,t^*)\frac{\alpha(\xi,t^*)}{\alpha_0}\frac{T(\xi,t^*)}{\Delta T}hd\xi+\\ \{A_{11}(\xi)-h\xi A_{21}(\xi)\}\int_0^1 \xi E(\xi,t^*)\frac{\alpha(\xi,t^*)}{\alpha_0}\frac{T(\xi,t^*)}{\Delta T}h^2d\xi\end{array}\right]\end{aligned} \tag{4.6}$$

where

$$A_{11}(t^*)=\int_0^1\frac{E(\xi,t^*)}{1-\nu^2(\xi,t^*)}d\xi \qquad A_{22}(t^*)=\int_0^1\frac{E(\xi,t^*)}{1-\nu^2(\xi,t^*)}\xi^2d\xi$$

$$A_{12}(t^*)=A_{21}(t^*)=\int_0^1\frac{E(\xi,t^*)}{1-\nu^2(\xi,t^*)}\xi d\xi \qquad A_0(t^*)=A_{11}(t^*)A_{22}(t^*)-A_{12}(t^*)A_{21}(t^*)$$

Moreover the values $E_0=E(\xi=0,t^*)$ and $\alpha_0=\alpha(\xi=0,t^*)$, i.e. correspond to the ceramic edge of the strip. An example of $\sigma_{yy}^{T}(\xi,t^*)$ distribution is shown in Fig. 27b.

Thermal residual stress due to technological cooling process. The thermal residual stress created during technological cooling of the FGM from the processing temperature has a significant influence on the material behaviour. According to Ravichandran (1995), the thermal residual stress for a strip as shown in Fig. 27 is

$$\sigma_{yy}^{res}(\xi,t^*) = \Delta T_{res} E(\xi,t^*) \left[\alpha(\xi,t^*) - \frac{A_1}{E_1} + \frac{\left(A_2 - \frac{A_1}{E_1} E_2\right)(\xi E_1 - E_2)}{E_1 E_3 - E_2^2} \right] \tag{2.7}$$

where ΔT_{res} denotes the difference between the process temperature and room temperature. The expressions for A_1 and A_2 are

$$A_1(t^*) = \int_0^1 \alpha(\xi,t^*) E(\xi,t^*) d\xi \qquad A_2(t^*) = \int_0^1 \alpha(\xi,t^*) E(\xi,t^*) \xi d\xi$$

and E_1, E_2, E_3 are given by

$$E_1(t^*) = \int_0^1 E(\xi,t^*) d\xi, \qquad E_2(t^*) = \int_0^1 E(\xi,t^*) \xi d\xi \qquad E_3(t^*) = \int_0^1 E(\xi,t^*) \xi^2 d\xi$$

Thermal stress intensity factor during thermal shock. As shown in Figure 28, the crack is perpendicular to the stress-free boundaries, because it was assumed that the problem is symmetric with respect to the y axis. Because the length of the crack after thermal shock is short compared to the specimen dimensions one can simplify the problem by assuming a constant Young modulus $E(\xi = 0, t^*) = E_0$. Then the thermal stress intensity factor in the FGM strip (Figure 28) can be found in a similar way as described in (Jin and Batra (1996), Erdogan and Wu (1996), Noda (1999). The thermal stress intensity factor is found by solution of the integral equation under the given tractions $p_{yy}(x, y = 0, t^*) = -\sigma_{yy}(x, y = 0, t^*)$ along the crack boundary, Figure 28b. Employing the edge crack opening displacement defined by

$$V_y(x, y = 0, t^*) = u_y(x, +0, t^*) - u_y(x, -0, t^*) \qquad \text{for} \quad (0 < x < b) \tag{4.8}$$

the problem can be reduced to the following integral equation

$$\int_0^b \frac{V_y(x,r,t^*)}{(r-x)^2} dr + \int_0^b V_y(x,r,t^*) K(x,r) dr = -\pi \left(\frac{4}{E_0} \right) p_{yy}(x,t^*) \quad \text{for} \quad (0 < x < b) \tag{4.9}$$

Here $K(x,r)$ is the integral kernel given by

$$K(x,r) = K_1(r,x) + K_1(h-r,h-x) + K_2(r,x) + K_2(h-r,h-x)$$

$$K_1(r,x) = -\frac{1}{(r+x)^2} + \frac{12x}{(r+x)^3} - \frac{12x^2}{(r+x)^4},$$

$$K_2(r,x)=\int_0^{\infty}\left[f_1(r,x,\gamma)e^{-\gamma(r+x)}+f_2(r,x,\gamma)e^{-\gamma(2h+x-r)}\right]d\gamma$$

$$f_1(r,x,\gamma)=\frac{\gamma}{D}e^{-2\gamma h}\left\{\begin{array}{l}8\gamma^4h^2rx-12\gamma^3h^2(r+x)+2\gamma^2\left[9h^2+h(r+x)+rx\right]+\\-3\gamma\left[2h+r+x\right]+5+e^{-2\gamma h}\left[-2\gamma^2rx+3\gamma(r+x)-5\right]\end{array}\right\}$$

$$f_2(r,x,\gamma)=\frac{\gamma}{D}\left\{\begin{array}{l}-4\gamma^3hx(h-r)+6\gamma^2\left[h^2+h(x-r)\right]+\\+\gamma\left[-10h+r-x\right]+3+e^{-2\gamma h}\left[\gamma(x-r)-3\right]\end{array}\right\}$$

$$D=1-(4\gamma^2h^2+2)e^{-2\gamma h}+e^{-4\gamma h}$$

Normalizing the interval $x\in(0,b)$ by defining

$$r=\frac{b}{2}(1+w),\qquad x=\frac{b}{2}(1+s),\qquad V_y(r,t^*)=\frac{b}{2}f(w,t^*)$$

the integral equation (4.9) becomes

$$\int_{-1}^{1}\frac{f(w,t^*)}{(w-s)^2}dw+\int_{-1}^{1}f(w,t^*)k(w,s)dw=g_{yy}(s,t^*),\tag{4.10}$$

where

$$k(w,s)=\left(\frac{b}{2}\right)^2K(r,x),\qquad g_{yy}(s,t^*)=-\pi\left(\frac{4}{E_0}\right)p_{yy}(s,t^*)$$

Let us assume the solution of the integral equation takes the form $f(w,t^*)=\sqrt{1-w}F(w,t^*)$, where $\sqrt{1-w}$ is a so called weight function and $F(w,t^*)=\sum_{m=0}^{N}a_m(t^*)w^m$. Solving (4.10) we get the expression for thermal stress intensity factor in the non-dimensional form

$$K_I^*(b,h,t^*)=\frac{1-\nu_0}{E_0\alpha_0\Delta T\sqrt{\pi h}}K_I(b,t^*)\tag{4.11}$$

4.3 Numerical simulation of unsymmetrical thermal shock in the strip

As an example an Al_2O_3/Al FGM prepared by the so called GMFC process (Neubrand et al. (2004)) was analysed. This material was chosen because it is one of the rare FGMs for which all thermomechanical properties including residual stresses and the crack growth resistance have been studied experimentally in detail (Neubrand et al. (2002 and 2004), Becker et al. (2001)). For the purpose of this work, the properties of the analysed Al_2O_3/Al FGM were expressed as a function of the volume content of Al in the composite c_{Al}. The Young's modulus at RT (in GPa) was described by the polynomial

$$E(c_{Al}) = -1482.6\left(c_{Al}\right)^3 + 1973\left(c_{Al}\right)^2 - 1096.9\left(c_{Al}\right) + 398.42 \tag{4.12}$$

and its temperature dependence was neglected. In a similar manner the thermal expansion coefficient of the composite between 20°C and 620°C was described by

$$\alpha\left(c_{Al}\right) = 281.24\left(c_{Al}\right)^3 - 102.98\left(c_{Al}\right)^2 + 15.112\left(c_{Al}\right) + 7.71 \quad (\text{in } 10^{-6}/\text{K}) \tag{4.13}$$

The appropriate function for thermal conductivity k (in W/mK) is given by

$$k\left(c_{Al}\right) = 37.71 + 363(c_{Al}^{1.45}) \cdot \exp[-1.5c_{Al}] \tag{4.14}$$

The thermal diffusivity κ (in cm^2/s) is

$$\kappa\left(c_{Al}\right) = 0.109 + 1.844(c_{Al}^{1.5}) \cdot \exp[-2.5c_{Al}] \tag{4.15}$$

The crack growth resistance as a function of crack length in the Al_2O_3/Al FGMs was determined earlier in Neubrand et al. (2004).

For the calculation of the residual stresses, it was assumed that the composite was stress free at 620°C (at this temperature the aluminium in the composite is still very soft and cannot exert high stresses on the ceramic backbone of the composite irrespective of volume content) and residual stresses during cooling to room temperature were calculated from the thermal expansion coefficients and elastic modulus data. It has been shown for specimens of a different geometry that the stresses calculated with these assumptions are in reasonable agreement with experimental data Neubrand (2002).

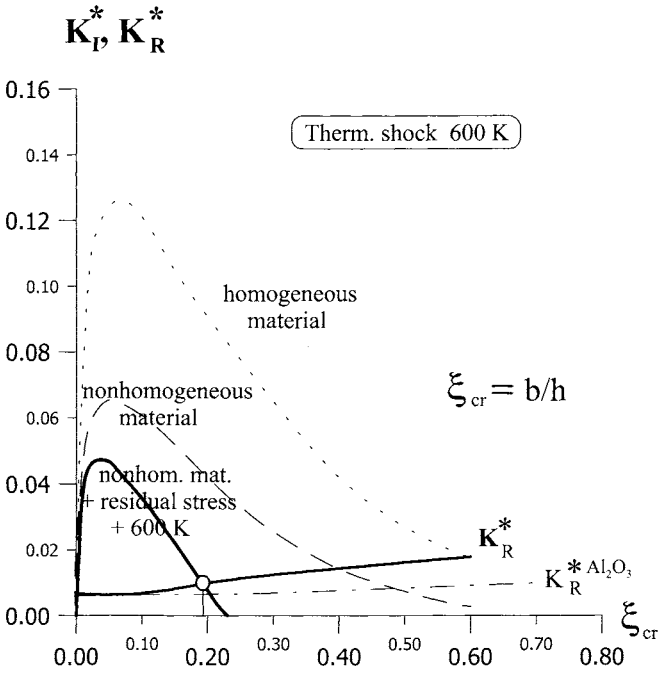

Figure 29. Maximum of the non-dimensional thermal stress intensity factors K_I^* and corresponding crack resistance curve K_R^* for linear change of Al content in FGM (n = 1);

For the calculations of residual stresses during thermal shock it was assumed that the temperature T_0 was 620°C and T_a was 20°C, i.e. the thermal shock temperature difference ΔT was 600°C. The strip had a width of h = 10 mm and a composition gradient along the x-direction which could be described by the function

$$c_{Al}(n,\xi) = c_{Al}^0 + c_{Al}^n \cdot \xi^n \tag{4.16}$$

Here, c_{Al}^0, c_{Al}^n and n are material parameters describing the composition gradient in the material. By introducing (4.16) to (4.12)-(4.15) and varying the material parameters, the thermal shock response of different FGMs can be investigated. In our study, c_{Al}^0 equalled 0.03 and c_{Al}^n = 0.3 throughout – at such volume fractions the material behaves macroscopically brittle, and thus plasticity could be neglected. For n=1 we have a linear composition gradient of the Al in Al_2O_3. For n < 1, the metal content increases quickly below the surface, and we have the case of a "metal rich material", whereas for n > 1 the metal content increases only slowly, and we have a "ceramic rich material".

The thermal stress intensity factor K_I^* depends on time, crack length and temperature. For a given crack length the stress intensity factor will reach a maximum at a certain time t which will increase with crack length. This non-dimensional maximum of the stress intensity factor K_I^* is plotted in Figure 29 as a function of crack length ξ_{cr} together with the crack growth resistance, K_R^* for Al_2O_3/Al and $K_R^{*Al_2O_3}$ for pure Al_2O_3. The point where the curve for the stress intensity factor intersects the R-curve represents the equilibrium crack length.

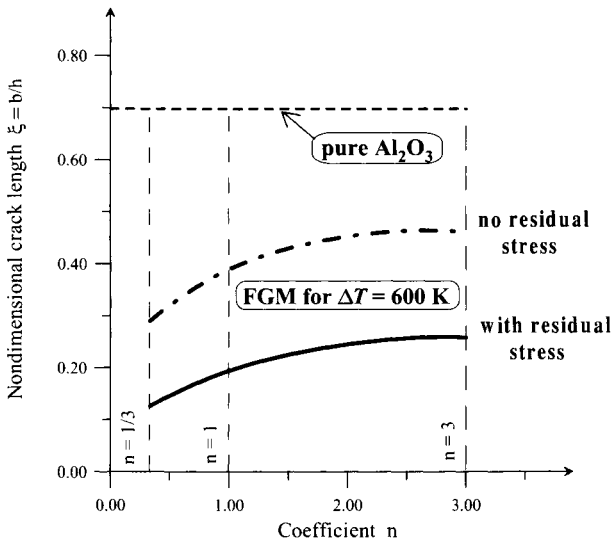

Figure 29. Equilibrium crack length for different kinds of FGM characterised by coefficient n

Figure 29 presents the equilibrium crack length for different values of n=1, 1/3 and 3. The crack lengths are much shorter in the graded Al_2O_3/Al composite than in a homogenous composite with a volume content of Al which corresponds to the surface composition of the FGM, $\xi = 0$.

Residual stresses in the graded composite are typically compressive near the surface and lead to smaller stress intensity factors and equilibrium crack length (for longer cracks the stress intensity factors even become negative indicating very efficient crack arrest). The effect of residual stresses is strongest for n = 1/3 where the equilibrium crack length is reduced by about 60% compared to a hypothetic stress free material. The composite with n = 1/3 shows also the shortest equilibrium crack length. The short crack length is not only caused by the residual stresses, but also by the crack growth resistance of the material, which increases quickly due to its metal-rich composition profile. Close examination of Figures 28 and 29 reveals that the graded material with n = 1/3 would show the lowest stress intensity factors under thermal shock even if residual stresses were absent. The current contribution thus corroborates earlier calculations by Noda (1999), which also predict that thermal shock stress intensity factors can be reduced by gradients. The findings of this work show, however, that significantly shorter equilibrium crack lengths are expected if the rising crack growth (R-curve) of an FGM is

combined with a controlled residual stress profile. Residual stress and the rising crack grow resistance should thus be included in any analysis of the thermal shock resistance of functionally graded materials.

5 Concluding remarks

The lectures deal with the description of stress concentration, defects nucleation and their growth leading to creation of macrodefect, which course the final failure of the material. Local stress concentration plays very important role in the damage initiation process. This process begins at *nano-* or *micro-scale* and is strictly related to the particular kind of the ceramic composite. The damage growth process can be related to *meso-* or *mili-scale*. Final failure corresponds to *macro-scale*. The problem of multiscale modelling of composites was illustrated by three examples presenting different approaches to the general topic of the course.

Acknowledgement

Tomasz Sadowski is currently supported by a Marie Curie Fellowship of the European Community programme "Improving Human Research Potential and Socio-economic Knowledge Base" under contract number HPMF-CT-2002-01859.

References

Altenbach, H., Becker, W. eds (2003) *Modern Trends in Composite Laminates Mechanics*, CISM Courses and and Lectures no. 448, Wien - New York: Springer Verlag.

Bahr, H.A., Balke, H., Fett, T., Hofinger, I., Kirchhoff, G., Munz, D., Neubrand, A., Semenov, A.S., Weiss, H.J., (2004) Cracks in graded materials, *Mat. Science and Engineering A* (accepted for publication)

Becker, H., Tschudi, T., Neubrand, A., Spatially (2001) Resolved Thermal Diffusivity Measurements for Functionally Graded Materials. In: Functionally Graded Materials 2000, *Ceramic Transactions* 114, American Ceramic Society, Westerville, Ohio, 1571-578.

Boccaccini, A.R., (1998) Influence of Stress Concentrations on the Mechanical Property-Porosity Correlation in Porous Materials. *J. Mat. Sci. Let.* 17:1273-75.

Bogy, D.B. (1970) On the problem of edge-bonded elastic quarter planes loaded at the boundary, *Int. Journal of Solids and Structures* 6, 1287-1313.

Davidge, R.W., (1979) *Mechanical behaviour of ceramics*, Cambridge Univ. Press.

Dröschel, M., Oberacker, R., Hoffman, M.J., Schaller, W., Yang, Y.Y., Munz, D. (1999) Silicon Carbide Evaporator Tubes with Porosity Gradient Designed by Finite Element Calculations In Functionally Graded Materials, *Proceedings of the 5th International Symposium on FGM*, W.R. Kaysser ed., Trans Tech Publications, Schweiz, 820-825.

Erdogan, F., Wu, B.H., (1996) Crack problems in FGM layers under thermal stresses. *J. Thermal Stress* :237-265.

Espinosa, H.D., Zavattieri, P.B. (2003) A grain level model for the study of failure initiation and evolution in polycrystalline brittle materials, Part I: Theory and numerical implementation. *Mech. Materials* 35:333-364.

Espinosa, H.D., Zavattieri, P.D. (2003) A grain level model for study of failure initiation and evolution in polycrystalline brittle materials. Part II: Numerical examples, *Mech. Materials* 35:365-394.

Fett, T. (2001) Mixed-mode stress intensity factors for partially opened cracks. *Int. J. Fracture* 111:L67-L72

Fett, T., Munz, D. (1997) *Stress intensity factors and weight functions*, Computational Mechanics Publications, Southampton, UK.

Fett, T., and Munz, D. (1999) *Mechanical Properties, Failure Behaviour, Materials Selection*, Ceramics, Springer, Berlin, Heidelberg, New York.

Flinn, B.D., Bordia, R.K., Zimmermann, A., and Roedel, J. (2000) Evolution of Defect Size and Strenght of Porous Alumina during Sintering, *J. Am. Ceram. Soc.* 20:2561-68.

Hu, M.S., Thouless, M.D., Evans, A.G. (1988) The decohesion of thin films from brittle substrates. *Acta Metall.* 36:1301-1307.

Hutchinson, J.W., Suo, Z., (1991) Mixed mode cracking in Layered Materials. *Adv. Appl. Mech.* 29:63-191.

Ishizaki, K., Komarneni, S., and Nanko, M. (1998) *Porous Materials: Process Technology And Applications*, Materials Technology Series, Kluwer Academic Publishers.

Itoh, Y., Kashiwaya, H. (1992) Residual stress characteristics of FGMs. *J. Ceram. Soc. Jap.* 100: 476-481.

Jayaseelan, D.D., Kondo, N., Brito, M.E., and Ohji, T. (2002) High-Strength Porous Alumina Ceramics by Pulse Electric Current Sintering Technique *J. Am. Ceram. Soc.* 85: 267-69.

Jeulin, D., and Ostoja-Starzewski, M., eds. (2001) *Mechanics of Random and Multiscale Microstructures*, CISM Courses and and Lectures no. 430, Wien - New York: Springer Verlag.

Jin, Z.H., Batra, R. (1996) Stress intensity relaxation at the tip of an edge crack in a functionally graded material subjected to a thermal shock. *J. Thermal Stress* 19:317-339.

Kachanov, M. (1993) Elastic Solids with Many Cracks and Related Problems, *Advances in Appl. Mech.* 30:259-445.

Kachanov, M. (1993) On The Effective Moduli of Solids With Cavities and Cracks. *Int. J. Fracture.* 59: R17-R21.

Kachanov, M., Sevostianov, I., Shafiro, B., (2001) Explicit cross-property correlations for porous materials with anisotropic microstructures, *J. Mech. Phys. Solids* 49:1-25

Krajcinovic, D. (1989) Damage Mechanics, *Mech. Materials* 8:117-197.

Lam, D.C.C., Lange, F.F., and Evans, A.G. (1994) *Mechanical Properties of Partially Dense Alumina Produced from Powder Compacts*. J. Am. Ceram. Soc., 77 :2113-17.

Nanjangud, S.C., Brezny, R., and Green, D.J., (1995) *Strenght and Young's Modulus Behaviour of a Partially Sintered Porous Alumina*. J. Am. Ceram. Soc., 78: 266-68.

Nemat-Nasser, S., and Horii, M., (1993) *Micromechanics: Overall Properties of Heterogeneous Materials*, Elsevier Sci. Publ.

Nemat-Nasser, S., and Obata, M. (1988) A Microcrack Model of Dilatancy in Brittle Materials. *J. Appl. Mech.* 55: 24-35.

Neubrand, A., Chung, T.J., Rödel, J., Steffler, E.D., Fett, T. (2002) Residual Stresses in Functionally Graded Plates. *J. Mater. Res.* 17: 2912-2920.

Neubrand, A., Chung, T.-J., Lucato, S., Fett, T., Rödel, J. (2004) R-curve behaviour of functionally graded composites. *J. Am. Cer. Soc.* (in review).

Noda, N. (1999) Thermal stresses in functionally graded materials. *J. Thermal Stress* 22:477-512.

Ostrowski, T., and Rödel, J. (1999) Evolution of Mechanical Properties of Porous Alumina during Free Sintering and Hot Pressing. *J. Am. Ceram. Soc.* 82 :3080 –86.

Owen, D.R.J., Hinton E. (1980) *Finite Elements in Plasticity, Theory and Practice*, Pineridge Press Ltd. Swansea, UK.

Pampuch, R., (1988) *Ceramic Materials. An Outline of Inorganic-Nonmetallic Materials Science*, Polish State Scientific Press, Warsaw, (in Polish).

Perzyna, P. (1971) Thermodynamic Theory of Viscoplaticity, in Advances in Applied Mechanics, Academic Press, New York, 11.

Ponte Castañeda, P., and Suquet, P., (1998) Nonlinear composites. *Adv. Appl. Mech.* 34:171-302.

Pordoen, T., Dumont, D., Deschamps, A., Brechet. Y. (2003) Grain boundary versus transgranular ductile failure. *J. Mech. Phys. Solids* 51: 637-665.

Raiser, G.F., Wise, J.L., Clifton, R.J., Grady, D.E., Cox D.E. (1994) Plate impact response of ceramics and glasses, *J. Appl. Phys* 75:3862- .

Ravichandran, K.S. (1995) Thermal residual stresses in a FGM system. *Mat. Sci. and Eng* A201: 269-276.

Rice, R.W. (1998) *Porosity of Ceramics.* Marcel Dekker, New York,

Sadowski, T. (1994) Modelling of semi-brittle MgO Ceramics Behaviour under Compression *Mech. Materials*, 18:1-16.

Sadowski, T., Boniecki, M., Librant, Z., and Ruiz, C. (1997) Fracture process of monolithic polycrystalline ceramics (Al_2O_3 and MgO) under quasi-static and dynamic loading. *Proceedings of Brittle Matrix Composites, 5.* Edited by A.Brandt, V.C.Li and I.H.Marshall, BIGRAF and Woodhead Publ., Warsaw, 567-576

Sadowski, T. (1999) Description of Damage Development and Limit States of Ceramic Materials, Technical Univ. of Lublin Press, (in Polish).

Sadowski, T., Samborski, S. (2003) Modelling of porous ceramics response to compressive loading, *J. Am. Cer. Soc.* 86:2218-2221.

Sadowski, T., Samborski, S. (2003) Predicition of mechanical behaviour of porous ceramics using mesomechanical modeling. *Computational Materials Science* 28:512-517.

Sadowski, T., Neubrand, A. (2003) Thermal shock crack propagation in functionally graded strip. *Proceedings of Brittle Matrix Composites, 7.* Edited by A.Brandt, V.C.Li and I.H.Marshall, BIGRAF and Woodhead Publ., Warsaw, 81-90.

Sadowski, T., Hardy S., Postek, E. (2004) Prediction of the mechanical response of polycrystalline ceramics containing metallic inter-granular layers under uniaxial tension, *Computational Materials Science* (subjected)

Sundaram, S., Clifton, R.J. (1998) The influence of a glassy phase on the high strain rate response of ceramics. *Mech. Materials* 29:233-251.

Suquet, P., ed. (1997) *Continuum Micromechanics*, CISM Courses and and Lectures no. , Wien - New York: Springer Verlag.

Tvergard, V. (1997) Studies of void growth in a thin ductile layer between ceramics. *Comput. Mech.* 20:186-191.

Vasudevan, A., Doherty, R. (1987) Grain boundary ductile fracture in precipitation hardened aluminium alloys. *Acta Metall.* 35:1193-1219.

Yang, Y.Y., Munz, D. (1995) Reduction of the stresses in a joint of dissimilar materials using graded materials as interlayer, *Fracture Mechanics* 26, ASTM STP 1256, W.G. Reuter, J.H. Underwood, J.C. Newman, Jr. (Hrsg.), American Society for Testing and Materials, Philadelphia, 1-15